A Comparative Study on Combustion Behaviours of Polyurethane Foams with Numerical Simulations using Pyrolysis Models

by

Dennis Pau

Supervised by

Charles Fleischmann and Michael Spearpoint

Fire Engineering Research Thesis

April 2013

A research thesis presented as partial fulfilment of the requirements for the degree of Doctor of Philosophy in Fire Engineering

Department of Civil and Natural Resources Engineering
University of Canterbury
Private Bag 4800
Christchurch
New Zealand

Abstract

This research investigates the decomposition and burning behaviours of polyurethane foams experimentally and compares the experimental results obtained with the numerical results from the pyrolysis model of Fire Dynamics Simulator, Version 5 (FDS 5[a]). Based on the comparison of model and experimental heat release rates, the accuracy of the pyrolysis model is quantified. In total, this research tested seven polyurethane foams consisting of three non-fire retardant (NFR) and four fire retardant (FR) foams. According to the simultaneous differential scanning calorimetry and thermogravimetric analysis (SDT) experiments, the decomposition behaviour of polyurethane foams under nitrogen environment is represented by two pyrolysis reactions. The first reaction consists of foam decomposition into melts and gases while the second reaction consists of the decomposition of the remaining melts into gases.

The kinetic properties which govern the rate of decomposition are the activation energy (E), pre-exponential factor (A), reaction order (n) and heat of reaction (Δh_r). Using graphical techniques, E, A and n of the first and second reactions are determined from the thermogravimetric analysis (TGA) results. Through analysing the differential scanning calorimetry (DSC) results, Δh_r is determined from the changes in heat flow and sample mass. The thermophysical properties govern the heat transfer through material and these are the thermal conductivity (λ) and specific heat (c_p) which are measured experimentally at ambient temperature through the Hot Disk method.

Through the Sample Feeding Vertical Cone, the decomposition and melting behaviours of polyurethane foams in a vertical orientation are investigated and the foams tested can be categorised into those which produce melts only after ignition and those which produce melts and char after ignition. The 1-dimensional burning behaviour of foams is obtained from the cone calorimeter experiments. The NFR foams show a change from plateau burning behaviour at low heat flux to two stage

[a] Version 5.5.3, SVN number 7031.

burning behaviour at high heat flux while the FR foams consistently show two stage burning behaviour. The combustion property governs the amount of heat released when fuel combusts and this is the effective heat of combustion ($\Delta h_{c,eff}$) which is determined from the heat released and mass consumed in the cone experiment.

The 1-dimensional burning behaviour is simulated using the pyrolysis model of FDS 5 and two different modelling approaches are considered. The direct method uses the material properties determined experimentally as FDS 5 inputs while the refined method uses the genetic algorithm of Gpyro to refine the kinetic properties which are later used as FDS 5 inputs. The heat release rate of the model and experiment are compared through linear regression analysis which quantifies the accuracy of both methods. The accuracy is defined as the percentage of data points within the boundary of acceptance which is bounded by 25 % of the greatest experimental heat release rate. This assessment method places greater emphasis on the accuracy of developed burning phases and lesser emphasis on the accuracy of initial growth and final decay. The accuracy of the direct method is found to be 56 % while the refined method with estimated kinetic properties achieves a higher accuracy of 75 %.

The 2-dimensional burning behaviours are investigated in the foam slab experiments for two different slab thicknesses, 120 and 100 mm. The opposed-flow spread of 120 mm slab is more intense and rapid while for the 100 mm slab, the flame spread is less intense and slow. FDS 5 is used to simulate the experimental results but when the material properties either developed experimentally or refined by Gpyro are used as inputs, the model fails to produce flame spread. This is because FDS 5 does not yet have the features which address the dynamics of foam melting and the reactive nature of the flame. In order to produce flame spread in the model, E of the reactions have been reduced to increase the decomposition rate.

UNIVERSITY OF CANTERBURY
Te Whare Wānanga o Waitaha
CHRISTCHURCH NEW ZEALAND

Deputy Vice-Chancellor's Office
Postgraduate Office

Co-Authorship Form

This form is to accompany the submission of any thesis that contains research reported in co-authored work that has been published, accepted for publication, or submitted for publication. A copy of this form should be included for each co-authored work that is included in the thesis. Completed forms should be included at the front (after the thesis abstract) of each copy of the thesis submitted for examination and library deposit.

Please indicate the chapter/section/pages of this thesis that are extracted from co-authored work and provide details of the publication or submission from the extract comes:

Chapter 3

D. S. W. Pau, C. M. Fleischmann, M. J. Spearpoint and K. Y. Li, "Determination of kinetic properties of polyurethane foam decomposition for pyrolysis modelling", *Journal of Fire Sciences*, 2013, DOI: 10.1177/0734904113475858.

Please detail the nature and extent (%) of contribution by the candidate:

Pau carried out the experimental investigations and analysis under supervision of the co-authors

Certification by Co-authors:

If there is more than one co-author then a single co-author can sign on behalf of all

The undersigned certifys that:

- The above statement correctly reflects the nature and extent of the PhD candidate's contribution to this co-authored work
- In cases where the candidate was the lead author of the co-authored work he or she wrote the text

Name: *Dennis Pau Su Wee* Signature: *Dennis* Date: *17/04/2013*

UNIVERSITY OF CANTERBURY
Te Whare Wānanga o Waitaha
CHRISTCHURCH NEW ZEALAND

Deputy Vice-Chancellor's Office
Postgraduate Office

Co-Authorship Form

This form is to accompany the submission of any thesis that contains research reported in co-authored work that has been published, accepted for publication, or submitted for publication. A copy of this form should be included for each co-authored work that is included in the thesis. Completed forms should be included at the front (after the thesis abstract) of each copy of the thesis submitted for examination and library deposit.

Please indicate the chapter/section/pages of this thesis that are extracted from co-authored work and provide details of the publication or submission from the extract comes:

Chapter 6

D. S. W. Pau, C. M. Fleischmann, M. J. Spearpoint and K. Y. Li, "Thermophysical properties of polyurethane foams and their Melts", *Fire and Materials*, 2013.

Please detail the nature and extent (%) of contribution by the candidate:

Pau carried out the experimental investigations and analysis under supervision of the co-authors

Certification by Co-authors:

If there is more than one co-author then a single co-author can sign on behalf of all
The undersigned certifys that:

- The above statement correctly reflects the nature and extent of the PhD candidate's contribution to this co-authored work
- In cases where the candidate was the lead author of the co-authored work he or she wrote the text

Name: *Dennis Pau Su Wee* Signature: *Dennis* Date: *17/04/2013*

Acknowledgements

I would like to thank the following who have contributed to this research. First and foremost is my senior supervisor, Professor Charles Fleischmann for his unwavering academic and emotional supports throughout this entire research. His technical inputs to this work have smoothed many obstacles faced during the experimental and numerical investigations. Associate Professor Michael Spearpoint for the proof reading he has done on a number of journal articles and the frequent constructive comments provided during various research meetings. Associate Professor Kai Yuan Li for the coorperation in experimental and numerical investigations during the last 2 years of my research. The various detailed discussions between us have shaped many paths of this research. Dr. Anthony Abu for his moral supports during the tough times in research. Professor Andrew Buchanan for his continuous support and involvements of the fire engineering group.

Grant Dunlop for working endlessly on various tasks and problems that surfaced throughout the experimental investigations. Bob Wilsea-Smith for lending a helping hand around the laboratory whenever possible. John Kooloos for working on the electronic device of experimental equipment. Joost Stenfert-Kroese for allocating numerous computers in his laboratory for my simulations and also troubleshooting any computer related issues that surface. Mike Van der Colk from Chemistry for helping me during my rather extensive time spent working in his laboratory.

The FDS 5 discussion community for answering my questions regarding the use of FDS 5. Dr. Chris Lautenberger for developing Gpyro and also taking time in answering my questions regarding the various features in Gpyro. Dr. Simo Hostikka and Dr. Guillermo Rein for answering the call as thesis examiners and conducted a very indepth review of the thesis. The feedbacks from the thesis examination have provided me with new insights to the ongoing issues and potential directions for the research.

Previous and present colleagues at the university, James O'Neill, Andrew Baird, Tobias Smith, Sam McHattie, Varun Joshi, Daniel Moroder, Francesco Sarti, Chris Watson, Maxim Millen, Harry Johnston, Jan Dormanns, Tim Huber, Reuben Costello, Shaz Sazegara, Tong Hong Haey, Ted Gu, Manoochehr Ardalany, Asif Iqbal, Daniel Wong, Marco Yip, Jenny Han, Kevin Tsai and Cheong Mun Kit. Of course, many more that I have not named whom I shared a laughter or two with throughout my stay at the university. Lastly, my beloved family who bears with me through the tough times.

Table of Contents

List of Figures

List of Tables

Nomenclature

A	pre-exponential factor, s^{-1}
A_{duct}	cross sectional area of exhaust duct, m^2
A_s	exposed sample surface area, m^2
α	fraction decomposed, $(W_0\text{-}W)/(W_0\text{-}W_f)$
α_1	fraction decomposed during first reaction, %
α_2	fraction decomposed during second reaction, %
α_t	fraction decomposed during transition, %
β	heating rate, K/s or °C/min
C	orifice constant
C_{old}	previous orifice constant
c_p	sample specific heat, J/kgK
$c_p(T)$	specific heat of material as a function of temperature, J/kgK
$c_{p,char}$	specific heat of char, J/kgK
$c_{p,wood}$	specific heat of wood, J/kgK
$D(\tau)$	dimensionless time function representing sensor design
D_{sam}	sample diameter, m
D_{sen}	sensor diameter, m
d	thickness, mm
$d_{probing}$	probing depth, m
d_{sam}	sample thickness, m
$d_{sen\text{-}bound}$	shortest distance from sensor to boundary, m
$\frac{dq}{dt}$	original heat flow measured by DSC, mW
$\left(\frac{dq}{dt}\right)_{bas}$	baseline heat flow, mW
$\left(\frac{dq}{dt}\right)_{char}$	calculated heat flow for heating char, mW
$\left(\frac{dq}{dt}\right)_{off}$	heat flow offset, mW

$\left(\frac{dq}{dt}\right)_{peak}$	heat flow magnitude measured at melting peak, mW
$\left(\frac{dq}{dt}\right)_{R}$	reaction heat flow, mW
$\left(\frac{dq}{dt}\right)_{rad}$	radiation heat flow, mW
$\frac{dT}{dt}$	heating rate, °C/min
dW/dt	rate of mass loss with time, %/s
$d\alpha/dT$	rate of fraction decomposed in temperature basis, 1/K
$d\alpha/dt$	rate of fraction decomposed with time, s^{-1}
$\Delta h_c/r_0$	heat release per unit mass of oxygen consumed, 13.1×10^3 kJ/kg (12.54×10^3 kJ/kg if methane is fuel)
$\Delta h_{c,eff}$	effective heat of combustion, MJ/kg
Δh_{dec}	heat of decomposition, J/g
$\Delta h_{f,known}$	known heat of fusion of zinc, 108.7 J/g
$\Delta h_{f,mea}$	measured heat of fusion of zinc, J/g
Δh_g	heat of gasification, J/g
Δh_{melt}	heat of melting, J/g
Δh_p	heat of pyrolysis for the primary decomposition of wood, J/g
Δh_p*	recalculated Δh_p, J/g
Δh_r	heat of reaction, J/g
Δh_s	heat of pyrolysis for the secondary decomposition of wood, J/g
Δh_s*	recalculated Δh_s, J/g
Δh_{tot}	total heat of pyrolysis of wood, J/g
Δh_{tot}*	recalculated Δh_{tot}, J/g
Δp	orifice meter pressure differential, Pa
$\Delta T_{ave}(\tau)$	temperature increase of sample surface in contact with sensor, °C
ΔT_i	constant temperature difference over sensor's insulating layer, °C
ΔT_{lag}	thermal lag, °C
$\Delta T_{sam\text{-}ref}$	temperature difference between sample and reference, °C
Δt	time increment, s
δ_{min}	smallest solid phase cell size, m

E	activation energy, J/mol
ε	emissivity
F	mass fraction
F_g	vapour mass fraction, %
F_m	melt mass fraction, %
F_s	variable pyrolysable fraction
$f(Re)$	instrument dependent correction, function of Reynolds number
$f(T,t)$	kinetic component of DSC measurements, mW
$f(W/W_0)$	kinetic model in terms of fraction remaining
$f(\alpha)$	kinetic model in terms of fraction decomposed
θ	function representing either λ, c_p or ρ
k	rate constant, s^{-1}
k_c	velocity shape factor
k_f	factory set calibration value
k_u	user set calibration value
$\kappa = \lambda / \rho c_p$	sample thermal diffusivity, m^2/s
λ	sample thermal conductivity, W/mK
$M_{loss,tot}$	total sample mass consumed, g
$m(T)$	instantaneous sample mass as a function of temperature, mg
m_0	original sample mass or mass of wood, mg
m_{10}	sample mass at 10 % mass loss, g
m_{90}	sample mass at 90 % mass loss, g
m_{end}	sample mass at T_{end}, mg
m_f	final sample mass or mass of char, mg
m_i	initial sample mass, mg
m_{sam}	mass of sample, mg
m_{shift}	mass of sample where primary decomposition ends and secondary decomposition starts, mg
m_{start}	sample mass at T_{start}, mg
$\dot{m}_{ave}$	average mass loss rate, g/s
$\dot{m}''_{ave}$	average mass loss rate per unit area, g/m^2s
$\dot{m}_e$	exhaust mass flow rate, kg/s

$\dot{m}''_{gas}$	vaporisation rate per unit area, g/m^{2}s
$\dot{m}''_{melt}$	melting rate per unit area, g/m^{2}s
$\dot{m}_{sam}$	sample mass loss rate, kg/s
$\dot{m}''_{sam}$	sample mass loss rate per unit area, g/m^{2}s
n	reaction order
P_0	output power delivered to sensor, mW
P_a	atmospheric pressure, 101325 Pa
PC	percentage of temperature range occupied by physical state of foam, mixture or melt, %
q_{tot}	total heat released, MJ
q''_{tot}	total heat released, MJ/m^2
$\dot{q}$	heat release rate, kW
$\dot{q}_{ave}$	average heat release rate, kW
$\dot{q}''_{ave}$	average heat release rate per unit area, kW/m^2
$\dot{q}''_{desired}$	desired heat flux at central position, kW/m^2
$\dot{q}''_{fl}$	flame heat flux, kW/m^2
$\dot{q}_i$	heat release rate at i^{th} scan after ignition, kW
$\dot{q}_{ign}$	heat release rate at ignition, kW
$\dot{q}_n$	heat release rate at n^{th} scan after ignition where the magnitude becomes insignificant, kW
$\dot{q}_{pk}$	peak heat release rate, kW
$\dot{q}''_{pk}$	peak heat release rate per unit area, kW/m^2
R	universal gas constant, 8.314 J/Kmol
$R(t)$	instantaneous sensor resistance, ohm
R_0	initial sensor resistance, ohm
R_t	thermal resistance, °C/mW
RH	relative humidity, %
r	rate of reaction in terms of fraction remaining, s^{-1}
r_{sen}	sensor radius, m
ρ	sample density, kg/m^3

$\overline{\rho}$	weighted bulk density, kg/m^3
$\overline{\rho}\big\|_{t=0}$	initial weighted bulk density, kg/m^3
ρ_{s0}	initial density of layer containing decomposing material, kg/m^3
$\rho_{s,i}$	density of decomposing material component, kg/m^3
S	cell size factor
T	reaction temperature or instantaneous temperature, K or °C
T_a	ambient temperature, °C or K
T_{cone}	cone heater temperature, °C
T_e	exhaust temperature at orifice meter, K
T_{end}	end temperature of the range selected for calculating heat of reaction, °C
T_f	temperature at the end of secondary decomposition, °C
T_i	temperature at the start of primary decomposition, °C
T_p	temperature where reaction initiates, °C
T_{pk}	peak temperature, °C
T_{shift}	temperature where the primary decomposition ends and secondary decomposition starts, °C
T_{start}	start temperature of the range selected for calculating heat of reaction, °C
TCR	temperature coefficient of resistivity, 1/K
t	measuring time, s
t_{10}	time at m_{10}, s
t_{90}	time at m_{90}, s
t_{cha}	characteristic time, s
t_d	time delay to melting, s
t_{ig}	ignition time, s
t_{tot}/t_{cha}	total to characteristic time ratio
$\tau = \frac{\sqrt{t\kappa}}{r_{sen}}$	square root of t_{tot}/t_{cha} presented in Equation (6-2)
v_{feed}	feeding rate of polyurethane foam, mm/s
W	instantaneous sample mass, %
W_0	initial sample mass, %

W_f	final sample mass, %
$X(T)$	dimensionless sample conversion
X_{CO}	measured mole fraction of carbon monoxide in exhaust flow
X_{CO_2}	measured mole fraction of carbon dioxide in exhaust flow
$X^0_{CO_2}$	measured mole fraction of carbon dioxide in combustion air
$X^0_{H_2O}$	actual mole fraction of water vapour in combustion air
X_{O_2}	measured mole fraction of oxygen in exhaust flow
$X^0_{O_2}$	measured mole fraction of oxygen in combustion air
$X^a_{O_2}$	ambient mole fraction of oxygen
X_s	ratio between instantaneous solid weight loss and initial solid weight
Y	mass fraction of condensed phase species undergoing reaction
Y_g	gaseous yield
Y_r	residue yield
ϕ	oxygen depletion factor
Φ	as defined in Equation (3-21)

Chapter 1. Introduction

1.1 Polyurethane Foam as Material Investigated in This Research

Approximately 75 % of the global application of polyurethane products is in the form of foam[1]. Flexible polyurethane foam has been widely used in upholstery (furniture and bedding), in automotive (interior finishes and seating), for thermal and acoustic insulations and for impact and vibration protections[2]. The wide application of foam is due to a number of its attractive qualities such as light weight, flexible, easily moulded and insulative ability for heat and sound. However, from a fire safety perspective, polyurethane foam is considered as a hazardous combustible due to a number of fire characteristics such as the ease of ignition, the high combustibility and the high toxicity of the gaseous products produced following combustion.

While the New Zealand Building Code Clauses, C1-C6 Protection from Fire[3] limits the combustibility of material used as the interior surface finishes of a building, there is currently no limitation regarding the combustibility of the upholstered furniture used in a building. According to the research by Wong[4], upholstered furniture was found to be involved in 35.4 % of New Zealand residential fire fatalities from 1996 to 2000. The common cause of death was smoke inhalation for the occupants outside the room of origin while the common cause of death for the occupants within the room of origin was identified to be the exposure to heat and smoke from the fire.

A number of fires involving polyurethane foam are highly publicised due to the rapid fire development and also the high casualties resulted. Table 1-1 listed a number of fire disasters where polyurethane foam had played a significant role alongside other factors such as the human behaviours and the inadequacies of the buildings' fire safety design. Due to the high fire risk posed by polyurethane foam and the well-known track record in fire disaster, this research selects polyurethane foam as the material for investigation.

Table 1-1: Fire disasters since year 2000 where polyurethane foam is known to have a significant role

Date	Fire Disaster	Location	Fatalities
February 20, 2003	The Station nightclub fire	West Warwick, Rhode Island	100
December 30, 2004	Republica Cromanon nightclub fire	Buenos Aires, Argentina	194
June 18, 2007	Charleston Sofa Super Store fire	Charleston, South Carolina	9
April 25, 2008	Rosamor Furniture factory fire	Casablanca, Morocco	55
November 15, 2010	2010 Shanghai fire	Shanghai, China	58
December 8, 2010	2010 Santiago prison fire	Santiago, Chile	81
January 27, 2013	Kiss nightclub fire	Santa Maria, Brazil	241

1.2 Combustion Characteristics of Upholstered Furniture

The burning behaviours of bench-scale polyurethane foam and medium-scale upholstered furniture have been widely reported and quantified in the literature[5,6,7]. From the research by Young[8], a summary of the combustion characteristic of upholstered furniture fires in the literature was provided. According to the findings, upholstered furniture can be ignited with ignition source as small as a cigarette and has the ability to smoulder for several hours before sustainable flaming takes place.

The burning behaviours of upholstered furniture differ from one design to another because of the different fuel load and its distribution around the furniture. Furniture with armrests have greater growth rate and achieve higher heat release rate due to the increase radiation feedback onto the seating of the chair. Furniture where the cushions are supported by webbings allows the fire to burn through and form pool fire inside the chair. Due to the enhanced radiation feedback, this results in greater growth rate and heat release rate. Certain furniture that do not have a frame are the most hazardous because they are often assembled from primarily soft combustible components.

The types of cover fabric used in upholstered furniture also affect the burning behaviour. Thermosetting fabric has the ability to char which slows the fire growth and lowers the heat release rate while thermoplastic fabric melts very quickly and exposes the foam to flame. Certain fabric covers use nylon zippers which can fail earlier than the cover itself, exposing the foam to fire. In general, the correlation between the heat release rate of furniture fires and the size of the furniture is found to

be greater than linear. This trend highlights the hazardous nature of polyurethane foam which is the primary soft combustible in upholstered furniture.

Hill's research[9] provided a more detailed description regarding the burning behaviours of upholstered furniture. Figure 1-1 shows the progress of an upholstered furniture fire involving an armchair made of domestic furniture foam with wool as the fabric cover. The burning process can be classified into four phases, namely Spread (1), Burn Through (2), Pool Fire (3) and Burn Out (4). In the experiment, the armchair was placed on a platform and the chair mass was measured by the chair load cell. A tray was located underneath the chair to collect the melts dripping from the armchair and this melt mass was measured by the tray load cell.

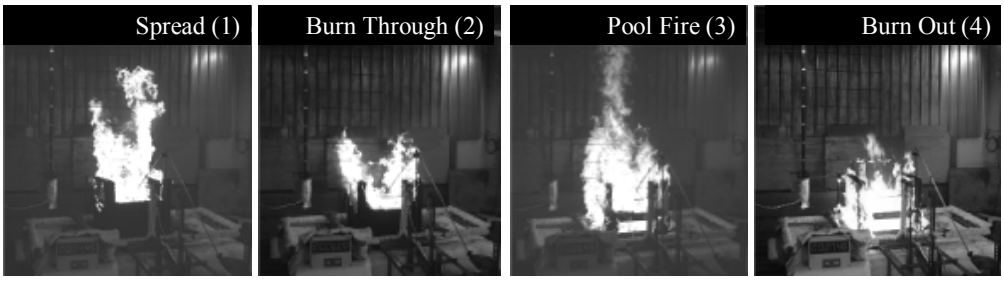

Figure 1-1: Spread, Burn Through, Pool Fire and Burn Out phases of armchair made of domestic furniture foam with wool as fabric cover[9]

Figure 1-2 shows the mass and heat release rate histories of the fire and on the plot, 'HRR' denotes the heat release rate of the armchair, 'Chair LC' denotes the armchair mass on the chair load cell and 'Tray LC' denotes the melt mass collected onto the tray load cell located underneath the armchair. The number 1 to 4 in Figure 1-2 denote the Spread, Burn Through, Pool Fire and Burn Out phases of the fire respectively.

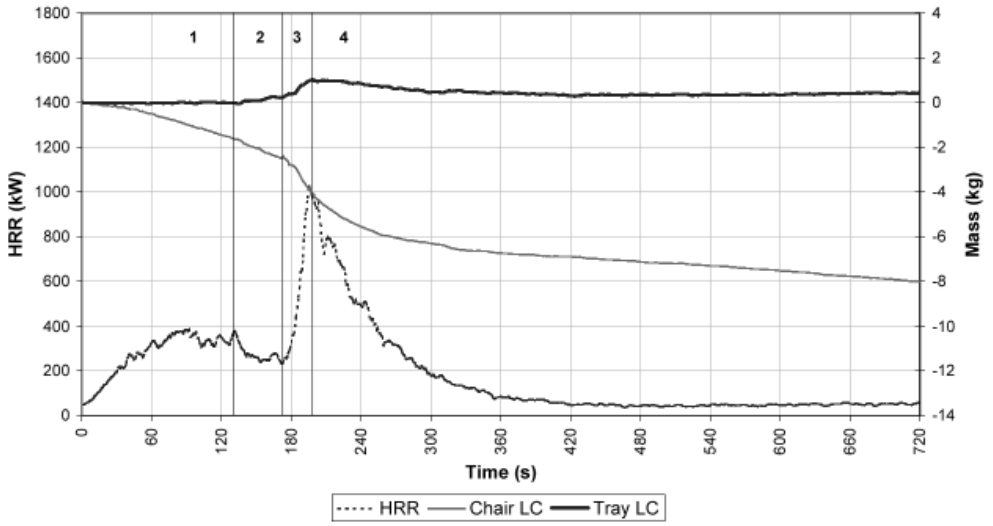

Figure 1-2: Mass and heat release rate histories of an upholstered armchair made of domestic furniture foam with wool as fabric showing Spread (1), Burn Through (2), Pool Fire (3) and Burn Out (4)[9]

A LPG gas burner was used as the ignition source and it was placed over the seating of the armchair. In the Spread phase, the seating was first ignited and then the fire propagated onto the seat back cushion. A seat pool fire was formed from the melts flowing down the back cushion and also the melts produced during the decomposition of the seating. As the seating fire developed, the armrest of the armchair also became involved. In this phase, the heat release rate of the fire was noted to increase steadily and the fire was becoming self-sustaining. The fire was limited to the seat area of the armchair as the Tray LC showed no melt mass collected. In the Burn Through phase, the Tray LC started to show gradual increase in the mass collected from the initial failing of the seat cushion due to the burn through of the seat fabric and webbing. As wool is a thermosetting material, the fabric was more effective in containing the fire in the seating. This resulted in a more apparent Burn Through phase where the heat release rate was noted to reduce slightly.

As the seating and webbing of the armchair failed, the melts pooled in the seat area poured onto the Tray LC increasing the mass collected and creating an initial pool fire below the chair. When coupled with the failure of the fabric in the lower part of the armchair, the air supply to the initial pool fire further increased the heat release rate and established the Pool Fire phase. This phase is characterised by the rapid increase

in both the heat release rate and the mass collected on the Tray LC while the armchair mass on Chair LC reduced rapidly. At this stage, the armchair was fully involved in the fire. In the Burn Out phase, the heat release rate and Tray LC mass started to reduce as the majority of the soft combustibles were consumed and the pool fire subsided.

As identified by Young[8], Hill[9] also found that the burning behaviour of upholstered furniture is influenced by the foam-fabric combination. The combination of thermosetting fabric and fire retardant (FR) polyurethane foam in some cases was found to be effective in mitigating the burning process where the fire self-extinguished during the Burn Through phase. On the other hand, the combination of thermoplastic fabric and non-fire retardant (NFR) polyurethane foam showed rapid growth where the fire directly entered into the Pool Fire phase from the Spread phase without having the Burn Through phase as seen in Figure 1-3. The characteristic decline in the heat release rate observed during the Burn Through phase is absence from the figure.

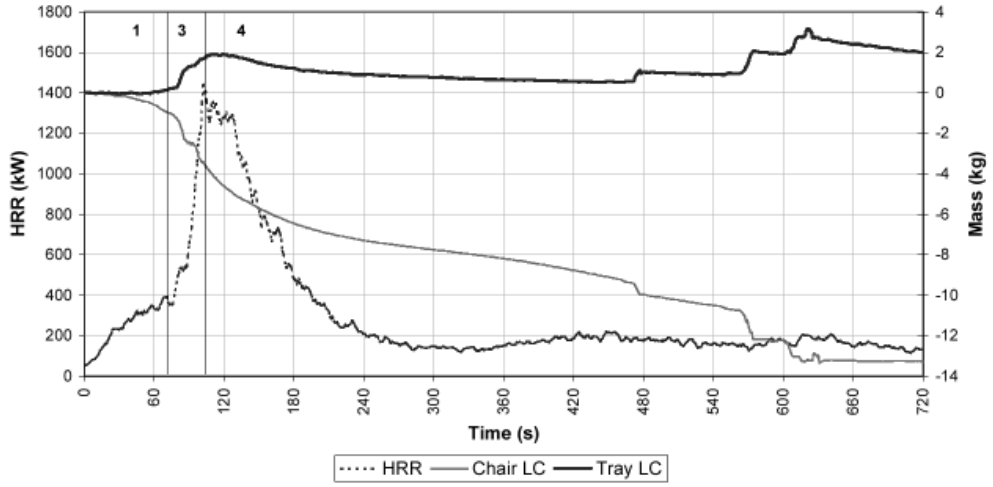

Figure 1-3: Mass and heat release rate histories of an upholstered armchair made of public auditorium foam with polypropylene as fabric showing Spread (1), Pool Fire (3) and Burn Out (4)[9]

1.3 Prediction of Heat Release Rate of Fires

The heat release rate of a fire is the single most important variable in quantifying the fire hazard[10] posed by a material even though there are a number of other factors which also contribute to the fire hazard such as the ignitability of the material and the toxicity of the gaseous combustion products. However, none are as definitive as the heat release rate. For instance, from the heat release rate of the armchair in Figure 1-3, the fire rapidly reaches a higher peak heat release rate and never enters the Burn Through phase before spilling the melts onto the tray below the armchair. Therefore, it is more hazardous than the armchair fire in Figure 1-2.

The implementation of oxygen depletion calorimetry[11] in fire experiments has allowed the heat release rate to be quantified accurately at bench-scale through the cone calorimeter[12] and at full-scale through the furniture calorimeter[13]. The quantification of the heat release rate of a fire is useful for fire engineering practice where it is adopted as the design fire for fire safety designs of building and also for use in fire disaster investigation to reconstruct the series of events that unfold. The fire hazards posed by polyurethane foam and its extensive application mean the material's heat release rate is often considered in the fire safety engineering design of buildings. In fact, combustion characteristics of polyurethane foam were a major consideration in the formulation of the design fire during the development of the new Verification Method C/ VM2[14,15]. This document was released in 2012 in New Zealand, describing the framework for fire safety design.

The common practice in fire engineering involves using the experimental heat release rate as input to a fire model and then assesses the effects from the fire such as flame spread, smoke movement and tenability. This is a cost effective approach and many fire models have this feature where the user can specify a heat release rate curve for the fire. The heat release rate applied as model input is measured experimentally and despite having accurate experimental technique, conducting fire experiments are often costly, laborious and in some cases not practical. For instance, industrial-scale test samples where the fire size approaches 10 MW.

Furthermore, there are also variations in the fuel loads and the heat release rate found within the literature might not be applicable. Changes to the type, amount and orientation of the fuel load could have significant effects on the heat release rate of the fire. For example, the simple change in the foam-fabric combination can result in different burning behaviours of the armchairs seen in Figure 1-2 and 1-3. Under these circumstances where the heat release rate of a fire is not known, it has to be predicted by the fire model. The heat release rate predictive capability of a fire model depends on the complexity of the model. The different level of complexity for two commonly used fire models, B-RISK[16] and Fire Dynamics Simulator, Version 5[17,18] (FDS 5[a]) in simulating heat release rate is discussed.

B-RISK[16] which is a zone model with probabilistic analysis capability has a design fire generator which allows the user to specify the heat release rate curve for rectilinear objects within a compartment. B-RISK starts to simulate the heat release rate of a fire when multiple objects are specified where sequential ignitions of the objects are determined based on the Flux-Time Product (FTP) method. The heat release rate of multiple objects is computed as the sum of heat release rate from the individual objects as each one achieves ignition. There is no compartment enhancement included in B-RISK and individual objects will burn according to a prescribed heat release rate which may be deterministic or probabilistic in nature.

While B-RISK has the capability to simulate item to item fire spread and the heat release rate of fire involving multiple objects, the heat release rate of each individual object is still defined by the user. The experimental heat release rate involving the individual combustible is often used as model input. Applying the individual heat release rates followed by the summation to determine the total heat release rate means the model assumes no interaction between the burning objects. As such, the enhancement of burning due to radiative contribution from the upper layer is also absence in this simplified process of defining heat release rate.

In order to actually simulate the heat release rate of burning object without the specification of known heat release rate curve, a pyrolysis model is required. The

[a] Version 5.5.3, SVN number 7031.

pyrolysis model is normally inbuilt within the fire modelling software such as the widely used computational fluid dynamics (CFD) model, FDS 5[17,18]. FDS 5 models the fire-driven fluid flow by numerically solving a form of the Navier-Stokes equations appropriate for low-speed, thermally-driven flow. The pyrolysis model in FDS 5 can be applied to govern the decomposition of a solid when it is burning. The pyrolysis model is flexible in the sense that it allows the user to design various schemes to represent the decomposition of a solid fuel into gaseous fuel. The user can define multiple material components with different material properties and some of which can be temperature dependent. These material components can then be specified within multiple layers and also be implemented to undergo multiple solid phase reactions. While the pyrolysis model of FDS 5 can be used to simulate the material burning behaviours and to predict the heat release rate, its application is not without complications.

The inputs of the FDS 5 pyrolysis model consist mainly of thermophysical, kinetic and combustion properties. The thermophysical properties govern the heat transfer through the solid fuel. The kinetic properties govern the rate of fuel decomposition when the solid fuel converts into gaseous fuel. The effective heat of combustion governs the amount of heat released per unit mass of gaseous fuel combusted. These properties are specific for each material and some of them are often not immediately available within the literature because they cannot be determined from common fire experiments such as bench-scale cone calorimeter. Specialised experimental techniques where sample is tested at material level are required and from the experimental results obtained, the material properties can be developed.

These material properties are mostly quantified in a laboratory environment which does not represent the actual fire condition so their suitability as model inputs to simulate fire phenomena have always been questionable. Furthermore, the experimental results obtained at elevated temperature or close to the actual fire condition often suffer from reduced accuracy and lack of resolution as the capability of the experimental technique and the data collection process are stretched. The numerous experimental challenges mean that currently, there is a lack of material properties in the literature for use in pyrolysis model of FDS 5. As such, the pyrolysis

model in FDS 5 is not well validated where the model's accuracy and sensitivity are not known.

The validation of the FDS 5 pyrolysis model is also hindered by some numerical challenges. Ideally, the boundary conditions within the fire modelling software and the equations constituting the pyrolysis model should accurately represent the actual phenomena. But these are not always possible as a result of computational limitations, modelling assumptions and the lack of understanding regarding the physical phenomena. As a result, there are inherent differences between the simulation and the actual phenomena. Using polyurethane foam as an example, the model still lacks in physics which address the foam porosity, the foam melting behaviours and the melt flow dynamics. For heat transfer through a solid, the model solves a 1-dimensional equation but the actual phenomena can be more complex, involving 3-dimensional heat transfer process. In terms of radiation transport and the representation of flame, there are also differences between the model which uses semi-empirical equations and the actual phenomena.

Significant research has been on-going to refine the experimental techniques and the data reduction techniques such that useful material properties are developed for modelling. Numerically, there is also a continuous effort to improve the features of a pyrolysis model such that the model better represents the actual physical phenomena. Nevertheless, these improvement are slow therefore, an alternative modelling approach has been implemented by several studies[19,20,21] to improve the predictive capability of a pyrolysis model. The approach utilises a mathematical tool known as genetic algorithm which refines the material properties based on a number of experimental results supplied. When these optimised properties are used as inputs to the pyrolysis model, the model results become more comparable with the experimental results. In line with the development of genetic algorithm and pyrolysis model, a few research bodies have been collaborating to establish a set of standardised guidelines[a] for the fire practitioners to estimate the required material properties for fire modelling using the pyrolysis model. Within the guidelines, the experimental techniques for obtaining the different material properties were described and the

[a] SFPE Engineering Guide for Estimating Material Pyrolysis Properties for Fire Modeling.

property estimation process was explained through a number of case studies where the decomposition schemes with different levels of complexity are considered.

1.4 Objectives and Outline of This Research

Directly specifying the heat release rate as input for fire modelling often neglects the actual dynamics of the fire which means the subsequent analysis on the effect of fire becomes less meaningful. Therefore, this research attempt to explore the capability of pyrolysis model in predicting the heat release rate. While the FDS 5 pyrolysis model is able to simulate the burning behaviours of material without requiring the specification of heat release rate, this is at the cost of the specification of numerous material properties which needed to be determined experimentally. Due to the lack of validation, the accuracy of FDS 5 pyrolysis model has not been assessed thoroughly. Thus, the objective of this research is to experimentally investigate the decomposition and burning behaviours of polyurethane foam and numerically assess the accuracy of the pyrolysis model in FDS 5 in predicting these behaviours. This objective comprises of the following five sub-objectives.

1. The study of the decomposition behaviours for a collection of polyurethane foams and the determination of the kinetic properties applicable for FDS 5 pyrolysis model.

    - This investigation is necessary because the foam's decomposition behaviour and the kinetic properties in the literature[22,23,24] are limited. The suitability of those determined kinetic properties as inputs in the pyrolysis model of FDS 5 is also not known.

    - In this research, the experimental tasks are carried out using the simultaneous differential scanning calorimetry and thermogravimetric analysis (SDT) and these are addressed in more details over Chapter 3, 4 and 5.

2. The determination of the thermophysical properties for the collection of polyurethane foams.

    - This investigation is necessary because the information on the thermophysical properties of foam is scarce in the literature[25] and their influence on the heat release rate predictions remains uncertain.

    - In this research, the experimental tasks are carried out using the Hot Disk Thermal Constants Analyser and these are addressed in more details in Chapter 6.

3. The study of the decomposition and melting behaviours for the collection of polyurethane foams in a vertical orientation and the quantification of these behaviours at constant exposure heat flux.

    - This investigation is necessary because the literature[9] shows that the foam melting behaviours leads to pool fire which causes the peak heat release rate in the upholstered furniture fire. While research[26] has already been done to investigate the foam melting behaviour and the subsequent melt flow dynamics, different foams are noted to behave differently so this aspect requires further investigations.

    - In this research, the experimental tasks are carried out using the Sample Feeding Vertical Cone and these are addressed in more details in Chapter 7.

4. The study of the simple 1-dimensional burning behaviour under cone calorimeter for the collection of polyurethane foams and the FDS 5 modelling of the heat release rate.

    - The upholstered furniture fire discussed earlier involves 3-dimensional flame spread due to the complex configuration of the fuel and the dynamic foam melting behaviour. But as a start in model validation,

this investigation assesses the accuracy of the pyrolysis model based on a simplistic 1-dimensional burning scenario.

- It is a methodological decision to start evaluating the accuracy of the pyrolysis model at small-scale cone experiment, rather than at material-scale thermogravimetric analysis (TGA) experiment. Also, the focus of this research is the burning behaviours of polyurethane foam which are at small-scale cone experiment and medium-scale foam slab experiment. The application of pyrolysis model to simulate decomposition of polyurethane foam at material-scale TGA experiment has previously been investigated by Valencia[25].

- The effective heat of combustion is derived from the experimental results obtained from the cone experiments. With all the necessary material properties determined, the inputs used for FDS 5 modelling are either determined experimentally or refined by genetic algorithm of Gpyro[27], both at small-scale. These experimental and numerical tasks are addressed in more details in Chapter 8.

5. The study of the 2-dimensional flame spread behaviours of mattress-scale polyurethane foam slab under furniture calorimeter and the FDS 5 modelling of the heat release rate.

    - Following on from the investigation on 1-dimensional burning, this investigation expanded the complexity of foam burning behaviour to 2-dimensional which involves the opposed-flow spread of flame on a mattress-scale foam slab. These experimental and numerical tasks are addressed in more details in Chapter 9.

Heat release rate of a fire is recognised as the basis of fire safety engineering practices. Therefore, quantifying the accuracy of the fire model in predicting the actual heat release rate of combustible fuels and improving the model predictive capability are crucial. A better representation of heat release rate produces a more

accurate prediction of the subsequent fire effects which often define the level of fire safety. This research details the experimental and numerical methodology in obtaining material properties for use in pyrolysis model. The research outcomes can be used as benchmark and validation to establish standardised guidelines for this type of modelling approach.

Chapter 2. Physical and Chemical Attributes of Polyurethane Foams and Melts

In this study, three non-fire retardant (NFR) and four fire retardant (FR) polyurethane foams are tested. The melts of these foams are also investigated and the melt samples are collected through the experiments involving the Sample Feeding Vertical Cone described in Chapter 7. During the experiments, 900 mm long foam sample situated on top of a conveyor platform was exposed at one end to a vertically oriented cone heater which imposed a constant radiative heat flux on the 75 by 75 mm cross section of the sample. As the sample began to decompose and recede, the conveyor platform moved the sample forward such that the distance between the decomposing surface and the heater remained constant thus maintaining a constant radiative heat flux on the exposed surface. The melt droplets formed on the surface of the decomposing foam flowed downwards with gravity and were eventually collected by a melt collecting unit. At the end of the experiment, the melts which remained in liquid form at ambient temperature were stored for the SDT and Hot Disk experiments from which the kinetic and thermophysical properties were obtained.

The Sample Feeding Vertical Cone experiments have been carried out in either non-flaming (NF) or flaming (F) conditions. Under non-flaming condition, the exposed surface of the foam decomposes but does not burn throughout the experiment while under the flaming condition, the exposed surface is pilot ignited. The FR foams are tested under both conditions but the NFR foams are only tested in flaming condition due to the experimental challenges in maintaining uniform exposed surface under non-flaming condition. The identification given to the foam and melt samples is based on the known combustion resistive nature of the foam, an internal code for the research, the foam density and the type of condition under which melts are obtained. Table 2-1 provides the identification, foam hardness, density and chemical formula of the samples.

Table 2-1: General description of polyurethane foams and their melts tested in this research

Identification	Foam Hardness[a] (N)	Sample Type	Density (kg/m^3)	Chemical Formula
NFR-SB-31	130	Foam	31	$C_{1.00}H_{1.77}O_{0.31}N_{0.06}$
		Melt (F)	1019	$C_{1.00}H_{1.98}O_{0.35}N_{0.01}$
NFR-DG-42	80	Foam	42	$C_{1.00}H_{1.84}O_{0.33}N_{0.05}$
		Melt (F)	1025	$C_{1.00}H_{2.03}O_{0.36}N_{0.01}$
NFR-C-19	60	Foam	19	$C_{1.00}H_{1.75}O_{0.31}N_{0.07}$
		Melt (F)	1034	$C_{1.00}H_{1.99}O_{0.36}N_{0.01}$
FR-Y-36	130	Foam	36	$C_{1.00}H_{1.69}O_{0.28}N_{0.17}Cl_{0.003}P_{0.0010}$
		Melt (NF)	1054	$C_{1.00}H_{1.95}O_{0.33}N_{0.05}Cl_{0.001}$
		Melt (F)	1047	$C_{1.00}H_{1.96}O_{0.33}N_{0.05}Cl_{0.001}$
FR-LG-38	80	Foam	38	$C_{1.00}H_{1.73}O_{0.28}N_{0.16}Cl_{0.003}P_{0.0002}$
		Melt (NF)	1052	$C_{1.00}H_{1.91}O_{0.32}N_{0.07}Cl_{0.001}$
		Melt (F)	1051	$C_{1.00}H_{1.89}O_{0.31}N_{0.07}Cl_{0.001}$
FR-W-50	120	Foam	50	$C_{1.00}H_{1.74}O_{0.32}N_{0.07}Cl_{0.002}P_{0.0004}$
		Melt (NF)	1046	$C_{1.00}H_{1.93}O_{0.34}N_{0.02}Cl_{0.002}$
		Melt (F)	1038	$C_{1.00}H_{1.98}O_{0.34}N_{0.02}Cl_{0.001}$
FR-G-32	140	Foam	32	$C_{1.00}H_{1.76}O_{0.32}N_{0.06}Cl_{0.016}P_{0.0050}$
		Melt (NF)	1035	$C_{1.00}H_{1.97}O_{0.35}N_{0.02}Cl_{0.001}$
		Melt (F)	1027	$C_{1.00}H_{1.99}O_{0.35}N_{0.01}Cl_{0.002}$

The density of the foams studied is found to vary widely from 19 to 50 kg/m^3, within the manufacturer specifications. These densities are measured from samples with 100 mm sides by 50 mm thick. According to the manufacturer, the foams studied are mainly recommended for the use as padding in upholstered furniture. Their range of density and hardness enable them to be applied to different parts of the furniture such as quilting, overlay, back, seat, arms, frame wrap and mattress. Comparing with foam, the density of melt appears more consistent on a percentage basis, ranging between 1019 to 1054 kg/m^3. There is also no significant difference in terms of the density and chemical composition between the melts collected from the non-flaming and flaming surfaces. The density is measured from 50 ml samples using a measuring cylinder. Despite the consistency in density, the melts of different foams vary in terms of their appearance, viscosity and solid contents.

In terms of appearance, the melt of NFR-SB-31, NFR-DG-42, NFR-C-19 and FR-G-32 are black liquids, FR-W-50 is a dark brown liquid and FR-Y-36 and FR-LG-38 are light brown liquids. The melts can also be grouped according to their viscosity and solid contents. The light coloured FR-Y-36 and FR-LG-38 melts are more viscous compared to the others and contain solid contents in the like of smaller char fractions. These char fractions are produced during the foam decomposition and although the majority have been removed for the Hot Disk experiments, some have blended

[a] Hardness as reported in manufacturer specifications.

together with the melt. The other remaining melts from NFR foams, FR-W-50 and FR-G-32 do not have ant solid content and they flow much more easily. The decomposition of FR-W-50 actually produces char layer but unlike FR-Y-36 and FR-LG-38, the layer does not blend with the melt and they are completely removed. Despite being recognised as having fire retardant additives, the decomposition of FR-G-32 does not produce char which is in contrast to the other FR foams in this research.

According to the manufacturer, the polyurethane foams are made from the reaction of mainly toluene diisocyanate, water and polyalkoxy polyether polyol. The polyol also contains styrene and acrylonitrile polymer. Other ingredients in smaller quantity include inorganic fillers, plasticisers, extenders, antimicrobial agents and pigments. The fire retardant FR-Y-36, FR-LG-38 and FR-W-50 contain melamine and halophosphate as fire retardant additives while FR-G-32 only has halophosphate. The precise concentration of these additives is unavailable due to commercial reasons. The proportion of halophosphate within FR-G-32 is reportedly between 10 to 20 % and the literature reported as much as 10 % melamine by weight in a certain polyurethane foam formulation[28]. The NFR foams do not adhere to any flame retardant standard but FR-Y-36, FR-LG-38 and FR-W-50 are tested to BS 5852: Source 5[29] and FR-G-32 complies with BS 4735[30]. FR-Y-36 is also specifically reported to comply with a few additional standards such as AS/NZS 1530.3:1999[31], Technical Bulletin 117[32] and § 25.853 of the Federal Aviation Regulations[33].

The chemical formula for the foams are obtained via elemental analysis and the results show carbon, hydrogen, oxygen and nitrogen as the primary elements with small traces of chlorine and phosphorus found in the FR foams. Similar elements are identified for the melts but phosphorus is not tested for during the elemental analysis involving melt samples. This is because the existing phosphorus content within the foams is considered low thus its concentration within the melts is not expected to affect the chemical formula of the melts. Chlorine and phosphorus detected in the foams originate from the halophosphate added into the formulation. Among the FR foams, FR-G-32 contains the highest chlorine and phosphorus composition which is at least five times that of the others. This result supports the manufacturer's information

where FR-G-32 only contains halophosphate as fire retardant additive which predominantly performs in the gas phase. FR-Y-36 and FR-LG-38 have a higher nitrogen content than other foams in Table 2-1 and this is an indication of the presence of melamine[34] as reported by the manufacturer.

Upon decomposition, halophosphate breaks down into a phosphate structure and releases chlorine. Chlorine is able to combine with the highly reactive radicals released by the foam decomposition to form inactive molecules which inhibit the fire[35]. While chlorine functions as a gas phase fire retardant, phosphorus performs in the solid phase. The phosphate structure creates an acidic environment through the formation of phosphoric acid[36,37]. The acidic environment catalyses the hydrolysis of the phosphate structure resulting in a cross-linking mechanism which leads to the formation of thermal insulating residue that slows the decomposition. The gaseous isocyanate which evolves from the polyurethane foam decomposition is known to react with the phosphate structure and acid to produce secondary products and residues. As a result, the amount of isocyanate released directly into the gas phase for immediate combustion is reduced[37].

The other fire retardant additives, melamine[38] ($C_3H_6N_6$) is able to function in both the gas and solid phases. Melamine initially sublimes and when heated further, it releases ammonia and nitrogen gas which are thermally stable thus diluting the combustible gases. The remaining melamine reacts with the phosphoric acid produced from halophosphate breakdown to form a thermally stable cross-linked residue, melam at 350 °C, melem at 450 °C and melon at 600 °C[34]. According to Price et al.[28], melamine is reactive towards isocyanate above 250 °C and from the resulting reaction, a polymeric structure is formed which later further degrades into char. Consistent with the gas and solid phase mechanisms of melamine and halophosphate, the chemical formula in Table 2-1 shows that N and Cl in melt are significantly less than foam as these elements are lost as gases when the fire retardant additives break down. Among the melts, FR-Y-36 and FR-LG-38 have the highest nitrogen content which suggests the solid contents within the melts are mostly degraded melamine. Good agreement is found between the chemical composition of polyurethane foams used in this research and those reported in the literature[39,40,41].

In terms of common applications, the manufacturer provides some information for the different foams tested in this research. Due to the lack of combustion resistive performance, NFR-SB-31 and NFR-C-19 are applicable for domestic, commercial and vehicle use. NFR-DG-42 with higher density is suitable for the applications within public auditorium and public transport but not in aviation. For FR foams, FR-Y-36 and FR-LG-38 are applicable in public auditorium, public transport, aviation and healthcare while for the more specific applications, FR-W-50 is used as healthcare mattress and FR-G-32 is used as acoustic panel and also in packaging.

Chapter 3. Determination of Kinetic Properties of Polyurethane Foam Decomposition for Pyrolysis Modelling

3.1 Introduction

The focus of this chapter is to use graphical techniques to develop the governing kinetic properties of polyurethane foam based on the decomposition in thermogravimetric analysis (TGA) experiments under a nitrogen environment. The developed parameters are activation energy (E in kJ/mol), pre-exponential factor (A in s^{-1}) and reaction order (n). These properties are often used as inputs to pyrolysis models which govern the thermal decomposition rate of a material. Hence, it becomes crucial to ensure that the graphical techniques applied to evaluate these parameters are compatible with the pyrolysis model incorporated in a specific combustion model. Other researchers[22,23] have investigated the decomposition of polyurethane foam under an air environment. The decomposition behaviour under air is different than nitrogen due to the additional oxidative reactions which means the governing kinetic properties are potentially different as well.

As mentioned in Section 1.4 of Chapter 1, this research focuses on the fire behaviour of polyurethane foam and the combustion modelling capability of Fire Dynamics Simulator, Version 5[18] (FDS 5[a]). In order to obtain a better comparison between experimental and simulated results, the inputs to FDS 5 are refined in Chapter 8 using a generalised pyrolysis model called Gpyro[27] with an inbuilt genetic algorithm. The algorithm is a search tool based on Darwinian evolution theory which is capable of finding the optimal solutions to nonlinear problems with multiple dimensions such as material decomposition governed by several kinetic properties. This chapter only introduces the graphical techniques used to develop the kinetic properties of polyurethane foam, the application of the developed kinetic properties and the results of FDS 5 and Gpyro are presented later in Chapter 8.

[a] Version 5.5.3, SVN number 7031.

The pyrolysis model of FDS 5 and Gpyro calculate the rate of decomposition through an Arrhenius equation which is a temperature dependent model and an n^{th} order reaction model which is mass dependent[18]. The rate of decomposition for FDS 5 is represented by Equation (3-1) and that for Gpyro is showed in Equation (3-2). Despite the difference in notation, the pyrolysis model in FDS 5 and Gpyro are essentially equivalent.

$$r = A\left(\frac{\rho_{s,i}}{\rho_{s0}}\right)^{n} e^{-\frac{E}{RT}} \tag{3-1}$$

$$r = \left(\frac{\overline{\rho} Y}{\overline{\rho}\big|_{t=0}}\right)^{n} A e^{-\frac{E}{RT}} \tag{3-2}$$

Three different graphical techniques using similar relationships as Equation (3-1) and (3-2) are selected for this study and they are Kinetic Analysis, the Arrhenius Plot Method and the Inflection Point Methods. The repeatability of the TGA results and the calculated kinetic properties are also addressed.

3.2 Published Kinetic Properties and Pyrolysis Models of Polyurethane Foams

A number of studies in the literature have estimated the kinetic properties of polyurethane foam decomposition from TGA experiments. Various techniques are used to obtain these properties including the graphical techniques and the computational-based optimisation programs. Table 3-1 summarises the kinetic properties from the literature on foam decomposition under a nitrogen environment. Despite being recognised as the fundamental material properties of polyurethane foam, there are differences among the values reported which are caused by the variation in polyurethane foams studied, the application of different methods to establish the kinetic properties and the multi-dimensionality aspect of foam

decomposition. In Table 3-1, the subscripts '*1*' and '*2*' denote the first and second reactions, '*pre*' denotes the pre-first reaction and '*NFR*' and '*FR*' indicate non-fire retardant and fire retardant.

Table 3-1: Published kinetic properties of polyurethane foam decomposition under nitrogen environment

Authors	Activation energy, E (kJ/mol)	Pre-exponential factor, A (s^{-1})	Reaction order, n
Prasad et al.[42]	$E_1 = 135$ $E_2 = 175$	$A_1 = 1.69\times10^{8}$ $A_2 = 8.75\times10^{9}$	$n_1 = 1.00$ $n_2 = 1.16$
Rein et al.[19]	$E_1 = 148$ $E_2 = 124$	$A_1 = 2.00\times10^{11}$ $A_2 = 1.58\times10^{8}$	$n_1 = 0.21$ $n_2 = 1.14$
Rein et al.[43]	$E = 200$	$A = 5.00\times10^{15}$	$n = 3$
Bilbao et al.[22]	$E_{pre} = 29$ $E_1 = 63$ $E_2 = 180$	$A_{pre} = 6.50\times10^{-1}$ $A_1 = 1.78\times10^{3}$ $A_2 = 1.57\times10^{12}$	$n_{pre} = 1.00$ $n_1 = 1.00$ $n_2 = 1.00$
Chao et al.[23]	$E_{1,NFR} = 99 – 120$ $E_{2,NFR} = 54 – 184$ $E_{1,FR} = 56 – 114$ $E_{2,FR} = 42 – 193$	$A_{1,NFR} = 1.00\times10^{2} – 2.34\times10^{22}$ $A_{2,NFR} = 2.23\times10^{2} – 8.89\times10^{8}$ $A_{1,FR} = 1.20\times10^{9} – 2.90\times10^{16}$ $A_{2,FR} = 1.83\times10^{1} – 1.62\times10^{9}$	$n_{1,NFR} = 6.90 – 18.40$ $n_{2,NFR} = 0.90 – 3.20$ $n_{1,FR} = 9.30 – 13.30$ $n_{2,FR} = 0.70 – 3.40$
Rogers et al.[24]	$E_1 = 218$ $E_2 = 163$	$A_1 = 5.67\times10^{17}$ $A_2 = 1.13\times10^{11}$	Not using n^{th} order model

3.2.1 Prasad et al.

Prasad et al.[42] used the FDS 5 pyrolysis model to simulate the decomposition of flexible poly-ether polyurethane foam in the TGA experiment. The research also simulated the foam burning behaviours in cone calorimeter and medium-scale flame spread slab experiments. The dimension of heat transfer is different for these experiments where TGA experiment is a lumped capacitance system, cone calorimeter is 1-dimensional and slab experiment is 2-dimensional. In their research, the genetic algorithm of Gpyro was applied to search for the kinetic properties within a defined search boundaries before using as inputs to FDS 5. The constraints of the algorithm are the allocated search duration and boundaries, both of which potentially have a significant influence on the final set of properties obtained.

3.2.2 Rein et al.

Rein et al.[19,43] investigated the smouldering combustion of open-cell, flexible polyurethane foam under microgravity. Smouldering combustion consists of two mechanisms which are pyrolysis and oxidation. The kinetic properties relating to the former are listed in Table 3-1. The pyrolysis mechanism is commonly represented by two reactions but Rein et al. have also employed a single reaction scheme in their research. A numerical model was used to simulate the foam decomposition in lumped model TGA experiments and also the foam smouldering in one-dimensional microgravity experiments. The pyrolysis model of the numerical model is presented in Equation (3-3).

$$r = Ae^{-\frac{E}{RT}}Y^n \tag{3-3}$$

The kinetic properties were estimated with a genetic algorithm called Genetic Algorithms for Optimisation Toolbox (GAOT)[44]. Unlike Gpyro which has an inbuilt pyrolysis model, GAOT provides the flexibility to incorporate a user defined pyrolysis model thus the numerical model in Equation (3-3) is used.

3.2.3 Bilbao et al.

In a study on the decomposition of polyurethane foam in a nitrogen environment and an air environment, Bilbao et al.[22] conducted TGA experiments in dynamic and isothermal modes to estimate the kinetic properties. The dynamic mode is a more common selection where the decomposition occurs across a range of temperatures. In the isothermal mode, the temperature is held constant once a set point temperature is reached. The foam studied was made from diisocyanate and polyether-type polyol. The pyrolysis model used for calculating the kinetic properties is presented in Equation (3-4) where the reaction order, *n* is assumed to be 1.

$$r = \left(F_s - X_s\right)^n Ae^{-\frac{E}{RT}} \tag{3-4}$$

To estimate E and A, other variables in Equation (3-4) are found from the dynamic experiments except for F_s which is obtained from the isothermal experiments and by rearranging, Equation (3-5) is obtained. By plotting ln(k) versus 1/T the foam decomposition was classified by Bilbao et al. into pre-first reaction, first reaction and second reaction regions. Subsequently, the kinetic properties for each region were graphically determined from the slope and y-intercept of the plot.

$$\ln(k) = \ln\left(\frac{r}{F_s - X_s}\right) = \ln(A) - \frac{E}{RT} \tag{3-5}$$

3.2.4 Chao et al.

Chao et al.[23] investigated the decomposition of non-fire retardant and fire retardant open-cell flexible polyurethane foam in a nitrogen environment and also in an air environment. The pyrolysis model used is represented by Equation (3-6) and the kinetic properties were estimated from the slope and y-intercept of ln($d\alpha/dt$) versus 1/T plot.

$$\ln\left(\frac{d\alpha}{dt}\right) = \ln A + n\ln(1-\alpha) - \frac{E}{RT} \tag{3-6}$$

3.2.5 Rogers et al.

Instead of using a reaction order, n, Rogers et al.[24] used two different rate laws to graphically evaluate the kinetic properties governing the decomposition of flexible polyurethane foam which is known to demonstrate a tendency to smoulder. From 16 rate laws available, Rogers et al. performed a 'reduced rate' assessment on each in order to select those suitable for the foam decomposition. Following the assessment, the first reaction was represented by a two-dimensional diffusion-controlled rate law while the second reaction was represented by a random nucleation rate law. The parameter evaluation started from a generalised rate equation seen in Equation (3-7).

$$\frac{d\alpha}{dT} = \frac{A}{\beta} e^{-\frac{E}{RT}} f(\alpha) \tag{3-7}$$

After some rearrangement and adopting the Gorbachev approximation for the exponential integral, Equation (3-8) is obtained[45]. For the first reaction, $g(\alpha)$ is defined by Equation (3-9) while for the second reaction, it is represented by Equation (3-10). The kinetic properties were estimated through the slope and y-intercept of $\ln[g(\alpha)/T^2]$ versus $1/T$ plot.

$$\int \frac{d\alpha}{f(\alpha)} = g(\alpha) = \frac{A}{\beta} \int e^{-\frac{E}{RT}} dT \approx \frac{ART^2}{\beta(E + 2RT)} e^{-\frac{E}{RT}} \tag{3-8}$$

$$g(\alpha) = (1 - \alpha)\ln(1 - \alpha) + \alpha \tag{3-9}$$

$$g(\alpha) = [-\ln(1 - \alpha)]^{2/3} \tag{3-10}$$

3.3 Thermogravimetric Analysis Experiments

The equipment used to conduct the decomposition experiments is a DSC-TGA Q Series™ instrument, SDT Q600 manufactured by TA Instruments. The TGA experiments are carried out in dynamic mode where the foam sample is subjected to a constant heating rate within a gas purged furnace from room temperature (~20 °C) up to the maximum temperature of 600 °C. A sample mass between 3 to 4 mg is prepared by shredding the polyurethane foam into fine fragments so as to half-fill a 90 μL alumina cup. Inside the furnace, the sample and reference cups are placed on the platinum platform of the sample and reference balance beams respectively. The equipment also simultaneously performs differential scanning calorimetry (DSC) which records the changes in enthalpy during sample decomposition. The DSC results for foam decomposition are discussed later in Chapter 5.

During the experiment, the equipment measures the sample mass based on a current signal required for correcting a taut-band meter movement caused by the changes in

sample mass[46]. The sample temperature is recorded through the thermocouple welded underneath the platforms. When the heating rate or purge gas is changed, the necessary calibrations are performed to obtain their respective signal correction factors. The calibrations are performed in sequence, starting with the mass calibration, the temperature calibration, the heat flow calibration and finally, the cell constant calibration. The mass calibration is more related to the TGA experiment and the procedure is discussed below. The others are more related to the DSC experiment so they are discussed further in Chapter 5.

The mass calibration is performed to establish the appropriate weight correction factors for the specific heating rate and temperature range applied. This calibration consists of two parts and the first involves an experiment with empty sample and reference platforms. The furnace temperature is increased from the room temperature (~20 °C) to the maximum temperature under constant heating rate and the results are collected. The second part consists of an experiment where the sample and reference platforms are loaded respectively with the sample and reference weight pieces provided by TA Instruments. This experiment proceeds under the same experimental conditions as the first and the collected results from both parts are loaded onto the analysis software where the appropriate weight correction factors are determined and applied.

The heating rates selected are 1, 5, 20 and 60 °C/min and these are chosen based on the temperature variation of a polyurethane foam smouldering front, reported to range between 1 and 150 °C/min[19]. The chosen rates are also below the maximum allowable limit of 100 °C/min for the equipment. The purge gas used is nitrogen which is delivered at a constant rate of 100 ml/min and since nitrogen is non-reactive, the foam decomposition is solely influenced by heat.

3.4 Decomposition of Base Case Polyurethane Foams

Two polyurethane foams from Table 2-1 of Chapter 2 are discussed to introduce the graphical techniques for estimating the kinetic properties and three repetitions at each

heating rate are conducted. These two foams are NFR-SB-31 and FR-Y-36 which are the base case NFR and FR foams of this research. The physical and chemical attributes of these foams are presented in Chapter 2. Figure 3-1 shows the changes in the mass of NFR-SB-31 during its decomposition in the nitrogen environment at 1, 5, 20 and 60 °C/min. The measured sample mass is plotted against the sample temperature. NFR-SB-31 fully decomposed over two regions of significant mass loss and for each heating rate the repeated results are reproducible. A transition region with a smaller mass loss exists between the two decomposition regions as indicated on the results at 1 °C/min in Figure 3-1. With increasing heating rate the decomposition of NFR-SB-31 shifts towards higher temperature while its overall trend remains consistent with only minute changes in the mass loss over each region. Indicated in Figure 3-1, 23 – 26 % of the sample mass is lost during the first reaction while in the transition and second reaction, 4 – 6 % and 69 – 71 % of the sample mass is lost respectively.

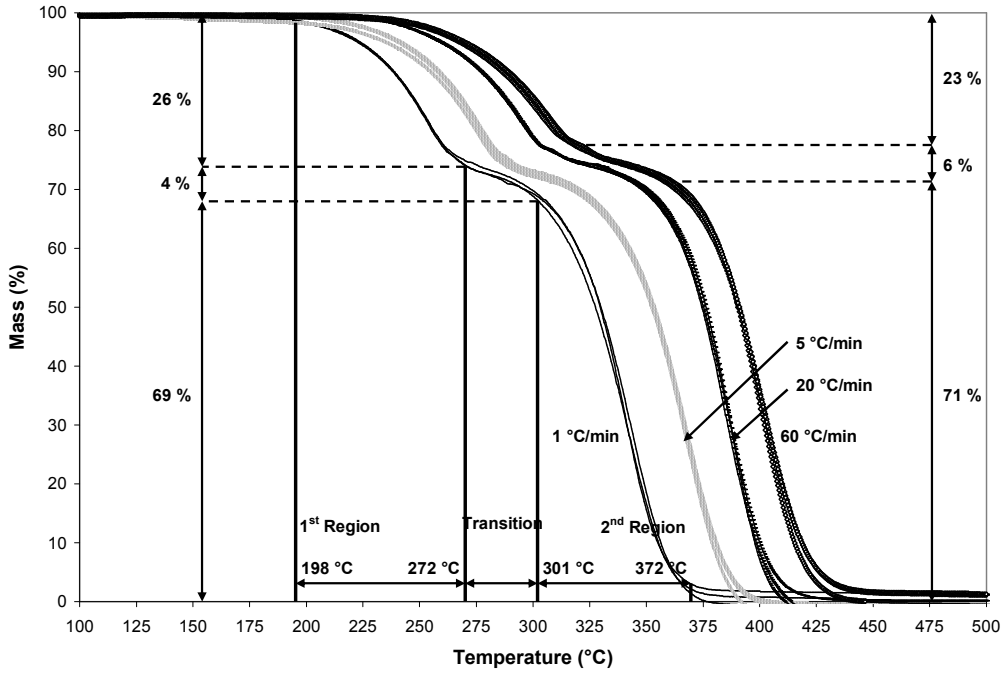

Figure 3-1: Sample mass versus temperature of NFR-SB-31 at 1, 5, 20 and 60 °C/min heating rates

FR-Y-36 also decomposed via two significant mass loss reactions as seen in Figure 3-2. The overall decomposition trend is similar to NFR-SB-31 except the changes in heating rate have more impact on the amount of sample decomposed during the first reaction and transition. From Figure 3-2, during the first reaction 19 – 31 % of the sample mass is lost, while during the transition and second reaction, 6 – 15 % and 63 – 66 % of the sample mass is lost respectively. For NFR-SB-31 the first reaction and transition shows negligible changes in sample decomposition, changing by 3 and 2 % respectively over the different heating rates but for FR-Y-36 these changes are more significant, varying by 12 and 9 % respectively.

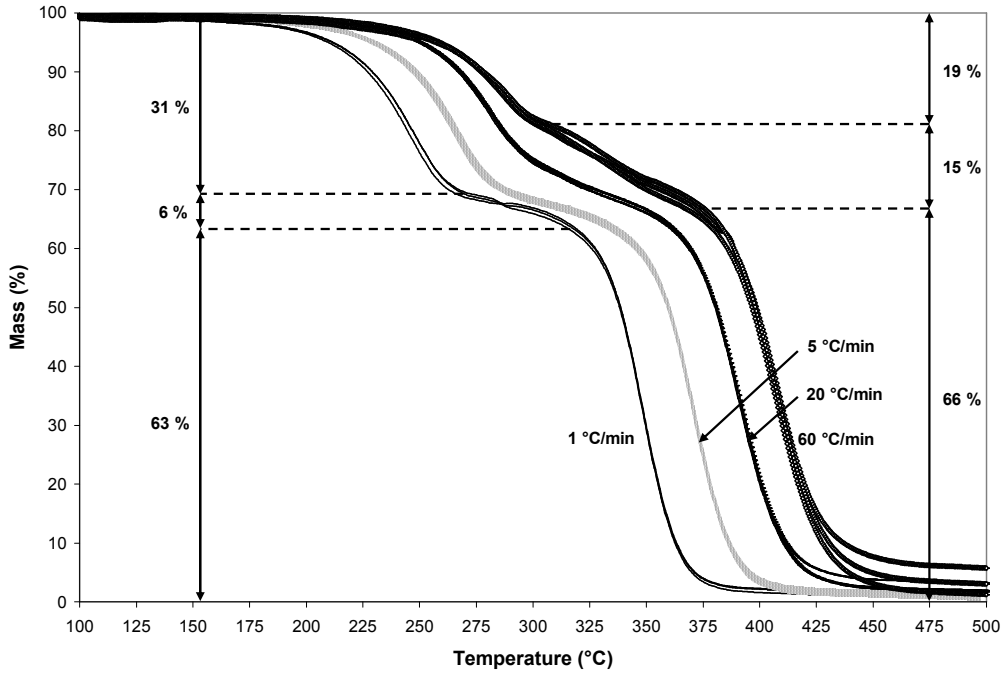

Figure 3-2: Sample mass versus temperature of FR-Y-36 at 1, 5, 20 and 60 °C/min heating rates

Figure 3-3 shows the mass loss/°C versus sample temperature of NFR-SB-31 for all four heating rates. Two significant mass loss reactions are seen as the prominent protuberances in Figure 3-3 and the peak of reaction occurs at the temperature where the maximum mass loss/°C is recorded. The peak magnitude of the second reaction is approximately three times greater than the first reaction and when the heating rate increases, the peak of the first reaction decreases while that of the second reaction remains effectively constant.

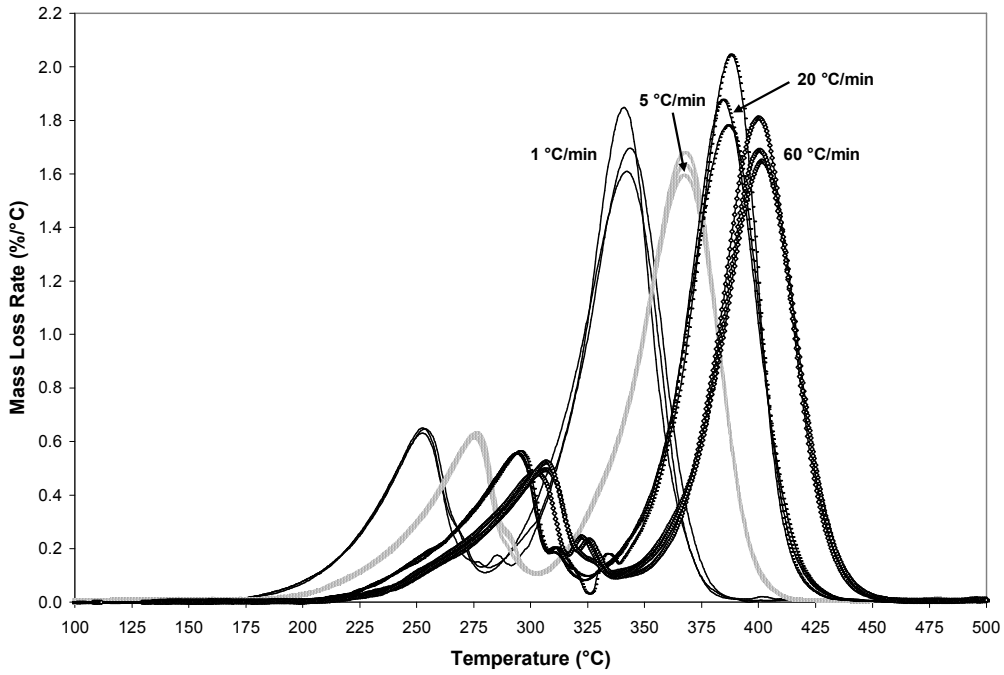

Figure 3-3: Mass loss/°C versus temperature of NFR-SB-31 at 1, 5, 20 and 60 °C/min heating rates

For FR-Y-36, the peak in both reactions decreases with increasing heating rate as seen from the mass loss/°C versus sample temperature plot in Figure 3-4. The systematic decrease in the peak magnitude is accompanied by a progressive increase of the overall magnitude during transition which is not observed in NFR-SB-31. At 60 °C/min, the mass loss/°C during transition has increased to more than 0.2 %/°C, doubling the magnitude at 1 °C/min.

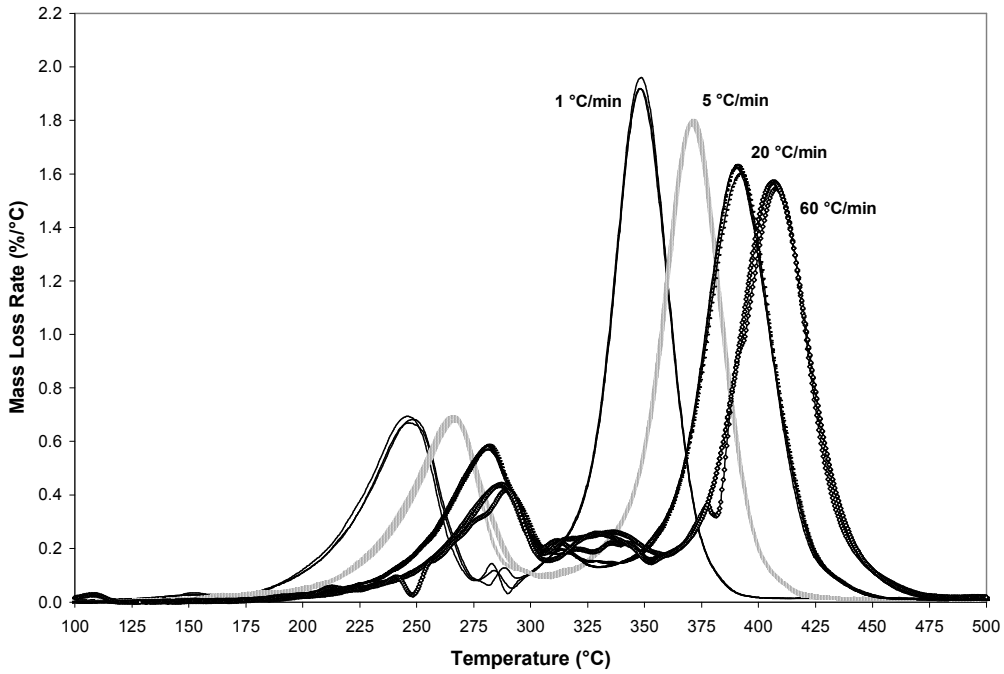

Figure 3-4: Mass loss/°C versus temperature of FR-Y-36 at 1, 5, 20 and 60 °C/min heating rates

Table 3-2 shows the decomposition temperature range of each reaction for NFR-SB-31 and FR-Y-36. The values presented are the average of the three repeated experiments and the values in brackets are the temperature where the maximum mass loss/°C is recorded. Based on the observed trend in Figure 3-3 and 3-4, the start and end temperatures of the decomposition are quantified as the temperature where the mass loss/°C is 10 % of the difference between the minimum and maximum of the specific reaction.

Table 3-2: Decomposition temperature of NFR-SB-31 and FR-Y-36

Heating rate, °C/min	Decomposition temperature (Temperature at peak of reaction), °C			
	NFR-SB-31		FR-Y-36	
	1st Reaction	2nd Reaction	1st Reaction	2nd Reaction
1	198 – 272 (253)	301 – 372 (342)	190 – 270 (247)	316 – 376 (348)
5	213 – 295 (276)	322 – 398 (368)	209 – 290 (266)	338 – 401 (371)
20	229 – 311 (294)	348 – 415 (386)	222 – 314 (281)	358 – 426 (391)
60	238 – 321 (305)	362 – 434 (401)	216 – 302 (288)	375 – 446 (407)

Over the range of heating rates tested, the consistently lower start and peak temperatures of the first reaction for FR-Y-36 indicate that it decomposes earlier than NFR-SB-31. According to Grassie et al.[36,37] and Price et al.[28], the decomposition of

fire retardant foam occurs at lower temperatures because the overall process is catalysed by the acidic environment created and the presence of ammonia following the breakdown of halophosphate and melamine respectively. The early decomposition of FR-Y-36 leads to the formation of residue which impacts on the remainder of the decomposition process.

Comparing the decomposition behaviours of NFR-SB-31 with FR-Y-36, the latter demonstrates greater resistance to decomposition as a result of the formation of residue from halophosphate and melamine. From Table 3-2, the transition region where the decomposition rate is minimal is wider for FR-Y-36, 44 – 73 °C compared to 27 – 41 °C for NFR-SB-31. According to the TGA results, the majority of the fuel is consumed during the second reaction thus in the event of fire, the decomposition of FR-Y-36 will have to overcome a greater temperature barrier due to the widened transition before the second reaction can initiate thus delaying the onset of significant fuel consumption. Figure 3-2 shows that the widening of transition also reduces the amount of sample decomposed during the first reaction from 31 % at 1 °C/min to 19 % at 60 °C/min thus the fuel gas released under a high heating rate has reduced.

For NFR-SB-31, the peak magnitude of the second reaction remains constant with increasing heating rate as seen in Figure 3-3. Due to residue formation of FR-Y-36 which interferes with the release of pyrolysates, the peak magnitude of the second reaction in Figure 3-4 actually decreases with the increasing heating rate. This indicates a reduction in the fuel gas released per increase of the material temperature. In terms of the total amount of fuel gas released, FR-Y-36 in Figure 3-2 is also 5 to 6 % less than NFR-SB-31 in Figure 3-1 when compared over the second reaction which is the major mass loss region. This shows the effectiveness of residue formation in reducing the release of pyrolysates into the gas phase.

From the reduction in peak magnitude and in the amount of fuel consumed during the second reaction and also the widening of transition region, FR-Y-36 has demonstrated greater resistance towards decomposition than NFR-SB-31. This shows that the halophosphate and melamine in FR-Y-36 are able to form a residue which slows decomposition by restricting the release of pyrolysates. The fire retardant mechanisms

are consistent with the descriptions provided in the literature and the differences seen in the decomposition pattern between NFR-SB-31 and FR-Y-36 are also compatible with the NFR and FR foams reported by Price et al.[28].

3.5 Determination of Kinetic Properties using Graphical Techniques

Three graphical techniques are employed on the TGA results for NFR-SB-31 and FR-Y-36 to evaluate the kinetic properties, *E*, *A* and *n* for the first and second reactions. First of these methods is Kinetic Analysis[47], also known as the "Model Free" Method[48] which calculates a set of global kinetic properties for all experiments. The other two methods, the Arrhenius Plot Method[47] and the Inflection Point Methods[49] determine the kinetic properties specific to each experiment. The individual kinetic properties are later involved in the assessment of their repeatability. To demonstrate the calculation involved, the experimental results of NFR-SB-31 are used.

3.5.1 Kinetic Analysis or "Model Free" Method

Equation (3-11) is the general kinetic equation[47] and is assumed to be an adequate representation of the thermal decomposition of polyurethane foam. The temperature dependence rate constant, *k* is represented by the Arrhenius equation as shown in Equation (3-12). The decomposition chemistry represented by the kinetic model, $f(W/W_0)$ is independent of temperature and solely a function of the instantaneous sample mass. The first kinetic parameter determined is *E* and since no knowledge of $f(W/W_0)$ is required at this stage, this method is considered "Model Free"[48].

$$(1/W_0)(dW/dt) = k \cdot f(W/W_0) \tag{3-11}$$

$$k = Ae^{-E/RT} \tag{3-12}$$

Substituting Equation (3-12) into (3-11) and taking the natural logarithm gives Equation (3-13).

$$\ln\left[\left(1/W_0\right)\left(dW/dt\right)\right] = \ln A + \ln f\left(W/W_0\right) - E/RT \tag{3-13}$$

Figure 3-5 shows the relationship between $\ln[(1/W_0)(dW/dt)]$ and $1/T$ for NFR-SB-31. The data is plotted for W/W_0 ranging between 0.95 and 0.05, at the interval of 0.01. The initial and final 5 % of the data are excluded to eliminate the uncertainties due to baseline offset while still retaining sufficient points for further analysis. Each line in Figure 3-5 corresponds to a specific W/W_0 and each point on a line represents the average of three repeated experiments at a given heating rate. At each W/W_0, E is determined from the slope, E/R thus it is a value dependent on the number of heating rates included in the analysis, in this case 1, 5, 20 and 60 °C/min.

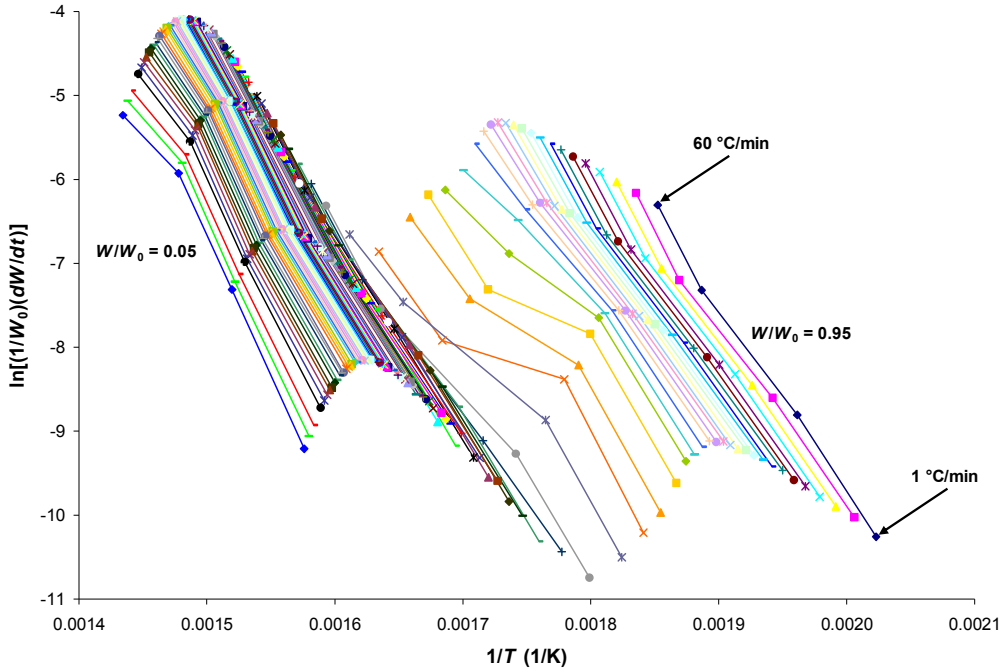

Figure 3-5: $\ln[(1/W_0)(dW/dt)]$ versus $1/T$ plotted for W/W_0 from 0.95 to 0.05 of NFR-SB-31

Figure 3-6 shows E plotted against W/W_0 where there are two regions in which E becomes relatively constant. The global E for each decomposition reaction is determined as the average of the respective regions. Since E varies from approximately 120 to 240 kJ/mol, selecting the data points for calculating the global E uses the R-squared values from $\ln[(1/W_0)(dW/dt)]$ versus $1/T$ of at least 0.99 and the difference in E between the adjacent W/W_0 not exceeding 5 kJ/mol. Based on such

selection criteria, the first decomposition reaction is determined to range from W/W_0 of 0.94 to 0.79 and the second reaction ranges from 0.61 to 0.07. The global E for the first and second reactions is 179 and 231 kJ/mol respectively. In the region between 0.78 and 0.62, E changes rapidly as the first reaction transitions into the second reaction.

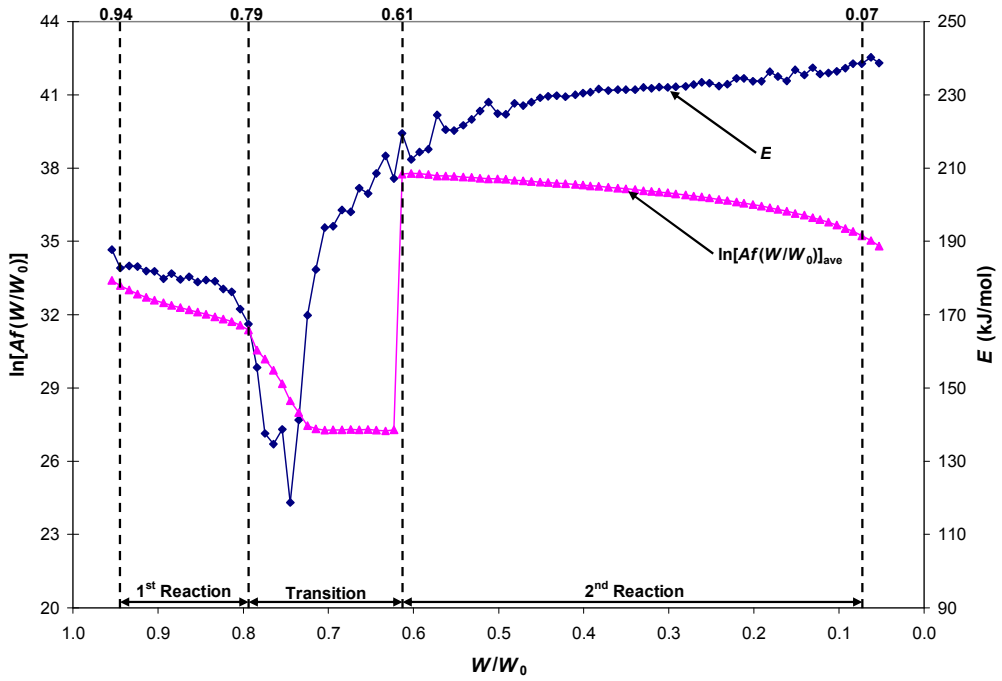

Figure 3-6: E and $\ln[Af(W/W_0)]_{ave}$ versus W/W_0 of NFR-SB-31

With E determined, n and A are calculated simultaneously. For each heating rate and each W/W_0, $\ln[Af(W/W_0)]$ is evaluated by substituting the global E into Equation (3-13). At each W/W_0, $\ln[Af(W/W_0)]_{ave}$ which is the average for all heating rates is calculated and plotted in Figure 3-6. At this stage, a kinetic model is required and the n^{th} order kinetic model in Equation (3-14) is assumed for the polyurethane foam decomposition.

$$f(W/W_0) = \left[(W - W_f)/W_0\right]^n \tag{3-14}$$

This kinetic model is applicable for modelling a solid reactant converting into a constant ratio of gaseous and solid product[47]. This is the case with polyurethane foam as the TGA results show the mass fraction of products from the first and second

reactions are consistent with respect to the heating rates included within the analysis. Multiplying both sides of Equation (3-14) by A and taking the natural logarithm yields Equation (3-15).

$$\ln\left[Af\left(W/W_0\right)\right]_{ave} = \ln A + n\ln\left[\frac{\left(W - W_f\right)}{W_0}\right] \tag{3-15}$$

In Figure 3-7, $\ln[Af(W/W_0)]_{ave}$ versus $\ln[(W\text{-}W_f)/W_0]$ is plotted for all three regions. Calculating the slope and y-intercept, the global n and A are determined. For the first and second reactions respectively, n are 9.51 and 1.23 while A are 3.61×10^{14} and 4.72×10^{16} s^{-1}.

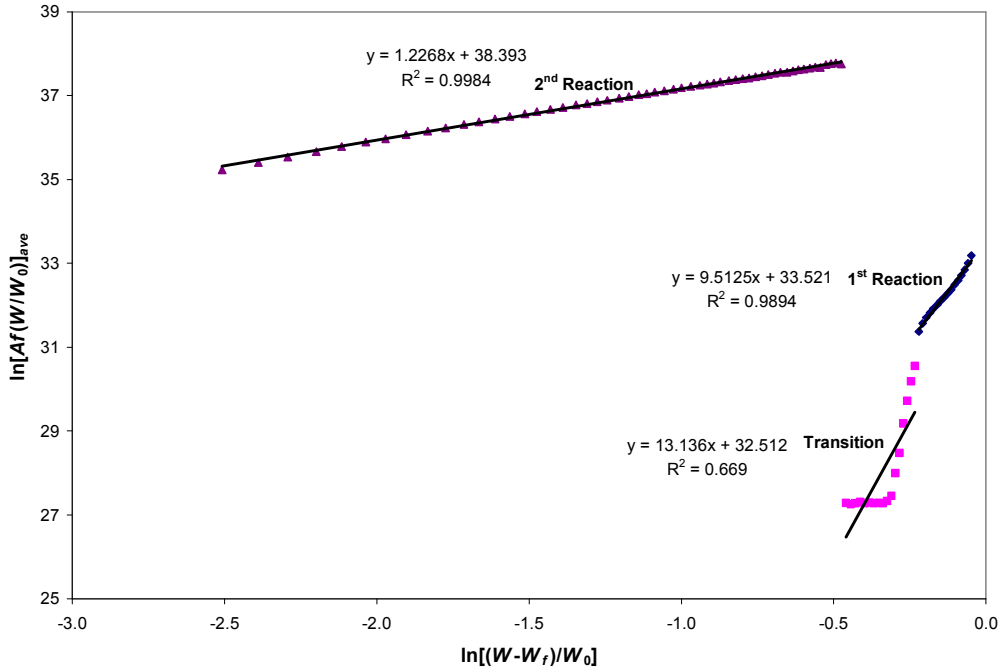

Figure 3-7: $\ln[Af(W/W_0)]_{ave}$ versus $\ln[(W\text{-}W_f)/W_0]$ of NFR-SB-31

As demonstrated, a single set of kinetic properties is derived using Kinetic Analysis on the TGA results over a range of heating rates and therefore, these properties are considered as the global representation of the polyurethane foam decomposition. Being global also means these properties are influenced by the heating rates included within the analysis.

3.5.2 Arrhenius Plot Method

Besides the global values derived above, the kinetic properties specific to each experiment are also estimated using the Arrhenius Plot Method[47] which utilises the global n from Kinetic Analysis. Using the general kinetic equation in (3-11) and assuming n^{th} order kinetic model in Equation (3-14), k is redefined in Equation (3-16).

$$k = \frac{(1/W_0)(dW/dt)}{\left[(W - W_f)/W_0\right]^n} \tag{3-16}$$

For each repeated experiment, k is evaluated by applying the global n found in Kinetic Analysis over the respective W/W_0 range of the first reaction, transition and second reaction. The natural logarithm form of the Arrhenius equation is given in Equation (3-17) and $\ln(k)$ is plotted against $1/T$ to estimate E and A from the slope and y-intercept as seen in Figure 3-8.

$$\ln(k) = \ln(A) - \frac{E}{RT} \tag{3-17}$$

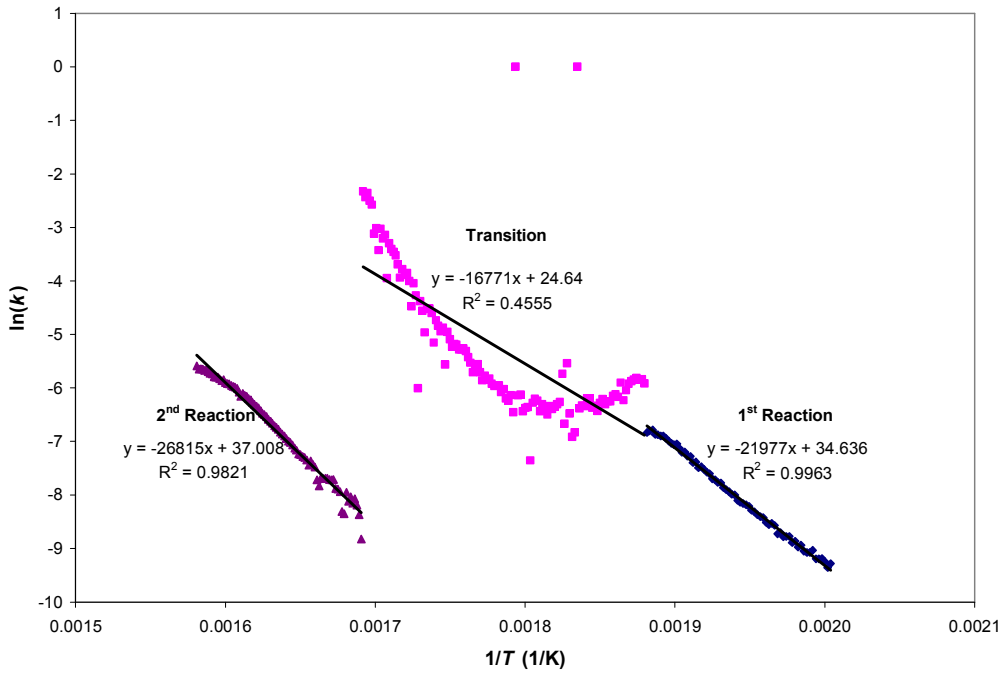

Figure 3-8: ln(k) versus 1/T at 1 °C/min, first repetition of NFR-SB-31

Again using NFR-SB-31 as an example, from the first repetition at 1 °C/min, E and A of the first reaction are 183 kJ/mol and 1.10×10^{15} s^{-1} while those of the second reaction are 223 kJ/mol and 1.18×10^{16} s^{-1}. Using the global n and analysing over the identical regions as described in Kinetic Analysis, the kinetic properties found from the Arrhenius Plot Method are expected to be close to Kinetic Analysis. The values of E and A for other repetitions are also determined using the outlined approach and these properties are discussed later. Starting with the Arrhenius Plot Method and later with the Inflection Point Methods, the determination of kinetic properties for each TGA experiment provides further details regarding the repeatability and trend of these properties.

3.5.3 Inflection Point Methods

Like the Arrhenius Plot Method, the Inflection Point Methods[49] are applied to evaluate the kinetic properties of each experiment. However, as an independent technique, the calculation methods and the analysis regions are different to the graphical approaches discussed previously. From Equation (3-11) and (3-16), k is

defined as the decomposition rate divided by the mass dependent kinetic model. Based on the same definition, k in Equation (3-18) is represented by the decomposition rate on a temperature basis, $d\alpha/dT$ divided by the n^{th} order kinetic model, $(1-\alpha)^n$ represented as a function of α, the fraction decomposed. Comparing k of Equation (3-11) and (3-16) with (3-18), the former are time-based and they are defined in terms of fraction remaining while the latter is temperature-based and it is defined in terms of fraction decomposed, α. On the right hand side of Equation (3-18), the equation is converted into a temperature basis by dividing A with the constant heating rate, β of an experiment.

$$\ln(k) = \ln\left[\frac{d\alpha/dT}{(1-\alpha)^n}\right] = -\frac{E}{RT} + \ln\left(\frac{A}{\beta}\right) \tag{3-18}$$

During the peak or maximum inflection point of mass loss/°C, $d\alpha/dT$ is a maximum while $d^2\alpha/dT^2$ is 0 and through solving these conditions, n is defined in Equation (3-19). The parameters with subscript S denote the values at the maximum inflection point.

$$n = \frac{(E/RT_S^2)(1-\alpha_S)}{(d\alpha/dT)_S} \tag{3-19}$$

Substituting Equation (3-19) into (3-18) yields (3-20) and the parameter Φ is calculated in Equation (3-21).

$$\ln(d\alpha/dT) = (E/R)\left(\left[\frac{\ln(1-\alpha)}{\Phi}\right] - \frac{1}{T}\right) + \ln\left(\frac{A}{\beta}\right) \tag{3-20}$$

$$\Phi = \frac{T_S^2 (d\alpha/dT)_S}{1-\alpha_S} \tag{3-21}$$

The analysis region of each reaction needs to be defined before solving for any parameters. The data points are plotted from the 'start of a reaction' to the peak $d\alpha/dT$ and 'start of a reaction' is defined as the temperature where $d\alpha/dT$ is 10 % of the

difference between the maximum and minimum $d\alpha/dT$. Figure 3-9 shows the defined analysis region of the first and second reactions from the first repetition at 1 °C/min for NFR-SB-31.

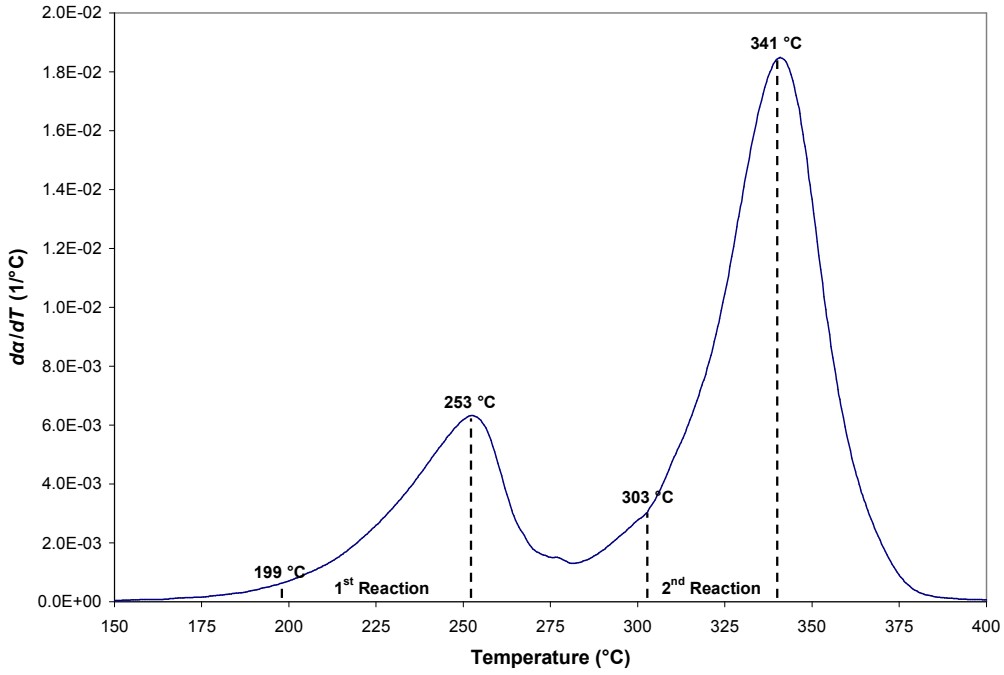

Figure 3-9: *dα/dT* versus temperature at 1 °C/min, first repetition of NFR-SB-31

Based on the analysis regions, $\ln(d\alpha/dT)$ against $[\ln(1-\alpha)/\Phi]-1/T$ is plotted in Figure 3-10 and E/R is determined from the slope. With E/R of the two reactions found, n values are calculated using Equation (3-19) and it is 7.92 and 1.07 for the first and second reactions respectively.

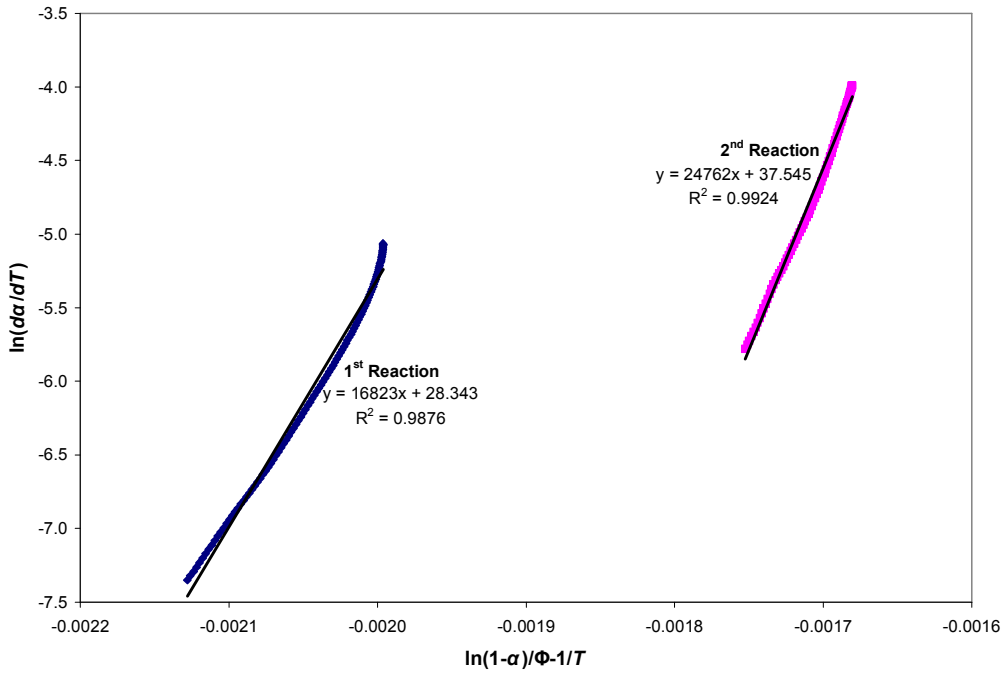

Figure 3-10: ln($d\alpha/dt$) versus [ln(1-α)/Φ]-1/T at 1 °C/min, first repetition of NFR-SB-31

Substituting n into Equation (3-18), ln(k) is evaluated and plotted against 1/T as shown in Figure 3-11. From the slope and y-intercept, E and A are evaluated. For the first reaction, E is 142 kJ/mol and A is 5.45×10^{10} s^{-1} while for the second reaction, E and A are 208 kJ/mol and 4.80×10^{14} s^{-1} respectively.

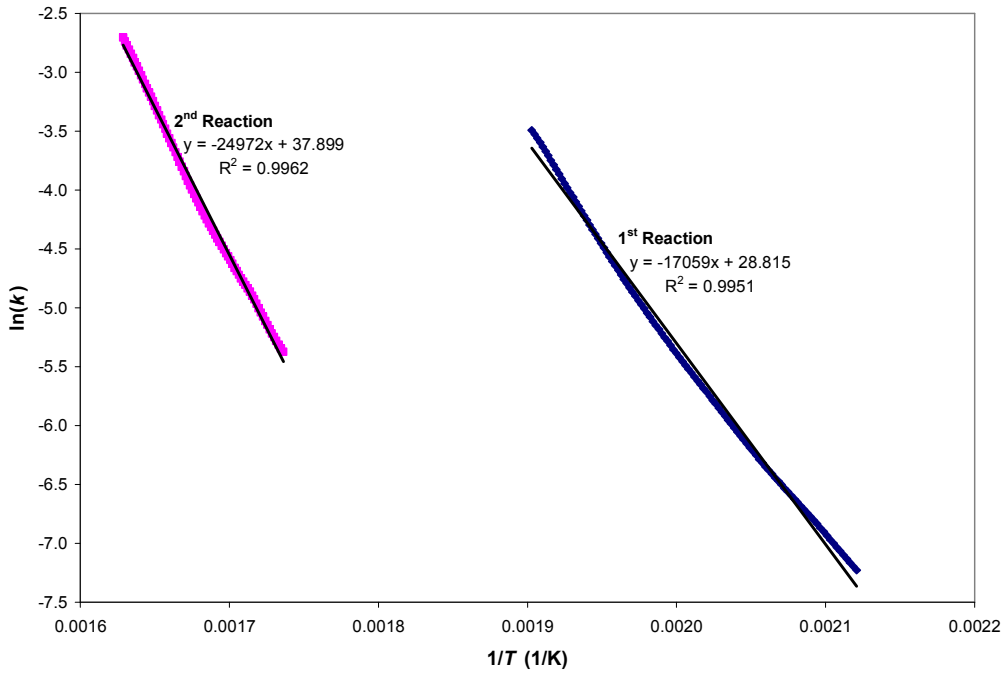

Figure 3-11: ln(k) versus 1/T at 1 °C/min, first repetition of NFR-SB-31

3.5.4 Normalisation of Inflection Point Methods

The flexibility of the pyrolysis model in FDS 5 and Gpyro allows the user to design various schemes to represent the intended type of decomposition. Despite the varying schemes, the decomposition rate of each scheme is still solved using the same equations, Equation (3-1) and (3-2). From all of the graphical techniques employed so far the decomposition of polyurethane foam is represented by Equation (3-11) where the decomposition rate is partially influenced by E and A within the temperature dependent model, k and also partially via n within the mass dependent model, $f(W/W_0)$. Subsequently, the calculated kinetic properties are suited to the more complex schemes where the solid fuel forms fuel gas and also solid residue or have material components that are not reacting during decomposition.

On the other hand, the simplest scheme involves the solid fuel completely converting into fuel gas causing the solid phase cells to shrink to maintain a constant solid density. Density preservation forces $\rho_{s,i}/\rho_{s0}$ in Equation (3-1) to unity as $\rho_{s,i} = \rho_{s0}$ causing n to become a redundant parameter. Thus, Equation (3-11) simplifies into

Equation (3-22) which becomes solely temperature dependent. Further discussions regarding the compatibility of kinetic properties with pyrolysis model are presented in Section 8.5.9 of Chapter 8.

$$(1/W_0)(dW/dt) = Ae^{-E/RT} \tag{3-22}$$

In this case, E and A need to be reassessed to include the decomposition effect previously shared by n. To achieve this, an alternate form of the Inflection Point Methods are employed where $f(W/W_0)$ is normalised by setting $n = 0$ for both reactions. This effectively brings $f(W/W_0)$ to unity, achieving the same effect as the density preservation in FDS 5 and Gpyro. Having $n = 0$ and once again utilising Equation (3-18), ln(k) against $1/T$ is plotted in Figure 3-12 for NFR-SB-31.

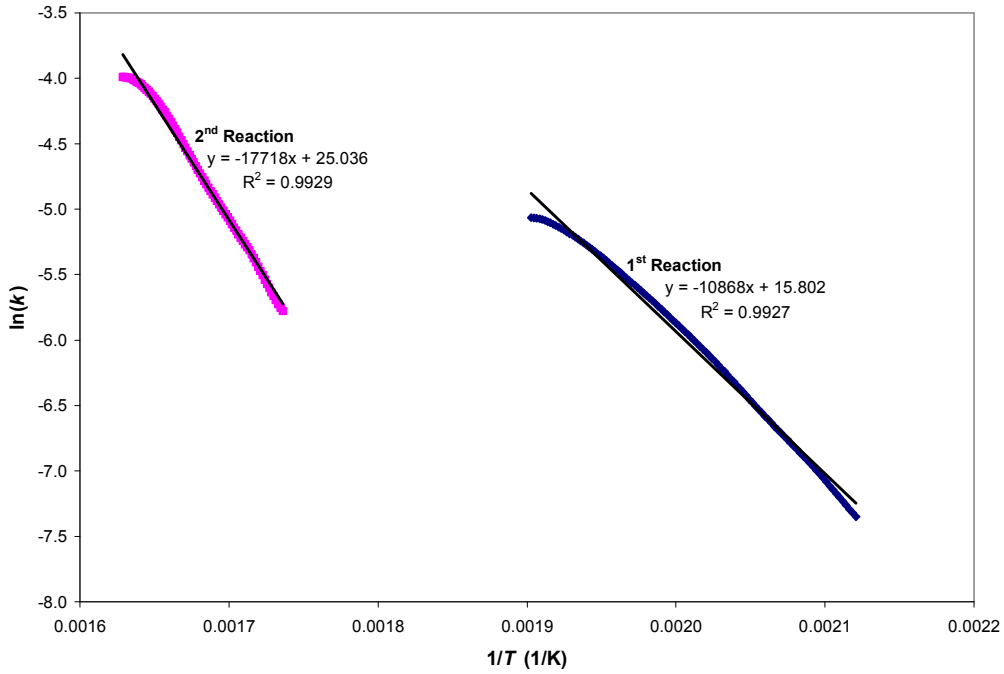

Figure 3-12: ln(k) versus $1/T$ at 1 °C/min, first repetition of NFR-SB-31

For the first repetition at 1 °C/min, E and A for the first and second reactions are 90 kJ/mol and 1.21×10^5 s^{-1} and 147 kJ/mol and 1.24×10^9 s^{-1}. Hence, besides the general compatibility of a graphical technique with a pyrolysis model, the intricate details of the decomposition schemes involved are also a crucial aspect affecting the kinetic properties calculated.

3.6 Kinetic Properties of Base Case Polyurethane Foams

The kinetic properties, *E*, *A* and *n* determined by each method and their trend with different heating rates are presented and discussed in this section. Figure 3-13 shows *E* of NFR-SB-31 for the three repeated experiments calculated using the Arrhenius Plot Method. For the repeatability study, the standard deviation as percentage of the average is included for each set of three repetitions. A larger spread is noted in the experiments with higher heating rates, 20 and 60 °C/min. Over different heating rates, *E* of the second reaction is consistently higher than the first reaction, ranging between 209 – 292 kJ/mol compared to 142 – 186 kJ/mol.

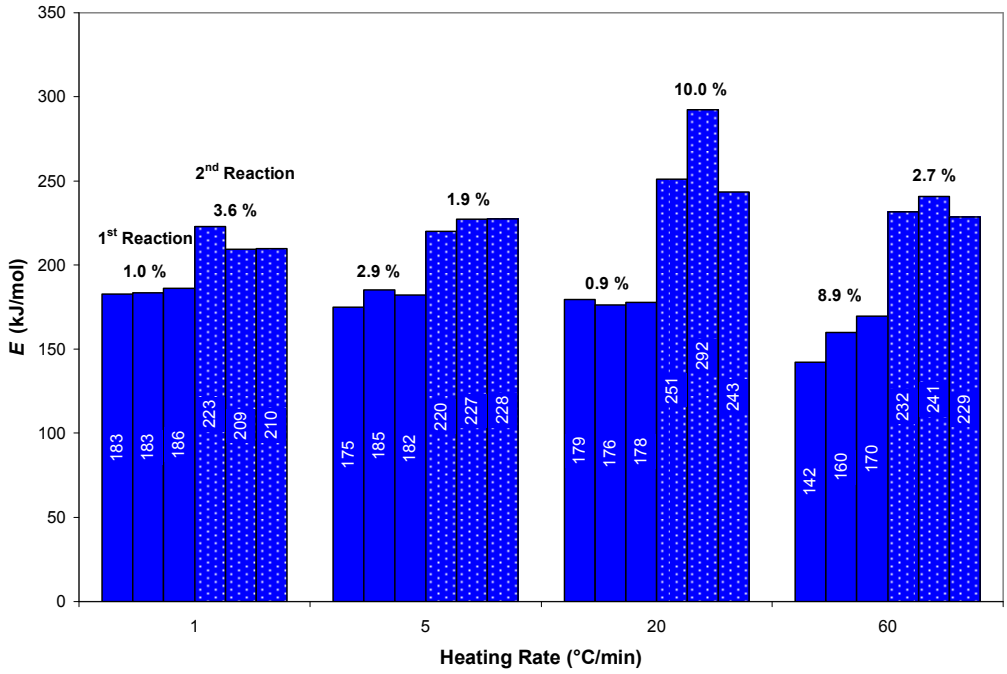

Figure 3-13: *E* of NFR-SB-31 from Arrhenius Plot Method

Since A relates to E through the natural logarithm, ln(A) of NFR-SB-31 from the Arrhenius Plot Method are shown in Figure 3-14. The trend and standard deviation of ln(A) is similar to those seen in E because within the Arrhenius equation, E and A function as a pair to model the temperature dependent aspect of the decomposition. From all the graphical techniques used, E is determined from the slope of the relationship between the rate and temperature while A is found from its y-intercept. The TGA results also shows a consistent decomposition behaviour over different heating rates thus in order to model this, any increase in E is matched by an appropriate increase in A. This trend is known as the kinetic compensation effect[47] and it is seen in all the parameters calculated. Since E and ln(A) share a similar trend, the subsequent discussions will focus solely on E.

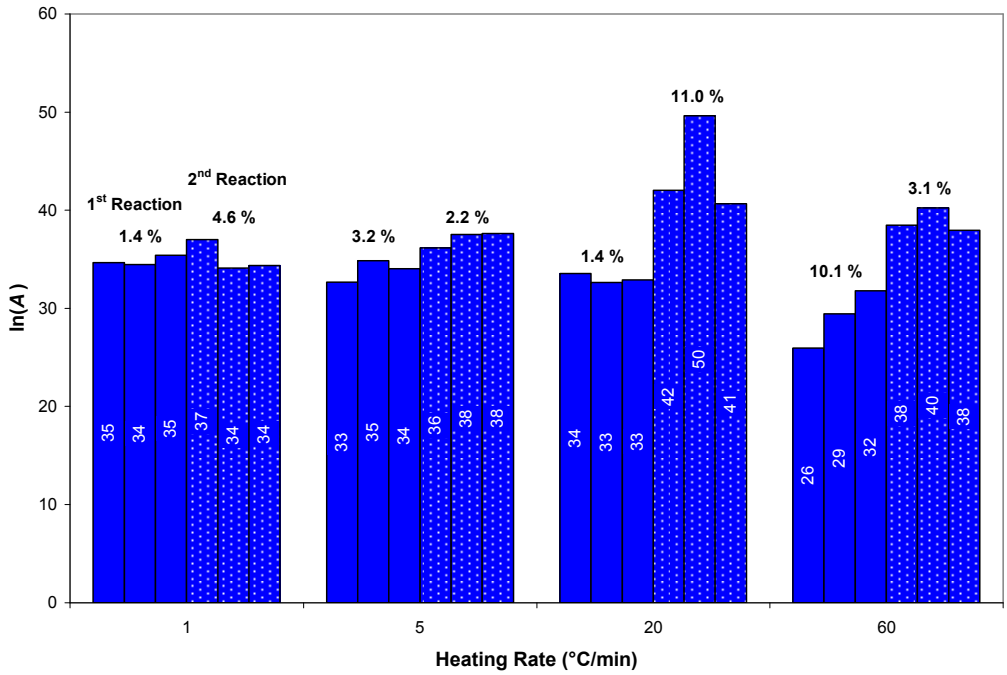

Figure 3-14: ln(A) of NFR-SB-31 from Arrhenius Plot Method

Figure 3-15 shows *E* of NFR-SB-31 determined using the Inflection Point Methods and they are different than those from the Arrhenius Plot Method. Nevertheless, the common trend where *E* of the second reaction is larger than the first reaction is still observed. The parameter has a greater deviation at the lowest and highest heating rates, 1 and 60 °C/min and also for the second reaction in comparison with the first reaction.

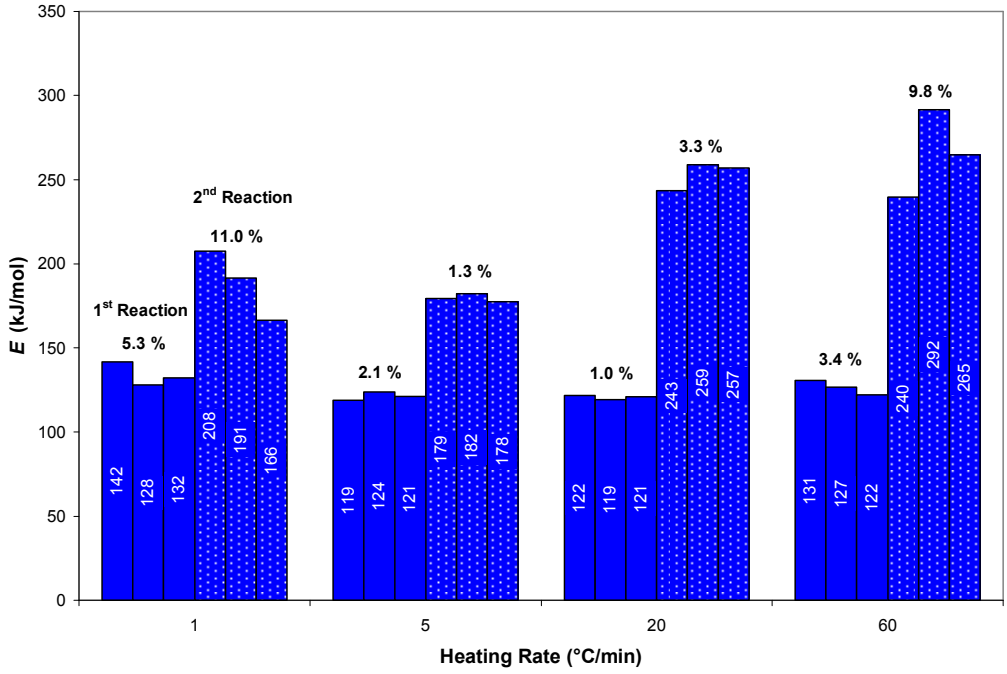

Figure 3-15: *E* of NFR-SB-31 from Inflection Point Methods

From Figure 3-16, the application of the Inflection Point Methods with normalised kinetic model on the TGA results has the effect of reducing *E* and its spread while preserving a trend identical to that with n^{th} order kinetic model.

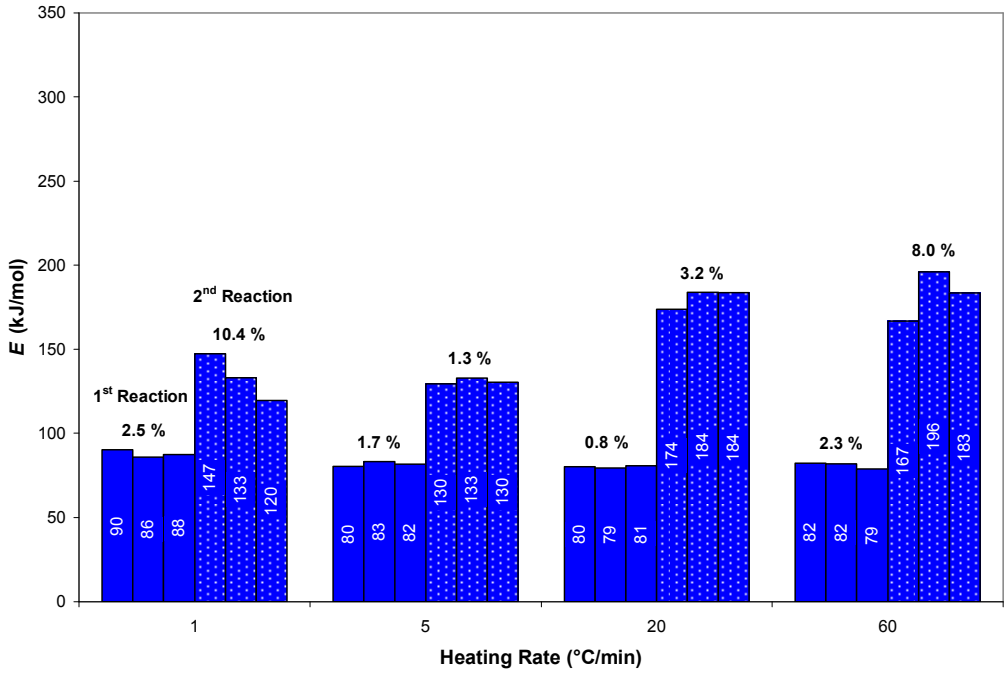

Figure 3-16: *E* of NFR-SB-31 from Inflection Point Methods with normalised kinetic model

Within the literature, the temperature dependent aspect of decomposition has been frequently described using the Arrhenius equation but the mass dependent aspect has been modelled by various types of kinetic model and the n^{th} order model used is one of many. In this study, the Inflection Point Methods calculate *n* for each experiment while Kinetic Analysis calculates the global *n* which is then applied in the Arrhenius Plot Method. Figure 3-17 shows *n* of NFR-SB-31 determined using the Inflection Point Methods. At each heating rate, *n* from the first reaction is consistently greater than the second reaction, ranging from 6.09 – 8.13 compared with 0.89 – 1.45. According to the percentage deviation, the data spread appears greater at the lowest and highest heating rates, 1 and 60 °C/min. In terms of absolute value, the deviation in the first reaction is greater than the second reaction.

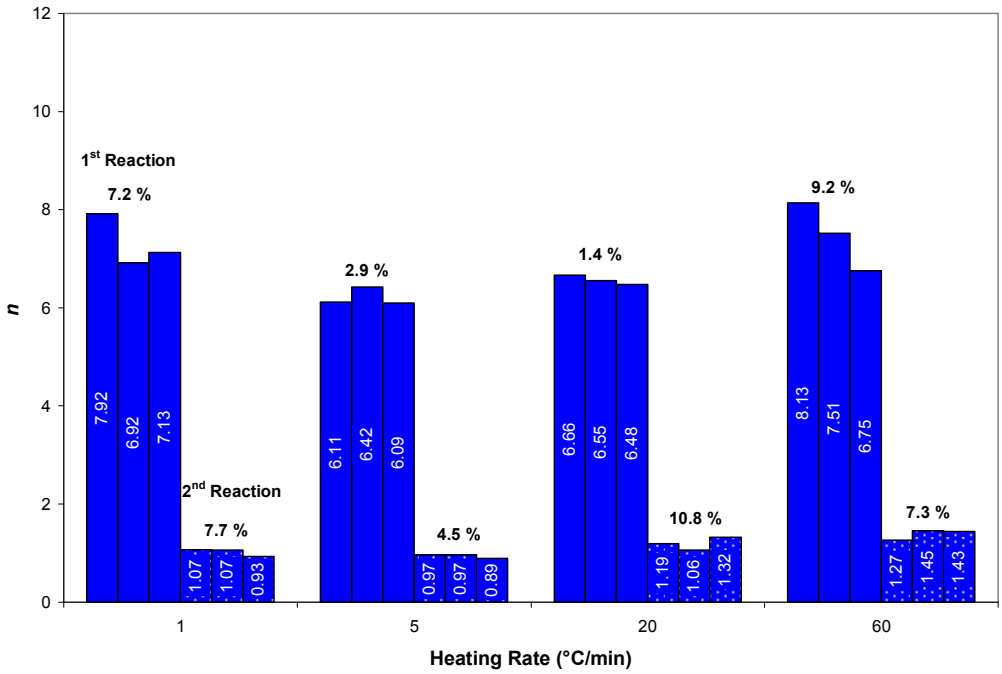

Figure 3-17: *n* of NFR-SB-31 from Inflection Point Methods

Thus far, the individual kinetic properties of NFR-SB-31 are presented and since FR-Y-36 shows a similar trend, its individual results are not repeated. For the comparison between different graphical techniques, Figure 3-18 shows the average *E* of NFR-SB-31 and FR-Y-36 calculated by each approach. The reported values are taken as the average over 1, 5, 20 and 60 °C/min. The values from the literature, reported by Chao et al.[23] on NFR and FR foams are also included in Figure 3-18 and the heating rates tested are 5, 10 and 20 °C/min.

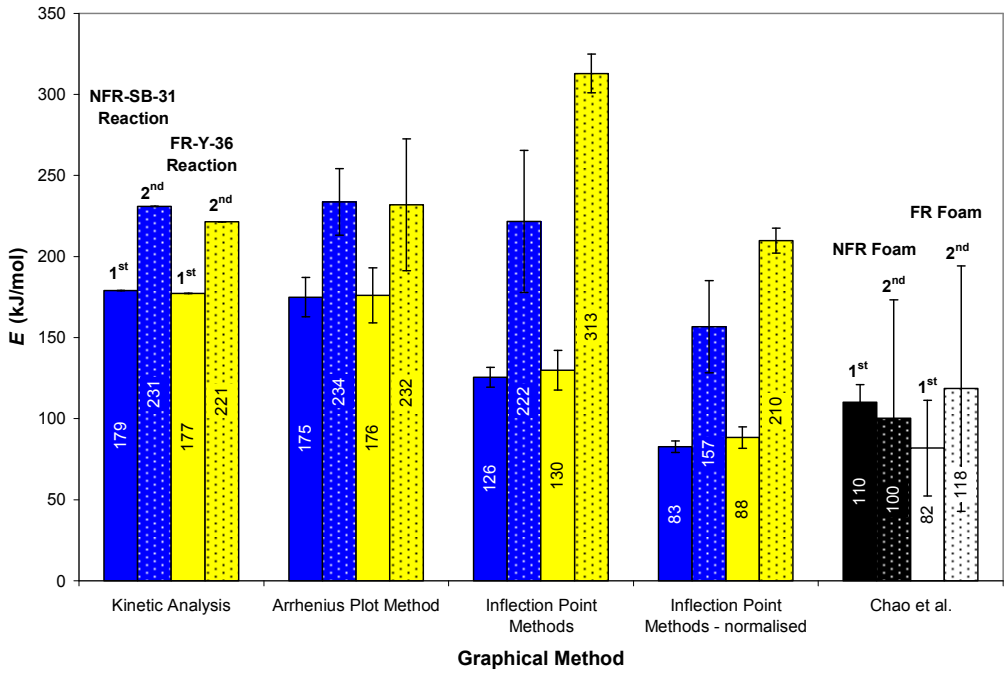

Figure 3-18: Comparison of average *E* of NFR-SB-31 and FR-Y-36 from different graphical techniques and values reported in the literature

The global values from Kinetic Analysis fall within one standard deviation of the average values from the Arrhenius Plot Method as the latter utilises the global *n* and also the similar analysis regions as Kinetic Analysis when calculating the kinetic properties. Due to the difference in the calculation method applied and also in the region analysed, the values from the Inflection Point Methods are different than those of Kinetic Analysis and the Arrhenius Plot Method. Nevertheless, these differences are similar to the variation reported by Matala et al.[50] in their assessment on the performance of different analytical methods for evaluating kinetic properties. Comparing between the original and normalised Inflection Point Methods, the normalised version resulted in lower *E*. Despite the differences in value, the overall trend between both foams is consistent for the different graphical techniques considered whereby the second reaction has higher *E*. In terms of spread, the standard deviation indicates the second reaction has the greater variation with respect to the changes in heating rate.

The effort to make a thorough comparison with the kinetic properties within the literature is complicated by the different methodologies and different polyurethane

foams used by different research. When compared with the *E* from Chao et al.[23], the trend observed is different where no distinct variation is noted between the *E* of the first and second reactions of Chao et al.. The analysis in this research is performed over a wider range of heating rates from 1 to 60 °C/min while the heating rate in Chao et al. ranges from 5 to 20 °C/min. Despite having a greater range of heating rate, the deviation in *E* determined in this research is smaller.

The average ln(*A*) of NFR-SB-31 and FR-Y-36 calculated from all graphical techniques are plotted in Figure 3-19. Since *E* and *A* function as pairs, the average ln(*A*) share a same trend as the average *E* in Figure 3-18. Again comparing with Chao et al.[23], a different trend in ln(*A*) is noted and the deviation determined by Chao et al. is greater compared to those found in this research.

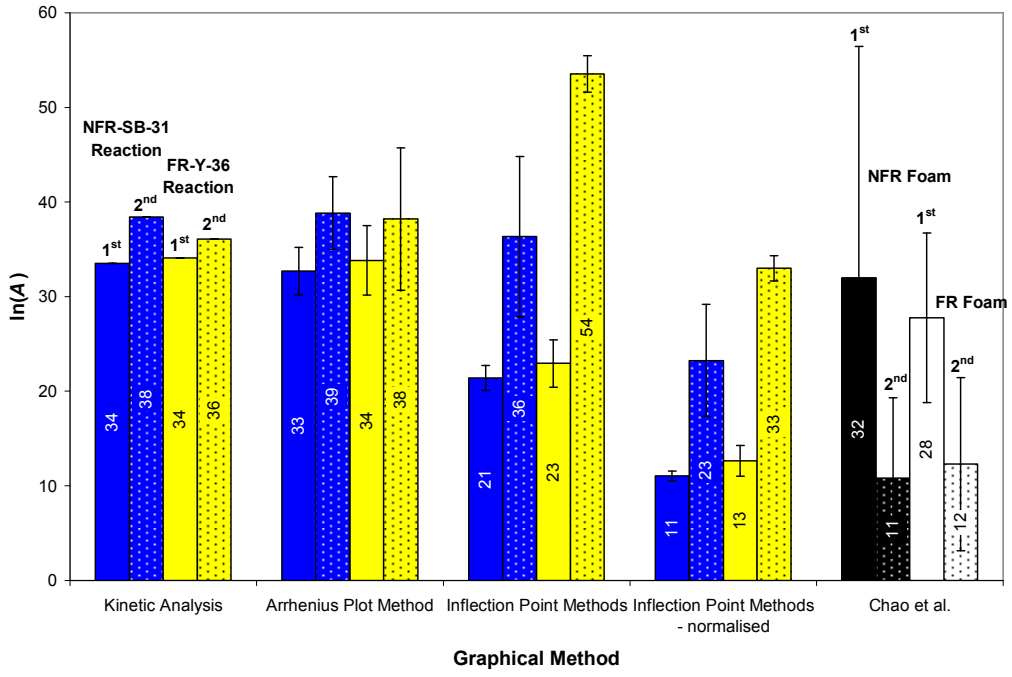

Figure 3-19: Comparison of average ln(*A*) of NFR-SB-31 and FR-Y-36 from different graphical techniques and values reported in the literature

Figure 3-20 shows the global *n* from Kinetic Analysis and the average *n* from the Inflection Point Methods. Although different values are obtained due to the application of different calculating methods, the trend between both methods remains identical where the first reaction has greater *n*. Over different heating rates, both foams show the spread of value among the first reaction is greater than the second

reaction. The magnitude and deviation of *n* obtained by Chao et al.[23] are greater than those reported in this research. Previously, the trend of *E* and ln(*A*) from Chao et al. differs from this research but for *n*, the trend is noted to be similar.

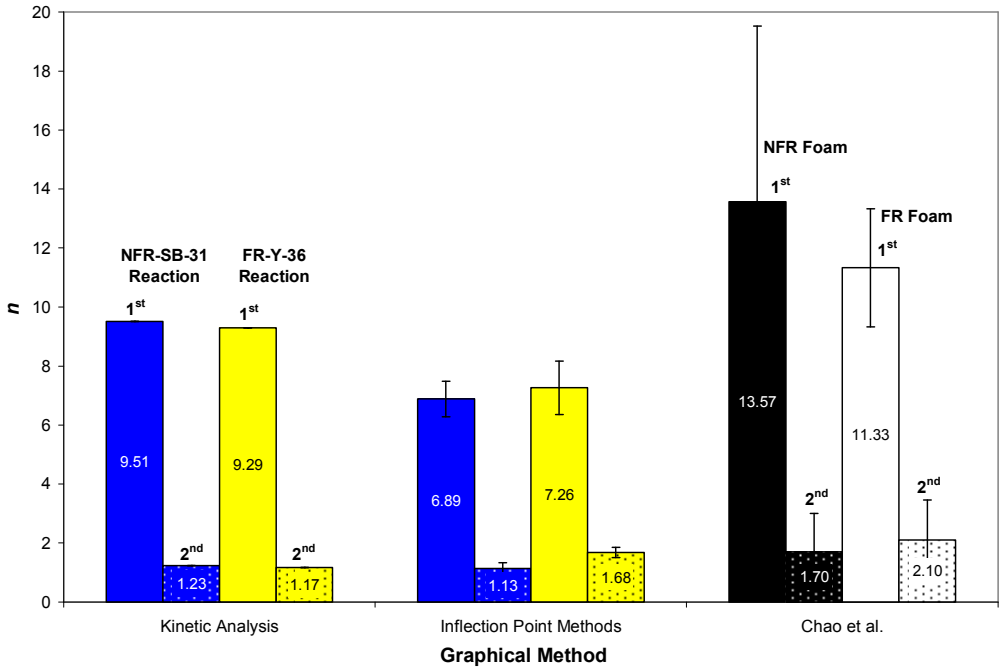

Figure 3-20: Comparison of average *n* of NFR-SB-31 and FR-Y-36 from different graphical techniques and values reported in the literature

Table 3-3 provides a summary of the kinetic properties of the polyurethane foams calculated via the graphical techniques discussed previously. The different relationships involved in estimating these properties have shown correlations with an average R-squared value ranging between 0.95 – 1.00. In Table 3-3, 'Average' denotes the average value over all heating rates and also the global value determined by Kinetic Analysis.

Table 3-3: Kinetic properties of NFR-SB-31 and FR-Y-36 developed using graphical techniques

Foam	Method	Parameter	1st Reaction					2nd Reaction				
			β=1	β =5	β =20	β =60	Average	β =1	β =5	β =20	β =60	Average
NFR-SB-31	Kinetic Analysis	E (kJ/mol)	N/A	N/A	N/A	N/A	179	N/A	N/A	N/A	N/A	231
		A (s^{-1})	N/A	N/A	N/A	N/A	3.61×10^{14}	N/A	N/A	N/A	N/A	4.72×10^{16}
		n	N/A	N/A	N/A	N/A	9.51	N/A	N/A	N/A	N/A	1.23
	Arrhenius Plot Method	E (kJ/mol)	184	181	178	157	175	214	225	262	234	234
		A (s^{-1})	1.35×10^{15}	4.96×10^{14}	2.20×10^{14}	4.17×10^{12}	1.57×10^{14}	1.86×10^{15}	1.28×10^{16}	1.41×10^{19}	7.73×10^{16}	7.15×10^{16}
		n	9.51	9.51	9.51	9.51	9.51	1.23	1.23	1.23	1.23	1.23
	Inflection Point Methods	E (kJ/mol)	134	121	121	127	126	188	180	253	265	222
		A (s^{-1})	7.91×10^{9}	5.80×10^{8}	7.38×10^{8}	4.76×10^{9}	2.00×10^{9}	9.64×10^{12}	1.84×10^{12}	2.61×10^{18}	2.75×10^{19}	5.97×10^{15}
		n	7.32	6.21	6.56	7.47	6.89	1.02	0.94	1.19	1.38	1.13
	Inflection Point Methods – normalised	E (kJ/mol)	88	82	80	81	83	133	131	180	182	157
		A (s^{-1})	6.83×10^{4}	3.62×10^{4}	4.93×10^{4}	1.21×10^{5}	6.21×10^{4}	7.17×10^{7}	7.69×10^{7}	1.55×10^{12}	2.84×10^{12}	1.25×10^{10}
		n	0.00	0.00	0.00	0.00	0.00	0.00	0.00	0.00	0.00	0.00
FR-Y-36	Kinetic Analysis	E (kJ/mol)	N/A	N/A	N/A	N/A	177	N/A	N/A	N/A	N/A	221
		A (s^{-1})	N/A	N/A	N/A	N/A	6.34×10^{14}	N/A	N/A	N/A	N/A	4.69×10^{15}
		n	N/A	N/A	N/A	N/A	9.29	N/A	N/A	N/A	N/A	1.17
	Arrhenius Plot Method	E (kJ/mol)	172	184	194	154	176	265	262	222	178	232
		A (s^{-1})	1.86×10^{14}	2.88×10^{15}	2.32×10^{16}	4.85×10^{12}	4.95×10^{14}	2.20×10^{19}	9.14×10^{18}	4.89×10^{15}	2.24×10^{12}	3.85×10^{16}
		n	9.29	9.29	9.29	9.29	9.29	1.17	1.17	1.17	1.17	1.17
	Inflection Point Methods	E (kJ/mol)	130	137	140	113	130	310	302	310	330	313
		A (s^{-1})	4.77×10^{9}	4.02×10^{10}	1.04×10^{11}	3.75×10^{8}	9.29×10^{9}	1.94×10^{23}	2.48×10^{22}	8.39×10^{22}	2.46×10^{24}	1.77×10^{23}
		n	6.58	6.45	7.66	8.37	7.26	1.59	1.52	1.73	1.91	1.68
	Inflection Point Methods – normalised	E (kJ/mol)	85	93	95	81	88	220	211	202	207	210
		A (s^{-1})	4.97×10^{4}	6.17×10^{5}	2.01×10^{6}	1.45×10^{5}	3.08×10^{5}	1.21×10^{15}	2.38×10^{14}	4.90×10^{13}	1.48×10^{14}	2.14×10^{14}
		n	0.00	0.00	0.00	0.00	0.00	0.00	0.00	0.00	0.00	0.00

The graphical techniques presented in this chapter are applicable to reactions that do not overlap. However, these methods will struggle to produce meaningful properties for the reactions that are not separable and have closely spaced peaks such as during foam decomposition in air where the additional oxidative reactions overlap with the pyrolysis reactions. In this case, the kinetic properties evaluated are expected to be different than those in nitrogen.

Table 3-4 provides a short description regarding the type of kinetic properties, the selection of data points for analysis and the compatibility with pyrolysis model for each of the method described in this chapter.

Table 3-4: Summary on the features of Kinetic Analysis, Arrhenius Plot Method and Inflection Point Methods

Method	Kinetic Analysis	Arrhenius Plot Method	Inflection Point Methods
Type of kinetic properties	Global	Individual	Individual
Selection of data points for analysis	Discrete sample mass fractions, W/W_0	Continuous W/W_0 and the range as defined in Kinetic Analysis	Continuous leading slope of decomposition rate curve
Compatibility with pyrolysis model	Temperature and mass dependent scheme	Temperature and mass dependent scheme	Temperature and mass dependent scheme Temperature dependent scheme (for normalised version)

Kinetic Analysis produces a set of global properties for the range of heating rates analysed while the Arrhenius Plot Method and the Inflection Point Methods calculate properties for each experiment. Kinetic Analysis utilises discrete W/W_0 in terms of selecting data points for analysis. The Arrhenius Plot Method and the Inflection Point Methods on the other hand use a continuous range of data points. The former uses continuous W/W_0 which range is defined in Kinetic Analysis and the latter analyses the leading slope of the decomposition rate curve. As mentioned previously, the compatibility of the kinetic properties found depends on the pyrolysis model and the decomposition scheme selected. From the equations discussed, the properties from all three methods are suitable for the pyrolysis model which is both temperature and mass dependent. However, properties from the normalised version of the Inflection Point Methods are more suited to the pyrolysis model which is temperature dependent only.

3.7 Conclusions

From the repeated TGA experiments of the base case NFR and FR polyurethane foams, the mass loss and mass loss/°C show good repeatability at heating rates from 1 to 60 °C/min. Consistent with the literature, the results show the foam decomposition under nitrogen environment occurs via two primary reactions with the second reaction consuming the majority of the fuel. Three graphical techniques compatible with the pyrolysis model in FDS 5 and Gpyro are used to estimate the kinetic properties governing the foam decomposition. These approaches are Kinetic Analysis, the Arrhenius Plot Method and the Inflection Point Methods. The constants of the Arrhenius equation, E and A are evaluated in all the methods while n is only calculated in Kinetic Analysis and the Inflection Point Methods as the Arrhenius Plot Method uses the global n from Kinetic Analysis.

The flexibility of the pyrolysis model of FDS 5 and Gpyro allows the user to design various decomposition schemes. The kinetic properties evaluated from the original graphical techniques are suitable for the complex schemes. These schemes involve the production of fuel gas and also solid residue or have non-reacting material components during the decomposition. However, the simplest scheme involves the solid fuel converting entirely into fuel gas and this causes n to become a redundant kinetic parameter. From the perspective of developing kinetic properties, this simplifies the original Inflection Point Methods where the mass dependent kinetic model is normalised by setting $n = 0$. In this normalised version, the decomposition rate becomes solely temperature dependent. Therefore, despite achieving the compatibility between the graphical techniques and the pyrolysis model, the suitability of the calculated kinetic properties also depends on the type of decomposition schemes adopted within the pyrolysis model. Chapter 8 will address the suitability of these properties via their application in the FDS 5 pyrolysis model.

The calculated kinetic properties for each experiment under the same method are repeatable but the deviation has been observed to increase especially at the two

extreme heating rates of 1 and 60 °C/min used in this research and also for the properties with greater magnitude, for instance, *E* of the second reaction with a greater magnitude has larger deviation than *E* of the first reaction with a smaller magnitude. When the different methods are used, the calculated parameters are noted to be different. However, the general trend for the first and second reactions is consistent among all methods, whereby *E* and *A* of the first reaction are 10 to 60 % smaller in magnitude than the second reaction and *n* of the first reaction has magnitude between 400 to 800 % greater than the second reaction. Comparing with the literature, the kinetic properties developed for polyurethane foam in this research show better consistency and have smaller deviation over a greater range of heating rates tested. Chapter 8 will utilise the range of kinetic properties found as the search boundaries of Gpyro's genetic algorithm in finding the optimal inputs for FDS 5 modelling.

Chapter 4. Decomposition Behaviours and Kinetic Properties of Polyurethane Foams

4.1 Introduction

From the literature[22,23,25], the decomposition of polyurethane foam in nitrogen environment and in air environment have been reported. Figure 4-1 shows the mass loss rates or the differential thermogravimetric (DTG) curves for a type of fire retardant foam during the thermogravimetric analysis (TGA) experiments reported by Chao et al.[23]. The experiments were carried out at three different heating rates, 5, 10 and 20 °C/min and under two separate environments, nitrogen and air.

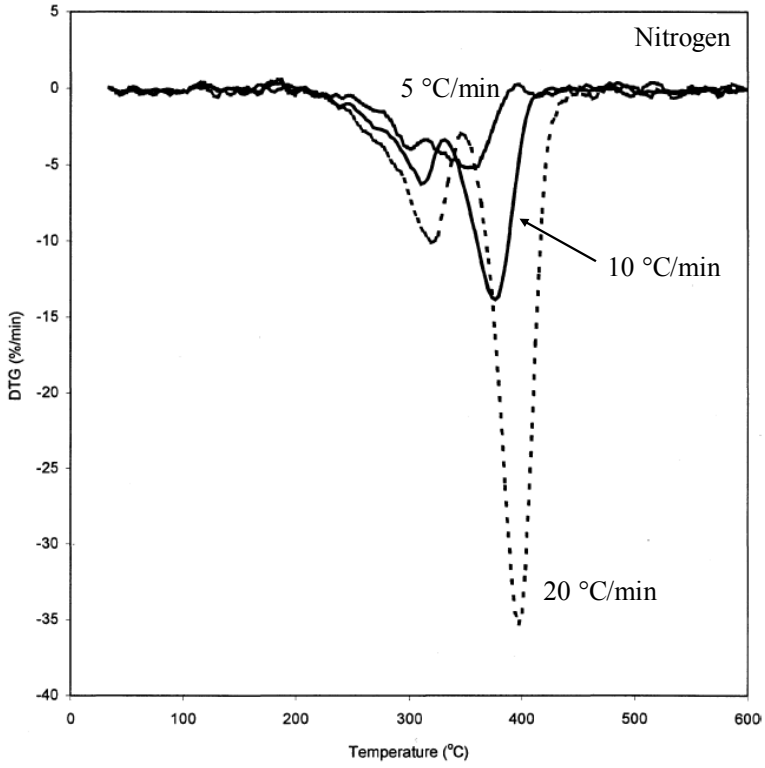

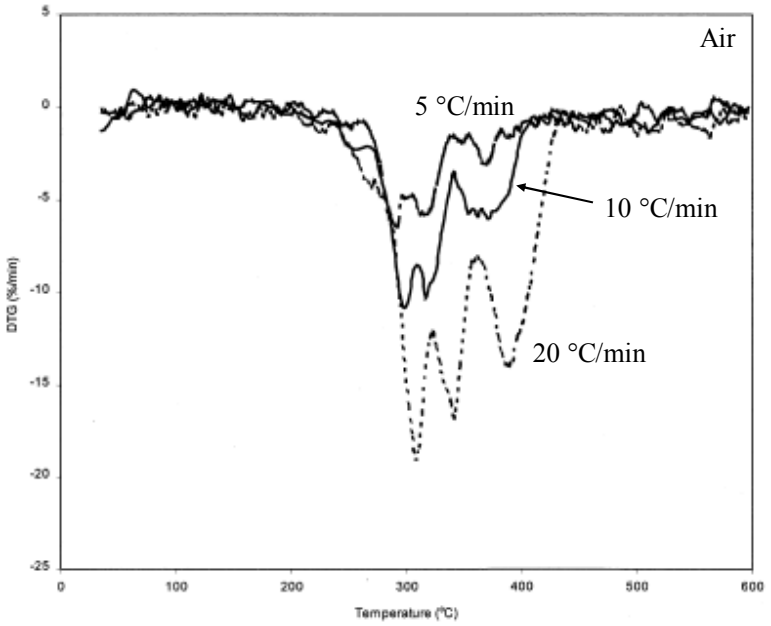

Figure 4-1: TGA mass loss rate of fire retardant polyurethane foam in nitrogen and air environments[23]

Comparing the TGA results from nitrogen with that from air, the decomposition behaviour is noted to have changed. Under nitrogen, two decomposition peaks are noted where the first peak has a smaller magnitude compared to the second peak. The decomposition behaviours under air are different to nitrogen, three decomposition peaks are noted and the magnitude is found to decrease from the first peak to the last peak.

The decomposition of polyurethane foam under nitrogen environment and air environment is described by Valencia[25]. Under nitrogen, the decomposition can be represented by two reactions as followed.

First reaction: Polyurethane foam → Melts + Gases
Second reaction: Melts → Char + Gases

The first reaction involves the breakdown of polyurethane foam into melts and gases, reportedly occurring between 200 and 340 °C. The second reaction involves the further decomposition of melts produced by the first reaction into mostly gases with small amount of char residue as solid product. The temperature range of the second

reaction is between 340 and 450 °C. These temperatures reported should be considered as nominal values because from Figure 4-1, the range of decomposition temperature is noted to increase with greater heating rate applied.

Under air, the decomposition becomes more complex with the additional oxidative reactions and it can be represented by five reactions described as followed.

First pyrolysis reaction:	Polyurethane foam → Melts + Gases
Second oxidative reaction:	Polyurethane foam + Oxygen → Char + Gases
Third oxidative reaction:	Melts + Oxygen → Char + Gases
Fourth pyrolysis reaction:	Melts → Char + Gases
Fifth oxidative reaction:	Char + Oxygen → Gases

The second oxidative reaction occurs between 200 and 275 °C, the third oxidative reaction occurs between 220 and 300 °C and the fifth oxidative reaction occurs between 300 and 450 °C. The second and third oxidative reactions compete for the same reactants as the pyrolysis reactions and also over similar temperature range. This explains the lack of separation between the decomposition peaks in air due to the overlapping of reactions.

As the continuation of Chapter 3 which has been published in a peer reviewed journal[51], this chapter investigates the decomposition behaviours of seven polyurethane foams and their melts experimentally and obtains the kinetic properties governing the decomposition. The general descriptions of these foams are presented in Chapter 2. As listed in Table 2-1, three non-fire retardant (NFR) and four fire retardant (FR) foams are tested at different heating rates in the TGA experiments. The NFR foams tested are NFR-SB-31, NFR-DG-42 and NFR-C-19 while the FR foams tested are FR-Y-36, FR-LG-38, FR-W-50 and FR-G-32. NFR-SB-31 and FR-Y-36 are the base case foams of this research which are tested more extensively than the others.

The governing kinetic properties are established from the TGA results through the application of four graphical techniques. The decomposition behaviours and the

kinetic properties of the base case foams have already been described in Chapter 3 in a nitrogen environment and are tested again in this chapter in the nitrogen environment and the air environment with the expanded collection of foams. These kinetic properties developed are eventually used as the model inputs of Fire Dynamics Simulator, Version 5[17] (FDS 5[a]) and also as the benchmark for the search boundaries of Gpyro's genetic algorithm[27] which is used to optimise the FDS 5 inputs, specifically the kinetic properties. Chapter 3 only investigates the foam decomposition at a constant sample size but in this chapter, the investigation is expanded to include different sample sizes.

4.2 Decomposition Behaviours of Polyurethane Foams in Nitrogen Environment

The foam samples are prepared by shredding a larger piece of foam specimen into fine fragments which are transferred into the 90 μL alumina cup. During the TGA experiments, the purge gas used is nitrogen delivered at a rate of 100 ml/min. More details on the mass calibration for TGA experiment and the experimental procedure are provided in Section 3.3 of Chapter 3. The following sections describe the sensitivity of the foam decomposition to heating rate and sample size. The range of decomposition temperature for the first and second reactions and their mass fractions are also discussed.

4.2.1 Sensitivity of Polyurethane Foam Decomposition to Heating Rate

The nominal sample mass is 3 mg and the different heating rates tested are 1, 5, 20 and 60 °C/min. As mentioned before in Section 3.3, the chosen range of heating rate is based on the temperature variation of a polyurethane foam smouldering front[19] and it is also less than the maximum allowable limit of the equipment. From Chapter 3, the repeated TGA experiments showed good repeatability under similar experimental conditions so for this chapter, only a single replicate is tested. Figure 4-2 shows the changes in sample mass with temperature for all the polyurethane foams tested at 1, 5,

[a] Version 5.5.3, SVN number 7031.

20 and 60 °C/min. Each foam is represented by a colour scheme as depicted below and this set of identification is applied throughout this thesis for illustrations containing these different polyurethane foams.

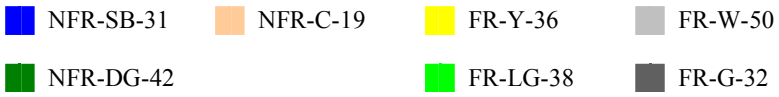

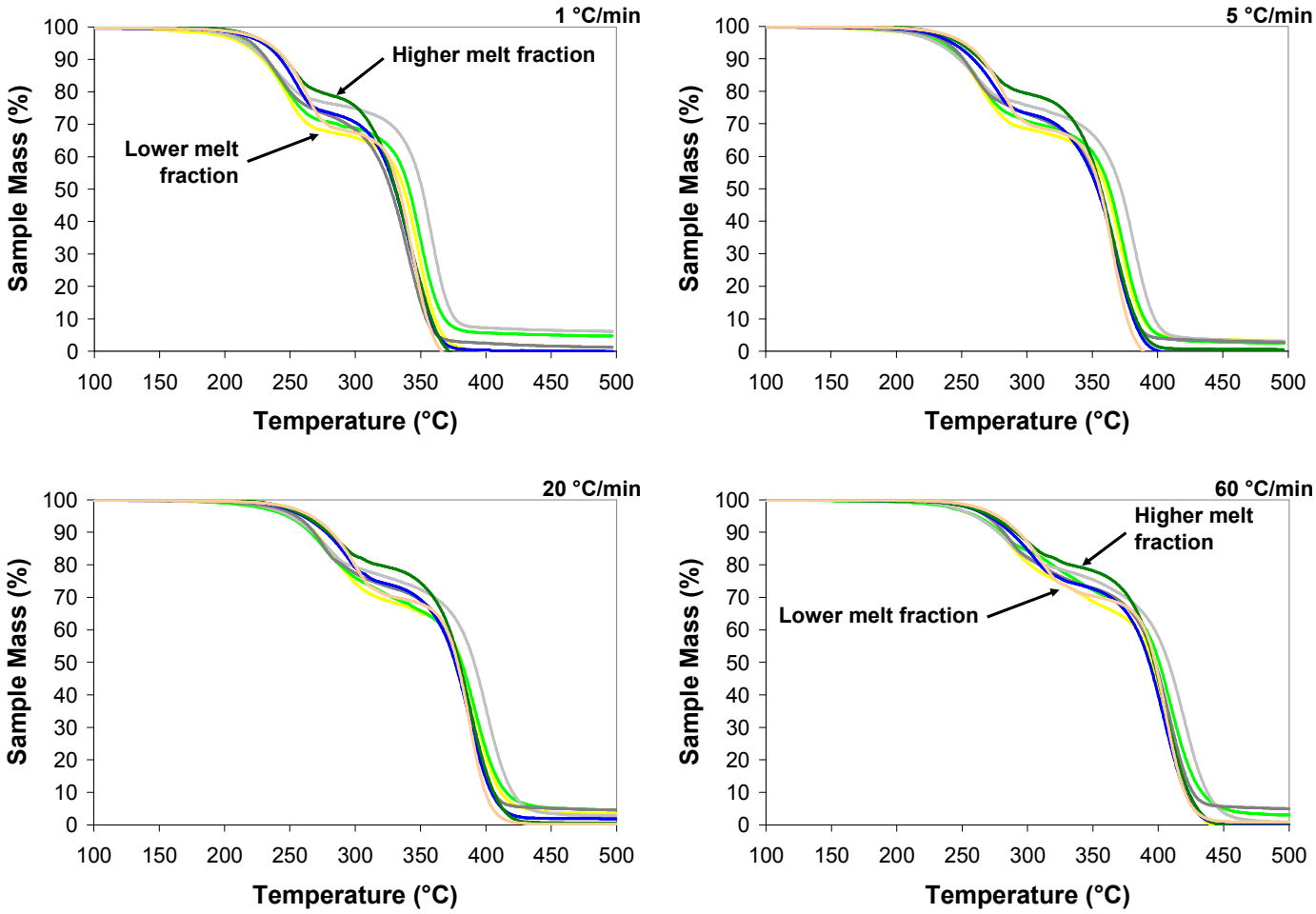

Figure 4-2: Sample mass versus temperature of ~3 mg polyurethane foams at 1, 5, 20 and 60 °C/min heating rates under nitrogen environment

Similar to the trend seen in the literature[22,23,25], the results show that the decomposition of polyurethane foam proceeds via two reactions with significant mass loss. In between the two reactions is a transition region where the mass loss is comparatively smaller. As the heating rate increases, the decomposition is found to shift towards higher temperature range. This is due to the thermal lag which exists between the sample and the thermocouple in the experiment and also the phenomenon known as heat hysteresis as suggested by Chao et al.[23]. These general trends are found to be similar to those reported previously in Chapter 3 on the base case foams.

According to the proposed decomposition reactions by Valencia[25], the completion of the first reaction means the original foam structure has completely collapsed into melts. This remaining mass fraction of the sample also known as the melt fraction becomes the fuel for the second reaction. For each heating rate, the results in Figure 4-2 collectively show that the polyurethane foams tested possess a varying range of melt fraction. Despite the variation, the polyurethane foams can be categorised into three groups according to their similarity in melt fraction. The first group is the foams with melt fraction nominally equal or greater than 80 % and this includes NFR-DG-42 and FR-W-50. The second group is the foams with melt fraction nominally between 75 and 80 % and this includes NFR-SB-31 and FR-G-32. The last group is for the foams with melt fraction nominally equal or less than 75 % which includes NFR-C-19, FR-Y-36 and FR-LG-38. Most of the foams show an increase in the melt fraction on the order of 3 to 5 % as the heating rate increases from 1 to 60 °C/min. However, a few foams are found to display different trends. FR-G-32 shows a constant melt fraction of 75 to 76 % at the different heating rates. FR-Y-36 and FR-LG-38 show a constant melt fraction between 1 and 20 °C/min, 69 to 70 % and 70 to 71 % respectively but at 60 °C/min, the melt fraction increases rapidly, 78 % for FR-Y-36 and 85 % for FR-LG-38.

Including all the heating rates, Table 4-1 shows the decomposition temperature of the polyurethane foams and the mass fraction of the sample consumed during the first reaction, transition and second reaction. The start and end temperatures for each reaction is defined as the temperature where the magnitude of the mass loss rate in %/°C or simply, mass loss/°C is at 10 % of the difference between the minimum and maximum of the specific reaction. The temperature where the peak mass loss/°C occurred for the first and second reactions is also included in brackets. The melt fraction reported earlier is the summation of the mass fraction decomposed during transition and second reaction.

Table 4-1: Decomposition temperature and mass fraction of sample consumed during first reaction, transition and second reaction for ~3 mg polyurethane foams at 1, 5, 20 and 60 °C/min heating rates under nitrogen environment

Foam	β, °C/min	Decomposition temperature and mass fraction decomposed					
		1st Reaction		Transition		2nd Reaction	
		T (T_{pk}), °C	α_1, %	T, °C	α_t, %	T (T_{pk}), °C	α_2, %
NFR-SB-31	1	206-272 (256)	26	272-302	4	302-373 (343)	70
	5	214-294 (276)	26	294-322	4	322-399 (369)	70
	20	229-304 (295)	22	304-345	7	345-420 (388)	71
	60	239-317 (306)	23	317-363	7	363-439 (404)	70
NFR-DG-42	1	201-272 (253)	20	272-297	4	297-376 (340)	76
	5	213-294 (275)	20	294-322	4	322-400 (366)	76
	20	226-301 (292)	17	301-344	7	344-423 (388)	76
	60	235-315 (300)	17	315-363	7	363-442 (404)	76
NFR-C-19	1	212-283 (264)	31	283-316	5	316-373 (343)	64
	5	229-304 (283)	30	304-337	5	337-394 (366)	65
	20	241-323 (301)	29	323-359	5	359-414 (388)	66
	60	248-326 (311)	26	326-378	7	378-435 (406)	67
FR-Y-36	1	193-271 (249)	31	271-317	6	317-377 (348)	63
	5	211-292 (265)	31	292-339	6	339-400 (372)	63
	20	226-318 (282)	30	318-359	6	359-424 (392)	64
	60	226-311 (288)	22	311-377	15	377-446 (409)	63
FR-LG-38	1	191-271 (245)	29	271-316	5	316-377 (349)	66
	5	205-300 (266)	29	300-340	6	340-402 (373)	65
	20	215-329 (277)	30	329-363	7	363-427 (392)	63
	60	221-294 (283)	15	294-377	18	377-449 (409)	67
FR-W-50	1	182-268 (245)	22	268-324	7	324-382 (359)	71
	5	194-280 (263)	22	280-343	9	343-409 (382)	69
	20	213-295 (280)	20	295-361	10	361-434 (400)	70
	60	218-305 (288)	19	305-374	11	374-456 (420)	70
FR-G-32	1	193-265 (241)	25	265-300	7	300-367 (341)	68
	5	215-291 (260)	25	291-329	7	329-394 (366)	68
	20	229-310 (276)	24	310-351	7	351-415 (388)	69
	60	236-332 (287)	25	332-369	6	369-436 (409)	69

Comparing the temperatures of the first reaction, particularly the start and peak temperatures, the FR foams are noted to start decomposing over lower temperature

range than the NFR foams. Comparing the temperatures of the second reaction, FR-Y-36, FR-LG-38 and FR-W-50 are found to decompose over higher temperature range than the rest of the foams. This decomposition pattern of earlier first reaction and later second reaction is associated with the fire retardant mechanisms of the FR foams.

According to the manufacturer, FR-Y-36, FR-LG-38 and FR-W-50 are known to contain halophosphate and melamine ($C_3H_6N_6$) as fire retardant additives while FR-G-32 only has halophosphate. During decomposition, halophosphate breaks down into chlorine and phosphate structure. Halophosphate is predominantly a gas phase fire retardant where the chlorine released is able to form inactive molecules with the highly reactive radicals from foam decomposition thus inhibiting combustion[35]. The remaining phosphate structure creates an acidic environment by forming phosphoric acid[36,37]. Together with the presence of ammonia from the breakdown of melamine[28], they act as catalysts to the decomposition thus allowing FR foams to start decomposing at lower temperature.

Melamine performs in both gas and solid phases. In gas phase, the breakdown of melamine releases inert gases such as ammonia and nitrogen which dilute the combustible gases. In solid phase, melamine is known to react with phosphoric acid[34] and also isocyanate[28] to create thermally stable char. The char produced restricts the release of pyrolysates and this has the impact of delaying the remainder of the decomposition. As a result, the second reaction of foams with melamine such as FR-Y-36, FR-LG-38 and FR-W-50 occurs over higher temperature range than those foams without. The ability of these foams to form char in actual combustion has been witnessed in the Sample Feeding Vertical Cone experiments which is described in further details in Chapter 7. Given the char formation ability of the FR foams containing melamine, the term melt fraction used in this research actually includes both melt and char.

From Table 4-1, the width of the transition region is found to be similar among the NFR foams, nominally ranging from 30 – 50 °C. However, for the FR foams, their transition region is wider, FR-Y-36 and FR-LG-38 show a transition width of 40 – 70 °C and 30 – 80 °C respectively while FR-W-50 has a transition width of 60 – 70 °C.

FR-G-32 show a constant transition width of 40 °C which is greater than the NFR foams at 1 and 5 °C/min but similar or less than the NFR foams at 20 and 60 °C/min. Again, the wider transition region is due to the presence of fire retardant additives and the FR foams with melamine appear to produce the greatest width in transition due to the formation of solid phase char.

From the mass fraction decomposed in the first reaction, α_1, NFR-DG-42 and FR-W-50 show the least mass loss, approximately 20 %. This is followed by NFR-SB-31 and FR-G-32 with ~25 % and NFR-C-19 with ~30 %. FR-Y-36 and FR-LG-38 are special cases where the mass fraction at 1, 5 and 20 °C/min is approximately 30 % but at 60 °C/min, the mass fraction reduces significantly where FR-Y-36 has 22 % and FR-LG-38 has 15 %. The trend reflected by α_1 corresponds directly with the trend of melt fraction discussed previously. During the transition region, the mass fraction decomposed, α_t shows that FR-Y-36, FR-LG-38 and FR-W-50 with char formation ability have mass loss ranging between 5 and 18 % while those foams without have mass loss between 4 and 7 %. Given the widen temperature gap during transition for FR-Y-36, FR-LG-38 and FR-W-50, the mass loss rate would still be considered insignificant despite the greater mass loss recorded. This is proven in the plot of mass loss rate presented later. For the second reaction, the mass fraction decomposed, α_2 shows that NFR-DG-42 has the greatest mass loss of 76 % and this is followed by NFR-SB-31, FR-W-50 and FR-G-32 at ~70 % and NFR-C-19, FR-Y-36 and FR-LG-38 with less than 70 %. In contrast to α_1 and α_t where significant changes with varying heating rate are noted in the cases of FR-Y-36 and FR-LG-38, α_2 has remained fairly consistent at the different heating rates for all foams, changing by 4 % the most.

The major fuel consumption occurs in the second reaction and the FR foams, particularly FR-Y-36 and FR-LG-38 have showed reduced mass loss over this region when compared to the other foams. Both foams also show reduced mass loss for the first reaction when the heating rate reaches 60 °C/min. The reduction of mass loss in the first and second reactions comes at the expense of increase mass loss during the transition region but given the extended temperature gap during transition, the mass loss rate would still be minimal. Similar to FR-Y-36 and FR-LG-38, FR-W-50 also shows extensive transition region but the mass loss is less in comparison. In the first

reaction, FR-W-50 performs well by consistently limiting the mass loss to 20 % but it is not able to match the reduction produced by FR-Y-36 and FR-LG-38 over the second reaction. Thus, given the foam's greater density, the more significant mass loss in the second reaction could be detrimental towards FR-W-50 fire retardant performance. Mainly relying on the performance of gas phase fire retardant, the decomposition of FR-G-32 is not significantly different from the NFR foams. The notable exception is FR-G-32 earlier decomposition temperature during the first reaction. FR-G-32 and the NFR foams are characterised by their low mass loss over the comparatively narrower transition region which indicates the absence of solid phase char formation. Despite the variations in decomposition between the different foams, the general trend where polyurethane foam decomposes through two significant mass loss reactions is still observed which is comparable to the results obtained from Chapter 3 on the base case foams.

Figure 4-3 shows the mass loss/°C versus temperature for all the polyurethane foams tested at 1, 5, 20 and 60 °C/min. The two significant mass loss reactions are seen as the two protuberances on the mass loss/°C plot with the second reaction achieving greater magnitude than the first reaction.

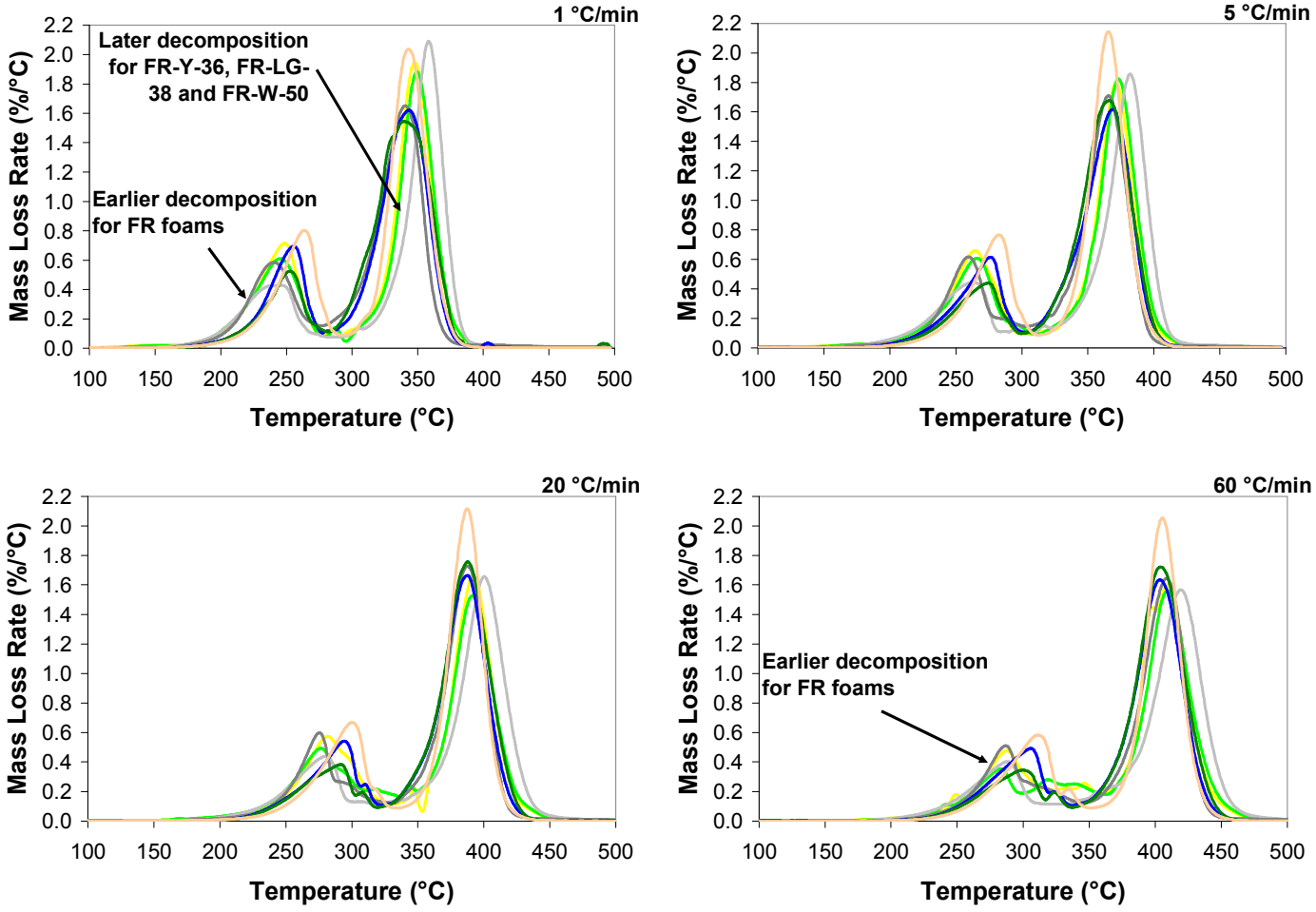

Figure 4-3: Mass loss/°C versus temperature for ~3 mg polyurethane foams at 1, 5, 20 and 60 °C/min heating rates under nitrogen environment

The results in Figure 4-3 reflect the trend described by the decomposition temperatures in Table 4-1 more clearly. For the first reaction, the FR foams consistently start to decompose at an earlier temperature than the NFR foams for all the heating rates tested. As explained before, this is due to the presence of phosphoric acid and ammonia which act as catalysts following the breakdown of halophosphate and melamine. For the second reaction, the FR foams containing melamine, FR-Y-36, FR-LG-38 and FR-W-50 shows a later decomposition compared to the other foams due to the foams' char formation ability.

The displayed trends are more explicit at the low heating rate such as 1 °C/min but as the heating rate increases towards 60 °C/min, the trend becomes less evident. The main mass loss reactions are constituted by many micro reactions occurring over discrete temperature range[52,53] and the high heating rate enables more micro reactions to become involved simultaneously. This is believed to produce a heating rate dependent effect that outweighs the much smaller difference seen between the decomposition of different foams and as a result, the decomposition pattern between the different foams become more closely spaced at high heating rate. Despite being FR foam, due to the absence of char formation mechanisms, the decomposition of FR-G-32 is actually comparable to the NFR foams over the second reaction where the major fuel consumption occurs. FR-G-32 only differs from the NFR foams in the first reaction where it experiences earlier decomposition due to the presence of phosphoric acid which acts as catalyst following the breakdown of halophosphate. Figure 4-4 and 4-5 respectively shows the plot of mass loss/°C for the individual NFR and FR foams. In order to investigate the effect of different heating rates on decomposition, the results at 1, 5, 20 and 60 °C/min are compared.

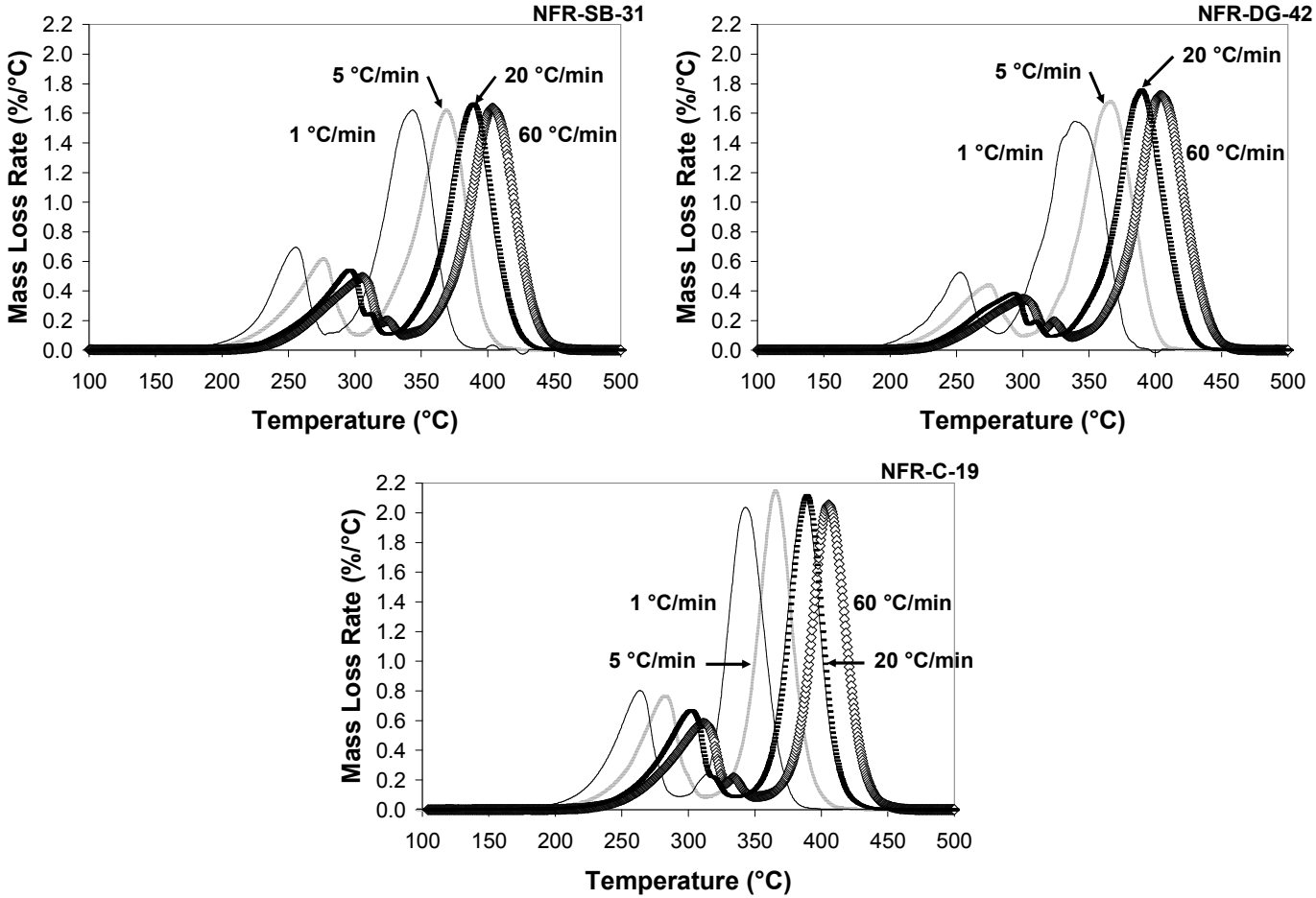

Figure 4-4: Mass loss/°C versus temperature at 1, 5, 20 and 60 °C/min heating rates under nitrogen environment for individual ~3 mg NFR foams

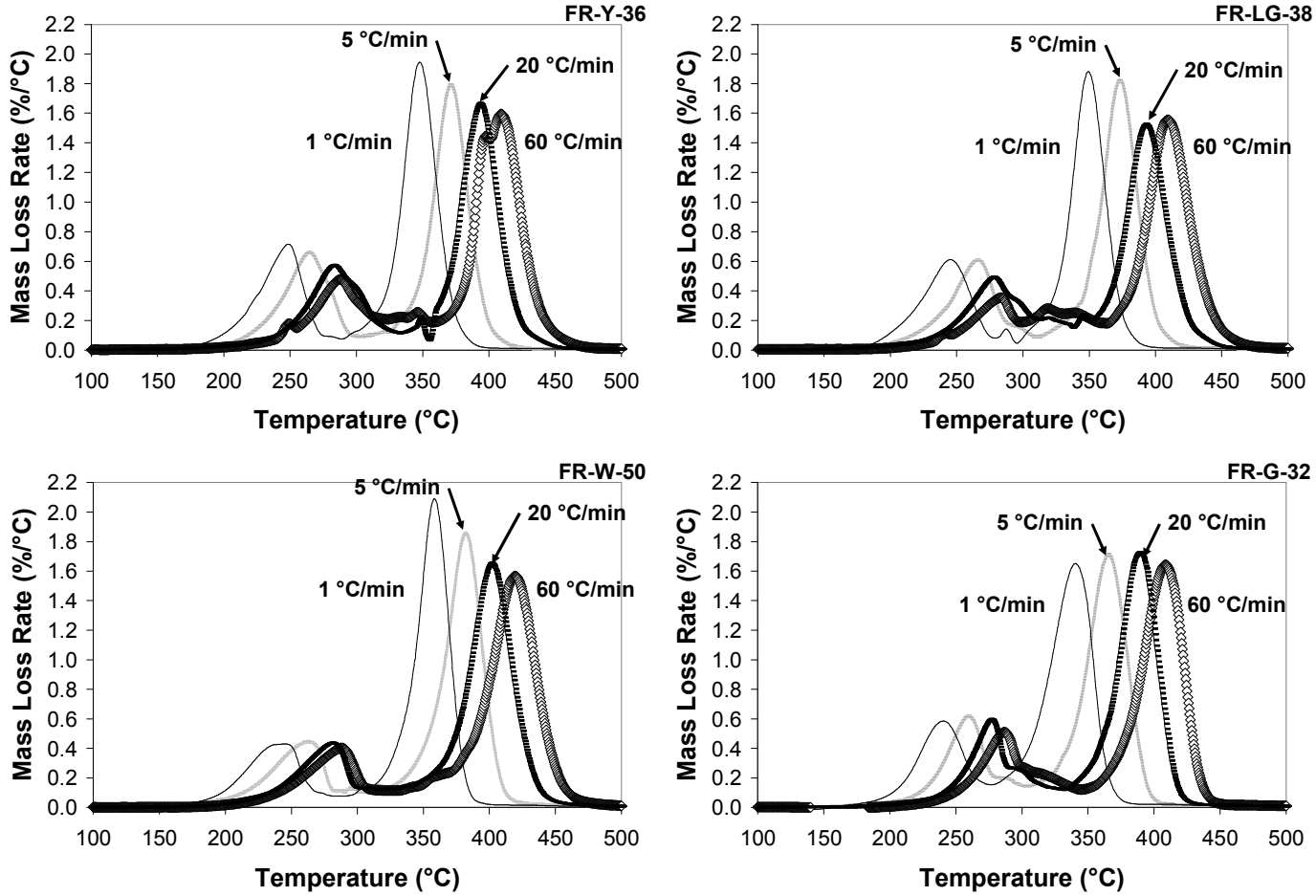

Figure 4-5: Mass loss/°C versus temperature at 1, 5, 20 and 60 °C/min heating rates under nitrogen environment for individual ~3 mg FR foams

For the first reaction, the increase in heating rate generally results in the reduction of peak magnitude in most of the foams with the exception to FR-W-50 and FR-G-32. During the transition region, most of the foams show a constant minimum mass loss rate of ~0.1 %/°C regardless of the change in heating rate. However, for FR-Y-36 and FR-LG-38, this minimum rate is noted to increase with heating rate and by 60 °C/min, it is approximately 0.3 %/°C. This increase in decomposition rate over the transition is caused by the greater mass loss reported previously in Table 4-1. As mentioned earlier, despite the increased mass loss, the extensive transition temperature gap of these FR foams means the decomposition rate over this region is still small compare to the other two reactions. In the second reaction, the increase in heating rate seems to produce a reduction in the peak magnitude of FR-Y-36, FR-LG-38 and FR-W-50 which is caused by the interference from the char formed during the first reaction. The other foams without char formation ability show that the peak magnitude either remains constant or shows slight increase with higher heating rate.

Thus far, there are some distinctive features between the NFR and FR foams tested. The FR foams are noted to possess earlier decomposition temperature of the first reaction, wider transition region, lesser fuel consumed in the second reaction and decreasing peak of the second reaction under increasing heating rate. The earlier decomposition of the FR foams seemingly indicates an inferior fire performance compared to NFR foam. This is not justified because part of the gaseous products formed such as chlorine, ammonia and nitrogen gas can either inhibit combustion or dilute the concentration of the combustible gases. The other features such as widen transition, reduction in fuel consumed and decreasing peak magnitude in the cases of FR-Y-36, FR-LG-38 and FR-W-50 are caused by the char formation. The char developed is thermally stable and it protects the combustible fuel, thereby also slowing the release of gaseous products. As such, these FR foams endure an extended transition where the mass loss is found to be greater than the other foams because the decomposition continues at a minimal rate. This continuous decomposition ensures that the amount of remaining fuel is reduced prior to the second reaction which consumes majority of the fuel. The reducing peak magnitude of the second reaction with increasing heating rate indicates that the process of char formation could be

influenced by heating rate. The aforementioned differences between the NFR and FR foams are found to be similar to those reported for the base case foams in Chapter 3.

4.2.2 Sensitivity of Polyurethane Foam Decomposition to Sample Size

Besides the nominal 3 mg sample, the alumina cup is also filled completely to investigate the effect of different sample sizes on decomposition. The nominal sample mass for a full cup is 10 mg and a single replicate of the sample is tested at heating rate of 5 °C/min. Figure 4-6 and 4-7 shows the plot of mass loss/°C for the individual NFR and FR foams respectively. The results from the 10 mg sample are compared with those from the 3 mg sample.

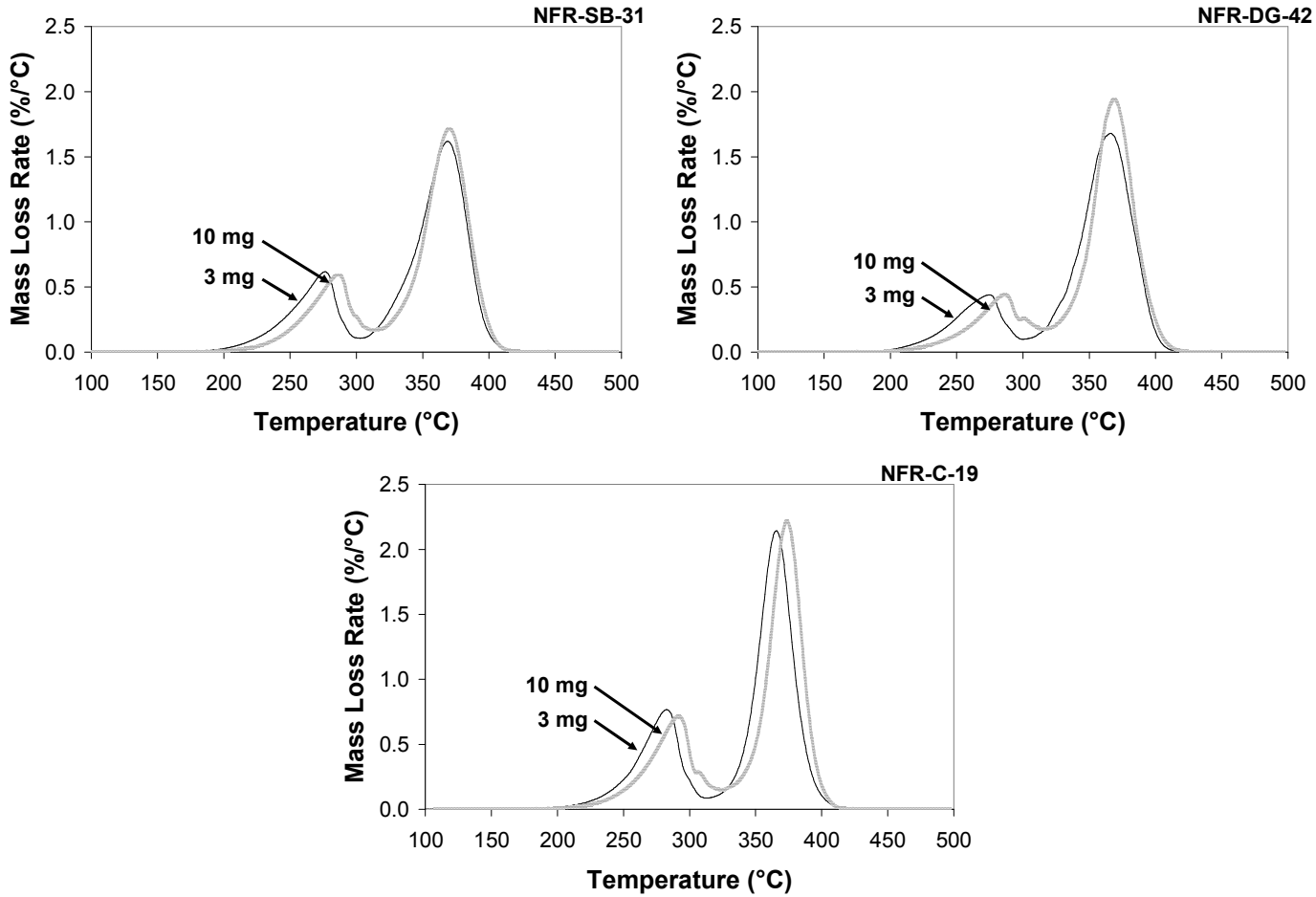

Figure 4-6: Mass loss/°C versus temperature for ~3 and ~10 mg NFR foams at 5 °C/min heating rate under nitrogen environment

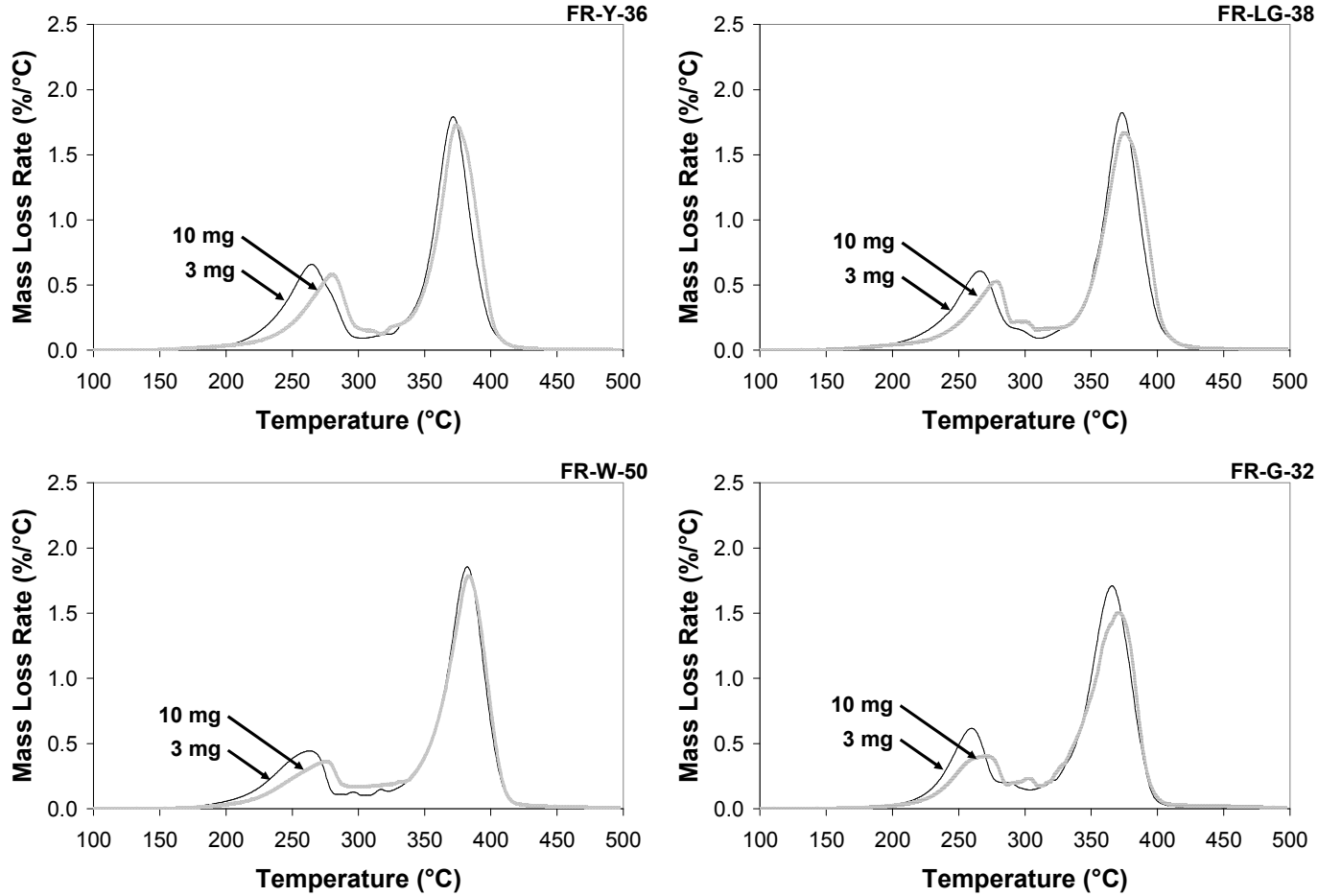

Figure 4-7: Mass loss/°C versus temperature for ~3 and ~10 mg FR foams at 5 °C/min heating rate under nitrogen environment

For all foams, the results consistently show that the 3 mg sample is able to decompose earlier than the 10 mg sample. This is believed to be caused by the higher density of the 10 mg sample which is more densely prepared such that the alumina cup is completely filled. Thus, the greater thermal inertia of the 10 mg sample results in its higher decomposition temperature. On the other hand, the 3 mg sample is loosely prepared such that the alumina cup is only half filled. The porous nature of the foam allows these prepared samples to be compressed differently.

Between the two reactions considered, the difference in decomposition temperature is more apparent in the first reaction where the sample is in the state of foam compared to the second reaction where the sample is in the state of melt. The trend is less apparent for melts because the sample has become a thin layer of non-porous liquid having consistent density. Hence, the thermal inertia of the melts from 3 and 10 mg samples are actually similar. Nevertheless, the melt decomposition temperature for the 10 mg sample is noted to be slightly higher because more melts cover the bottom of the alumina cup while for the 3 mg sample, there are less melts. This effect is also illustrated later in the analysis on the sensitivity of different melt sample sizes. Table 4-2 compares the decomposition temperature and the mass fraction decomposed between the 3 and 10 mg samples. The start and end temperatures are presented as a range and the temperature of the decomposition peak is included in brackets.

Table 4-2: Decomposition temperature and mass fraction of sample consumed during first reaction, transition and second reaction for ~3 and ~10 mg polyurethane foams at 5 °C/min heating rate under nitrogen environment

Foam	Mass, mg	Decomposition temperature and mass fraction decomposed at 5 °C/min					
		1st Reaction		Transition		2nd Reaction	
		T (T_{pk}), °C	α_1, %	T, °C	α_t, %	T (T_{pk}), °C	α_2, %
NFR-SB-31	3	214-294 (276)	26	294-322	4	322-399 (369)	70
	10	231-304 (286)	24	304-334	6	334-401 (370)	70
NFR-DG-42	3	213-294 (275)	20	294-322	4	322-400 (366)	76
	15	227-309 (286)	20	309-336	6	336-402 (369)	74
NFR-C-19	3	229-304 (283)	30	304-337	5	337-394 (366)	65
	11	237-313 (292)	29	313-346	6	346-399 (374)	65
FR-Y-36	3	211-292 (265)	31	292-339	6	339-400 (372)	63
	10	219-300 (280)	25	300-343	7	343-403 (374)	68
FR-LG-38	4	205-300 (266)	29	300-340	6	340-402 (373)	65
	10	213-305 (278)	24	305-343	7	343-405 (375)	69
FR-W-50	4	194-280 (263)	22	280-343	9	343-409 (382)	69

	13	204-288 (275)	17	288-347	12	347-410 (384)	71
FR-G-32	3	215-291 (260)	25	291-329	7	329-394 (366)	68
	12	213-284 (271)	18	284-326	9	326-396 (371)	73

Similar to the mass loss/°C plots, the results in Table 4-2 show that the decomposition temperature is generally higher for the 10 mg sample and this pattern is more apparent over the first reaction. While the 10 mg samples are only tested at 5 °C/min, some of the temperatures are actually noted to be comparable to the values reported at 20 °C/min for the 3 mg sample tested. The values of α_1, α_t and α_2 for NFR foams are generally comparable between the 3 and 10 mg samples, varying 2 % at most. However, for the FR foams, the 10 mg sample has consistently lower α_1 where the difference compared to the 3 mg sample ranges between 5 and 7 %. Oppositely, for α_2, the 10 mg sample is noted to have consistently greater magnitude, by 2 to 5 %. For α_t, the value of the 10 mg sample is slightly greater but the difference is essentially negligible. In conclusion, the increase in sample mass has affected the decomposition of FR foams by reducing the amount of fuel released in the first reaction while increasing the amount of fuel released in the second reaction. Previous sensitivity analysis on the effect of heating rates on decomposition indicates that the char formation of FR foams could be heating rate dependent. Similarly, the mass fraction decomposed in Table 4-2 suggests that the fire retardant mechanisms could also be sample mass dependent.

4.3 Kinetic Properties of Polyurethane Foams in Nitrogen Environment

The kinetic properties developed from the TGA results are intended for use as inputs for the pyrolysis model in FDS 5 which represents the decomposition rate of a material via Equation (3-1)[18] in Chapter 3. From Equation (3-1), the kinetic properties of interest are the activation energy, E, the pre-exponential factor, A and the reaction order, n. Each reaction of the decomposition has one set of E, A and n which are determined by graphical techniques. In this research, the graphical techniques employed are Kinetic Analysis[47], the Arrhenius Plot Method[47], the Inflection Point Methods[49] and the normalised version of Inflection Point Methods. The detailed

differences between these techniques and their respective calculation process are discussed in Chapter 3.

In general, Kinetic Analysis produces a single set of global kinetic properties from the TGA results at multiple heating rates which are included into the analysis. The Arrhenius Plot Method and the Inflection Point Methods produce the kinetic properties for the individual TGA experiment. The analysis regions of the Arrhenius Plot Method are the same as Kinetic Analysis and the technique also utilises the same *n* determined from Kinetic Analysis. The Inflection Point Methods analyse the TGA results over the leading slope of the decomposition rate curve. The normalised version is similar to the original Inflection Point Methods except in the treatment of *n*. In the original Inflection Point Methods, *n* is calculated but in the normalised version, *n* is assumed as zero in order to produce kinetic properties that are representative of specific decomposition schemes implemented in FDS 5. The feature of these schemes is the solid phase cells experience shrinking when the solid fuel converts completely into gaseous fuel during decomposition[17,18].

4.3.1 Kinetic Properties for ~3 mg Polyurethane Foams Tested at Heating Rates of 1, 5, 20 and 60 °C/min

This section presents the kinetic properties for the nominal 3 mg samples which are tested at 1, 5, 20 and 60 °C/min of heating rates. Figure 4-8 shows *E* determined with the different graphical techniques for all the polyurethane foams. *E* of the first and second reactions are labelled on the plots and the reported values are the global values or the average for all the heating rates tested. The standard deviation which indicates the spread of *E* over different heating rates is included as error bars on the plot. The results from Kinetic Analysis do not have error bars because the analysis produce a single set of global kinetic properties from the different heating rates included into the analysis. This is different to the other methods where the kinetic properties of each individual heating rate are determined from which the standard deviation is derived.

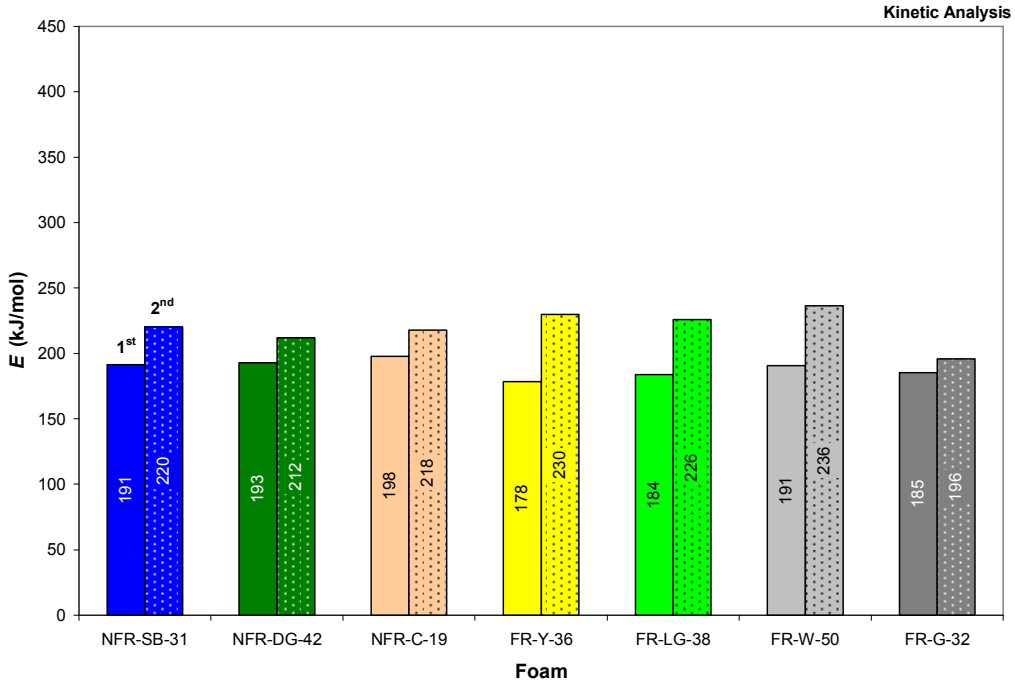
Kinetic Analysis
E (kJ/mol)
450
400
350
300
250
200
150
100
50
0
1st
2nd
191
220
193
212
198
218
178
230
184
226
191
236
185
196
NFR-SB-31
NFR-DG-42
NFR-C-19
FR-Y-36
FR-LG-38
FR-W-50
FR-G-32
Foam

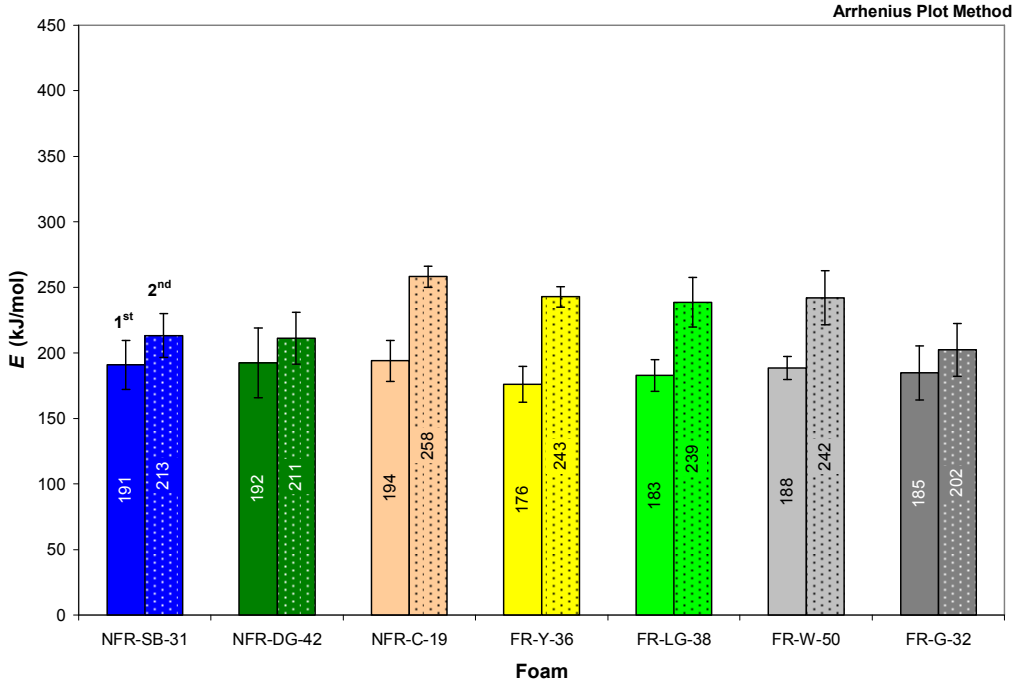
Arrhenius Plot Method
E (kJ/mol)
450
400
350
300
250
200
150
100
50
0
1st
2nd
191
213
192
211
194
258
176
243
183
239
188
242
185
202
NFR-SB-31
NFR-DG-42
NFR-C-19
FR-Y-36
FR-LG-38
FR-W-50
FR-G-32
Foam

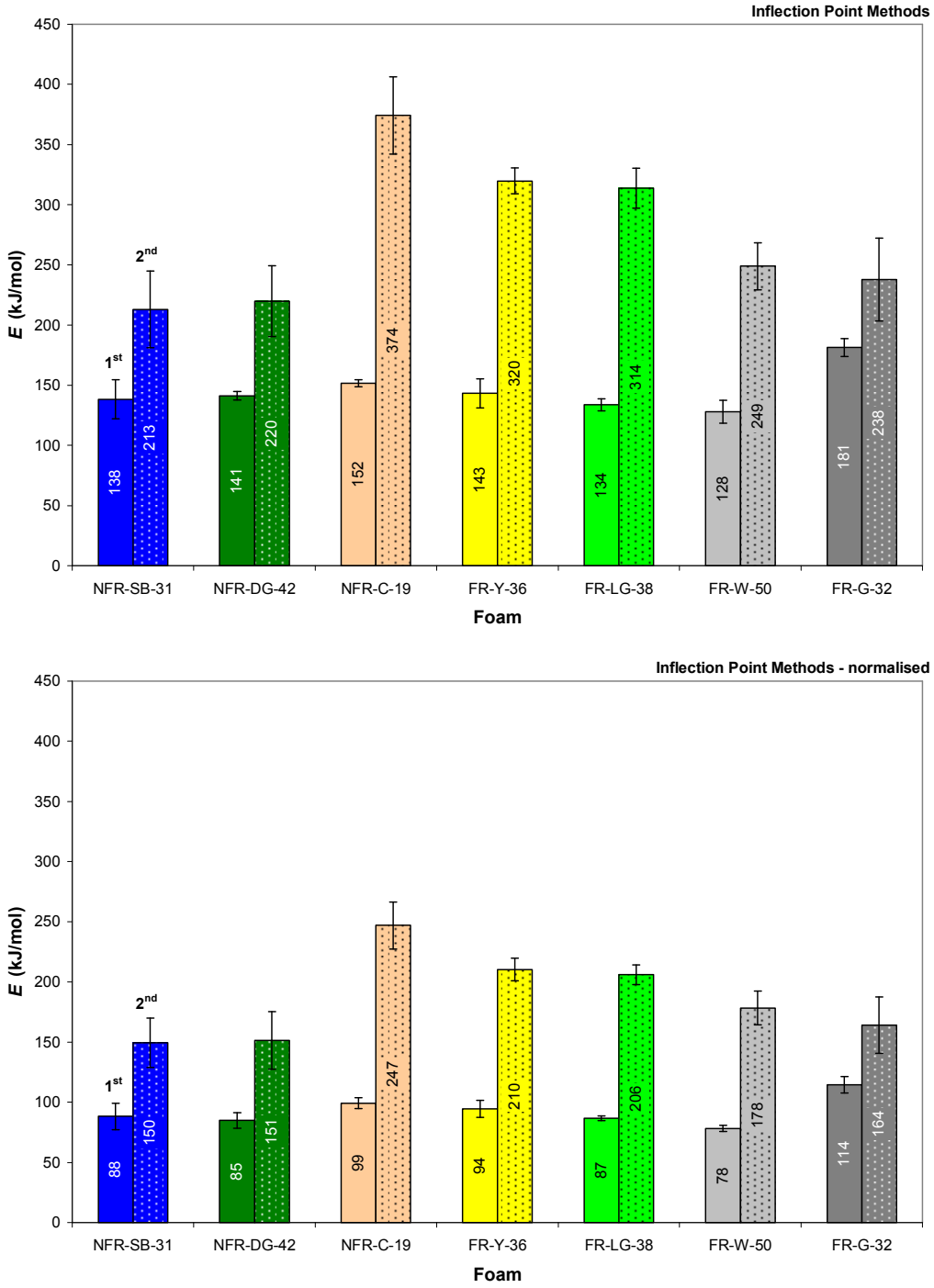

Figure 4-8: Comparison of average *E* from different graphical techniques for all ~3 mg polyurethane foams

For all the graphical techniques applied, the general trend shows that *E* of the second reaction is consistently greater than the first reaction. The magnitude of *E* between Kinetic Analysis and the Arrhenius Plot Method is comparable because of the

similarity between the two techniques where the Arrhenius Plot Method utilises the identical analysis regions and n as Kinetic Analysis. E produced by the original and normalised Inflection Point Methods are found to be different than those from Kinetic Analysis and Arrhenius Plot Method. As documented in Chapter 3, these techniques differ in terms of analysis regions and calculation approach. Forcing $n = 0$ in the normalised version has lowered the magnitude of E, nevertheless, the general trend between the reactions and among the foams are still similar to the original Inflection Point Methods.

Kinetic Analysis and the Arrhenius Plot Method show that E of the first reaction is very similar among the different polyurethane foams and the same for E of the second reaction. Differently, the original and normalised Inflection Point Methods show that there are variations among the foams. For the first reaction, all the foams possess similar E except for FR-G-32 which has a comparatively larger magnitude. For the second reaction, NFR-C-19, FR-Y-36 and FR-LG-38 are noted to have greater E compared to the other foams. The original and normalised Inflection Point Methods also show a more distinctive difference in E between the first and second reactions when compared to Kinetic Analysis and the Arrhenius Plot Method. In terms of spread, the original and normalised Inflection Point Methods show that the spread of E is greater for the second reaction in comparison to the first reaction. Differently, the Arrhenius Plot Method shows that the spread of E is actually fairly similar between both reactions. Again, these trends are believed to be caused by the differences between the graphical techniques applied.

According to Equation (3-1), the decomposition rate consists of a mass dependent function known as the kinetic model and a temperature dependent function known as the rate constant. The kinetic model is the density function in Equation (3-1) while the rate constant is the Arrhenius expression represented by Equation (3-12). Therefore, E and A function as a pair and the linearisation of Equation (3-12) using natural logarithm shows that E is related to $\ln(A)$. Similar to the comparison of E in Figure 4-8, Figure 4-9 compares $\ln(A)$ from the different graphical techniques for all the polyurethane foams. The presented values are the global values or the average for heating rates of 1, 5, 20 and 60 °C/min.

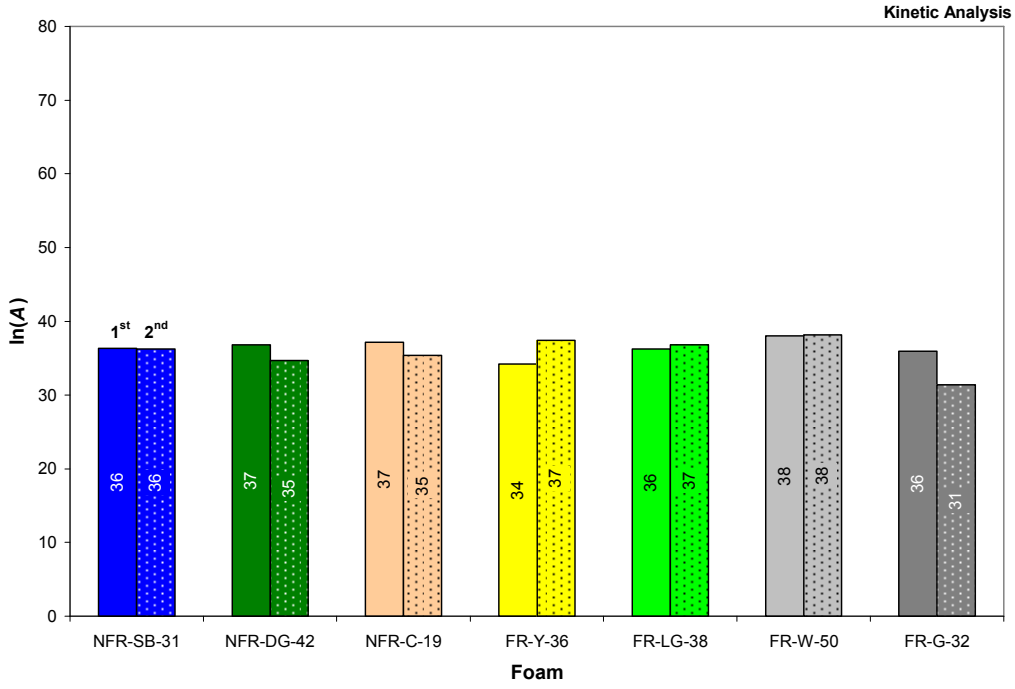
Kinetic Analysis
ln(A)
80
70
60
50
40
30
20
10
0
1st
2nd
36
36
37
35
37
35
34
37
36
37
38
38
36
31
NFR-SB-31
NFR-DG-42
NFR-C-19
FR-Y-36
FR-LG-38
FR-W-50
FR-G-32
Foam

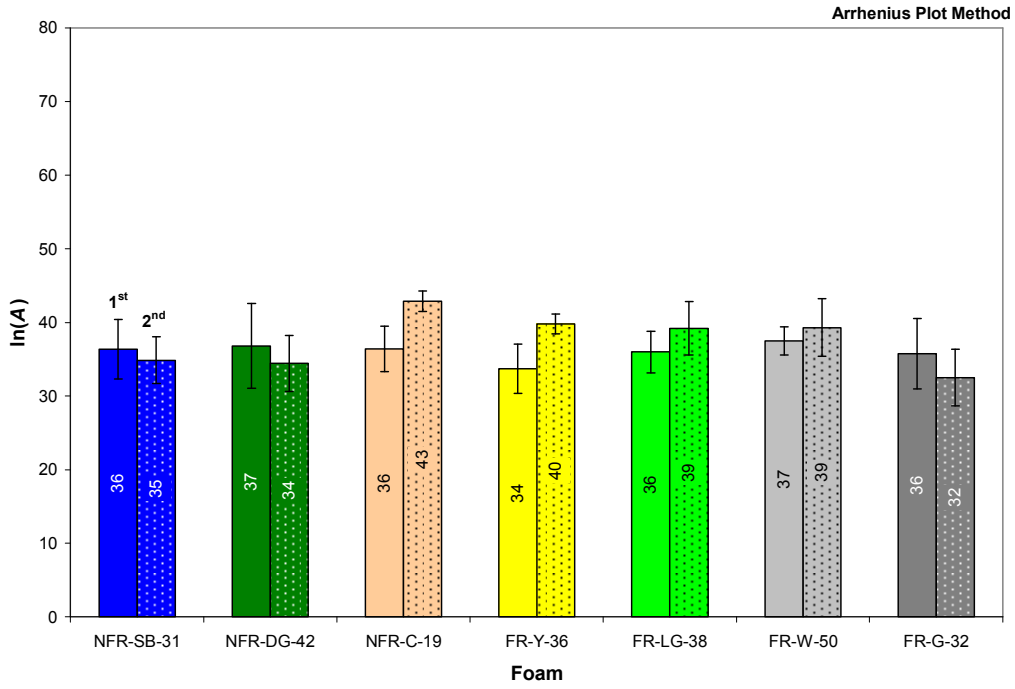
Arrhenius Plot Method
ln(A)
80
70
60
50
40
30
20
10
0
1st
2nd
36
35
37
34
36
43
34
40
36
39
37
39
36
32
NFR-SB-31
NFR-DG-42
NFR-C-19
FR-Y-36
FR-LG-38
FR-W-50
FR-G-32
Foam

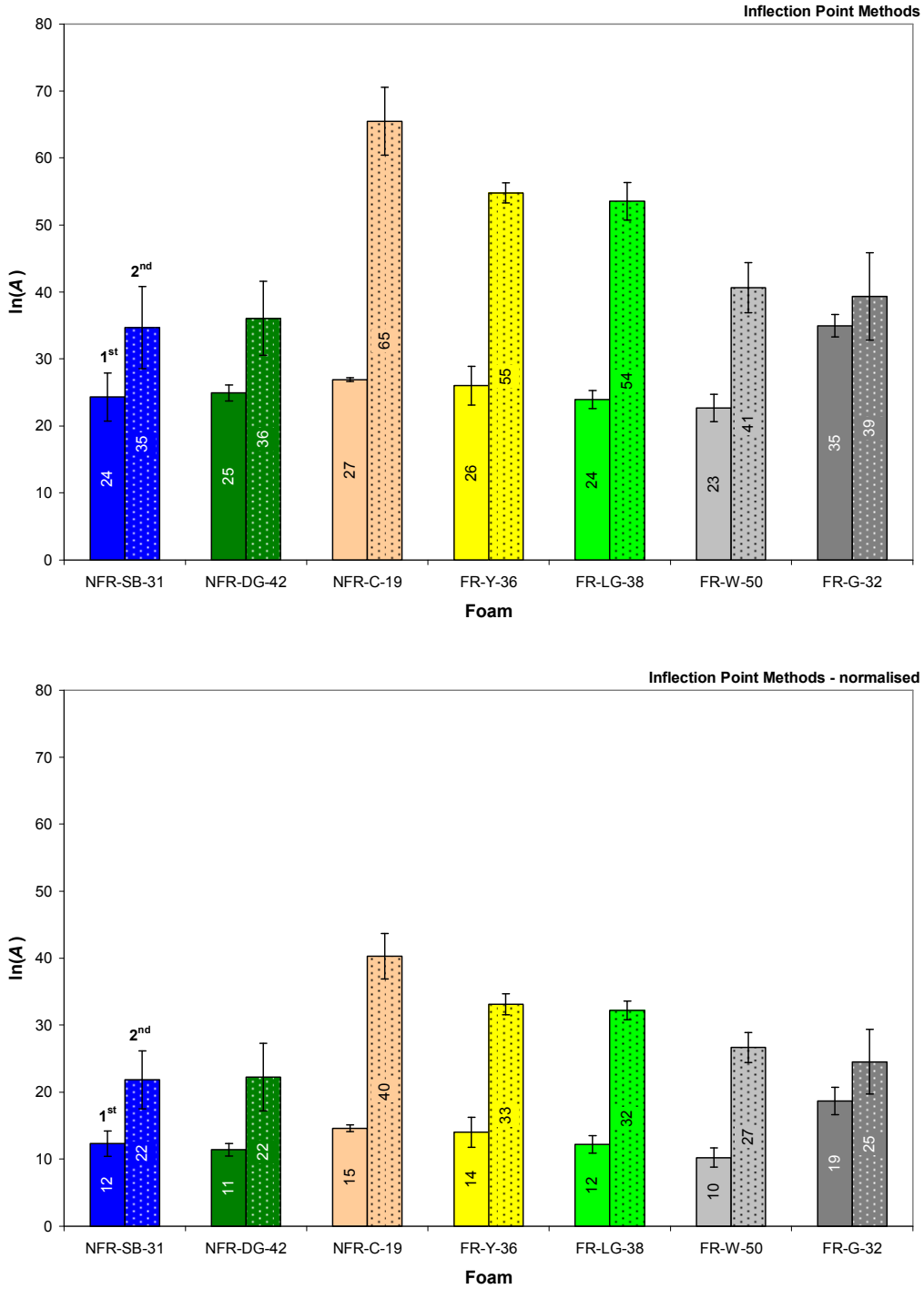

Figure 4-9: Comparison of average ln(*A*) from different graphical techniques for all ~3 mg polyurethane foams

ln(*A*) generally shares the same trend as *E* where the increase or decrease in *E* also results in a similar increase or decrease in ln(*A*). This is known as the kinetic

compensation effect in the literature[47] where the decomposition rate essentially remains consistent because the increase in E which acts to reduce the rate is compensated by an equivalent increase in A which increases the rate and vice versa. Since E of the second reaction is greater than the first reaction, theoretically, ln(A) of the second reaction should also be greater than the first reaction. This trend is consistently evident in the original and normalised Inflection Point Methods but not in Kinetic Analysis and the Arrhenius Plot Method where ln(A) of the first and second reactions are fairly similar in magnitude. This is perhaps a reflection of the less distinctive difference seen between E of the first and second reactions for Kinetic Analysis and the Arrhenius Plot Method as depicted in Figure 4-8. The standard deviation indicating the spread of ln(A) at different heating rates is included as error bars in the plot. The spread pattern of ln(A) is similar to E whereby the second reaction generally has a greater spread than the first reaction. This trend is more obvious for the original and normalised Inflection Point Methods but for the Arrhenius Plot Method, the spread in both reactions are actually comparable.

Among the graphical techniques considered, only Kinetic Analysis and the original Inflection Point Methods calculate n since the Arrhenius Point Method uses n found from Kinetic Analysis while for the normalised Inflection Point Methods, $n = 0$. Figure 4-10 shows n from Kinetic Analysis and Inflection Point Methods for all the polyurethane foams. The presented results are the global values or the average for heating rates of 1, 5, 20 and 60 °C/min.

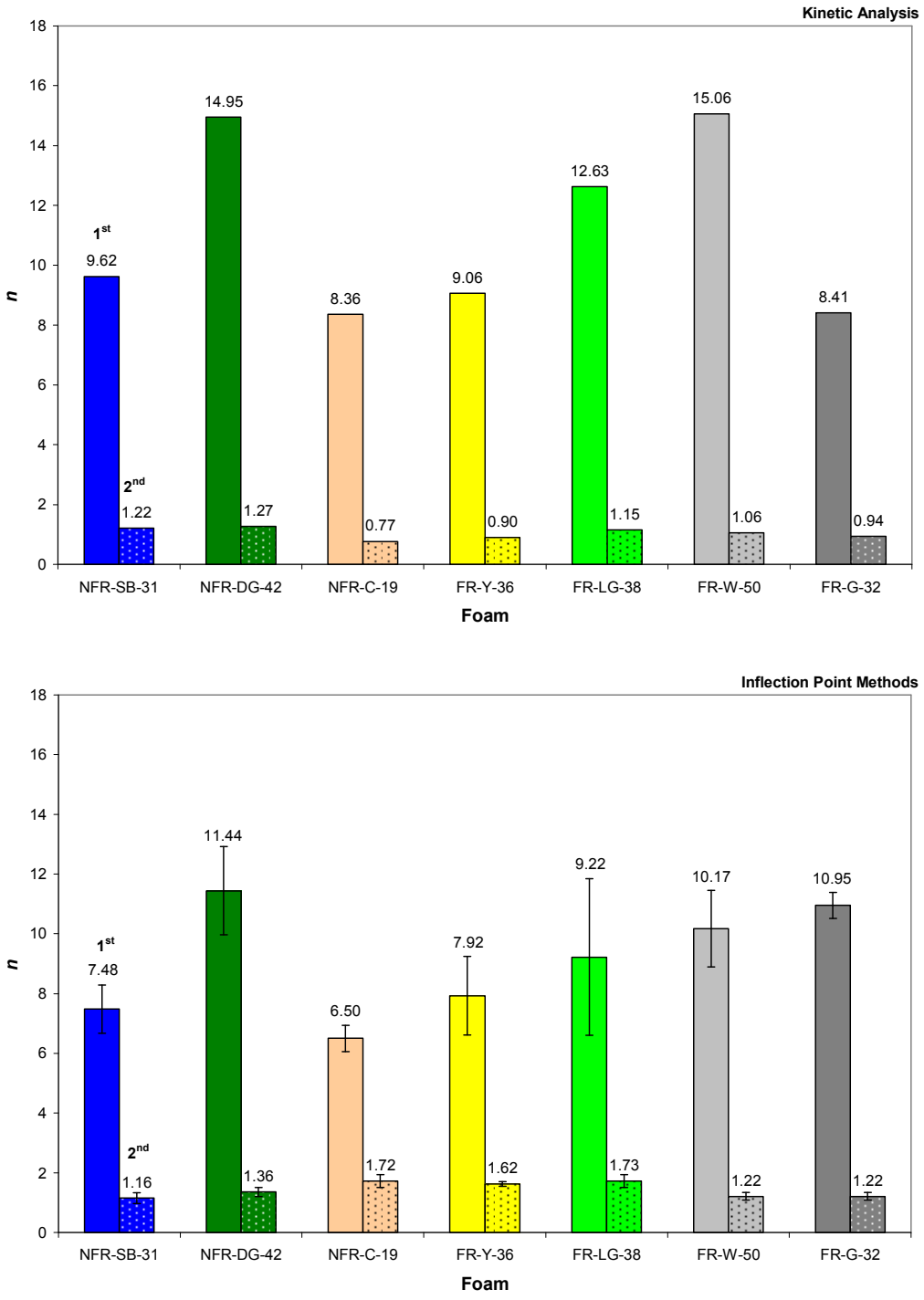

Figure 4-10: Comparison of average *n* from Kinetic Analysis and Inflection Point Methods for all ~3 mg polyurethane foams

The general trend shows that *n* of the first reaction are consistently greater than *n* of the second reaction for all the polyurethane foams tested. In terms of magnitude, *n* of

the second reaction is close to unity while *n* of the first reaction is found to range from 4 to 14 times greater than that of the second reaction. From the Inflection Point Methods, the deviation in *n* with respect to the changes in heating rate is found to be greater for the first reaction compared to the second reaction. For a nominal sample size of 3 mg, the trends observed in the kinetic properties of interest, *E*, *A* and *n* obtained from heating rate between 1 and 60 °C/min are found to be consistent with those described for the base case foams in Chapter 3 which are also tested using the same sample size and heating rates.

4.3.2 Kinetic Properties for ~10 mg Polyurethane Foams Tested at Heating Rate of 5 °C/min

The kinetic properties of the nominal 10 mg samples are also determined but since the experiments are carried out at a single heating rate of 5 °C/min, only the original and normalised Inflection Point Methods are utilised. Kinetic Analysis is not applicable because this technique requires the TGA results from multiple heating rates. The Arrhenius Plot Method is also not applicable because this technique relies on the analysis regions and *n* determined in Kinetic Analysis. Table 4-3 compares the kinetic properties of the 10 mg samples at 5 °C/min against the minimum and maximum values found for the 3 mg samples tested between 1 and 60 °C/min. The minimum and maximum values of the 3 mg samples are presented as a range with the standard deviation in brackets. The kinetic properties of the 10 mg samples with magnitude exceeding the range of the 3 mg samples are marked. A single asterisk denotes one standard deviation apart and two asterisks denote two or more standard deviations apart.

Table 4-3: Comparison of kinetic properties for ~10 mg polyurethane foams against minimum and maximum values of ~3 mg polyurethane foams

Method	Foam	Reaction	*E* (kJ/mol)		ln(*A*)		*n*	
			~3 mg sample	~10 mg sample	~3 mg sample	~10 mg sample	~3 mg sample	~10 mg sample
Inflection Point Methods	NFR-SB-31	1	126-161 (16)	158	21-29 (4)	28	6.57-8.28 (0.81)	8.35*
		2	176-250 (32)	242	27-42 (6)	40	0.92-1.36 (0.18)	1.30
	NFR-DG-42	1	138-146 (3)	143	24-27 (1)	24	10.05-13.45 (1.47)	10.67
		2	189-258 (29)	285*	30-43 (5)	49**	1.23-1.50 (0.15)	1.55*
	NFR-C-19	1	148-155 (3)	159**	27-27 (0)	28**	6.17-7.14 (0.44)	6.69
		2	343-419 (32)	346	60-72 (5)	60	1.53-1.98 (0.21)	1.39*
	FR-Y-36	1	131-157 (12)	137	23-29 (3)	23	6.29-9.20 (1.31)	7.37
		2	311-333 (11)	308*	53-57 (1)	52*	1.53-1.71 (0.08)	1.74*
	FR-LG-38	1	127-139 (5)	124*	22-25 (1)	21*	6.88-12.95 (2.62)	7.55
		2	298-333 (17)	294*	51-57 (3)	50*	1.50-1.93 (0.21)	1.71
	FR-W-50	1	120-141 (10)	123	21-25 (2)	21	9.22-12.05 (1.28)	11.51
		2	226-270 (19)	241	36-45 (4)	39	1.09-1.40 (0.13)	1.16
	FR-G-32	1	174-188 (7)	174	33-37 (2)	33	10.44-11.35 (0.43)	14.59**
		2	188-266 (35)	183*	30-45 (7)	29*	1.05-1.34 (0.13)	0.99*
Inflection Point Methods – normalised	NFR-SB-31	1	81-105 (11)	99	11-15 (2)	14	0	0
		2	128-173 (20)	161	18-27 (4)	24	0	0
	NFR-DG-42	1	79-94 (6)	92	10-12 (1)	12	0	0
		2	123-178 (24)	186*	16-28 (5)	29*	0	0
	NFR-C-19	1	94-104 (4)	105*	14-15 (1)	15	0	0
		2	232-274 (19)	238	38-45 (3)	38	0	0
	FR-Y-36	1	86-103 (7)	91	11-16 (2)	12	0	0
		2	198-220 (9)	202	31-35 (2)	31	0	0
	FR-LG-38	1	85-89 (2)	86	11-13 (1)	11	0	0
		2	197-215 (8)	186**	31-34 (1)	28**	0	0
	FR-W-50	1	75-81 (3)	75	9-12 (1)	9	0	0
		2	162-196 (14)	166	24-29 (2)	24	0	0
	FR-G-32	1	106-121 (7)	97**	16-21 (2)	14*	0	0
		2	131-183 (23)	125*	18-28 (5)	17*	0	0

The 10 mg samples share the common general trends as the 3 mg samples whereby E and A of the second reaction is consistently greater than the first reaction while for n, the magnitude of the first reaction is found to be greater than the second reaction. Comparing with the minimum and maximum of the 3 mg samples, the kinetic properties of the 10 mg samples are generally comparable where more than half are within the range specified in Table 4-3 and approximately 90 % are within one standard deviation apart. The kinetic compensation effect is again noted whereby the increase in E beyond the boundaries also leads to the increase in A beyond the boundaries and vice versa.

4.4 Decomposition Behaviours of Melts in Nitrogen Environment

The melt samples tested in the TGA experiments is obtained from the Sample Feeding Vertical Cone experiments detailed in Chapter 7. During the experiment, 75 by 75 mm cross section area of a 900 mm long foam sample is exposed to the radiative heat flux from a vertically oriented cone heater and the sample surface is pilot ignited. As the exposed foam starts to burn, the melts produced flow downwards, across the surface and eventually into the melt collecting unit. The decomposed section of the foam is compensated by feeding the sample forward on a conveyor platform hence the decomposing front is exposed to a constant radiative heat flux as a constant distance is maintained between the decomposing sample surface and the cone heater. At the end of the experiment, the collected melts are stored in a sealed container at ambient temperature for further testing in the TGA experiments. For the FR foams which produce char, the solid residues are separated and removed from the liquid.

The melt samples for the TGA experiments are prepared by freezing the melt droplets in liquid nitrogen. This allows the droplets to be transferred easily into the 90 μL alumina cup. The TGA experiments involving melt samples are performed under nitrogen with a purge rate of 100 ml/min. Figure 4-11 shows the changes in the sample mass and mass loss/°C with temperature for all melts with a nominal mass of 20 mg at heating rate of 5 °C/min.

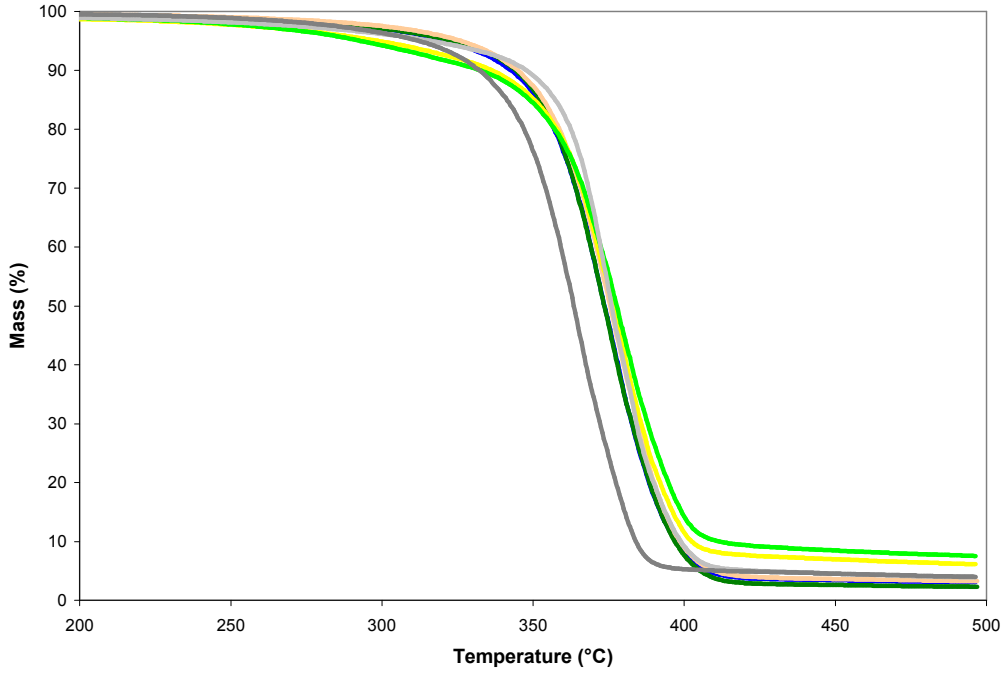

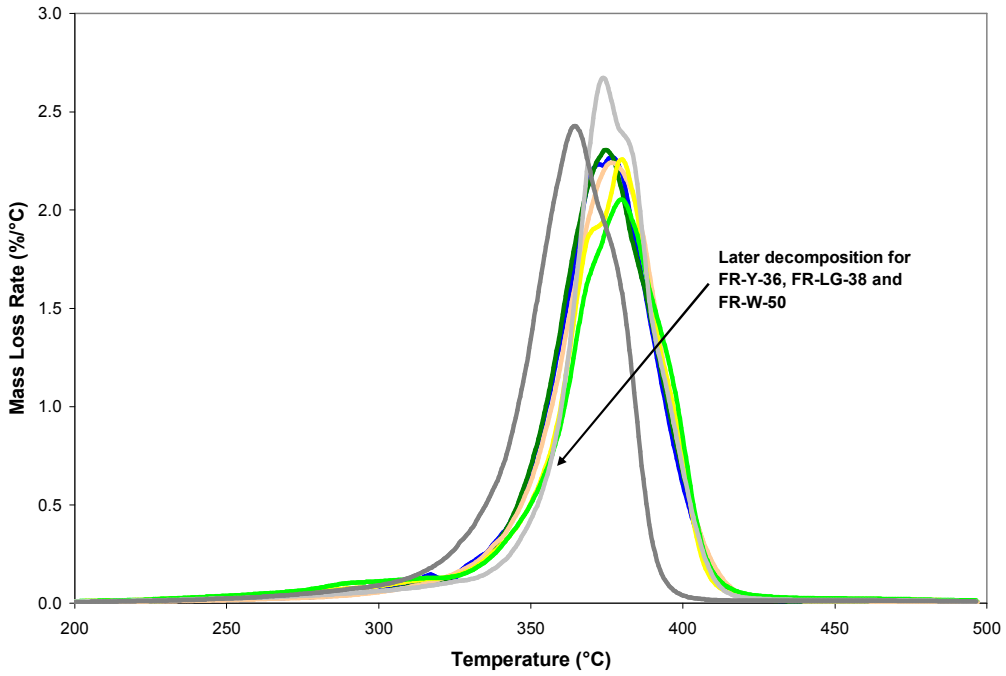

Figure 4-11: Sample mass and mass loss/°C versus temperature of ~20 mg melts at 5 °C/min heating rate under nitrogen environment

The results show that the melt decomposition only consists of one reaction where the melts decomposes completely into gaseous fuel and this expectedly corresponds to the second reaction of the proposed decomposition mechanism of polyurethane foam. From the mass loss/°C plot, the melts of FR-Y-36, FR-LG-38 and FR-W-50 appear to decompose at higher temperature compared to the melts of the other foams. However, this temperature difference is not pronounced because in the preparation of the melt samples, the char formed has been removed. In contrast, the temperature difference in the second reaction of the foam decomposition is more pronounced between the aforementioned FR foams and the other foams. This is depicted in Figure 4-3 for the same heating rate applied to the melt samples, 5 °C/min where the presence of char has slowed the foam decomposition.

The second reaction of FR-G-32 in foam decomposition is seen to coincide with the second reaction of the NFR foams but in the melt decomposition, the decomposition temperature of FR-G-32 is visibly earlier than the other melts as seen in Figure 4-11. Based on the chemical formula of the polyurethane foams, FR-G-32 is noted to

possess 5 to 25 times more phosphorus than the other FR foams. Therefore, FR-G-32 earlier decomposition is believed to be caused by the remnant of phosphoric acid from the breakdown of halophosphate during the Sample Feeding Vertical Cone experiment. The collected phosphoric acid then acts as catalyst to the melt decomposition[36] in the TGA experiments. For foam decomposition in TGA experiment, the phosphorus catalysed the first reaction but it is believed to have converted into residue over the transition region hence it does not catalyse the second reaction. The ability of the other FR foams to create char is a process known to consume phosphorus[34]. As a result, the meagre amount of phosphorus presents in those FR foams is fully involved with the char formation process during the Sample Feeding Vertical Cone experiments, thus not available as the catalyst for the melt decomposition in the TGA experiments. The following sections respectively discuss the sensitivity of the melt decomposition to the samples collected under non-flaming and flaming conditions, at different heating rates and at different sample sizes.

4.4.1 Sensitivity of Melt Decomposition to Samples Collected under Non-Flaming and Flaming Conditions

Both the NFR and FR foams are tested under flaming condition in the Sample Feeding Vertical Cone experiments where the exposed surface is ignited with a hand held methane burner. Only the FR foams are tested under non-flaming condition where the exposed surface undergoes decomposition but does not burn throughout the experiment. The NFR foams are not tested under non-flaming condition because of the difficulties in maintaining an even exposed surface under such experimental condition. Unless specifically identified, the melts discussed in this chapter should be taken as the flaming melts. Figure 4-12 compares the mass loss/°C of the melts from the FR foams obtained under non-flaming and flaming conditions. These TGA experiments are performed at heating rate of 5 °C/min under nitrogen environment with a nominal sample mass of 20 mg.

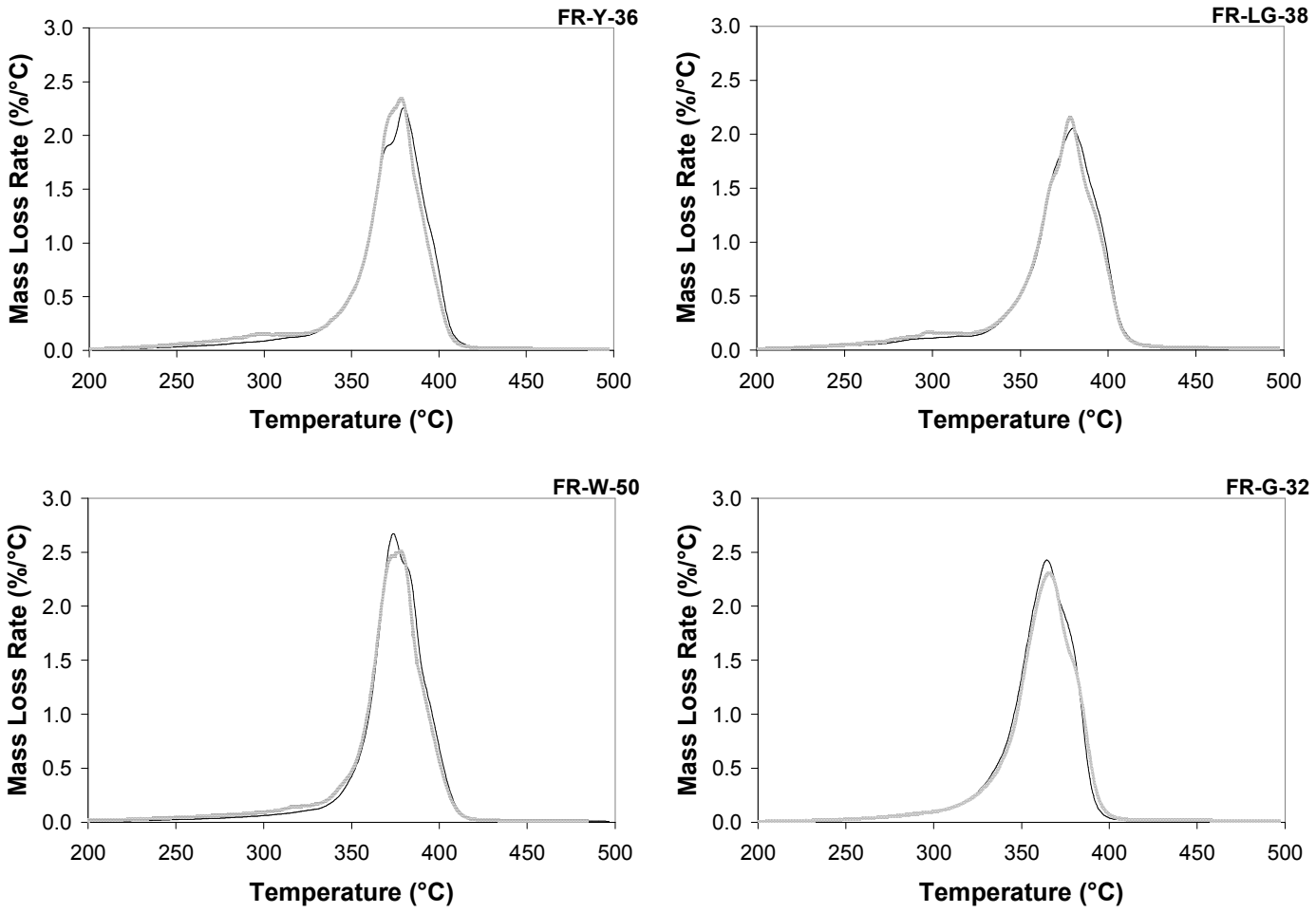

Figure 4-12: Mass loss/°C versus temperature for ~20 mg non-flaming and flaming melts at 5 °C/min heating rate under nitrogen environment

The results show that the difference in the decomposition pattern between the non-flaming and flaming melts is negligible. The char forming foams, FR-Y-36, FR-LG-38 and FR-W-50 shows the non-flaming melts possess a slightly greater decomposition rate than the flaming melts at the start. This is believed to be caused by the breakdown of isocyanate remnants or foam fragments which are collected in greater quantity under the non-flaming condition.

Table 4-4 contains the decomposition temperature of the nominal 20 mg melts under non-flaming (NF) and flaming (F) conditions at 5 °C/min. Also included for reference is the comparative decomposition temperature for the second reaction of foam decomposition at the same heating rate. While the nominal mass of the foam samples is 3 mg, the mass remaining for the second reaction is reduced to nominally 75 % of the original due to the mass loss in the first reaction. The start and end temperatures are presented as a range with the temperature of the decomposition peak in brackets.

Table 4-4: Decomposition temperature for ~20 mg non-flaming and flaming melts and decomposition temperature during second reaction for ~3 mg polyurethane foams at 5 °C/min heating rate under nitrogen environment

Sample		Decomposition temperature at 5 °C/min, °C
NFR-SB-31	Melt (F)	333-408 (377)
	Foam	322-399 (369)
NFR-DG-42	Melt (F)	335-409 (375)
	Foam	322-400 (366)
NFR-C-19	Melt (F)	334-409 (377)
	Foam	337-394 (366)
FR-Y-36	Melt (NF)	336-404 (379)
	Melt (F)	336-406 (380)
	Foam	339-400 (372)
FR-LG-38	Melt (NF)	334-407 (379)
	Melt (F)	335-408 (380)
	Foam	340-402 (373)
FR-W-50	Melt (NF)	340-406 (378)
	Melt (F)	345-406 (374)
	Foam	343-409 (382)
FR-G-32	Melt (NF)	323-394 (366)
	Melt (F)	323-391 (364)
	Foam	329-394 (366)

As depicted previously in Figure 4-12, the decomposition temperature for the non-flaming and flaming melts in Table 4-4 shows no significant differences. For most melts, the decomposition temperature is found to be higher when compared to that of

the foams because the 20 mg melt samples have more melts covering the bottom of the alumina cup than the 3 mg foam samples. The melts that show lower or similar decomposition temperature compared to the foams are FR-W-50 and FR-G-32. In the case of FR-W-50, the removal of char during the melt sample preparation means the char is absence to slow the melt decomposition. As a result, this is believed to have allowed the melt to decompose at lower temperature. The other char forming FR foams, FR-Y-36 and FR-LG-38 also have char removed during the preparation of melt sample but different to FR-W-50, these foams produce smaller char fractions and some of which remain inseparable from the melts. Thus, the presence of these char fractions in the melt samples couples with the more complete coverage of the sample at the bottom of the alumina cup result in the higher decomposition temperature for the melts of FR-Y-36 and FR-LG-38 when compared to the foams. In the case of FR-G-32, the effect of phosphoric acid acting as catalyst as discussed previously is the likely cause for the similar decomposition temperature compared to foam.

4.4.2 Sensitivity of Melt Decomposition to Heating Rate

The sensitivity analysis only involves the base case foams, NFR-SB-31 and FR-Y-36 and the different heating rates tested are 1, 5, 20 and 60 °C/min. The nominal sample mass is 20 mg and a single replicate is tested for each heating rate. Figure 4-13 shows the mass loss/°C of NFR-SB-31 and FR-Y-36.

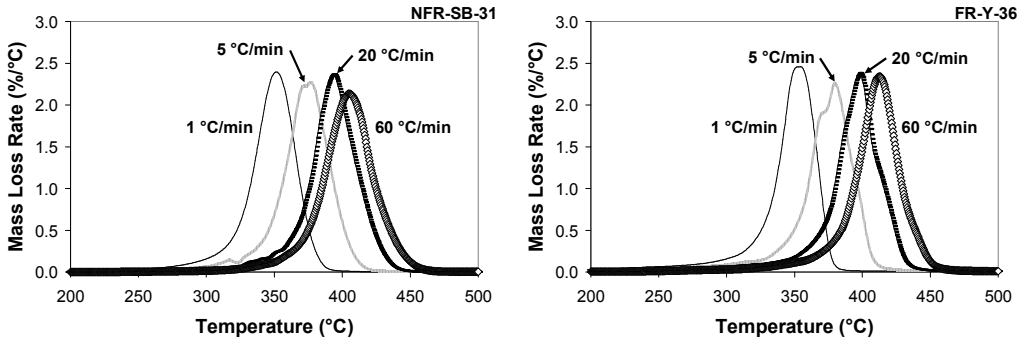

Figure 4-13: Mass loss/°C versus temperature for ~20 mg melts of NFR-SB-31 and FR-Y-36 at 1, 5, 20 and 60 °C/min heating rates under nitrogen environment

Similar to the trend seen in foam decomposition, the results show that the single reaction in melt decomposition shifts towards higher temperature range as the heating

rate increases. For both NFR-SB-31 and FR-Y-36, the peak magnitude of the decomposition in Figure 4-13 appears to be constant with varying heating rates. However, different trends are noted previously in Figure 4-5 for foam decomposition. The peak magnitude of the second reaction for FR-Y-36 is found to decrease consistently with the increase in heating rate due to the heating rate dependency of the char formation process. This trend of decreasing peak magnitude is absence in the melt decomposition because the char has been removed during the melt sample preparation thus unable to slow the decomposition. At different heating rates, Table 4-5 compares the decomposition temperature for the melts of NFR-SB-31 and FR-Y-36 with the decomposition temperature for the second reaction of the same foams. The nominal mass of the melts is 20 mg while for foams, it is 3 mg but given the mass loss in the first reaction, the actual mass remaining for the second reaction is approximately 75 % of the original.

Table 4-5: Decomposition temperature for ~20 mg melts of NFR-SB-31 and FR-Y-36 and decomposition temperature during second reaction for ~3 mg NFR-SB-31 and FR-Y-36 foams at 1, 5, 20 and 60 °C/min heating rates under nitrogen environment

Sample	β, °C/min	Decomposition temperature, °C	
		~20 mg melt	~3 mg foam
NFR-SB-31	1	310-381 (352)	302-373 (343)
	5	333-408 (377)	322-399 (369)
	20	351-429 (393)	345-420 (388)
	60	360-445 (405)	363-439 (404)
FR-Y-36	1	313-376 (353)	317-377 (348)
	5	336-406 (380)	339-400 (372)
	20	355-428 (398)	359-424 (392)
	60	370-446 (413)	377-446 (409)

The decomposition temperatures for melts tabulated in Table 4-5 agrees with the trends described in Figure 4-13 where the increase in heating rate shifts the decomposition towards higher temperature range. Over the heating rates tested, the decomposition temperature of the melts is generally greater than the foams and again, this is a result of more melts covering the bottom of the alumina cup achieved by the 20 mg melt samples. For the 3 mg foams, the decomposition temperature of FR-Y-36 is consistently greater than NFR-SB-31 at the different heating rates and this trend is most noticeable for the start temperature where FR-Y-36 is approximately 14 to 17 °C higher. The peak and end temperatures show similar trend but with much smaller difference. Due to the removal of the majority of char, the difference in

decomposition temperature between the melt samples of NFR-SB-31 and FR-Y-36 has reduced where the start temperature of FR-Y-36 is approximately 3 to 10 ℃ higher as the small quantity of remaining char which is inseparable from the melts is no longer effective in slowing the melt decomposition.

4.4.3 Sensitivity of Melt Decomposition to Sample Size

Similar to the sensitivity analysis of heating rate, the sensitivity analysis of sample size only involves the base case foams, NFR-SB-31 and FR-Y-36. The TGA experiments are conducted at 5 °C/min and the different sample sizes used are 3, 10, 20 and 50 mg which are nominal values. At the maximum sample size of 50 mg, the alumina cup is filled completely. A single replicate is tested for each sample size and Figure 4-14 shows the mass loss/°C of NFR-SB-31 and FR-Y-36.

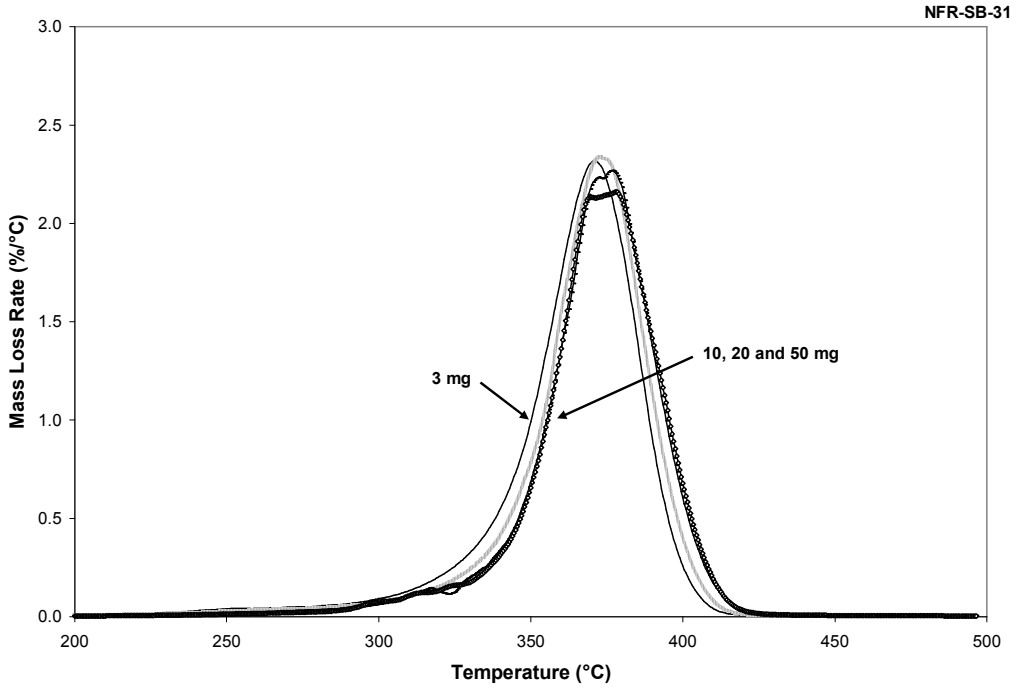

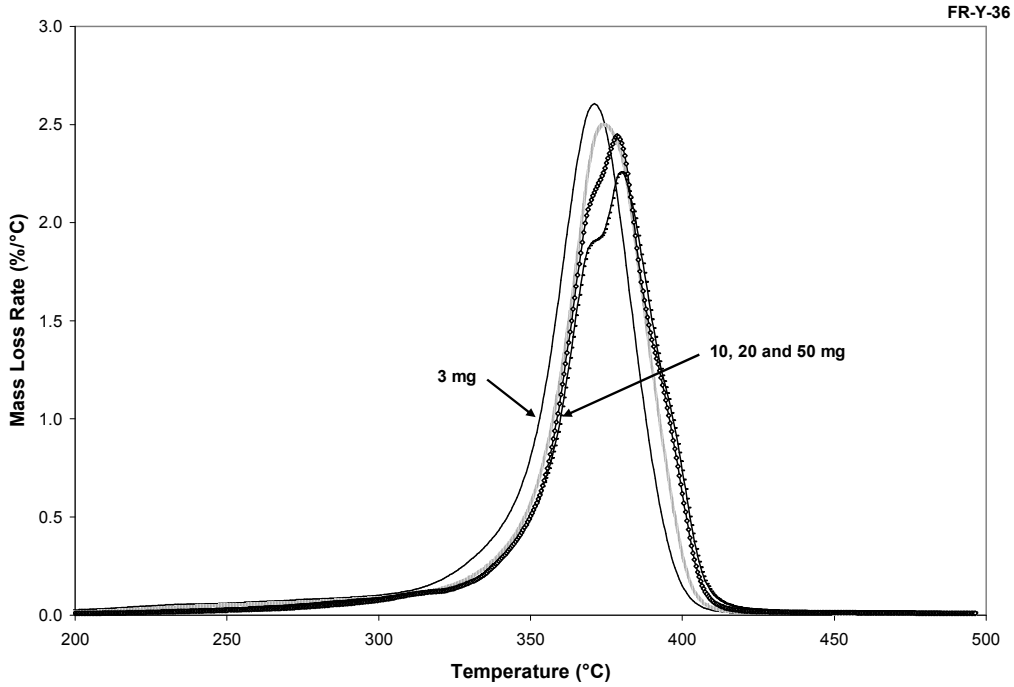

Figure 4-14: Mass loss/°C versus temperature for ~3, ~10, ~20 and ~50 mg melts of NFR-SB-31 and FR-Y-36 at 5 °C/min heating rate under nitrogen environment

From the results, only the 3 mg melt sample decomposes at an earlier temperature than the other samples. As mentioned earlier and also seen in Figure 4-6 and 4-7, this is due to the smaller sample size used where the bottom of the alumina cup is covered by small amount of melts. The difference in decomposition temperature for the 10, 20 and 50 mg melt samples is negligible as the bottom of the alumina cup is covered by more melts. Aside from the variation in decomposition temperature, the decomposition pattern and the peak magnitude among the different sample size are similar. Table 4-6 compares the decomposition temperature between the 3, 10, 20 and 50 mg melts of NFR-SB-31 and FR-Y-36 at 5 °C/min. Also included is the decomposition temperature for the second reaction of 3 and 10 mg NFR-SB-31 and FR-Y-36 foams at the same heating rate. As mentioned previously, the amount of foam mass remaining for the second reaction is approximately 75 % of the original.

Table 4-6: Decomposition temperature for ~3, ~10, ~20 and ~50 mg melts of NFR-SB-31 and FR-Y-36 and decomposition temperature for ~3 and ~10 mg NFR-SB-31 and FR-Y-36 foams at 5 °C/min heating rate under nitrogen environment

Sample		Mass, mg	Decomposition temperature at 5 °C/min, °C
NFR-SB-31	Melt	5	323-401 (371)

	Melt	10	330-404 (373)
	Melt	26	333-408 (377)
	Melt	46	334-409 (378)
	Foam	3	322-399 (369)
	Foam	10	334-401 (370)
FR-Y-36	Melt	4	329-397 (371)
	Melt	12	336-401 (374)
	Melt	33	336-406 (380)
	Melt	49	338-405 (379)
	Foam	3	339-400 (372)
	Foam	10	343-403 (374)

Similar to the trend in Figure 4-14, the 3 mg melts decompose at lower temperature while the decomposition temperature for 10, 20 and 50 mg melts is much closer, particularly between 20 and 50 mg which show a maximum variation of only 2 °C. The effect of char in the foams is noted by comparing the decomposition temperature between the melts and the second reaction of the polyurethane foams at similar mass of 3 and 10 mg. In the case of FR-Y-36, the decomposition temperature of the foams is consistently greater than the melts, especially for the start temperature by approximately 10 °C. This higher decomposition temperature is due to the formation of char in the case of the foam while in the case of melt, the char has been removed during the melt sample preparation so it does not slow the melt decomposition, resulting in the lower decomposition temperature. In the case of NFR-SB-31, the decomposition temperature of the foams and melts are found to be fairly similar because NFR-SB-31 does not contain melamine that forms the char.

4.5 Kinetic Properties of Melts in Nitrogen Environment

From the TGA results of the melts decomposition, the original and normalised Inflection Point Methods are applied to determine the governing kinetic properties. Kinetic Analysis and the Arrhenius Plot Method have not been applied because most of the melts are tested at a single heating rate. Figure 4-15 compares *E* determined for the melt decomposition and *E* of the second reaction from foam decomposition. The values for both the non-flaming and flaming melts are reported. The nominal mass of foam and melt samples compared are 3 and 20 mg respectively. The different physical states of the sample are denoted on the plot, ‘foam’ indicates the polyurethane foam, ‘NF’ indicates the non-flaming melt and ‘F’ indicates the flaming melt.

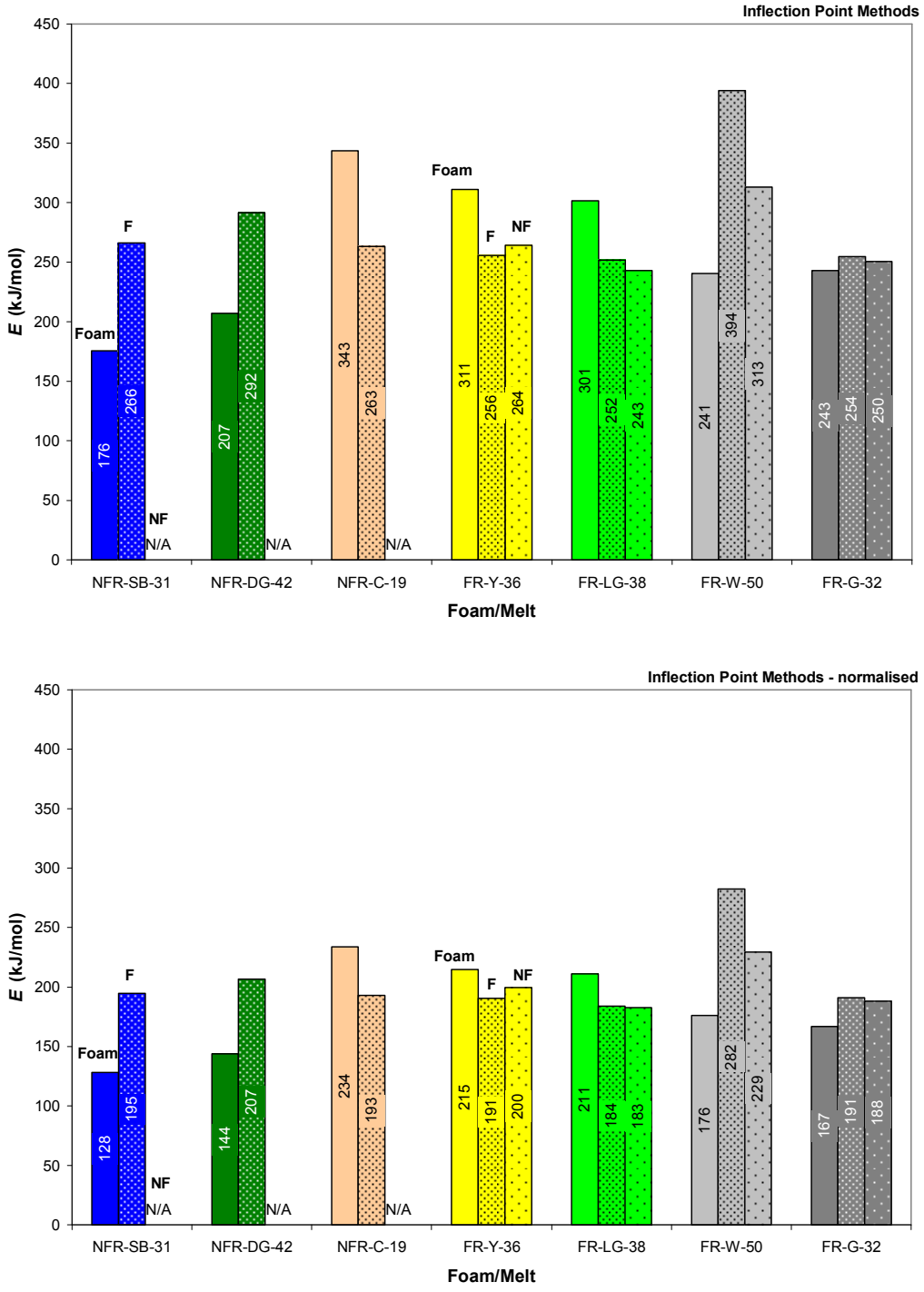

Figure 4-15: Comparison of *E* from original and normalised Inflection Point Methods for second reaction of ~3 mg polyurethane foams and ~20 mg melts at 5 °C/min heating rate

As discussed before, the non-flaming melts are not available for the NFR foams due to the experimental difficulties of the Sample Feeding Vertical Cone. The results

show that a consistent trend is not apparent between E of the foams and melts as certain cases show greater magnitude for the melts while the others show greater magnitude for the foams.

This inconsistent trend is caused by two issues. The first issue is the differences in TGA results between the second reaction of foam decomposition and the melt decomposition. These differences influence the calculated kinetic properties for foam and melt decompositions. The affected results include the peak decomposition rate, the temperature at peak decomposition, the mass fraction decomposed at peak decomposition and the temperature range included in the graphical analysis. These differences in TGA results are directly related to the physical aspect of the samples tested such as the different sample mass used for foam and melt samples and the absence of char in the prepared melt samples. The second issue is the exponential nature of the Arrhenius expression used to represent the decomposition rate which has contributed to the sensitive nature of E.

Despite the inconsistent trend, the magnitude of E for melt decomposition is within the same range as E for the second reaction of foam decomposition. As such, when compared with the first reaction of foam decomposition, E of melt decomposition is still consistently greater. Thus, this trend is exactly the same as depicted in Figure 4-8 where E of the second reaction is greater than E of first reaction. From Figure 4-15, having $n = 0$ in the normalised Inflection Point Methods results in lower E compared to the original Inflection Point Methods. This is again similar to the trend seen in foam decomposition thus justifying the consistency of the graphical techniques when applied to samples in different physical states such as solid foams and liquid melts.

Figure 4-16 compares $\ln(A)$ from the decomposition of melts with that from the second reaction of the polyurethane foams. As E functions together with A according to Equation (3-12), the trend in $\ln(A)$ is similar to that of E.

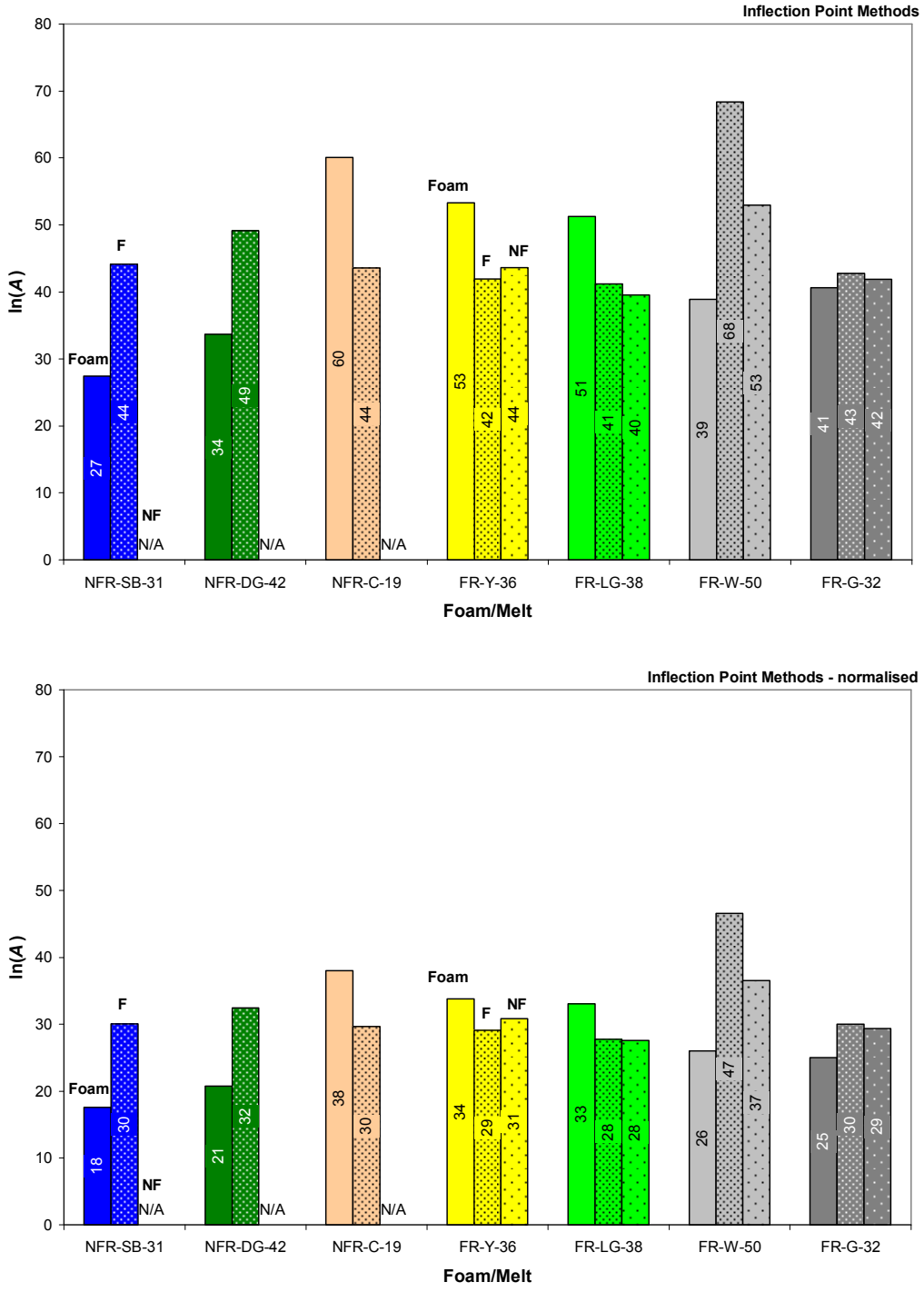

Figure 4-16: Comparison of ln(*A*) from original and normalised Inflection Point Methods for second reaction of ~3 mg polyurethane foams and ~20 mg melts at 5 °C/min heating rate

The results demonstrate the kinetic compensation effect[47] which is seen previously in the foam decomposition whereby the change in *E* is compensated by a similar change

in ln(A) so that the decomposition rate stays consistent. The trend of ln(A) is similar between the original and normalised Inflection Point Methods but the magnitude of the former is much greater compared to the latter which is again similar to the trend in foam decomposition, justifying the consistency of the graphical techniques.

Lastly, Figure 4-17 compares n from the decomposition of melts with that from the second reaction of the polyurethane foams. The comparison is only for the original Inflection Point Methods since $n = 0$ in the normalised version.

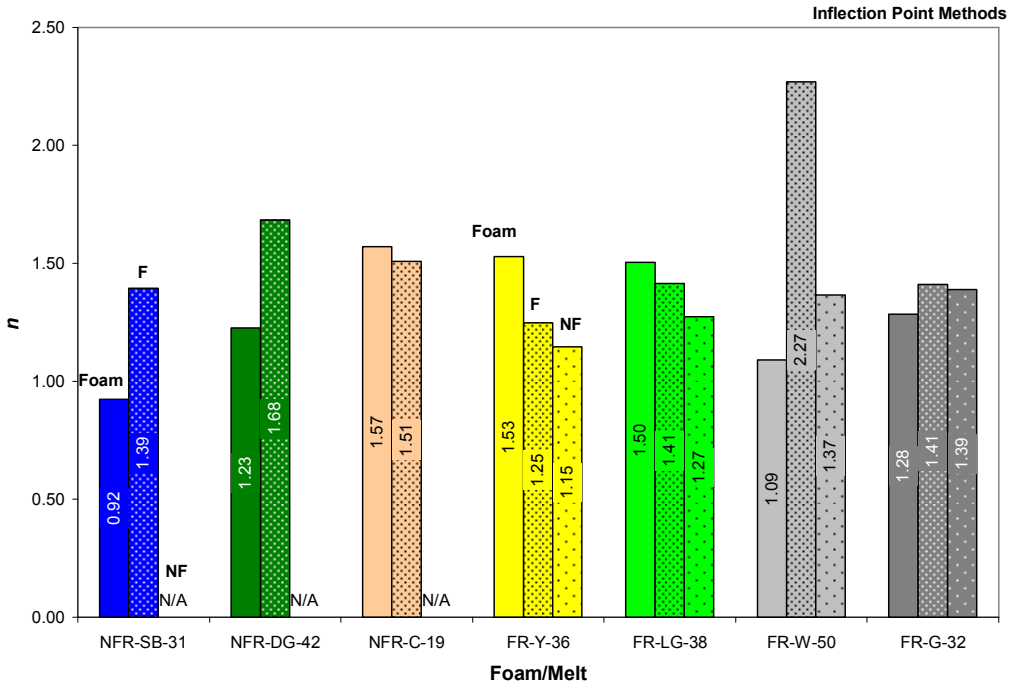

Figure 4-17: Comparison of n from original Inflection Point Methods for second reaction of ~3 mg polyurethane foams and ~20 mg melts at 5 °C/min heating rate

The results show that except for the flaming melt of FR-W-50, *n* of other melts are fairly close to the value of unity. This is similar in magnitude to *n* for the second reaction of polyurethane foams. The sensitivity of melt decomposition to different heating rates and sample sizes is only investigated for the base case foams so Table 4-7 tabulates the kinetic properties for the melts of NFR-SB-31 and FR-Y-36 at the heating rates and sample sizes tested. The original and normalised Inflection Point Methods are the graphical techniques used. The average value over the heating rates and sample mass tested is also reported with the standard deviation in brackets.

Table 4-7: Kinetic properties for melts of NFR-SB-31 and FR-Y-36 at different heating rates and sample mass

Method	Melt	Mass, mg	β, °C/min	E, kJ/mol	ln(A)	n
Inflection Point Methods	NFR-SB-31	21	1	254	42	1.41
		26	5	266	44	1.39
		22	20	284	47	1.54
		22	60	283	48	1.65
		Average		272 (14)	45 (3)	1.50 (0.12)
	FR-Y-36	22	1	259	43	1.28
		33	5	256	42	1.25
		23	20	278	46	1.32
		25	60	294	49	1.40
		Average		272 (18)	45 (3)	1.31 (0.06)
	NFR-SB-31	5	5	218	35	1.12
		10	5	254	42	1.36
		26	5	266	44	1.39
		46	5	276	46	1.43
		Average		253 (25)	42 (5)	1.33 (0.14)
	FR-Y-36	4	5	250	41	1.12
		12	5	292	49	1.46
		33	5	256	42	1.25
		49	5	287	48	1.30
		Average		271 (22)	45 (4)	1.28 (0.14)
Inflection Point Methods – normalised	NFR-SB-31	21	1	188	29	0
		26	5	195	30	0
		22	20	213	34	0
		22	60	205	33	0
		Average		200 (11)	31 (2)	0
	FR-Y-36	22	1	196	30	0
		33	5	191	29	0
		23	20	210	33	0
		25	60	221	35	0
		Average		204 (14)	32 (3)	0
	NFR-SB-31	5	5	168	25	0
		10	5	189	29	0
		26	5	195	30	0
		46	5	195	30	0
		Average		187 (13)	29 (2)	0
	FR-Y-36	4	5	196	31	0
		12	5	220	35	0

		33	5	191	29	0
		49	5	211	33	0
		Average		204 (14)	32 (3)	0

As discussed for the plots of kinetic properties, the magnitude of E and ln(A) determined from the original Inflection Point Methods is greater than the normalised version. Also, the kinetic properties in Table 4-7 representing the melt decomposition are in the same range as those for the second reaction of foam decomposition in Table 4-3. For the changes in heating rate, the overall standard deviation of the kinetic properties governing melt decomposition is found to be 7 % of the average. This overall percentage deviation includes the standard deviation of all the kinetic properties determined by both graphical techniques. Similarly for the changes in sample mass, the overall standard deviation is found to be 9 %. These relatively low deviations indicate that the calculated properties are consistent with respect to the changes in these experimental conditions. For the foam decomposition, the overall deviation is 9 % which includes the additional standard deviations from the first reaction and the Arrhenius Plot Method. Therefore, the overall deviation in kinetic properties between foams and melts is comparable.

4.6 Decomposition Behaviours of Polyurethane Foams in Air Environment

The polyurethane foams tested under air environment are the base case foams, NFR-SB-31 and FR-Y-36. Air is delivered as purge gas at the rate of 100 ml/min and the different heating rates tested are 1, 5, 20 and 60 °C/min. The nominal sample mass is 3 mg and three replicates in total are tested for each heating rate. Figure 4-18 compares the mass loss/°C versus temperature for NFR-SB-31 and FR-Y-36 in air and in nitrogen.

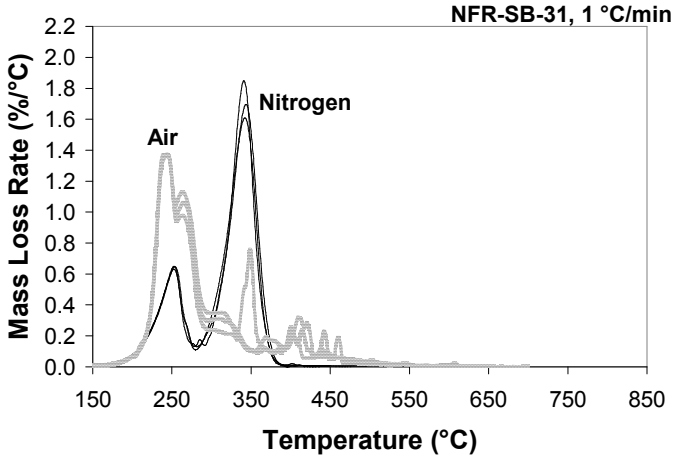
NFR-SB-31, 1 °C/min
Mass Loss Rate (%/°C)
Temperature (°C)
Air
Nitrogen

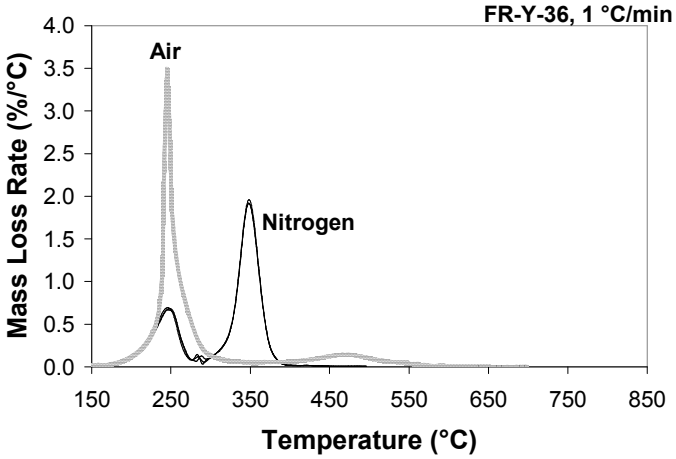
FR-Y-36, 1 °C/min
Mass Loss Rate (%/°C)
Temperature (°C)
Air
Nitrogen

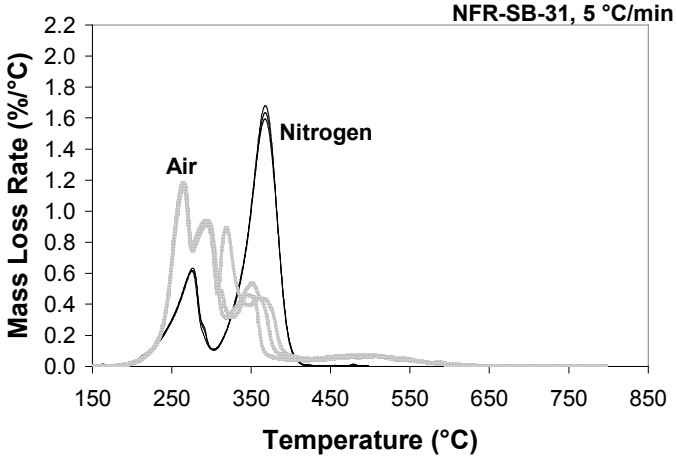
NFR-SB-31, 5 °C/min
Mass Loss Rate (%/°C)
Temperature (°C)
Air
Nitrogen

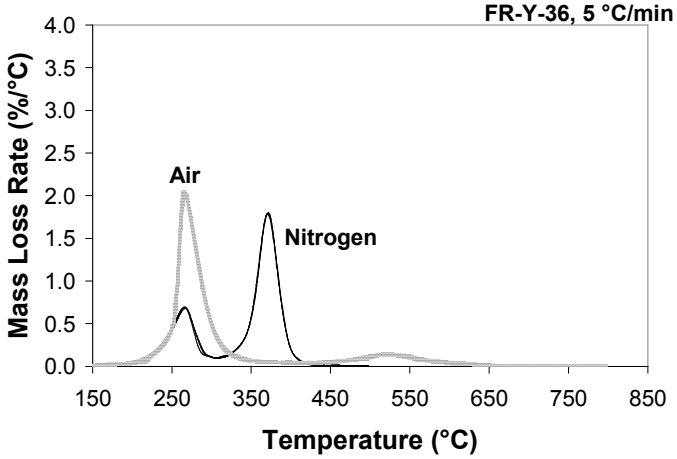
FR-Y-36, 5 °C/min
Mass Loss Rate (%/°C)
Temperature (°C)
Air
Nitrogen

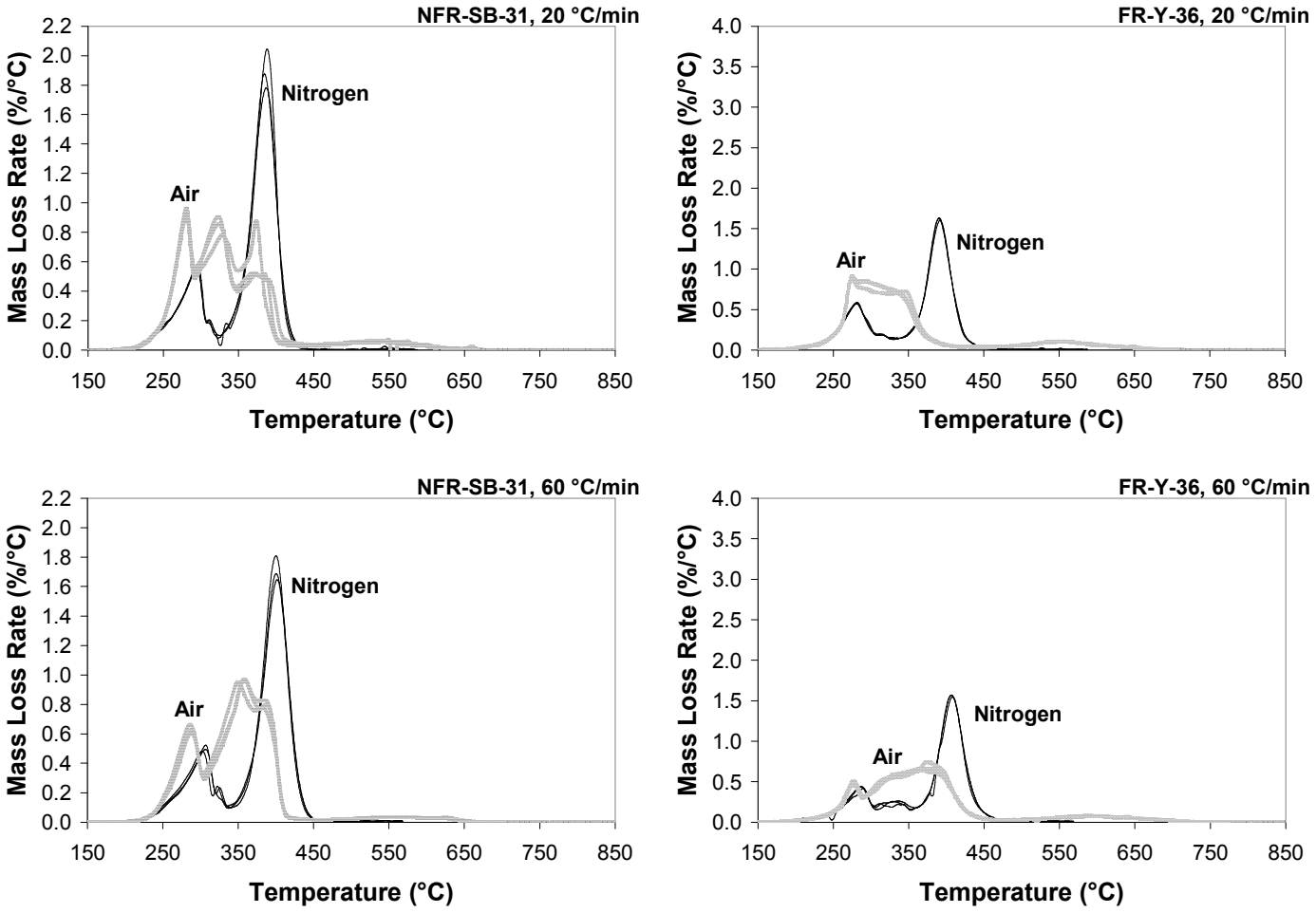

Figure 4-18: Mass loss/°C versus temperature for ~3 mg NFR-SB-31 and FR-Y-36 at 1, 5, 20 and 60 °C/min heating rates under nitrogen and air environments

Focusing on the decomposition behaviours in air, at 1 °C/min, NFR-SB-31 and FR-Y-36 shows a single primary peak at approximately 250 °C but the magnitude of former is significantly smaller than the latter, 1.4 %/°C compared to 3.5 %/°C. NFR-SB-31 also shows multiple smaller non-repetitive peaks between 350 and 450 °C and these peaks are not noted in the results of FR-Y-36 which has better repeatability among its replicates. After the primary decomposition peak, FR-Y-36 shows that there is a slow decomposition region over 375 to 600 °C. At 5 °C/min, FR-Y-36 still shows a single primary peak at approximately 270 °C but NFR-SB-31 has developed from a single peak into two or three peaks, ranging between 200 and 400 °C. The peak at 270 °C has the greatest magnitude and is considered as the primary peak. The repeatability of NFR-SB-31 has improved and a slow decomposition region similar to FR-Y-36 has developed between 425 and 650 °C. Compared to 1 °C/min, the maximum decomposition rate in both foams at 5 °C/min has decreased, 1.2 and 2.0 %/°C for NFR-SB-31 and FR-Y-36 respectively.

At 20 °C/min, the second and third peaks of NFR-SB-31 at 320 and 370 °C have showed increased influence when compared to 5 °C/min previously. The influence of a peak is a comparison of its maximum relative to the primary peak. While the first peak at 280 °C is still the primary decomposition peak, the peak magnitude of 1.0 %/°C is comparable to the magnitude of the second and third peaks. For FR-Y-36, the single primary peak has developed into an extended plateau ranging from 275 to 350 °C with magnitude ranging between 0.7 and 0.9 %/°C. The slow decomposition region is noted between 450 and 650 °C for both foams. At 60 °C/min, the magnitude of the second peak for both NFR-SB-31 and FR-Y-36 has surpassed the first peak to become the primary decomposition peak. This trend is unique for this heating rate as it has not been observed at any of the lower heating rates tested. Due to the familiar presence of the two peaks in the main region of decomposition, this decomposition behaviour at 60 °C/min in air is more comparable to the decomposition behaviours in nitrogen. For NFR-SB-31 and FR-Y-36, the peak magnitude is 1.0 and 0.7 %/°C respectively. The slow decomposition region is noted between 450 and 650 °C for NFR-SB-31 and slightly higher for FR-Y-36, between 475 and 750 °C.

In general, the decomposition in air can be separated into two regions, the main decomposition region and the slow decomposition region. The former consists of pyrolysis and oxidation of foam and melts while the latter consists of oxidation of the char which is a product of those earlier reactions. The repeatability of NFR-SB-31 has improved with increasing heating rate as the comparison between the replicates at 60 °C/min is much closer than the comparison at 1 °C/min. Overall, the TGA results of FR-Y-36 demonstrates better repeatability than those of NFR-SB-31, as the latter contains multiple non-repetitive peaks at lower heating rates such as 1 and 5 °C/min. In nitrogen, the results show that the decomposition behaviours are consistent at different heating rates. Therefore, the pyrolysis reactions involved are confirmed to be independent of heating rate. In air, the decomposition behaviours are more sensitive and are noted to change drastically at different heating rates as seen in Figure 4-18. This indicates that under air, the decomposition has become dependent on heating rate which are caused by the additional oxidative reactions.

In air, the variations in the decomposition involve the changes to the influence or the comparative magnitude of the peaks as a result of the varying degree of oxidation at different heating rates. Low heating rate such as 1 °C/min appear to favour the oxidative reactions that consume foams and melts. According to Valencia[25], these oxidative reactions occur over similar temperature ranges which are lower compared to the pyrolysis reaction of melts. As a result, the melts formed by the first pyrolysis reaction are mainly consumed through oxidation rather than pyrolysis. The solid product of these oxidative reactions is char and the favouring of oxidations leads to a greater amount of char formed as evidenced in Figure 4-19. The char is formed over the main decomposition region at lower temperatures where the decomposition rate is rapid. The char then decomposes over the slow decomposition region at higher temperature which corresponds to the tail of the curves where the slope or decomposition rate declines suddenly. Therefore, besides being heating rate and sample mass dependent, the char formation process is also dependent on the concentration of the oxidiser in the environment.

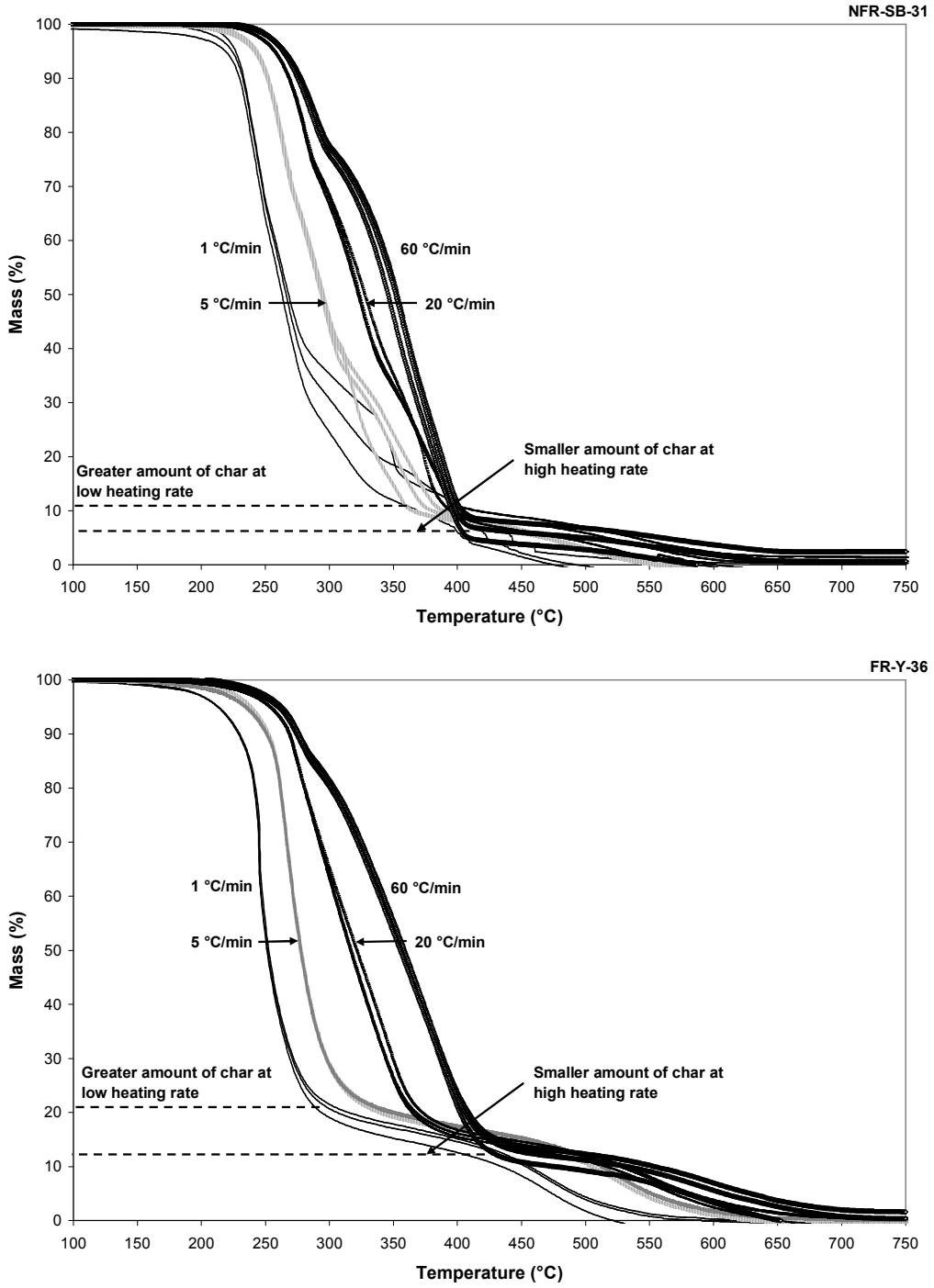

Figure 4-19: Sample mass versus temperature for ~3 mg NFR-SB-31 and FR-Y-36 at 1, 5, 20 and 60 °C/min heating rates under air environment

At high heating rate such as 60 °C/min, the pyrolysis reactions become increasingly favoured during the foam decomposition in air. This is evidenced by the closer resemblance of the decomposition rate curve to that under nitrogen as seen in Figure

4-18. In air, at 60 °C/min, the magnitude of the second reaction surpasses the magnitude of its first reaction to become the primary decomposition peak. Similar trend demonstrating the change in primary decomposition peak at high heating rate is presented by Kramer et al.[54]. The research investigated the decomposition behaviour of foam under air environment in TGA experiments with two reported heating rates, 5 and 176 °C/min. The favouring of the pyrolysis reactions is also evidenced from the amount of char depicted in Figure 4-19 which is noted to reduce under high heating rate as a result of the inferior competition from the oxidative reactions.

The oxidative reactions are the causes for the differences noted between the foam decomposition under nitrogen and air. Under nitrogen, the two decomposition peaks are more distanced as the two reactions occur over distinct temperature ranges but in air, due to the overlaps between the pyrolysis and oxidative reactions, the multiple peaks are closely spaced during the main region of decomposition. The solid phase product of oxidation is char which is thermally stable. Char only decomposes at high temperature via oxidation hence the slow decomposition region is only presence under air. Figure 4-18 shows that the initial foam decomposition in air and nitrogen is similar but the decomposition in air eventually overtakes the decomposition in nitrogen as they approach their respective first peak. As discussed before, this is due to the melts produced from the first pyrolysis reaction undergoing oxidation rather than pyrolysis in air because oxidation occurs over lower temperature range[25]. This trend is more obvious at low heating rates such as 1 and 5 °C/min because at these heating rates, the influence of oxidation on decomposition is stronger over pyrolysis. This is reflected by the significantly greater magnitude of the first peak in air compared to that in nitrogen.

From the TGA results in air, especially at 1 and 5 °C/min, FR-Y-36 is noted to have greater decomposition peak than NFR-SB-31. This seemingly indicates that the fire performance of this FR foam is inferior compared to the NFR foam. However, this is by no means conclusive as the decomposition in air is more representative of the environment during a smouldering fire where oxygen is able to diffuse to the pyrolysis front[19]. In a fully developed fire, oxygen is assumed to be fully consumed in the flame which means it does not have any significant impact on the decomposition

of the fuel[42]. Thus, the decomposition in nitrogen is actually more representative of the fully developed fire and previously, the comparison of decomposition behaviours of NFR and FR foams in nitrogen has indicated that the FR foams have features that show a better performance in fire. Furthermore, the decomposition of FR-Y-36 is known to release inert gases that dilute the combustible gas concentration, produce gas phase inhibitor that disrupt combustion and also form char that interfere with combustion at solid phase. The effectiveness of these fire retardant mechanisms is not fully evident through experiments such as TGA.

Table 4-8 summarises the decomposition temperature for NFR-SB-31 and FR-Y-36 at different heating rates in air environment. The reported temperature is the average of the three replicates tested at each heating rate. The start and end temperatures of the main decomposition region and the slow decomposition region are presented with the peak temperature in brackets. The main decomposition region consists of the closely spaced oxidative and pyrolysis reactions consuming foam and melts while the slow decomposition region consists of the oxidative reaction of char which is the product of those earlier reactions.

Table 4-8: Decomposition temperature for ~3 mg NFR-SB-31 and FR-Y-36 at 1, 5, 20 and 60 °C/min heating rates under air environment

Foam	β, °C/min	Decomposition temperature, °C	
		Main decomposition region	Slow decomposition region
NFR-SB-31	1	212-434 (244)	N/A
	5	228-375 (265)	432-610 (497)
	20	236-400 (281)	457-637 (544)
	60	245-410 (356)	479-664 (558)
FR-Y-36	1	224-281 (245)	374-572 (468)
	5	235-313 (267)	453-641 (522)
	20	236-382 (275)	471-688 (557)
	60	234-434 (373)	502-723 (593)

Similar to the trend in nitrogen, the results shows that the increase of heating rate shifts the decomposition towards higher temperature range. The peak temperature of the main decomposition region differs significantly between 20 and 60 °C/min due to the change in primary decomposition peak as the magnitude of the second reaction surpasses that of the first reaction. The slow decomposition region occurs at temperature range higher than the main decomposition region as reflected in Figure 4-18.

Comparing between NFR and FR foams, the trends in nitrogen previously show the FR foams tends to start decomposing earlier than the NFR foams but this is no longer notable in air because the oxidative reactions occurring over similar range of temperature have masked this difference. Nevertheless, FR-Y-36 is noted to possess higher temperature range for the slow decomposition region where oxidation of char occurs. This comparison indicates that the char formed in the presence of fire retardant additives is thermally more stable than the char formed without. Despite having greater peak magnitude at 1 and 5 °C/min, the temperature range of the main decomposition region for FR-Y-36 is at least half of NFR-SB-31 and the main decomposition of FR-Y-36 also completes at a lower temperature than NFR-SB-31. This means the gaseous fuel from FR-Y-36 is released over lower and narrower temperature range. Given the closely spaced and overlapping reactions of foam decomposition under air, the kinetic properties that govern each reaction cannot be determined using the conventional graphical techniques discussed so far. The calculated kinetic properties are only meaningful for reactions that are well separated.

4.7 Conclusions

The decomposition behaviours of the seven different polyurethane foams tested in the TGA experiments under nitrogen environment are comparable to those reported in Chapter 3 which only involves the base case foams. Over a range of heating rates, the foam decomposes via two pyrolysis reactions where the second reaction consumes majority of the fuel in the form of melts. The melt fraction varies for different foams which can be categorised into those with melt fraction greater than 80 %, those between 75 and 80 % and those with less than 75 %. The FR foams are reported to contain fire retardant additives such as melamine and halophosphate which causes some differences between the decomposition behaviours of FR and NFR foams. The FR foams are noted to have earlier decomposition temperature in the first reaction, wider transition region, lesser fuel consumed in the second reaction and decreasing peak of the second reaction under increasing heating rate. Most of these features are indicative of a potentially better fire performance for the FR foams.

The melts of the different polyurethane foams are also tested in the TGA experiments under nitrogen environment and the decomposition of melt consists of a single reaction which is basically the second reaction of the foam decomposition. The melts tested are collected from the Sample Feeding Vertical Cone experiments discussed in Chapter 7 and during the preparation of the melt samples, the char formed in certain FR foams is separated and removed from the liquid melts. Previously, from the FR foams decomposition, the insulative char formed is able to lower the decomposition peak of the second reaction under increasing heating rate and it also delays the decomposition by increasing the start temperature of the second reaction. However, with the char removed, these trends disappear and the decomposition behaviours of melts from NFR and FR foams become similar. The foam and melt samples are tested at different sample mass, the results show that sample with greater mass decomposes at higher temperature because more mass covers the bottom of the alumina cup.

The decomposition of polyurethane foams in air is also investigated and it is found to be significantly different than in nitrogen due to the additional oxidative reactions which overlaps closely with the pyrolysis reactions. The decomposition can be separated into mainly two regions, the main region of decomposition followed by the slow decomposition region. The main region of decomposition consists of the overlapping oxidation and pyrolysis of foam and melts while the slow decomposition region involves the oxidation of char, the product of the earlier reactions. In comparison with the decomposition in nitrogen, the decomposition in air is more sensitive where the changes in heating rate alters the degree of oxidation causing the increase in influence or comparative magnitude of certain peaks. By 60 °C/min, the primary peak of the decomposition has shifted as the magnitude of the second reaction surpasses the first reaction. Low heating rate appears to favour the oxidative reactions while high heating rate favours the pyrolysis reactions.

Previously, the decomposition in nitrogen shows FR foams to possess potentially better fire performance compared to NFR foams but the decomposition in air shows the peak magnitude of FR-Y-36 is significantly greater than NFR-SB-31 at heating rates of 1 and 5 °C/min. This seemingly indicates the fire performance of the FR foam

is inferior but the TGA results are not an accurate representation of the actual fire performance since the effectiveness of the gas and solid phase fire retardant mechanisms are not evaluated. Furthermore, despite the greater peak magnitude, the decomposition temperature range of FR-Y-36 is lower and shorter than NFR-SB-31 thus the gaseous products released are less susceptible to combustion. This research shows that the fire retardant mechanisms are potentially dependent on the heating rate, the sample mass and also the environment.

From the TGA results obtained under nitrogen, the kinetic properties are calculated using graphical techniques and the respective trend of E, A and n are found to be comparable to those obtained in Chapter 3. Over the different heating rates and sample mass tested, E and A of the first reaction is consistently smaller than the second reaction while n of the first reaction is consistently greater than the second reaction. For the range of heating rate and sample mass tested, the deviation in kinetic properties of the foam samples and the melt samples are similar, less than 10 % of the average. Since the decomposition of melt is essentially the same as the second reaction of foam, their kinetic properties are comparable in magnitude. This justifies the consistency of these graphical techniques when applied to samples in different physical states. For air, the kinetic properties for the individual reactions of foam decomposition are not calculated because they overlap and are closely spaced. The graphical techniques applied are only suited for reactions that are well separated. In order to develop a better understanding on the intrinsic nature of the kinetic properties and the decomposition they governed, future research should identify the primary TGA results that produce the current trends seen among the kinetic properties.

Chapter 5. Heat of Reaction of Polyurethane Foams

5.1 Introduction

According to the literature, a number of studies[19,55] proposed that the decomposition of polyurethane foam in a nitrogen environment proceeds via the two pyrolysis reactions presented in Section 4.1 of Chapter 4. According to the proposed scheme, when the polyurethane foam reaches the decomposition temperature, it decomposes into melts and gases through the first reaction. From the thermogravimetric analysis (TGA) results, by the end of the first reaction, the melts remained are approximately 75 % of the original sample mass. When the temperature increases further, the melts decompose almost entirely into gases through the second reaction, leaving behind small amount of char residue.

During the smouldering phase of a fire or before piloted ignition, polyurethane foam exposed to heat will be oxidised to some degree by the oxygen in the air. However, oxidation is seldom included to describe the foam decomposition under sustainable flaming because after ignition, any available oxygen will be consumed within the flame before reaching the fuel bed to cause oxidation[42]. Therefore, the two pyrolysis reactions listed in Section 4.1 remain as a simple mean of describing the combustion of polyurethane foam.

From the fundamental of thermochemistry, in order for a reaction such as the decomposition of material to initiate or to progress further, an amount of energy is absorbed or released by the material[56]. The reactions absorbing energy are endothermic in nature while those releasing energy are exothermic. The amount of energy that changes is termed the heat of reaction and this is a user defined input in many combustion models available such as Fire Dynamics Simulator, Version 5[17] (FDS 5[a]) and Gpyro[27]. The objective of this chapter is to experimentally determine the heats of reaction during the decomposition of polyurethane foams which are later used as inputs into FDS 5 to simulate the burning behaviours of polyurethane foams in

[a] Version 5.5.3, SVN number 7031.

Chapter 8 and 9. The experimental technique applied is known as simultaneous differential scanning calorimetry and thermogravimetric analysis (SDT).

5.2 Literature Review on Terminology of Heat of Reaction, Type of Differential Scanning Calorimetry and Common Practice

Since the primary fire model in this research is FDS 5, the model's terminology on heat of reaction is applied in this thesis. The heat of reaction, Δh_r in J/g is defined as the change in the amount of energy per unit mass of reactant converting into products. However within the literature, the heat of reaction is also known as the enthalpy of reaction, the heat of pyrolysis, the heat of volatilisation, the heat of vaporisation and the heat of decomposition. Also used in the field of fire modelling is the heat of gasification which includes the additional sensible heat or the energy required to heat up the material before a reaction occurs[57,58,59]. The definition for the heat of gasification is illustrated by Equation (5-1) where the first term on the right hand side represents the sensible heat while the second term is the heat of reaction[60].

$$\Delta h_g = \int_{T_a}^{T_p} c_p(T)dT + \Delta h_r \tag{5-1}$$

In practice, the heat of reaction is not measured directly but calculated through the changes of heat flow measured in mW. There are several equipment[61,62] capable of measuring heat flow and one of those is the family of differential scanning calorimetry (DSC) which is categorised into two operating modes, power compensation and heat flux. For power compensation DSC, the sample contained within a cup is placed in the sample furnace while an empty cup which serves as reference is placed in another furnace. During the experiment, both furnaces are heated at an identical rate and when the sample undergoes reaction, the amount of power compensated to maintain the heating rate is used to compute the changes of heat flow. For heat flux DSC, the sample and reference are contained within a single furnace and during the experiment, the temperature of the sample and reference are measured by their respective thermocouple, usually beneath the cup. The temperature

difference between the sample and reference is used to compute the changes in heat flow.

While there are only two operation modes, there are a few types of DSC equipment with different features. These include the typical standalone DSC which measures heat flow only, the modulated DSC (MDSC) which has sinusoidal oscillation superimposed on its temperature increase, the pressure DSC (PDSC) which allows an experiment to proceed under high pressure or vacuum, the dual sample DSC which allows the simultaneous testing of two samples and the SDT which simultaneously measures the changes in heat flow via DSC and the changes in sample mass via TGA. Alternatively, SDT is also known as simultaneous thermal analysis (STA). Besides the family of DSC, there is differential thermal analysis (DTA) which predates DSC. The equipment has the same setup as the heat flux DSC but the temperature difference between the sample and reference is not converted into heat flow and remains as a voltage signal. There is also differential photocalorimetry (DPC) which utilises ultraviolet radiation to initiate the reaction and determines the change in heat flow from the temperature difference between the sample and reference[63].

The cup used in DSC experiment is made from either metallic element such as aluminium, copper, gold and platinum or non-metallic such as graphite and alumina. These cups can be tested in different configurations such as open, non-hermetically sealed or hermetically sealed. Open configuration suits the experiments where the sample will be tested until the end of decomposition and the pyrolysates produced are allowed to escape. However, this reduces the accuracy of the heat flow measured as larger thermal gradient develops across the sample and the pyrolysates are released within the equipment. The thermal gradient invalidates the lumped capacitance assumption of DSC experiment and the contamination wears the furnace. In sealed modes, the cups are covered with lid and the thermal gradient and contamination are minimised but the experiments are normally terminated before the start of decomposition to prevent pressure build up within the sealed cup from the volatiles released. By slowing the release of volatiles, Rath et al.[64] in their research has showed that this can lead to secondary reactions which alter the nature of the decomposition.

According to the recommended practice[65], the amount of sample to be tested normally ranges between 10 to 20 mg but this is reduced to less than 5 mg if the sample is corrosive and increased to between 50 and 100 mg if volatilisation is significant. The heat flow measured is also recommended to range between 0.1 to 10 mW and the baseline needs to stabilise before and after the reaction of interest. Commonly, chemically inert gases such as nitrogen and helium are used for furnace purging and the selected flow rate varies, depending on the manufacturer's recommendation. In general, excessively high purge flow rate tends to increase the noise level in the measurements while decreasing it extremely causes the accumulation of decomposition products which damages the furnace. In terms of heating rate, values from 2 to 20 °C/min are often applied in DSC experiment. Heating rates less than 2 °C/min result in extended experimental duration while those greater than 20 °C/min are considered too fast for the sample to achieve thermal equilibrium and also create thermal gradient across the sample.

5.3 Literature Review on Issues Surrounding Differential Scanning Calorimetry and Available Solutions

The use of DSC as a research tool in fire engineering is significantly hampered by the complications involved with analysing the measured heat flow results. Some of the known issues are discussed in this section. Figure 5-1 shows a typical DSC heat flow curve which often contains several baseline artefacts such as start up hook, offset, slope and curvature. These artefacts are either caused by the sample undergoing reaction or the unwanted experimental errors. Sources for these experimental errors include the sample-reference side asymmetry from the inherent design and manufacture of the equipment[66], the changes in the heating rate applied[67] and also the changes of the sample characteristic such as the heat capacity[67] and emissivity[64] after decomposition.

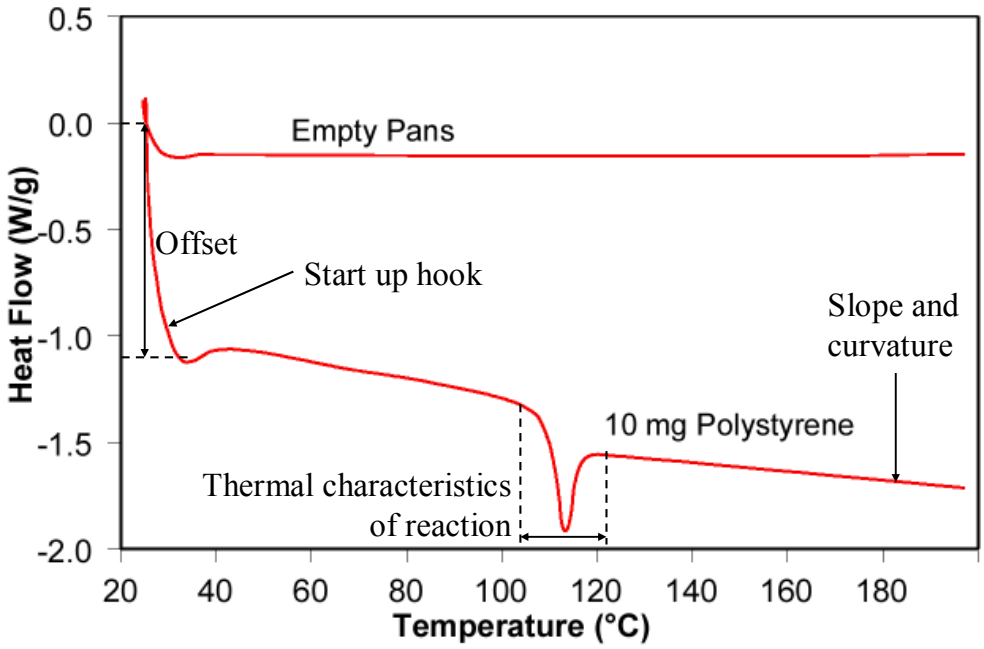

Figure 5-1: Common baseline artefacts and reaction thermal characteristics on DSC heat flow curve[62]

From Figure 5-1, the inconsistent offset and start up hook is influenced by the changes in the heating rate applied and the changes in the heat capacity of the sample. The presence of curvature is contributed by the changes in the emissivity of the sample during decomposition. The DSC heat flow also experiences reduction in resolution indicated by the smearing of heat flow from a reaction into the temperature range outside the reaction region as seen in Figure 5-2[68]. The phenomenon of smearing arises from the in-built assumptions made regarding the heat flow imbalance of the equipment which relates to its thermal resistance, thermal capacitance and heating rate.

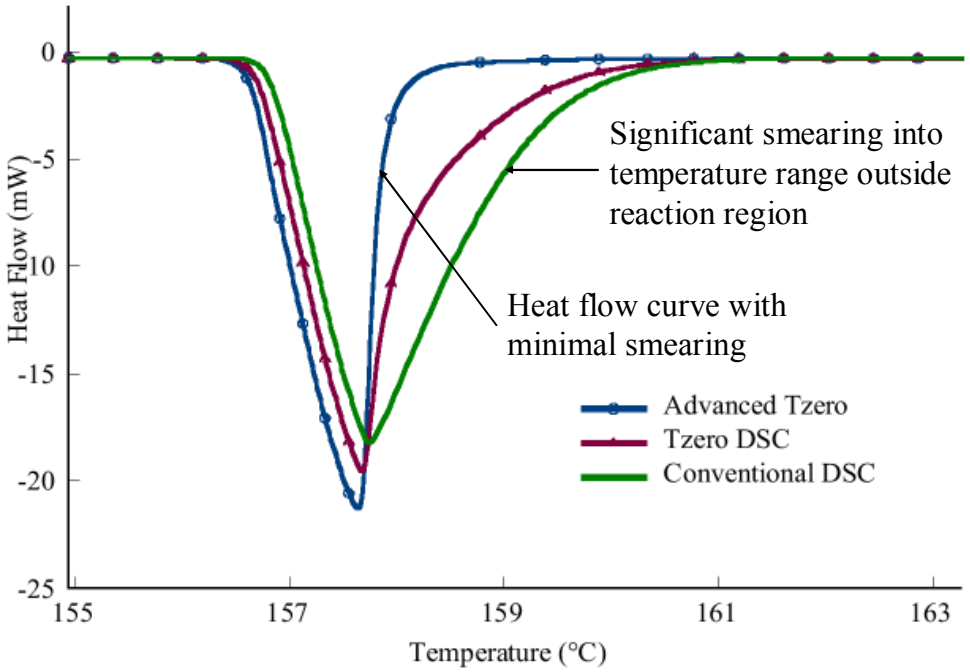

Figure 5-2: Smearing of heat flow by different models of DSC equipment[68]

Figure 5-3 shows the DSC heat flow containing thermal lag which is influenced by the setup of the equipment and also by the cup in use which acts as thermal barrier[69]. The severity of the lag depends largely on the specific heat of the sample and cup, the thermal contact between the cup and thermocouple and the selected heating rate of the experiment[70]. Generally, large sample mass with high specific heat, cup with open configuration, poor thermal contact and high heating rate are factors which increase the thermal lag.

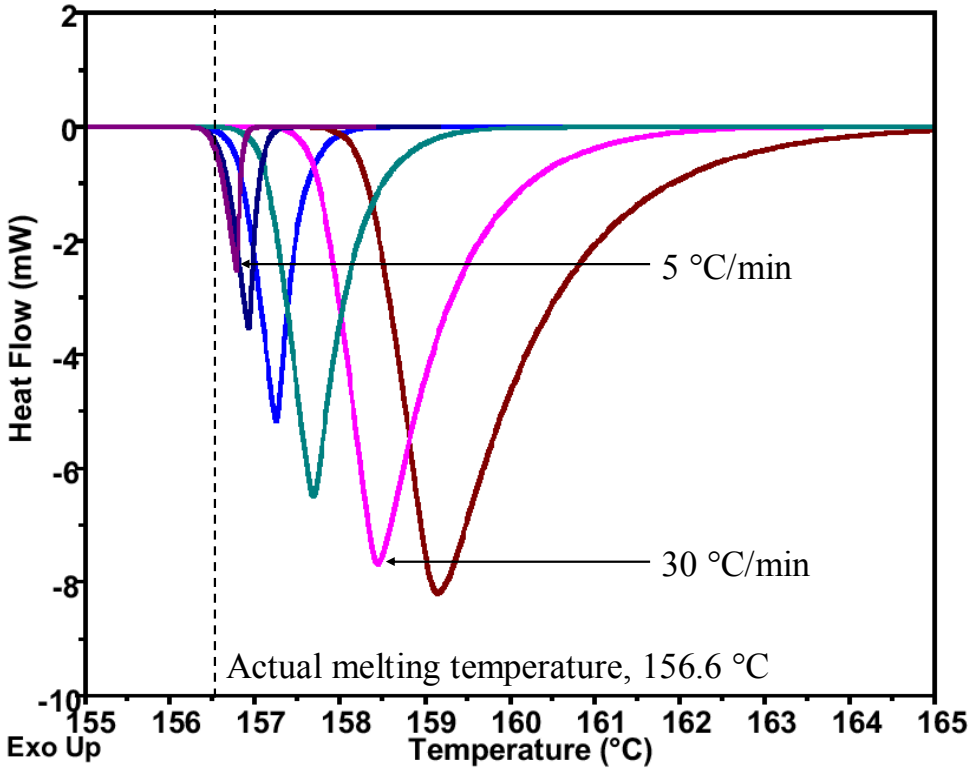

Figure 5-3: Thermal lag on DSC heat flow curve[69]

Some conventional treatments aimed at mitigating the errors mentioned above are reported in the literature. One of the recommendations involves subtracting the measured heat flow for empty cups from the experimental heat flow as the former is assumed to be free of inconsistencies. In their research, Stoliarov et al.[71] found that due to the heat losses between the furnace and the surrounding, the baselines for the empty cups still vary even after extended equilibration of the equipment. The non-reproducible inconsistencies such as offset, slope and curvature are known to vary with the heating rate applied and the changes in the thermophysical properties of the sample following decomposition. The baseline offset can be estimated using Equation (5-2)[67] and the offset is a function of the heat capacity of the sample and the heating rate of the experiment.

$$\left(\frac{dq}{dt}\right)_{off} = m_{sam} c_p \frac{dT}{dt} \tag{5-2}$$

According to Rath et al.[64], the baseline curvature caused by the changes in the sample's emissivity can be removed by quantifying the additional radiative exchange between the sample and the furnace. However, the technique is rather laborious and this is discussed further in the next section. In the literature[25,62], a simpler treatment had been used for correcting both the offset and the curvature. This technique involves subtracting the measured heat flow with a mathematically fitted baseline defined by the user or an analysis program as seen in Figure 5-4. The baseline for subtraction can also be constructed experimentally as described in the research by Stoliarov et al.[71]. By assuming linear dependence between the heat losses and temperature, Stoliarov et al. constructed the baseline from the isothermal heat flow measured at several selected temperatures.

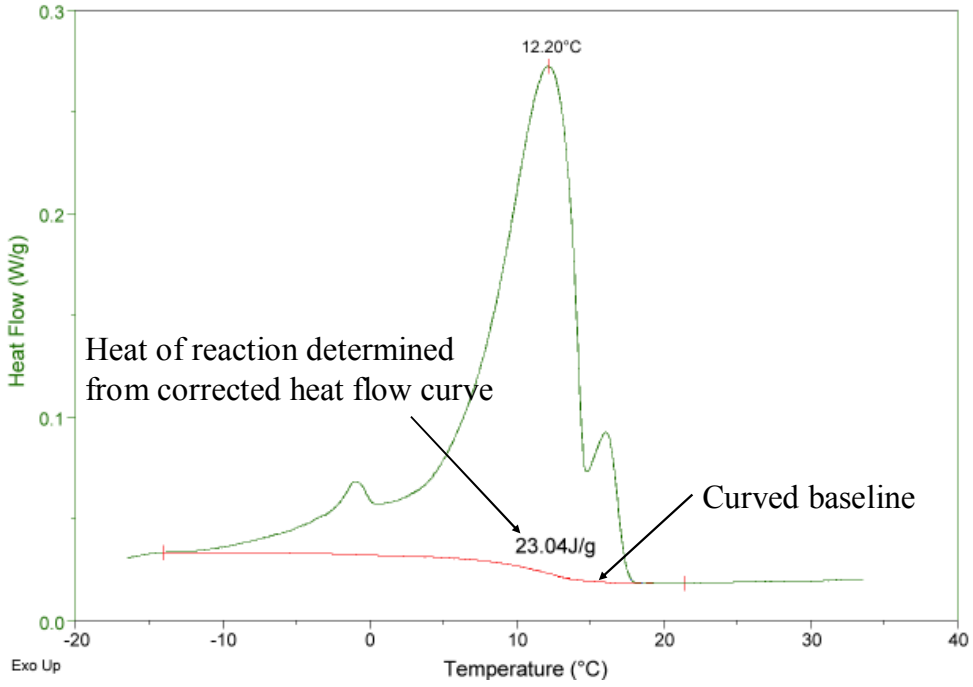

Figure 5-4: Application of curved baseline for correcting heat flow measurements[62]

Besides the mathematical approaches, there are also few experimental practices which can minimise the unwanted errors. Utilising greater heating rate and higher sample mass help in reducing the curvature[62]. Another alternative involves reducing the asymmetry between the sample and reference sides by filling the reference side with material of similar heat capacity as the sample[62]. This allows the baseline to stabilise faster but the technique is often impractical because the selected material should not experience any reaction over the temperature range investigated. Lowering the

thermal inertia of the sample and allowing it to heat through thoroughly improve the resolution of the heat flow. The practices include using low mass flat pan and small sample mass, ensuring good thermal contact between the sample and the bottom of the pan, employing slow heating rate and using helium gas which has better thermal conductivity than nitrogen gas for purging. As the criteria for improving resolution contradicts those for reducing curvature, the user is required to consider the trade-off between heat flow resolution and baseline curvature when preparing DSC experiments. Lastly, the thermal lag is often corrected by shifting the measured heat flow by an appropriate temperature calculated based on Equation (5-3)[69].

$$\Delta T_{lag} = \left(\frac{dq}{dt}\right)_{peak} \cdot R_t \tag{5-3}$$

This technique involves melting a pure material in DSC experiment to determine the equipment specific parameters for the type of cup used and for the heating rate applied. From the heat flow curve of melting, the thermal resistance, R_t is determined as the inverse of the leading slope while $(dq/dt)_{peak}$ is the peak magnitude measured. Despite obtaining those parameters, the heat capacity of a polymer is known to be different than a pure material thus ΔT_{lag} found might not be applicable in the case of polymer sample.

Currently, a few advanced technologies have been installed into specific standalone DSC equipment to improve the accuracy of the heat flow measurements. These technologies include highly sensitive thermocouples, extra thermocouple to accurately address the instrumental effects and the changes in furnace orientation for accurate temperature measurements[72]. These have been developed to ensure the heat flow baseline is stable by addressing the asymmetries and thermal effects of the equipment through a more complete heat flow equation. Other improvements in heat flow measurements include providing accurate heat flow measurements for low mass (~1 mg) sample, compensating the heat flow imbalances to improve the resolution and automatically correcting the thermal lag caused by cup, equipment and heating rate. However, these equipment are more delicate and sample testing until decomposition

is not possible due to the amount of contamination and corrosion that could damage the furnace[73].

5.4 Literature Review on Determination of Heat of Reaction for Common Solid Fuels

As illustrated by Equation (5-4), the changes of heat flow measured in DSC experiment compose of two terms. The first term is a heat capacity component and the second term is a kinetic component[62].

$$\frac{dq}{dt} = m_{sam} c_p(T) \frac{dT}{dt} + f(T,t) \tag{5-4}$$

The heat capacity component is influenced by the heating rate applied and the material's heat capacity. Examples of heat capacity component include phenomenon such as glass transition and melting. The kinetic component is a function of temperature and time. The examples of kinetic component include enthalpic relaxation[61], mechanical stress relief, melting, evaporisation and decomposition. As illustrated in Equation (5-1), the changes in enthalpy due decomposition also known as the heat of reaction is embedded within the kinetic component. Thus, further data reduction is required to extract the heat of reaction from the DSC heat flow. A few studies in the literature have described the data reduction techniques to extract the heat of reaction for several materials and they are discussed below.

5.4.1 Rath et al.

Under nitrogen environment, Rath et al.[64] determined the heat of pyrolysis of woods using standalone DSC and SDT at heating rate of 10 °C/min. The wood samples studied were spruce and beech and the authors also investigated the effect of using non-hermetic lid, different sample mass and different purge flow rates. When the pierced lid was used to seal the sample and reference cups, the emissivity of the sample and reference sides were identical throughout the experiment which resulted

in the same radiative exchange with the furnace[74]. Without the lid, additional radiation heat flow was present due to the difference in emissivity between the sample and reference. As a result, a sloping baseline was developed. Thus, for the experiments without lid, the reaction heat flow due to pyrolysis is calculated via Equation (5-5) which includes the radiation heat flow term. For the experiments with lid, the radiation heat flow is omitted from the equation.

$$\left(\frac{dq}{dt}\right)_R = \frac{dq}{dt} - \left(\frac{dq}{dt}\right)_{bas} - m_{sam} c_p(T) \frac{dT}{dt} - \left(\frac{dq}{dt}\right)_{rad} \tag{5-5}$$

The baseline heat flow, $\left(\frac{dq}{dt}\right)_{bas}$ is measured from the DSC experiment with empty sample and reference cups. The heat flow due to the heat capacity of the sample is determined using Equation (5-6) which accounts for the conversion of wood into char and the changes in the specific heat of wood and char with respect to temperature.

$$m_{sam} c_p(T) \frac{dT}{dt} = \left[(1 - X(T)) m_0 c_{p,wood} + X(T) m_f c_{p,char}\right] \frac{dT}{dt} \tag{5-6}$$

The conversion of wood into char is governed by a dimensionless sample conversion, $X(T)$ calculated using Equation (5-7) while the changes in $c_{p,wood}$ and $c_{p,char}$ are governed by the temperature based empirical correlations in Equation (5-8) and (5-9).

$$X(T) = \frac{m_0 - m(T)}{m_0 - m_f} \tag{5-7}$$

$$c_{p,wood} = 1113.68 + 4.8567(T - 273.15) \tag{5-8}$$

$$c_{p,char} = \frac{8314}{5.75}\left[e^{\frac{380}{T}}\left(\frac{e^{\frac{380}{T}} - 1}{\frac{380}{T}}\right)^{-2} + 2e^{\frac{1800}{T}}\left(\frac{e^{\frac{1800}{T}} - 1}{\frac{1800}{T}}\right)^{-2}\right] \tag{5-9}$$

The radiation heat flow, $\left(\frac{dq}{dt}\right)_{rad}$ from the additional radiative exchange between the sample and the furnace is estimated based on the difference between the measured experimental heat flow for heating char and the calculated values using Equation (5-10).

$$\left(\frac{dq}{dt}\right)_{char} = m_f c_{p,char} \frac{dT}{dt} \tag{5-10}$$

After determining the respective heat flow due to baseline, sample heat capacity and radiation, the offset and curvature from the original DSC heat flow are removed using Equation (5-5) to produce the reaction heat flow. In sequence, Figure 5-5 shows the TGA sample mass loss (a), the TGA mass loss/°C (b) and the reaction heat flow from DSC experiment without lid (c) and with lid (d) of spruce wood at 10 °C/min.

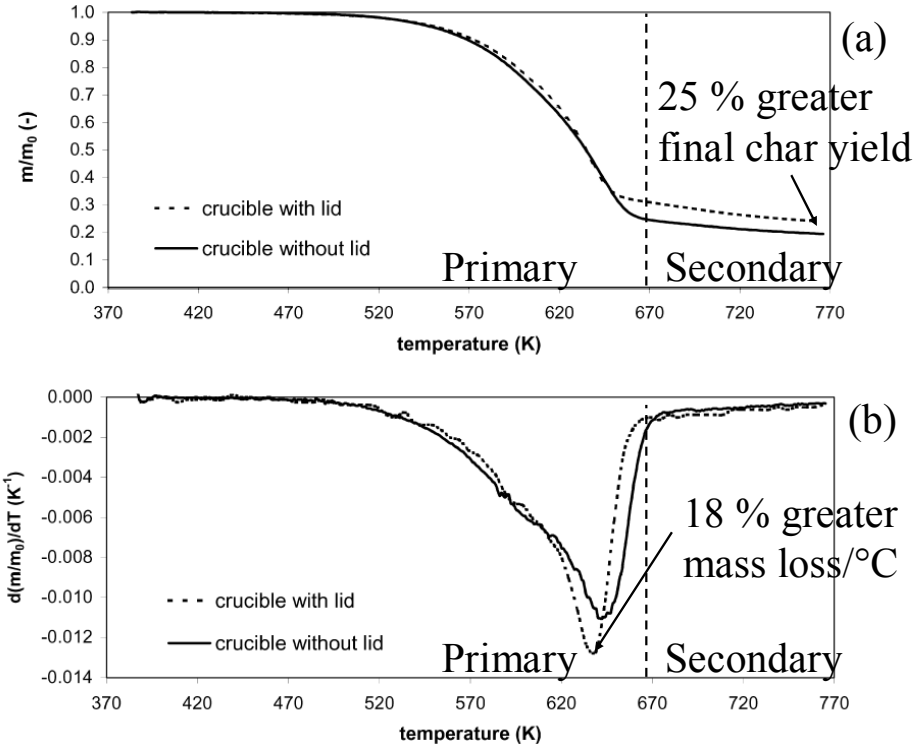

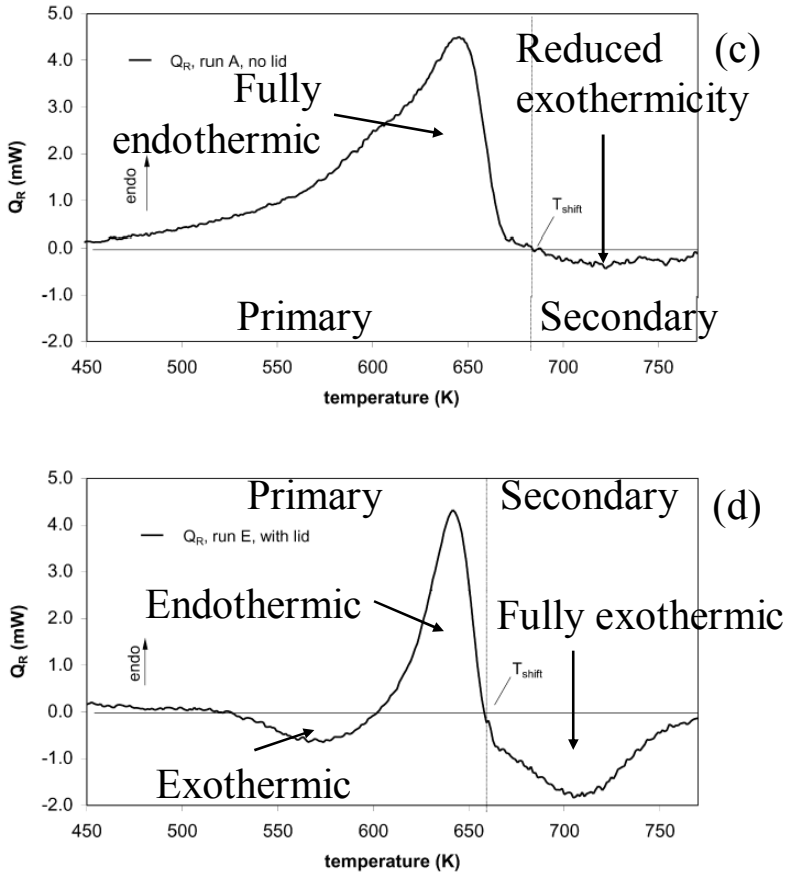

Figure 5-5: TGA sample mass loss in mass fraction (a), TGA sample mass loss/°C (b) and reaction heat flow of DSC experiment without lid (c) and with lid (d) for spruce at 10 °C/min under nitrogen environment[64]

From the TGA results, between the experiment with and without lid, the former achieves approximately 18 % greater peak mass loss/°C than the latter over the primary decomposition. Over the secondary decomposition, the experiment with lid maintains approximately 25 % higher final char yield than the experiment without lid. From the DSC results, more notable differences are observed between the experiment with and without lid. With lid, the heat flow shows the primary decomposition has an initial exothermic region followed by an endothermic region while the secondary decomposition is fully exothermic. Without lid, the first exothermic region is absent as the primary decomposition is fully endothermic. In the secondary decomposition, its exothermic region has reduced and the peak heat flow is approximately 25 % of the peak heat flow when the lid was used.

The heat of pyrolysis for the primary, secondary and total decomposition is calculated using Equation (5-11). T_{shift} as depicted in Figure 5-5 is the temperature where the primary decomposition ends and the secondary decomposition begins.

$$\Delta h_{tot} = \Delta h_p + \Delta h_s = \frac{1}{m_0}\int_{T_i}^{T_{shift}} \left(\frac{dq}{dt}\right)_R dt + \frac{1}{m_0}\int_{T_{shift}}^{T_f} \left(\frac{dq}{dt}\right)_R dt \qquad (5\text{-}11)$$

From Equation (5-11), the heat of pyrolysis determined by Rath et al. is on the basis of the original mass, m_0 rather than per unit mass of reactant converted into product which is the terminology used in this thesis. By adopting the latter, the heats of pyrolysis are represented in Equation (5-12).

$$\Delta h^*_{tot} = \Delta h^*_p + \Delta h^*_s = \frac{1}{m_i - m_{shift}}\int_{T_i}^{T_{shift}} \left(\frac{dq}{dt}\right)_R dt + \frac{1}{m_{shift} - m_f}\int_{T_{shift}}^{T_f} \left(\frac{dq}{dt}\right)_R dt \qquad (5\text{-}12)$$

The initial and final mass, m_i and m_f are provided by Rath et al. but the mass at T_{shift}, m_{shift} is not reported. Since the mass loss over the secondary decomposition as seen in Figure 5-5(a) and (b) is negligible, m_{shift} is assumed to be m_f as an approximation. This enables the recalculation of Δh_p and Δh_{tot} but without knowing m_{shift}, Δh_s cannot be estimated. Table 5-1 provides a range of heat of pyrolysis and final char yield for spruce and beech reported by Rath et al.. The recalculated heat of pyrolysis, Δh_p* and Δh_{tot}* which are based on unit mass of reactant consumed are also included. The negative sign denotes the exothermic nature of the decomposition.

Table 5-1: The range of heat of pyrolysis and final char yield for spruce and beech at 10 °C/min reported by Rath et al.[64]

Sample	Lid	Final char yield	Δh_p (J/g)	Δh_p* (J/g)	Δh_s (J/g)	Δh_{tot} (J/g)	Δh_{tot}* (J/g)
Spruce	With	0.22 to 0.25	42 to 162	56 to 209	-42 to -63	120 to -19	155 to -25
	Without	0.18 to 0.21	241 to 387	300 to 472	-24 to -29	213 to 364	264 to 443
Beech	With	0.23 to 0.25	-86 to -156	-111 to -207	-50 to -66	-135 to -222	-175 to -295
	Without	0.18	145 to 148	177 to 180	-17 to -32	116 to 128	141 to 156

The results in Table 5-1 show the decomposition are more endothermic in nature when no lid was used and this corresponds well with the reduced exothermicity seen

in Figure 5-5(c). For beech, changing from with to without lid even causes the primary decomposition to change from exothermic into endothermic.

Rath et al. discovered a linear relationship between the final char yield and the heat of pyrolysis of woods as seen in Figure 5-6. The increase in final char yield causes both Δh_p and Δh_s to become more exothermic with the former changing more drastically than the latter.

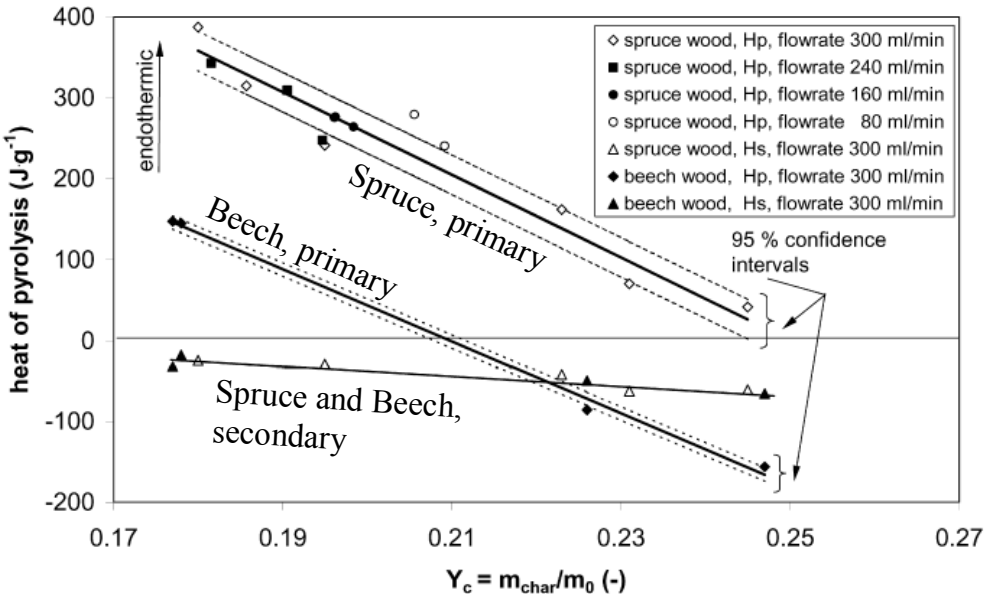

Figure 5-6: Heat of pyrolysis versus final char yield for primary and secondary decomposition of spruce and beech[64]

The changes in final char yield are dependent on several experimental conditions. First of all, from Table 5-1, the final char yield is affected by the lid where its presence encourages char formation resulting in the higher yield. Rath et al. also investigated the effects of different sample mass and purge flow rate have on char yield. Sample mass from 2 to 15 mg and flow rate of nitrogen from 80 to 300 ml/min were tested. The results in Figure 5-7 show that lower sample mass and higher purge flow rate potentially decrease the final char yield.

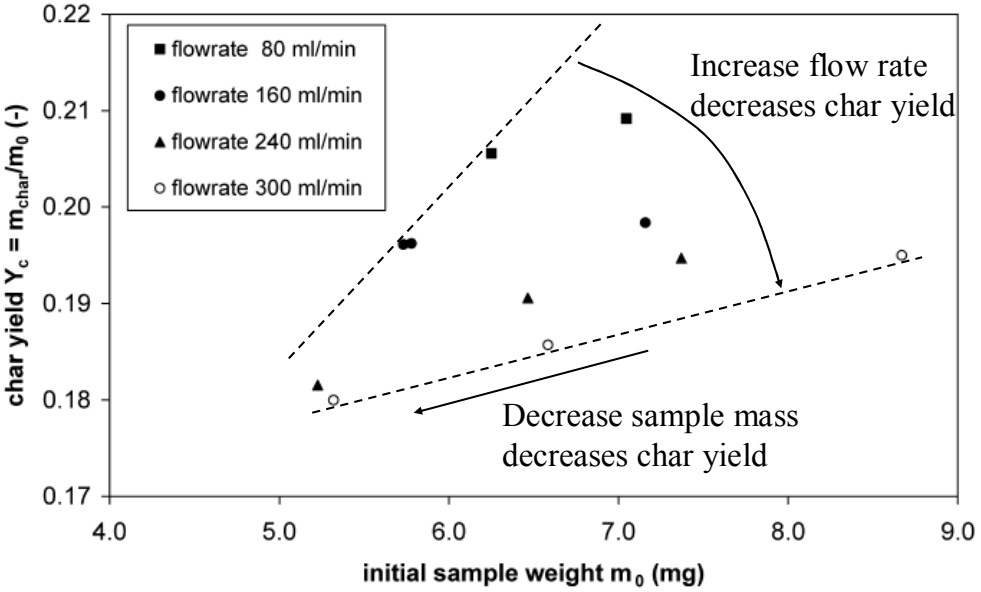

Figure 5-7: Effect of initial sample mass and purge flow rate on final char yield[64]

From the results in Table 5-1 and Figure 5-7, the final char yield is noted to decrease for experiments without lid, with low sample mass and with high purge flow rate. So according to the correlations in Figure 5-6, the wood decomposition is expected to become more endothermic under these experimental conditions. The primary decomposition was reported to consist of the competition between endothermic volatilisation and exothermic char formation, both reactions utilise virgin wood as the reactant. Due to such competition, Δh_p is more strongly influenced by the char yield than Δh_s. The secondary decomposition is reported to consist of reactions such as char aromatisation and dehydrogenation.

Rath et al. did not explicitly plot the relationships of the heat of pyrolysis versus the sample mass and the purge flow rate. Therefore to ascertain these relationships, the available results from Rath et al. are utilised here. The recalculated primary heat of pyrolysis, Δh_p* is plotted against the sample mass and the purge flow rate respectively in Figure 5-8 and 5-9. A trend line is fitted through the most repeated series of experiments involving spruce wood without lid.

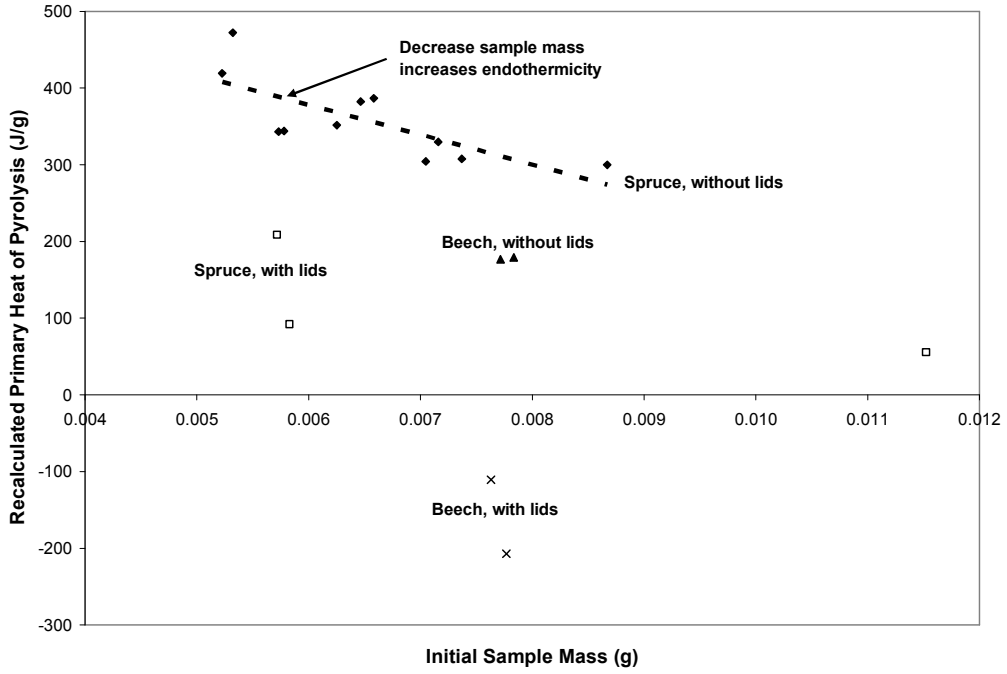

Figure 5-8: Recalculated primary heat of pyrolysis versus initial sample mass from DSC experiments with and without lid on spruce and beech

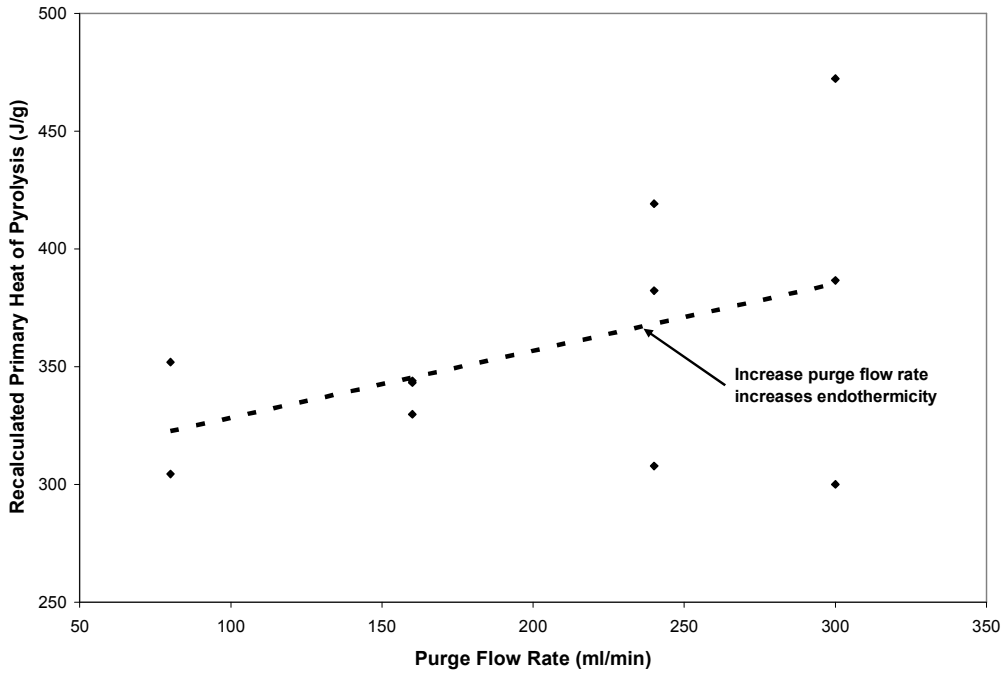

Figure 5-9: Recalculated heat of pyrolysis versus purge flow rate from DSC experiments without lid on spruce

The results confirm that the decrease in sample mass and the increase in purge flow rate shift the heat of pyrolysis towards endothermic which support the relationships obtained by Rath et al. in Figure 5-6 and 5-7.

Rath et al. offered some qualitative explanations regarding the continuous changes in the heat of pyrolysis under the different experimental conditions. The competition between endothermic volatilisation and exothermic char formation was identified as the main cause. The exothermic char formation is favoured by the experimental conditions such as the use of lid, high sample mass and low purge flow rate. Collectively, these conditions result in the greater resistance towards the transport of volatiles and the enhancement of charring and other exothermic reactions of the remaining residues at low temperatures. Overall, Rath et al. showed that the heat of reaction potentially has a wide range which changes as a function of the yield of decomposition products. The heat of reaction varies for different wood samples and it is sensitive to the changes in the experimental conditions. These variations are capable of altering the nature of the decomposition that often contains several competing reactions which are favoured differently under different conditions.

5.4.2 Valencia

Valencia's research contains the experimental and numerical investigations of polyurethane foam decomposition[25]. A power compensated standalone DSC was used to measure the heat flow during the decomposition under nitrogen and air environments. The experiments were performed under a constant heating rate of 8 °C/min from the room temperature up to 500 °C with a purge flow rate of 50 ml/min. Sample mass measuring 7 mg was contained within an aluminium cup and sealed by a lid. According to the author, the original heat flow results were reported to contain the common inconsistencies such as offset and curvature due to the changes in the sample mass and its thermophyscial properties during decomposition. Utilising a sigmoid baseline, these inconsistencies were removed. The author also reported the TGA results of the polyurethane foam under the same heating rate. Figure 5-10 shows the TGA mass loss rate and DSC heat flow during the decomposition in air and nitrogen environments respectively. The negative sign on DSC heat flow is indicative of the exothermic nature of the reaction.

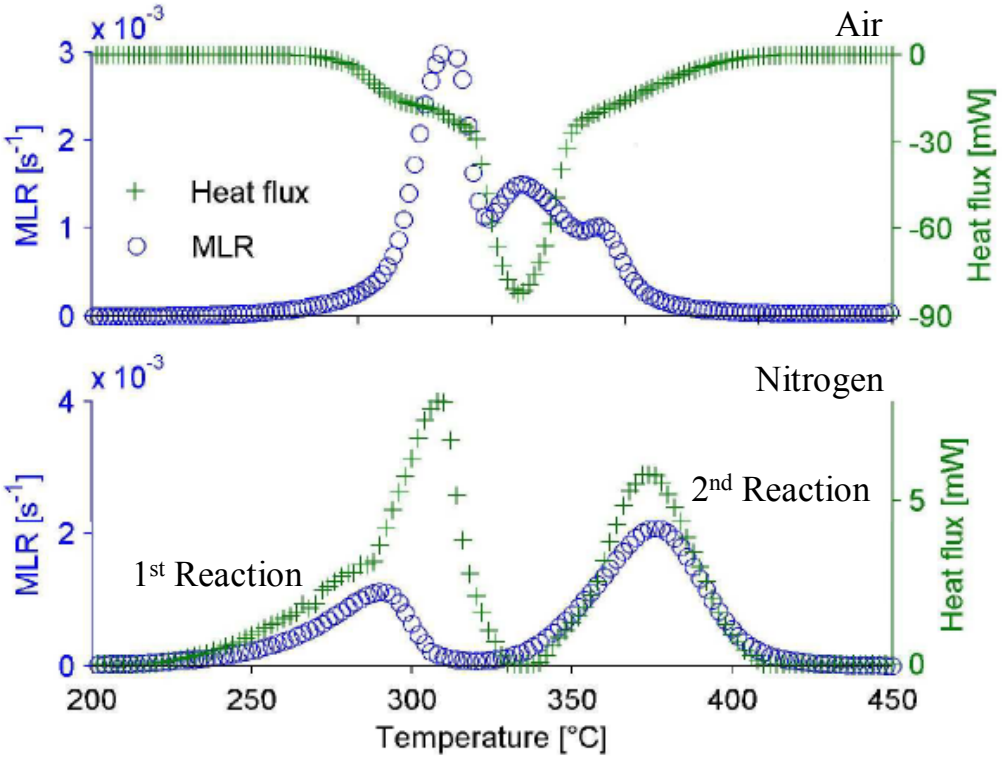

Figure 5-10: TGA mass loss rate and DSC heat flow of polyurethane foam decomposition in air and nitrogen environments[25]

According to the TGA results, significant mass loss starts above 200 °C and the DSC results show that the decomposition reactions under nitrogen are endothermic in nature while under air, the decomposition is exothermic. Under nitrogen, the temperature mismatch seen between DSC heat flow and TGA mass loss rate over the first reaction indicates the presence of thermal lag in the heat flow measurements. The heat flow from the first reaction also appears to smear into the temperature region where the first reaction has completed. Nevertheless, the trend between DSC and TGA results is reasonably similar. Under air, the differences between DSC and TGA results are more pronounced. According to Valencia, these dissimilarities are caused by the different heating mechanism between the DSC and TGA equipment. In the DSC experiment, the heat was transferred through the bottom of the cups while in the TGA experiment, the heat transfer occurred around the sample. Another likely cause is the different purge flow rate between both equipment where DSC used 50 ml/min and TGA used 20 ml/min. The decomposition under air was reported to be strongly dependent on the ventilation, very different results were obtained when hermetic and non-hermetic lids were used.

Valencia reported that the heat of reaction for the air experiment is exothermic 3891 J/g and for the nitrogen environment, the first and second reactions are endothermic 318 and 236 J/g respectively. The heat of reaction developed was subsequently used to model the burning behaviours of polyurethane foam in FDS 5. The standalone DSC equipment does not monitor the changes in sample mass so the heat of reaction reported by Valencia is per the original sample mass. Once again by adopting the terminology for the heat of reaction in this thesis, the heat of reaction from Valencia's research is recalculated. For the nitrogen experiment, the assumptions made include the original sample mass is precisely 7 mg as reported by Valencia and the smeared heat flow noted between the first and second reactions originates completely from the first reaction. The recalculated endothermic heat of reaction for the first and second reactions and also the total is 1009, 331 and 547 J/g respectively. For the air experiment, the recalculation is not necessary because the decomposition is assumed to be a single reaction where the entire sample mass was consumed.

5.4.3 Stoliarov et al.

Stoliarov et al.[71] tested several common plastics and engineering polymers in nitrogen using the power compensation DSC and a separate TGA equipment. The heat of melting, the heat of decomposition and the heat of gasification of those materials were determined from the DSC heat flow and the TGA mass loss obtained. The materials tested include polymethylmethacrylate (PMMA), polyoxymethylene (POM), polyethylene (PE), polypropylene (PP), polystyrene (PS), polyamide 6,6 (PA 66), polyethylene terephthalate (PET), bisphenol A polycarbonate (PC), polyvinylidene fluoride (PVDF) and polyvinyl chloride (PVC). The experiments were performed using different sample sizes, heating rates and cup configurations and the most reproducible results were found for 2 to 4 mg of sample mass at 5 °C/min with aluminium pan covered by bent lid.

From Figure 5-11(a), the original heat flow curve contains offset and curvature. To remove these inconsistencies, isothermal heat flow were measured at discrete temperatures from which a new baseline was developed for subtraction from the original heat flow curve. The positive heat flow denotes endothermicity.

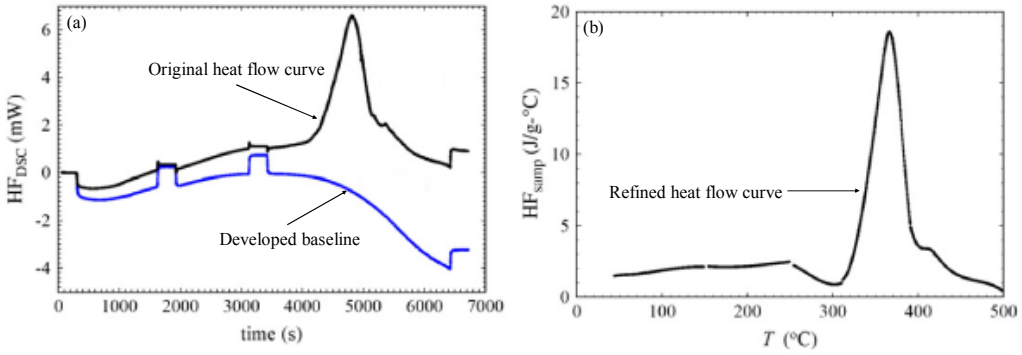

Figure 5-11: Original heat flow curve and developed baseline (a) with refined heat flow curve (b) of PMMA sample[71]

After baseline subtraction, the refined heat flow curve as seen in Figure 5-11(b) was obtained and integrated over the selected regions to obtain the change in enthalpy related to heat capacity, melting and decomposition. Dividing the change in enthalpy by the amount of sample mass involved, the heat of melting, the heat of

decomposition and the heat of gasification were determined and tabulated in Table 5-2 for the different materials tested by Stoliarov et al..

Table 5-2: Heat of melting, heat of decomposition and heat of gasification for materials tested in Stoliarov et al. research[71]

Polymer	Δh_{melt} (J/g)	Δh_{dec} (J/g)	Δh_g (J/g)
PMMA	0	870	1610
POM	141	2540	3370
PE	218	920	2510
PP	80	1310	2540
PS	0	1000	1800
PA 66	55	1390	2500
PET	37	1800	2570
PC	0	830	1740
PVDF	47	2120	3080
PVC	0	710	1420

All values are found to be endothermic and among the three parameters calculated, the heat of decomposition obtained from the decomposition peak is the same as the heat of reaction discussed thus far. Included as reference, the heat of melting is determined over the melting peak only while the heat of gasification as defined earlier includes the contribution from heat capacity, melting and decomposition.

5.4.4 Matala et al.

Matala et al. measured the heat flow during the decomposition of birch, oak, pine, PVC, PMMA, graphite and various wood components which include cellulose, lignin and xylan to determine their respective heat of reaction[21,75]. The equipment used were power compensated standalone DSC and STA where 10 to 50 mg of samples were tested at heating rate of 2, 5, 10 and 20 °C/min in nitrogen and air environments. The selected range of heating rate ensures the entire sample achieves thermal equilibrium during the decomposition. Matala et al. reported the decomposition nature of each material based on their heat flow behaviours and these are summarised in Table 5-3.

Table 5-3: Number of reactions and their decomposition nature for materials tested in Matala et al. research[75]

Material	Nitrogen environment		Air environment	
	Number of reaction	Nature of reaction	Number of reaction	Nature of reaction
Birch	1	Endothermic	2	Exothermic

Oak	1	Endothermic	2	Exothermic
Pine	1	Endothermic	2	Exothermic
PVC	2	Endothermic	3	Endothermic and exothermic[a]
PMMA	1	Endothermic	1	Endothermic
Graphite	2[b]	Endothermic	1	Exothermic

In Table 5-3, under nitrogen environment, the reactions are endothermic and these consist of pyrolysis and evaporisation. Under air environment, the reactions are mostly exothermic due to oxidation except for PVC and PMMA which contain endothermic reactions. For the materials tested, the heat flow curve of nitrogen experiments show the presence of curvature while the air experiments show a more level baseline. As example, the heat flow curve of pine is reproduced in Figure 5-12.

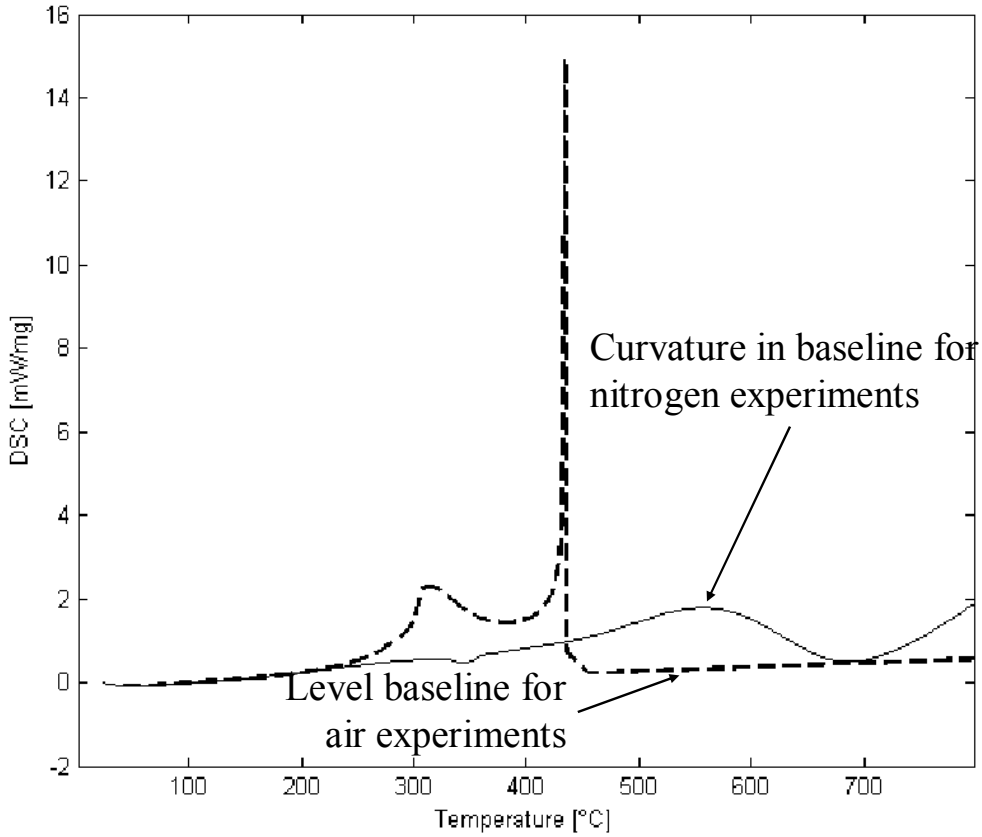

Figure 5-12: Heat flow curve of pine tested under nitrogen and air environments[75]

Matala et al. reported that a consistent endothermic heat of reaction for cellulose and birch was obtained at all the heating rates tested under nitrogen. The heat of reaction

[a] Under air environment, PVC experiences three reactions in total and the first reaction is endothermic while the remaining two are exothermic.
[b] Under nitrogen environment, graphite experiences two non-decomposition reactions where there are changes in enthalpy but no mass loss is recorded.

for other materials was less consistent, caused by the diminishing accuracy of the DSC equipment due to the occurrence of multiple parallel reactions during decomposition. Matala et al. used the same heat of reaction terminology as this thesis and the consistent heat of reaction for cellulose and birch is endothermic 482 and 230 J/g respectively. The developed values were used as the input for the decomposition modelling in FDS 5 and also for the material property refinement with Genetic Algorithm Toolbox for Matlab[76].

5.4.5 Peterson et al.

The endothermic heat flow reported by Matala et al.[75] during PMMA oxidation under air is also seen in the research of Peterson et al.[77]. The heat flow during the decomposition of PMMA under nitrogen and air environments was measured using standalone DSC at heating rate of 20 °C/min with a purge flow rate of 80 ml/min. The sample mass used was 9.8 mg for nitrogen experiment and 15.5 mg for air experiment. Endothermic heat flow was recorded in both experiments and the heat of reaction found is 1080 and 550 J/g for nitrogen and air respectively. The smaller endothermic heat of reaction in air shows that the exothermic oxidation has reduced the overall endothermicity of the decomposition.

5.5 Literature Review on Heat of Reaction for Polyurethane Foam

For the purpose of modelling the flaming combustion of polyurethane foam, the heats of reaction associated with the two pyrolysis reactions introduced earlier are of interest. However, the values on the heat of reaction for polyurethane foam are not widely available in the literature and those reported are mostly the heat of gasification. Table 5-4 contains the endothermic heat of gasification and heat of reaction for polyurethane foam from various research.

Table 5-4: Heat of gasification and heat of reaction for polyurethane foam reported in the literature

Authors	$\Delta h_g/\Delta h_r$	1st Reaction (J/g)	2nd Reaction (J/g)	Total (J/g)
Tewarson[40]	Δh_g	N/A	N/A	1400

Prasad et al.[42]	Δh_g	N/A	N/A	1960
Valencia[25]	Δh_r	1009	331	547

Tewarson[40] and Prasad et al.[42] reported a single value which is the heat of gasification that includes the contribution from the heat capacity as well as the first and second reactions of the decomposition. Comparing with the recalculated total heat of reaction from Valencia[25], the values from Tewarson and Prasad et al. are greater in magnitude by at least three times. Such variation is not surprising because the heat of reaction does not include contribution from the heat capacity. Furthermore, the heat flow measurements from each research could be different as the results are very sensitive to many experimental conditions such as sample mass, heating rate, type of cup, presence of lid and instrumental effects. Lastly, the data reduction technique employed to analyse the DSC results could also be different for each research.

5.6 Differential Scanning Calorimetry Experiments

A simultaneous DSC-TGA Q Series™ instrument, SDT 600 manufactured by TA Instruments is used to carry out the DSC experiments in this research and as mentioned in Chapter 3 and 4, the equipment also simultaneously conducts the TGA experiments by recording the changes in sample mass. The process of the TGA experiment is discussed in details in Section 3.3. For the aspect of DSC, SDT 600 operates based on the heat flux concept where the heat flow is determined from the thermal equivalent of Ohm's Law as seen in Equation (5-13)[62].

$$\frac{dq}{dt} = \frac{\Delta T_{sam-ref}}{R_t} \cdot k_f \cdot k_u \tag{5-13}$$

$\Delta T_{sam-ref}$ is the difference between the sample and reference temperatures measured by the individual thermocouple located underneath the platinum lined platform. R_t, k_f and k_u are the constants obtained through a series of calibrations. The sample mass is measured through the current signal required to correct a taut-band meter movement[46] caused by the changes in sample mass. The calibrations for the equipment are performed in the following sequence, mass calibration, temperature calibration, heat

flow calibration and cell constant calibration. The calibrations are carried out when there are changes to the heating rate and purge gas and also after crucial maintenance of the equipment such as the replacement of the beam set. Unless specified otherwise, these calibrations are performed at the specific heating rate and temperature range which are applicable to the intended experiments. The mass calibration relating to the TGA experiments are discussed in details in Section 3.3.

The temperature calibration is performed to establish the accurate temperature measurements. This is achieved by relating the measured temperature with the actual known temperature of a chemical or physical transition[78]. The process involves melting a high purity metal and the choices of sample include tin, zinc, aluminium, silver, gold and nickel which provide a range of melting point between 232 and 1455 °C. According to TA Instruments, performing this calibration at multiple points can improve the calibration's accuracy. From the TGA results obtained in Chapter 3 and 4, the foams tested experience significant mass loss between 180 and 460 °C. As such, only tin and zinc with their respective melting point of 232 and 419 °C falls within this range. For this research, a single point calibration was decided to be sufficient and 3 to 10 mg of zinc was used as calibrant. The selected calibrant is placed in the sample cup while an empty cup is used as reference. Under the intended heating rate, the furnace temperature is increased from 200 °C below the onset of melting to 200 °C above. The collected results are analysed over the endothermic melting region and any difference between the measured and actual melting temperature is compensated.

The heat flow calibration is performed to develop the proportionality factor for converting the measured voltage signal into heat flow[78]. The calibration involves two parts and the first consists of experiment with empty cups on sample and reference platforms. In the second part, a sapphire standard issued by TA Instruments is placed in the sample cup while the reference cup remains empty. Both parts are conducted under the same experimental conditions where the furnace temperature is increased from the room temperature to the maximum temperature under constant heating rate. The collected results are converted by the analysis software into the heat capacity of

sapphire. This is then compared with the built in literature values over multiple temperatures to mathematically produce a heat flow calibration curve.

Lastly, the heat flow calibration curve produced is further refined through the cell constant calibration. The previous cell constant is set to unity and 3 to 10 mg of zinc used as metal standard is placed in the sample cup while the reference cup remains empty. The standard is first equilibrated at 550 °C and then at 250 °C before being heated to 500 °C at a heating rate of 20 °C/min. The heat of fusion of zinc is determined from the collected heat flow by analysing the endothermic region. The new cell constant is calculated through Equation (5-14) and then implemented into the software.

$$cell\ constant = \frac{\Delta h_{f,known}}{\Delta h_{f,mea}} \tag{5-14}$$

5.6.1 Sample Preparation and Experimental Conditions

In this research, seven polyurethane foams and their melts as listed in Table 2-1 of Chapter 2 are tested. The melts are collected from the Sample Feeding Vertical Cone experiments discussed in Chapter 7 where the foam sample decomposes with non-flaming (NF) or flaming (F) surfaces. The foam samples tested in SDT 600 range from 3 to 10 mg while the melt samples range from 3 to 50 mg. The mass of 10 and 50 mg for foam and melt samples are the respective maximum limit for the current setup based on the capacity of the alumina cups used. The foam sample is prepared by shredding the polyurethane foam into fine fragments and then transferring these fragments into the cup. The melt sample is prepared by freezing the melt droplets with liquid nitrogen for easy transfer into the cup and then the sample is allowed to return to ambient temperature before the start of experiment.

All experiments are carried out in dynamic mode where the prepared sample is heated at constant heating rate from the room temperature to the maximum temperature. The purge flow rate is 100 ml/min and the effect of two different purge gases, nitrogen and air have on the decomposition is investigated. Nitrogen purge gas creates a non-

reactive environment where the decomposition occurs under the sole influence of heat. Under air environment, the decomposition proceeds under the influence of both heat and oxidation. As discussed earlier, the decomposition under nitrogen environment is theoretically similar to the decomposition of foam during combustion where oxygen is consumed by the flame[42]. The decomposition under air is more representative of the decomposition of foam during smouldering where oxygen can diffuse to the pyrolysis front[19]. The sample is tested in open configuration without the presence of lid so the volatiles produced from decomposition can escape without being obstructed.

The selected heating rates are 1, 5, 20 and 60 °C/min while the maximum temperature is 600 and 900 °C for the nitrogen and air environments respectively. The heating rates chosen are based on the temperature variation of polyurethane foam smouldering front[19] which are also below the maximum allowable limit of 100 °C/min for the equipment. Throughout the series of experiments, the cups and platforms are often contaminated by the decomposition products thus the equipment requires routine cleaning. Soot accumulated on the cup is burned off using a propane torch while the contaminated platform is cleaned by heating the furnace to 1000 °C under air environment at heating rate of 20 °C/min.

5.7 Data Reduction to Determine Heat of Reaction from Simultaneous DSC-TGA Experiments

The results of 26 mg NFR-SB-31 (F) melt at 5 °C/min is used to illustrate the data reduction process involved to obtain the reaction heat flow from the original DSC heat flow. The DSC results of melt are used as example because of the relative simplicity of the decomposition. According to the pyrolysis mechanism of polyurethane foam proposed in Section 4.1 of Chapter 4, the melt samples only undergo a single reaction to decompose completely into gases. Thus in Figure 5-13, the melt decomposition is depicted by the single protuberance in the TGA mass loss/°C curve.

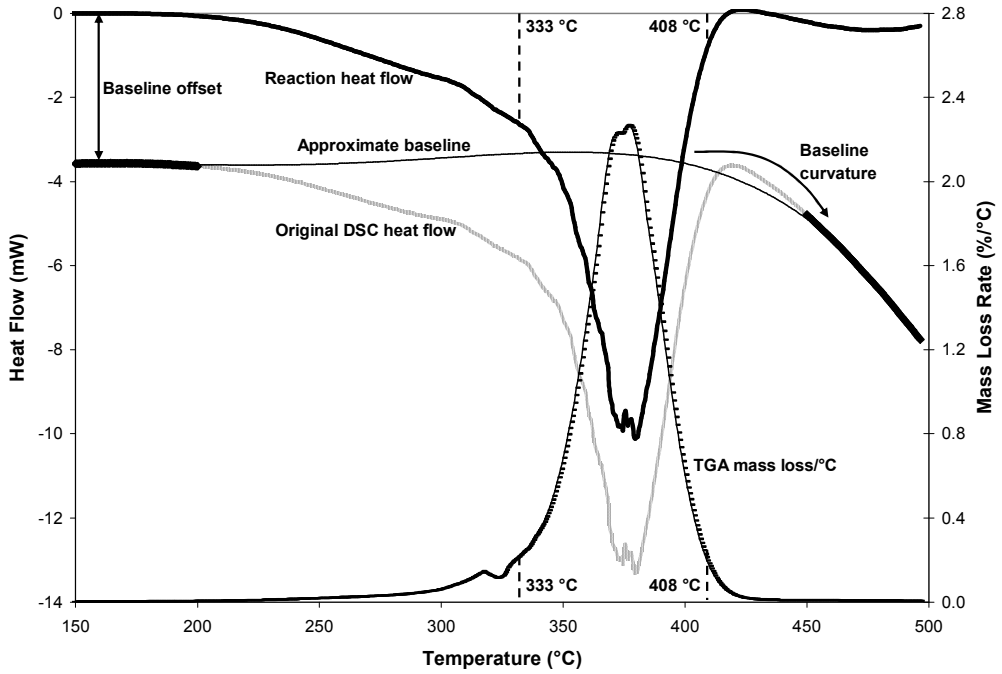

Figure 5-13: TGA mass loss/°C and DSC heat flow (original and reaction) for 26 mg NFR-SB-31 (F) melt at 5 °C/min under nitrogen environment

Over the identical temperature range of the protuberance, the original heat flow curve shows an endothermic region indicated by the negative heat flow measured. This is the sign convention adopted for the DSC results of this research hence exothermicity is indicated by positive magnitude in the heat flow. The curve contains two baseline artefacts, a baseline offset from the start and a negative gradient curvature initiating at the end of decomposition. The curvature continues until the experiment is terminated at the final temperature. The baseline offset when a melt sample is tested can be calculated using Equation (5-2). The curvature in the baseline can be determined following the method proposed by Rath et al.[64] where the heat flow associated with the heat capacity of the sample and the additional radiative exchange within the furnace are accounted. But without the temperature correlations governing the heat capacity of polyurethane foam and its melts and also not knowing the additional radiative exchange within the current furnace, the simplified approach by correcting the original curve with a user defined baseline is used instead.

The approximate baseline is developed based on the trend of heat flow observed over the non-decomposition regions. From the TGA mass loss/°C in Figure 5-13, the non-

decomposition regions are identified as 100 – 200 °C and 450 – 500 °C. The resulting approximate baseline generated from the non-decomposition regions is indicated in the figure. Subtracting the approximate baseline from the original curve, the reaction heat flow without offset or curvature is obtained. Subsequently, Equation (5-15) which is similar to Equation (5-12) is used to calculate the heat of reaction.

$$\Delta h_r = \frac{1}{m_{start} - m_{end}} \int_{T_{start}}^{T_{end}} \left(\frac{dq}{dt} \right)_R dT \cdot \frac{dt}{dT} \tag{5-15}$$

The numerator of Equation (5-15) contains the temperature integral of the reaction heat flow between two selected temperatures, T_{start} and T_{end} which are 333 and 408 °C as indicated in Figure 5-13. The selected temperatures are where the TGA mass loss/°C is 10 % of the difference between the maximum and minimum values of the specific reaction. The resulting integral is in unit of mW°C. The amount of energy involved with the reaction is determined by dividing this integral with the heating rate used as the temperature increase within the experiment is governed by the constant heating rate applied. The denominator of Equation (5-15) consists of the amount of sample mass consumed between T_{start} and T_{end}. For NFR-SB-31 (F) at 5 °C/min, the heat of reaction for the melt decomposition is endothermic 231 J/g.

5.8 Heat of Reaction for Decomposition of Melts (Second Reaction) in Nitrogen and Sensitivity to Heating Rate and Sample Mass

The decomposition of melt is the second reaction of the overall decomposition of polyurethane foam. The heat of reaction for melt decomposition is introduced first because the results are simpler and the data reduction process is much more straightforward compared to that of polyurethane foam decomposition which is discussed in the next section. The sensitivity of the heat of reaction towards the changes in heating rate and sample mass are investigated on two melts, NFR-SB-31 (F) and FR-Y-36 (F). Both melts are the respective decomposition product of non-fire retardant and fire retardant foams. The results of NFR-SB-31 (F) melts are used to

illustrate the sensitivity towards the heating rate and sample mass. Figure 5-14 shows the original heat flow, the reaction heat flow and the calculated heat of reaction for ~20 mg NFR-SB-31 (F) melts at heating rate of 1, 5, 20 and 60 °C/min. Again, the negative heat flow denotes endothermicity.

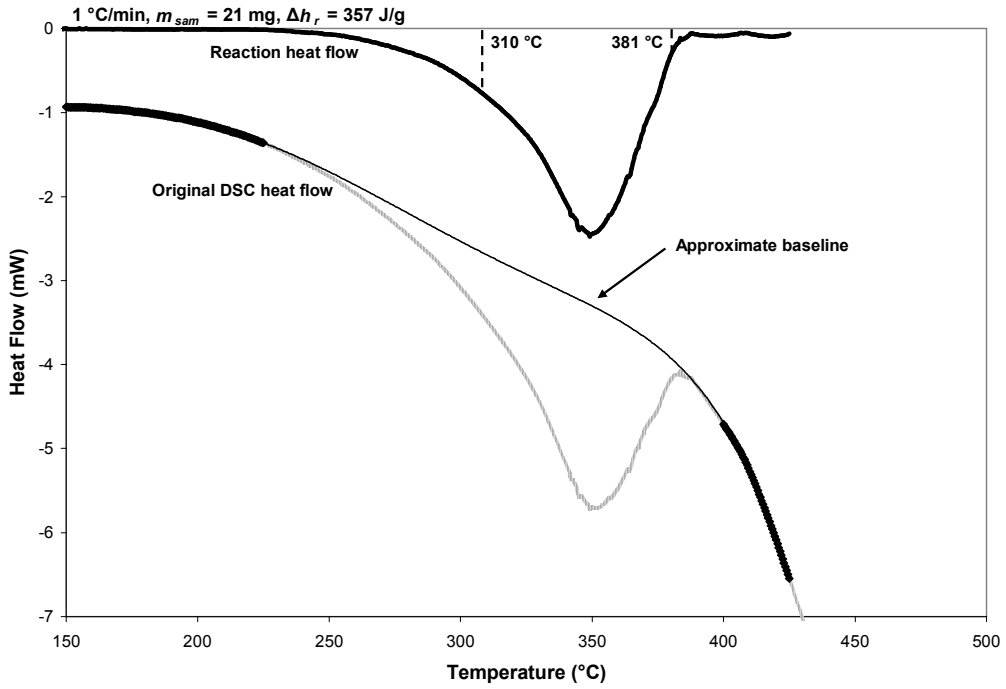

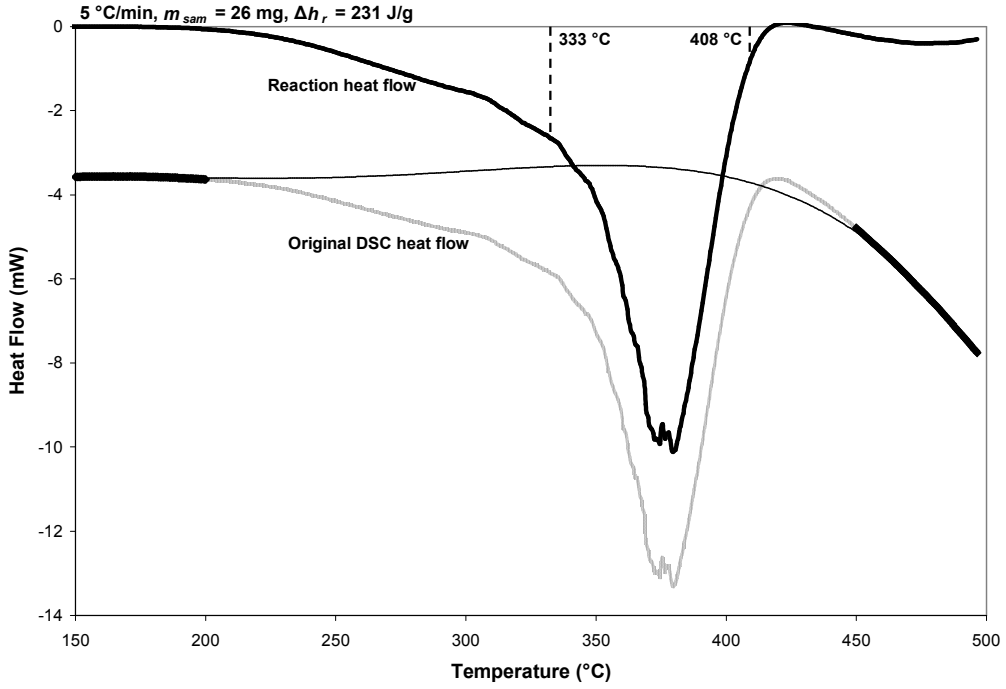

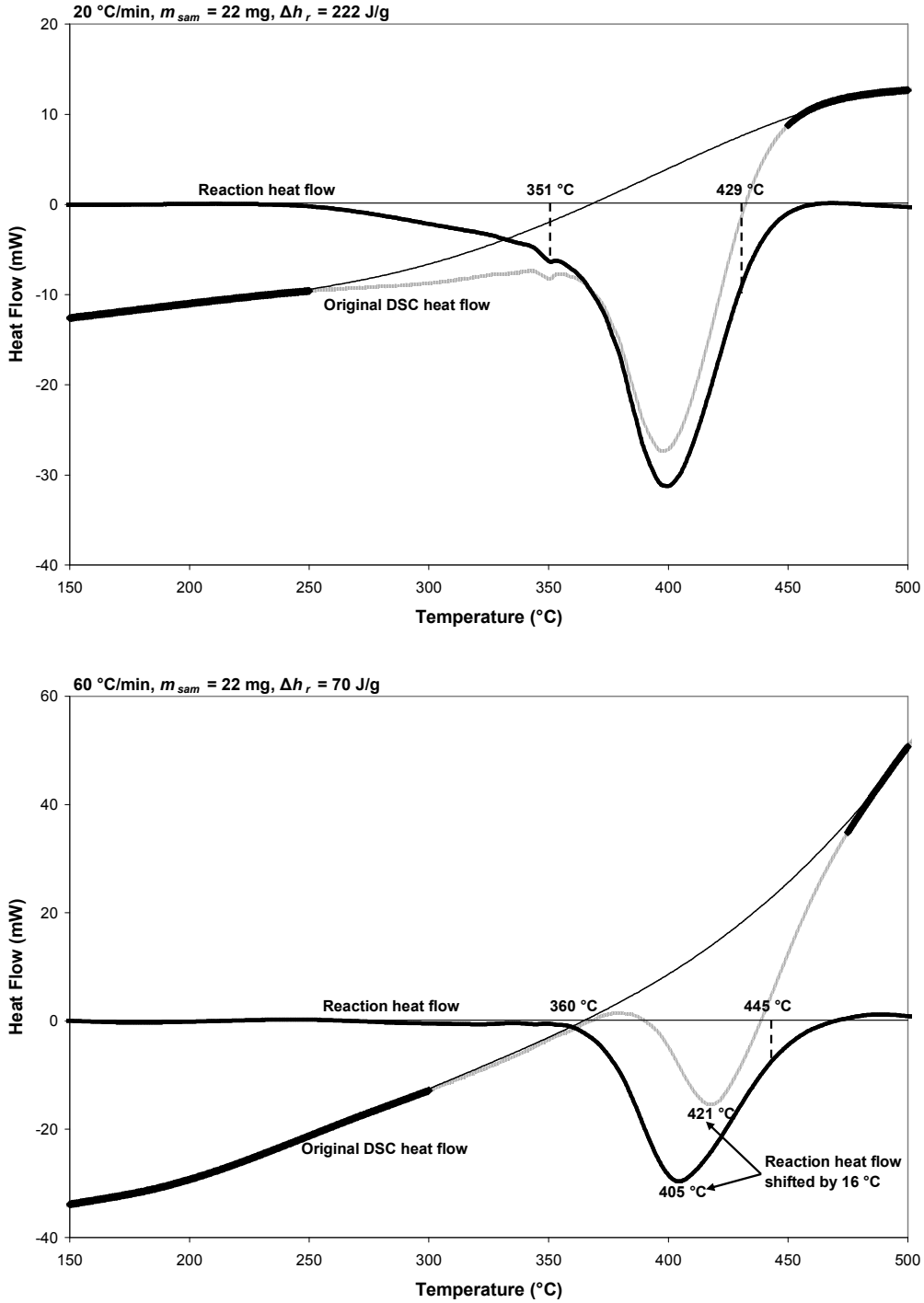

Figure 5-14: Original DSC heat flow, reaction heat flow after baseline correction and heat of reaction for ~20 mg NFR-SB-31 (F) melts at 1, 5, 20 and 60 °C/min heating rates under nitrogen environment

The offset and curvature on the original heat flow changes significantly with different heating rate. In accordance with the relationship in Equation (5-2), the offset at 150

°C shows greater endothermic magnitude as the heating rate increases, from -1 mW at 1 °C/min to almost -40 mW at 60 °C/min. The curvature shows the changes in gradient from negative to positive under increasing heating rate. Adopting the same baseline correction as described before, the reaction heat flow curve is obtained. Despite having performed the required temperature calibration, there is still a temperature lag in the experiment at 60 °C/min. A temperature difference of 16 °C is present between the peak of the original DSC heat flow and the TGA mass loss/°C. This mismatch is subsequently corrected in the reaction heat flow curve as indicated on Figure 5-14. Integrating the reaction heat flow between T_{start} and T_{end}, the heat of reaction determined using Equation (5-15) for the second reaction is found to reduce greatly from endothermic 357 – 70 J/g between 1 and 60 °C/min. Despite this significant variation, a region of consistency is noted between 5 and 20 °C/min, where the heat of reaction changes between 231 and 222 J/g.

The sensitivity towards sample mass is investigated at 5 °C/min where Figure 5-15 shows the original heat flow, the reaction heat flow and the calculated heat of reaction for 5, 10, 26 and 46 mg NFR-SB-31 (F) melts. The sample mass of ~50 mg is the maximum limit based on the cup capacity.

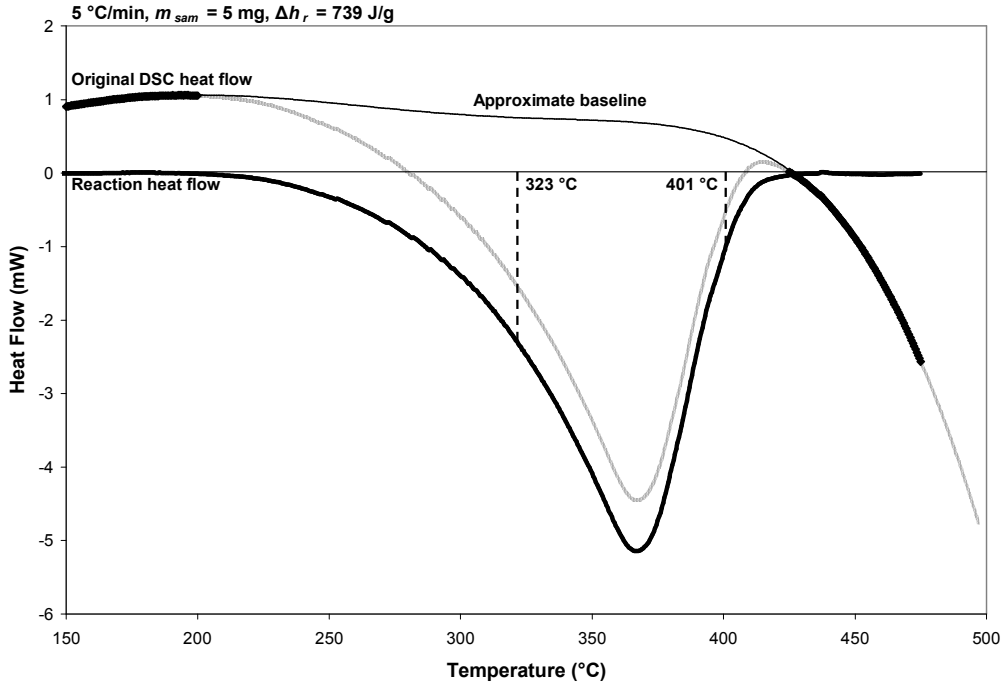

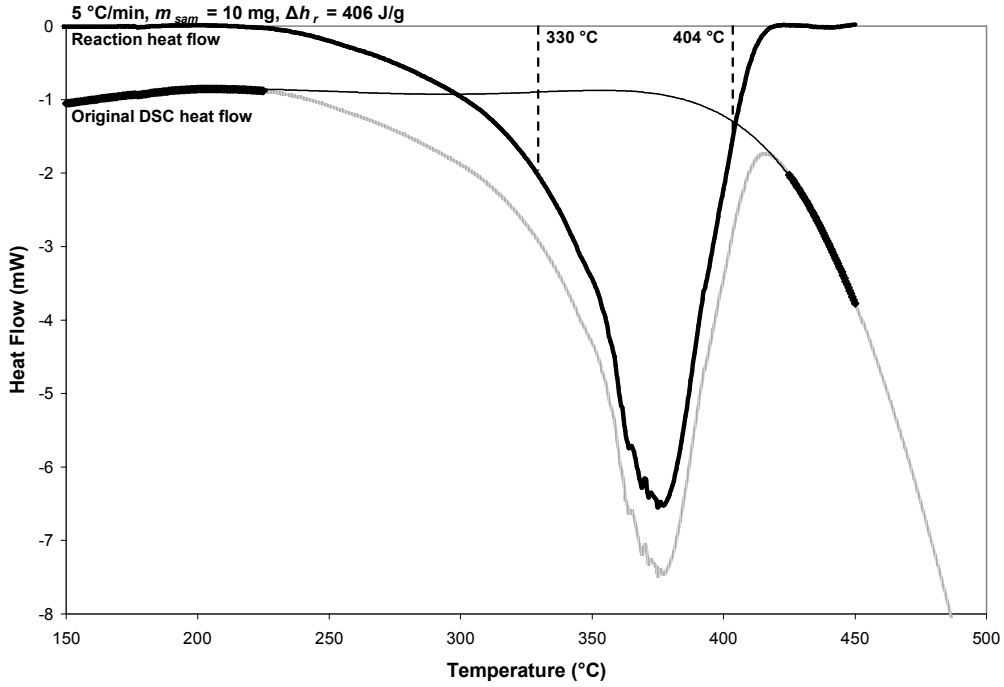
5 °C/min, m_{sam} = 10 mg, Δh_r = 406 J/g
Reaction heat flow
Original DSC heat flow
330 °C
404 °C
Heat Flow (mW)
Temperature (°C)

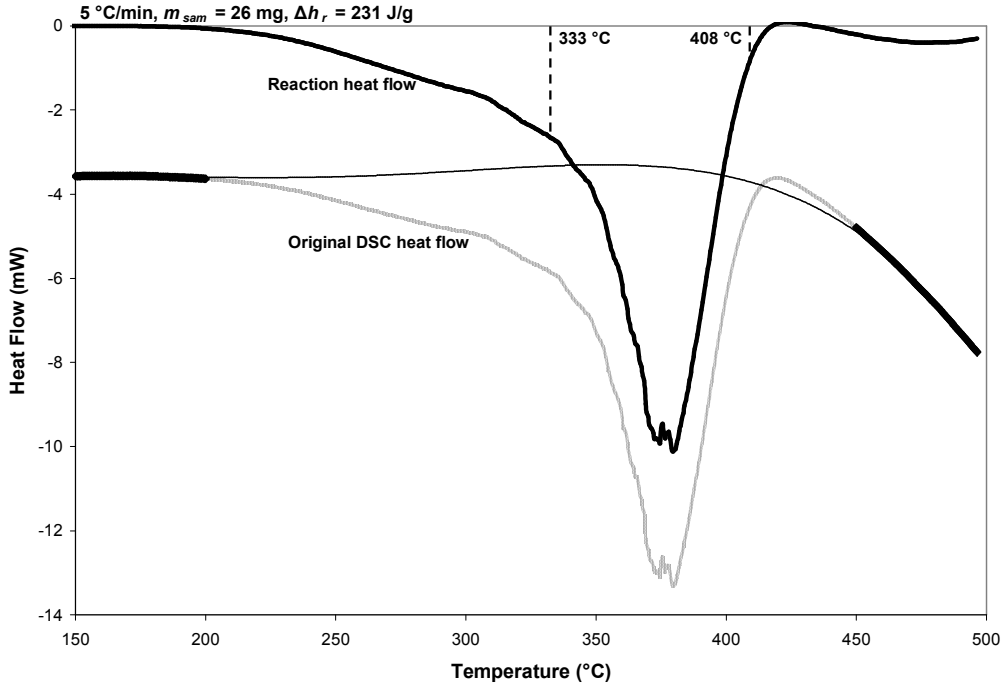
5 °C/min, m_{sam} = 26 mg, Δh_r = 231 J/g
Reaction heat flow
Original DSC heat flow
333 °C
408 °C
Heat Flow (mW)
Temperature (°C)

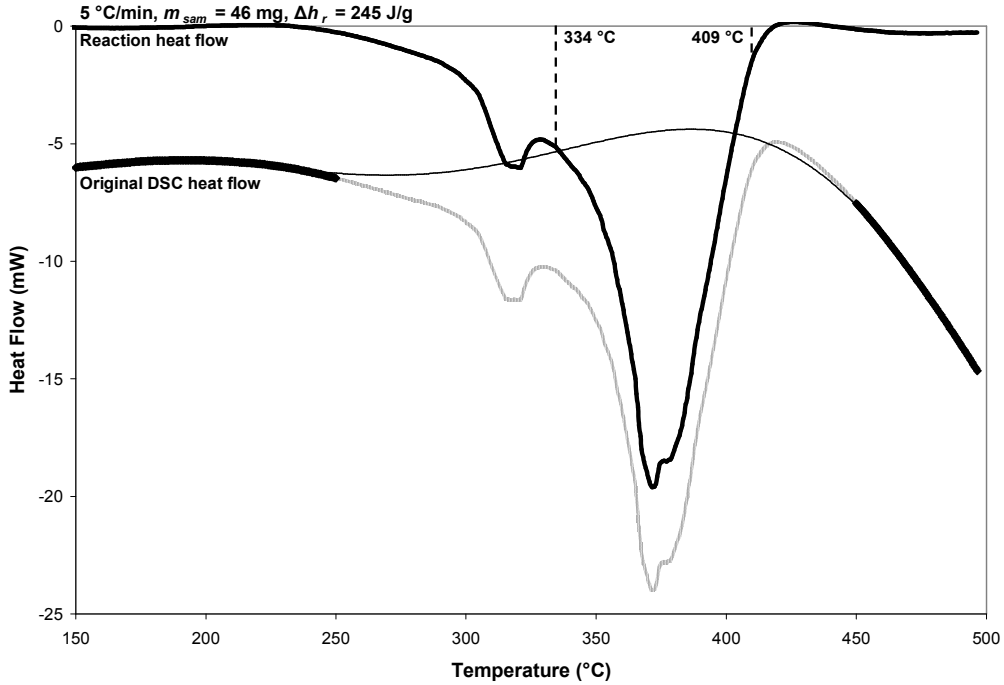

Figure 5-15: Original DSC heat flow, reaction heat flow after baseline correction and heat of reaction for 5, 10, 26 and 46 mg NFR-SB-31 (F) melts at 5 °C/min under nitrogen environment

Despite the changes in sample mass, the curvature in the original heat flow curves shows a consistent negative gradient and there is also no significant thermal lag between the DSC and TGA results at the heating rate applied. Once again, in accordance with Equation (5-2), the baseline offset at 150 °C shows greater endothermic magnitude with the increase in sample mass, from 1 mW at 5 mg to -6 mW at 46 mg. After correcting the baseline and integrating the reaction heat flow, the calculated heat of reaction from Equation (5-15) is found to be endothermic and its magnitude reduces exponentially when the sample mass increases. At 5 mg, the heat of reaction is largest at 739 J/g and it diminishes to 406 J/g by 10 mg. Then it plateaus at 26 and 46 mg with consistent values of 231 and 245 J/g respectively.

From the sensitivity analysis, the region of consistent heat of reaction is established which is between the heating rate of 5 and 20 °C/min and between the sample mass of ~20 and ~50 mg. Similar heat flow patterns and region of consistency are also noted for the other melt sample, FR-Y-36 (F). From 5 to 20 °C/min, the consistent values of FR-Y-36 (F) vary between endothermic 203 and 179 J/g and from ~20 to ~50 mg, the values vary between endothermic 203 and 212 J/g. The melts of other polyurethane

foams are tested within the region of consistency, at heating rate of 5 °C/min and with sample mass of ~20 mg. Similar to Figure 5-13, all the results collectively show the melt decomposition as a single endothermic reaction. Figure 5-16 shows the consistent heat of reaction for all melts tested under nitrogen environment and the values range from 164 – 295 J/g. The results show that the melts of FR-Y-36 and FR-LG-38 have a slightly lower heat of reaction than the other foams. The heat of reaction between the melts produced under non-flaming and flaming conditions during the Sample Feeding Vertical Cone experiments is similar with no distinctive trend. Since NFR-SB-31 (F) and FR-Y-36 (F) melts are tested at multiple heating rates and sample mass, the average of the values from the consistent region is reported in Figure 5-16.

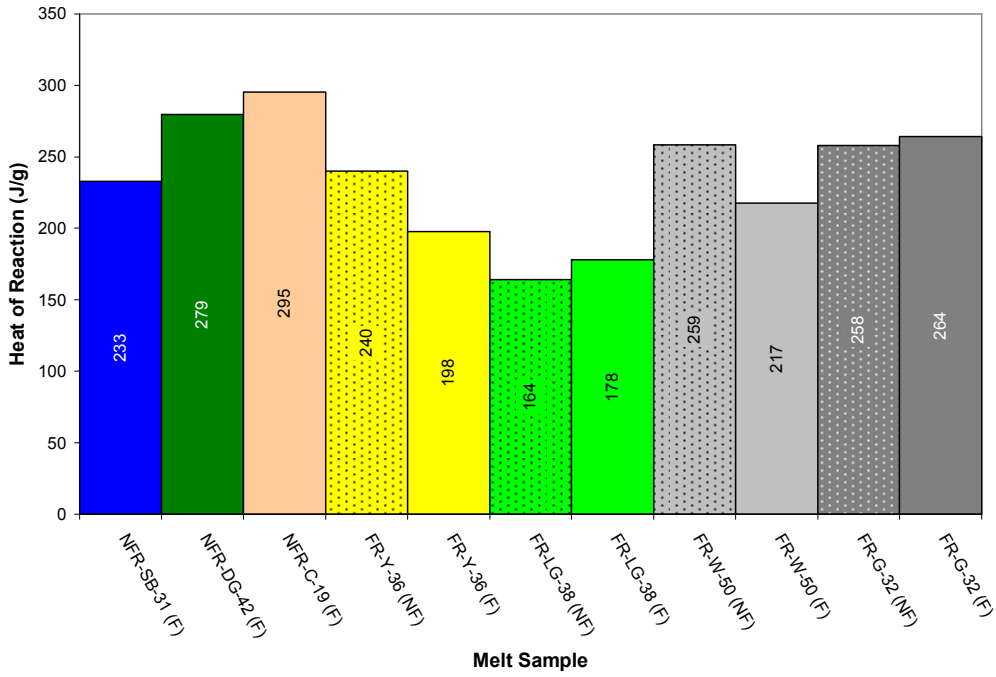

Figure 5-16: Consistent heat of reaction for the second reaction, melt decomposition under nitrogen environment

5.9 Heat of Reaction for Decomposition of Polyurethane Foams (First Reaction) in Nitrogen and Sensitivity to Heating Rate and Sample Mass

The previous section focuses on the heat of reaction for melt decomposition which corresponds to the second reaction in the complete decomposition of polyurethane foam in nitrogen. In this section, the heat of reaction for the first reaction involving the decomposition of foam into melts and gases is analysed. The results of NFR-SB-31 are presented to illustrate the sensitivity towards the heating rate and sample mass. Figure 5-17 shows the original heat flow, the reaction heat flow, the calculated heat of reaction and the mass loss/°C for ~3 mg NFR-SB-31 at heating rate of 1, 5, 20 and 60 °C/min. The negative heat flow denotes endothermicity. The sample decomposes completely over two reactions and this is depicted by the two protuberances in the TGA mass loss/°C. Since the pattern of mass loss/°C is similar over the different heating rates tested, it is only repeated for 1 and 60 °C/min.

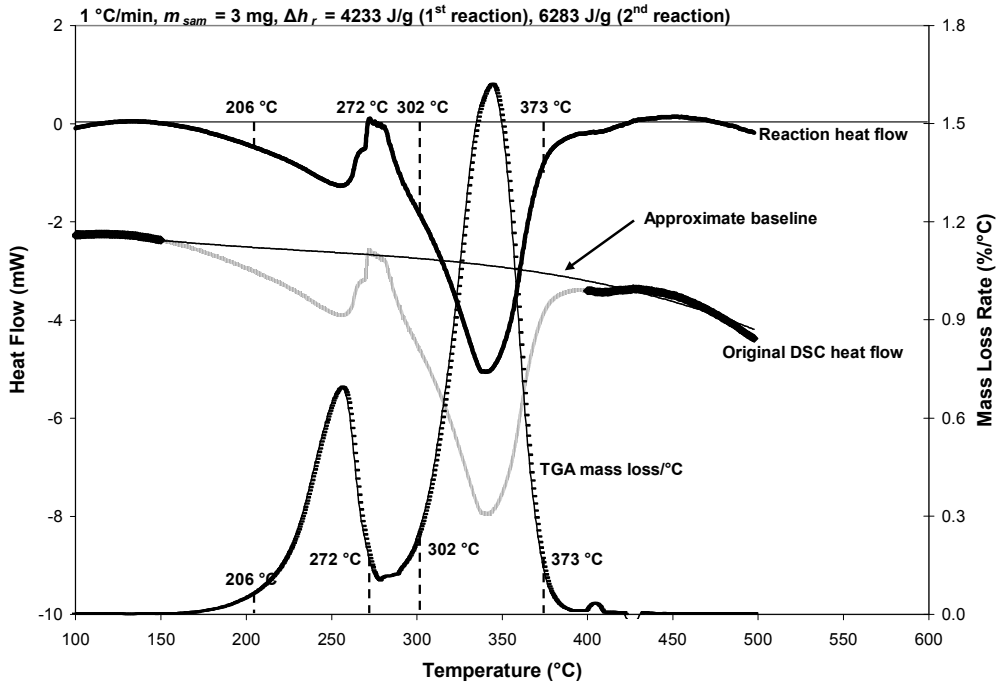

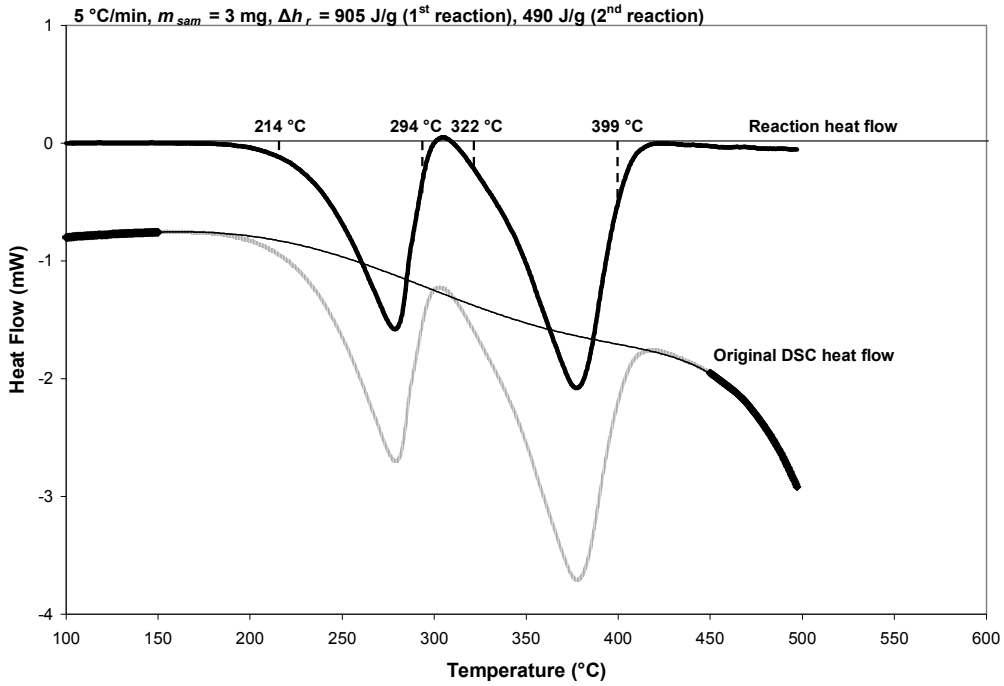
5 °C/min, m_{sam} = 3 mg, Δh_r = 905 J/g (1st reaction), 490 J/g (2nd reaction)
214 °C
294 °C
322 °C
399 °C
Reaction heat flow
Original DSC heat flow
Heat Flow (mW)
Temperature (°C)

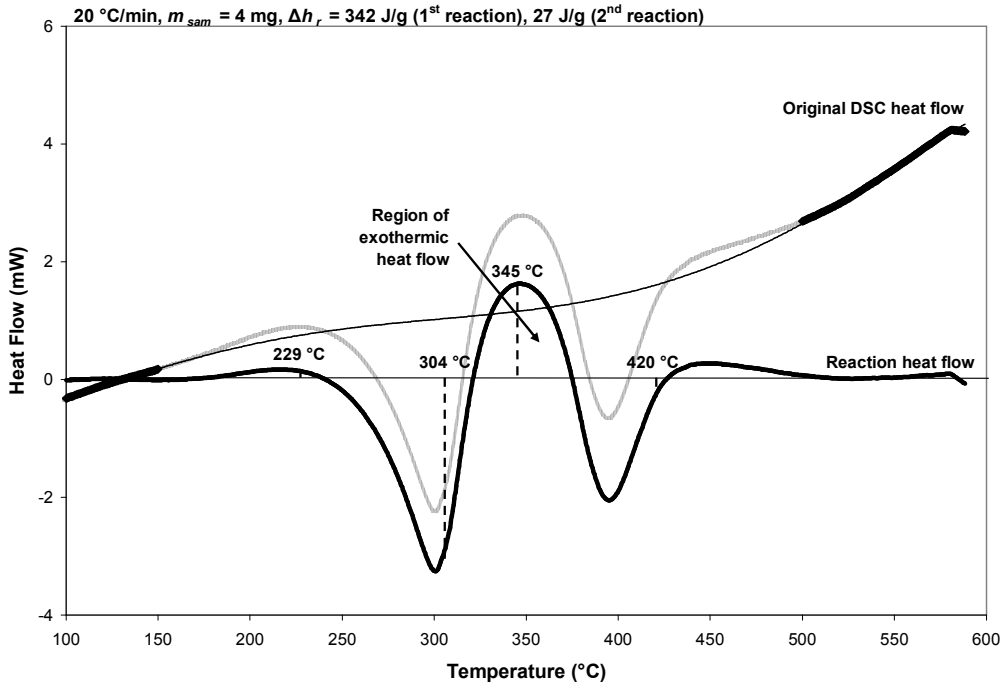
20 °C/min, m_{sam} = 4 mg, Δh_r = 342 J/g (1st reaction), 27 J/g (2nd reaction)
Original DSC heat flow
Region of exothermic heat flow
345 °C
229 °C
304 °C
420 °C
Reaction heat flow
Heat Flow (mW)
Temperature (°C)

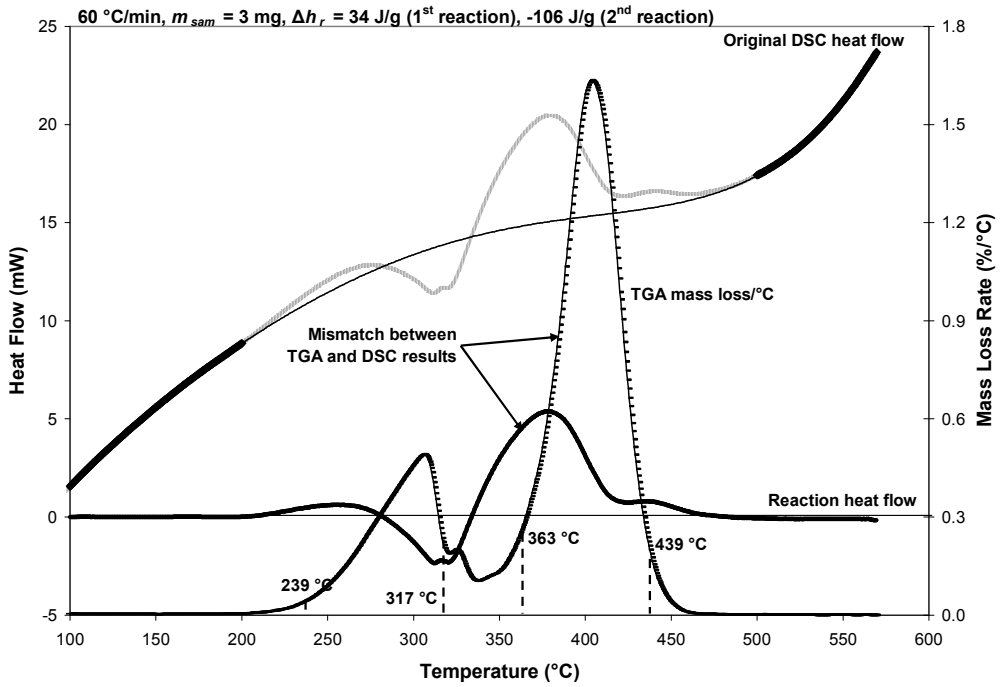

Figure 5-17: Original DSC heat flow, reaction heat flow after baseline correction, heat of reaction and TGA mass loss/°C for ~3 mg NFR-SB-31 at 1, 5, 20 and 60 °C/min heating rates under nitrogen environment

Figure 5-17 shows the curvature of the original heat flow curve changes from negative to positive gradient from 1 to 60 °C/min which is similar to the trend in the melt results. However, different to the melt samples, the changes in baseline offset with increasing heating rate are not in accordance with the relationship described in Equation (5-2). Another trend noted is the deterioration of the heat flow resolution as the heating rate increases. At 1 and 5 °C/min, the two protuberances of the TGA mass loss/°C compare well with the two endothermic regions of the reaction heat flow but at 20 °C/min, the reaction heat flow shows the presence of an exothermic region in between the first and second reactions and by 60 °C/min, the TGA and DSC results has become incomparable as the heat flow resolution deteriorates severely.

The sensitivity of sample mass is investigated at 5 °C/min where Figure 5-18 shows the original heat flow, the reaction heat flow, the calculated heat of reaction and the mass loss/°C for 3 and 10 mg NFR-SB-31. The sample mass of ~10 mg for foam is the maximum limit of the cup capacity. The baseline curvature maintains the negative gradient at the different sample mass tested. Similar to the sensitivity with heating

rate, the changes in baseline offset do not correspond with Equation (5-2) and this seems to be an inherent feature of the foam sample. The TGA mass loss/°C shows the foam sample decomposes via two reactions and at 5 °C/min, the heat flow obtained has distinguishable resolution.

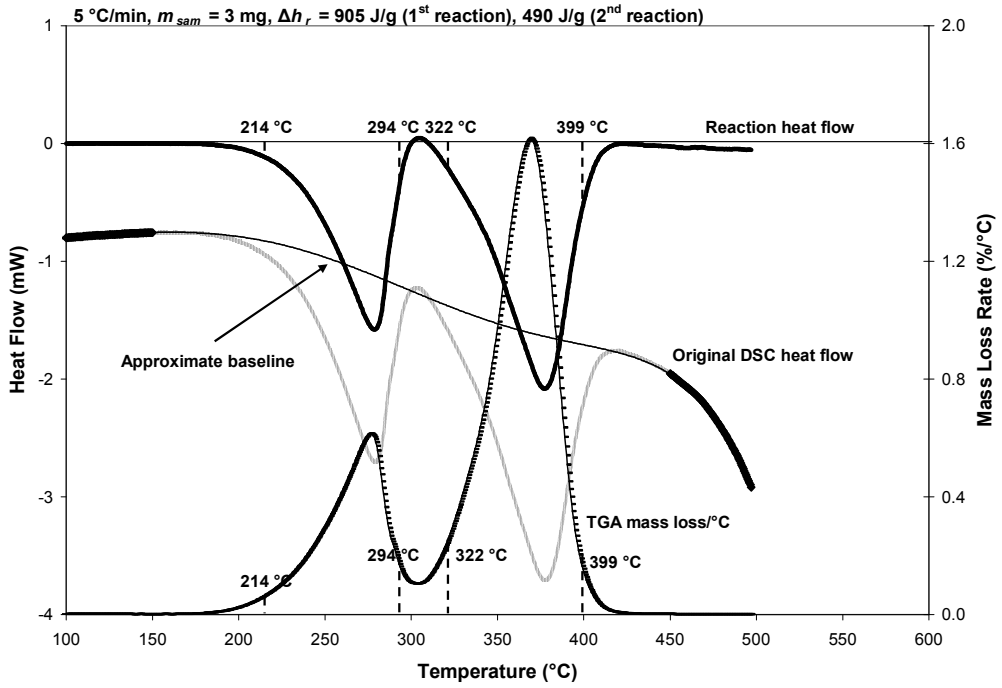

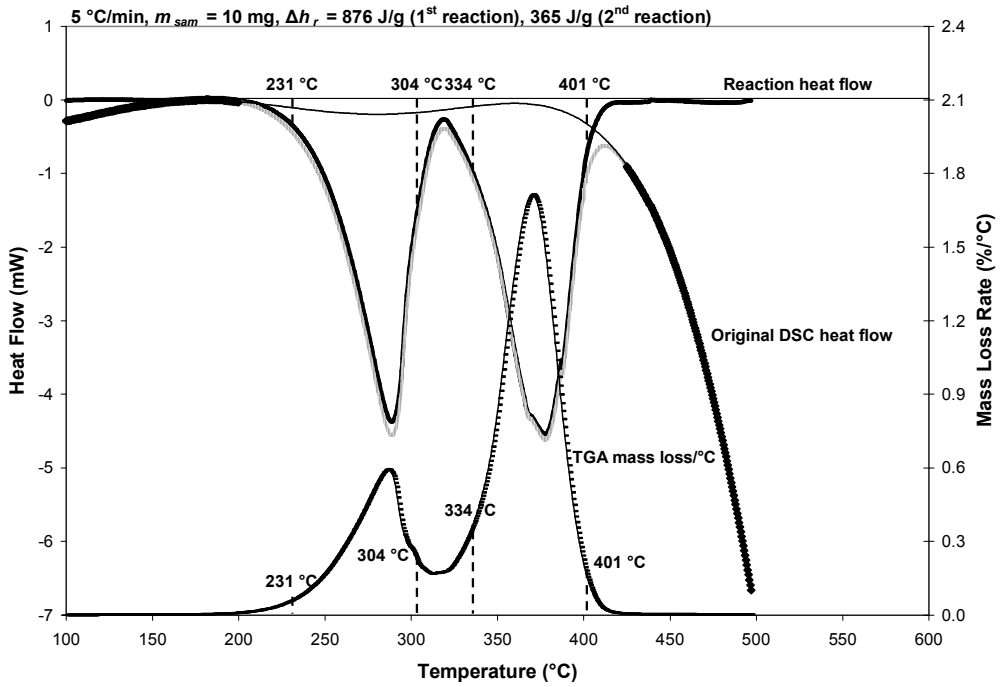

Figure 5-18: Original DSC heat flow, reaction heat flow after baseline correction, heat of reaction and TGA mass loss/°C for 3 and 10 mg NFR-SB-31 at 5 °C/min under nitrogen environment

At the different heating rates in Figure 5-17, the heat of reaction for the first reaction is obtained from Equation (5-15) which involves integrating the reaction heat flow over the first reaction and then dividing by the mass loss over the same interval. The results show a significant reduction in magnitude when the heating rate increases. While discrediting the results at 20 and 60 °C/min on the basis of deteriorated resolution, the endothermic value still changes greatly from 4233 – 905 J/g between 1 and 5 °C/min. When the sample mass changes from 3 to 10 mg as seen in Figure 5-18, the heat of reaction for the first reaction remains similar, varying between endothermic 905 and 876 J/g.

All the other foams are tested at the same sets of experimental conditions, ~3 mg sample at 1, 5, 20 and 60 °C/min and ~10 mg sample at 5 °C/min. The ~10 mg sample is not tested as extensively as the ~3 mg because fully filled sample cup often contaminates the equipment which affects the heat flow measurements. The changes in the heat of reaction for the other foams are noted to be similar to NFR-SB-31. For foam sample, the maximum mass tested is only ~10 mg and this is outside the region of consistency previously determined for the melt sample which requires at least 20

mg. The heat of reaction for the second reaction after the foam decomposition is also available but given the current foam sample size, the results are considered less reliable. Different to the melt sample, the region of consistent heat of reaction is not found for the foam sample so among the heating rates tested, the results from 5 °C/min are recommended. The basis of the recommendation is that the heat flow resolution and accuracy appear least affected and the magnitude of the heat of reaction for the second reaction is closest to that of the melt sample.

Figure 5-19 shows the recommended heat of reaction for the first reaction under nitrogen environment which ranges between endothermic 610 and 1023 J/g for the different polyurethane foams tested. The reported values are the average determined from the heat of reaction for ~3 and ~10 mg samples at 5 °C/min.

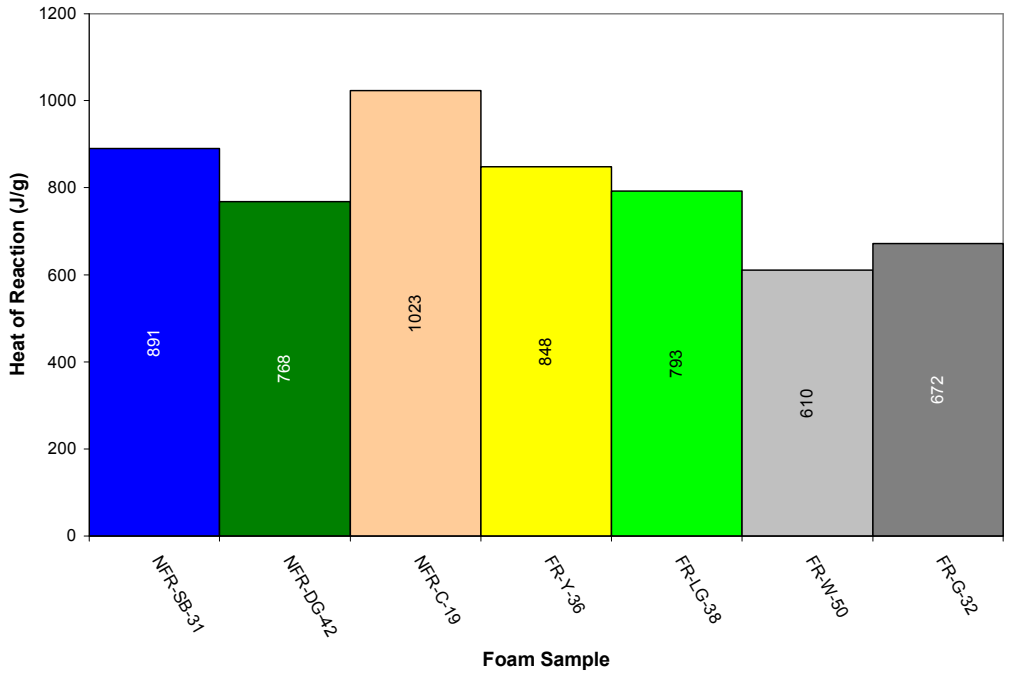

Figure 5-19: Recommended heat of reaction for the first reaction, foam decomposition under nitrogen environment

The repeatability of the heat flow is investigated with NFR-SB-31 and FR-Y-36. Figure 5-20 shows the repeated reaction heat flow curves at 5 °C/min involving three ~3 mg replicates for each foam. The heat flow among the three replicates is repeatable showing similar trend.

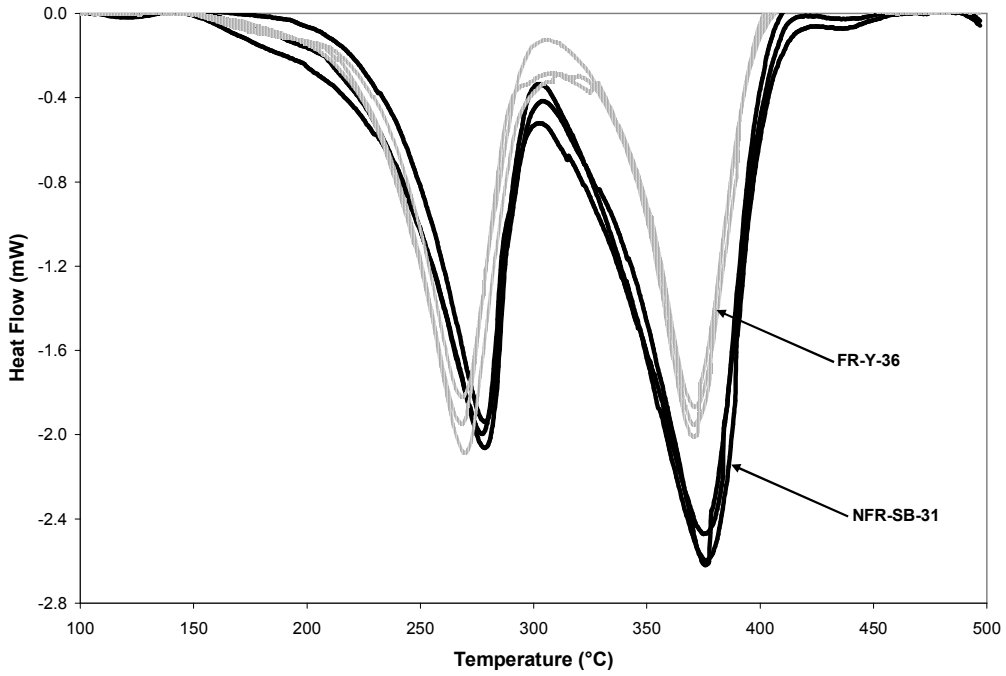

Figure 5-20: Reaction heat flow of the three repetitions of NFR-SB-31 and FR-Y-36 at heating rate of 5 °C/min and sample mass of ~3 mg

5.10 Physical and Experimental Issues on Heat of Reaction from Nitrogen Experiments

From Figure 5-17, the extreme changes noted in the heat of reaction obtained for the foam sample are related to the sample's porous nature. The thermal contact between the sample and the bottom of the alumina cup is crucial to the accuracy of the heat flow measurements. According to Equation (5-13), the heat flow is determined from the temperature difference measured by the thermocouples located underneath the sample and reference cups. The porous structure of the sample means that there are inherent voids between the foam fragments and these fragments also do not form a good thermal contact with the cup. Thus during heating, a localised convective heat flow is believed to develop within these gaps and the impact of this varies with different heating rates which affects the temperature difference measured. The foam sample is prepared by shredding a larger block of foam into smaller fragments and when packed into the cup, the prepared sample becomes more condensed than the

original foam. The poor thermal contact and the variation in the density of the prepared sample become the sources of uncertainty in the experiments.

As a result, the heat flow measurements of the foam samples are considered less reliable when compared to the melt samples which have better thermal contact and more consistent density. This is illustrated in Figure 5-21 which shows the calculated baseline offset using Equation (5-2) versus the experimentally measured offset at 100 °C, a temperature prior to any significant decomposition. The data points plotted are for all the SDT experiments conducted in this research, including the results under air environment.

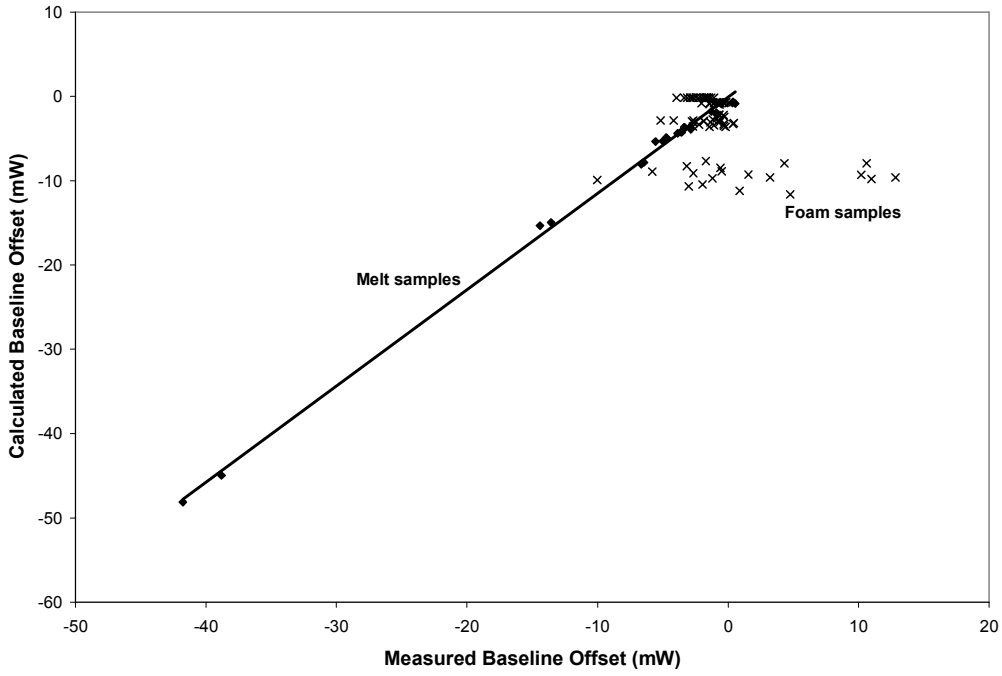

Figure 5-21: Calculated baseline offset versus measured baseline offset at 100 °C for all SDT experiments conducted in this research

The results show that in the case of foam samples, the calculated values do not correlate well with the measured values. This is caused by the poor thermal contact and also by the poor representation of the sample heat capacity in Equation (5-2) which uses the original heat capacity of the foam where in fact, the prepared sample has become more condensed. In the case of the melt samples, a clear linear correlation

is established due to the improved thermal contact and the accurate representation of the sample heat capacity.

While the trend of the baseline offset relates to the physical condition of the sample, the changes in the gradient of the heat flow curvature relates to the experimental variables such as the instrumental effect and the use of lid with the alumina cups. The changes in gradient observed in this research is consistent with those reported in the literature. Price et al.[28] and Denecker et al.[34] had performed DSC experiments on polyurethane foam at 10 °C/min. Despite having the same heating rate, the former obtained a curvature with positive gradient while the latter obtained one with negative gradient due to the different equipment used. In their research on woods, Rath et al.[64] show that the curvature is caused by the additional radiation heat flow developed from the difference in emissivity between the sample and reference. When a lid was used, the radiative exchange with the furnace between the sample and the reference are similar and the baseline becomes more level. But in the study from Denecker et al., the heat flow curvature has a negative gradient despite the use of a pierced lid. A possible explanation is the amount of pyrolysates released is sufficient to contaminate the sample lid and subsequently, the additional radiation heat flow is generated from this change in emissivity.

Besides the offset and curvature, the heat flow measurements also experience thermal lag and reduced resolution. Since the necessary temperature calibration has been performed to correct for the experimental temperature lag, its continuing presence at 60 °C/min as seen in Figure 5-14 requires further explanations. A similar post calibration lag is also noted in Valencia's study[25], Figure 5-10 shows the presence of lag in the first reaction between the TGA mass loss rate and the DSC heat flow in nitrogen. One explanation for the continuous presence of thermal lag is the difference in the heat capacity of the sample and the metal standard used for calibration, zinc. Comparing the specific heat of foams and melts with zinc, the formers range from 2000 – 3000 J/kgK as reported later in Chapter 6 while the latter is 389 J/kgK[79]. This shows the specifc heat of foams and melts are 5 to 8 times that of zinc. Also, the melting and vaporisation of a pure material such as zinc often take place over a narrow and specific temperature interval. Although represented by two reactions,

polyurethane foam consists of many complex chemicals and the decomposition occurs over wider range due to the different reacting temperatures. Hence, the decomposition of a complex material becomes more susceptible to the changes in experimental conditions such as heating rate. Another explanation is the lower accuracy of the single point temperature calibration performed thus for future research, multiple points calibration should be performed within the temperature range of interest. Regarding reduced resolution, the deterioration is caused by the collapse of porous foam structure into a thin layer of melt which introduces experimental noise into the heat flow signal. High heating rate severely deteriorates the resolution of foam sample experiment as seen in Figure 5-17 because at 60 °C/min, the foam sample decomposes rapidly into melt over 10 minutes while at 1 °C/min, the same process occurs slowly over 8 hours. In contrast, the melt samples have identifiable resolution at all the heating rates tested as they do not experience as much disturbances as the foam samples during decomposition.

5.11 Chemical Issues on Heat of Reaction from Nitrogen Experiments

In the previous section, the poorly correlated baseline offset of foam samples is explained by the sample porosity which is the physical issue. The experimental issues such as instrumental effects and presence of lid explain the changes to the gradient of the heat flow curvature. However, these do not explicitly explain the significant changes in the heat of reaction with respect to heating rate and sample mass, especially in the case of melt sample where it is not porous. Therefore, the changes in heat of reaction are believed to be related to the decomposition chemistry of material. Through detailed gas chromatography and mass spectrometry (GC/MS) techniques, there are often more than twenty different complex chemicals detected following the decomposition of polyurethane. Bilbao et al.[22] described the decomposition of polyurethane as involving multiple competitive micro reactions which produce several decomposition products. Some of the products are intermediate chemicals which are able to further dissociate into a number of atomic, molecular and free radical species[80]. The micro reactions and secondary dissociations either absorb or

release energy to proceed which causes the changes in enthalpy and affects the heat flow measured[81]. These processes are also affected by the changes in heating rate which alter the reaction rate and the composition of the decomposition products. This sensitive nature of polyurethane foam decomposition is considered as a likely explanation for the trend seen in its heat of reaction and a few studies have investigated the type of species and their yield during polyurethane decomposition. The findings of these studies are discussed in this section.

Grassie et al. investigated the decomposition of polyurethane[82] and its primary segments which are the polyether segment[36,83] and the urethane link[37,84]. Through GC/MS, Grassie et al. discovered approximately 10 to 20 different chemicals produced following the individual decomposition of the polyether segment and the urethane link and more than 20 chemicals in the case of polyurethane. Similarly, Font et al.[52] and Zhang et al.[53] also analysed the decomposition products of polyurethane using GC/MS. Font et al. identified as many as 60 different chemicals while Zhang et al. found approximately 20 but noted that there are a few that remain inseparable. The difference in the amount of chemicals detected between the two studies is due to the differences in the equipment used, the experimental conditions such as the decomposition temperature and duration, the libraries of mass spectra used for the chemical identification and also the polyurethane samples tested. The findings of Font et al. and Zhang et al. are described further in the following sections.

5.11.1 Font et al.

In their research, Font et al.[52] utilised two furnaces joined in series to investigate the decomposition of polyurethane. The first furnace was a pyroprobe and the second furnace was known as the secondary reactor. In turn, the temperature of each furnace was varied over a range while the other furnace stayed at constant temperature. The changes in yield for some of the main decomposition products reported by Font et al. are showed in Figure 5-22.

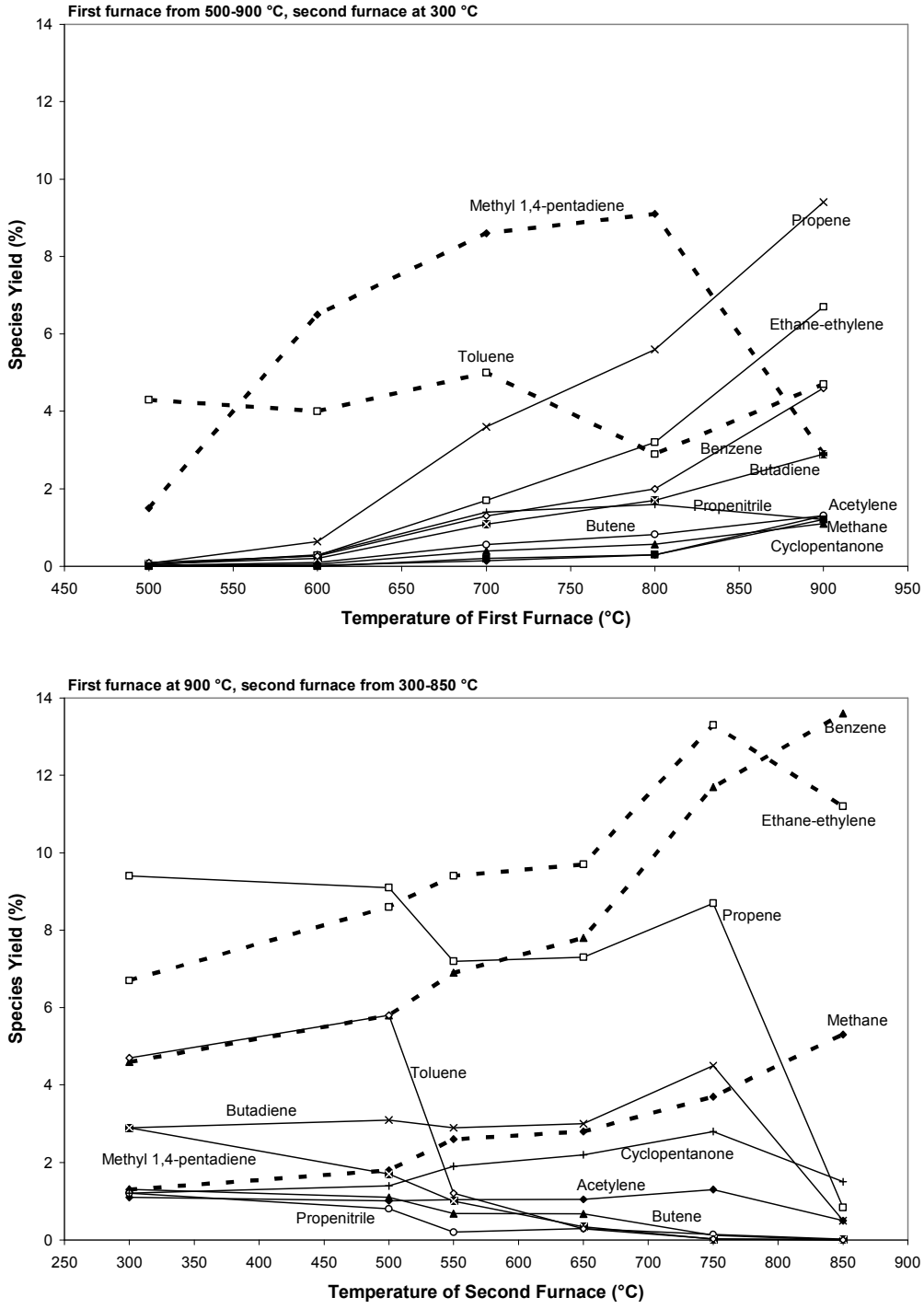

Figure 5-22: Yield of products from polyurethane decomposition versus the varying temperature of the first and second furnaces[52]

When the first furnace was varied from 500 to 900 °C while the second furnace remained at 300 °C, the yield for most of the products increases except for toluene

and methyl 1,4-pentadiene which are represented by the dashed lines. The former remains constant over 500 to 900 ℃ while the latter shows increase towards the plateau between 700 and 800 °C and then decreases beyond 800 °C. With the first furnace maintained at 900 ℃ while the second furnace was varied from 300 to 850 °C, the yield for most of the products remains consistent before showing decrease above two specific temperatures, 550 and 750 °C. Only methane, ethane-ethylene and benzene represented by the dashed lines show the increase in yield with respect to temperature. This indicates that they are the more stable chemicals from the pyrolysis of polyurethane. From both sets of results, most of the species are intermediate chemicals which experience further decomposition within the second furnace and are only present over specific temperature interval.

5.11.2 Zhang et al.

In their study, Zhang et al.[53] were able to identify the chemicals from the decomposition of polyurethane and those associated with the solvents and additives used in its manufacturing. The chemicals from the decomposition of polyurethane were classified into those from the breakdown of urethane link, polyether-polyol and both. The changes in yield of decomposition products from polyurethane decomposition reported by Zhang et al. are showed in Figure 5-23.

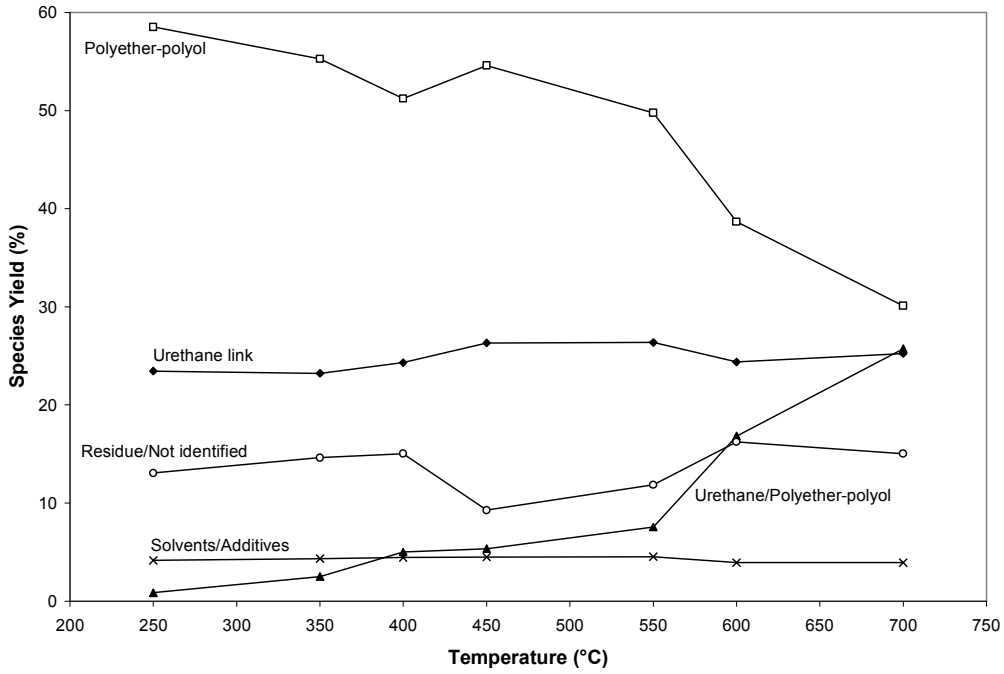

Figure 5-23: Yield of products from polyurethane decomposition at different temperature[53]

The yield of solvents and additives is constant and due to their small quantity in the formulation, their yield is significantly less than the other products. The yield of products associated with the breakdown of urethane link appears constant in Figure 5-23 but the yield of its individual chemicals actually varies as seen in Figure 5-24. The individual yields are represented by the solid lines and the combined yield is represented by the dashed line. The possible cause for these changes is the competition between the micro reactions relating to the dissociation of urethane link. Two competitive paths had been identified by Zhang et al. and they are the

dissociation into isocyanate and alcohol and the dissociation into primary amine, olefin and carbon dioxide[53].

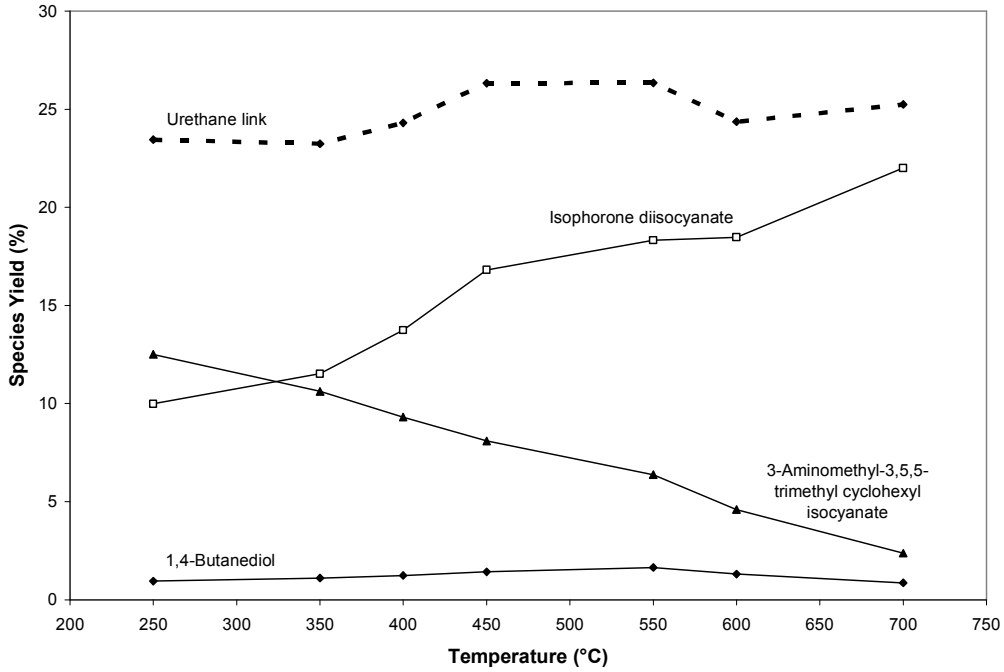

Figure 5-24: Yield of products from urethane link dissociation at different temperature[53]

From Figure 5-23, the yield of products from the breakdown of polyether-polyol shows a gradual reduction with increasing temperature until 550 °C where a more rapid reduction occurs. Similar trend is also collectively reflected by its individual yields in Figure 5-25. According to Zhang et al., the breakdown of polyether-polyol is also competitive in nature and the reactions involved include thermal degradation, dehydration, hydrogen transfer and ester exchange[53].

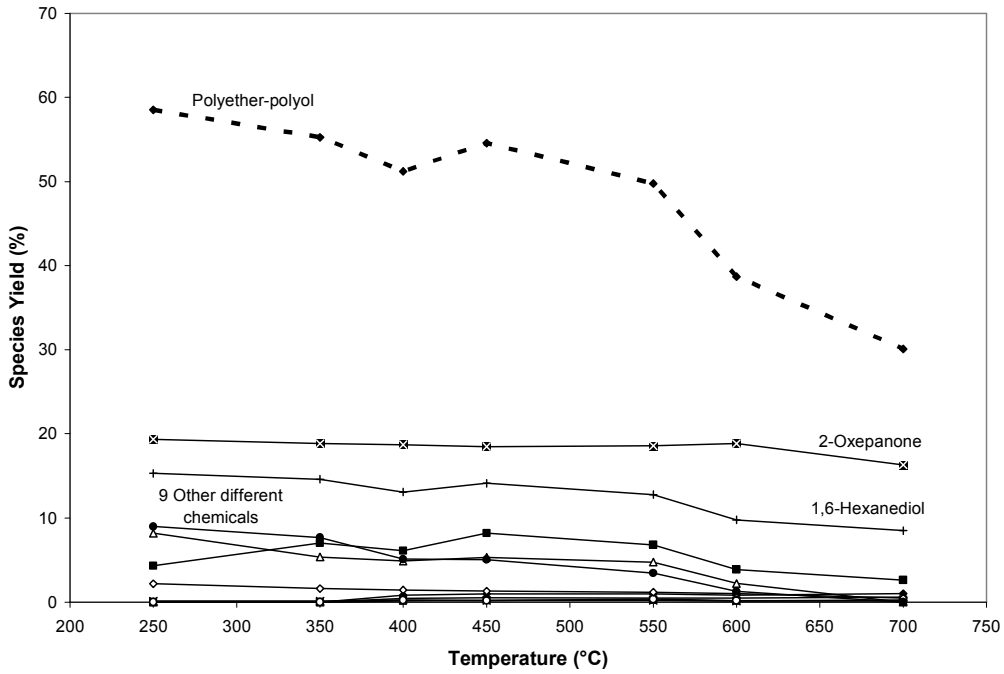

Figure 5-25: Yield of products from breakdown of polyether-polyol at different temperature[53]

A number of decomposition products remain inseparable as they originate from both urethane link and polyether-polyol. From Figure 5-23, these yields become more significant above 550 °C which coincides with the rapid reduction in the yield of polyether-polyol hence these two phenomena might be related to some extent. From the individual yields in Figure 5-26, this rapid increase of the combined yield is mainly influenced by the rapid rise in carbon dioxide.

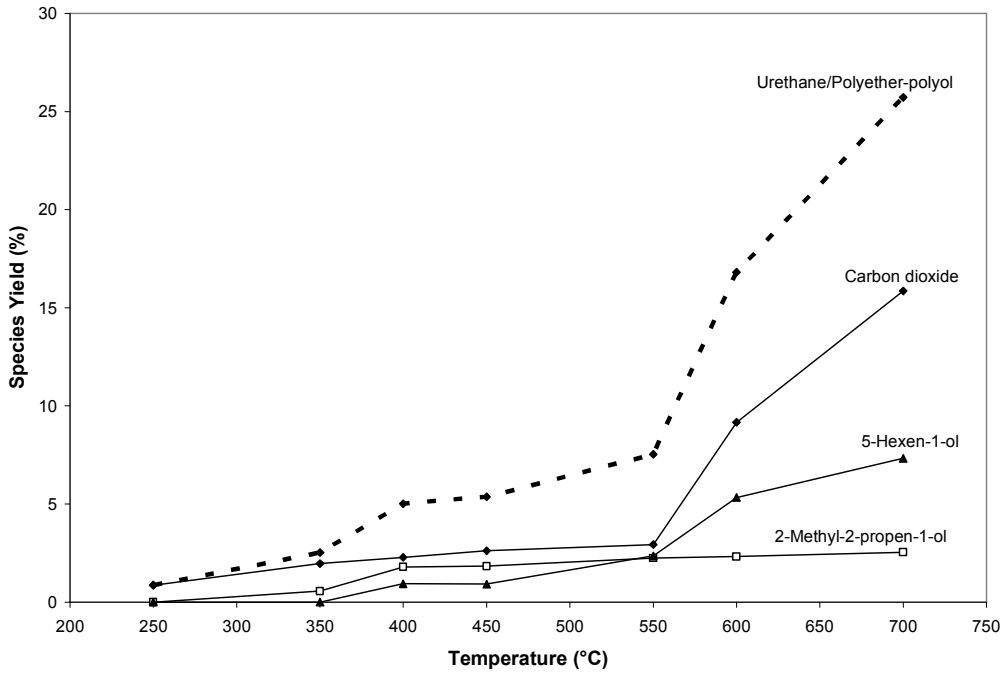

Figure 5-26: Yield of products from dissociation of urethane link and breakdown of polyether-polyol at different temperature[53]

Despite the variations in yield over the entire temperature range, the region between approximately 400 to 550 °C shows both the combined and individual yields of products from urethane link, polyether-polyol and both are relatively constant. Although the decomposition temperature does not translate directly into heating rate, this consistent relationship exhibited by the product yield and temperature over a specific region as demonstrated by Zhang et al.[53] indicates the possibility of a similar trend between the product yield and heating rate. This should be investigated in the future and if such trend exists, then the changes in the yield and composition of decomposition products with heating rate will hopefully justify the region of consistency found and explain the changes noted in the heat of reaction. This hypothesis is also supported by the findings from Rath et al.[64] where a linear relationship is found between the final char yield of woods and their heat of pyrolysis.

5.11.3 Effect of Fuel Containing Oxygen and Amount of Sample Mass Tested

Other possible factors which affect the heat of reaction of polyurethane foam decomposition include the oxygen content in the fuel[85] and the amount of sample

mass tested. The release of oxygen from fuel causes exothermic oxidation and the degree of oxidation depends strongly on the heating rate. Thus, under different heating rate, the varying degree of oxidation could change the endothermicity of foam decomposition in nitrogen. Regarding the amount of sample mass tested, Rath et al.[64] show in Figure 5-8 that the increase in sample mass decreases the endothermic heat of pyrolysis of woods due to the increase influence from exothermic char formation. Hence, changing the mass of foam and melt samples could also have a profound impact on the heat of reaction during decomposition.

5.11.4 Effect of Fire Retardant Additives

According to the manufacturer's information, the raw ingredients in NFR and FR foams are similar with the exception that fire retardant additives such as melamine and halophosphate are presence in the FR foams. The effects these fire retardant additives have on the heat of reaction are not obvious. However, in Figure 5-16, the melts of FR-Y-36 and FR-LG-38 shows lower endothermic value than the others and this is believed to be a result of the exothermic char formation from the breakdown of melamine remnants in the melts. The mechanism of melamine as fire retardant additive was studied by Price et al.[28] and Denecker et al.[34] but their findings were inconclusive. The former reported an exothermic process as a result of char formation by melamine while the latter reported an endothermic process as a result of melamine sublimation. This is believed to be dependent on the melamine concentration which can vary for different foam formulations. As melamine experiences both endothermic sublimation and exothermic char formation[38], its varying concentration affects the competition between both reactions and has a direct impact on the heat of reaction.

5.12 Heat of Reaction for Decomposition of Polyurethane Foams in Air and Sensitivity to Heating Rate

Experiments under air environment are performed at 1, 5, 20 and 60 °C/min with ~3 mg sample mass and the polyurethane foams tested are NFR-SB-31 and FR-Y-36. Figure 5-27 and 5-28 shows the original heat flow curve at all heating rates tested for

NFR-SB-31 and FR-Y-36. The positive heat flow denotes exothermicity. Comparing with the baseline curvature seen in the nitrogen experiments, the baseline of the air experiments is relatively level. Due to the porous nature of the foam samples, the experimental offset in air experiments does not correlate with their calculated offset as seen previously in Figure 5-21.

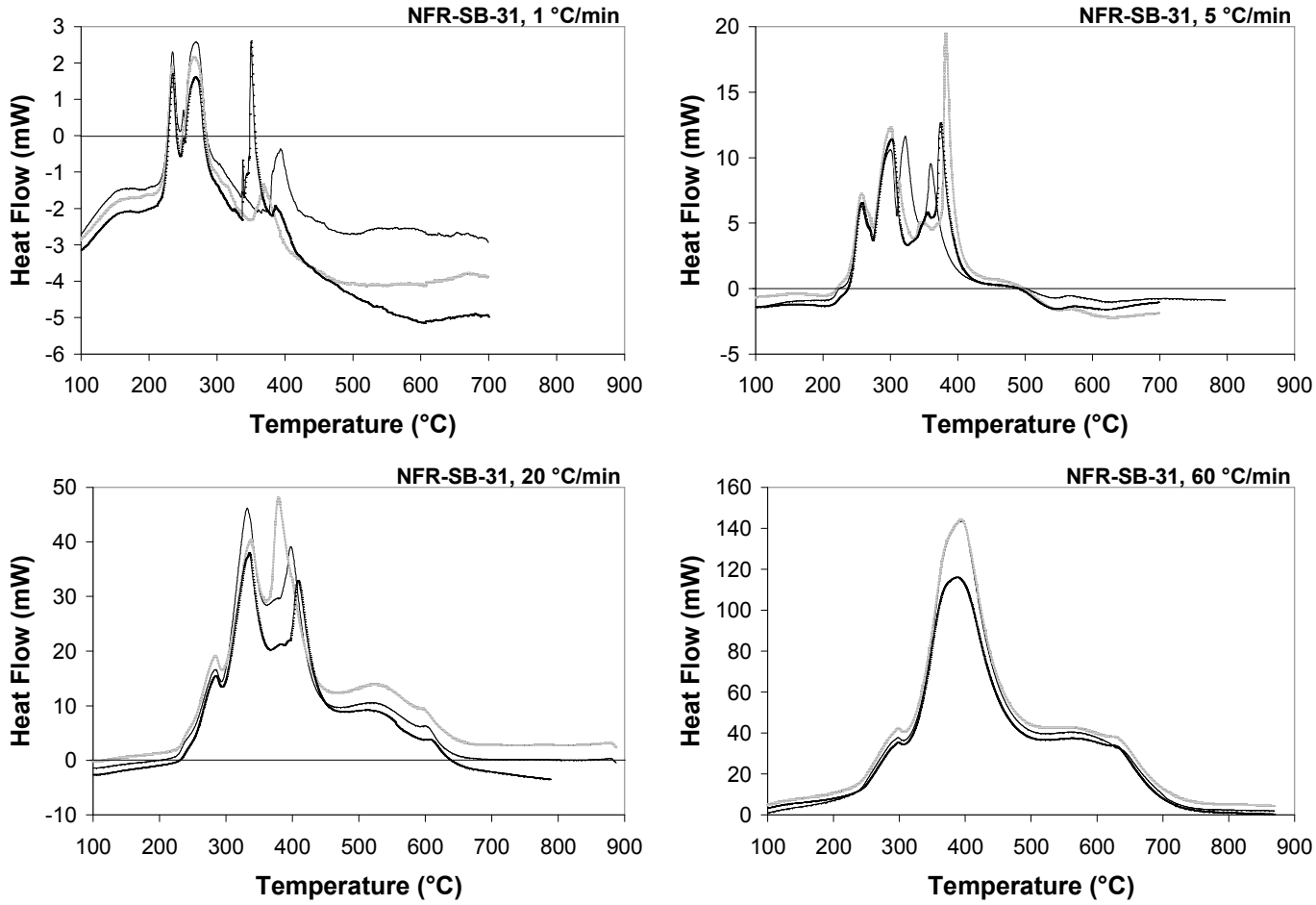

Figure 5-27: Original heat flow curve of ~3 mg NFR-SB-31 at 1, 5, 20 and 60 °C/min heating rates under air environment

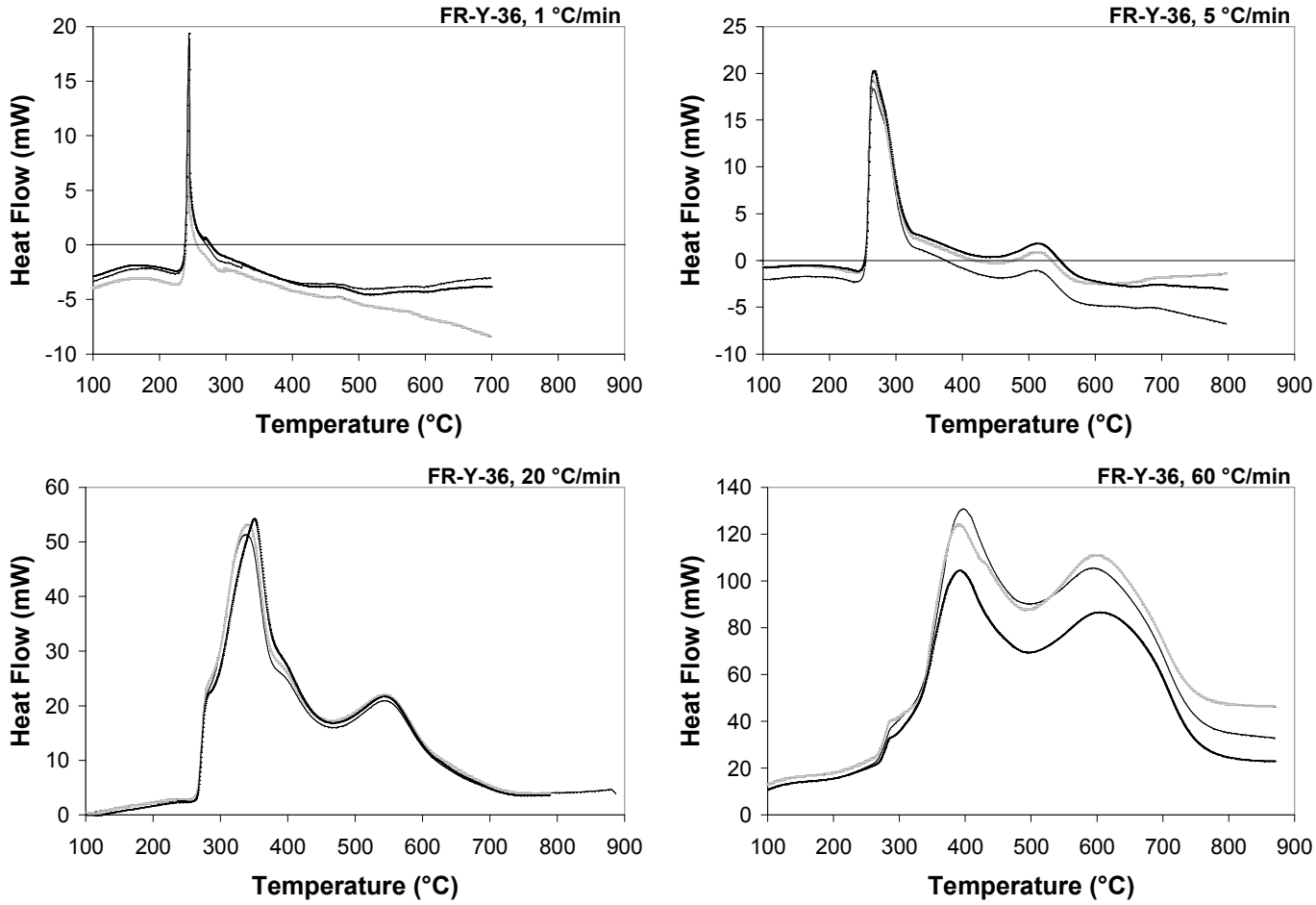

Figure 5-28: Original heat flow curve of ~3 mg FR-Y-36 at 1, 5, 20 and 60 °C/min heating rates under air environment

Applying the analysis principle adopted for the nitrogen experiments, the reaction heat flow curve are obtained and Figure 5-29 shows the mass loss/°C and reaction heat flow curve for NFR-SB-31. Different to the decomposition in nitrogen, the pattern of decomposition in air changes significantly over the different heating rates tested. For NFR-SB-31, the mass loss/°C at 1 °C/min shows one primary peak at 250 °C and several smaller non-repetitive peaks between 350 and 450 °C. At 5 and 20 °C/min, there are two to three peaks over the main region of decomposition ranging between 200 and 400 °C followed by a slow decomposition region above 425 °C which lasts until 650 °C. Increasing the heating rate from 5 to 20 °C/min increases the influence of the second and third peaks such that their magnitude is similar to that of the first primary peak. At 60 °C/min, there are two distinct peaks between 200 and 400 °C and the slow decomposition region initiates around 450 °C. The significant difference seen at 60 °C/min compared to the other heating rates is the magnitude of the second peak has surpassed the first peak to become the primary decomposition peak. At each heating rate tested, the decomposition of NFR-SB-31 in air produces exothermic reaction heat flow.

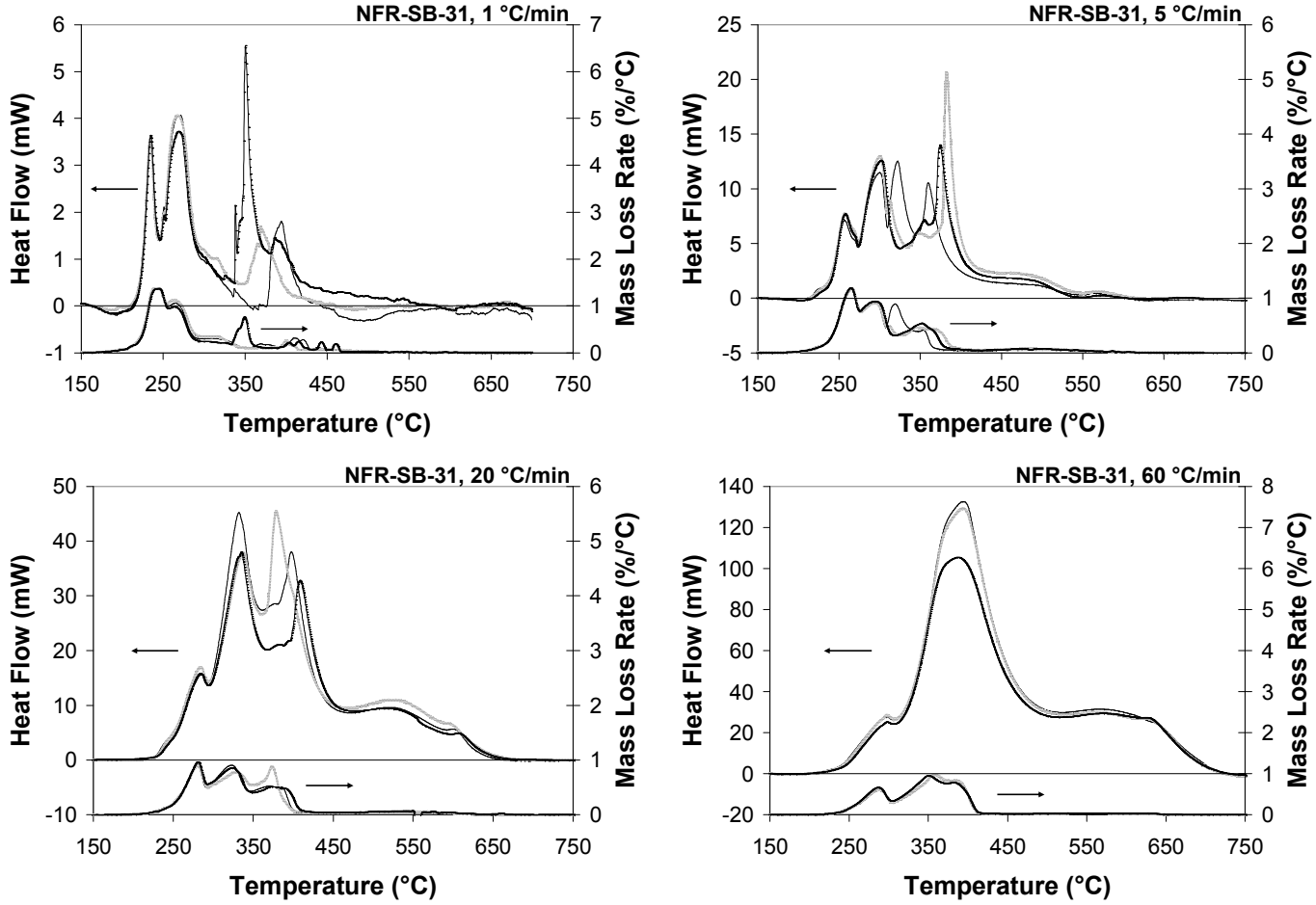

Figure 5-29: Reaction heat flow and mass loss/°C of ~3 mg NFR-SB-31 at 1, 5, 20 and 60 °C/min heating rates under air environment

Different to the similarity seen between the decomposition of NFR-SB-31 and FR-Y-36 in the nitrogen environment, the decomposition in air of FR-Y-36 in Figure 5-30 is not the same as NFR-SB-31. At 1 and 5 °C/min, the mass loss/°C show an initial single primary peak and its magnitude decreases with increasing heating rate. At 20 °C/min, the primary peak reduces to a level plateau ranging from 275 to 350 °C. At 60 °C/min, the decomposition pattern is similar to that of NFR-SB-31 where two peaks are noted over the main region of decomposition. For FR-Y-36, the slow decomposition region is present at all heating rates tested and it starts between 375 and 475 °C. Overall, the decomposition pattern of FR-Y-36 shows better repeatability than NFR-SB-31. However, similar to NFR-SB-31, the decomposition of FR-Y-36 in air also produces exothermic reaction heat flow for each of the heating rate tested.

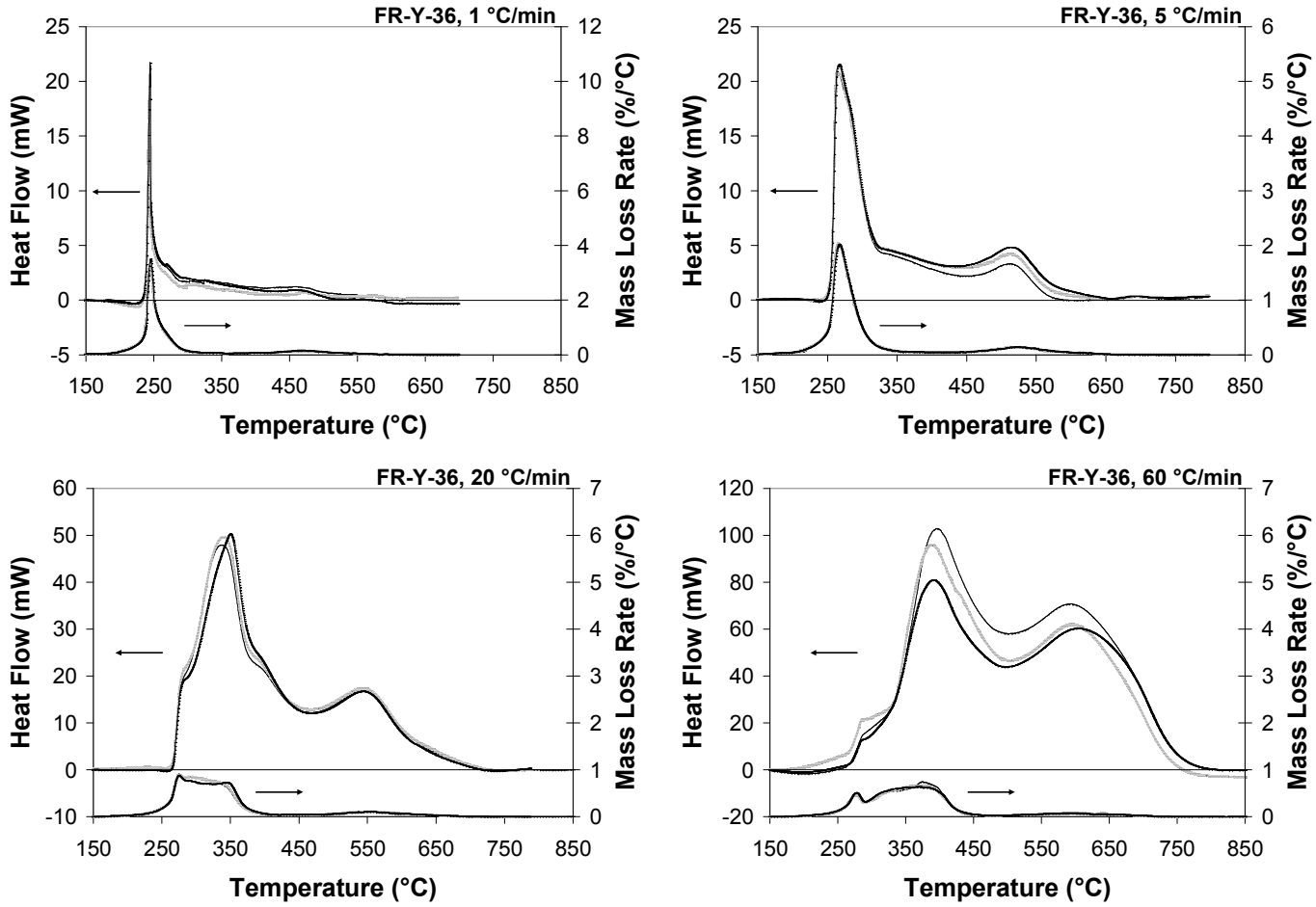

Figure 5-30: Reaction heat flow and mass loss/°C of ~3 mg FR-Y-36 at 1, 5, 20 and 60 °C/min heating rates under air environment

The multiple peaks of the mass loss/°C curve indicate multiple reactions but the absence of clear separation between the peaks means that these reactions overlap closely and it is not possible to accurately decide the start and end of the individual reactions. Hence, the total heat of reaction is reported which is determined from Equation (5-15). The calculation involves integrating the heat flow from the start to end of the entire decomposition and then divided by the mass loss over the same interval. In this case, T_{start} is temperature where the TGA mass loss/°C is 10 % of the difference between the maximum and minimum values of the main decomposition region. T_{end} has the same definition as T_{start} except it is determined for the slow decomposition region. In Figure 5-31, the reported values are the average of three repetitions and the standard deviation is included as error bars.

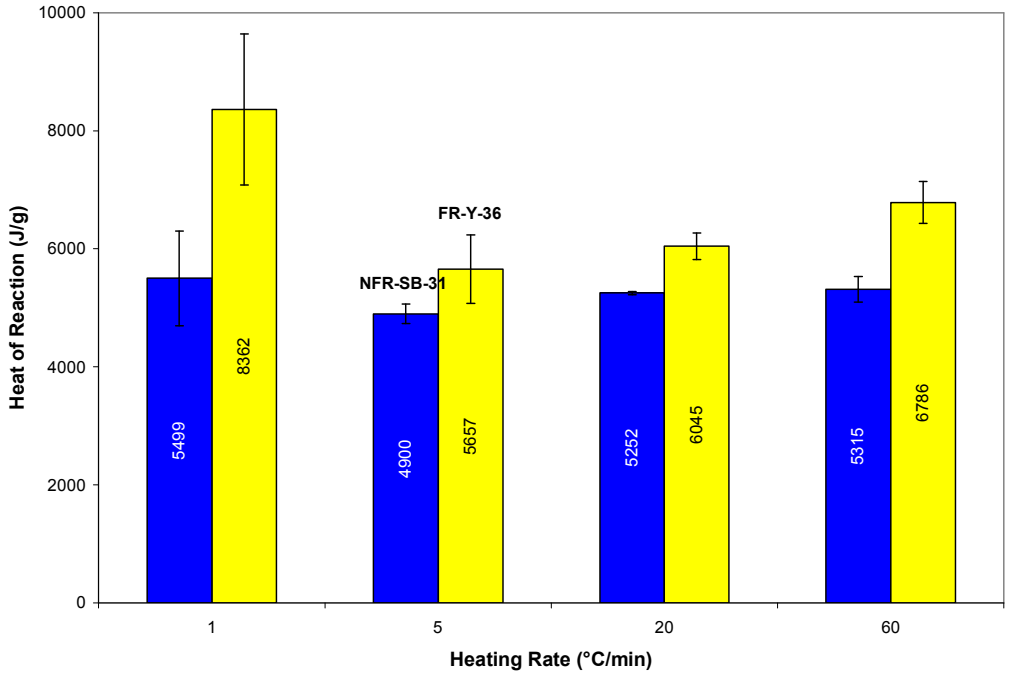

Figure 5-31: Average total heat of reaction for foam decomposition under air environment

The heat of reaction for NFR-SB-31 is less than FR-Y-36, the former ranges from exothermic 4900 – 5499 J/g and the latter ranges from exothermic 5657 – 8362 J/g. When compared with the endothermic pyrolysis reactions in nitrogen, the magnitude of the air experiments is at least five times greater. Despite using ~3 mg of porous foam sample, the heat of reaction for air experiments does not appear to change

significantly with varying heating rates. This is different to the trend seen among the nitrogen experiments. From Figure 5-31, the heat of reaction for NFR-SB-31 shows better consistency than FR-Y-36. At 1 °C/min, FR-Y-36 shows its greatest magnitude but decreases greatly at 5 °C/min and then increases slightly towards 60 °C/min. From the error bars, NFR-SB-31 has smaller deviation among its repeated experiments comparing with FR-Y-36. The greatest deviation is consistently noted at 1 °C/min for both foams.

5.13 Heat Flow Characteristics of Polyurethane Foam Decomposition in Air

Comparing the original heat flow curves, the baselines of air experiments are more level than the nitrogen experiments. As discussed before, the presence of curvature relates closely to the emissivity of the sample and reference sides. Figure 5-32 compares the different end condition of the alumina sample cups from nitrogen and air experiments. The cups from nitrogen experiments are covered by a layer of char residue while the cups from air experiments are effectively cleaned by oxidation.

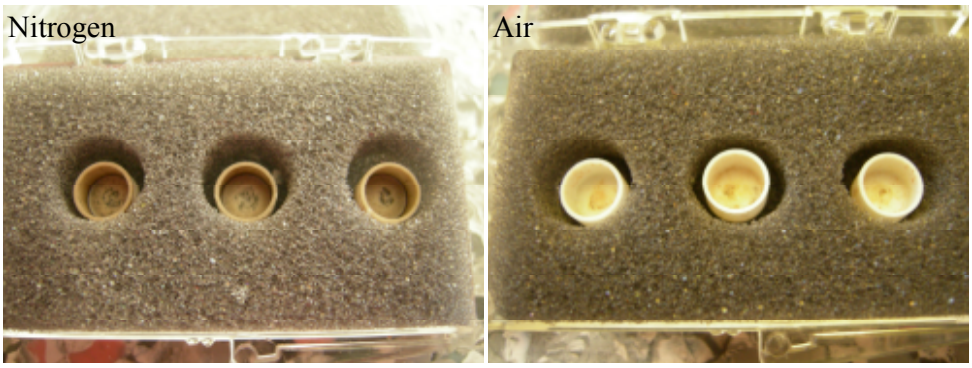

Figure 5-32: End condition of sample cups for nitrogen and air experiments on NFR-SB-31

As the reference cup remains clean throughout the experiment, in the case of nitrogen experiment, there is a difference in the emissivity between the sample and the reference. This generates the additional radiation heat flow which results in the curved baseline. In the air experiments, the emissivity of sample and reference remains the

same thus the level baseline is obtained. This is consistent with the baselines under air environment obtained by Matala et al.[75] and Denecker et al.[34].

In air, the oxygen is able to diffuse onto the pyrolysing surface and the effect of oxidation on the overall decomposition is significant. Valencia et al.[55] and Rein et al.[19] had introduced three more reactions to the existing two pyrolysis reactions to describe the decomposition under air. This proposed scheme listed in Section 4.1 of Chapter 4 shows the increase complexity of foam decomposition under air as both pyrolysis and oxidation compete after the same reactants over similar temperature range. This is supported by the TGA mass loss/°C from this research which show the presence of multiple peaks with a lack of separation between them. The changes in the decomposition pattern seen in both Figure 5-29 and 5-30 indicate the varying degree of oxidation under different heating rates. Given the overall exothermic nature of the decomposition, it shows that the exothermic oxidation generates greater heat flow magnitude which suppresses the heat flow relating to the endothermic pyrolysis. The reported decomposition and heat flow patterns for the foam decomposition in air have been consistent with the literature[22,23,25].

Details of the decomposition behaviours of NFR-SB-31 and FR-Y-36 in air are presented in Section 4.6. In general, the influence of pyrolysis becomes greater than oxidation in the overall decomposition of foam when the heating rate increases. As a result, more melts are produced from the foam pyrolysis than the formation of char residue through the foam oxidation. This is supported by the TGA mass history in Figure 4-19 where the amount of char residue available for oxidation over the slow decomposition region is noted to reduce with the increase of heating rate. Between NFR-SB-31 and FR-Y-36, the former shows less char available for oxidation and this indicates that the fire retardant additives within FR-Y-36 are responsible for its higher char content. Consequently, the heat of reaction for FR-Y-36 is consistently higher than NFR-SB-31 as seen in Figure 5-31 due to the exothermic oxidation of the extra char residue.

5.14 Conclusions

In this research, SDT is used to determine the heat of reaction from the decomposition of polyurethane foams and their melts under nitrogen environment. By changing the purge gas, the decomposition of polyurethane foam under air environment is also investigated. Under nitrogen environment, the foam samples experience two separate pyrolysis reactions while the melt samples which have already undergone the first reaction experience the second reaction only. From the DSC results, the nature of the decomposition for both the first and second reactions is endothermic. The heat of reaction for the first reaction is obtained from the decomposition of polyurethane foam samples while the heat of reaction for the second reaction is obtained from the decomposition of the melt samples. The heat of reaction for the second reaction is also available from the decomposition of the foam sample but these values are not recommended because of the inherent reduced heat flow accuracy for a foam sample.

Despite the large variation in the heat of reaction obtained with respect to the changes in heating rate and sample mass tested, a consistent region is established for the second reaction involving the decomposition of melt. This region includes heating rate from 5 to 20 °C/min and sample mass from ~20 to ~50 mg. No consistent region is determined in the case of the first reaction which involves the decomposition of foam sample. This is caused by the porous nature of the sample which creates a poor thermal contact with the bottom of the cup and this produces uncertainties in the heat flow measurements. In addition, the inconsistency of the heat of reaction may also be caused by the changes in the yield and composition of the decomposition products. Through GC/MS techniques, several studies in the literature have revealed that the yield and composition of the products from polyurethane decomposition varies with respect to temperature. The consistent heat of reaction for the second reaction ranges from endothermic 164 – 295 J/g while the recommended values of the first reaction ranges from endothermic 610 – 1023 J/g. The recommendations for the first reaction are made on the basis of distinguishable heat flow resolution and accuracy for the experiments involving foam samples and also the second reaction having the closest magnitude to the reported consistent values of melt samples. The variations in the heat of reaction for different NFR and FR foams and also NF and F melts are considered to

be within the experimental uncertainties. Comparing with values in Table 5-4, the range of heat of reaction reported for the first and second reactions are similar to the recalculated values of Valencia[25] which are endothermic 1009 and 331 J/g respectively.

The decomposition of polyurethane foam under air is more complicated than nitrogen. It is commonly described by five different reactions which involves both oxidation and pyrolysis. Some of these reactions overlap closely in terms of temperature and are also competitive as they consume the same reactant. While the decomposition pattern under nitrogen environment is consistent over different heating rate, the decomposition pattern under air environment varies. The reason is the changes in the degree of oxidation with heating rate. Higher heating rate is noted to encourage foam pyrolysis over foam oxidation. The overall nature of the decomposition is exothermic indicating that the exothermic oxidation has greater heat flow magnitude than the endothermic pyrolysis. Since multiple reactions overlap closely in the air experiments, the determination of individual heat of reaction is not possible and a total value is reported instead. For NFR-SB-31, the total heat of reaction ranges from exothermic 4900 – 5499 J/g while for FR-Y-36, the value ranges from exothermic 5657 – 8362 J/g. Again, comparing with the literature, the heat of reaction reported for air experiments is close to the value reported by Valencia[25], exothermic 3891 J/g.

Chapter 6. Thermophysical Properties of Polyurethane Foams and Their Melts

6.1 Introduction

As mentioned in Chapter 4 and 5, the decomposition of polyurethane foam in fire is represented by two main pyrolysis reactions[19,55] where the first reaction involves the foam decomposition into melts and gases while the second reaction involves the decomposition of the remaining melts into gases. Although oxidation occurs to some degree prior to ignition as the material heats up, it is reasonable to omit the effect of oxidation on the overall decomposition process. The assumption is that once the flame becomes sustainable, the oxygen will be fully consumed within the flame before reaching the fuel bed to cause any oxidation[42].

According to the results from thermogravimetric analysis (TGA) experiments under nitrogen environment in Chapter 3 and 4, the temperature range of the first and second reactions varies with the changes in the heating rate. However, nominally, the temperature ranges from 180 to 330 °C for the first reaction and from 300 to 460 °C for the second reaction. During the first reaction, the polyurethane foam experiences a phase change when it decomposes from the originally porous solid into the coagulated melt and simultaneously releases some combustible gases. A phase change disrupts the molecular arrangement of a material and often leads to the changes in its thermophysical properties which affect the heat transfer through the material.

The melting phenomenon of polyurethane foam has been widely reported in the literature[6,26]. It is not the typical solid to liquid transformation which only involves a simple phase change without alteration to the chemical composition of the material. From the two reactions proposed, the melting of foam is actually part of the first reaction in the overall decomposition process. Through the first reaction, polyurethane foam decomposes into its raw ingredients, the urethane link and the polyether-polyol[53]. The urethane link decomposes further into gaseous products over the first

reaction while the polyether-polyol remains stable in liquid melt form. Over a higher temperature range, the melt produced in the first reaction will undergo the second reaction to form more combustible gases and by the end of the decomposition, a small amount of char residue is left behind. In certain special application foams that contain fire retardant additives, a complete layer or some fraction of char are formed to inhibit the combustion as seen in Figure 6-1. The formation of insulative char further alters the thermophysical properties of the decomposing foam.

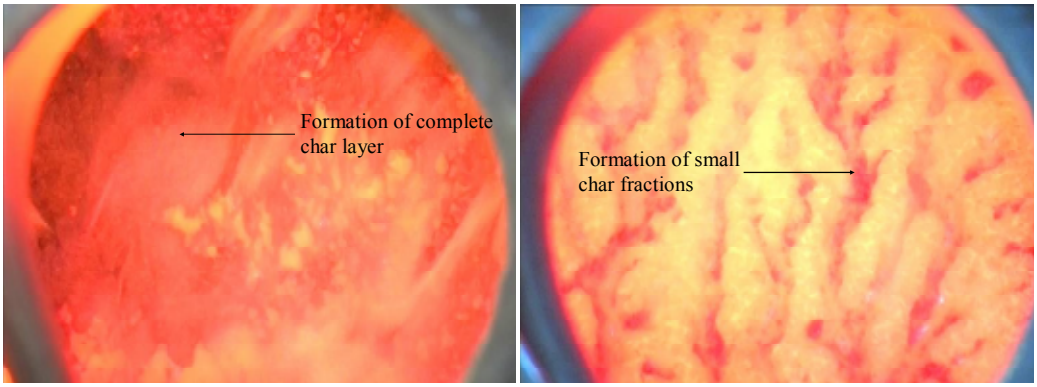

Figure 6-1: Photographs of the decomposing surface of different fire retardant polyurethane foams showing the complete char layer and the smaller char fractions

According to the two pyrolysis reactions of foam decomposition, Chapter 3, 4 and 5 have developed the kinetic properties governing decomposition. This chapter describes the methodology for measuring the thermophysical properties of polyurethane foam and its melt at ambient temperature. A transient plane source method is used and it is commonly called the Hot Disk method[86] which is performed in accordance with ISO 22007-2:2008[87]. Seven polyurethane foams and their melts listed in Table 2-1 of Chapter 2 are tested. As discussed in Chapter 7, the melts tested are obtained from the Sample Feeding Vertical Cone experiments where the foam sample decomposes with either non-flaming (NF) or flaming (F) surfaces.

The properties measured using Hot Disk method are the thermal conductivity, λ which governs the rate of heat transfer through a material, the specific heat, c_p which represents the material's heat storing capacity and the thermal diffusivity, κ which is a measure of the material's thermal inertia. Among these properties, the thermal conductivity and specific heat are of interest to this research as they are the required

inputs to Fire Dynamics Simulator, Version 5[17] (FDS 5[a]). Other research[27] focusing on estimating material properties as inputs for fire modelling have also used these thermophysical properties as the inputs or variables during the estimation process. Lastly, the thermal conductivity and specific heat of material are also useful for the prediction of solid ignition[58,88] and melt flow[89].

In the Hot Disk experiment, the thermophysical properties of material are measured over a transient period where the sample temperature does not achieve steady state. The advantages of this method over the conventional steady state technique such as the guarded hot plate[90] include shorter measuring time, smaller sample size and simplified experimental setup. Within the literature, the Hot Disk method has been successful in finding the thermophysical properties of building materials with varying density and level of porosity[91,92]. Using this transient plane source technique, the properties found have been comparable to those reported by the materials' manufacturers. With the simple experimental setup, the Hot Disk method has also been applied to determine the thermophysical properties of several liquids with different viscosity such as nano fluid[93], milks[94] and thermal greases[95].

6.2 Published Thermophysical Properties of Polyurethane Foam and Its Melt

Three sources in the literature have reported the thermophysical properties of polyurethane foam and melt as shown in Table 6-1. The italicised '*Polyol*' in Table 6-1 is the terminology adopted by Prasad et al.[42] and Valencia[25] to denote the melt produced from the foam decomposition. Meanwhile, the non-italicised 'Polyol' is the original raw material which is used in the foam production reported by the manufacturers[96]. Since the liquid produced during the foam decomposition includes some solid contents in this research, this liquid is termed melt rather than polyol which specifically implies the raw material.

[a] Version 5.5.3, SVN number 7031.

Table 6-1: Thermophysical properties of polyurethane foam and its melt (polyol) in the literature

Authors	Prasad et al.		Valencia		MatWeb
Sample type	Foam	*Polyol*	Foam	*Polyol*	Polyol
Density, ρ (kg/m^3)	23	1012	22	800	1025
Thermal conductivity, λ (W/mK)	0.050	0.150	0.045 – 0.085	0.8	0.157
Specific heat, c_p (J/kgK)	1000	2000	2000 – 2400	2000	1917

Using the reported values as inputs, Prasad et al. and Valencia used FDS 5 to model the burning behaviours of polyurethane foam from different scales of experiments. Prasad et al. reported thermophysical properties that are independent of temperature change but it remains unclear if these are obtained at ambient or elevated temperatures. The range of thermal conductivity and specific heat of polyurethane foam reported by Valencia were measured using the guarded hot plate and the differential scanning calorimetry (DSC) respectively, from the room temperature to 200 °C. Both properties are found to increase with increasing temperature. Comparing several manufacturer specifications in MatWeb[96], the thermophysical properties of different polyols are found to be fairly similar. The average density, thermal conductivity and specific heat in Table 6-1 are from six different polyols at 20 °C. With respect to increasing temperature from 20 to 100 °C, the manufacturer values have suggested on average, a 10 % decrease in the thermal conductivity and a 19 % increase in the specific heat.

6.3 Hot Disk Experimental Setup and Preliminary Calculations

The version of equipment used in this research is the Hot Disk Thermal Constants Analyser, Windows 2000/XP Version 5.9.1. The setup consists of Hot Disk sensors, sourcemeter, bridge unit, multimeter, computation device and desktop computer as seen in Figure 6-2.

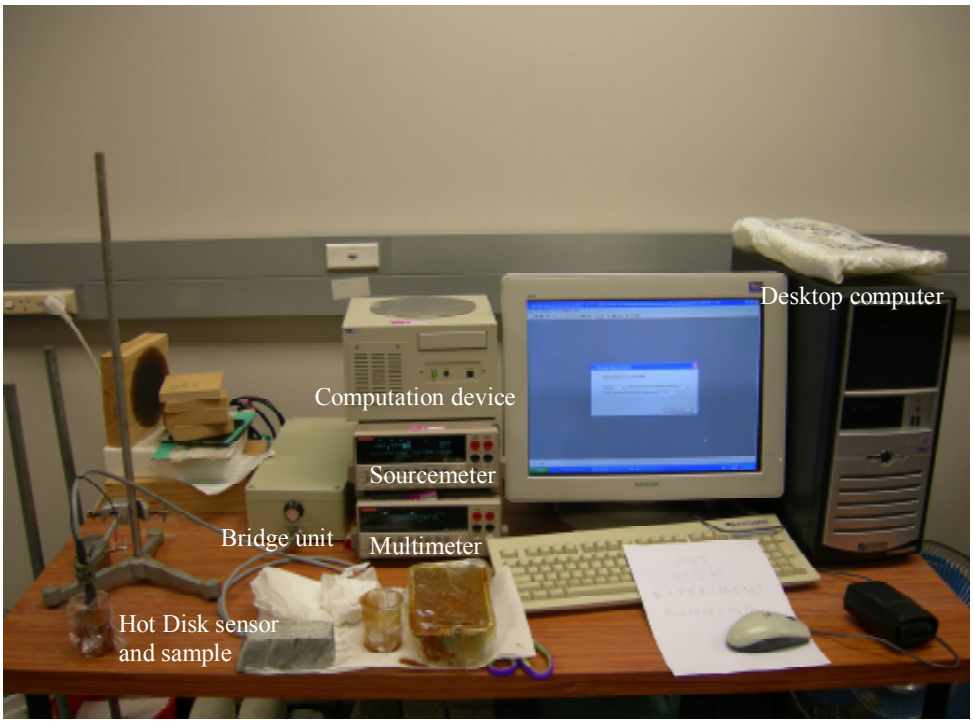

Figure 6-2: Setup for Hot Disk experiment

The fundamental assumption behind the Hot Disk experiment is that the sensor must be located within an infinitely thick sample where the temperature increase of the sensor is free of any influence from the outside boundaries. Due to the difference in the sample size of foam and melt, sensor 4921 of 9.719 mm radius is used for the foam sample while sensor C5465 of 3.189 mm radius is used for the melt sample as seen in Figure 6-3. The appropriate sensor size is determined according to several experimental criteria[87,97] relating to the fundamental assumption made and these criteria are discussed further in the preliminary calculations.

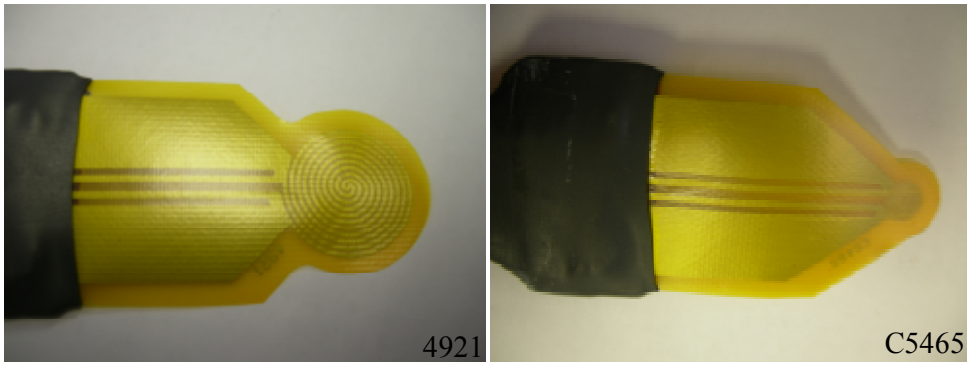

Figure 6-3: Hot Disk sensor, 4921 used for polyurethane foam and C5465 used for melt

During the experiment, the Hot Disk sensor is enclosed by the material tested and it acts as both a heat source and a temperature sensor. In Figure 6-4, the sensor is sandwiched between two foam samples on the left and surrounded by the melt sample on the right.

Figure 6-4: Hot Disk sensor sandwiched by polyurethane foam and by melt

Due to the relatively low weight of the foam sample, the contact between the sample and the sensor is imperfect and this generates heat loss which diminishes the accuracy of the results. To improve the thermal contact, an extra object is added to the top of the sample as seen in Figure 6-4 and in this case, it is a medium density fibreboard (MDF). The object selected should have even surfaces and also the same size as the samples tested such that it provides a consistent and reproducible pressure from the top. The mass of the object should not be excessive to the extent that it compresses and deforms the microstructure of the samples and for the MDF in use, it weighs approximately 120 g. For the melt sample, transparent films are used to cover the open beaker to prevent contamination to the sample.

The sourcemeter is a Keithley 2400 instrument which records and delivers the necessary electrical current to the sensor for heating the sample. The bridge unit is used to balance the potential difference across the sensor at the start of an experiment. During the experiment, this unit becomes increasingly unbalanced as the sensor resistance increases due to heating. The multimeter is a Keithley 2000 instrument which measures the change in potential difference across the bridge. The computation

device and desktop computer provide the analysis interface to edit the experimental information and to evaluate the thermophysical properties.

As mentioned earlier, several experimental criteria must be fulfilled to ensure the Hot Disk sensor is embedded within an infinitely thick medium and the temperature increase of the sensor is free of any influence from the outside boundaries. These criteria are related to the experimental inputs in Table 6-2 which are the sample size, sensor radius and measuring time. Hence, before the Hot Disk experiments proceed, the preliminary calculations are performed to estimate the inputs suitable for the different polyurethane foams and melts used in this research.

Table 6-2: Experimental criteria for sample size, sensor radius and measuring time of Hot Disk experiment

Experimental input	Experimental criteria
Sample size and sensor radius	$d_{sen\text{-}bound} > r_{sen}$ and $d_{sen\text{-}bound} > d_{probing}$
	$r_{sen} < d_{probing} < D_{sen}$
	r_{sen} > size of porosity
	$D_{sam} > 2D_{sen}$
	$d_{sam} > D_{sen}$
	Roughness is one magnitude smaller than D_{sen}
Measuring time	$0.33 < t_{tot}/t_{cha} < 1.00$
	$t = t_{cha}$ for large sample
	t > 10 s for materials with high thermal conductivity and thermal diffusivity
	Discrete selection of t, 2.5, 5, 10, 20, 40, 80, 160, 320 and 640 s

A majority of the variables within Table 6-2 are measured directly from the sample and sensor used. Two variables requiring further calculations are the probing depth, $d_{probing}$ and the total to characteristic time ratio, t_{tot}/t_{cha}. $d_{probing}$ is the heat penetration depth through the sample and it is determined via Equation (6-1)[97].

$$d_{probing} = 1.4(\kappa t)^{1/2} \tag{6-1}$$

Estimating $d_{probing}$ requires the thermal diffusivity, κ of the sample which is a function of the thermophysical properties, λ and c_p which are still unknown and the sample density, ρ. Nevertheless, a close estimate of the thermophysical properties can be used and for polyurethane foam, λ is 0.050 W/mK and c_p is 2440 J/kgK. These properties were previously obtained via the Hot Disk experiment conducted on a polyurethane

foam which is no longer produced commercially and these values are also found to be close to those reported by Valencia[25]. For melt, the λ and c_p from MatWeb[96] in Table 6-1 are applied. For ρ, the density reported in Table 2-1 for the respective foam and melt are applied.

t_{tot}/t_{cha} is a dimensionless parameter and it is deduced from Equation (6-2)[97]. t_{tot} is only the portion of the measuring time which is selected for calculating the thermophyscial properties but in the preliminary calculations, the entire measuring time is used instead. t_{cha} is represented as $t_{cha} = r_{sen}{}^2 / \kappa$ which relates to the sensor radius and the thermal diffusivity of the sample.

$$t_{tot} / t_{cha} = t\kappa / r_{sen}{}^2 \tag{6-2}$$

Table 6-3 summarises the calculated t_{tot}/t_{cha} and $d_{probing}$ from the preliminary calculations for the different polyurethane foams and melts. The table also includes the calculated κ and t_{cha} and the estimated measuring time, t.

Table 6-3: Preliminary estimate of t_{tot}/t_{cha} and $d_{probing}$ of polyurethane foams and melts for Hot Disk experiment

Sample		κ (m^2/s)	t_{cha} (s)	t (s)	t_{tot}/t_{cha}	$d_{probing}$ (mm)
NFR-SB-31	Foam	6.64×10^{-7}	143	160	1.12	14.4
	Melt (F)	8.05×10^{-8}	127	80	0.63	3.6
NFR-DG-42	Foam	4.90×10^{-7}	193	160	0.83	12.4
	Melt (F)	8.00×10^{-8}	128	80	0.62	3.5
NFR-C-19	Foam	1.06×10^{-6}	90	80	0.89	12.9
	Melt (F)	7.93×10^{-8}	129	80	0.62	3.5
FR-Y-36	Foam	5.71×10^{-7}	166	160	0.96	13.4
	Melt (NF)	7.78×10^{-8}	132	80	0.61	3.5
	Melt (F)	7.83×10^{-8}	131	80	0.61	3.5
FR-LG-38	Foam	5.45×10^{-7}	174	160	0.92	13.1
	Melt (NF)	7.79×10^{-8}	131	80	0.61	3.5
	Melt (F)	7.80×10^{-8}	131	80	0.61	3.5
FR-W-50	Foam	4.11×10^{-7}	231	160	0.69	11.4
	Melt (NF)	7.84×10^{-8}	131	80	0.61	3.5
	Melt (F)	7.90×10^{-8}	130	80	0.62	3.5
FR-G-32	Foam	6.33×10^{-7}	150	160	1.07	14.1
	Melt (NF)	7.92×10^{-8}	129	80	0.62	3.5
	Melt (F)	7.99×10^{-8}	128	80	0.62	3.5

For the selected sensor radius, the measuring time estimated for polyurethane foams and melts is 160 and 80 s respectively to satisfy the criteria, $0.33 < t_{tot}/t_{cha} < 1.00$. An

exception is made for NFR-C-19 due to its low density and the measuring time is lowered from 160 to 80 s such that t_{tot}/t_{cha} remains within the recommended bounds. The calculated t_{tot}/t_{cha} is considered to be closer towards the high end value because during the actual Hot Disk analysis it is necessary to exclude certain data points in order to obtain accurate results which will reduce t_{tot}.

During the experiment, the sensor is centred within the sample as depicted in Figure 6-4, the foam sample measures 100 mm along the sides with a thickness of 50 mm while the melt sample is contained within a 100 ml beaker that measures approximately 50 mm in diameter and 45 mm in depth. The selected sample size and the current setup are able to adequately contain the $d_{probing}$ reported in Table 6-3 thus ensuring that the heat does not penetrate beyond the boundaries. As demonstrated through these preliminary calculations, the sample dimensions, the selected sensor radius and the estimated measuring time for the polyurethane foams and melts have satisfied all the experimental criteria. In the subsequent Hot Disk experiments, three repetitions are performed for each experiment with a 60 minutes rest interval in between. Sensitivity analysis is carried out on a few selected foams and melts to obtain the optimal output power and measuring time which produces the most accurate results.

6.4 Hot Disk Analysis Procedure and Operational Theory

Before discussing the sensitivity analysis, this section introduces the analysis procedure[97] and the operational theory[98] of the Hot Disk method in evaluating the thermophysical properties. A number of equations involved in the analysis performed are also discussed. The results of NFR-SB-31 (F) with 15 mW output power and 80 s measuring time are used as illustration. At the start of each experiment, the equipment records 25 s of temperature drift as seen in Figure 6-5. The results provide an indication to the thermal state of the sample. Under a constant ambient environment, the results should show a random distribution of data points such as Figure 6-5 which means that the sample temperature is at equilibrium. If the results show any form of correlation then the experiment should not proceed further as the sample temperature

is still adjusting to reach equilibrium. The three sets of data points in Figure 6-5 represent the three repetitions of the experiment.

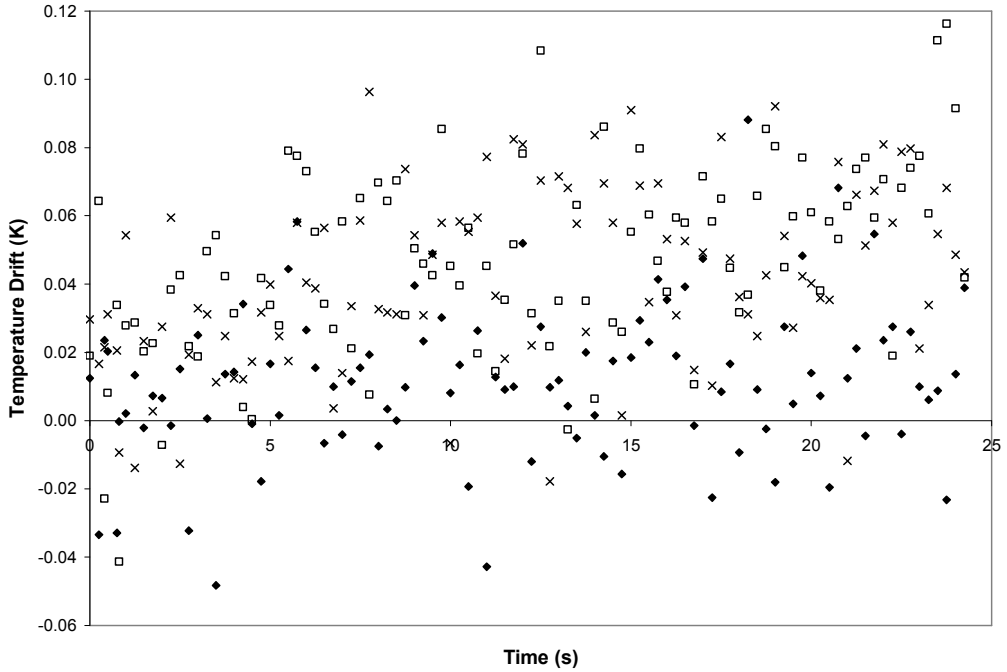

Figure 6-5: Temperature drift versus time of NFR-SB-31 (F)

After the temperature drift assessment, the electrical current is delivered and the sensor heats up which raises its resistance. The sensor resistance is recorded indirectly by the multimeter in terms of the potential difference across the bridge unit. The time varying relationship between the sensor resistance, $R(t)$ and the temperature increase of the sample surface in contact with the sensor, $\Delta T_{ave}(\tau)$ is represented by Equation (6-3).

$$R(t) = R_0\left[1 + TCR\{\Delta T_i + \Delta T_{ave}(\tau)\}\right] \tag{6-3}$$

Due to the thin insulating layer of the sensor, ΔT_i approximates zero and Equation (6-3) is rearranged to solve for $\Delta T_{ave}(\tau)$ in Equation (6-4).

$$\Delta T_{ave}(\tau) = \frac{1}{TCR} \cdot \left[\frac{R(t)}{R_0} - 1\right] \tag{6-4}$$

There are three sets of results analysis before the thermophysical properties are found, the first set is the relationship of $\Delta T_{ave}(\tau)$ versus time. Regardless of the selected measuring time, the Hot Disk experiment constantly records 200 data points over the specified duration. Throughout the entire experiment, the sample is heated continuously thus $\Delta T_{ave}(\tau)$ versus time is expected to show an increasing trend as depicted in Figure 6-6. The trend among the three repetitions shows good agreement.

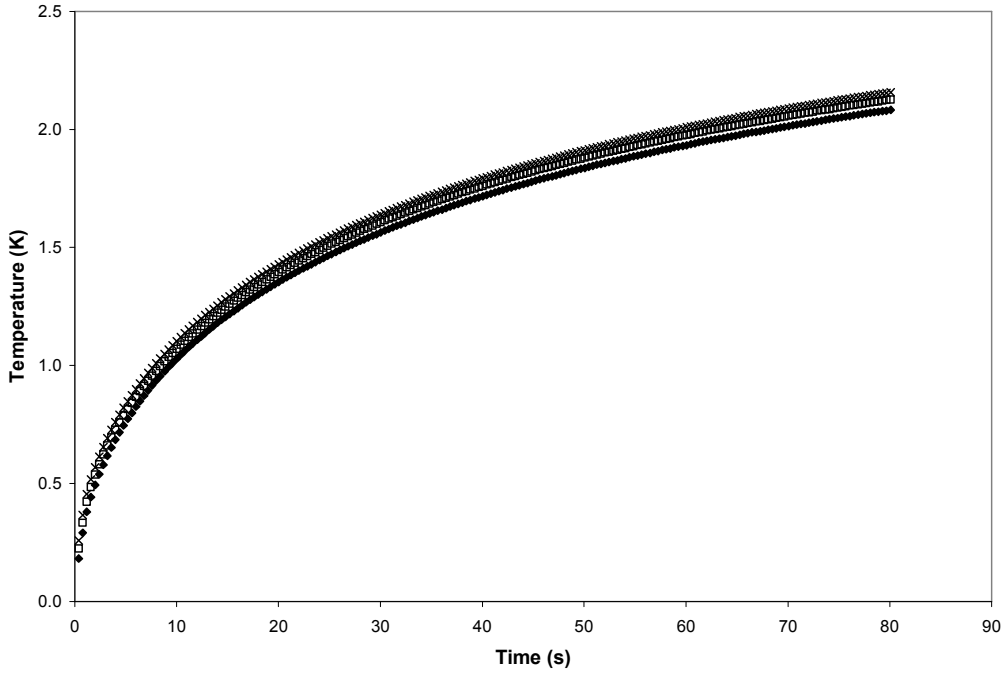

Figure 6-6: Temperature increase versus time of NFR-SB-31 (F)

He[98] demonstrated the mathematical representation for the concentric rings design of the sensor which allows $\Delta T_{ave}(\tau)$ to be expressed as Equation (6-5).

$$\Delta T_{ave}(\tau) = \frac{P_0}{\pi^{3/2} r_{sen} \lambda} \cdot D(\tau) \tag{6-5}$$

$D(\tau)$ is evaluated numerically and the relationship of $\Delta T_{ave}(\tau)$ versus $D(\tau)$ is linear with $P_0/\pi^{3/2} r_{sen}\lambda$ as the slope. Since P_0 and r_{sen} are known inputs, the thermal conductivity of the sample, λ can be determined. However, before evaluating λ, the variable within function D, $\tau = \frac{\sqrt{t\kappa}}{r_{sen}}$ is related to the thermal diffusivity of the

sample, κ which is still unknown. The second set of results analysis solves for κ based on the plot of difference temperature versus square root of time[98]. The aim of this analysis is to achieve a final plot displaying randomly distributed data points after several iterative refinements on the selectable analysis range[97]. Figure 6-7 is the initial plot containing all 200 data points recorded and it shows the early influence from heating the sensor insulating layer.

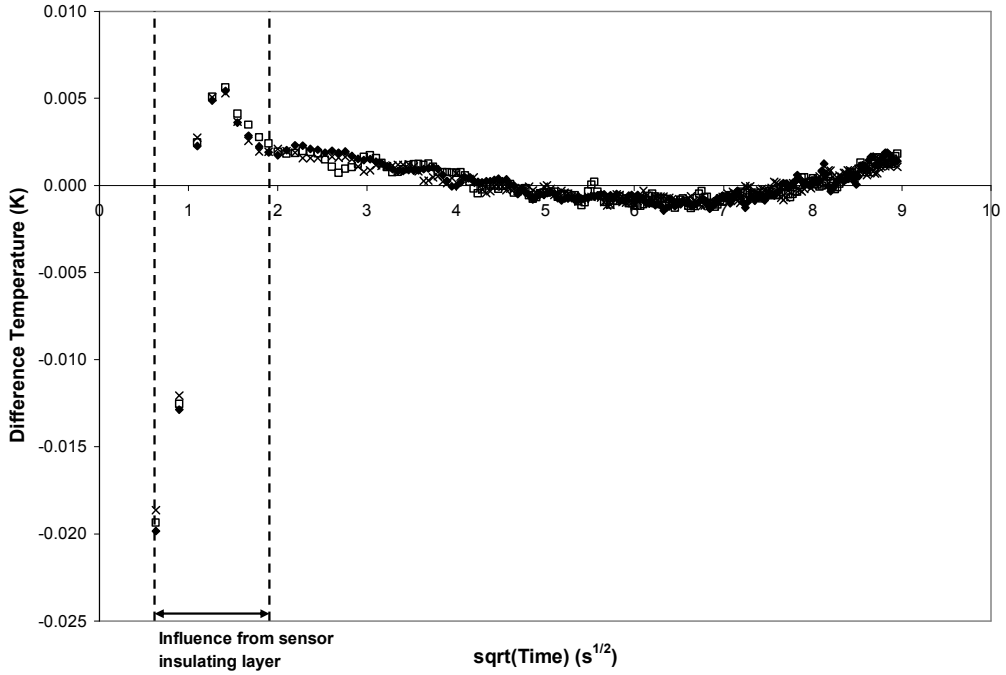

Figure 6-7: Difference temperature versus square root of time with 1 – 200 points of NFR-SB-31 (F)

Following on from Figure 6-7, the first 9 data points are excluded in the attempt to remove the initial effect from heating the insulating layer. The subsequent results containing 10 – 200 points is seen in Figure 6-8 and it shows some residual effect from heating the insulating layer, as well as the influence of the lateral boundaries near the end of experiment[97].

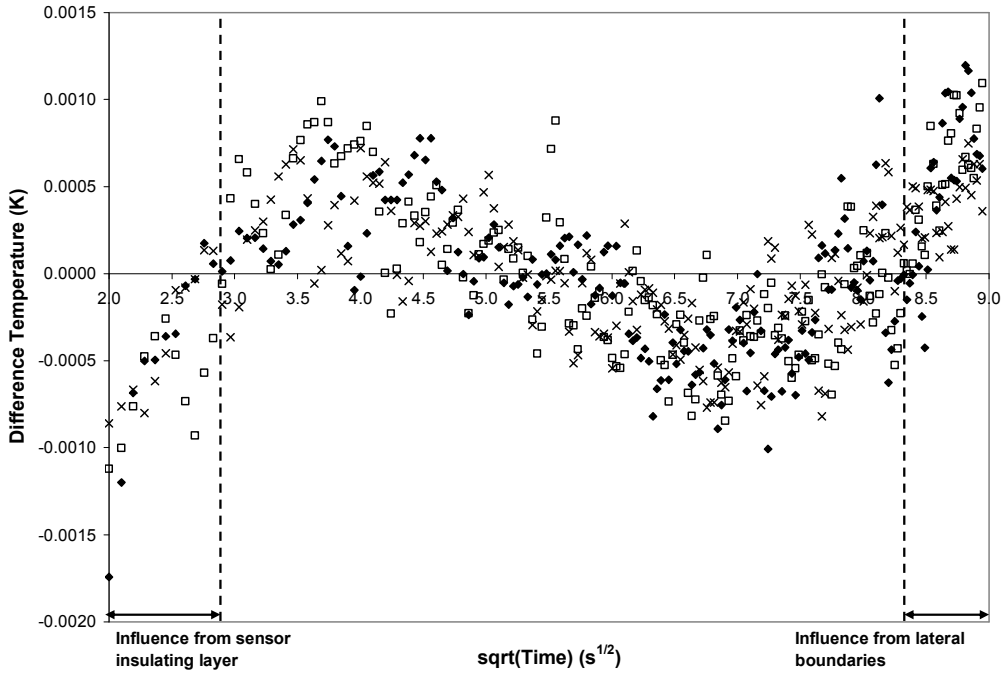

Figure 6-8: Difference temperature versus square root of time with 10 – 200 points of NFR-SB-31 (F)

The data exclusion continues until 31 – 145 points remain as seen in Figure 6-9 which shows the random distribution. This random scatter also means that in the third and final set of analysis, the data points along the linear plot of $\Delta T_{ave}(\tau)$ versus $D(\tau)$ is of random statistical distribution thus the optimum κ has been found.

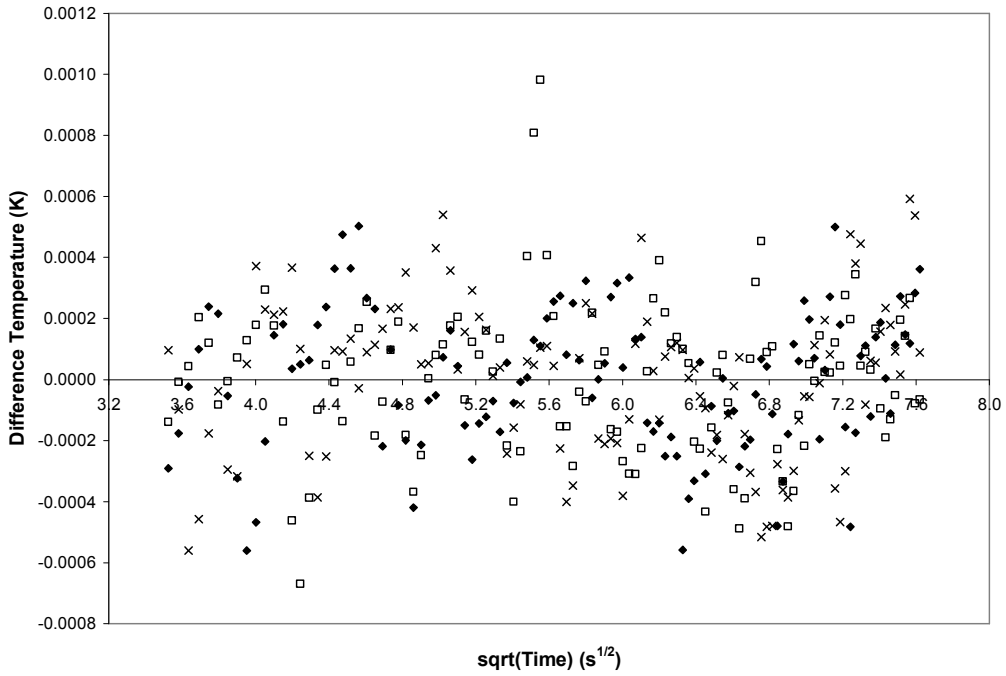

Figure 6-9: Difference temperature versus square root of time with 31 – 145 points of NFR-SB-31 (F)

While data exclusion is necessary for refining the results, it is still important to use at least 100 points for the analysis to maintain sufficient accuracy. The third and final set of results analysis involves the plot of $\Delta T_{ave}(\tau)$ versus $D(\tau)$ which according to Equation (6-5) is a linear straight line as depicted in Figure 6-10. This relationship is plotted over the same optimum range found in Figure 6-9 and based on the slope, λ is determined.

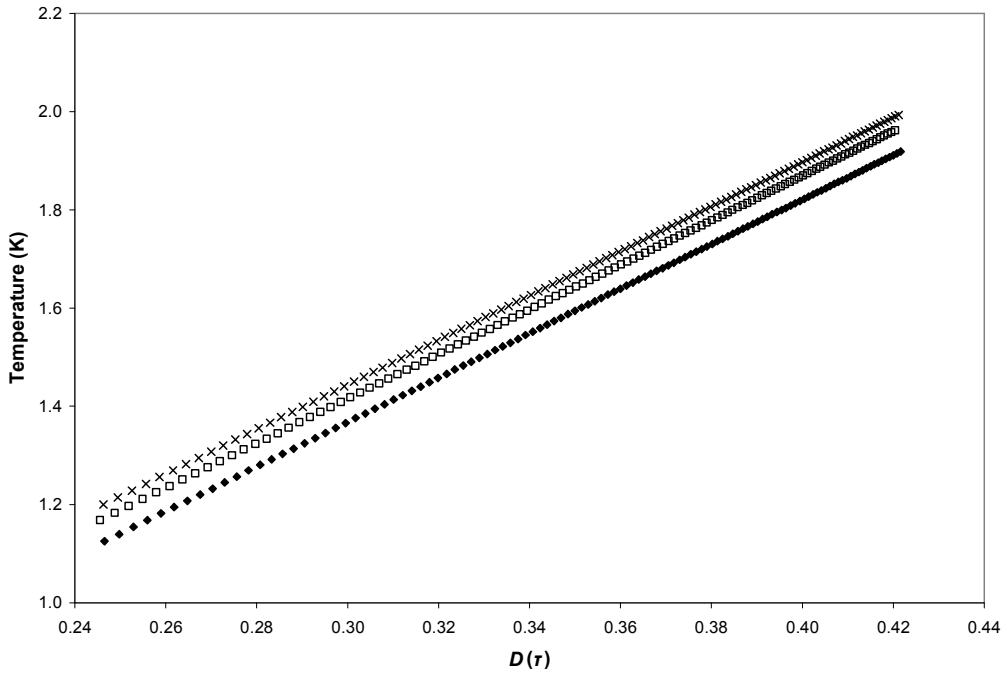

Figure 6-10: Temperature increase versus $D(\tau)$ of NFR-SB-31 (F)

For NFR-SB-31 (F), the density of the melt, ρ is 1019 kg/m^3 and with κ and λ solved, the specific heat of the sample, c_p is determined via the relationship, $\kappa = \lambda / \rho c_p$. The analysis software records $d_{probing}$, temperature increase and t_{tot}/t_{cha} associated with the optimum range applied. The average probing depth for the three repetitions is 4.5 mm which is sufficiently contained within the sample size. The average temperature increase is 0.81 °C and the average t_{tot}/t_{cha} is 0.44, both are within the acceptable region indicated by the analysis software. The average value of κ, λ and c_p for NFR-SB-31 (F) is 8.90×10^{-8} m^2/s, 0.186 W/mK and 2053 J/kgK.

6.5 Sensitivity Analysis on Measuring Time and Output Power

Table 6-2 provides the experimental criteria for the appropriate sample size, sensor radius and measuring time. Through the preliminary calculations, the sample size and sensor radius have satisfied those criteria. Although the measuring time, t is also estimated in the preliminary calculations, the suitable t together with the output power, P_0 are only established from a series of sensitivity experiments. The selection

of t and P_0 are based on the assessment of several experimental outputs from the sensitivity experiments. The outputs assessed include $d_{probing}$, the temperature increase (ΔT), t_{tot}/t_{cha}, the number of data points analysed (N) and the repeatability of the evaluated thermophysical properties. The outputs are compared against their respective acceptance criteria listed in Table 6-4 which are based on the recommendations from the Hot Disk equipment's manufacturer[97].

Table 6-4: Experimental outputs and acceptance criteria for selection of t and P_0

Experimental output	Acceptance criteria
$d_{probing}$	Less than sample thickness, d_{sam}
ΔT	'Lamp indicator' of the analysis interface shows 'green' means the sample temperature increase is adequate
t_{tot}/t_{cha}	'Lamp indicator' of the analysis interface shows 'green' means this ratio is between 0.33 and 1.00
N	More than 100 points analysed
Repeatability of λ and c_p	Standard deviation of the repetitions is less than 2 % for λ and 7 % for c_p

The selected samples for the sensitivity analysis are NFR-C-19, FR-Y-36 and FR-W-50 for polyurethane foams and NFR-SB-31 (F) and FR-Y-36 (NF) for melts. The selected foams cover the range of foam density while the selected melts covers the different viscosity and appearance of the liquid.

For melts, the selected t for the sensitivity analysis are 20, 40, 80 and 160 s during which P_0 is constant at 25 mW. The selection of t is based around the estimated t from the preliminary calculations. Figure 6-11 shows λ and c_p of the three repetitions for each experiment at the selected t. The standard deviation of the repetitions is also included in the figure as percentage of the average value.

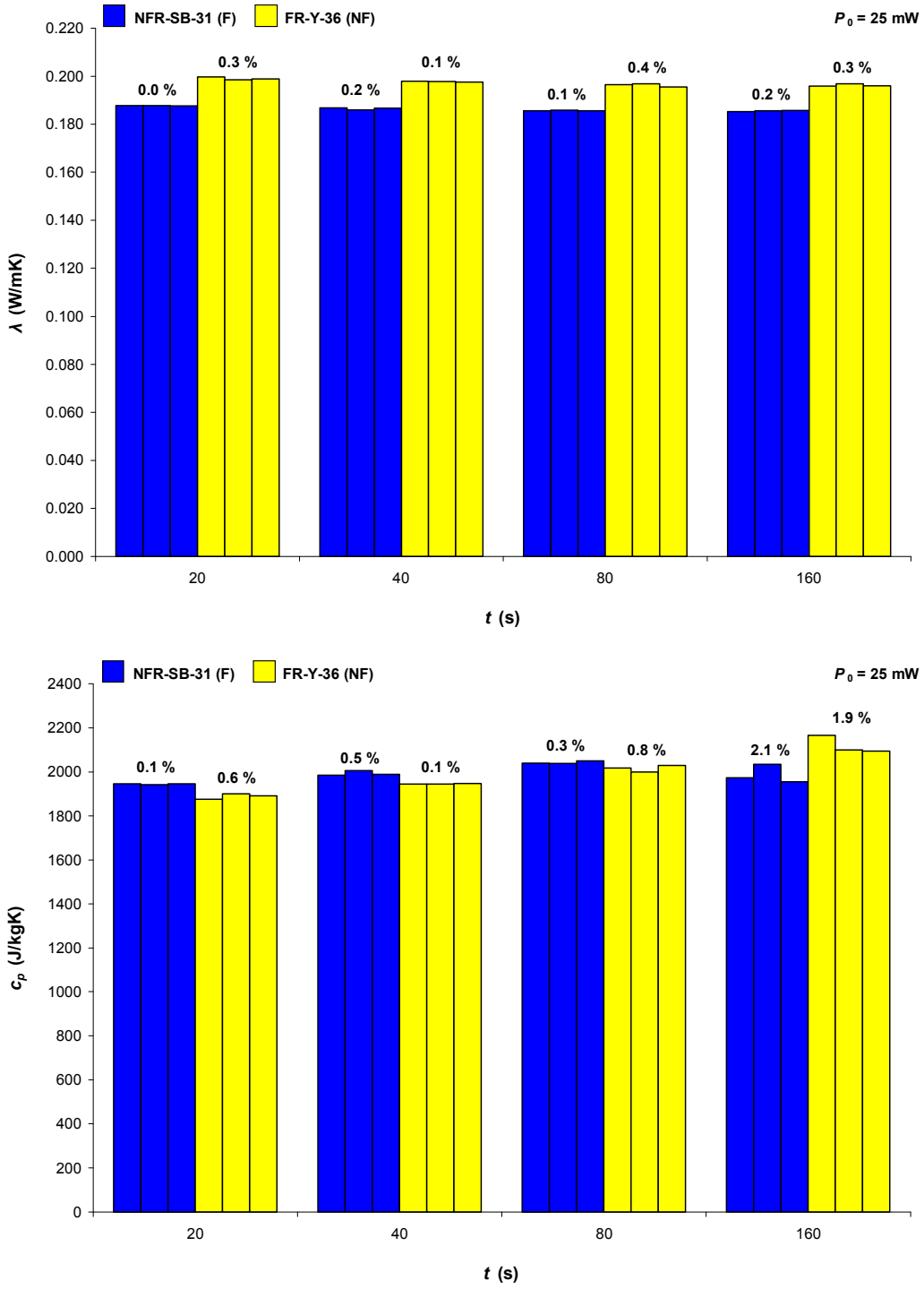

Figure 6-11: Sensitivity analysis of t on λ and c_p of melt

The sensitivity analysis of t reveals that the thermophysical properties are consistent over the range of t tested and most of the standard deviations are less than 1 % of the average except for c_p at 160 s which is the largest at 2 %. These are within the

acceptance criteria of repeatability in Table 6-4. It is noted that λ of FR-Y-36 (NF) is consistently higher than NFR-SB-31 (F) by approximately 0.01 W/mK while c_p is similar between both foams and shows no obvious trend. Table 6-5 lists $d_{probing}$, ΔT, t_{tot}/t_{cha} and N for the sensitivity analysis on melts. These experimental outputs are assessed according to the acceptance criteria listed in Table 6-4 to select the suitable t and P_0. The outputs which are outside the acceptable range are marked with an asterisk.

Table 6-5: $d_{probing}$, temperature increase, t_{tot}/t_{cha} and number of data points analysed for sensitivity analysis of melts

P_0 (mW)	t (s)	NFR-SB-31 (F)				FR-Y-36 (NF)			
		$d_{probing}$ (mm)	ΔT (°C)	t_{tot}/t_{cha}	N	$d_{probing}$ (mm)	ΔT (°C)	t_{tot}/t_{cha}	N
25	20	2.6	1.46	0.15*	166	2.7	1.40	0.16*	166
	40	3.5	1.28	0.27*	135	3.6	1.22	0.28*	135
	80	4.5	1.33	0.43	110	4.7	1.32	0.48	121
	160	5.8	0.68	0.71	60*	5.6	0.93	0.68	75*
5	80	5.3	0.37*	0.62	177	5.4	0.35*	0.63	177
10		4.9	0.68	0.51	145	5.0	0.56	0.54	139
15		4.5	0.81	0.44	114	4.9	0.81	0.51	129
40		4.5	2.45	0.43	114	4.4	1.28	0.42	81*
60		4.2	1.53	0.38	58*	4.4	1.93	0.42	81*

Based on the results in Table 6-5, the suitable t to use for melts is 80 s as all the outputs are satisfactory at a constant P_0 of 25 mW. Other t values are not suitable, 20 and 40 s have t_{tot}/t_{cha} outside the acceptable range while 160 s has insufficient data points for evaluating the thermophysical properties. The subsequent sensitivity analysis of P_0 is performed using constant t of 80 s and P_0 at 5, 10, 15, 25, 40 and 60 mW. The selection of P_0 is based on the range used for nano fluids[93]. The thermophysical properties from the sensitivity experiments are showed in Figure 6-12.

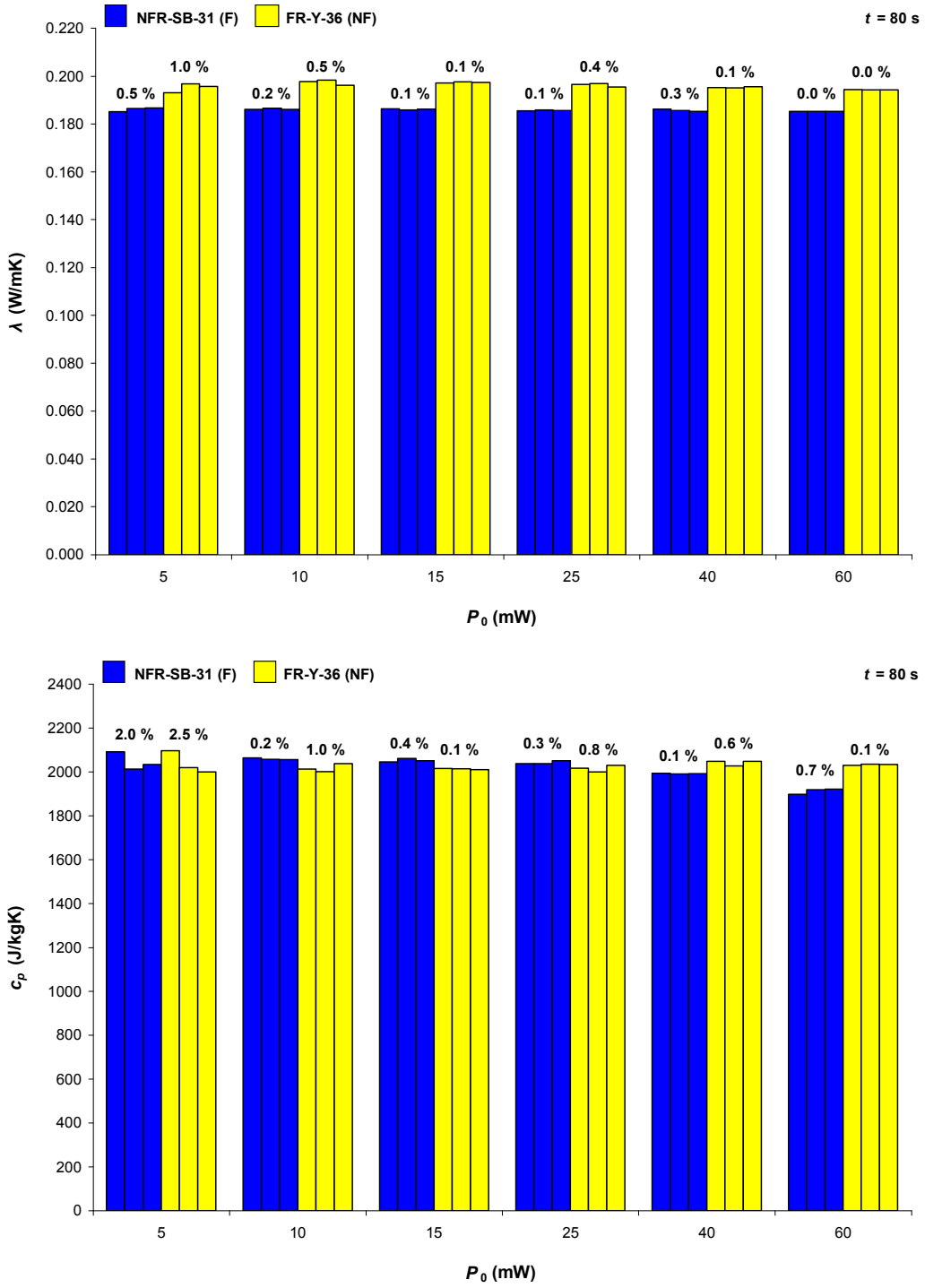

Figure 6-12: Sensitivity analysis of P_0 on λ and c_p of melt

Similar to the sensitivity analysis of t, λ and c_p are consistent over the range of P_0 tested and most of the standard deviations are less than 1 % of the average except for c_p at 5 mW which is between 2 and 3 %. Once again, these fall within the acceptance

criteria of repeatability in Table 6-4. According to Table 6-5, the suitable P_0 ranges between 10 to 25 mW and for this research, the mid value of 15 mW is used. Low P_0 such as 5 mW fails to produce acceptable temperature increase as a result of insufficient energy for heating. On the other hand, high P_0 such as 40 and 60 mW require excessive data exclusion before the plot of difference temperature versus square root of time displays a random distribution. As a result, insufficient data points are used in the analysis. According to the literature, the convection within liquid has been a concern when applying the Hot Disk method to measure the thermophysical properties of a liquid[93,94] and it is normally caused by extended t and high P_0. So far, the results for melts have showed no sign of erratic trends thus any effects of convection is considered insignificant for the t and P_0 applied.

The sensitivity analysis of t and P_0 are also performed for polyurethane foams and the trends are similar to the melts thus the foam results are not reproduced here. The different t values investigated are 40, 80, 160 and 320 s while for P_0, the selections are 3, 5, 7 and 10 mW. Like melts, the sensitivity results of foams show higher spread among the thermophysical properties of the repeated experiments when the extreme t and P_0 are applied. While most of the standard deviations are within the acceptance criteria of repeatability in Table 6-4, FR-W-50 has standard deviation outside the acceptable range between 4 to 7 % for λ and 8 to 40 % for c_p at extreme values of t and P_0.

The maximum and minimum densities of the foams tested change by more than a factor of two so the suitable t and P_0 applied also varies. t of 160 s is applicable to all foams except for NFR-C-19. This foam has the lowest density and the suitable measuring time is 80 s. P_0 of 5 mW is applied to the denser foams such as NFR-DG-42 and FR-W-50 while higher P_0 of 7 mW is required for the others in order to maintain a sufficient temperature increase. The other choices of t and P_0 are not suitable because some of their experimental outputs are outside the acceptance criteria in Table 6-4.

6.6 Thermophysical Properties of Polyurethane Foam and Its Melt

For the polyurethane foams and melts tested, Figure 6-13 shows λ and c_p from the three repetitions using the optimal t and P_0 determined from the sensitivity analysis. The standard deviation as percentage of the average value is also included in the figure.

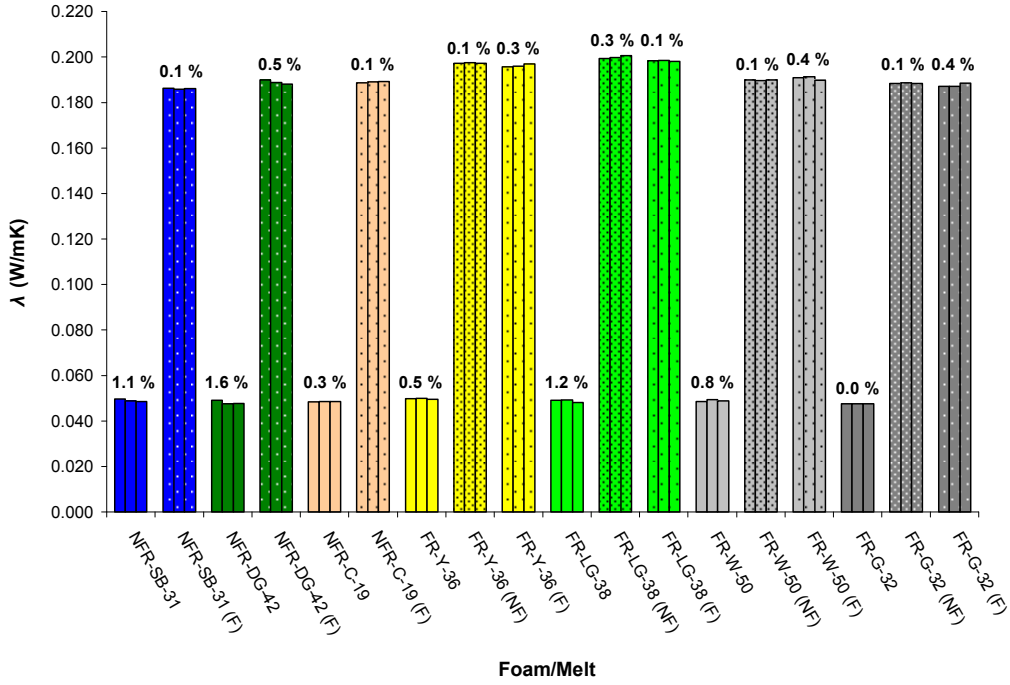

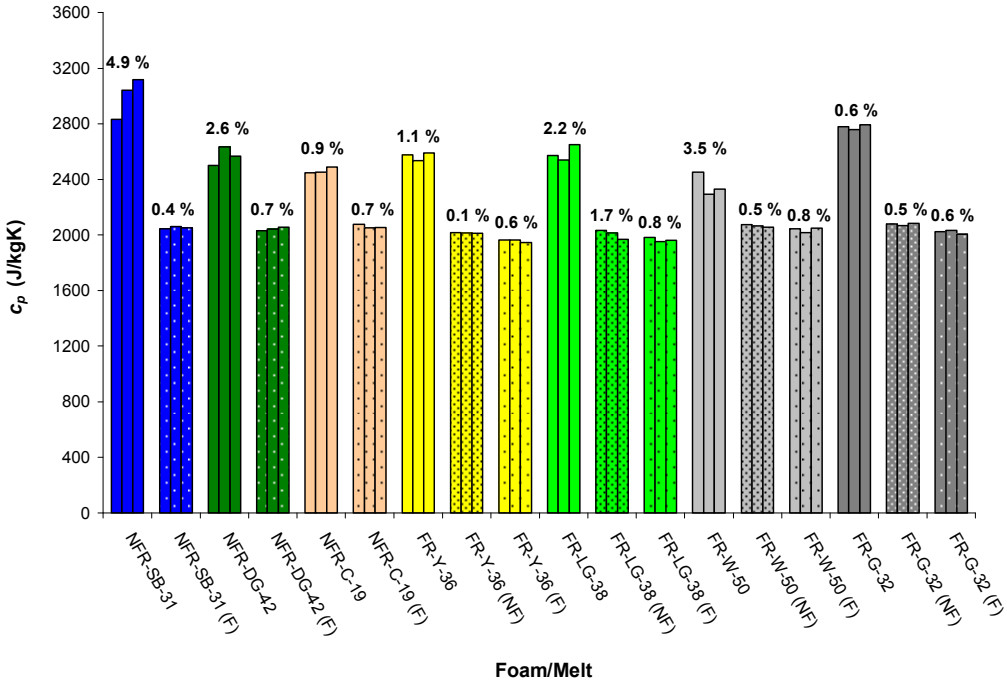

Figure 6-13: λ and c_p of polyurethane foams, non-flaming (NF) melts and flaming (F) melts

Based on the results, the thermophysical properties among different polyurethane foams have been consistent and the same applies to the melts. The thermophysical properties of the melts produced from non-flaming and flaming surfaces are found to be comparable, supporting the similarity seen in their chemical formula from Table 2-1. Table 6-6 shows the average λ and c_p of the three repetitions for the different foams and melts. Also included are their standard deviations which are within the repeatability limits mentioned by the manufacturer in Table 6-4, 2 % for λ and 7 % for c_p.

Table 6-6: Average λ and c_p of polyurethane foams and melts

Sample		λ (W/mK)	c_p (J/kgK)
NFR-SB-31	Foam	0.049±1.1 %	2996±4.9 %
	Melt (F)	0.186±0.1 %	2053±0.4 %
NFR-DG-42	Foam	0.048±1.6 %	2567±2.6 %
	Melt (F)	0.189±0.5 %	2043±0.7 %
NFR-C-19	Foam	0.049±0.3 %	2462±0.9 %
	Melt (F)	0.189±0.1 %	2061±0.7 %
FR-Y-36	Foam	0.050±0.5 %	2566±1.1 %
	Melt (NF)	0.197±0.1 %	2014±0.1 %
	Melt (F)	0.196±0.3 %	1958±0.6 %
FR-LG-38	Foam	0.049±1.2 %	2587±2.2 %
	Melt (NF)	0.200±0.3 %	2005±1.7 %
	Melt (F)	0.198±0.1 %	1966±0.8 %

FR-W-50	Foam	0.049±0.8 %	2359±3.5 %
	Melt (NF)	0.190±0.1 %	2064±0.5 %
	Melt (F)	0.191±0.4 %	2036±0.8 %
FR-G-32	Foam	0.048±0.0 %	2776±0.6 %
	Melt (NF)	0.188±0.1 %	2076±0.5 %
	Melt (F)	0.188±0.4 %	2021±0.6 %

The value of λ for polyurethane foams is found to range between 0.048 – 0.050 W/mK. A global standard deviation is calculated from all the average λ for foams reported in Table 6-6 and it is found to be 1.5 %. For melts, λ ranges from 0.186 – 0.200 W/mK and the global standard deviation is 2.6 %. The value of c_p for polyurethane foams ranges between 2359 – 2996 J/kgK and the global standard deviation is 8.0 %. For melts, c_p ranges from 1958 – 2076 J/kgK and the global standard deviation is 1.9 %. The global standard deviation of λ is slightly higher for melts than foams because the λ for the melts of FR-Y-36 and FR-LG-38 is 0.01 W/mK greater than the other melts. This is believed to be due to the presence of solid contents which have blended into the liquids. The higher global standard deviation seen in c_p of the foams compared to melts is believed to be caused by the unaccounted convective heat losses through the pores of the foams during the heating process in the experiments. The thermophysical properties of foams and melts presented in this chapter are in good agreement with the majority of the values reported in the literature[25,42,96].

The overall results show polyurethane foam has lower λ and higher c_p than melt which means slower heat transfer and more heat storing capacity. Therefore, polyurethane foam is more insulative than its decomposition product, melt. When the decomposition to melt occurs, λ increases by approximately 300 % while c_p reduces by approximately 20 %. These changes effectively promote the heat transfer through the material. Polyurethane foam also experiences volume reduction and mass transport when the foam structure collapses into a thin layer of melt. The formation of melt increases the overall density of the sample which increases its thermal inertia and slows the heat transfer. Acting oppositely, the collapse of the heated front onto the virgin layer together with the changes in the thermophyiscal properties improve the heat transfer.

Despite the overall improvements in heat transfer as foam decomposes into melt, in certain FR foams, the heat transfer process is further complicated by the char formation which acts as an insulative barrier that slows the heat transfer to the virgin foam and inhibits the flow of oxygen necessary for combustion[23,26,28]. The thermophysical properties of char are not addressed in this research because of the experimental difficulty in establishing a reasonably even surface for char which is necessary for the proper sensor contact.

6.7 Conclusions

The thermophysical properties of a variety of polyurethane foams and their melts are measured using the transient plane source technique. On average, λ ranges between 0.048 – 0.050 W/mK for polyurethane foams and 0.186 – 0.200 W/mK for melts while c_p ranges between 2359 – 2996 J/kgK for polyurethane foams and 1958 – 2076 J/kgK for melts. These properties are found to be consistent among the different types of foams and the same applied for the different melts. The sensitivity analysis performed reveals that the thermophysical properties are also fairly consistent over the range of t and P_0 tested. The thermophysical properties presented in this chapter are in good agreement with the values reported in the literature thus showing that the Hot Disk technique is applicable to porous material such as polyurethane foam and also to viscous liquid such as melt.

At this stage, only the properties at ambient temperature are found. To better represent the foam decomposition in fire, the properties at elevated temperature are of much interest. However, the experimental setup and procedure involved at elevated temperature are more complicated and such investigation is the focus of future research. The properties relating to char and partially decomposed foam are also useful since these layers could affect the overall heat transfer but the difficulties are these residues do not have a reasonably even surface for proper sensor contact and they are difficult to gather in large quantity. The suitability of the developed thermophysical properties of polyurethane foams and melts as the inputs into fire models and pyrolysis models will be addressed in Chapter 8.

Chapter 7. Experimental Technique to Quantify Decomposition and Melting Behaviours of Polyurethane Foams in Vertical Orientation

7.1 Introduction

The thermogravimetric analysis (TGA) results in the literature[19,51,55] and from Chapter 3 and 4 show that the polyurethane foam decomposition is commonly described by two pyrolysis reactions as seen in Section 4.1. The first reaction includes a melting phenomenon and nominally, the melts produced accounts for 75 % of the original mass. Thus, a significant amount of fuel is consumed later by the second reaction over higher temperature range as a result of the melting of foam. The variability in foam density and hardness allow the material to be used for many applications. In the case of upholstered furniture, the foams of different density are used on the various parts of the same furniture such as the seat, back, arms and around the base. In upholstered furniture fires, the impact of foam melting is amplified when a pool fire forms below the seat causing the sudden increase in the heat release rate[5,6].

Given the significance of the melting phenomenon in foam decomposition and also in furniture fire, this chapter describes a new experimental apparatus called the Sample Feeding Vertical Cone which is used for investigating the two-dimensional decomposition and melting behaviours of vertically oriented foam. The foam melting experiment involves a foam sample being exposed on one surface to a constant user defined irradiance which causes the decomposition of the solid foam into liquid melts that flow down the decomposing surface. This chapter introduces the general features of the apparatus, the necessary calibrations and a set of experimental results at 50 kW/m^2 of heat flux. The outcomes from the experiments include the qualitative observation of the surface decomposition and the quantitative measurements of the decomposition and melting behaviours. The quantitative results include the sample mass loss rate, the melting rate, the vaporisation rate, the melt and vapour mass fractions, the sample feeding rate and the time delay before melting.

7.2 Existing Experimental Techniques to Investigate Melting Behaviours of Thermoplastics

In this chapter the term melting is used to describe the behaviour of a material that will soften and become fluid when heated sufficiently. Within the literature, many methods had been developed to investigate the melting behaviours of thermoplastic. The most applicable methodologies are discussed below, ranging from small-scale to large-scale. Wang et al.[99] investigated the burning and dripping phenomena of eight different polymers using UL 94 vertical burning test[100]. The samples were hung vertically and ignited on the bottom edge using a Bunsen burner. The samples measured 100 mm in length and 10 mm in width with a thickness varying from 2 to 10 mm.

Ohlemiller et al.[26] conducted two-dimensional radiation driven experiments and three-dimensional pool fire experiments to study the burning and melting behaviours of seven different polyurethane foams. In the two-dimensional radiation driven experiments, a vertically oriented cone heater was used as the heat source. The exposed surface of the sample was 50 mm square and in order to maintain a constant irradiance, the sample measuring 400 mm in length was driven forward throughout the experiment to compensate for the decomposed foam. This concept of sample compensation has become the impetus to this research. The melts produced were collected into a deep bottle which was water cooled. Two kinds of experiments, non-flaming and flaming were conducted and in the latter, a multiple jet methane flame was used as the ignition source to ignite the exposed foam surface. During the three-dimensional burning experiments, the flame spread rate and the contribution of pool fire towards burning were investigated. The samples measured 300 mm tall and 600 mm long with a thickness ranging between 75 to 100 mm. In the experiments, either a single slab was tested or two slabs were tested in a 30° Vee configuration. A catch plate was placed underneath the setup to contain the melts. Using a propane Tee burner as the ignition source, the setup was ignited along one 300 mm edge for the single slab and along the narrow end for the Vee configuration.

Zhang et al.[101] investigated the melting behaviours of six different thermoplastics using the cone calorimeter and in large-scale wall panel fire test. Under the cone calorimeter, a 3 mm cone sample was exposed to a vertically mounted cone heater. The melts produced were collected into a container and measured at the end of the experiment. In the large-scale wall panel fire test, a sample was mounted as a wall panel and ignited using wood crib placed at mid position by the bottom of the sample. Using the same thickness as the cone sample, the wall panel sample measured 800 mm in width and 2200 mm in height.

Sherratt[102] developed a number of large-scale experimental methods to investigate the burning and melt flow behaviours of thermoplastic commodities. In the full polyethylene roll test, the sample consisted of a thin polyethylene sheet rolled onto a hollow cardboard core. The 2 m long sample was suspended over one of the two equally sized square trays which measured 1.2 m along the sides and 25 mm deep. The sample was ignited at the bottom using wood crib and midway through the experiment, the sample was moved to the adjacent square section for further study on the effect of pool fire development. In the sedan rig test, several polypropylene crates were tested by igniting the setup with a blowtorch and an oil filled pan was used to collect the melts. The oil was used to quench the molten material thus preventing the pool fire from developing.

Prior to developing the Sample Feeding Vertical Cone, a few exploratory experiments[103] on the decomposition and melting behaviours of non-fire retardant foam under non-flaming condition were investigated using the cone calorimeter. The experiments involved testing foam samples of 100 mm sides and 50 mm thick in a vertical orientation at a series of constant heat fluxes. The melts produced was collected by a catch tray located underneath the heater and sample setup. These experiments were the precursor to the Sample Feeding Vertical Cone described below.

7.3 Sample Feeding Vertical Cone

From the literature review, simple small-scale experiments such as the UL 94 vertical burning test[100] and the vertical cone calorimeter experiment are able to provide sufficient qualitative observations of the decomposition and melting behaviours. However, these experiments are lacking in accurate quantitative assessments due to the relatively small sample size tested. Conversely, the large-scale experiments such as those conducted by Sheratt[102] have a challenging setup and are dimensionally complex. Therefore, the results obtained are less repeatable which complicate the accurate quantification of the decomposition and melting behaviours. Hence, the ideal setup is a well-controlled small-scale experiment with expanded features similar to the methodology used by Ohlemiller et al.[26]. Based on the experimental challenges noted by the other studies mentioned above, the experience gathered from the exploratory experiments[103] and also over the course of developing the Sample Feeding Vertical Cone, a number of complicating phenomena relating to foam melting are identified that warrant further explanations.

1. First of all is the progressive reduction of irradiance on the exposed sample surface when the sample position is fixed such as in a cone calorimeter experiment. The reduction in irradiance occurs when the foam decomposes and recedes under heat thus the decomposition and melting behaviours are not quantified at constant heat flux.

2. Secondly, the uneven, non-planar or three-dimensional decomposition front developed due to a series of complicated phenomena. These include the heat losses around the sample perimeter[26], the reradiation from the surrounding heated surfaces of the apparatus, the shielding effect[23,26,28] from the mixture of char and melts accumulating near the bottom of the sample and the flame propagation along the sample. In order to maintain a constant irradiance on the decomposition front, the position of the front has to be tracked and compensated accordingly. However, the formation of an uneven front complicates the sample compensation process and ruins the experimental consistency. The changing surface area of the uneven front means it is not

possible to quantify the decomposition and melting behaviours on a consistent per unit area basis. While the mixture of char and melts forming on the exposed surface could be removed to lessen the significance of the uneven front[26]. The removal process unavoidably introduces noise into the mass measurements recorded.

3. Third issue, the small-scale experimental setup such as the cone calorimeter has limited sample mass. The density of the commercially available polyurethane foams in upholstered furniture ranges from 16 to 65 kg/m^3 which give between 8 to 33 g of mass for a typical cone sample. This range of mass is insufficient for an accurate assessment of the decomposition and melting behaviours.

4. Lastly, the melts are often collected in close proximity to the cone heater and often during flaming experiments, flaming droplets drip continuously into the collected melts which can lead to ignition. The subsequent pool fire is undesirable as it consumes the collected melts and produces additional unknown radiative feedback that enhances the burning rate of the sample. This practically ruins the objective of the research which is to quantify decomposition and melting behaviours of foam at specific heat flux.

The experimental apparatus developed in this research incorporates specific features designed to resolve or at least mitigate the majority of the issues outlined above. Figure 7-1 shows the experimental apparatus which consisted of three main components, the vertical cone housing, the automated sample feeder and the load cell system which were supported on top of the common frame. The vertical cone housing contained a vertically mounted cone heater as the heat source which imposed a user defined heat flux onto the sample's exposed surface. The automated sample feeder conveyed the foam sample forward to compensate for the decomposed foam while the load cell system continuously monitored the changes in the sample and melt mass.

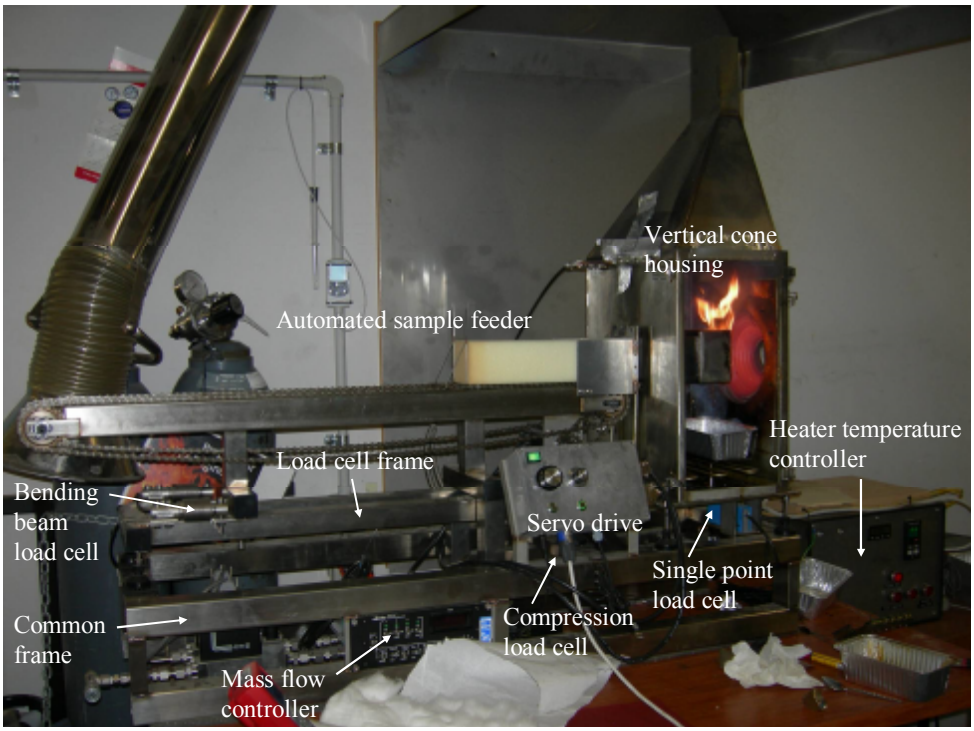

Figure 7-1: Photograph of the Sample Feeding Vertical Cone and its primary components.

7.3.1 Vertical Cone Housing

The heating element of the cone heater was made from 8 mm diameter calrod which consists of nichrome wire centred within a tubular stainless steel sheath filled with ceramic insulation[104]. The design of the cone heater was adopted from ISO 5657:1997[105]. Figure 7-2 shows the setup of the cone heater where the heating element was wound on a mould into a coil, the formed coil was then backed by 15 mm kaowool insulation and fastened onto the heater casing.

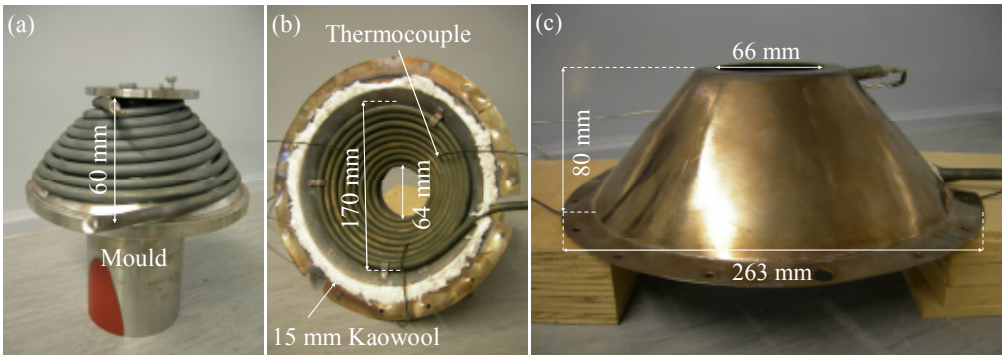

Figure 7-2: Dimensions and setup of cone heater showing the heating element wound on a mould (a), the heating element fastened onto the heater casing (b) and the completed cone heater (c)

Three type K thermocouples with metal sheath were embedded at different locations around the heater. The heater temperature controller seen in Figure 7-1 adjusted the cone heater temperature to produce the desired irradiance at the sample surface. The set point temperature entered by the operator was compared to the average temperature measured by the heater's thermocouples. This prompted the controller to either increase or decrease the power delivered to the heater to achieve the specified set point. The cone heater has a maximum power rating of 4.5 kW at 230 V.

Figure 7-3 shows the setup of the vertical cone housing which was made of stainless steel. The cone heater was installed on a latch door in one wall of the vertical cone housing. This door provided easy access for the maintenance and inspection of the apparatus.

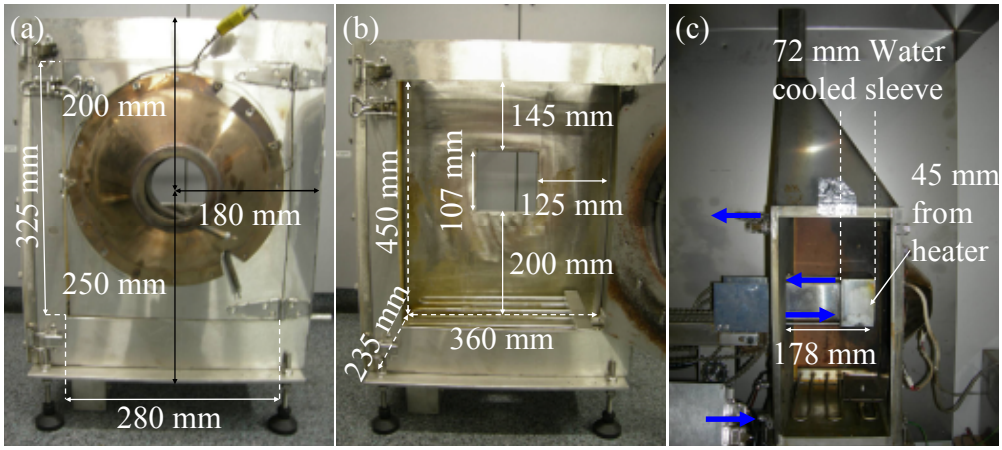

Figure 7-3: Dimensions and setup of vertical cone housing showing the cone heater installed on one wall of the housing (a), the housing with opened latch door (b) and the protrusion of water cooled sleeve into the housing (c)

The square opening in the wall opposite the heater enabled part of the automated sample feeder to extend into the housing. The wall opposite the heater was water cooled as shown by the blue arrows in Figure 7-3(c) where the cooling water entered at the base of the wall and exited via the top. The side wall further from the operator was lined with 5 mm millboard to prevent the steel wall from becoming too hot during the experiment. The side wall closer to the operator remained open for experimental observation and also for mitigation of pool fire on the collected melts. At the top of the housing, a chimney was used to channel the smoke produced into the exhaust hood above the apparatus.

7.3.2 Automated Sample Feeder

Figure 7-3(c) shows the automated sample feeder with the water cooled sleeve. Water cooling minimised the reradiation from the sleeve and also helped to maintain a constant temperature around the sample perimeter. This prevented the decomposition and flame spread along the sides of the sample thus the decomposition and melting of

polyurethane foam remained as two-dimensional. Figure 7-4(a) shows the water cooled sleeve was attached to the conveyor platform which carried the bulk of the foam sample during the foam melting experiment. A pair of roller chains which covered the entire length of the platform was used as moving tracks and the chains were meshed onto the sprockets at both ends. A vertical end support was welded onto the chains to assist and guide the foam forward.

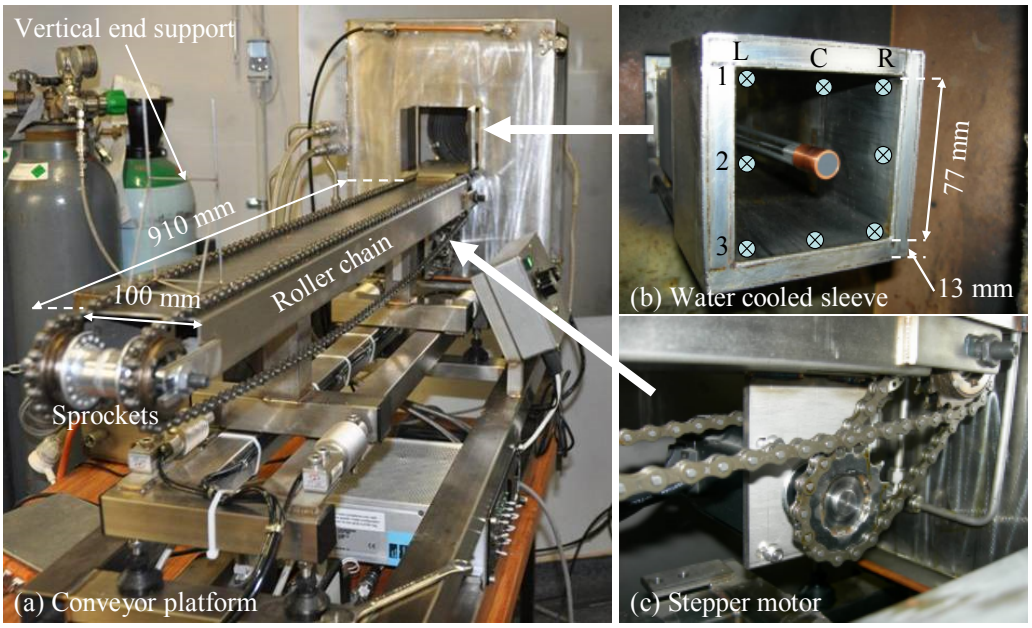

Figure 7-4: Dimensions and setup of automated sample feeder showing the conveyor platform (a), the water cooled sleeve serving as the benchmark position for experiment and heat flux calibration (b) and the stepper motor driving the tracks forward (c)

During the experiment, the sample was pushed through the water cooled sleeve shown in Figure 7-4(b). The edge of the water cooled sleeve served as the benchmark position for tracking the decomposition front and for positioning the heat flux gauge. The heat flux was measured at the different positions indicated on Figure 7-4(b) to quantify the heat flux distribution on the sample surface in an experiment. On the opening, 'L', 'C' and 'R' denote the left, centre and right columns while '1', '2' and '3' denote the first, second and third rows. The moving tracks were driven at the housing end of the apparatus by a shorter chain meshed onto the sprocket of a 300 W three-phase stepper motor as seen in Figure 7-4(c). The operation of the motor was controlled via a servo drive.

The servo drive provided manual and automatic control of the feeding mechanism. Under manual mode, the operator has the full control of the conveyor tracks. This was usually adopted prior to the start of the experiment where the exposed surface of the foam was adjusted to the benchmark position and also at the end of the experiment where the feeding mechanism needed to stop. Under automatic mode, the motor moved the tracks at a user defined speed which consistently fed the sample forward to compensate for the decomposed section. The servo drive's reprogrammable microprocessor was able to provide feeding rate ranging between 0.5 and 4.0 mm/s. This is applicable for foam with density from 20 to 50 kg/m^3 tested between 30 and 80 kW/m^2. The vibrations generated from the track movements and the sprockets rotation were reduced by allowing the chains to fit loosely. This minimised the noise in the mass measurements.

7.3.3 Load Cell System

The load cell system measured the sample mass on the automated sample feeder and the melt mass in the melt collecting unit. The automated sample feeder was supported on two 5 kg bending beam load cells seen in Figure 7-5(a) located at the back of the apparatus and a single 25 kg compression load cell seen in Figure 7-5(b) located near the front of the apparatus. Each bending beam load cell was attached to the load cell frame at one end and the other end was attached to the automated sample feeder. The compression load cell sat on a plate of the load cell frame and supported the automated sample feeder pressing from the top. During the foam melting experiment, the mass distribution on each load cell would vary as the foam sample moved along the conveyor platform. Thus, the sample mass was determined by combining the measurements from the three load cells. Figure 7-5(c) shows the melt collecting unit consisting of an aluminium pan placed on a tray. The unit was attached to the melt load cell pedestal which protruded into the vertical cone housing. The melt load cell used was a 2 kg single point load cell located underneath the housing thus shielded from any thermal radiation.

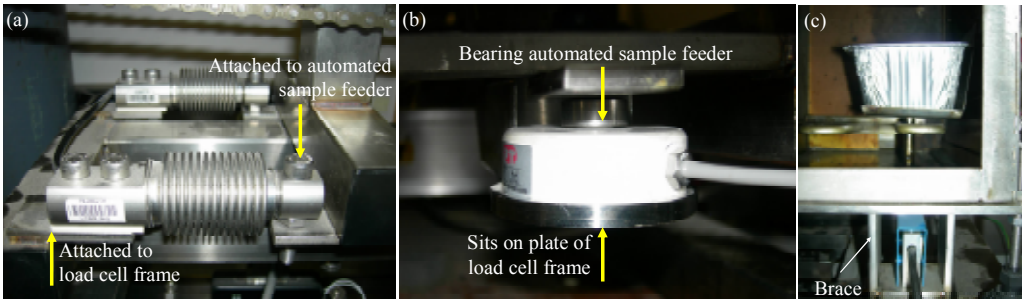

Figure 7-5: Setup of load cell system showing the bending beam load cells (a), the compression load cell (b) and the single point load cell with the melt collecting unit (c)

For accurate mass measurements, the automated sample feeder and the melt collecting unit needed to be physically isolated from the rest of the apparatus and supported only on their respective load cells. The melt collecting unit was successfully decoupled as the opening in the bottom plate of the vertical cone housing offered sufficient clearance for the protrusion of the load cell pedestal and the tray containing the aluminium pan also has adequate clearance from the adjacent wall, as indicated in Figure 7-5(c). For the automated sample feeder, the rear wall opening of the vertical cone housing provided sufficient separation for the protrusion of the water cooled sleeve seen in Figure 7-3(c) and 7-4(b). However, the automated sample feeder was not fully isolated as it remained connected by the electrical leads to the motor and by the plastic tubes to the cooling water supply, both of which are not weighed by the load cell system. In order to minimise the significance of these external loads have on the mass measurements, the electrical leads and plastic tubes were arranged in such a way that they produced minimal and consistent effects on the load cells.

7.3.4 Supplementary Features

This section discusses the supplementary features of the apparatus that facilitated the foam melting experiment. A pool fire suppressing unit was used to prevent the ignition of heated melts collected in the aluminium pan during the experiment. Carbon dioxide (CO_2) gas from a pressurised cylinder was intermittently injected via a hand held nozzle to put out any flame developing in the pan. A video camera with adjustable exposure was aimed through the opening of the cone heater to capture the decomposition phenomenon on the surface. A data logger and a desktop computer were used to record the experimental data and to monitor the real time results.

Although not investigated in this research, the apparatus was also equipped with features that accommodated the experiment under oxygen vitiated condition. A nitrogen and air inflow of known concentration can be achieved using the mass flow controller and then supplied into the vertical cone housing via a series of tubes at the bottom. For the oxygen vitiated experiment, a fire rated glass panel can be latched across the outer wall to close the housing yet still providing the necessary visual observation.

7.4 Calibrations of Sample Feeding Vertical Cone

Since the objective of this chapter is to quantify the decomposition and melting behaviours of polyurethane foams at known heat flux, it is important that the mass measurements and the experimental heat fluxes are accurate. Given the complexity of the apparatus, the mass calibrations and the heat flux calibration are performed daily before the start of experiment. Additionally, the heat flux calibration is also carried out whenever the level of heat flux changes between experiments.

7.4.1 Mass Calibrations

Both static and dynamic mass calibrations were performed to ensure that the load cells were functioning properly and any disturbance on the mass measurements was minimal and within the experimental uncertainty. The static calibration checked the operation of the load cell system and the significance of the external load from the plastic water tubes and the electrical leads under a static condition. During the calibration, a 150 g load was applied in turn at different positions, the back, middle and front of the conveyor platform. The 150 g load is representative of the typical mass of the foam sample. For each position, the measurement was recorded for 60 s. Measuring at all three locations helped to identify the problematic section along the lengthy platform when invalid results were encountered. The melt collecting unit was left empty during the static calibration. Figure 7-6 shows the typical results for the static mass calibration.

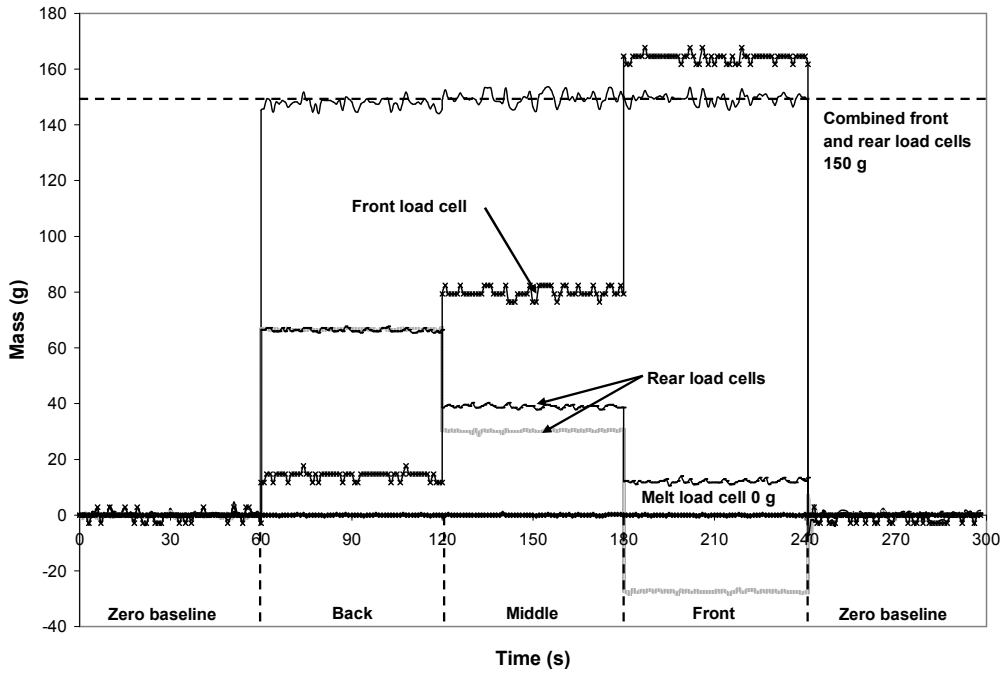

Figure 7-6: Mass measurements from static mass calibration

At the start and end of the calibration, a baseline of zero mass was recorded for 60 s and when the applied load was positioned from back to front, the rear load cells showed a decrease in the measured value while the front load cell showed an increase. The combined measurement was close to the applied load and the fluctuations in the results were due to the digital noise of the data logger. Thus, the static calibration ascertained that the sample load cells were functioning normally and the impact of the external loads were minimal.

The dynamic calibration checked the impact of vibration and also the significance of the continuous shift in the apparatus' centre of mass caused by the feeding mechanism. Figure 7-7 shows the typical results for the dynamic mass calibration. During the calibration, the 150 g load was transferred along the platform at three different speed settings and these are 1.4, 2.0 and 3.8 mm/s for the case in Figure 7-7. The range of speed calibrated should be applicable for the subsequent experiments. Without the aluminium pan, an 84 g load was added on the tray of the melt collecting unit. The 84 g load is representative of the typical mass of melts collected.

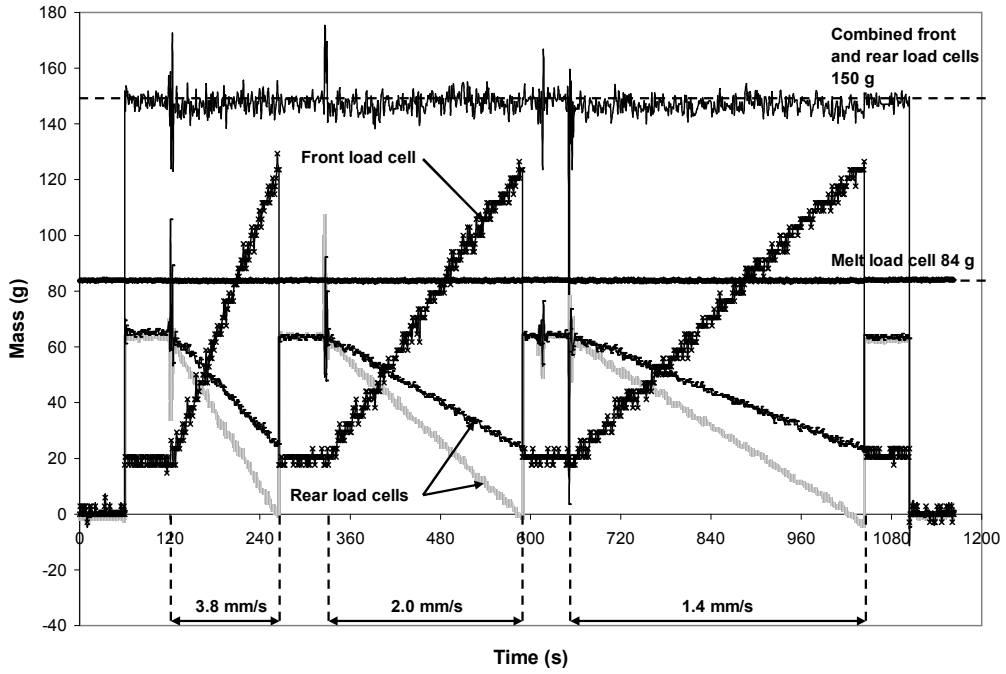

Figure 7-7: Mass measurements from dynamic mass calibration

In addition to the 60 s zero mass baseline at the start and end of calibration, a 60 s static mass baseline was also recorded between the interchange of different speed settings. The large spike at the end of each static mass baseline was caused by the initiation of the feeding mechanism. In agreement with the static calibration, the results show the rear load cells recorded continuously decreasing value while the front load cell recorded continuously increasing value. The combined measurement was close to the applied load on the platform which indicated the vibration and the shift in the centre of mass due to the feeding mechanism have little effect on the sample mass measurements. The vibration from the feeding mechanism has been moderated

significantly by the rubber dampers fitted underneath the load cell frame and the common frame. In this calibration, the melt load cell accurately measured the applied load of 84 g added onto the tray.

7.4.2 Heat Flux Calibration

The heat flux calibration was performed to achieve the user defined heat flux intended for the subsequent foam melting experiments. As seen in Figure 7-4(b), an end mounted, water cooled Schmidt-Boelter gauge was aligned with the benchmark position at the centre of the hollow space. The temperature of the heater was adjusted to achieve the desired irradiance and the measurements were taken after the thermal equilibrium was reached. For the calibration, the measurement at the centre of the sample was deemed sufficient but to understand the heat flux distribution over the sample surface, Table 7-1 presents the average heat flux measured at all nine locations depicted in Figure 7-4(b). In brackets is the percentage deviation from the desired heat flux at the central position, $\dot{q}''_{desired}$. The different positions are identified by two notations where the first notation denotes the column while the second notation denotes the row. T_{cone} is the heater temperature calibrated to produce the required irradiance centrally.

Table 7-1: Heat flux distribution of cone heater

Position	$\dot{q}''_{desired}$ = 30 kW/m^2	$\dot{q}''_{desired}$ = 50 kW/m^2	$\dot{q}''_{desired}$ = 65 kW/m^2
	T_{cone} = 719 °C	T_{cone} = 859 °C	T_{cone} = 938 °C
L1	27 (-10)	46 (-8)	60 (-8)
L2	28 (-7)	48 (-4)	62 (-4)
L3	25 (-17)	45 (-10)	58 (-11)
C1	29 (-4)	48 (-4)	62 (-4)
C2	30 (0)	50 (0)	65 (0)
C3	28 (-8)	47 (-7)	62 (-5)
R1	26 (-13)	45 (-10)	58 (-11)
R2	27 (-9)	46 (-8)	61 (-5)
R3	26 (-14)	43 (-14)	56 (-15)

As expected, the results show no deviation from $\dot{q}''_{desired}$ at the centre of the exposed surface but the irradiance diminishes towards the boundaries. The irradiance is noted to be slightly lower at the bottom right area of the exposed surface and the average deviation for all the positions measured is approximately 8 %.

7.5 Polyurethane Foams Tested in Sample Feeding Vertical Cone

The sample length of 900 mm offers sufficient mass and experimental duration for an accurate quantitative analysis on the decomposition and melting behaviours of the polyurethane foams. From the observations made during the exploratory experiments[103], the edge effect was more pronounced at low heat flux where the sample's edge decomposed at a much slower rate compared to the rest of the sample due to the significant perimeter heat losses. To rectify this problem, the exposed surface was reduced from former 100 mm to the recommended size of 75 mm which also fitted the dimensions of the conveyor platform and the opening of the automated sample feeder.

Based on experience, a few types of polyurethane foam are not suitable for the current setup. These include foams where the density approaches 100 kg/m^3, foams where the hardness is less than 60 N or foams with visco-elastic feature. The feeding mechanism was not able move the foam sample with high density as the large amount of mass exceeds the capability of the stepper motor. Likewise, the foam samples that exhibit visco-elastic behaviour or with low hardness were too easily compressed and could not be transported along the conveyor platform. Three non-fire retardant (NFR) and four fire retardant (FR) polyurethane foams listed in Table 2-1 of Chapter 2 are tested in the Sample Feeding Vertical Cone.

7.6 Experimental Procedure

At the start, the cone heater thermocouples are inspected and any detachment is rectified. A detached thermocouple will misread the actual temperature and also risks damaging the heating element. The water source is checked to supply the cooling water needed for the apparatus and any leakage is mended. The load cells are zeroed with no weights on the automated sample feeder and the melt collecting unit. The mass and heat flux calibrations are performed for the subsequent foam melting

experiments and the required feeding speed is set on the servo drive. The heater is shielded completely using a 5 mm millboard inserted through a slot on the top of the housing as seen in Figure 7-8(a).

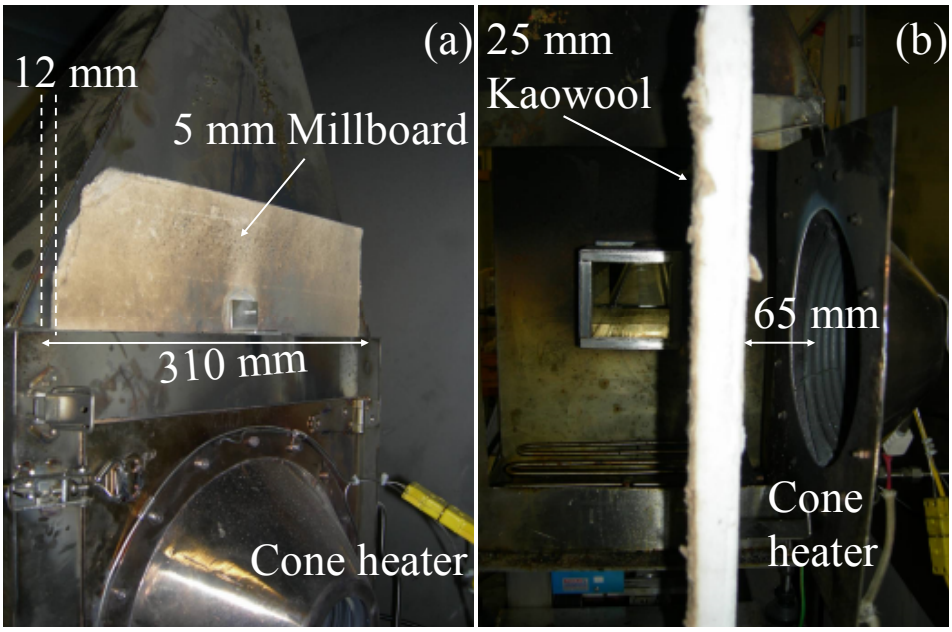

Figure 7-8: Millboard shielding cone heater prior to start of experiment (a), kaowool shielding cone heater during routine cleaning (b)

The foam sample is positioned on the conveyor platform and manually adjusted such that the exposed surface extends nominally 5 mm beyond the edge of the benchmark water cooled sleeve. This is necessary especially at high heat flux because without a sufficient offset, the foam sample which starts to recede immediately upon the heat flux exposure will contaminate the inner walls of the water cooled sleeve and potentially jam the feeding mechanism.

The video recording is initiated and a 60 s baseline is recorded. Then the experiment starts with the removal of the millboard shield followed by the initiation of the feeding mechanism. A hand held methane burner is used as the ignition source to ignite the exposed surface and the pool fire supressing unit is readied to extinguish any sign of flame in the aluminium pan. Throughout the experiment, the foam sample decomposes and it is also guided forward by the vertical end support. When the end

support reaches the end of the platform, the feeding mechanism is halted and the experiment is completed.

The water cooled sleeve requires cleaning after every experiment where acetone is used to remove the melts and hardened residue. Normally, the heater is not powered down between experiments due to the lengthy interval needed to achieve thermal equilibrium. For cleaning, the latch door is opened and a 25 mm thick kaowool board is hung onto the door to shield the heater as shown in Figure 7-8(b). The shield is 65 mm from the cone heater and it is prevented from touching the heater because that could cause the thermocouple to detach due to rapid cooling when the shield is removed.

7.7 Qualitative Results of Polyurethane Foams at Heat Flux of 50 kW/m^2

To prevent the melt from being consumed by flame, Sample Feeding Vertical Cone was originally intended for investigating the decomposition and melting behaviours of polyurethane foams under non-flaming conditions. During the development phase, the polyurethane foams were noted to produce char which mixes with the melt when tested under non-flaming condition. For the NFR foams, this mixture accumulated over the exposed surface forming into char skin. The formation of char skin obstructed the melt flow and caused uneven decomposition surface due to the skin's shielding ability. Ohlemiller et al.[26] had reported similar phenomenon during the radiation driven experiment where the char skin needed to be physically removed. This uneven decomposition front complicated the experiments and the subsequent analysis. For the FR foams, the melt flow was able to carry the char into the melt collecting unit thus the mixture did not accumulate to form char skin such as the case of NFR foams.

It is possible to maintain an even front by manually removing the accumulated char skin but this technique also introduces significant noise on the mass measurements. Furthermore, such melting behaviour is no longer gravity driven but stimulated by the

skin removal process. The current solution to this problem is to perform the foam melting experiments under flaming condition during which the char skin is seen to break up and do not accumulate on the exposed surface. Despite some melts being consumed by the flame, the melt flow has remained effectively unhindered and this method allows the experiments to proceed with a comparatively steady melting rate that can be quantified more accurately.

The results from the foam melting experiments at heat flux of 50 kW/m^2 are used to demonstrate the application of Sample Feeding Vertical Cone. From the video observation of the surface phenomenon, the polyurethane foams tested can be categorised into two groups, Group 1 consists of foams which produce only melts after ignition and Group 2 are those which produce melts and char after ignition. Group 1 includes all NFR foams and FR-G-32, their surface phenomenon at different intervals are depicted in Figure 7-9 which includes 3, 6 and 9 s after exposure, the ignition and the steady burning period.

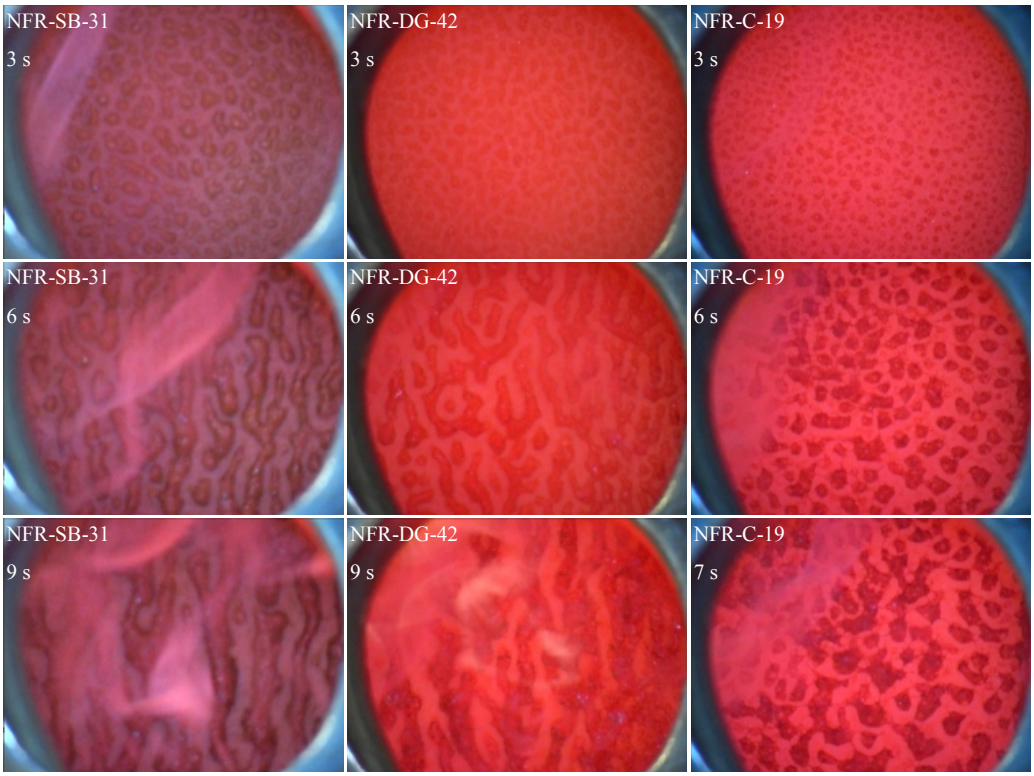

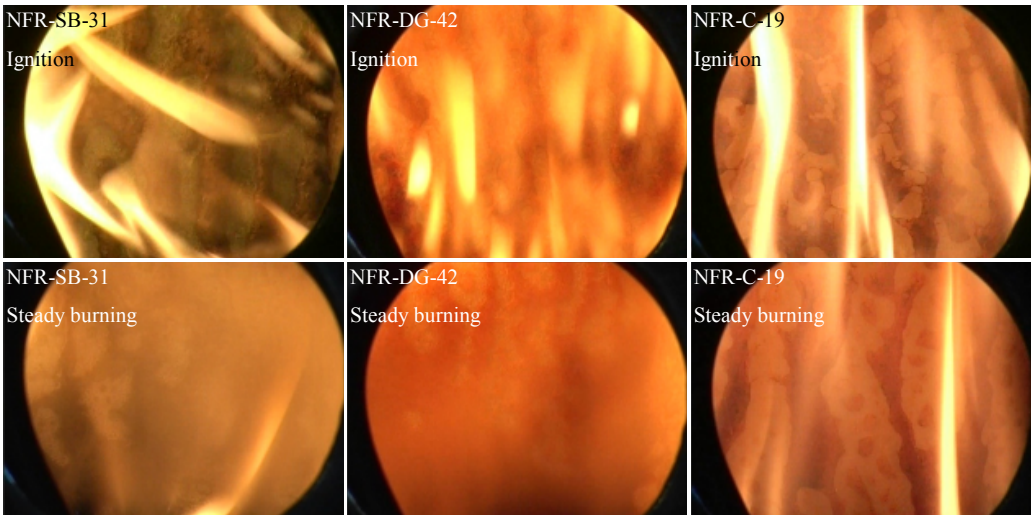

Figure 7-9: Surface phenomenon of Group 1 foams at different intervals under 50 kW/m^2

After 3 s exposure to 50 kW/m^2, static melt droplets are formed over the exposed surface of the foam. By 6 s, the droplets grow in size and start to merge into larger droplets. For NFR-SB-31 and NFR-DG-42, the large droplets start to flow downward due to their increased mass and begin to form elongated melt streams. For NFR-C-19, the static droplets have increased in size but they appeared to be held in place by thin strands developing between the droplets. At 9 s, the elongated segments of NFR-SB-31 and NFR-DG-42 have formed columns of melt but at this stage, no significant melt flow is noted. NFR-C-19 ignites within 9 s so the last pre-ignition surface phenomenon is captured at 7 s which shows the merging of large droplets to form the elongated melt segments. Before ignition, these Group 1 foams are observed to have developed small fractions of char skin which is able to hold the melts in place, slowing their downwards movement and preventing any further merging of the melt droplets or columns.

When the surface is ignited with open flame, the char skin immediately breaks up causing rapid melt flow down the exposed surface. During the steady burning phase, the decomposed surface is continuously replenished by the virgin foam and a consistent surface phenomenon is established. NFR-SB-31 and NFR-DG-42 show the top half of the sample consists of several downward flowing melt streams that join together towards the lower half of the surface, forming a wall of melt. These are not clear in Figure 7-9 due to the opacity of the flame and the darker colour of the foam

samples. For NFR-C-19, several melt streams are formed but they remain separated over the exposed surface. For these Group 1 foams, a closer inspection of the footage shows the newly formed melt droplets either merge into the existing streams or create new streams as they merge and grow in size.

During steady burning, the surface phenomenon of NFR-C-19 shows wider melt streams and larger droplet size but the melt coverage area is smaller when compared with the other Group 1 foams. This is caused by the lower density of NFR-C-19 which results in the low thermal inertia of the sample and consequently, the decomposition front heats up faster resulting in more vaporisation than melting. Despite being a FR foam, FR-G-32 decomposes similarly to NFR-SB-31 and NFR-DG-42 but its surface phenomena are not included due to the opacity of the flame and the darker colour of the foam sample which in this case, completely obscures the visualisation.

Group 2 consists of the three remaining FR foams with the ability to form char after ignition. Figure 7-10 shows the surface phenomenon of Group 2 foams at the same intervals as Group 1 foams.

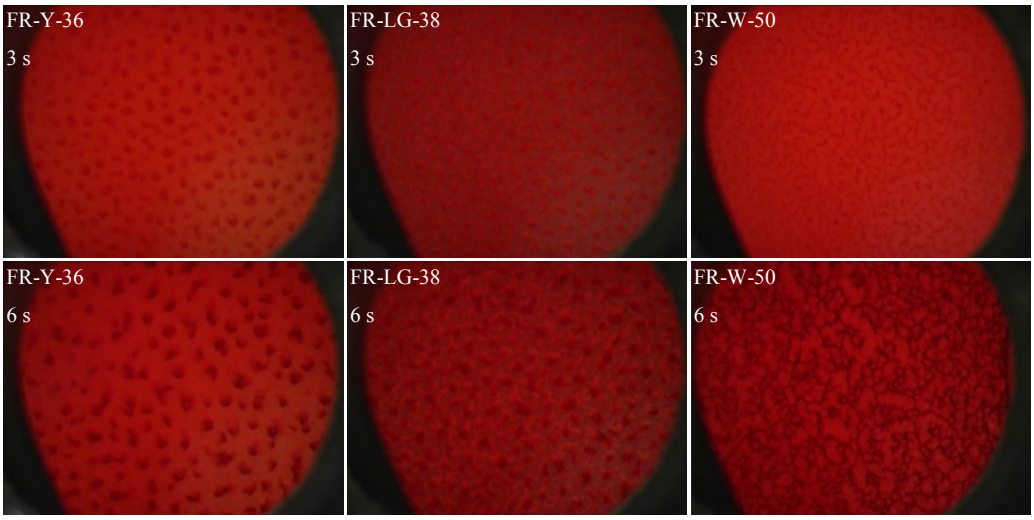

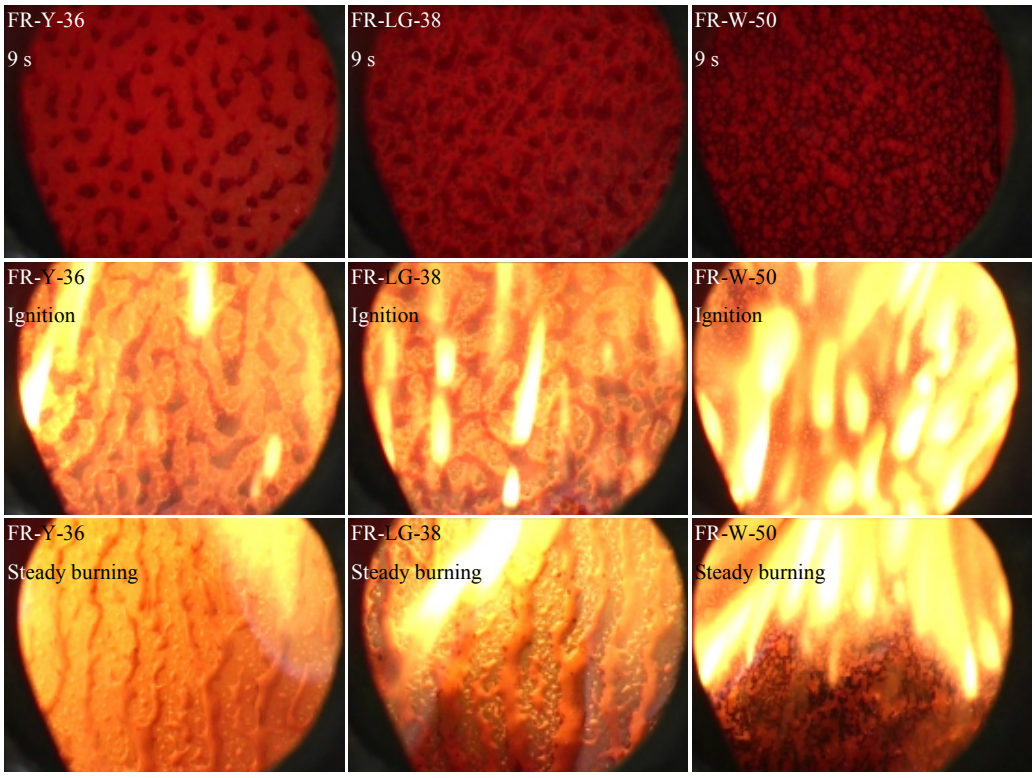

Figure 7-10: Surface phenomenon of Group 2 foams at different intervals under 50 kW/m^2

After 3 s exposure, the melt droplets are seen developing on the exposed surface of FR-Y-36 and FR-LG-38. For FR-W-50, no droplets are observed but fine strands are seen forming over the exposed surface. Over 6 and 9 s exposure, the droplets of FR-Y-36 and FR-LG-38 increase in size and merging occurs. Due to prolonged exposure, fractions of char have developed on the exposed surface of both foams. For FR-W-50, the amount of fine strand increases rapidly and a crust is formed. Prior to ignition, the melt flow is not significant but after ignition, the rapid melt flow carries the char formed into the melt collecting unit. Comparing with Group 1, Group 2 has thinner and weaker flame front and multiple flame outs are noted over the course of the experiment. This is due to the fire retardant mechanisms within these foams such as the release of gas phase combustion inhibitors and the continuous production of char after ignition. The thermally stable char is able to resist burning and at the same time, it also interrupts the solid phase burning by shielding the virgin foam behind and also obstructing the release of fuel vapours.

During steady burning, several independent melt streams are formed on the exposed surface of FR-Y-36 and FR-LG-38. In Figure 7-10, the melt flow carries the fractions of char downwards and the newly formed melt droplets are seen merging into the existing streams or creating new streams. The amount of char formed on the surface by FR-W-50 is significantly more than FR-Y-36 and FR-LG-38 and the crust formed is carried downwards by a wall of continuous melt flow where multiple pockets of flame are seen projecting through the uncovered area.

7.8 Quantitative Results of Polyurethane Foams at Heat Flux of 50 kW/m^2

The load cell system continuously records the changes in sample and melt mass during the foam melting experiments while the vapour mass is computed by subtracting the melt mass from the sample mass. All the polyurethane foams tested using Sample Feeding Vertical Cone has similar trends, the set of results for NFR-SB-31 at 50 kW/m^2 are presented in Figure 7-11. The results of the other foams are compared together later.

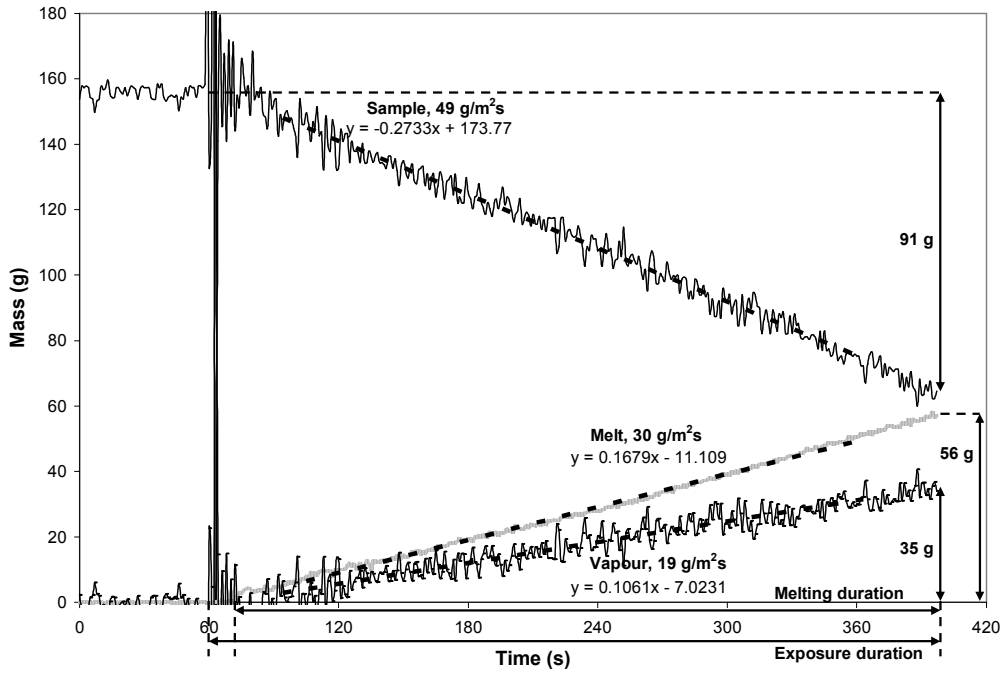

Figure 7-11: Sample, melt and vapour mass of NFR-SB-31 at 50 kW/m^2

After the 60 s baseline, the sample starts to decompose into melts and gases when exposed to heat flux of 50 kW/m^2. The sample mass loss rate and the vaporisation rate are computed from the slope of a linear trendline fitted through their respective results between 10 and 90 % of the exposure duration. The melting rate is computed similarly but between 10 and 90 % of the melting duration. The exposure duration is the amount of time between the start of heat source exposure, at 60 s and the end of experiment while the melting duration is the amount of time between the melt mass exceeding 1 g and the end of experiment. All rates are presented in a per unit area basis, the sample mass decreases linearly at a constant rate of 49 g/m^{2}s and after a short delay of 13 s, the melt mass begins to increase linearly at a constant rate of 30 g/m^{2}s. The initial delay is associated with the time for the melt to flow over the exposed surface and into the melt collecting unit. The calculated vapour mass increases linearly at a constant rate of 19 g/m^{2}s. The feeding rate of foam, v_{feed} is calculated using Equation (7-1) and it is found to be 1.6 mm/s.

$$v_{feed} = \frac{\dot{m}_{sam}}{\rho \cdot A_s} \tag{7-1}$$

For the NFR-SB-31 sample in Figure 7-11, a total of 91 g of foam has decomposed by the end of the experiment with 56 g as melt and 35 g as gases released. These translate into 61 % of melt mass fraction and 39 % of vapour mass fraction.

Figure 7-12 shows the changes in the sample mass for all polyurethane foams tested. The sample mass loss rate per unit area, $\dot{m}''_{sam}$ ranges from 40 – 65 g/m^{2}s where higher density is noted to produce a greater mass loss rate as a result of higher fuel content per unit of exposed sample surface area.

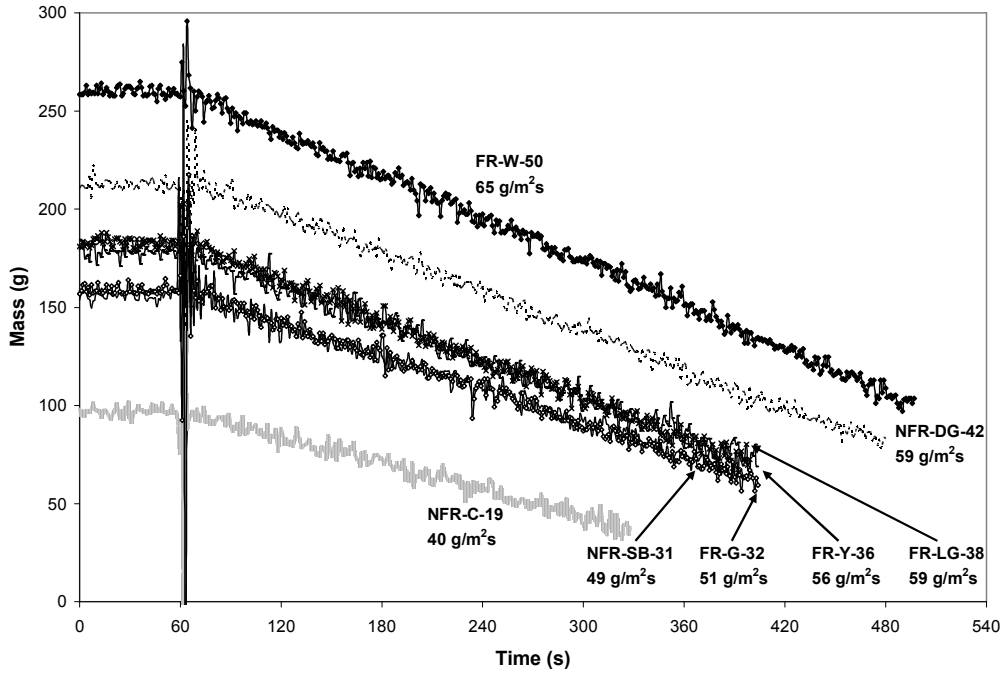

Figure 7-12: Sample mass of all polyurethane foams tested at 50 kW/m^2

Figure 7-13 shows the changes in the melt mass for all polyurethane foams tested. The melting rate per unit area, $\dot{m}''_{melt}$ ranges from 18 – 53 g/m^{2}s. Similar to $\dot{m}''_{sam}$, the higher foam density leads to greater $\dot{m}''_{melt}$ as the greater thermal inertia of the decomposition front causes more sample to decompose into melts rather than vaporising into gaseous fuel. However, NFR-DG-42 shows an exception to this trend. Despite having higher density, the melting rate of NFR-DG-42 is slightly less than FR-Y-36 and FR-LG-38 of lower density. This is believed to be due to NFR-DG-42 lack of combustion resistive nature which allows more melts to be consumed within the flame when flowing over the exposed surface.

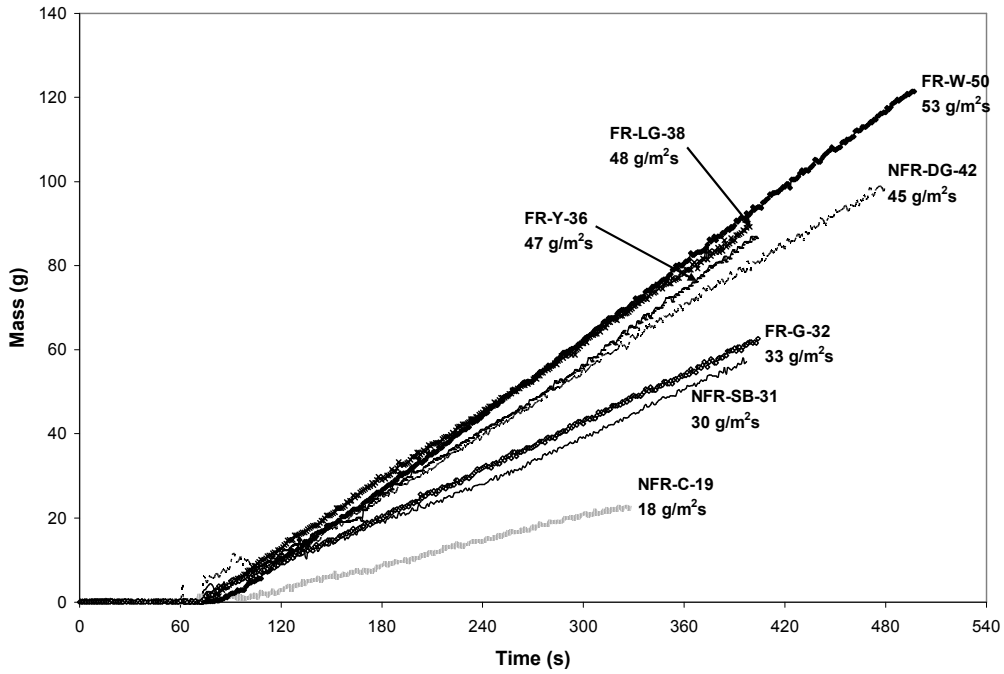

Figure 7-13: Melt mass of all polyurethane foams tested at 50 kW/m^2

In Figure 7-14, the calculated vaporisation rate per unit area, $\dot{m}''_{gas}$ ranges between 10 – 23 g/m^{2}s. Previously, $\dot{m}''_{sam}$ and $\dot{m}''_{melt}$ show good correlation with the foam density but this is not immediately obvious for $\dot{m}''_{gas}$.

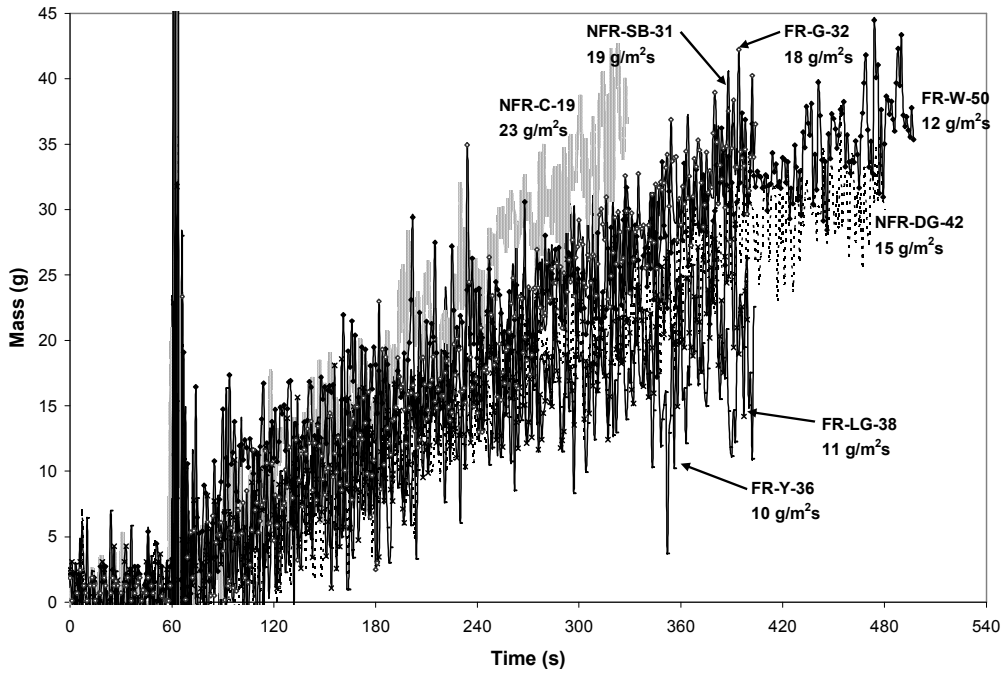

Figure 7-14: Vapour mass of all polyurethane foams tested at 50 kW/m^2

The results can be categorised according to the foams' fire characteristics. Group 1 foams which produce only melts after ignition shows that $\dot{m}''_{gas}$ decreases with increasing foam density due to the increasing thermal inertia of the sample. As mentioned before, this group of foams include all NFR foams and FR-G-32. Group 2 foams which produce both melts and char after ignition shows $\dot{m}''_{gas}$ remains constant despite significant changes in the foam density. Foams in this group are FR-Y-36, FR-LG-38 and FR-W-50. The consistent $\dot{m}''_{gas}$ of Group 2 is attributed to the fire retardant mechanisms of those foams, particularly the solid phase char formation mechanism which is effective in lowering the vaporisation rate.

Table 7-2 summarises the remaining results of the foam melting experiments including v_{feed}, time delay to melting (t_d), melt mass fraction (F_m) and vapour mass fraction (F_g). As F_g is the complement of F_m, the subsequent discussions focus only on F_m. While the melts collected for Group 1 foams are purely liquid melts, those for Group 2 contain the both melts and char. Thus, the melt mass fraction reported in this research includes both liquid melts and solid char.

Table 7-2: v_{feed}, t_d, F_m and F_g from Sample Feeding Vertical Cone experiments

Sample	Group	Sample Feeding Vertical Cone results			
		v_{feed} (mm/s)	t_d (s)	F_m (%)	F_g (%)
NFR-SB-31	1	1.6	13	61	39
NFR-DG-42	1	1.4	13	74	26
NFR-C-19	1	2.1	47	39	61
FR-G-32	1	1.6	15	63	37
FR-Y-36	2	1.6	21	79	21
FR-LG-38	2	1.6	17	78	22
FR-W-50	2	1.3	27	76	24

A range of melt mass fractions is obtained for the polyurethane foams tested due to the further melt consumption by the flame as the melt droplets formed flow across the exposed surface. From Table 7-2, FR-Y-36 and FR-LG-38 have the highest melt fraction, 79 and 78 % respectively. This is due to the superior fire retardant performance of these foams which produce char fractions that prevent further vaporisation of melts as they flow across the exposed surface. FR-Y-36 and FR-LG-38 are followed closely by FR-W-50 and NFR-DG-42 which have melt mass fraction of 76 and 74 % respectively. The fire retardant performance of FR-W-50 is perhaps not as effective as FR-Y-36 and FR-LG-38 given its lesser melamine content indicated by the lower nitrogen content in its chemical formula in Table 2-1. Thus, this results in the slightly lower melt mass fraction of FR-W-50 compared to FR-Y-36 and FR-LG-38. Despite being non-fire retardant, NFR-DG-42 achieves 74 % of melt fraction due to its high density which means greater thermal inertia and this encourages melting over vaporisation. For the remaining foams, the melt fraction is less than 70 % where NFR-SB-31 and FR-G-32 have 61 and 63 % while NFR-C-19 has the lowest melt fraction, 39 %. FR-G-32 has lower melt fraction compared to the other FR foams because FR-G-32 only has gas phase fire retardant mechanism which is not as effective as the solid phase char formation at preventing melt vaporisation. The melt fraction of FR-G-32 is actually comparable to NFR-SB-31 which has a

similar density and is non-fire retardant. Due to its low density, NFR-C-19 has low thermal inertia which favours vaporisation and thus resulting in the lower melt fraction.

The melt fraction from the Sample Feeding Vertical Cone can be grouped according to the previously assigned Group 1 and 2 which are based on the decomposition and melting behaviours observed. For the Group 1 foams, those with lower density are noted to have lower melt fraction. Again, this is related to the smaller thermal inertia of the foams causing most of the sample to vaporise rather than melt. Due to the char formation ability of the Group 2 foams, their melt fraction remains constant, ranging between 76 and 79 % which is greater compared to Group 1, between 39 and 74 %. This is indicative that with the presence of char, the melts from Group 2 foams are thermally more stable than Group 1.

For the different polyurethane foams, v_{feed} ranges from 1.3 – 2.1 mm/s where the foam with lower density requires a greater feeding speed. The results show that NFR-C-19 potentially has the fastest flame spread rate despite having the lowest mass loss rate. In terms of t_d, NFR-C-19 has the longest delay followed by FR-W-50, the rest of Group 2 and finally, the Group 1 foams. The magnitude of t_d is influenced by the surface phenomenon of each foam. The melting delay of NFR-C-19 is almost two times that of FR-W-50 due to the formation of thin strands prior to ignition which hold back the melt droplets and also the significant vaporisation rate after ignition meaning more melts are consumed instead of being collected. Among the Group 2 foams, FR-W-50 has a longer delay due to its ability to form crust as seen in Figure 7-10 prior to ignition which is better at slowing the melt flow compared to FR-Y-36 and FR-LG-38. Lastly, the inability of FR-G-32, NFR-SB-31 and NFR-DG-42 to form char after ignition results in their short t_d.

7.9 Effects of Density and Fire Retardant Additives on Decomposition and Melting Behaviours of Vertically Oriented Polyurethane Foams

From the results at 50 kW/m^2, the foam density is found to be one of the two crucial factors influencing the decomposition and melting behaviours of polyurethane foams. The foam density is found to correlate with the sample mass loss rate, the melting rate and the feeding rate. Polyurethane foams with low density also have low thermal inertia causing these foams to heat up faster and vaporise rather than melt. Consequently, this increases the feeding rate, vaporisation rate and vapour fraction while lowering the melting rate and melt fraction. These trends show that low foam density encourages combustion which is also supported by the literature. Statistical study conducted by Lefebvre et al.[106] demonstrates that the low density of foam correlates to rapid melting and significant contribution to flame propagation. The research analysed various physical properties of foam, including chemical formulation, porosity and density, and various fire parameter in standardised tests, including flame spread rate, peak heat release rate and maximum mass loss rate.

The second crucial factor is the ability of certain foams to produce char during decomposition which is a fire retardant mechanism that affects the vaporisation rate, the melt and vapour mass fractions and the time delay to melting. The results also show that aside from FR-G-32, all FR foams are categorised into Group 2 due to the continuous char formation after ignition. Char formation is effective in mitigating fire growth and as shown during experiments, char formation constantly causes flame out by interrupting the surface decomposition and the combustion. In contrast, the absence of continuous char formation after ignition allows the Group 1 foams to burn more readily than the Group 2 foams. The thermal insulative char has improved thermal stability and it limits the vaporisation rate and vapour fraction and thereby resulting in high melt fraction as most fuel remains in the form of liquid melts and char. Therefore, the foams with char forming ability have reduced combustibility.

Despite being FR foam, the results show that FR-G-32 has poorer combustion resistive performance than the other FR foams where it has demonstrated a very

similar decomposition and melting behaviours as the NFR foams. The absence of char formation after ignition observed during the experiments agrees with the manufacturer specification that only halophosphate is used as fire retardant additive in FR-G-32. Halophosphate breaks down into chlorine which functions predominantly in gas phase and this is very susceptible to several local conditions such as ventilation, fuel concentration and reaction rate. Therefore, the gas phase fire retardant is believed to be less effective than the solid phase fire retardant that promotes char formation which stays in place for longer and shields the foam from the external radiation.

7.10 Conclusions

The Sample Feeding Vertical Cone has been used to provide qualitative and quantitative assessment on the decomposition and melting behaviours of different types of polyurethane foam. The apparatus consists of the vertical cone housing, the automated sample feeder and the load cell system. The vertical cone housing is where decomposition and melting of vertically oriented polyurethane foam occur. The automated sample feeder conveys the foam forward at a user defined rate to compensate for the decomposed sample. The mass of the foam sample and the melts produced are continuously monitored throughout the foam melting experiment by the load cell system.

Several features of the Sample Feeding Vertical Cone ensure that the issues encountered by other research and also during the apparatus development are addressed. By having the foam sample continuously fed forward to maintain the decomposition front at a fixed position, the accuracy in quantifying decomposition and melting behaviours at specific heat fluxes is improved. Subsequently, to prevent the development of three-dimensional front, a water cooling system is used which prevents the decomposition and flame spread from propagating along the sides of the sample. The smaller exposed surface of 75 by 75 mm for the sample is also adopted to ensure the irradiance on the surface is more evenly distributed and the edge effect is minimised. Furthermore, conducting the experiments under flaming condition overcomes the necessity to remove the accumulated char skin which introduces

experimental uncertainties. Without a three-dimensional front, the sample mass loss rate, melting rate and vaporisation rate can be expressed accurately in per unit of exposed area.

Insufficient sample mass for testing is resolved by using a 900 mm long sample which also provides ample time for the melting behaviour of foam to reach steady state. Lastly, the introduction of intermittent injection of CO_2 gases to extinguish any sign of flame in the melt collecting unit has been successful at preventing pool fire. However, there are some drawbacks as CO_2 gas interferes with combustion and it does little in preventing the heated melt from evaporating slowly throughout the experiment. Nevertheless, the quantity of melt loss through evaporisation is insignificant. Ohlemiller et al.[26] had employed a water cooling system on the collecting bottle which has been successful in preventing pool fire development so further research should explore such techniques.

The foam melting experiments at 50 kW/m^2 reveals that the polyurethane foams tested can be categorised into two groups based on their surface phenomenon during decomposition. Group 1 consists of foams which produce melts after ignition while Group 2 consists of foams which produce melts and char after ignition. For the foams tested, the sample mass loss rate ranges from 40 – 65 g/m^{2}s, the melting rate ranges from 18 – 53 g/m^{2}s and the vaporisation rate ranges from 10 – 23 g/m^{2}s. The feeding rate ranges from 1.3 – 2.1 mm/s. In terms of melt fraction, Group 1 foams ranges from 39 – 74 % while Group 2 foams ranges from 76 – 79 %.

The results show the decomposition and melting behaviours are mainly affected by the foam density and the formation of char. Low foam density promotes fire spread and combustion due to the low thermal inertia of the sample. Char formation which is the attribute of Group 2 foams limits the vaporisation rate and vapour fraction. As such, the combustibility is lower because most of the fuel remains in liquid melts and char which give rise to the higher melt fraction of Group 2. In Chapter 4, 5 and 6, the melts collected from the Sample Feeding Vertical Cone are tested further to obtain the thermophysical and kinetic properties of melts. Future research should investigate the effects of different heat fluxes and oxygen concentrations have on the decomposition

and melting behaviours. These results can then be used in the development of a foam melting model and to serve as the model validation.

Chapter 8. 1-Dimensional Burning Behaviour of Polyurethane Foams and FDS 5 Modelling

8.1 Introduction

From Section 1.4 of Chapter 1, the overall objective of the research is to investigate the fire behaviours of polyurethane foam and to assess the combustion modelling capability of Fire Dynamics Simulator, Version 5[17,18] (FDS 5[a]). Polyurethane foam is typically used as the paddings in upholstered furniture which is a common type of commodity found in most types of occupancy and residential dwellings. Fire involving upholstered furniture are often selected as the design fire in fire safety designs of buildings due to the foam's wide application and its hazardous fire characteristics such as ease of ignition[107], rapid fire growth and high peak heat release rate[6,7]. In addition, the excessive production of toxic products from the combustion of foam including carbon monoxide and hydrogen cyanide cause incapacitation with relatively short exposure period[108,109,110].

Within the literature, Kramer et al.[54] provided a brief description on the decomposition chemistry of polyurethane foam. The degradation of the foam initiates above 110 °C, involving the least stable bonds, biuret and allophanate. The number of cross-links reduces but the trifunctional polyether bounded by urethane groups still maintains the foam structure. Hence, there is no significant mass loss until above 200 °C where urethane and urea bonds break down. These result in the collapse of foam structure which releases toluene diisocyanate and liquid polyol. Above 300 °C, the polyol further decomposes into volatile fragments.

The majority of the furniture's volume consists of soft combustibles including fabric and polyurethane foam. As discussed by Kramer et al.[54] and also seen in Chapter 7, the foam exhibits melting and flowing behaviours in a fire[26,103]. Under heating, the collapse of the foam structure leads to melting and subsequently, the formation of

[a] Version 5.5.3, SVN number 7031.

pool fire. This changes the burning behaviour of furniture fire due to the increased burning area. Commercially, there are a variety of furniture designs with different features[6] such as angled back and upholstered legs. As a result of the dynamic melting nature of polyurethane foam and the variation in fuel arrangements, the burning behaviours of furniture often consist of 3-dimensional flame spread.

FDS 5 is a computational fluid dynamics (CFD) model containing a pyrolysis model which enables the user to create solid phase fuel in a more complex manner. The features of FDS 5 pyrolysis model include the specification of solid fuel with multiple layers, different material components and multiple solid phase reactions. However, the model is still limited in certain aspects for modelling polyurethane foam fires such as having only a single gas phase reaction and the inability to address the melting phenomenon and the porous nature of a material such as foam. Also, the heat transfer through the solid fuel in FDS 5 is simplified such that a 1-dimensional calculation is solved even though the actual heat transfer is 2 and 3-dimensional. In order to obtain a meaningful assessment on the accuracy of FDS 5's pyrolysis model in simulating polyurethane foam fires, it is necessary to start with a burning geometry that is simpler than the multi-dimensional flame spread of furniture fire. Therefore, this chapter focuses on the 1-dimensional burning behaviour of polyurethane foam under cone calorimeter and the heat release rate modelling using the pyrolysis model of FDS 5. As explained in Section 1.4 of Chapter 1, a methodological decision is made to initiate the investigation at small-scale cone experiment, rather than at material-scale thermogravimetric analysis (TGA) experiment as the focus of this research is on the burning behaviours of polyurethane foam. Application of pyrolysis model to simulate the decomposition of foam at material-scale TGA experiment has been investigated by Valencia[25]. The details of the research are provided later in Section 8.2.2.

Under the cone calorimeter, the burning front progresses through the thickness of the material in one direction and any lateral temperature difference over the burning surface is assumed to be negligible. Most of the published research in the literature[6,111,112] have reported the burning behaviour of polyurethane foam under the cone calorimeter as having two stages as seen in Figure 8-1(a). The first stage involves the burning of foam and the second stage involves the burning of melt which

is the decomposition product from the first stage. However, the burning behaviour consisting of a single stage is also reported within the literature[39] as seen in Figure 8-1(b). Such difference is due to the variation among the commercially available polyurethane foams and also the different types of sample holder used during experiment which result in different boundary conditions.

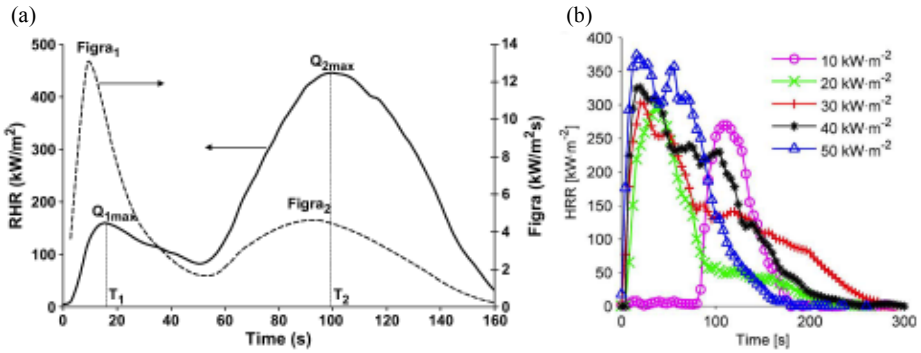

Figure 8-1: Two stage[112] (a) and single stage[39] (b) burning behaviours of polyurethane foam under cone calorimeter

Research on the material-scale decomposition of polyurethane foam using TGA experiments shows it consists of two reactions under nitrogen environment[19,55]. As listed in Section 4.1 of Chapter 4, the first reaction involves the decomposition of foam into both melts and gases while the second reaction is the decomposition of the remaining melts into gases at higher temperature. To some extent, the nitrogen decomposition pattern in TGA experiments is similar to the small-scale two stage burning behaviour seen in the cone experiment which proceeds under air environment. Despite the difference between the environments, the similar two stage behaviour is explained by the assumption that the oxygen required for combustion in the cone experiments is fully consumed within the flame front[42]. As such, no oxygen is available for the oxidation of solid fuel at the decomposition front thus the foam decomposition in cone experiments actually occurs under a similar fashion as the TGA experiments in nitrogen environment.

The accuracy of FDS 5 pyrolysis model in simulating the heat release rate of material has not been assessed thoroughly because the application is complicated by the significant amount of model inputs required to govern heat transfer, decomposition and combustion. Most of these inputs are difficult to measure experimentally and are not readily available from the literature. In this chapter, the material properties of

polyurethane foams are categorised into the thermophysical properties which are developed from the Hot Disk experiments[97] discussed in Chapter 6, the kinetic properties which are developed from the simultaneous differential scanning calorimetry and thermogravimetric analysis (SDT) experiments[113] discussed in Chapter 3, 4 and 5 and the effective heat of combustion which are developed from the cone calorimeter experiment[12,114] discussed in this chapter. To further improve FDS 5's heat release rate predictions, the kinetic properties are refined using the genetic algorithm of Gpyro[27,115] which contains a generalised pyrolysis model that solves a similar set of decomposition equations as the pyrolysis model in FDS 5. The genetic algorithm utilised is a process that searches for a set of kinetic properties within the user defined boundaries that produces the closest agreement between the outputs of the pyrolysis model and the experimental results supplied for comparison.

8.2 Literature Review on Decomposition and Burning Behaviours of Materials and Numerical Simulations using Pyrolysis Models

As mentioned before, the use of a pyrolysis model addresses the heterogeneous composition of a material and its complex physical processes such as charring and multiple competitive reactions. The pyrolysis model of FDS 5 allows the user to specify multiple layers and multiple material components where each component can have up to 10 reactions and the chain of consecutive reactions can have a maximum of 20 steps. Despite governing the fundamental processes in the pyrolysis model such as heat transfer and decomposition, the model inputs calculated experimentally or estimated by genetic algorithm are not regarded as the fundamental properties of the material. The reason being, these material properties are essentially derived from equations with simplified assumptions. As a result, these properties become model dependent and can potentially change if the underlying physics and assumptions are altered. The material properties which are inputs of FDS 5 are listed in Table 8-1 and the experimental techniques used to develop them are also included. Due to the lack of measurement techniques available, a few properties are not investigated. The default values of the model are used in simulation and are assumed to be the best estimate of those properties.

Table 8-1: Material properties which are FDS 5 inputs and their experimental techniques

Material Properties		Experimental Techniques
Thermophysical	Thermal conductivity, λ	Transient plane source, Hot Disk
	Specific heat, c_p	Transient plane source, Hot Disk
	Density, ρ	Measured from sample or calculated effectively
	Thickness, d	Measured from sample or calculated effectively
	Emissivity, ε	Not investigated, 0.9
	Absorption coefficient	Not investigated, 50000 m^{-1}
Kinetic	Activation energy, E	Thermogravimetric analysis
	Pre-exponential factor, A	Thermogravimetric analysis
	Reaction order, n	Thermogravimetric analysis
	Heat of reaction, Δh_r	Differential scanning calorimetry
	Mass fraction, F	Thermogravimetric analysis
	Residue yield, Y_r	Thermogravimetric analysis
	Gaseous yield, Y_g	Thermogravimetric analysis
Combustion	Effective heat of combustion, $\Delta h_{c,eff}$	Cone calorimetry

Rein et al.[19], Valencia[25] and Prasad et al.[42] had simulated the decomposition and burning behaviours of polyurethane foam. The material properties for use in their respective pyrolysis models were estimated from the experimental results using a genetic algorithm. In addition to foam, the material properties estimated by the genetic algorithm had also been applied to predict the decomposition and burning behaviours of woods, thermoplastics and composite materials. The research adopting the property estimation approach in pyrolysis modelling are discussed briefly in this section. Experiments of different setups and scales were modelled such as TGA, cone calorimeter, fire propagation apparatus (FPA) and large-scale fire experiments.

8.2.1 Rein et al.

Rein et al.[19] modelled the decomposition of polyurethane foam in TGA experiments and validated the material properties estimated from a genetic algorithm by simulating the 1-dimensional smouldering behaviours of foam. The authors proposed a five-step mechanism to address the decomposition of polyurethane foam under air environment. This was based on the decomposition pattern in the TGA results under nitrogen and air environments. The TGA results correlated with the changes in the structure of foam and its residues observed using a binocular instrument and the scanning electron microscopy (SEM).

First pyrolysis reaction:	Polyurethane foam → Polyol + Gases
Second pyrolysis reaction:	Polyol → Char + Gases
Third oxidative reaction:	Polyurethane foam + Oxygen → Char + Gases
Fourth oxidative reaction:	Polyol + Oxygen → Char + Gases
Fifth oxidative reaction:	Char + Oxygen → Residue + Gases

A lumped model representing the foam decomposition in the TGA experiment was developed by the authors and GAOT[44] was used to estimate the kinetic properties from the mass loss rate of TGA experiments at 20 °C/min under nitrogen and air environments. The developed properties were further validated by simulating the mass loss rate from the TGA experiments at 5 and 10 °C/min as seen in Figure 8-2. The solid lines are the model results while the individual markers are the experimental results.

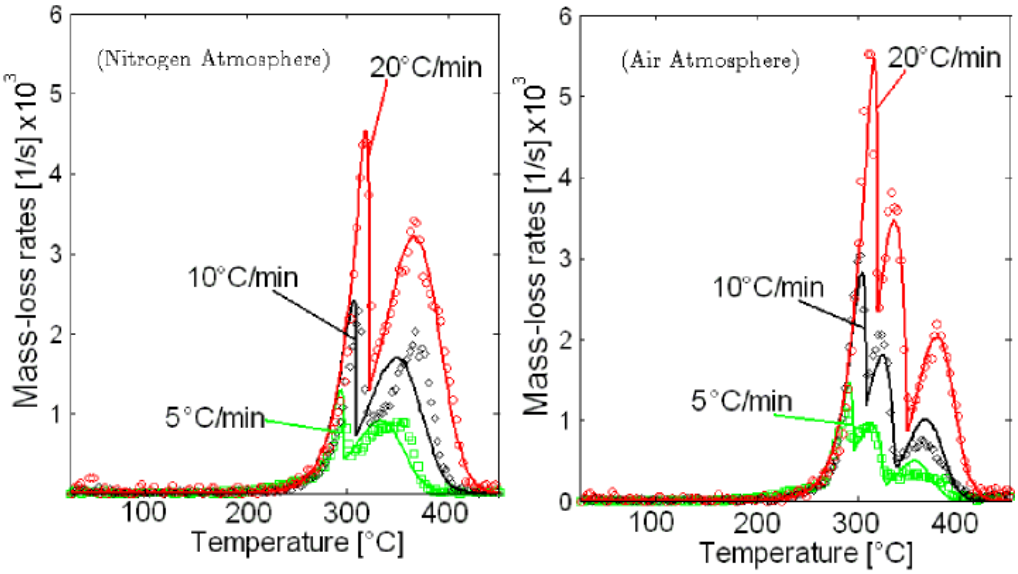

Figure 8-2: Mass loss rate of polyurethane foam in TGA experiment and from lumped model under nitrogen and air environments[19]

The kinetic properties were then used in the modelling of concurrent and opposed-flow smouldering experiments of polyurethane foam. The smouldering model in use is 1-dimensional and it solves the species conservation equations. The energy conservation equation was replaced by a prescribed temperature distribution and the smouldering velocity was also specified. From the modelling results, the smouldering front in the concurrent and opposed-flow modes consumes all the oxygen from the

supplied air. During concurrent smouldering, two distinct fronts are established from the model results where the oxidation front trails the pyrolysis front. In this case, less char remained as most are oxidised into residue by the concurrent flow of oxygen rich air. During opposed-flow smouldering, the model results show a single combined front of pyrolysis and oxidation. In this case, more char is obtained due to the insufficient oxygen in the air available for char oxidation. These modelling phenomena agree with the experimental results.

8.2.2 Valencia

The author[25] modelled the decomposition of polyurethane foam in material-scale TGA experiment and its 1-dimensional burning behaviour in the cone experiment. As listed in Section 4.1, five-step mechanism was proposed to model the burning behaviour of foam, two of which consist of the pyrolysis reactions under nitrogen environment. The proposed mechanism is similar to the one introduced by Rein et al.[19], except for the differences in the sequence of reaction and the solid residue produced.

Using Genetic Algorithms for Optimization Toolbox[44] (GAOT), the kinetic properties including E, A and n for each step of the mechanism were estimated based on the results supplied from the material-scale experiments. These results included the mass loss rate and the yield of different species. The mass loss rate was obtained from TGA experiments conducted at heating rate of 5, 8, 10 and 15 °C/min. The species yields were determined following the analysis using Fourier transform infrared (FTIR) spectroscopy on the gaseous products released from the TGA and tubular furnace (TF) experiments at 10 °C/min. Another kinetic property, the heat of reaction was determined from the differential scanning calorimetry (DSC) experiments at heating rate of 8 °C/min. For the thermophysical properties, the thermal conductivity and specific heat of polyurethane foam were determined respectively using the guarded hot plate technique and the DSC experiments.

The developed material properties were used as the inputs for modelling the 1-dimensional burning behaviour of foam under cone calorimeter at 50 kW/m^2. From

Figure 8-3(a), the simulated heat release rate per unit area and the burning rate had mostly underpredicted the experimental results. The author then investigated the effect of changing the thermophysical properties, the heat of reaction and the fraction of residue produced but the modifications did not improve the results as seen in Figure 8-3(b). Nevertheless, a change in the pattern of the modelled burning rate is observed in Figure 8-3(c) when the last solid species, 'Residue' was removed from the decomposition scheme implemented.

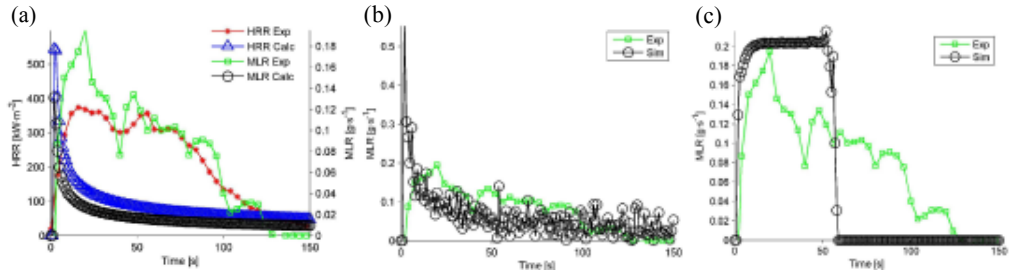

Figure 8-3: Comparison of polyurethane foam cone results and FDS 5 results with originally developed properties as inputs (a), trial and error properties as inputs (b) and 'Residue' removed from five-step mechanism (c)[25]

With 'Residue' removed, the polyurethane foam will fully decompose into gaseous fuel at the end of the decomposition scheme without any solid residue. Despite this change, the experimental trend was still not captured as the simulated burning rate overpredicted the experimental results.

The research had also developed a calculation for predicting the mass loss rate of TGA experiment. Figure 8-4 compares the experimental mass loss rate against the calculated mass loss rate for the original decomposition scheme with four species and the scheme where 'Residue' is removed. The comparison shows that the removal of 'Residue' does not affect the prediction at the scale of a TGA sample but as seen from Figure 8-3, this can potentially have a much greater impact at the scale of a cone sample.

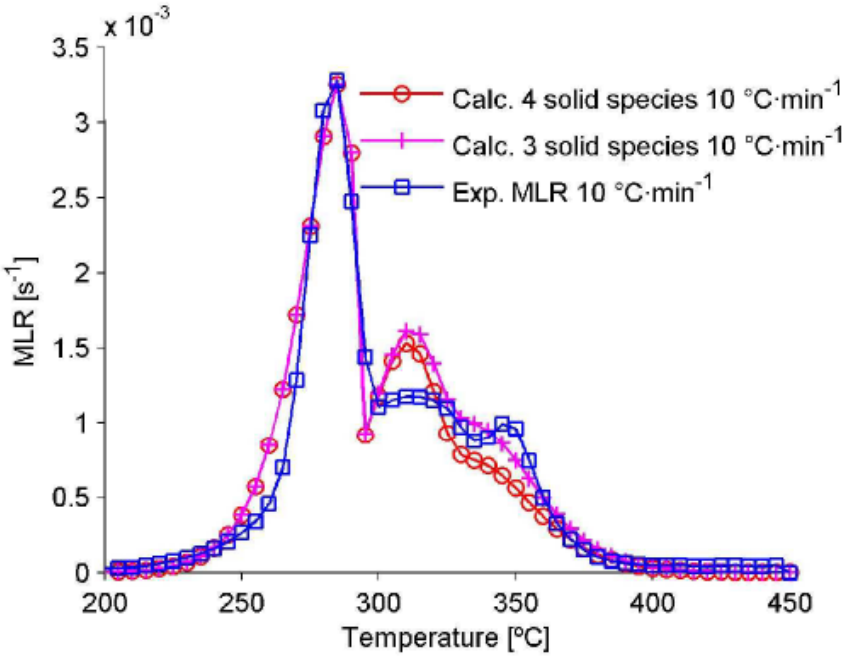

Figure 8-4: Mass loss rate of polyurethane foam in TGA experiment and results calculated with original four species and with 'Residue' removed[25]

8.2.3 Prasad et al.

The authors[42] modelled the decomposition and burning behaviours of polyurethane foam at several scales. Initially, the kinetic properties were developed at the material-scale using TGA experiments conducted at 5 and 10 °C/min under a nitrogen environment. Using the genetic algorithm of Gpyro[27], the kinetic properties of the first and second reactions were estimated with the experimental TGA mass loss rate supplied for comparison. This was followed by FDS 5 simulation on the 1-dimensional cone calorimeter experiment and the 2-dimensional foam slab experiment. In modelling the cone and foam slab experiments, the authors considered an alternative way of defining the kinetic properties in FDS 5. Instead of specifying E and A directly, the reference temperature, reference rate and heating rate from the TGA results were specified and based on those, FDS 5 calculated a set of values for E and A.

The flexibility of FDS 5 in defining the fuel composition and the solid phase reactions give rise to a variety of decomposition schemes. Prasad et al. had investigated four

different schemes to model the cone experiment performed at 45 kW/m^2. The effective heat of combustion was obtained using a microcalorimeter and the other material properties were either the values in the literature or the model defaults. The best scheme found was to model the solid fuel as two separate layers, the top layer contained the foam properties and the second layer underneath contained the melt properties. The simulation was performed without gas phase combustion and flame was represented as a heat flux of 40 kW/m^2. Hence, the foam surface was exposed to a combined heat flux of 85 kW/m^2. The sample mass from the model and the actual experiment are compared in Figure 8-5. The results show the model captures the two stage burning behaviour of foam.

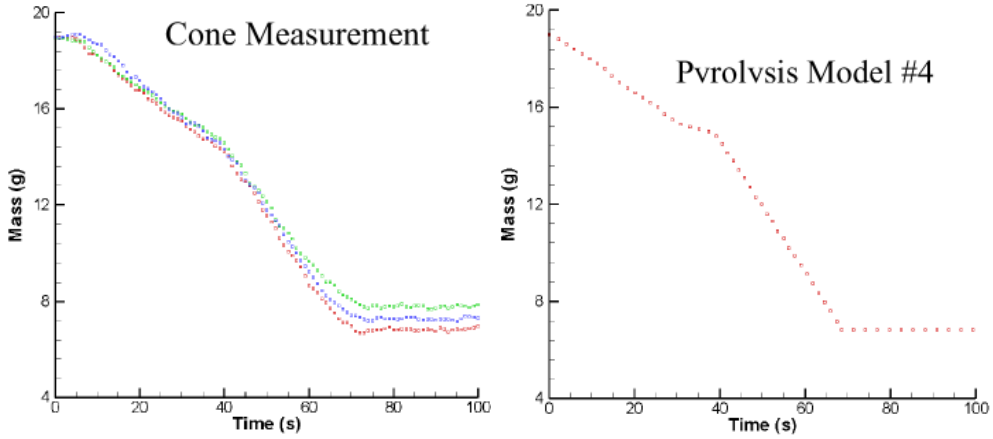

Figure 8-5: Sample mass loss of polyurethane foam in cone experiments and from FDS 5 pyrolysis model[42]

Lastly, the same scheme was further applied for the flame spread modelling of a 100 mm polyurethane foam slab measuring 1200 mm along the sides. The comparison between simulation and experiment is shown in Figure 8-6. The simulation overpredicts the start and growth of the foam slab fire but underpredicts the peak heat release rate.

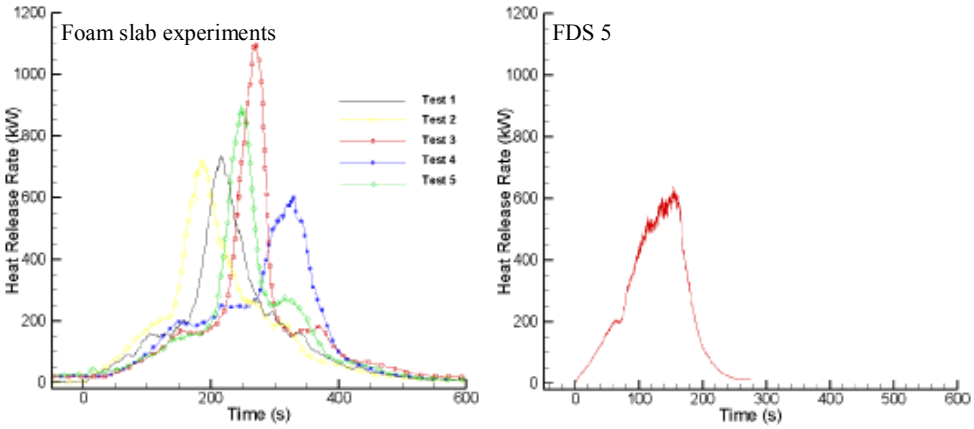

Figure 8-6: Heat release rate of polyurethane foam in foam slab experiments and from FDS 5 pyrolysis model[42]

8.2.4 Other Studies

Majority of the simulations on polyurethane foam have showed promising results at material-scale TGA experiment when a pyrolysis model is used and the model inputs are optimised with a genetic algorithm. Similar outcomes have been found when the same approach is applied to the modelling of other materials such as woods, thermoplastics and composite materials. Figure 8-7 shows some of the comparison between the model and experiment. The examples include redwood under cone experiment (a)[116], polymethylmethacrylate (PMMA) in TGA experiment (b)[21] and fiber reinforced polymer (FRP) in FPA (c)[20] and large-scale experiments (d)[117].

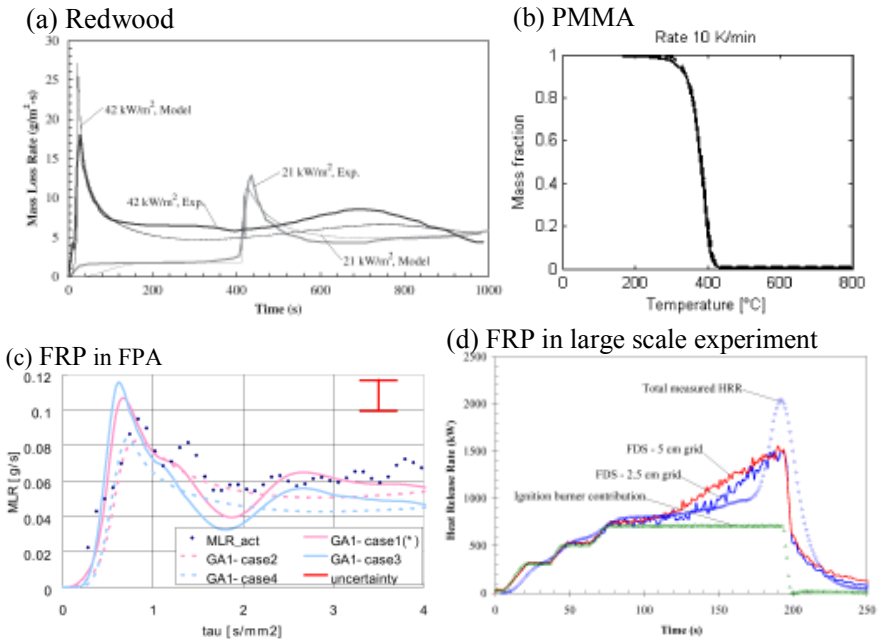

Figure 8-7: Comparison of model and experimental results for redwood under cone calorimeter (a)[116], PMMA in TGA experiment (b)[21] and FRP in FPA (c)[20] and large-scale experiments (d)[117]

Lautenberger et al.[116] developed a methodology using the genetic algorithm to estimate the material properties required for simulating the burning behaviours of materials in fire models. The materials investigated were the charring materials, red oak and redwood and the thermoplastic material, polypropylene. The thermophysical and kinetic properties were estimated from the mass loss rate and surface temperature profiles measured in the cone calorimeter experiments. Matala et al.[21] modelled the decomposition of wood components, birch wood, polyvinyl chloride (PVC) and PMMA with material properties estimated by the genetic algorithm from the TGA experiments. The mechanisms describing the decomposition of each material were developed and evaluated numerically. In both studies, the model results are compared with the experimental results from which the model inputs are estimated hence the comparisons are expected to be good as seen in Figure 8-7(a) and (b).

Kim et al.[20] modelled the decomposition and burning behaviours of FRP which consists of a mixture of resin and glass. The resin was initially tested in TGA experiments and the experimental mass loss rate obtained was used to develop different decomposition mechanisms and their governing kinetic properties. The FPA experiments were carried out and the measured mass loss rate and temperature

distribution within the solid were used to estimate the heat of reaction and the thermophysical properties for two different microstructures. The heterogenous structure has multiple layers consisting of resin, glass or the mixture of both while the homogenous structure consisted of a single layer determined from the mass fraction of resin and glass within the sample. From the modelling results, the heterogenous structure, case 1 and 3 in Figure 8-7(c) are able to resolve the oscillation within the experimental mass loss rate giving a better comparison than the homogenous structure, case 2 and 4. The research also reported that the different decomposition mechanisms do not improve the comparison significantly. The optimised material properties were also used to model a different FRP of higher glass content but the comparison is unsatisfactory due to the uncertainty associated with the microstructure at the material's surface.

In a later research, Lautenberger et al.[117] modelled the decomposition and burning behaviours of PMMA and FRP in small and large-scale experiments. The material properties for modelling were estimated from the small-scale experiments. The research reported that the large-scale experiments involved flame spread and the simulation results were sensitive to the selected mesh sizes. The model produces good prediction for the concurrent flame spread in the case of PMMA but for FRP, the model underpredicts the maximum heat release rate as seen in Figure 8-7(d) because the fire modelled consisted of both concurrent and opposed-flow flame spread. The authors explained that in concurrent flame spread, the preheat region is greater thus more meshes are involved to resolve the heat transfer. However, in the opposed-flow flame spread scenario, the preheat region is smaller resulting in a reduced amount of meshes for solving the heat transfer thus this causes the underprediction in heat release rate by the model.

8.3 Cone Calorimeter and Oxygen Depletion Calorimetry

Three non-fire retardant (NFR) and four fire retardant (FR) polyurethane foams listed in Table 2-1 of Chapter 2 are tested using the cone calorimeter. The preparation of the foam sample for the cone calorimeter experiment follows the procedure outlined in

Combustion Behaviour of Upholstered Furniture (CBUF)[114] and Figure 8-8 shows the readied cone sample and the sample holder used for testing. Using a band saw, the polyurethane foam cone specimen is prepared by cutting a block measuring 100 mm along the sides and 50 mm in thickness from a larger slab of foam. The sample cup containing the foam specimen is a folded aluminium foil which exposes only the top surface of the foam, an area measuring 0.01 m^2. The sample holder consists of a square pan with 18 mm high density calcium silicate board as the backing for the foam specimen.

Figure 8-8: Polyurethane foam sample and sample holder used for cone calorimeter experiment

The 1-dimensional burning behaviour of polyurethane foams are obtained using the cone calorimeter seen in Figure 8-9 and the experimental procedures outlined in ISO 5660-1:1993[12] are followed. During the experiment, the cone heater provides a constant and uniform heat flux on the sample surface located 25 mm from the bottom of the cone heater. The ignition of the sample is piloted by a spark ignitor located 13 ± 0.5 mm above the sample surface. The sample is seated on the load cell and the change in sample mass is monitored continuously. The combustion products from the burning of the sample are removed through the exhaust and the fan speed is set to produce a flow rate of 0.024 ± 0.002 m^3/s. Located before the fan, a ring probe continuously samples the combustion products from the exhaust stream. According to the schematic[12] in Figure 8-9, the sampled gases travel through a series of components to remove soot and moisture before being analysed by the oxygen (O_2), carbon dioxide (CO_2) and carbon monoxide (CO) gas analysers. The measured gas concentrations are used in calculating the heat release rate of the fire through oxygen depletion calorimetry.

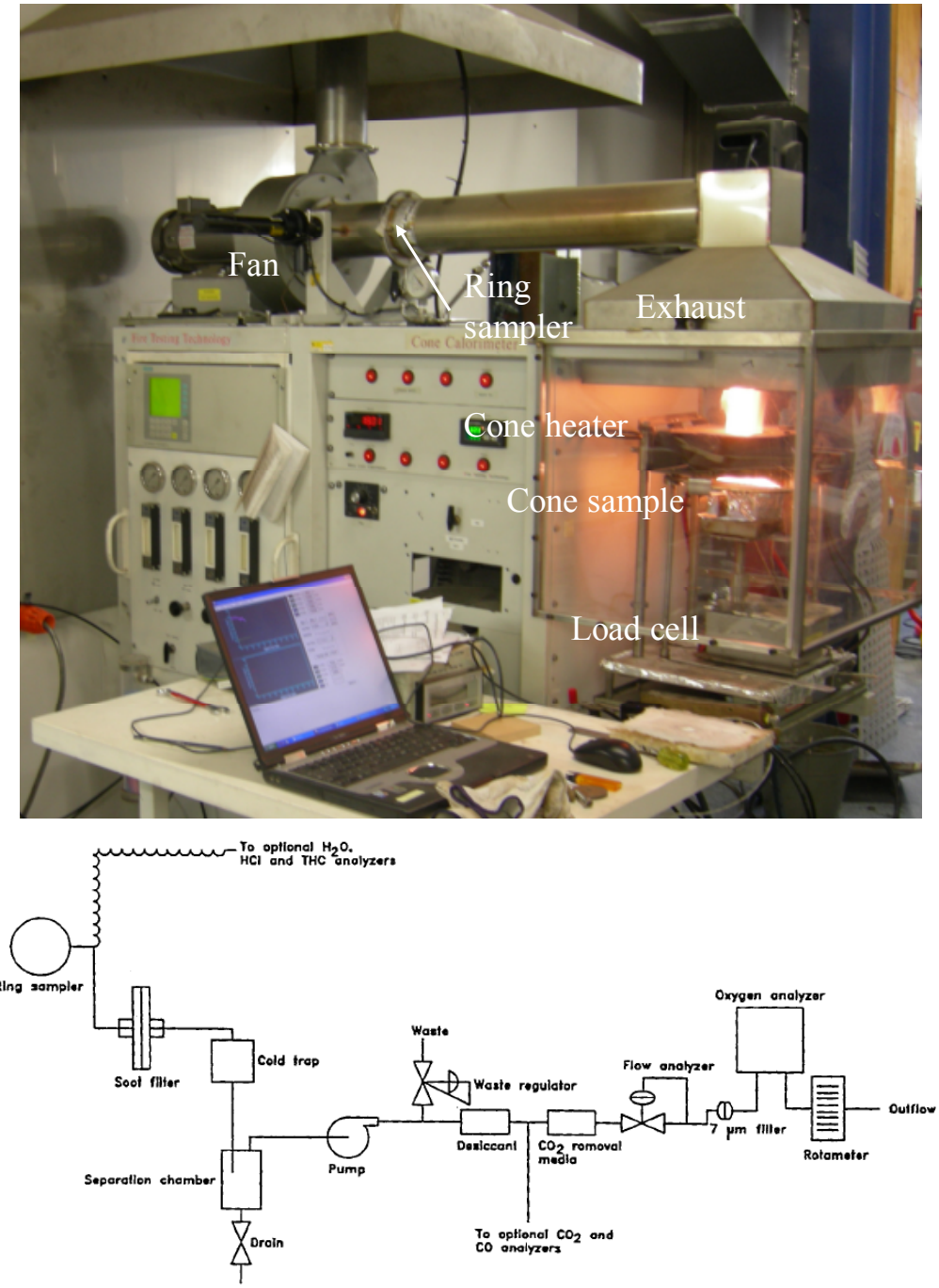

Figure 8-9: Cone calorimeter setup and schematic of gas sampling system[12]

By assuming a constant amount of heat is released when a unit mass of oxygen is consumed during combustion, Equation (8-1) is used to determine the heat release rate of the polyurethane foams tested[11].

$$\dot{q} = 1.10\left[\frac{\Delta h_c}{r_0}\right] X_{O_2}^a \left[\frac{\phi - 0.172(1-\phi)X_{CO}/X_{O_2}}{(1-\phi)+1.105\phi}\right]\dot{m}_e \tag{8-1}$$

For small-scale experiment, the heat release rate is commonly reported in per unit of exposed sample area (HRRPUA). The other combustion parameters such as the mass loss rate and the total heat released are also reported in similar fashion. Within Equation (8-1), the ambient mole fraction of oxygen ($X_{O_2}^a$), the actual mole fraction of water vapour in the combustion air ($X_{H_2O}^0$), the oxygen depletion factor (ϕ) and the exhaust mass flow rate ($\dot{m}_e$) are determined respectively from Equation (8-2) to (8-5). The value of *C* in Equation (8-5) is obtained from the orifice constant calibration described later.

$$X_{O_2}^a = \left(1 - X_{H_2O}^0\right) X_{O_2}^0 \tag{8-2}$$

$$X_{H_2O}^0 = \frac{RH}{100} \cdot \frac{\exp\left(23.2 - \dfrac{3816}{T_a - 46}\right)}{P_a} \tag{8-3}$$

$$\phi = \frac{X_{O_2}^0\left(1 - X_{CO_2} - X_{CO}\right) - X_{O_2}\left(1 - X_{CO_2}^0\right)}{X_{O_2}^0\left(1 - X_{CO_2} - X_{CO} - X_{O_2}\right)} \tag{8-4}$$

$$\dot{m}_e = C\sqrt{\frac{\Delta p}{T_e}} \tag{8-5}$$

To use the cone calorimeter, a few calibrations are carried out to ensure the experimental measurements are correct. First and foremost is the mass calibration of the load cell and this involves verifying the measured mass against the standard weight pieces of known mass. This is followed by the zero and span calibrations of the gas analysers. During zero calibration, the gas analysers are supplied with nitrogen

gas and the measured concentration of O_2, CO_2 and CO are calibrated to zero. During span calibration, the ambient air is supplied to the O_2 analyser while span gas with known CO_2 and CO concentrations are supplied to the CO_2 and CO analysers. The measured concentration of O_2 is calibrated to 20.95 % for ambient air while the measured concentration of CO_2 and CO is calibrated to their respective known values. With the gas analysers calibrated, the orifice constant calibration is performed which involves conducting a methane burner experiment at constant heat release rate of 5 kW. From the measured results, the orifice constant, *C* for use in Equation (8-5) is determined from Equation (8-6).

$$C = \frac{C_{old} \cdot \dot{q}_{act}}{\dot{q}_{cal}} \tag{8-6}$$

$\dot{q}_{act}$ is the average actual heat release rate determined from the methane supply rate while $\dot{q}_{cal}$ is the average calculated heat release rate based on C_{old}. The average heat release rates are taken over 4 minutes of constant burning. Lastly, the heat flux calibration is performed with a side mounted water cooled Schmidt-Boelter heat flux gauge to produce a list of cone heater temperatures that correspond to the desired heat fluxes at the sample surface.

8.4 1-Dimensional Burning Behaviours of Polyurethane Foams

NFR-SB-31 and FR-Y-36 are the base case foams selected from the group of NFR and FR foams tested in this research. Both foams are tested at four different heat fluxes under cone calorimeter, 30, 40, 50 and 60 kW/m^2 while the other five foams are only tested at 30 and 50 kW/m^2. At least three replicates are tested at each heat flux to assess the repeatability of the results obtained. Figure 8-10 shows the repeatability of HRRPUA for the replicates of the base case foams at 50 kW/m^2 exposure. Also explained on the plots are some of the common terminologies used to describe the burning behaviours of the polyurethane foams.

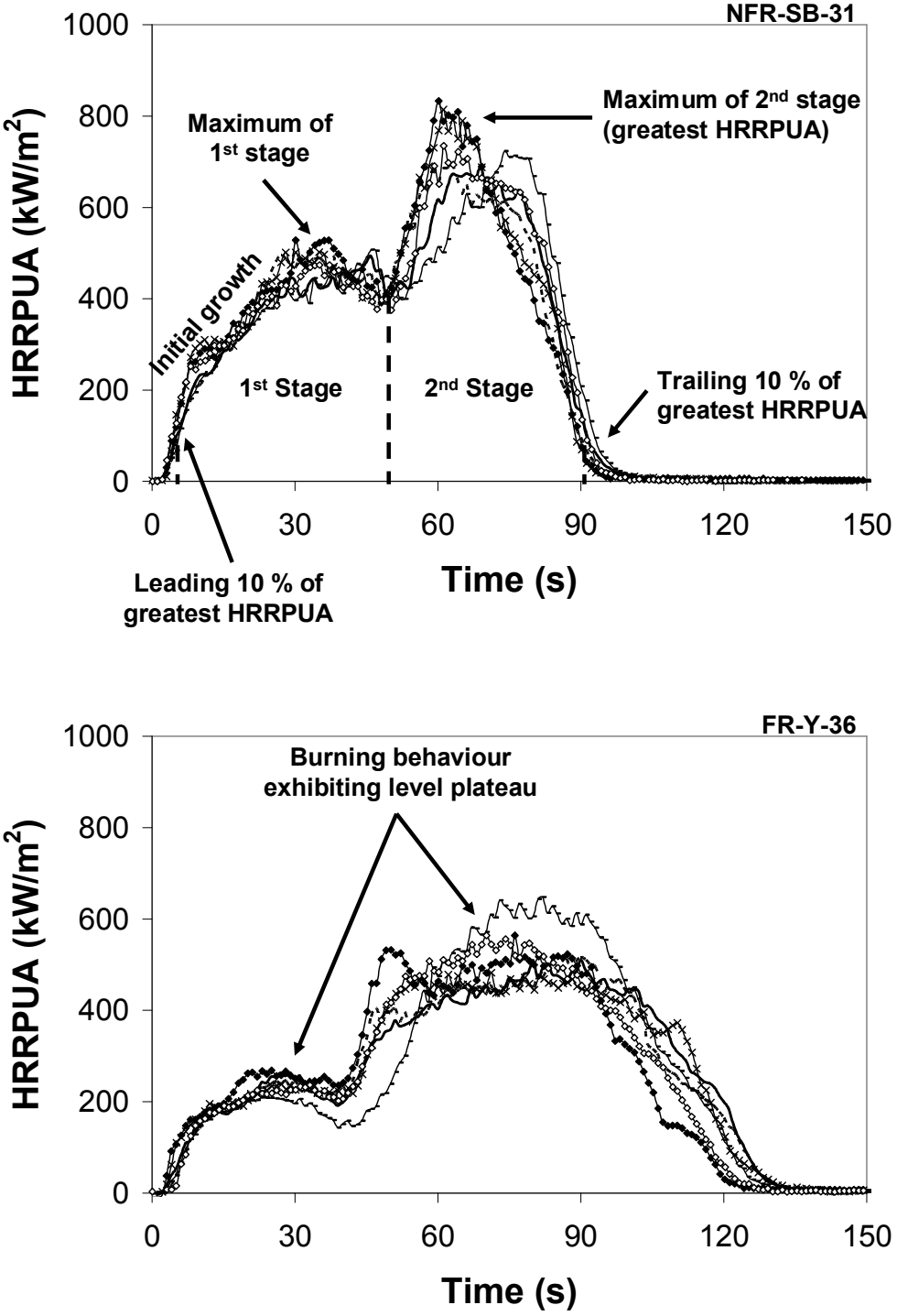

Figure 8-10: HRRPUA repeatability of NFR-SB-31 and FR-Y-36 replicates at 50 kW/m^2

The results for the base case foams at 50 kW/m^2 shows the two stage burning behaviour which is common for the polyurethane foams investigated in this research.

The first stage starts with the initial growth phase where the heat release rate increases sharply towards the maximum of the first stage. The first stage in the case of NFR-SB-31 resembles a peak while the first stage in the case of FR-Y-36 resembles a plateau. The second stage initiates with the rapid increase in heat release rate from the first stage towards the greatest heat release rate. The second stage of NFR-SB-31 resembles a sharp peak while the second stage of FR-Y-36 again resembles a plateau. The second stage ends with the decay in heat release rate.

From Figure 8-10, the results show that the maximum deviation between the replicates is approximately 100 kW/m^2 for both foams. The repeated HRRPUA of other foams show similar trend of repeatability as the base case foams. The repeatability among the replicates is noted to deteriorate at the higher exposure heat fluxes but the comparison is still considered reasonable with the maximum variation within 10 % of the average. Averaging the HRRPUA of the replicates, Figure 8-11 shows the average results at 30, 40, 50 and 60 kW/m^2 for the base case foams, the heat flux tested is included for identification. The burning behaviours exhibited by the base case foams is the typical burning behaviours for the other NFR and FR foams investigated in this research.

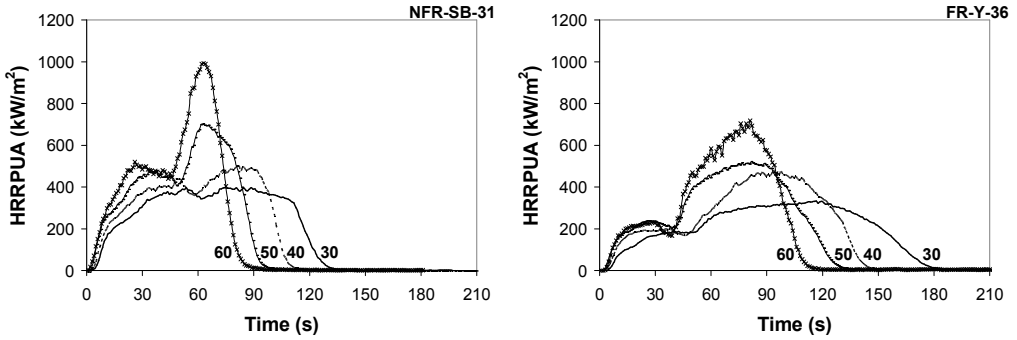

Figure 8-11: Average HRRPUA for NFR-SB-31 and FR-Y-36 at 30, 40, 50 and 60 kW/m^2

The results show the burning duration shortens and the HRRPUA increases with greater exposed heat flux. For NFR-SB-31, the burning behaviour changes from being a level plateau at 30 kW/m^2 to having two distinct stages at 60 kW/m^2 but for FR-Y-36, the two stage burning behaviour is consistent across all the tested heat fluxes. For NFR-SB-31, the two stage burning behaviour corresponds to the burning of two different fronts. Following the initial decomposition of the exposed low density foam

into condensed high density melt, the first front consists of a mixture of foam and melt which burns with lower heat release rate. As the amount of melt accumulates over the burning process while the amount of foam reduces, the second front consists mostly of condensed melt burns with higher heat release rate. The level burning behaviour of NFR-SB-31 at 30 and 40 kW/m^2 points to the burning of the first front only. At these low heat fluxes, due to insufficient thermal penetration, the pyrolysis zone is believed to be narrower than those at 50 and 60 kW/m^2. As a result, the amount of condensed melt accumulated for burning is reduced and the second front fails to develop. For FR-Y-36, the two stages in burning are due to the interference from the fire retardant mechanisms discussed further below.

From Figure 8-11, the increase of heat flux systematically increases the initial fire growth rate of NFR-SB-31 but for FR-Y-36, the trend is not obvious except for the slower growth rate noted at 30 and 40 kW/m^2. During this growth phase, the fire retardant additives in FR-Y-36 start to break down where halophosphate releases chlorine[35] and melamine releases ammonia and nitrogen gases[38]. These gas phase fire retardants neutralise the highly reactive radicals released and dilute the concentration of the combustion products. Besides gas phase mechanisms, there is also the solid phase mechanism through the formation of char which is non-combustible thus protecting the virgin foam underneath and disrupting the progression of the pyrolysis front. The combination of both gas and solid phase fire retardant mechanisms restricts the maximum HRRPUA of the first stage to approximately 200 kW/m^2 regardless of increase in the exposed heat flux. The constancy of the first stage with respect to the changes in heat flux emphasises the two stage burning behaviour of FR-Y-36. Without fire retardant additives, the maximum HRRPUA of NFR-SB-31 over the first stage is allowed to grow. Between 30 and 60 kW/m^2, the magnitude increases from 400 – 500 kW/m^2.

The second stage is driven by the pool fire developed following the collapse of the initial foam structure into melts which potentially increases the burning area as melts being non-porous cover the entire exposed surface. Furthermore, Prasad et al.[42], Kramer et al.[54], Lefebvre et al.[112] and Pitts[118] have reported that the combustion of melts in the second stage produces higher amount of heat released. Consequently, the

HRRPUA of the second stage is greater than the first stage as seen in Figure 8-11. Comparing across the tested heat fluxes, the maximum HRRPUA of NFR-SB-31 over the second stage ranges from 400 – 1000 kW/m^2. While the second stage of FR-Y-36 is also due to the burning of more melts, the HRRPUA never quite achieves the same maximum as NFR-SB-31. The magnitude is consistently lower, ranging from 300 – 700 kW/m^2. This is again a result of the fire retardant mechanisms of FR-Y-36, mainly the shielding of fuel by the char. The influence from the gas phase fire retardants at this stage is not considered to be significant since the majority of the gas phase fire retardants have been released over the first stage. This is in agreement with the findings from Kramer et al.[54] where the research investigated the effect of brominated-phosphorous fire retardant in polyurethane foam. Despite being FR foam, the increase in HRRPUA from the first to second stage is considerable, ranging from 1.5 to 3.5 times the maximum of the first stage. From the experimental observations during the Sample Feeding Vertical Cone experiments in Chapter 7, the char is noted to break up more easily towards higher heat flux and also under the presence of flame. This exposes the melt and foam underneath the char which leads to rapid decomposition thus the HRRPUA of the second stage is not as restricted as the first stage.

Figure 8-12 shows the average HRRPUA of all the polyurethane foams in this research tested at 30 and 50 kW/m^2 and each foam is represented by the colour scheme listed in Section 4.2.1 of Chapter 4. The foam with higher density has a longer burning duration due to the larger amount of fuel available. Similar to the base case foams, the burning behaviour of the NFR foams show the changes from a level plateau at 30 kW/m^2 to two stages at 50 kW/m^2 while the FR foams show the consistent two stages at both heat fluxes.

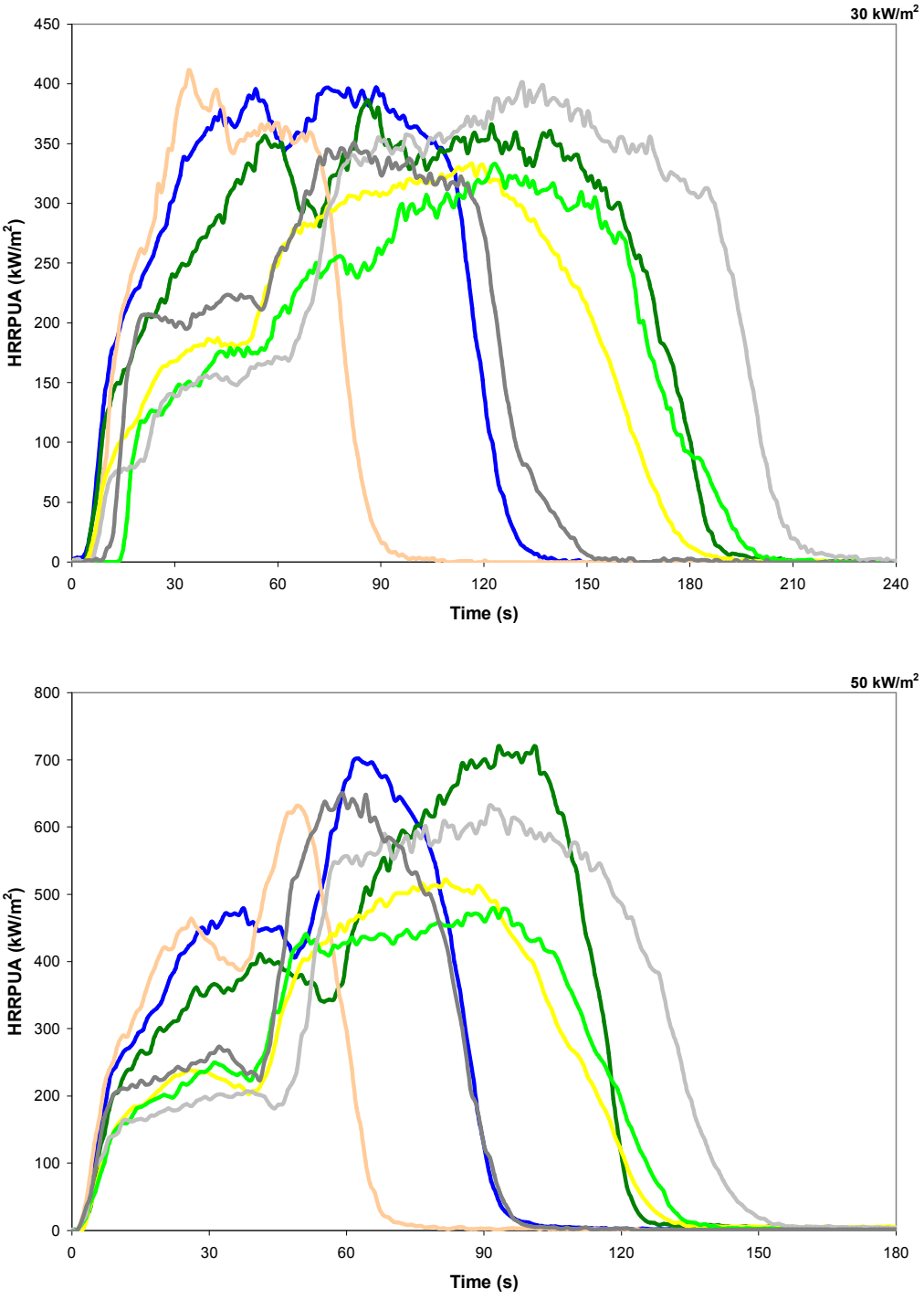

Figure 8-12: Average HRRPUA for all polyurethane foams at 30 and 50 kW/m^2

Between the two groups of foams, the NFR foams show a more rapid initial growth than the FR foams. Within each group, the foam with higher density shows a slower initial growth and also produces lower HRRPUA over the first burning stage due to

the greater heat capacity of the sample. However, towards the region of greatest HRRPUA, a higher foam density does not necessarily produce a higher peak despite the greater fuel content. The reason being the melting of the foam has created a mixed front of foam and melts and the unknown density of this front affects the HRRPUA. As the foam decomposes, approximately 75 % of the original mass remains as melts according to the TGA results presented in Chapter 3 and 4. From Table 2-1, the melt density is noted to be significantly greater than the foam density. So given the remaining mass at the decomposition front is mostly melts with high density, the density of the mixed front would approximate the melt density. Since the variation in the density among different melts in Table 2-1 is negligible, the greatest HRRPUA of the different foams are mostly comparable.

Comparing the fire performance of both foams, all FR foams show the ability to limit the maximum HRRPUA to approximately 200 kW/m^2 over the first stage while the HRRPUA of NFR foams grows to more than 400 kW/m^2. But over the second stage, only FR-Y-36 and FR-LG-38 shows lower HRRPUA, 300 kW/m^2 at 30 kW/m^2 and 500 kW/m^2 at 50 kW/m^2. The other foams achieve greater magnitude, 350 – 400 kW/m^2 and 600 – 700 kW/m^2 for the same heat fluxes respectively. The better fire performance of FR-Y-36 and FR-LG-38 is believed to be related to the higher melamine concentration within the foam indicated by their higher N composition in Table 2-1 compared to the other foams. Although FR-W-50 also contains melamine, the concentration is believed to be lower given the low N composition of FR-W-50. Despite the capability of melamine to produce char, the high density of FR-W-50 means the fuel content is also greater thus allowing it to achieve higher HRRPUA than FR-Y-36 and FR-LG-38. FR-G-32 only contains halophosphate which performs predominantly in the gas phase by releasing chlorine gas. Without the char formation mechanism like melamine, at 50 kW/m^2, the second stage of FR-G-32 is similar to the NFR foams showing a sharper peak than the other FR foams. Due to the insulative nature of char, the second stage of FR-Y-36, FR-LG-38 and FR-W-50 appears as an extended plateau as decomposition and combustion are constantly interrupted at the solid phase.

Table 8-2 contains the ignition time (t_{ig}), average mass loss rate ($\dot{m}''_{ave}$), total heat released (q''_{tot}), effective heat of combustion ($\Delta h_{c,eff}$), peak HRRPUA ($\dot{q}''_{pk}$) and average HRRPUA ($\dot{q}''_{ave}$) for all the polyurethane foams tested at 30, 40, 50 and 60 kW/m^2. The subscripts '*pl*', '*1*' and '*2*' for $\dot{q}''_{pk}$ denote the peak HRRPUA of the single plateau, the first stage and the second stage and similarly, '*tot*', '*1*' and '*2*' for $\dot{q}''_{ave}$ denote the average HRRPUA for the entire burning phase, the first stage and the second stage. The reported values are the average of all the replicates and the standard deviation as percentage of the average is included in the brackets. The trends of each parameter are explained in their respective section below.

Table 8-2: Ignition time, average mass loss rate, total heat released, effective heat of combustion, peak HRRPUA and average HRRPUA of all polyurethane foams tested at 30, 40, 50 and 60 kW/m^2

Experimental Parameter	Polyurethane foams and heat fluxes (kW/m^2) tested																	
	NFR-SB-31				NFR-DG-42		NFR-C-19		FR-Y-36				FR-LG-38		FR-W-50		FR-G-32	
	30	40	50	60	30	50	30	50	30	40	50	60[a]	30	50	30	50	30	50
t_{ig} (s)	5.1 (20.8)	3.4 (9.5)	2.5 (9.6)	2.0 (5.9)	5.1 (2.5)	3.2 (24.3)	7.4 (38.3)	2.1 (19.7)	7.8 (69.6)	4.2 (56.0)	3.0 (29.7)	2.2 (9.2)	87.2 (145.4)	3.5 (50.8)	11.0 (70.5)	2.4 (47.6)	11.8 (13.9)	2.6 (40.5)
$\dot{m}''_{ave}$ (g/m^{2}s)	15.0 (5.2)	17.1 (2.8)	20.4 (2.9)	23.0 (3.6)	13.6 (8.1)	20.1 (1.2)	14.8 (3.8)	19.0 (4.6)	12.1 (8.1)	14.4 (1.9)	16.9 (3.7)	19.3	12.1 (7.1)	17.0 (3.3)	14.1 (2.8)	20.4 (4.6)	13.6 (7.4)	19.9 (3.0)
q''_{tot} (MJ/m^2)	37.8 (2.2)	37.7 (0.4)	39.3 (1.8)	40.9 (1.1)	51.3 (0.7)	53.0 (1.4)	23.5 (1.3)	24.7 (1.3)	38.3 (2.3)	39.7 (0.4)	39.5 (2.0)	40.5	36.6 (12.7)	40.5 (0.8)	52.8 (0.7)	54.2 (1.9)	31.4 (0.4)	32.9 (1.2)
$\Delta h_{c,eff}$ (MJ/kg)	24.8 (1.3)	24.9 (0.7)	25.0 (1.8)	26.9 (1.4)	24.4 (0.2)	24.9 (0.7)	24.2 (1.9)	25.0 (2.3)	22.5 (3.1)	23.5 (1.0)	22.8 (2.5)	23.2	22.6 (5.4)	22.1 (1.7)	21.9 (0.1)	22.0 (0.4)	20.5 (2.5)	21.3 (0.2)
$\dot{q}''_{pk,pl}$ (kW/m^2)	432 (4.4)	-	-	-	400 (6.3)	-	421 (6.9)	-	-	-	-	-	-	-	-	-	-	-
$\dot{q}''_{pk,1}$ (kW/m^2)	-	458 (6.4)	503 (3.6)	542 (6.4)	-	422 (6.3)	-	465 (5.5)	194 (12.1)	209 (9.8)	245 (8.7)	231	185 (30.0)	251 (10.7)	172 (10.7)	215 (6.9)	236 (13.0)	276 (8.9)
$\dot{q}''_{pk,2}$ (kW/m^2)	-	520 (4.5)	748 (8.2)	1029 (11.9)	-	750 (1.5)	-	647 (8.4)	361 (10.2)	487 (8.5)	548 (10.7)	718	362 (1.6)	504 (4.8)	418 (5.2)	653 (6.5)	370 (8.9)	694 (11.2)
$\dot{q}''_{ave,tot}$ (kW/m^2)	319 (4.6)	368 (1.6)	447 (3.0)	536 (4.2)	295 (5.7)	455 (0.4)	302 (2.9)	401 (1.5)	240 (7.5)	296 (2.3)	330 (3.1)	393	246 (8.7)	326 (2.1)	273 (4.0)	393 (5.1)	256 (9.5)	370 (2.4)
$\dot{q}''_{ave,1}$ (kW/m^2)	-	333 (3.3)	376 (2.9)	413 (1.5)	-	322 (3.5)	-	360 (2.7)	155 (7.5)	174 (8.5)	198 (7.0)	193	149 (19.2)	196 (6.3)	143 (7.3)	176 (3.0)	199 (15.7)	227 (7.8)
$\dot{q}''_{ave,2}$ (kW/m^2)	-	408 (5.8)	527 (3.6)	685 (8.7)	-	554 (1.5)	-	452 (5.9)	273 (9.9)	350 (2.6)	387 (4.9)	493	272 (5.7)	374 (3.3)	319 (3.3)	486 (7.2)	288 (13.4)	471 (6.1)

[a] The value from a single replicate is reported for FR-Y-36 at 60 kW/m^2 except for the ignition time.

8.4.1 Ignition Time

The ignition time of polyurethane foam shortens with the increase in heat flux according to the results in Table 8-2. At 30 kW/m^2, the average ignition time of FR foams, from 8 – 87 s is longer than NFR foams, from 5 – 7 s. But at 50 kW/m^2, the fire retardant additives no longer have a significant impact on ignition and the average ignition time of FR and NFR foams is essentially the same, from 2 – 4 s. The average ignition time of 87 s for FR-LG-38 at 30 kW/m^2 is significantly longer than the other FR foams due to the extensive delay of the second replicate tested which only ignites after 234 s of exposure.

The delayed ignition is caused by the performance of the gas and solid phase fire retardants and also due to the collapse of the thick foam structure into thin layer of melts which subsequently extends the distance between the fuel bed and the spark ignitor, complicating the ignition process. Excluding the second replicate, the average ignition time of FR-LG-38 is 14 s which narrows the range of ignition time for FR foams to 8 – 14 s. In comparison with NFR foams, the mechanisms of fire retardant additives introduce greater deviation among the ignition times of the FR foams' replicates. The repeatability of the ignition time deteriorates as the exposure heat flux nears the minimum heat flux for ignition. This is because ignition is a complex phenomenon which is sensitive to many localised conditions such as air current, fuel concentration, oxygen concentration, heat flux and presence of pilot ignition source.

8.4.2 Average Mass Loss Rate

The average mass loss rate represented as per unit area is calculated from Equation (8-7) which is the change in mass divided by the change in time over the 10 and 90 % mass loss[12].

$$\dot{m}''_{ave} = \frac{m_{10} - m_{90}}{t_{90} - t_{10}} \cdot \frac{1}{A_s} \tag{8-7}$$

From Table 8-2, the average mass loss rate shows an increase in magnitude when the heat flux increases. Among the foams, the superior fire retardant mechanisms of FR-Y-36 and FR-LG-38 are reflected by their consistently lower magnitude. At 30 and 50 kW/m^2, both FR-Y-36 and FR-LG-38 have 12 and 17 g/m^{2}s respectively while the others have 14 – 15 g/m^{2}s and 19 – 20 g/m^{2}s. The maximum deviation among the replicates is no more than 8 % of the average mass loss rate reported.

8.4.3 Total heat released

The total heat released is calculated from ignition to where the HRRPUA becomes insignificant using the trapezium rule of integration in Equation (8-8)[12]. The HRRPUA is defined as insignificant when the changes between the successive scans are of the same magnitude as the experimental noise. From all the results analysed, this is a nominal value of less than 6 kW/m^2.

$$q''_{tot} = \left[0.5\dot{q}_{ign} + \sum_{i=1}^{n-1} \dot{q}_i + 0.5\dot{q}_n \right] \Delta t \cdot \frac{1}{A_s} \tag{8-8}$$

The total heat released from different polyurethane foams correlates well with their respective foam density where a higher density results in more total heat released due to the greater fuel content. The total heat released remains consistent with heat flux but it does show a slight increase in magnitude as a result of more complete combustion at high heat flux. The total heat released for the foams tested ranges from 24 – 54 MJ/m^2 and the maximum deviation among the replicates is mostly no more than 2 % except for FR-LG-38 at 30 kW/m^2 which shows 13 %. This outlier is caused by the extended ignition of the second replicate where the sample experiences the loss of fuel without combustion for an extensive duration.

8.4.4 Effective Heat of Combustion

From Equation (8-9), the effective heat of combustion is calculated as the summation of the heat released from ignition to the end of test which is divided by the difference between the initial and final sample mass[12].

$$\Delta h_{c,eff} = \frac{\sum \dot{q} \cdot \Delta t}{m_i - m_f} \tag{8-9}$$

From Table 8-2, the effective heat of combustion remains constant with heat flux. However, similar to the total heat released, the magnitude increases slightly at higher heat flux as a result of more complete combustion. The NFR foams with higher effective heat of combustion, 24 – 27 MJ/kg have greater combustibility than the FR foams. The lower effective heat of combustion for the latter, 21 – 24 MJ/kg is caused by the interference of the fire retardants on the combustion. The effective heat of combustion of NFR-SB-31 shows a sudden increase at 60 kW/m^2. This is believed to be due to enhanced burning as the strong thermal penetration causes a more rapid collapse of the foam structure producing a higher proportion of melts. A similar sudden increase is not seen in the other base case foam, FR-Y-36, again due to the fire retardants. The maximum deviation among the replicates is no more than 5 % of the average value reported.

8.4.5 Peak and Average Heat Release Rate Per Unit Area

The plateau peak HRRPUA reported in Table 8-2 is the maximum for the experiments exhibiting single plateau burning behaviour. The first and second peak HRRPUA are the respective maximum for the first and second stages of the experiments with two stage burning behaviour. The total average HRRPUA is the average taken over the entire burning duration which is between the leading and trailing 10 % HRRPUA of the greatest peak. For the experiments with two stage burning behaviour, the average HRRPUA over each stage is also reported. The first stage is determined from the leading 10 % HRRPUA of the greatest peak to the point after the maximum of the first stage where the slope starts to increase rapidly. The second stage continues from the end point of the first stage to the trailing 10 % HRRPUA of the greatest peak.

The maximum HRRPUA of the NFR foams are found to be consistently greater than the FR foams. At 30 kW/m^2, NFR foams range from 400 – 430 kW/m^2 while FR foams range from 360 – 420 kW/m^2. At 50 kW/m^2, NFR foams range from 650 – 750

kW/m^2 while FR foams range from 500 – 690 kW/m^2. The same trend is also noted for the total average HRRPUA. At 30 kW/m^2, NFR foams range from 290 – 320 kW/m^2 while FR foams range from 240 – 270 kW/m^2. At 50 kW/m^2, NFR foams range from 400 – 450 kW/m^2 while FR foams range from 330 – 390 kW/m^2. From Table 8-2, the deviation among the replicates is generally greater for the FR foams compared to the NFR foams due to the uncertainty introduced by the fire retardants during the combustion.

8.5 Decomposition Schemes and Features in FDS 5 for Simulating Burning Behaviours of Polyurethane Foam

As seen in the literature, the pyrolysis model such as the one within FDS 5 allows the user to device different types of scheme to represent the heterogeneity of the fuel content and the complexity of the decomposition. Five different schemes with varying level of complexity are investigated in this research and their suitability is assessed by comparing the model and experimental HRRPUA. The cone results of NFR-SB-31 at 50 kW/m^2 are used for comparison because NFR-SB-31 is the simpler base case foam without fire retardant additives. Furthermore, its burning behaviour at 50 kW/m^2 is representative of the common two stage burning behaviour seen at other heat fluxes and for other foams.

For the assessment, the FDS 5 model is constructed with a coarse gas phase mesh of 25 mm to reduce the simulation time and the cone heater is represented as an external heat source which imposes a constant 50 kW/m^2 radiation heat flux on the surface of the foam. The foam sample is modelled as a solid obstruction of 100 by 100 by 50 mm. To simulate the 1-dimensional burning behaviour, only the top surface of the obstruction is assigned as the foam surface which has the specified decomposition scheme while the other surfaces remain inert. The assessment utilises material properties which are determined experimentally in Chapter 3, 4, 5 and 6 as FDS 5 inputs.

Figure 8-13 shows the Smokeview set up of the FDS 5 model for assessing the suitability of the different decomposition schemes. The simulated domain is relatively large in comparison with the sample size which encloses the flame produced thus capturing the model heat release rate and total heat released. In FDS 5, the amount of heat released is calculated in the gas phase which is decoupled from the solid phase relating to material decomposition. The total heat released in the model and in the experiment is compared in Section 8.5.10 to validate the accuracy of FDS 5 in converting solid phase mass loss into gas phase heat released.

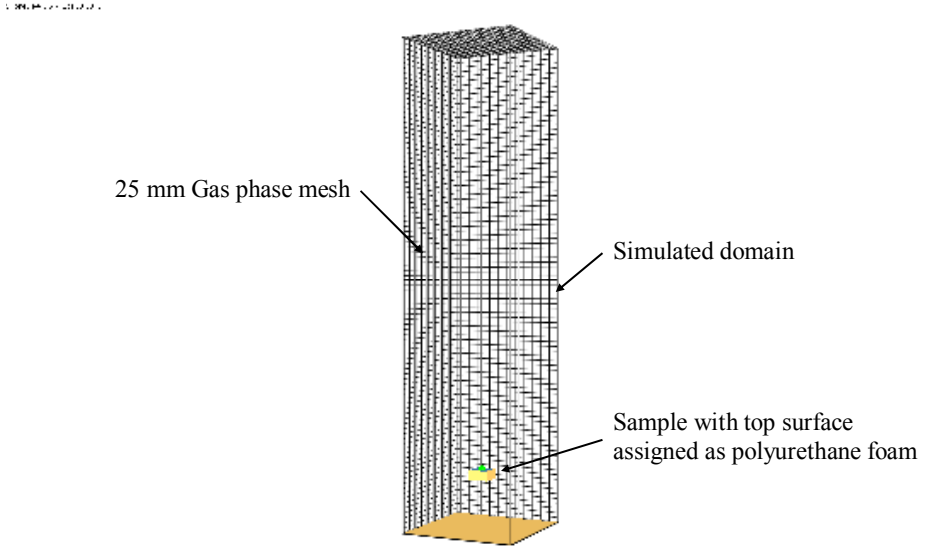

Figure 8-13: Smokeview set up of FDS 5 model with 25 mm gas phase mesh for assessing the suitability of five different decomposition schemes for polyurethane foam

Besides the selection of the decomposition schemes, a few features in FDS 5 such as the solid phase cell size, the back side boundary condition and the gas phase cell size are investigated and the sensitivity of the model results to these parameters are discussed in this section, Section 8.5. The compatibility between the graphically determined kinetic properties and the FDS 5 pyrolysis model is also discussed. Lastly, a summary on the assessment of decomposition schemes is provided and the best scheme for further modelling is chosen.

8.5.1 Scheme 1, Single Reaction Scheme

Scheme 1 is the simplest solid phase decomposition path in FDS 5 which involves a single solid phase reaction that converts a single material component completely into

gaseous fuel. Figure 8-14 shows the schematic of the decomposition path and the material properties required as inputs.

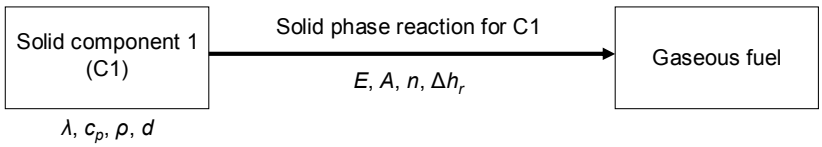

Figure 8-14: Scheme 1, single reaction scheme

The purpose of testing this scheme is to assess the suitability of this simplest scheme in representing the actual 1-dimensional burning behaviour of polyurethane foam. Some of the material properties tabulated in Table 8-1 are used as inputs and as discussed earlier, these properties are determined through a number of different experimental techniques presented in Chapter 3, 4, 5 and 6. Three different sets of material component are tested and the values used for the thermophysical and kinetic properties are tabulated in Table 8-3. Also included as input is the effective heat of combustion and specifically for NFR-SB-31, it is 25 MJ/kg in all the simulations. The effective heat of combustion for the other foams is discussed later.

Table 8-3: Material properties as FDS 5 inputs for Scheme 1

Set	s1-1	s1-2	s1-3
λ (W/mK)	0.049	0.186	0.186
c_p (J/kgK)	2996	2053	2053
ρ (kg/m^3)	31	1019	1019
***d* (mm)**	50.00	1.50	1.50
***E* (kJ/mol)**	88	150	200
***A* (s^{-1})**	2.18×10^{5}	3.06×10^{9}	4.17×10^{13}
n	0.00	0.00	0.00
Δh_r (J/g)	891	233	233

s1-1 has the thermophysical properties of NFR-SB-31 foam and uses the kinetic properties governing the first reaction of the foam sample decomposition. s1-2 and s1-3 have the thermophysical properties of NFR-SB-31 melt but each set uses different kinetic properties. The kinetic properties in s1-2 govern the second reaction of the foam sample decomposition while those in s1-3 govern the single reaction of the melt sample decomposition. The actual cone sample thickness, 50 mm is used as the model input for s1-1 but for s1-2 and s1-3, the thickness is 1.5 mm. This melt thickness is calculated based on the exposed surface area of 0.01 m^2 and the melt density of 1019 kg/m^3 to produce the same fuel content as the actual foam sample.

The values of E and A listed in Table 8-3 are calculated using the normalised Inflection Point Methods where $n = 0$. According to the original Inflection Point Methods[49] depicted in Equation (8-10), when $n = 0$, the mass dependent function, $(1-\alpha)^n$ becomes unity and in the graphical calculations performed, the decomposition effect supposedly allocated to $(1-\alpha)^n$ is transferred to E and A, the constants of the temperature dependent exponential function. Equation (8-10) is a rearranged form of Equation (3-18).

$$\frac{d\alpha}{dT} = \frac{A}{\beta} \cdot e^{-\frac{E}{RT}} (1-\alpha)^n \tag{8-10}$$

These normalised kinetic properties calculated graphically are compatible for use with Scheme 1 because the FDS 5 solid phase cells of this scheme experience shrinking when the solid fuel is consumed during reactions[17,18]. This shrinking phenomenon is applicable to a decomposition scheme where the material components within the reacting layer convert fully into gaseous fuel without the presence of any non-reacting components or the formation of solid residue. As solid fuel is consumed, the shrinking cells reduce in thickness to maintain a constant material density. According to Equation (3-1) which governs the decomposition rate in FDS 5, the constant material density means $\rho_{s,i} = \rho_{s0}$ and n becomes a redundant input as the function of density is unity. Despite the different approach of the normalised Inflection Point Methods where $n = 0$, it actually achieves the same effect as cell shrinking of FDS 5 where n becomes redundant. In both cases, the mass dependent function, $(1-\alpha)^n$ of Equation (8-10) and $(\rho_{s,i}/\rho_{s0})^n$ of Equation (3-1) become unity which makes the decomposition rate solely dependent on temperature. In the subsequent schemes, this redundancy of n is investigated further.

For assessing the suitability of different decomposition schemes, the solid phase cell size is uniformly 0.1 mm and the back side boundary condition is 'VOID'. These same criteria are also applied in Scheme 2 to 5. The solid phase cell is not the same as the gas phase cell visualised using Smokeview, the solid phase cell is applied in the heat transfer calculation through solid. The 'VOID' back side boundary condition

which is the model default assumes the last layer of solid fuel is backed up against an air gap at ambient temperature. In later sections, the sensitivity of the model results to different solid and gas phase cell sizes and different back side boundary conditions are investigated. Figure 8-15 compares the model HRRPUA using Scheme 1 with the experimental HRRPUA of NFR-SB-31 at 50 kW/m^2.

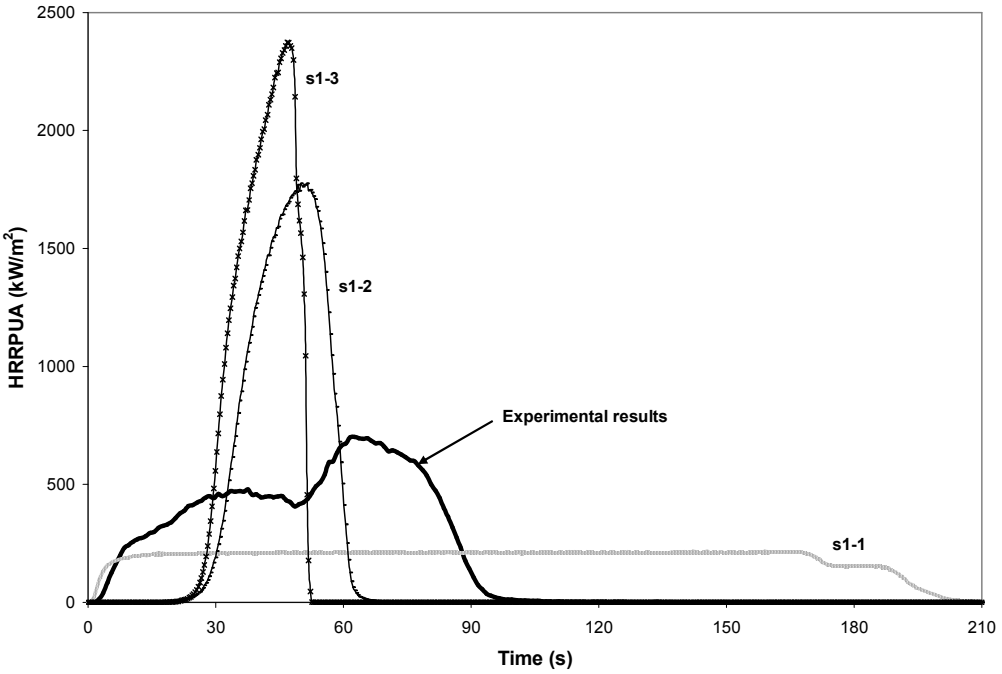

Figure 8-15: Comparison between FDS 5 HRRPUA using Scheme 1 and experimental HRRPUA of NFR-SB-31 at 50 kW/m^2

From the comparison, Scheme 1 does not capture the two stage burning behaviour of the experimental HRRPUA. s1-1 predicts the initiation of the burning process and part of the initial growth but once the model HRRPUA reaches 200 kW/m^2, it remains constant until burnout. The HRRPUA of s1-2 and s1-3 share very similar trend showing a delay of 30 s before rapidly rising to their respective peak, 1800 and 2400 kW/m^2.

s1-1 is able to predict the start and initial growth in the first stage with better accuracy than s1-2 and s1-3. This is because the kinetic properties of s1-1 are developed from the first reaction of foam decomposition which occurs over a lower range of reaction temperature than the second foam reaction implemented in s1-2 and the melt reaction

implemented in s1-3. Also, s1-1 uses the thermophyiscal properties of foam which produce lower heat capacity than melt thus the material component of s1-1 heats up faster. However, over the second stage, s1-1 underpredicts the subsequent increase in HRRPUA while s1-2 and s1-3 overpredicts because the kinetic properties of s1-2 and s1-3 are developed respectively from the second foam reaction and the melt reaction that possess greater reaction rate than the first foam reaction implemented in s1-1. From Figure 8-15, the growth and peak of the HRRPUA of s1-3 is greater than s1-2 despite both having the kinetic properties that essentially govern the same reaction relating to the decomposition of melt. This difference is related to the physical variations between the foam and melt samples tested in the SDT experiments, the variations in the TGA results obtained and the sensitive nature of the exponent based decomposition rate equation from which the kinetic properties are developed.

8.5.2 Scheme 2, Multi Reactions Scheme

In Scheme 2, the single material component undergoes two solid phase reactions and converts fully into gaseous fuel. Instead of using either the thermophysical properties of foam or melt, the single material component is a combination of both materials in terms of density and thickness while the thermal conductivity and specific heat change as a function of temperature. Figure 8-16 shows the schematic of the decomposition path and the material properties required as inputs.

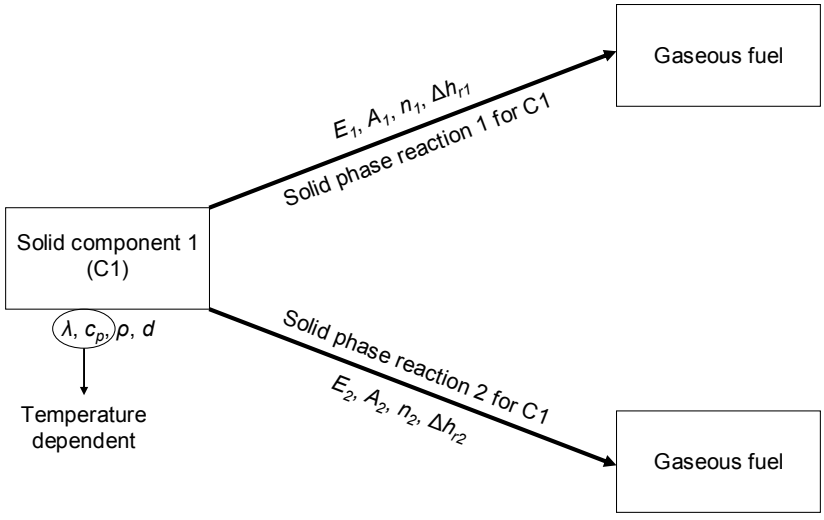

Figure 8-16: Scheme 2, multi reactions scheme

Three different sets of material component are simulated and the values used are tabulated in Table 8-4. The temperature range and the corresponding values of thermal conductivity and specific heat are reported. The two sets of kinetic properties specified are from the first and second reactions of the polyurethane foam decomposition, denoted by the subscript '*1*' and '*2*'.

Table 8-4: Material properties as FDS 5 inputs for Scheme 2

Set	s2-1	s2-2	s2-3
λ (W/mK)	Less than 222 °C, 0.049 222-310 °C, 0.049-0.186 Greater than 310 °C, 0.186	Less than 222 °C, 0.049 222-310 °C, 0.049-0.186 Greater than 310 °C, 0.186	Less than 222 °C, 0.049 222-310 °C, 0.049-0.186 Greater than 310 °C, 0.186
c_p (J/kgK)	Less than 222 °C, 2996 222-310 °C, 2996-2053 Greater than 310 °C, 2053	Less than 222 °C, 2996 222-310 °C, 2996-2053 Greater than 310 °C, 2053	Less than 222 °C, 2996 222-310 °C, 2996-2053 Greater than 310 °C, 2053
ρ (kg/m^3)	297	297	297
d (mm)	5.20	5.20	5.20
E_1 (kJ/mol)	138	138	88
A_1 (s^{-1})	3.69×10^{10}	3.69×10^{10}	2.18×10^{5}
n_1	7.48	0.00	0.00
Δh_{r1} (J/g)	891	891	891
E_2 (kJ/mol)	213	213	150
A_2 (s^{-1})	1.15×10^{15}	1.15×10^{15}	3.06×10^{9}
n_2	1.16	0.00	0.00
Δh_{r2} (J/g)	233	233	233

Similar to Scheme 1, the material component of this scheme converts fully from solid into gaseous fuel which means the solid phase cells experience shrinking during reactions. The redundancy of n is investigated through s2-1 and s2-2 where both sets have essentially the same material properties except for n which is calculated by the original Inflection Point Methods[49] in the former and forced to 0 in the latter. s2-1 and s2-2 uses E and A determined from the original Inflection Point Methods while s2-3 uses E and A determined from the normalised version where the decomposition is assumed to be temperature dependent only.

The TGA results provide some useful insights on the temperature range where the physical state of the sample changes due to decomposition. From this information, the temperature dependent function of thermal conductivity and specific heat are derived. The TGA sample mass and mass loss/°C in Figure 8-17 show the first and second reactions of polyurethane foam decomposition and their respective temperature range at the heating rate of 1 °C/min. Table 8-5 defines the characteristic temperatures

separating the three different physical states of the sample identified as foam, mixed and melt in Figure 8-17.

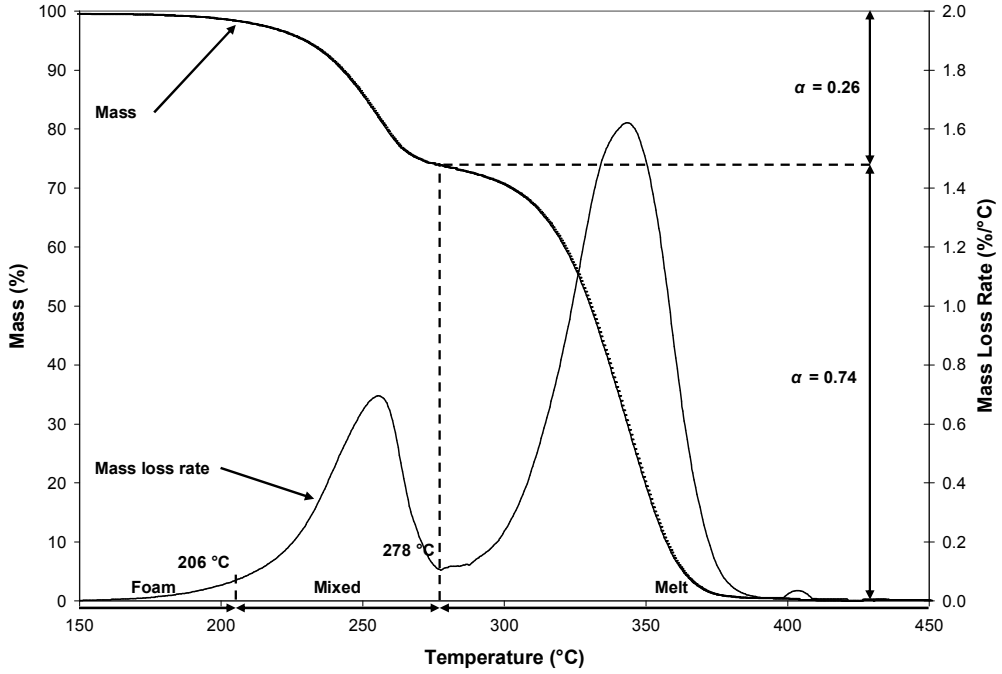

Figure 8-17: TGA sample mass and mass loss/°C versus temperature at 1 °C/min, a repetition of NFR-SB-31

Table 8-5: Definition of characteristic temperatures separating the foam, mixed and melt states of the decomposing polyurethane foam

Characteristic temperature (°C)	Definition
206	Temperature where the mass loss/°C is 10 % of the first peak. Prior to this temperature, the sample is in the state of polyurethane foam. After this temperature, the foam starts to break down into melt and the sample becomes a mixture of foam and melt.
278	Temperature between two peaks where the mass loss/°C is at minimum. At this temperature, the first reaction is completed where the fraction of sample decomposed, α is 0.26 and the remaining 0.74 is in the final state, melt.

The same definitions of characteristic temperatures are applied to describe the changes in thermal conductivity and specific heat of Scheme 2 in Table 8-4. But instead of basing on a specific heating rate, the average characteristic temperatures from all the heating rates tested, 1, 5, 20 and 60 °C/min are used. The averages are found to be 222 and 310 °C respectively. Prior to 222 °C, the sample has not experienced any reactions and remains in the state of polyurethane foam so over this

temperature range, the foam properties are used. Between 222 and 310 °C, the sample undergoes the first reaction and it remains in the state of a mixture of foam and melt. As foam structure starts to collapse into melts over this temperature range, the thermophysical properties are modelled to change linearly from those of foam into those of melt. After the completion of the first reaction, the sample has become melt and it undergoes the second reaction from 310 °C until the end of decomposition. Assuming the foam structure has completely collapsed into melts by the start of the second reaction, the melt properties are used from 310 °C onwards. While the thermal conductivity and specific heat in FDS 5 can be a function of temperature, the density and thickness are not temperature dependent. Therefore, for the density and thickness, the material component modelled is designed as a combination of foam and melt properties which requires the calculation of effective values.

The effective density is determined based on the thermal influence from the three different physical states. Between the initial temperature in FDS 5, 20 °C and the average final temperature from the TGA results of NFR-SB-31, 408 °C, the sample occupies 52 % of this temperature range as foam, 25 % as melt and 23 % as the mixture of both. The density of the foam and melt measures 31 and 1019 kg/m^3 respectively and these are obtained directly from Table 2-1. The density of the mixture is calculated based on the mass fraction of foam and melt obtained from the TGA results. From all the heating rates tested, the average fraction of mass remaining at the minimum mass loss/°C, at 310 °C is 0.74. Assuming all the gaseous fuel is lost instantly at 310 °C, the sample consists of 26 % foam and 74 % melt during the mixture state between 222 and 310 °C. This mixture state is assumed to be made up of a layer of foam and a layer of melt. For ease of demonstrating the calculation of mixture density, assumes the foam and melt layers respectively has 0.26 and 0.74 kg of mass. For a surface area of 1 m^2 for each layer, the thickness of the foam and melt are 8.50 and 0.72 mm, determined from their respective density of 31 and 1019 kg/m^3. The combined thickness of both layers is 9.22 mm thus for the surface area of 1 m^2 and the total mass of 1 kg, the mixture density is found to be 108 kg/m^3.

Based on the foam, mixture and melt densities found and the percentage of temperature range each state occupied, the effective density is calculated using

Equation (8-11). The subscript '*eff*', '*foam*', '*mix*' and '*melt*' respectively denote the effective value, the foam value, the mixture value and the melt value. For NFR-SB-31, the effective density is 297 kg/m^3.

$$\rho_{eff} = \rho_{foam} \cdot \frac{PC_{foam}}{100} + \rho_{mix} \cdot \frac{PC_{mix}}{100} + \rho_{melt} \cdot \frac{PC_{melt}}{100} \tag{8-11}$$

The cone sample mass of NFR-SB-31 is 15.4 g so with the effective density of 297 kg/m^3 and the sample sides measuring 100 mm, the effective thickness is found to be 5.2 mm. Figure 8-18 compares the model HRRPUA using Scheme 2 with the experimental HRRPUA of NFR-SB-31 at 50 kW/m^2.

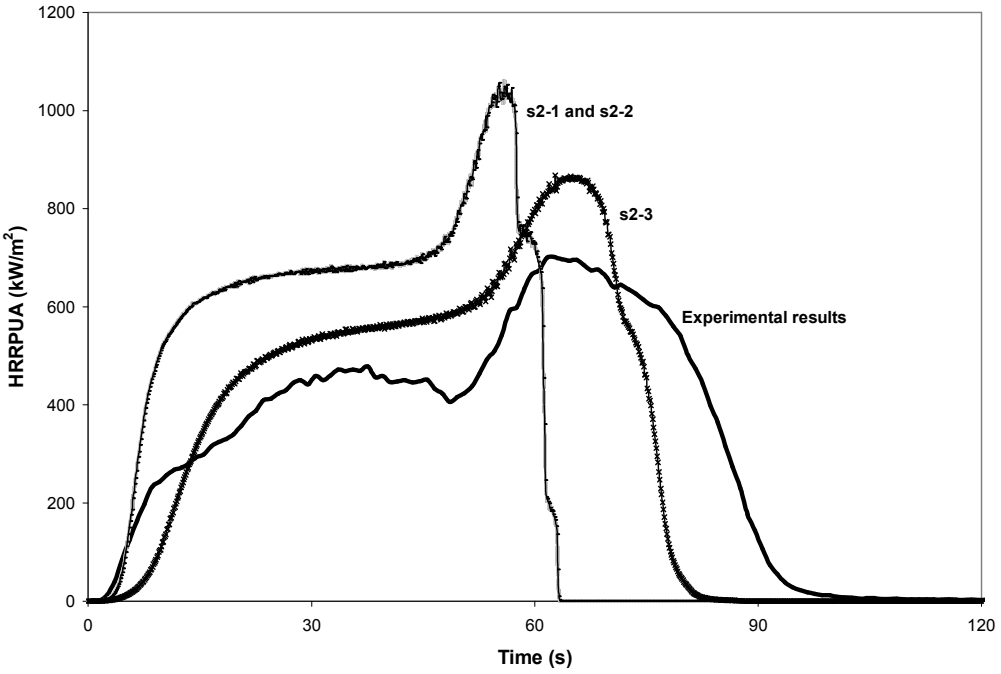

Figure 8-18: Comparison between FDS 5 HRRPUA using Scheme 2 and experimental HRRPUA of NFR-SB-31 at 50 kW/m^2

The comparison shows that with Scheme 2, the modelled material is able to burn in a similar two stage fashion as depicted in the experimental results. The results of s2-1 and s2-2 where the material properties differ only in *n* are exactly identical thus proving the redundancy of *n* in this scheme. Therefore, it is necessary to allocate the decomposition effect of *n* to *E* and *A* by recalculating the kinetic properties using the

normalised Inflection Point Methods. Using the normalised kinetic properties as inputs, s2-3 shows an improved comparison with the experimental HRRPUA.

8.5.3 Scheme 3, Multi Layers Scheme

In Scheme 3, two separate layers each containing one material component undergoes a single solid phase reaction converting from solid into gaseous fuel. Both layers are contained within the same top surface of the obstruction that defines the foam sample. The scheme is developed in accordance with the changes in the sample's physical state during the TGA experiment where the first layer consists of foam component while the second layer consists of melt component. Figure 8-19 shows the schematic of the decomposition path and the material properties required as inputs.

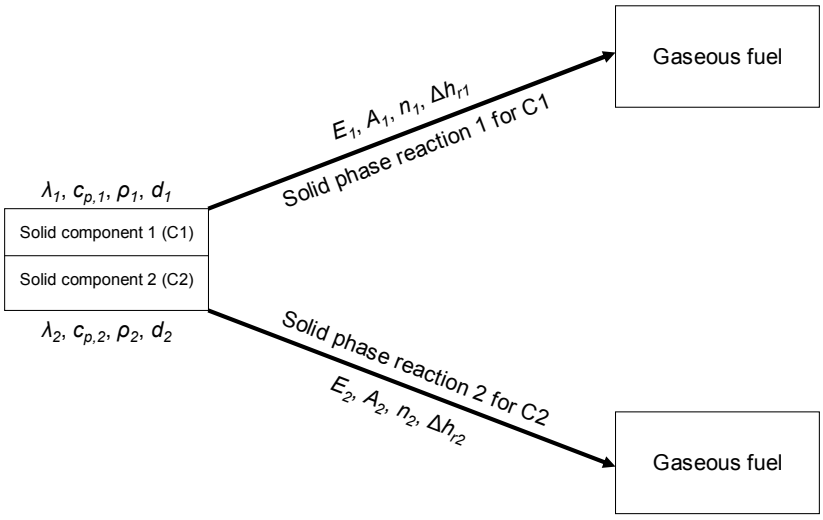

Figure 8-19: Scheme 3, multi layers scheme

Again, three different sets of material component tabulated in Table 8-6 are simulated. Two sets of thermophysical and kinetic properties denoted by the subscript '*1*' and '*2*' represent the foam and melt layers respectively.

Table 8-6: Material properties as FDS 5 inputs for Scheme 3

Set	s3-1	s3-2	s3-3
λ_1 **(W/mK)**	0.049	0.049	0.049
$c_{p,1}$ **(J/kgK)**	2996	2996	2996
ρ_1 **(kg/m^3)**	31	31	31
d_1 **(mm)**	13.11	13.11	13.11
λ_2 **(W/mK)**	0.186	0.186	0.186

$c_{p,2}$ (J/kgK)	2053	2053	2053
ρ_2 (kg/m^3)	1019	1019	1019
d_2 (mm)	1.12	1.12	1.12
E_1 (kJ/mol)	138	138	88
A_1 (s^{-1})	3.69×10^{10}	3.69×10^{10}	2.18×10^{5}
n_1	7.48	0.00	0.00
Δh_{r1} (J/g)	891	891	891
E_2 (kJ/mol)	213	213	150
A_2 (s^{-1})	1.15×10^{15}	1.15×10^{15}	3.06×10^{9}
n_2	1.16	0.00	0.00
Δh_{r2} (J/g)	233	233	233

Similar to Scheme 2, to investigate the redundancy of *n* on decomposition, *n* of s3-1 is determined using the original Inflection Point Methods[49] while for s3-2, *n* is forced to 0. The values of *E* and *A* for s3-1 and s3-2 are determined using the original Inflection Point Methods. On the other hand, s3-3 uses the normalised *E* and *A* as inputs. The mass of NFR-SB-31 cone sample is 15.4 g and distributing this mass according to the TGA mass fraction of foam and melt determined previously, 0.26 and 0.74, the mass allocated in the foam and melt layer is 4.0 and 11.4 g. Given the exposed top surface area is 0.01 m^2, using the density and the fuel content of both layers, the thickness of the foam and melt layers is calculated to be 13.1 and 1.1 mm. Figure 8-20 compares the model HRRPUA using Scheme 3 with the experimental HRRPUA of NFR-SB-31 at 50 kW/m^2.

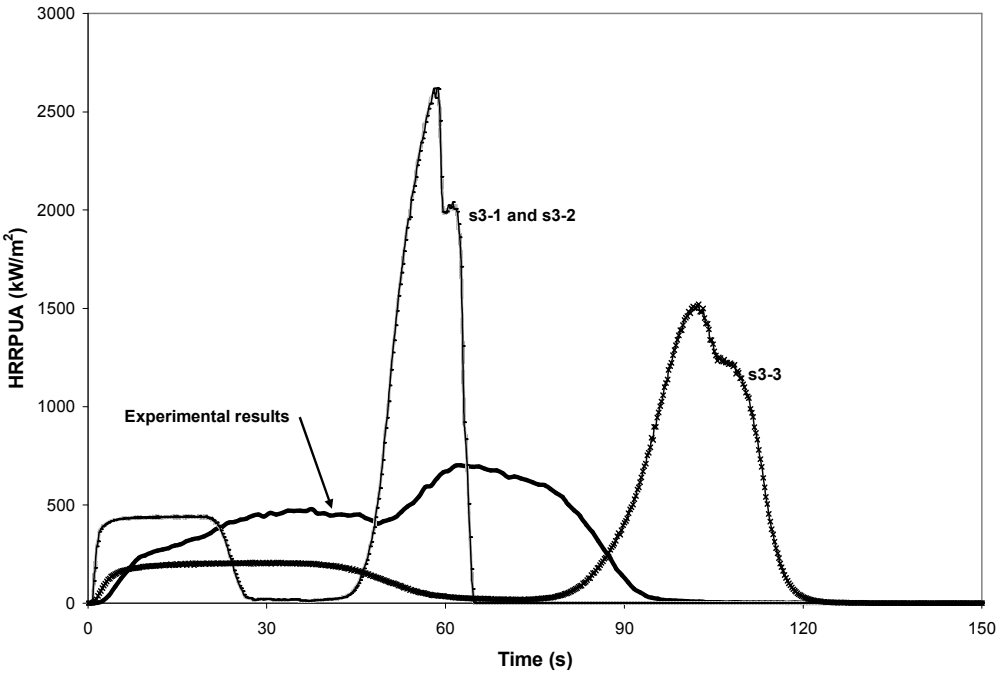

Figure 8-20: Comparison between FDS 5 HRRPUA using Scheme 3 and experimental HRRPUA of NFR-SB-31 at 50 kW/m^2

From Figure 8-20, the simulation results show that Scheme 3 produces a distinct two stage burning behaviour but it cannot predict the experimental HRRPUA due to the discontinuity of burning between layers and the overprediction during the burning of the second melt layer. Since the reacting material component in both layers converts fully into gaseous fuel, *n* becomes a redundant parameter due to density preservation. This is proven by the results of s3-1 and s3-2 which are effectively identical despite having different *n*. Therefore, it is necessary to distribute the decomposition effect of *n* to *E* and *A* as implemented in s3-3. The results show that this has the effect of lowering the HRRPUA and extending the burning duration.

8.5.4 Scheme 4, Mass Fraction Scheme

Scheme 4 defines the sample as a single layer comprising of two material components. The amount of fuel contributed by each material component is governed by the user specified mass fractions and each component undergoes one solid phase reaction converting the solid fuel into gaseous fuel. This scheme essentially assumes

the pyrolysis front consists of a constant mass fraction of foam and melt. Figure 8-21 shows the schematic of the decomposition path and the material properties required as inputs.

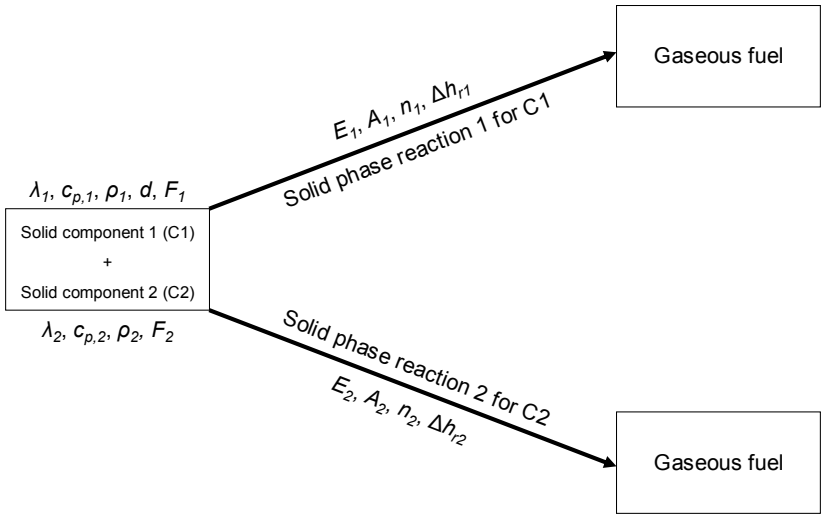

Figure 8-21: Scheme 4, mass fraction scheme

Table 8-7 contains the thermophysical and kinetic properties of the scheme. The additional parameter specified for this scheme which is the mass fraction of each material component is also included. Subscript '*1*' and '*2*' denote the material properties for the two material components, foam and melt. Since both components are within a single layer, one combined thickness is specified.

Table 8-7: Material properties as FDS 5 inputs for Scheme 4

Set	s4-1	s4-2
λ_1 **(W/mK)**	0.049	0.049
$c_{p,1}$ **(J/kgK)**	2996	2996
ρ_1 **(kg/m^3)**	31	31
d **(mm)**	14.23	14.23
F_1	0.26	0.26
λ_2 **(W/mK)**	0.186	0.186
$c_{p,2}$ **(J/kgK)**	2053	2053
ρ_2 **(kg/m^3)**	1019	1019
F_2	0.74	0.74
E_1 **(kJ/mol)**	138	138
A_1 **(s^{-1})**	3.69×10^{10}	3.69×10^{10}
n_1	7.48	0.00
Δh_{r1} **(J/g)**	891	891
E_2 **(kJ/mol)**	213	213
A_2 **(s^{-1})**	1.15×10^{15}	1.15×10^{15}
n_2	1.16	0.00
Δh_{r2} **(J/g)**	233	233

The values of E and A of s4-1 and s4-2 are calculated using the original Inflection Point Methods[49]. To investigate the redundancy of n, n of s4-1 is calculated from the original Inflection Point Methods while n of s4-2 is forced to 0. As inputs, the mass fraction of foam and melt in the single layer is 0.26 and 0.74, in accordance with the TGA results of NFR-SB-31. Although the individual value for thermal conductivity, specific heat and density are specified for each material component, the simultaneous presence of both components in the same layer means a single thickness needs to be determined for this mixture. From the thickness calculation in Scheme 3 which utilises the same mass fractions, the combined thickness of foam and melt mixture is 14.2 mm for an exposed surface area of 0.01 m^2. Although not required as an input, the density of this mixture can be back-calculated to 108 kg/m^3 for the known sample mass, 15.4 g. This density is the same as the mixture density previously derived in Scheme 2. Figure 8-22 compares the model HRRPUA using Scheme 4 with the experimental HRRPUA of NFR-SB-31 at 50 kW/m^2.

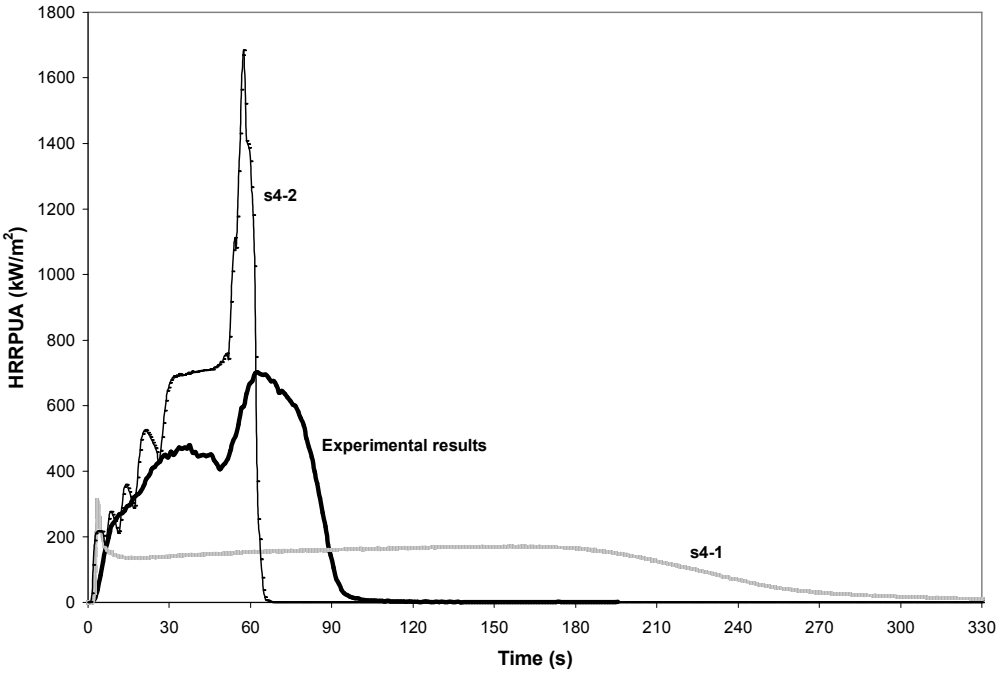

Figure 8-22: Comparison between FDS 5 HRRPUA using Scheme 4 and experimental HRRPUA of NFR-SB-31 at 50 kW/m^2

According to Scheme 1, the foam component has been shown to react earlier but at a slower rate than the melt component as seen in Figure 8-15. Since both components are currently within the same layer for Scheme 4, this difference between the foam and melt components means that there will be unreacted melt component as the decomposition progresses. The unreacted melt alters the instantaneous density of the layer and $\rho_{s,i}/\rho_{s0}$ in Equation (3-1) is no longer in unity which means n will influence the decomposition rate. This is proven in Figure 8-22 where a significant difference in HRRPUA is noted between s4-1 and s4-2 which only differs in n. Between the two simulations, s4-1 shows the correct results because it uses the proper n that includes the mass dependent decomposition effect. The model HRRPUA shows a level plateau suggesting a rather uniform burning behaviour and underpredicts the experimental HRRPUA.

8.5.5 Scheme 5, Residue Formation Scheme

In Scheme 5, a single material component is contained within a single layer and it undergoes one reaction to decompose into solid residue and gaseous fuel. The proportion of residue and gaseous fuel produced following this initial breakdown are governed by a pair of user defined yields. The gaseous fuel contributes immediately towards the gas phase combustion while the solid residue remains for the second reaction at higher temperature where the residue decomposes completely into gaseous fuel. Based on the TGA results, the first reaction of Scheme 5 represents the breakdown of the foam structure while the second reaction represents the further decomposition of the melts. Figure 8-23 shows the schematic of the decomposition path and the material properties required as inputs.

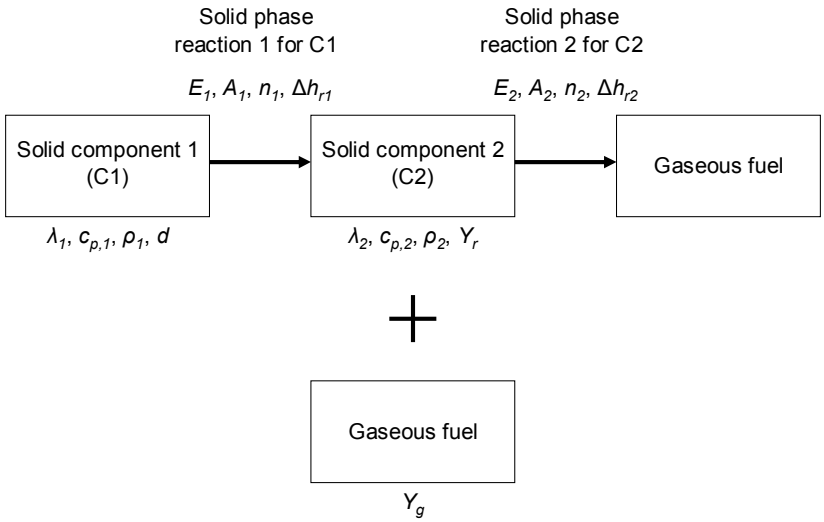

Figure 8-23: Scheme 5, residue formation scheme

The thermophysical and kinetic properties of the scheme are tabulated in Table 8-8 and subscript '*1*' and '*2*' denote the material properties for foam and melt respectively. The additional parameters, the yields of the residue and gaseous fuel which are produced following the first reaction are also included in the table.

Table 8-8: Material properties as FDS 5 inputs for Scheme 5

Set	s5-1	s5-2
λ_1 (W/mK)	0.049	0.049
$c_{p,1}$ (J/kgK)	2996	2996
ρ_1 (kg/m^3)	31	31

d (mm)	50.00	50.00
λ_2 (W/mK)	0.186	0.186
$c_{p,2}$ (J/kgK)	2053	2053
ρ_2 (kg/m^3)	1019	1019
Y_r	0.74	0.74
Y_g	0.26	0.26
E_1 (kJ/mol)	138	138
A_1 (s^{-1})	3.69×10^{10}	3.69×10^{10}
n_1	7.48	0.00
Δh_{r1} (J/g)	891	891
E_2 (kJ/mol)	213	213
A_2 (s^{-1})	1.15×10^{15}	1.15×10^{15}
n_2	1.16	0.00
Δh_{r2} (J/g)	233	233

Similar to Scheme 4, *E* and *A* of s5-1 and s5-2 are determined by the original Inflection Point Methods[49]. To investigate the redundancy of *n*, *n* of the former is determined by the original Inflection Point Methods while *n* of the latter is forced to 0. This scheme requires the specification of melt component as the solid residue of the first reaction and also the yields which govern the amount of residue and gaseous fuel produced following the first reaction. Again, using the information from the TGA experiments of NFR-SB-31, the residue yield is 0.74 and the gaseous yield is 0.26. Since the initial state of the fuel is foam and the experimental sample dimensions are also modelled, the actual thickness of the cone sample, 50 mm is used as the model thickness. Figure 8-24 compares the model HRRPUA using Scheme 5 with the experimental HRRPUA of NFR-SB-31 at 50 kW/m^2.

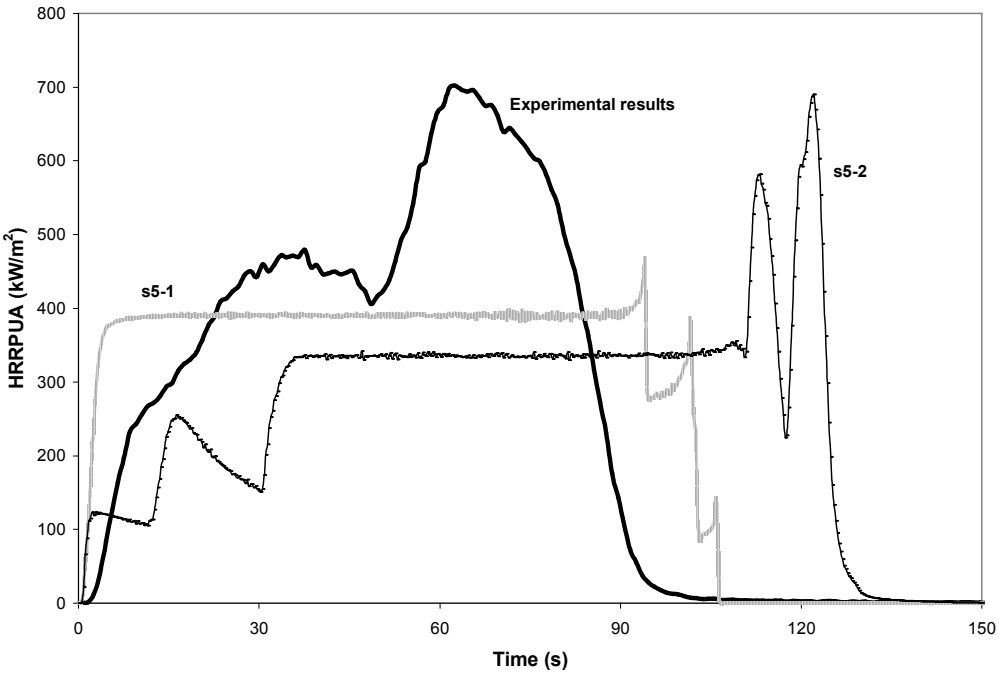

Figure 8-24: Comparison between FDS 5 HRRPUA using Scheme 5 and experimental HRRPUA of NFR-SB-31 at 50 kW/m^2

As foam decomposes into melt, the thermophysical properties change from those of foam into those of melt. Due to the formation of melt as residue which has a different density than the original foam component, $\rho_{s,i}/\rho_{s0}$ of Equation (3-1) is not unity. Therefore, n has influence on the decomposition rate which is proven by the different results seen between s5-1 and s5-2 that differ only in n. Focusing on the correct results in s5-1 where n is specified correctly to include the mass dependent decomposition effect, the pattern of burning shows a level plateau similar to s4-1 but with greater magnitude, approximately 400 kW/m^2. This scheme overpredicts the initial growth rate and final decay of the HRRPUA but underpredicts the magnitude over the majority of the first and second stages.

8.5.6 Effect of Different Solid Phase Cell Sizes

Different to the gas phase cell which is visualised by Smokeview in Figure 8-13, the solid phase cell is applied to each material layer specified under the designated surface of the solid obstruction. The solid phase cells are used to solve the 1-

dimensional heat transfer equation through the solid. By default, FDS 5 utilises non-uniform solid phase cell where the finest mesh is assigned to the boundaries of the layer and moving inwards, the mesh size becomes progressively coarser. The uniformity of the solid phase cell in FDS 5 is controlled by a user defined parameter known as the stretch factor which is a number between 1 and 2[17]. The former produces a uniform mesh and the latter is the model default. The effect of non-uniform and uniform 0.1 mm cell sizes has on the simulated HRRPUA is investigated and Figure 8-25 shows the comparison between the simulated results and the actual experimental results.

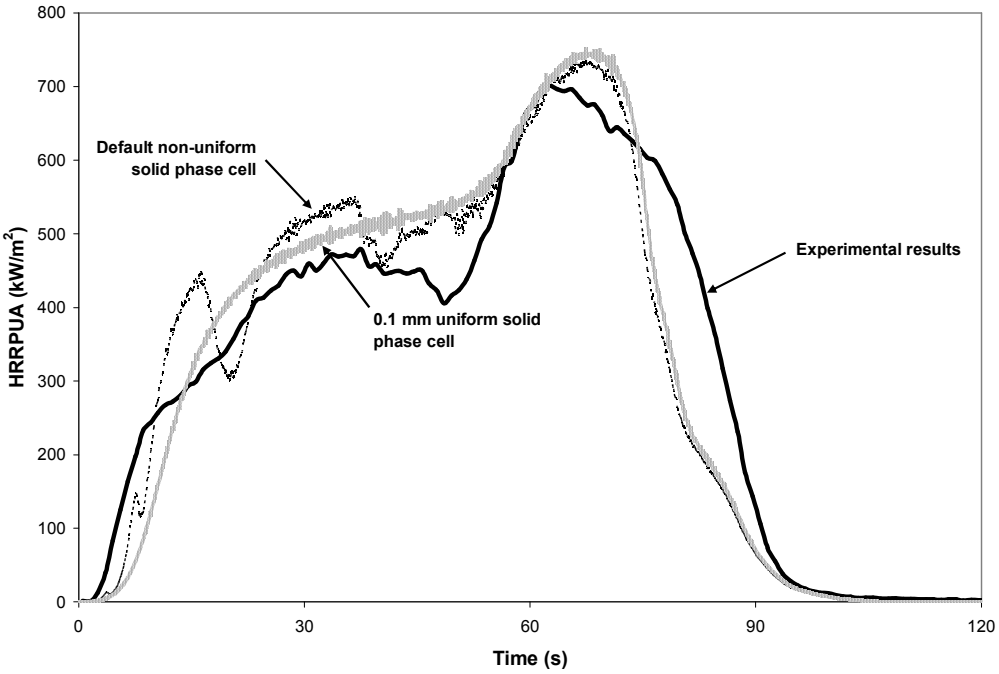

Figure 8-25: Effect of solid phase cell uniformity on FDS 5 HRRPUA of Scheme 2 in comparison with experimental HRRPUA of NFR-SB-31 at 50 kW/m^2

The simulations with non-uniform and uniform solid phase cell sizes are performed using the material properties of s2-3. For this cell uniformity investigation, the gas phase cell size in both simulations is 10 mm and instead of using an external heat flux, the cone heater is modelled based on the actual heater's dimensions. Since this 10 mm mesh is finer in comparison with the 25 mm mesh in Figure 8-18, this expectedly changes the simulated HRRPUA. The effect of different gas phase cell sizes on HRRPUA is discussed later in more details. From Figure 8-25, the use of the

default non-uniform solid phase cell has resulted in the increase of simulation noise which has no relation to the actual physical process.

Besides the stretch factor, another parameter known as the cell size factor also governs the solid phase cell size in FDS 5. The smallest cell size, δ_{min} is determined according to Equation (8-12)[18] which relates to the cell size factor, S and the square root of the material thermal diffusivity, $\sqrt{\frac{\lambda}{\rho c_p}}$.

$$\delta_{\min} < S\sqrt{\frac{\lambda}{\rho c_p}} \tag{8-12}$$

By setting the stretch factor to 1 for uniformity and establishing the thermal diffusivity of the material, S can then be adjusted to produce solid phase cell of any intended size. This is done to investigate the sensitivity of the model results to the different cell sizes. The determination of the appropriate S for Scheme 1, 2 and 5 is straightforward. The single set of thermophysical properties in Scheme 1 and 2 are used while for Scheme 5, the properties of foam which is the sample's initial state are used. Both the stretch factor and the cell size factor are applied to a surface so for Scheme 3 where two layers are contained within the same surface, S is determined using the thermophysical properties of the melt layer which is allocated the greater fuel content compared to the foam layer. In Scheme 4, the foam and melt components are simultaneously present in the same layer so the thermophysical properties for calculating S are the combination of the two components according to their respective mass fractions. The combined properties are calculated using Equation (8-13) where θ represents the values of λ, c_p and ρ of the foam and melt components denoted by subscript '*1*' and '*2*' respectively. The subscript '*comb*' denotes the value for the combined properties.

$$\theta_{comb} = \theta_1 \cdot F_1 + \theta_2 \cdot F_2 \tag{8-13}$$

Thus for Scheme 4, the combined value of λ, c_p and ρ is found to be 0.150 W/mK, 2298 J/kgK and 762 kg/m^3. The density found from Equation (8-13), 762 kg/m^3

differs from 108 kg/m^3 reported previously for Scheme 4. 762 kg/m^3 is used in the solid phase heat transfer calculation while 108 kg/m^3 is used in the fuel content calculation. Table 8-9 shows the cell size factor required for each scheme to produce three different solid phase cell sizes, 0.50, 0.10 and 0.05 mm.

Table 8-9: Cell size factors and the corresponding solid phase cell sizes for different schemes

Cell size, δ_{min} (mm)	Cell size factor, S for different schemes				
	Scheme 1[a]	Scheme 2	Scheme 3	Scheme 4	Scheme 5
0.50	1.68	2.13	1.68	1.71	0.69
0.10	0.34	0.43	0.34	0.34	0.14
0.05	0.17	0.21	0.17	0.17	0.07

The effect of different cell sizes on the simulated HRRPUA is depicted in Figure 8-26 for the five schemes considered. The simulation sets in each scheme only differs in the solid phase cell size, the other material properties are obtained from s1-3, s2-3, s3-3, s4-1 and s5-1 respectively.

[a] The cell size factor presented for Scheme 1 is when the thermophysical properties of melt are used. Similar sensitivity analysis is not performed for the foam properties. For the single simulation involving foam properties, s1-1, 0.1 mm cell size is used and for that, S is 0.14.

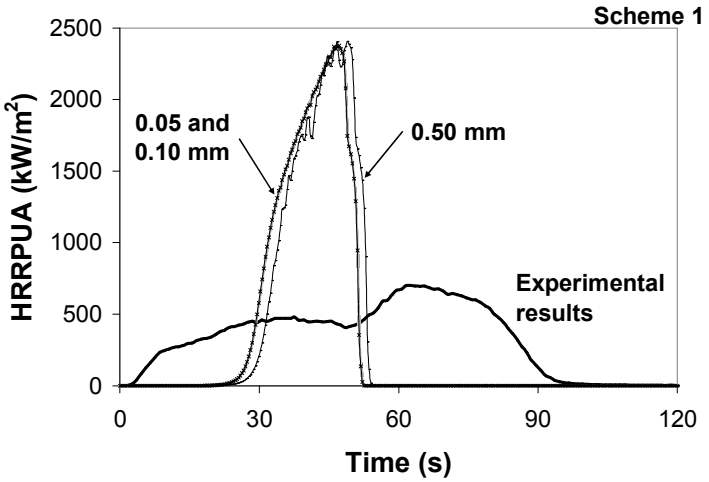
Scheme 1
HRRPUA (kW/m2)
2500
2000
1500
1000
500
0
0.05 and
0.10 mm
0.50 mm
Experimental
results
0
30
60
90
120
Time (s)

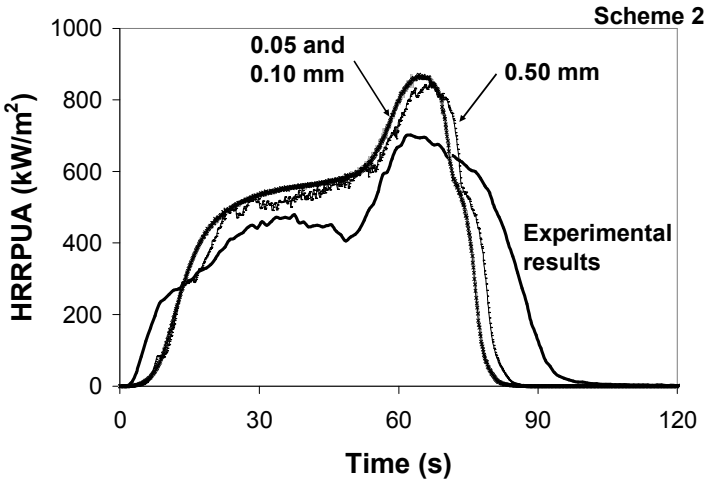
Scheme 2
HRRPUA (kW/m2)
1000
800
600
400
200
0
0.05 and
0.10 mm
0.50 mm
Experimental
results
0
30
60
90
120
Time (s)

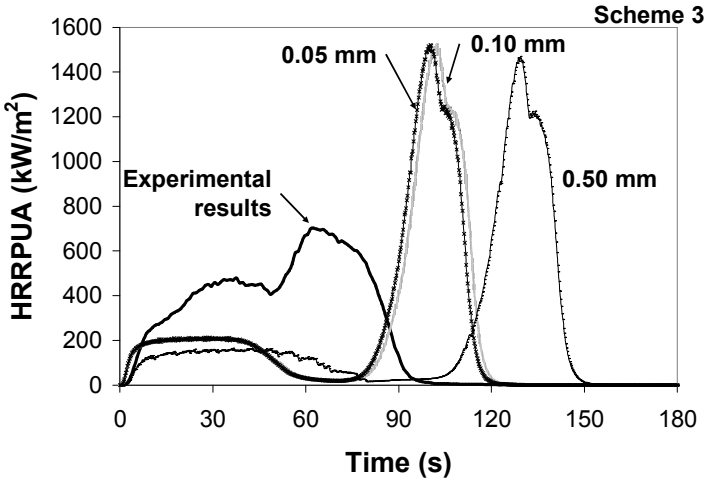
Scheme 3
HRRPUA (kW/m2)
1600
1400
1200
1000
800
600
400
200
0
0.05 mm
0.10 mm
Experimental
results
0.50 mm
0
30
60
90
120
150
180
Time (s)

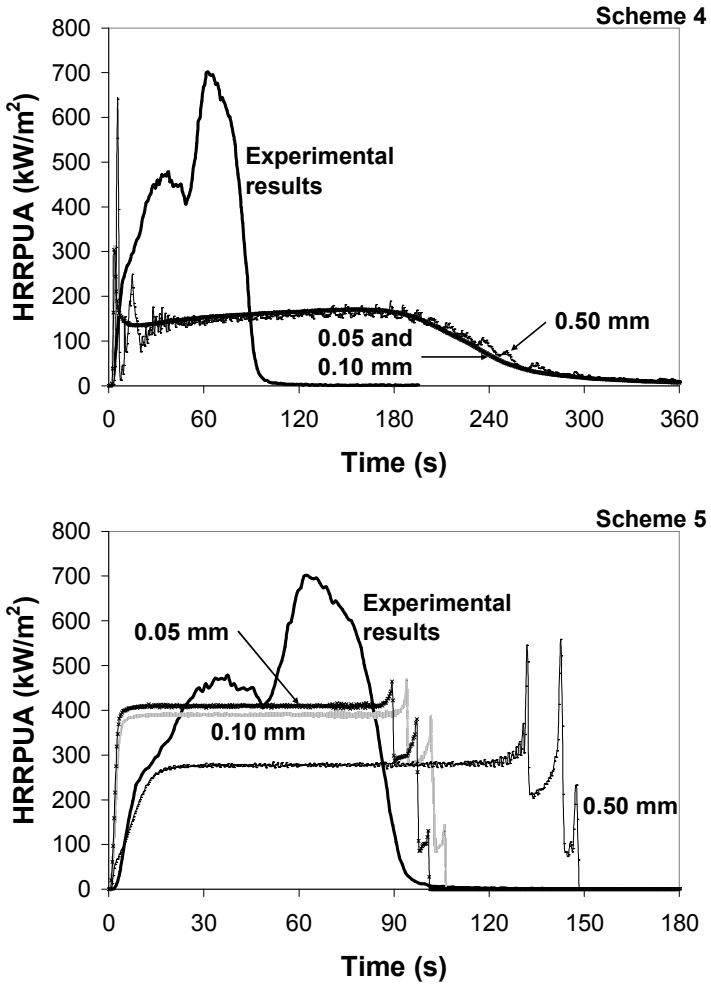

Figure 8-26: Effect of different uniform solid phase cell sizes, 0.50, 0.10 and 0.05 mm on FDS 5 HRRPUA of different schemes in comparison with experimental HRRPUA of NFR-SB-31 at 50 kW/m^2

In all schemes, the coarsest mesh, 0.50 mm tends to produce greater simulation noise when compared with the finer meshes, 0.10 and 0.05 mm. The HRRPUA of Scheme 1, 2 and 4 is not sensitive to the solid phase cell as their results appear to have negligible changes at different cell sizes. However, certain schemes are definitely more sensitive, particularly those having multiple layers within the same surface such as Scheme 3 and those with the formation of residue such as Scheme 5. In Scheme 3, the burning trend of the second melt layer is actually similar among the different cell sizes except for a ~30 s delay in the case of 0.50 mm. This is due to an equivalent extension during the burning of the first foam layer. The changes in cell size appear to

affect Scheme 5 the most as the results show the HRRPUA increases by ~50 % when the cell size changes from 0.50 to 0.05 mm.

8.5.7 Effect of Different Back Side Boundary Conditions

The effect that different back side boundary conditions have on the simulated HRRPUA in FDS 5 is investigated for Scheme 2, the multi reactions scheme. Three different conditions are considered and these are 'VOID' which is the default, 'INSULATED' and the specification of the backing material used in the actual cone experiments. Except for the different boundary conditions, the material properties used in the different simulations are identical to s2-3. According to the definition in FDS 5[17,18], 'VOID' means the layer of material component is backed to an open space at ambient temperature while 'INSULATED' means the layer is backed to a perfectly insulated boundary. The backing material of the cone sample is a type of high density calcium silicate board and it is modelled as the second layer beneath the sample which forms the first layer. The structure of this model is similar to Scheme 3, the multi layers scheme described previously. The backing material is non-combustible so the kinetic properties are not required. For the thermophysical properties, λ is 0.257 W/mK, c_p is 609 J/kgK, ρ is 932 kg/m^3 and thickness is 18 mm. The thermal conductivity and specific heat are measured from the Hot Disk experiment[97] while the density and thickness are measured from the physical object itself. Figure 8-27 compares the simulated HRRPUA using different back side boundary conditions with the experimental HRRPUA of NFR-SB-31 at 50 kW/m^2.

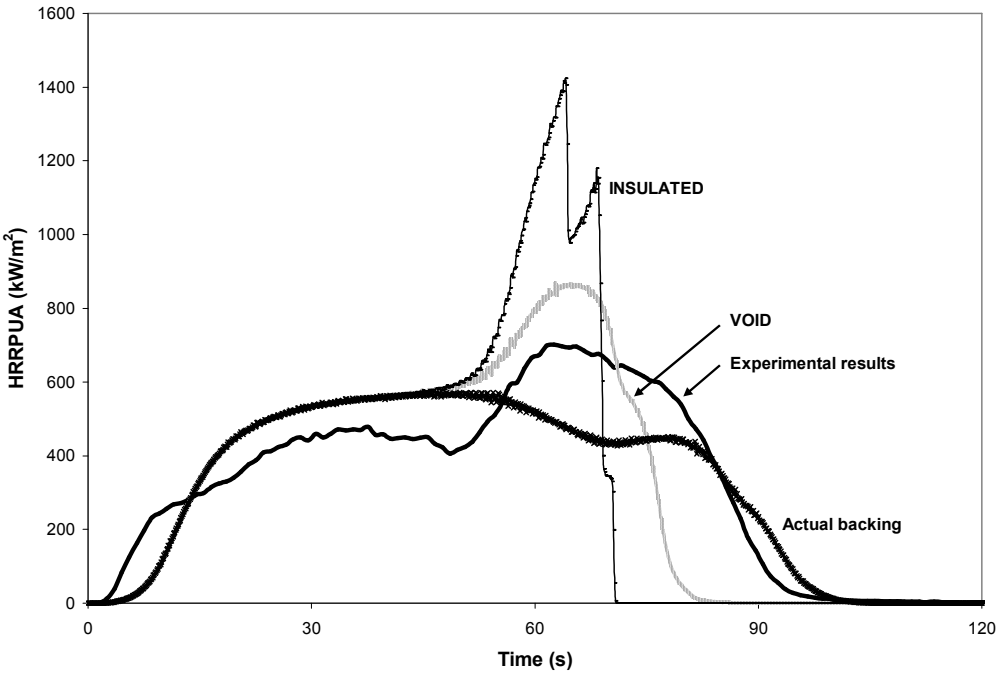

Figure 8-27: Effect of different back side boundary conditions, 'VOID', 'INSULATED' and actual backing on FDS 5 HRRPUA of Scheme 2 in comparison with experimental HRRPUA of NFR-SB-31 at 50 kW/m^2

The comparison shows that the different back side boundary conditions affect the HRRPUA towards the end of burning and the default 'VOID' produces the closest comparison with the experimental results. 'INSULATED' overpredicts the HRRPUA while specifying the backing material as a second layer underpredicts the results. 'INSULATED' indicates no heat losses from the back side and all the energy supplied by the heat sources in the model is absorbed within the layer for pyrolysis which results in the high HRRPUA towards the end. The heat sources in the model include the user defined external heat flux and the flame heat flux. There are heat losses from the back side in the other two conditions and the greater HRRPUA of 'VOID' shows this particular condition is more insulative than the option of modelling the backing material as a second layer.

During the actual experiments, the foam sample is by no means flushed against the backing layer as seen in Figure 8-28. Small gaps do exist between the bottom of the sample and the backing layer hence the thermal contact is not considered ideal. Furthermore, the four sides of the sample are not insulated and remain exposed to the surrounding air resulting in convective heat losses.

Figure 8-28: Current foam sample setup under cone calorimeter showing four sides exposed to air and small gaps between sample and backing

The bottom and the four sides of the sample made up the total unexposed surface of the sample and from which at least 67 % in terms of area is exposed to air. Based on this information, the definition of 'VOID' in FDS 5 and the results comparison seen in Figure 8-27, 'VOID' is decided to best represent the back side boundary of the current cone sample setup within FDS 5.

8.5.8 Gas Phase Reaction and Effect of Different Gas Phase Cell Sizes

The solid phase reactions in FDS 5 produce the gaseous fuel which is released into the gas phase to undergo combustion with the presence of oxygen. Through combustion, the gaseous fuel converts into several gaseous species including CO_2, H_2O, CO, soot, N_2, H_2 and other user defined chemicals. This gas phase reaction proceeds according

to a single user defined chemical equation. The yield of the different combustion products is based on several model inputs and these are the chemical composition of the gaseous fuel, the yields of CO, soot and H_2 and the amount of hydrogen in the soot. Since the species production from foam decomposition is not part of the focus of this research, most of these inputs remain as model default except for the chemical composition of the gaseous fuel. Model defaults are used for the yields of CO, soot and H_2 and also the amount of hydrogen in the soot. These default values are not expected to affect the heat release rate simulated which is the primary focus of this research. For the different foams, their respective chemical formula listed in Table 2-1 is used as the chemical composition of the gaseous fuel in FDS 5. Besides species production, the gas phase reaction also generates heat and the amount is controlled by the effective heat of combustion specified. The global effective heat of combustion listed in Table 8-10 for the different foams is used as the model input. The value is determined as the average of all replicates from the cone experiments, at the two commonly investigated heat fluxes of this research, 30 and 50 kW/m^2.

Table 8-10: Global effective heat of combustion for different polyurethane foams

Sample code	NFR-SB-31	NFR-DG-42	NFR-C-19	FR-Y-36	FR-LG-38	FR-W-50	FR-G-32
$\Delta h_{c,eff}$ (MJ/kg)	25	25	25	22	22	22	21

The size of the gas phase cell is defined by the size of the simulated domain in x, y and z directions and also the number of mesh allocated to each. Three different cell sizes are investigated in this research and Figure 8-29 shows the setups in Smokeview for 25, 10 and 5 mm cell sizes. In terms of simulation run time, using a computer system with 3.4 GHz of processing speed and 16 GB of processing memory, the 25 mm mesh simulations with ~50 k cells require ~40 minutes, the 10 mm mesh simulations with ~90 k cells require ~4 hours and the 5 mm mesh simulations with ~700 k cells require ~70 hours.

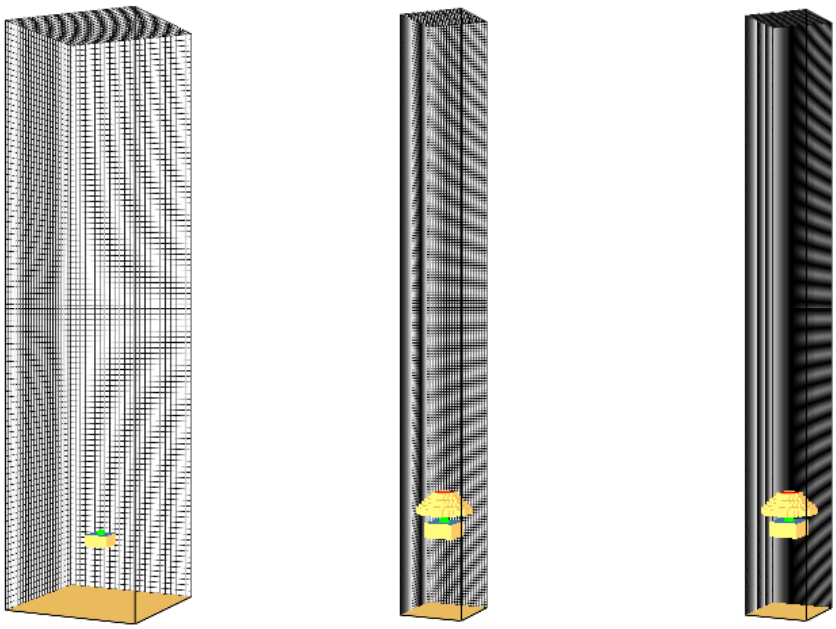

25 mm Gas phase mesh 10 mm Gas phase mesh 5 mm Gas phase mesh

Figure 8-29: Smokeview set up of FDS 5 model with different gas phase meshes

The 25 mm mesh is used to evaluate the suitability of the five decomposition schemes. As mentioned before, for this mesh size, the cone heater is replaced by the user defined external heat source which imposes a constant heat flux on the sample surface. The cone heater seen in the setups of 10 and 5 mm meshes has the same geometry. It is constructed based on the dimensions of the actual heater reported in ISO 5660-1:1993[12] using obstructions that fit the 10 mm mesh. Other components of the cone calorimeter such as the exhaust hood, fan and draught screen have been omitted from the simulation. These omissions are made on the basis that radiation is the main mode of heat transfer experienced by the sample surface and the standard airflow rate during the experiments is known to have no significant influence on the burning behaviour[119].

To simulate the heating element, the entire inner surface of the modelled cone heater is defined as a surface with fixed temperature which can be adjusted to produce the desired heat flux on the sample surface. In the experiments, the separation between the bottom of the heater and the sample is 25 mm and this is accurately portrayed by the 5 mm mesh. However, the 10 mm mesh is unable to resolve this separation so a 30

mm gap is used instead. Table 8-11 shows the temperature specified to obtain the desired heat flux at sample surface for 10 and 5 mm meshes.

Table 8-11: Temperatures of cone heater and the corresponding heat fluxes at sample surface for 10 and 5 mm meshes

Mesh size (mm)	Cone temperature (°C) to produce the desired heat flux at sample surface (kW/m^2)			
	30	**40**	**50**	**60**
10	657	727	783	832
5	648	717	773	822

Figure 8-30 compares the experimental HRRPUA of NFR-SB-31 at 50 kW/m^2 with the simulated HRRPUA of 25, 10 and 5 mm gas phase meshes. The gas phase cell size is the only variable between these simulations where Scheme 2 is adopted as the decomposition scheme and the material properties of s2-3 are used. Also, uniform solid phase cell of 0.1 mm is specified and 'VOID' is applied as the back side boundary condition.

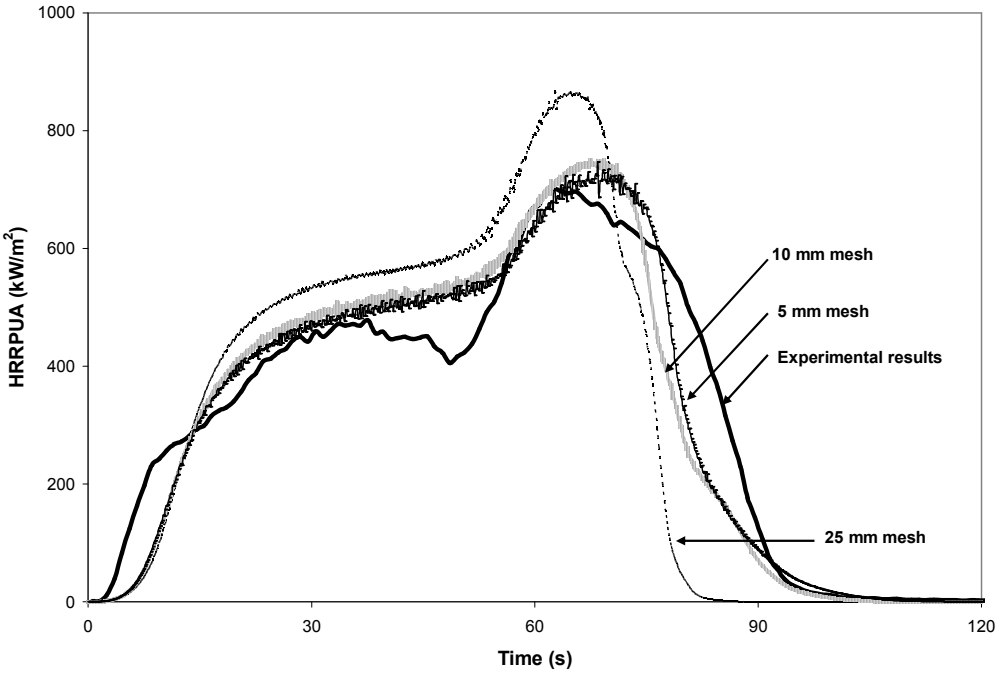

Figure 8-30: Effect of different gas phase cell sizes, 25, 10 and 5 mm on FDS 5 HRRPUA of Scheme 2 in comparison with experimental HRRPUA of NFR-SB-31 at 50 kW/m^2

With Scheme 2, the simulations manage to capture the two stage burning behaviour of the experiment and the comparison shows that using a coarser mesh produces greater

HRRPUA. The greatest difference of interest in the model HRRPUA is noted between the peak of the 25 and 5 mm meshes, approximately 140 kW/m^2. As no flame spread or multi-dimensional burning is involved, the changes in gas phase mesh do not have a significant impact on the burning behaviour.

8.5.9 Compatibility of Kinetic Properties with Pyrolysis Model

The compatibility of the kinetic properties, mainly E, A and n applied in FDS 5 depends on the decomposition scheme adopted by the user within the pyrolysis model. The five decomposition schemes considered for foam can be categorised into two groups differentiated by the shrinking and non-shrinking behaviours of the solid phase cells during decomposition. Cell shrinking is applicable to the decomposition schemes where the solid material components are converted into gaseous fuel without the formation of residues and without the presence of non-reacting components, for example, Scheme 1, 2 and 3. Non-shrinking behaviour is applicable to schemes which have the formation of residues or the presence of non-reacting components, for example, Scheme 4 and 5. The rate of decomposition in FDS 5 is calculated by Equation (3-1) which is applicable to the schemes with non-shrinking behaviour. This decomposition rate depends on both the temperature and mass of the material.

The shrinking of solid phase cell results in the preservation of the material density where $\rho_{s,i} = \rho_{s0}$ because the mass loss of the material component is accompanied by an appropriate reduction in the cell volume. With $\rho_{s,i}/\rho_{s0}$ being unity, the kinetic property, n becomes a redundant parameter in Equation (3-1). This is supported by the assessment on n redundancy performed in Scheme 2 to 5 where the outcomes confirm n to be redundant in Scheme 2 and 3 as a result of cell shrinking. Therefore, with shrinking behaviour, the mass dependent function becomes unity and the rate of decomposition in Equation (3-1) is solely dependent on the temperature of the material, represented by Equation (8-14).

$$r = Ae^{-\frac{E}{RT}} \tag{8-14}$$

Hence in FDS 5, the rate of decomposition can be calculated differently through Equation (3-1) or (8-14) depending on the choice of decomposition scheme. As a result, the graphical methodology that is compatible with the intended scheme needed to be used for developing the kinetic properties as the model inputs. Using Inflection Point Methods[49] as an example, the original decomposition rate is represented by Equation (8-10). Multiplying both sides of the equation with heating rate, β and substituting the fraction decomposed, α as $(W_0\text{-}W)/(W_0\text{-}W_f)$, Equation (8-15) is obtained.

$$\frac{d\left(\frac{W_0 - W}{W_0 - W_f}\right)}{dt} = A \cdot e^{-\frac{E}{RT}} \left(\frac{W - W_f}{W_0 - W_f}\right)^n \tag{8-15}$$

For the non-shrinking behaviour, the decomposition rate is calculated through Equation (3-1) in FDS 5 and since the instantaneous and original volume remains the same, Equation (3-1) can be represented as Equation (8-16). Comparing Equation (8-16) with (8-15), both equations are similar because the final mass, W_f for foam approaches zero for Equation (8-15).

$$r = A\left(\frac{W}{W_0}\right)^n e^{-\frac{E}{RT}} \tag{8-16}$$

With cell shrinking, the decomposition rate in FDS 5 becomes Equation (8-14) which is temperature dependent only. For Inflection Point Methods, a solely temperature dependent decomposition rate can be achieved by having $n = 0$ in Equation (8-10) which produces the normalised Inflection Point Methods as seen in Equation (8-17). Multiplying both sides of the equation with heating rate, β produces the exact same expression as Equation (8-14).

$$\frac{d\alpha}{dT} = \frac{A}{\beta} \cdot e^{-\frac{E}{RT}} \tag{8-17}$$

For more accurate modelling, it is crucial to select the appropriate decomposition scheme and based on the selection made, the suitable graphical method is used to determine the kinetic properties as model inputs. For schemes with cell shrinking behaviour, Equation (8-17) should be used for calculating the kinetic properties while for those without, Equation (8-10) is more appropriate.

8.5.10 Summary on Assessment of Decomposition Schemes

Figure 8-31 compares the selected model HRRPUA from different schemes with the experimental HRRPUA of NFR-SB-31 at 50 kW/m^2. The selected results are s1-1, s1-3, s2-3, s3-3, s4-1 and s5-1 as noted on the plot.

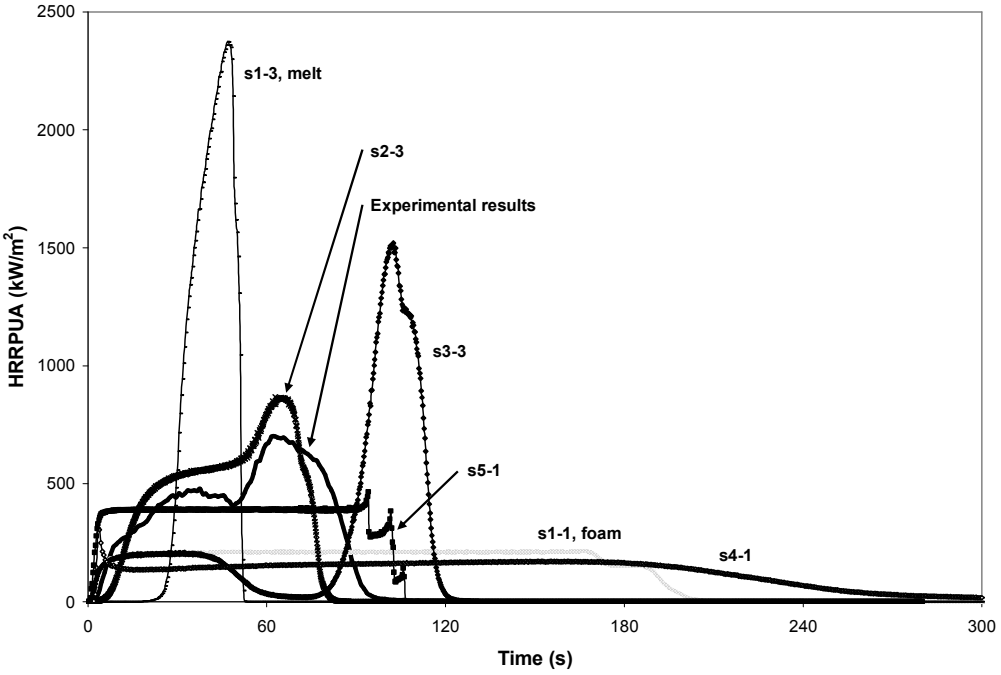

Figure 8-31: Comparison between FDS 5 HRRPUA of different schemes and experimental HRRPUA of NFR-SB-31 at 50 kW/m^2

The density and thickness for each decomposition scheme have been specified to produce the same amount of sample mass as the actual experiment. The effective heat of combustion has also been specified to generate similar amount of heat released within the gas phase. Table 8-12 compares the sample mass consumed, $M_{loss,tot}$ and the total heat released, q''_{tot} between the experiment and the simulations in Figure 8-31.

The sample mass consumed and the total amount of heat released from the simulations are slightly less than the experimental values but the maximum deviation is no more than 3 %.

Table 8-12: Comparison of total mass loss and total heat released between simulations with different schemes and experiment of NFR-SB-31 at 50 kW/m^2

Experimental Parameter	NFR-SB-31 experiment	Decomposition scheme sets					
	50 kW/m^2	s1-1	s1-3	s2-3	s3-3	s4-1	s5-1
$M_{loss,tot}$ (g)	15.7	15.5	15.3	15.4	15.5	15.5	15.5
q''_{tot} (MJ/m^2)	39.3	38.7	38.2	38.6	38.7	38.8	38.7

From the five different decomposition schemes assessed, the multi reactions scheme, Scheme 2 has produced the closest comparison with the experimental results as seen in Figure 8-31. This scheme consists of two reactions within a single material component having the thermophysical properties of foam and melt combined. The first reaction corresponds to the decomposition of foam while the second reaction corresponds to the decomposition of melt. The other schemes have not performed as well due to their respective limitations and assumptions.

The single reaction scheme, Scheme 1 comprising of either foam (s1-1) or melt (s1-3) component is too simplistic and is not adequate in capturing the two stage burning behaviour of the experiment. The multi layers scheme, Scheme 3 is able to capture the two stage burning behaviour but the discontinuity in burning between the foam and melt layers and the overprediction of HRRPUA during the burning of melt deteriorates the comparison. Despite having addressed both foam and melt as material components, the simulation results from the mass fraction scheme, Scheme 4 and the residue formation scheme, Scheme 5 produce a constant HRRPUA throughout the entire burning process, failing to capture the two stage burning behaviour.

The limitation of Scheme 4 and 5 lies with the representation of the material components within the model which differs from the actual experimental phenomenon. From the experiment, the sample's original state is foam but it eventually collapses into melt and the rate of collapse depends on the strength of the thermal penetration. Throughout the burning process, the pyrolysis front essentially changes from being foam into a combination foam and melt and then completely into

melt. These changes result in different burning behaviours which are not addressed by the material components in Scheme 4 and 5. In Scheme 5, the exposed solid phase cells of foam would convert into melt during decomposition but the unexposed solid phase cells underneath would still remain as foam due to the inherent 1-dimensional heat transfer model of FDS 5. In Scheme 4, the foam and melt components are distributed according to their respective mass fractions which remain identical throughout the entire layer thus the sample is essentially a homogenous material.

Through Scheme 2 and 3, the change from foam to melts is addressed to some extent. In Scheme 3, the foam layer is defined as the first layer followed by the melt as the second layer to simulate the full collapse of the foam structure into melt. The abrupt change in thermophysical properties between the two layers might be the cause for the discontinuity in burning seen in the simulated results. Despite having a single material component, the thermal conductivity and specific heat of the material in Scheme 2 gradually changes from foam to melt under increasing temperature thus simulating the conversion of foam to melt in the actual experiment. Based on the comparison in Figure 8-31, Scheme 2 is chosen as the decomposition mechanism for modelling polyurethane foam in FDS 5 with the material properties developed from the normalised Inflection Point Methods[49] and 'VOID' as the back side boundary condition. The sensitivity analysis performed in Figure 8-26 and 8-30 shows the changes to the solid and gas phase cell sizes do not yield a significant change in the simulated HRRPUA of Scheme 2. Nevertheless, the non-uniform solid phase cell in Figure 8-25 is shown to introduce unwanted simulation noises thus it is crucial to have uniform cells.

From Figure 8-27, 'VOID' as the back side boundary condition has shown to produce the closest HRRPUA comparison with the experimental results. 'VOID' is actually a closer representation of the experimental condition than the other two options, 'INSULATED' and the modelling of the actual backing material. With 'INSULATED', the back side is modelled as perfectly insulated with no heat losses but in the experiment, there are convective heat losses from the sides of the sample and also from the bottom of the sample due to the imperfect thermal contact with the backing material. In the second option, the backing material is modelled as a second

layer beneath the sample with a perfect thermal contact but in fact, this is not the case as the sample is by no means flushed against the backing material in the experimental setup.

The five decomposition schemes discussed so far are different from one another and each has their own unique features as depicted in their respective decomposition schematic. The flexibility of the pyrolysis model in FDS 5 means that modelling solid fuel decomposition is not limited to any particular scheme and in fact, the user is allowed to specify more than one scheme to represent the solid fuel. The use of more complex decomposition scheme to simulate the burning behaviour of foam should be considered in the future.

8.6 Experimentally Determined Material Properties as FDS 5 Inputs

This section provides a summary of the material properties of polyurethane foams which are used as the inputs for modelling the cone calorimeter experiments in FDS 5. The foams are tested at 30 and 50 kW/m^2 with two additional heat fluxes, 40 and 60 kW/m^2 included for the base case foams, NFR-SB-31 and FR-Y-36. As mentioned before, Scheme 2 is the chosen decomposition scheme and the material properties used as model inputs are categorised into thermophysical, kinetic and combustion properties. Other specified inputs include the chemical formula of the polyurethane foams, the cell sizes used in the solid and gas phases and the backside boundary condition. The inputs for all foams are listed in Table 8-13 and these reported values are the average of the repeated experiments from which the properties are derived.

Table 8-13: Experimentally determined material properties as FDS 5 inputs for different polyurethane foams tested

FDS 5 Inputs		Polyurethane foams tested						
		NFR-SB-31	**NFR-DG-42**	**NFR-C-19**	**FR-Y-36**	**FR-LG-38**	**FR-W-50**	**FR-G-32**
Thermophysical	λ (W/mK)	$T \leq 222$ °C, 0.049 $T \geq 310$ °C, 0.186	$T \leq 218$ °C, 0.048 $T \geq 310$ °C, 0.189	$T \leq 232$ °C, 0.049 $T \geq 323$ °C, 0.189	$T \leq 214$ °C, 0.050 $T \geq 320$ °C, 0.196	$T \leq 208$ °C, 0.049 $T \geq 330$ °C, 0.198	$T \leq 202$ °C, 0.049 $T \geq 307$ °C, 0.191	$T \leq 218$ °C, 0.048 $T \geq 314$ °C, 0.188
	c_p (J/kgK)	$T \leq 222$ °C, 2996 $T \geq 310$ °C, 2053	$T \leq 218$ °C, 2567 $T \geq 310$ °C, 2043	$T \leq 232$ °C, 2462 $T \geq 323$ °C, 2061	$T \leq 214$ °C, 2566 $T \geq 320$ °C, 1958	$T \leq 208$ °C, 2587 $T \geq 330$ °C, 1966	$T \leq 202$ °C, 2359 $T \geq 307$ °C, 2036	$T \leq 218$ °C, 2776 $T \geq 314$ °C, 2021
	ρ (kg/m^3)	297	326	243	289	275	364	281
	d (mm)	5.20	6.40	4.00	6.20	6.80	6.80	5.70
Kinetic	E_1 (kJ/mol)	88	85	99	94	87	78	114
	A_1 (s^{-1})	2.18×10^{5}	8.87×10^{4}	2.19×10^{6}	1.23×10^{6}	2.01×10^{5}	2.80×10^{4}	1.30×10^{8}
	n_1	0.00						
	Δh_{r1} (J/g)	891	768	1023	848	793	610	672
	E_2 (kJ/mol)	150	151	247	210	206	178	164
	A_2 (s^{-1})	3.06×10^{9}	4.60×10^{9}	3.07×10^{17}	2.42×10^{14}	9.52×10^{13}	3.81×10^{11}	4.58×10^{10}
	n_2	0.00						
	Δh_{r2} (J/g)	233	279	295	198	178	217	264
Combustion	$\Delta h_{c,eff}$ (MJ/kg)	25	25	25	22	22	22	21
Others	S	0.43	0.42	0.35	0.39	0.38	0.42	0.40
	Back side	VOID						
	Chemical formula	$C_{1.00}H_{1.77}O_{0.31}N_{0.06}$	$C_{1.00}H_{1.84}O_{0.33}N_{0.05}$	$C_{1.00}H_{1.75}O_{0.31}N_{0.07}$	$C_{1.00}H_{1.69}O_{0.28}N_{0.17}Cl_{0.003}P_{0.0010}$ [a]	$C_{1.00}H_{1.73}O_{0.28}N_{0.16}Cl_{0.003}P_{0.0002}$ [a]	$C_{1.00}H_{1.74}O_{0.32}N_{0.07}Cl_{0.002}P_{0.0004}$ [a]	$C_{1.00}H_{1.76}O_{0.32}N_{0.06}Cl_{0.016}P_{0.0050}$ [a]
	Gas phase mesh	Specify the size of the simulated domain and the number of meshes allocated to achieve 5 mm [b]						

[a] Besides C, H, O and N, FDS 5 allows the user to specify one other element. For the FR foams, Cl is specified because it has a higher composition than P.
[b] Simulations at 10 mm gas phase mesh are also performed for all the foams at the different heat fluxes tested.

For the thermophysical properties, the thermal conductivity (λ) and specific heat (c_p) of the foam and melt samples are developed from the Hot Disk experiments under ambient condition. The Hot Disk method is discussed in Chapter 6 and the values listed in Table 6-6 are used as model inputs. The two temperatures specified in Table 8-13 are the characteristic temperatures determined based on the trend observed in the TGA results. The first temperature is the final temperature where the foam properties apply and the second temperature is the initial temperature where the melt properties apply. Between the first and second temperatures, λ and c_p change linearly from foam to melt. The effective density (ρ_{eff}) is calculated according to the method discussed under Scheme 2 that utilises the density of the sample in the state of foam, mixture and melt and also the percentage of temperature range each state occupied. Based on ρ_{eff} and the experimental fuel content of each foam, the effective thickness (d_{eff}) is specified such that the fuel content in the model is the same as the actual fuel content.

For the kinetic properties, the activation energy (E), pre-exponential factor (A) and reaction order (n) are developed from the TGA results in Chapter 4. As Scheme 2 incorporates cell shrinking, the kinetic properties are developed using the normalised Inflection Point Methods. The heat of reaction (Δh_r) is developed from the DSC results in Chapter 5. The TGA and DSC results were obtained from the SDT experiments which are carried out on the foam and melt samples at heating rates of 1, 5, 20 and 60 °C/min under nitrogen environment. The values of E and A for the first and second reactions used as model inputs are obtained from Figure 4-8 and 4-9. As discussed before, n is set to zero for normalised Inflection Point Methods. For Δh_r, the value of the first reaction is the average from a recommended region of the DSC experiments on foam samples while the value of the second reaction is the average from a consistent region of the DSC experiments on melt samples. The values in Figure 5-19 and 5-16 are used as model inputs for the first and second reactions respectively. The effective heat of combustion ($\Delta h_{c,eff}$) is obtained from Table 8-10.

The chemical formula of each polyurethane foam listed in Table 2-1 is developed from the elemental analysis. The composition of C, H, O and N are specified and as FDS 5 only allows one other element to be included, Cl with higher composition is specified instead of P for the FR foams. The cell size factor is calculated for each

foam such that the solid phase cell size is uniform 0.1 mm. By adjusting the simulated domain and the amount of meshes allocated, the gas phase mesh is set to 5 mm. An identical set of simulations are performed for 10 mm gas phase mesh but since the difference in HRRPUA between different cell sizes is not significant, these results are not reproduced here. From the sensitivity analysis conducted on different back side boundary conditions, 'VOID' is found to be the suitable model input.

8.7 FDS 5 Modelling of 1-Dimensional Burning Behaviours of Polyurethane Foams using Experimentally Determined Material Properties as Inputs, Direct Method

The direct method uses the experimentally derived material properties listed in Table 8-13 as FDS 5 inputs. The simulations at 5 mm gas phase mesh are carried out for each of the exposure heat flux tested in the cone calorimeter. Figure 8-32 shows the HRRPUA comparison between the model and experiment of the base case foams, NFR-SB-31 and FR-Y-36 at all the exposure heat fluxes. The vertical dashed lines on the plot bound the separate regions for the model accuracy assessment which is discussed later.

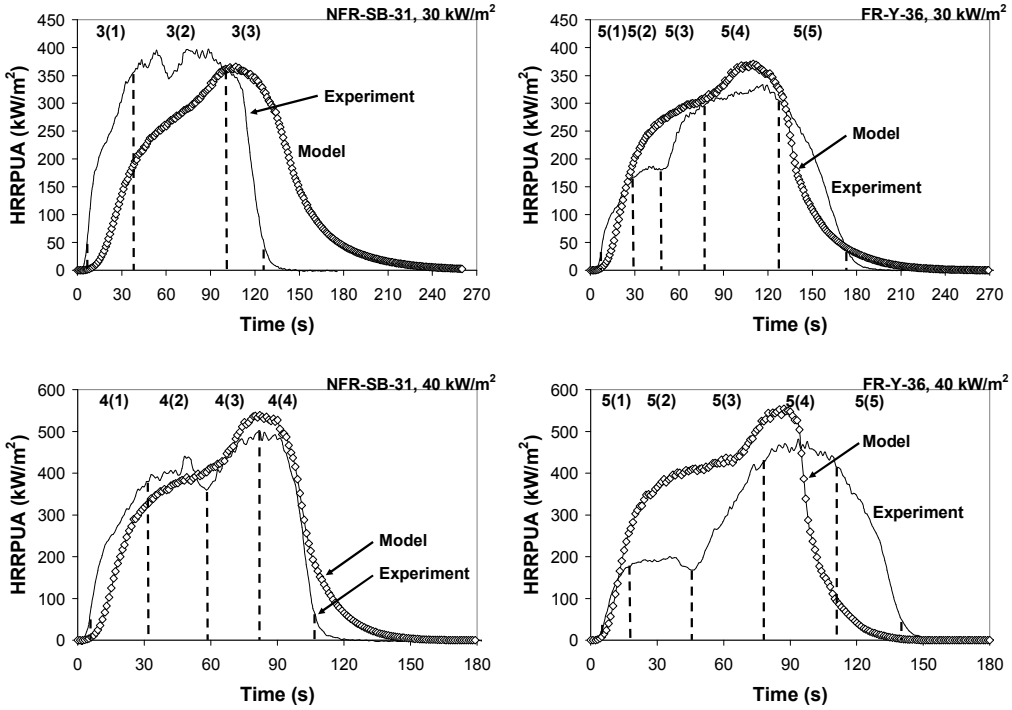

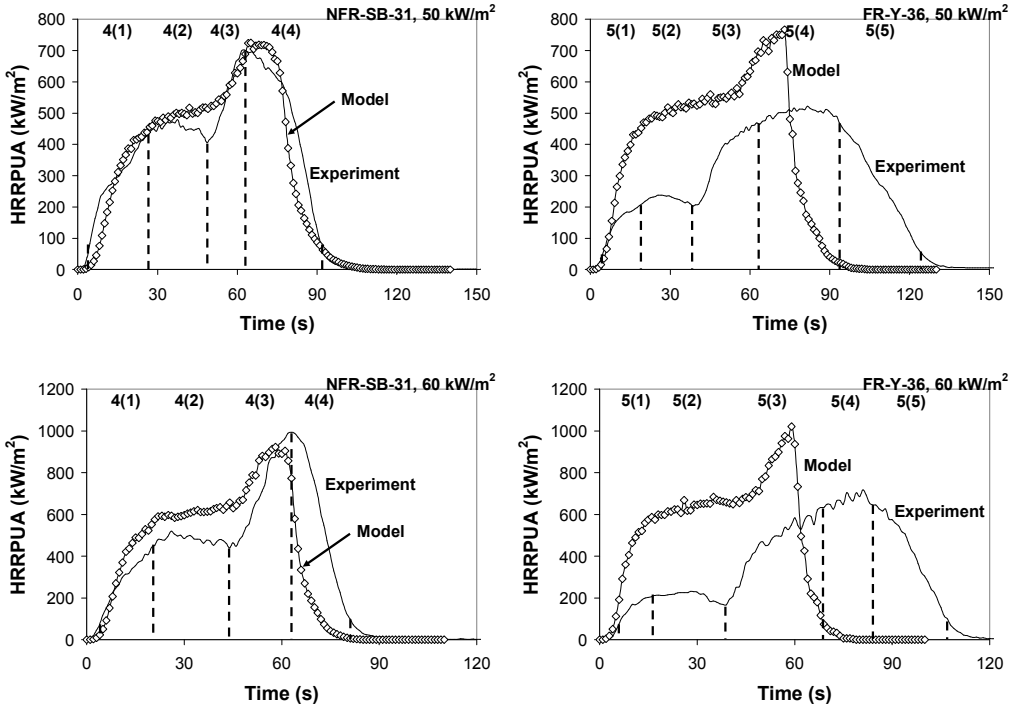

Figure 8-32: Comparison between FDS 5 HRRPUA by direct method and experimental HRRPUA at 30, 40, 50 and 60 kW/m^2 for NFR-SB-31 and FR-Y-36

For NFR-SB-31, the comparison shows the model results have a notable delay in the initial growth at 30 kW/m^2. At other heat fluxes, the model prediction improves and the closest comparison is at 40 and 50 kW/m^2 where the trend of the entire burning process is well captured. At 60 kW/m^2, the model starts to overpredict the HRRPUA of the first burning stage by as much as 100 kW/m^2. For FR-Y-36, the model shows the closest prediction at 30 kW/m^2 and towards higher exposure heat fluxes, the model starts to overpredict. At 60 kW/m^2, the model overpredicts the HRRPUA by approximately 400 kW/m^2 over the first stage and part of the second stage.

Showing similarity to NFR-SB-31 and FR-Y-36, the results for the other foams are not reproduced here. For the other NFR foams, at 30 kW/m^2, the initial growth has the characteristic delay seen in the results of NFR-SB-31. For the other FR foams, the model results at 30 kW/m^2 is similar to those of FR-Y-36 which show a two stage burning behaviour. Comparing with the experimental results at 30 kW/m^2, the model results at 30 kW/m^2 of FR foams achieve a better comparison than the model results at 30 kW/m^2 of NFR foams. Despite the improvement in comparison, the model still

cannot resolved the HRRPUA of FR foams over the first stage and the extensive burning plateau of the second stage. For the HRRPUA comparison at 30 kW/m^2, the maximum difference between the model and experiment is approximately 50 kW/m^2 for all the foams simulated. This is approximately 0.5 kW for the sample size investigated. For the HRRPUA comparison at 50 kW/m^2, the model results of the other NFR and FR foams show overprediction with similar magnitude as the model results of FR-Y-36. Based on this qualitative comparison, the direct method mostly produces better prediction at low heat flux than at high heat flux.

8.7.1 Linear Regression Analysis for Direct Method

In order to evaluate the accuracy of FDS 5 prediction, the linear regression analysis is performed to assess the comparison between the model and experimental HRRPUA. As noted in Figure 8-32, the experimental HRRPUA curve can be categorised into 3, 4 or 5 different regions for linear regression analysis depending on the type of polyurethane foams and the heat flux involved. The definition for each region in the different types of analysis and the application of the analysis to different kinds of HRRPUA curve are summarised in Table 8-14. Figure 8-33 shows the linear regression analysis on HRRPUA of NFR-SB-31 and FR-Y-36, the different symbols used on the plot corresponds to the different regions described in Table 8-14 which are also identified on Figure 8-32. The x axis is the experimental HRRPUA and the y axis is the model HRRPUA.

The diagonal solid line on the plot indicates the perfect correlation between the model and experiment. On either sides of the perfect correlation is the boundary of acceptance which is formed by the two parallel dashed lines set to 25 % of the greatest experimental HRRPUA. The data points that fall within this boundary are considered to achieve the acceptable accuracy. This criteria of accuracy assessment provide more emphasis or weighting on the accuracy of predicting HRRPUA with greater magnitude such as during the developed burning over the first and second stages while less emphasis is placed on the accuracy of predicting HRRPUA with smaller magnitude such as during the initial growth and the final decay. This is considered reasonable as during the initial growth and final decay, the experimental

and model HRRPUA change rapidly over a short duration which makes a meaningful assessment on the accuracy more challenging.

Table 8-14: Types of linear regression analysis, definition of each region and application to HRRPUA curves with different burning behaviours

Type of analysis		Definition	Application
3 regions	3(1)	Initial growth region – From 10 to 90 % of the single peak.	Single plateau burning behaviour. Examples include all NFR foams and FR-LG-38 at 30 kW/m^2.
	3(2)	Single plateau region – From leading 90 % to trailing 90 % of the single peak.	
	3(3)	Decay region – From 90 to 10 % of the single peak.	
4 regions	4(1)	Initial growth region – From 10 % of the second (greatest) peak to 90 % of the first peak.	Two stage burning behaviour with sharp peaks. Examples include all NFR foams at 40, 50 and 60 kW/m^2.
	4(2)	First peak region – From 90 % of the first peak to the minimum between the first and second peaks.	
	4(3)	Leading second peak region – From the minimum between peaks to the second peak.	
	4(4)	Trailing second peak region – From the second peak to 10 % of the second (greatest) peak.	
5 regions	5(1)	Initial growth region – From 10 % of the second (greatest) peak to 90 % of the first peak.	Two stage burning behaviour with plateaus. Examples include all FR foams at all heat fluxes tested except for FR-LG-38 at 30 kW/m^2.
	5(2)	First plateau region – From 90 % of the first peak to the minimum between the first and second peaks.	
	5(3)	Secondary growth region – From the minimum between peaks to 90 % of the second (greatest) peak.	
	5(4)	Second plateau region – From leading 90 % to trailing 90 % of the second (greatest) peak.	
	5(5)	Decay region – From 90 % to 10 % of the second (greatest) peak.	

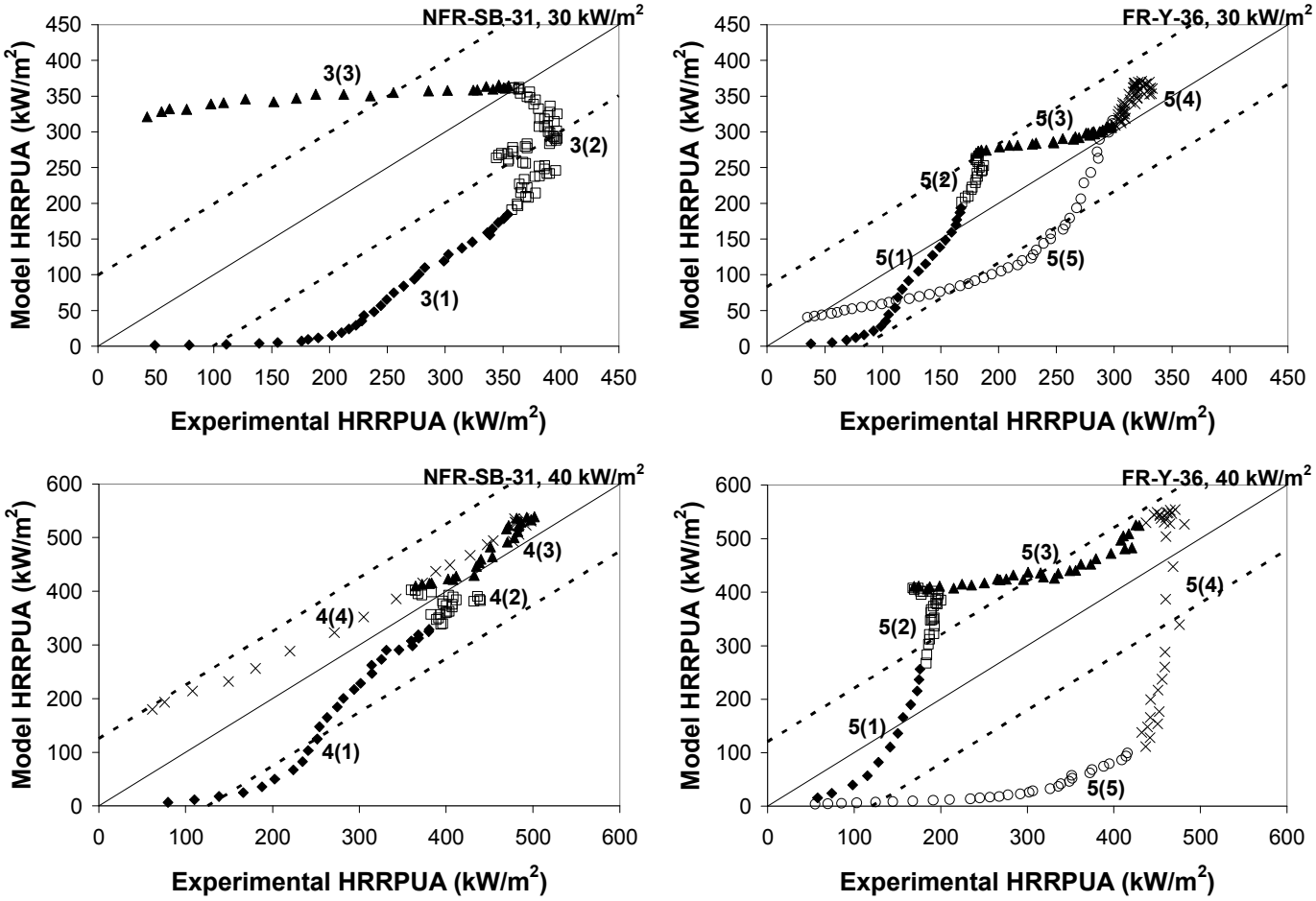
NFR-SB-31, 30 kW/m2
Model HRRPUA (kW/m2)
Experimental HRRPUA (kW/m2)
3(3)
3(2)
3(1)
FR-Y-36, 30 kW/m2
5(4)
5(3)
5(2)
5(1)
5(5)
NFR-SB-31, 40 kW/m2
4(3)
4(2)
4(4)
4(1)
FR-Y-36, 40 kW/m2
5(3)
5(4)
5(2)
5(1)
5(5)

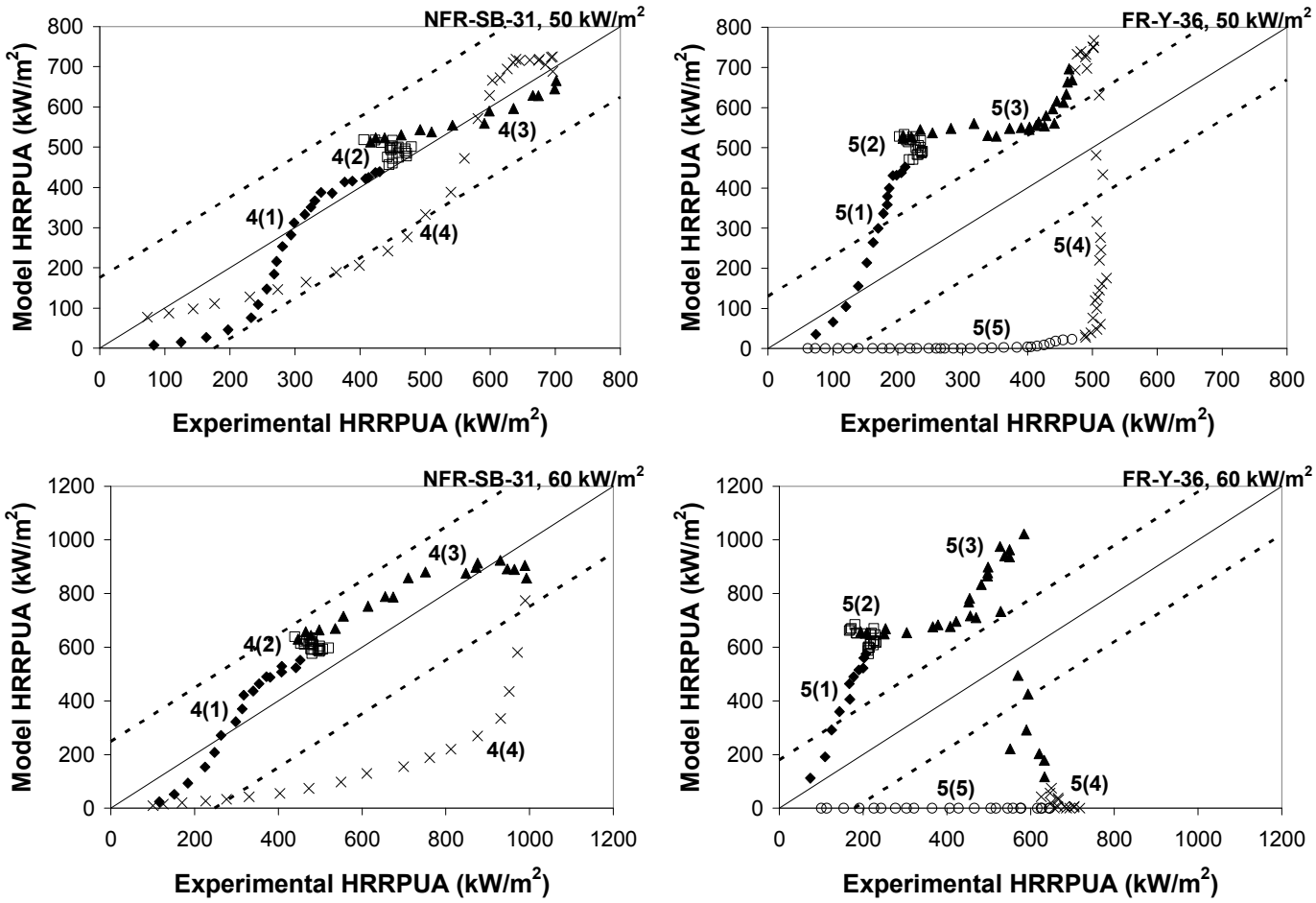

Figure 8-33: Linear regression analysis on HRRPUA between direct method and experiments for NFR-SB-31 and FR-Y-36 at 30, 40, 50 and 60 kW/m^2

From the linear regression analysis, the model predictions are assessed by comparing the trend of the data points with the perfect correlation and the boundary of acceptance. The results from both foams at 30 and 50 kW/m^2 are used as examples to illustrate the interpretation of the linear regression analysis performed. For NFR-SB-31 at 30 kW/m^2, the linear regression analysis shows the model has underpredicted over the initial growth and single plateau regions. However, over the decay region, the model starts to overpredict the HRRPUA. For FR-Y-36, the model at 30 kW/m^2 produces better prediction than NFR-SB-31 as most of the data points are within the boundary of acceptance except during part of the decay region where the model underpredicts outside this boundary.

For higher heat flux at 50 kW/m^2, the linear regression analysis shows the results of NFR-SB-31 are mostly within the boundary of acceptance. Good comparison is achieved during the initial growth region, the first peak region and the leading second peak region. Over part of the trailing second peak region, the model underpredicts slightly outside the boundary of acceptance. For FR-Y-36 at 50 kW/m^2, the model mostly overpredicts the initial growth region, the first plateau region and the secondary growth region. As the fuel burns out earlier in the model due to the higher heat release rate, the model underpredicts the second plateau region and the decay region. The pattern seen in the linear regression analysis consistently reflects the same trends seen between the model and experimental HRRPUA curves in Figure 8-32. Given the similarity between the other foams and the base case foams presented, the plots of linear regression analysis for the other foams are not reproduced here.

From Figure 8-32, the model and experimental comparison of NFR-SB-31 at 30 kW/m^2 is poor due to the delay in the initial growth, otherwise, the comparison is actually very similar in terms of the burning behaviour. For FR-Y-36, the model constantly struggles to capture the restricted HRRPUA of the first stage which remains at ~200 kW/m^2 regardless of the increase in exposure heat flux and also fails to capture the extensive plateau burning behaviour of the second stage. These mismatches are due to a few assumptions made during modelling and also the complexity of the actual physical phenomena modelled.

From the perspective of modelling, specifying a single effective density and effective thickness might not be an accurate representation of the actual phenomena where the decomposing sample experiences the change from thick layer of low density foam into thin layer of high density melt. Also, the magnitude of the thermophysical properties specified are ambient properties measured in Hot Disk experiments. Although the thermophysical properties are temperature dependent in the model, the temperatures specified are developed from the TGA results, not from the Hot Disk experiments. Hence, the potential changes of those properties at elevated temperatures such as during a fire are not addressed adequately. Lastly, the kinetic properties as inputs are mathematically developed from the TGA results obtained at different heating rates ranging from 1 to 60 °C/min. This tested experimental range is considerably lower than the heating rate in an actual fire, reportedly greater than 500 °C/min[85].

From the perspective of physical phenomena, the process of ignition and the fire retardant mechanisms are not adequately addressed in the model. FDS 5 assumes the formation of flame when the fuel gas encounters oxygen but this might not be the case in reality as fuel gases are noted to leave unburned prior to ignition. Furthermore, the ignition process in the cone experiments is piloted while in FDS 5, the sample undergoes auto ignition because the mechanism of the spark ignitor cannot be modelled. Lastly, for the FR foams, the solid phase char formation is not explicitly addressed by the selected solid phase decomposition scheme and the performance of the gas phase combustion inhibitors is also not implemented within the single gas phase reaction specified.

Due to the modelling assumptions made and the complexity of physical phenomena modelled, simulating ignition, growth and decay phases of foam burning process is challenging. During these phases, the heat release rate changes rapidly and substantially over relatively short period compared with the developed burning phase. In order to place more emphasis on the accuracy of pyrolysis model in simulating the developed burning phase, the linear regression analysis is also repeated with the model HRRPUA shifted for comparison over developed burning phase. Two different

curve fitting shifts are considered, the first method is an averaged 3 point shift and the second method involves a single point shift.

The averaged 3 point shift involves adjusting the model HRRPUA by a single time shift determined as the average difference from matching three selected characteristic points between the simulated HRRPUA and the experimental HRRPUA. These points are the HRRPUA of the greatest peak and the two 80 % HRRPUA of the greatest peak. The averaged 3 point shift has a minimal time shift of 5 s which means any adjustment less than that is not performed because of the negligible impact on the accuracy. The single point shift involves adjustment made after matching only one characteristic point, the leading 10 % HRRPUA of the greatest peak. No minimal time shift is applied for the single point method but in certain cases, the time shift of less than 1 s is not performed, again due to the negligible impact on the accuracy. Figure 8-34 shows the adjusted results of NFR-SB-31 at 30 kW/m^2 and FR-Y-36 at 50 kW/m^2 using the averaged 3 point shift. The rest of the results are characteristically similar to these two examples so they are not reproduced here.

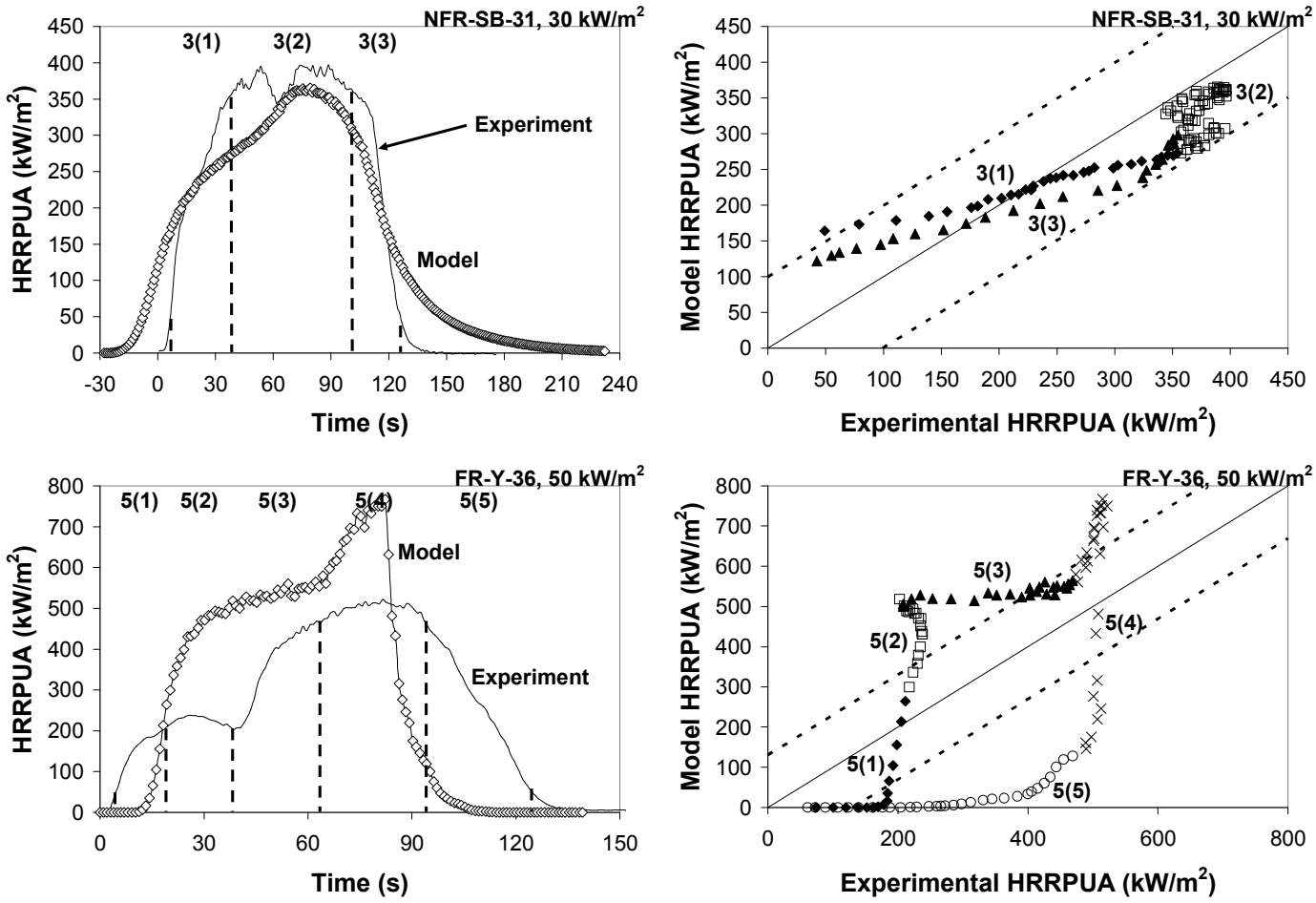

Figure 8-34: HRRPUA comparison and linear regression analysis of NFR-SB-31 at 30 kW/m^2 and FR-Y-36 at 50 kW/m^2 after adjustment by averaged 3 point shift

From Figure 8-34, the comparison between the model and experimental results for NFR-SB-31 at 30 kW/m^2 shows great improvement after the implementation of the averaged 3 point shift. The three selected characteristic points place more emphasis on matching the developed burning and as a result, part of the initial growth region is moved beyond the start of experiment noted by the negative time on the plot. The shifted curve shows a better comparison in terms of HRRPUA and the linear regression analysis shows that almost all the data points are within the boundary of acceptance. For FR-Y-36 at 50 kW/m^2, the model and experimental results comparison is not enhanced by the averaged 3 point shift. In terms of HRRPUA comparison, the model mainly overpredicts the extensive burning plateau of the first and second stages while underpredicting the initial growth and decay regions. This poor comparison is reflected in the linear regression analysis where a majority of the data points are outside the boundary of acceptance. These trends are discussed further in the next section.

8.7.2 Accuracy Assessment of Direct Method

In order to quantify the accuracy of FDS 5 predictions, a few classes of accuracy are introduced. First and foremost is the region specific accuracy which is calculated as the percentage of data points within the boundary of acceptance over a particular region. By including all the regions, the heat flux specific accuracy which is essentially the accuracy at a particular heat flux is determined. The two curve fitting shifts discussed above are only applied to the simulation results with the original heat flux specific accuracy of less than 80 %. Table 8-15 shows the region specific and heat flux specific accuracies of the direct method for all the polyurethane foams tested at the different exposure heat fluxes. The values in brackets are the accuracies determined respectively with the averaged 3 point shift and the single point shift and '-' indicates the shift produces negligible change to the accuracy.

Table 8-15: Region specific accuracies and heat flux specific accuracies of direct method for all polyurethane foams tested at 30, 40, 50 and 60 kW/m^2

Sample code	Heat flux (kW/m^2)	Number of regions	Region specific accuracies (%)					Heat flux specific accuracy (%)
			1	2	3	4	5	
NFR-SB-31	30	3	6 (97,75)	57 (100,71)	46 (100,58)	N/A	N/A	41 (99,69)
	40	4	74	100	100	100	N/A	93
	50	4	100	100	100	90	N/A	97
	60	4	100	100	100	33	N/A	84
NFR-DG-42	30	3	51	100	100	N/A	N/A	87
	50	4	87 (65,39)	35 (65,20)	76 (87,47)	7 (41,7)	N/A	56 (66,31)
NFR-C-19	30	3	35 (87,100)	85 (85,98)	40 (53,100)	N/A	N/A	62 (80,99)
	50	4	50 (19,25)	0 (61,0)	17 (0,17)	19 (38,19)	N/A	21 (32,15)
FR-Y-36	30	5	100	94	83	100	64	87
	40	5	100 (33,92)	11 (39,0)	52 (58,49)	58 (90,48)	17 (17,17)	41 (50,35)
	50	5	47 (53,27)	0 (16,0)	8 (44,0)	10 (24,10)	16 (16,16)	14 (29,10)
	60	5	27 (64,-)	0 (26,-)	7 (57,-)	0 (21,-)	13 (13,-)	8 (35,-)
FR-LG-38	30	3	89	80	51	N/A	N/A	78
	50	5	32 (36,9)	0 (0,0)	0 (9,0)	6 (12,8)	22 (22,22)	13 (17,10)
FR-W-50	30	5	100	68	94	100	70	86
	50	5	55 (-,25)	0 (-,0)	65 (-,65)	42 (-,30)	19 (-,19)	36 (-,28)
FR-G-32	30	5	100 (-,-)	81 (-,-)	80 (-,-)	74 (-,-)	57 (-,-)	74 (-,-)
	50	5	33 (-,29)	0 (-,0)	60 (-,70)	88 (-,75)	16 (-,16)	35 (-,33)

From Table 8-15, the accuracies of NFR-SB-31 shows relatively good comparison between the model and experiment at 40, 50 and 60 kW/m^2, agreeing with the comparison of HRRPUA curves seen in Figure 8-32 and the linear regression analysis in Figure 8-33. The delay in the initial growth region means the results at 30 kW/m^2 compares poorly as reflected by the low accuracy of 6 % over the initial growth region. Nonetheless, the region specific and heat flux specific accuracies are shown to improve significantly with the application of the averaged 3 point shift. Different to NFR-SB-31, the accuracies of FR-Y-36 shows that the comparison is actually the closest at 30 kW/m^2 and it diminishes as the heat flux increases, especially for regions beyond the initial growth region due to overprediction of HRRPUA. The curve fittings shifts applied do not produce much improvement for FR-Y-36 because the mismatch is not in the horizontal time but primarily in the vertical HRRPUA. The other foams collectively shows the similar trend as FR-Y-36 where the prediction at low heat flux, 30 kW/m^2 is better than those at high heat flux, 50 kW/m^2 due to the consistent overprediction of HRRPUA at 50 kW/m^2.

From the heat flux specific accuracies, the foam specific accuracy is determined as the average accuracy of all the heat fluxes and this also becomes the accuracy for the specific polyurethane foam. Lastly, the method specific accuracy includes the average accuracy of all the foams and this represents the accuracy of the methodology applied, in this case the direct method. Table 8-16 shows the heat flux specific accuracies, the foam specific accuracies and the method specific accuracy relating to the direct method. The values reported in brackets are the results when the averaged 3 point shift and the single point shift are applied.

Table 8-16: Heat flux specific accuracies, foam specific accuracies and method specific accuracy of direct method for all polyurethane foams

Sample code	Heat flux specific accuracy (%) at different heat fluxes (kW/m^2)				Foam specific accuracy (%)
	30	40	50	60	
NFR-SB-31	41 (99,69)	93	97	84	79 (93,86)
NFR-DG-42	87	N/A	56 (66,31)	N/A	72 (77,59)
NFR-C-19	62 (80,99)	N/A	21 (32,15)	N/A	41 (56,57)
FR-Y-36	87	41 (50,35)	14 (29,10)	8 (35,-)	37 (50,35)
FR-LG-38	78	N/A	13 (17,10)	N/A	45 (47,44)
FR-W-50	86	N/A	36 (-,28)	N/A	61 (-,57)
FR-G-32	74 (-,-)	N/A	35 (-,33)	N/A	55 (-,54)
Method specific accuracy (%)					56 (63,56)

For all the foams simulated, their heat flux specific accuracies collectively demonstrates that the direct method mostly produces better prediction at low heat flux than at high heat flux with the only exception to NFR-SB-31. By default without any shifts, the results of NFR-SB-31 and FR-Y-36 discussed above are the best and worst cases among the foams with 79 and 37 % foam specific accuracy. Among the other foams, only NFR-DG-42 has foam specific accuracy above 70 % while the rests are between 41 and 61 %. The method specific accuracy of the direct method is 56 % without any curve fitting shifts. Using the averaged 3 point shift, the majority of the predictions are improved and the method specific accuracy increases to 63 %. The best and worst foam specific accuracies in this case are 93 and 47 % recorded for NFR-SB-31 and FR-LG-38 respectively. The single point shift improves certain predictions while diminishing the others so as a result, the method specific accuracy remains at 56 %. The best and worst foam specific accuracies are 86 and 35 % recorded for NFR-SB-31 and FR-Y-36 respectively.

Figure 8-35 shows the linear regression analysis performed on the maximum HRRPUA, the average HRRPUA and the burning duration between the direct method results and the experimental results. The analysis includes all the foams and the different heat fluxes. The maximum HRRPUA is the magnitude of the greatest peak, the average HRRPUA is calculated as the average between the two 10 % HRRPUA of the greatest peak and similarly, the burning duration is determined as the time difference between the same pair of points. For each parameter, the boundary of acceptance (BOA) is set to 25 % of the experimental values in conjunction with the same boundary of acceptance allocated to the linear regression analysis performed previously on the individual set of model and experimental results.

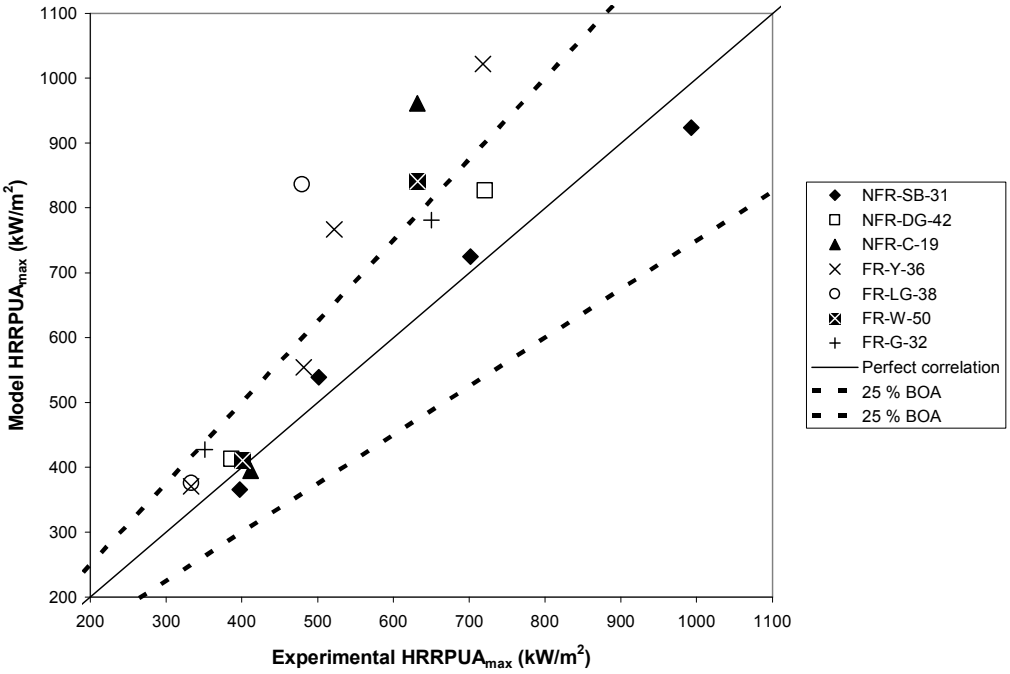
Model HRRPUA$_{max}$ (kW/m^2)
Experimental HRRPUA$_{max}$ (kW/m^2)
1100
1000
900
800
700
600
500
400
300
200
200
300
400
500
600
700
800
900
1000
1100
NFR-SB-31
NFR-DG-42
NFR-C-19
FR-Y-36
FR-LG-38
FR-W-50
FR-G-32
Perfect correlation
25 % BOA
25 % BOA

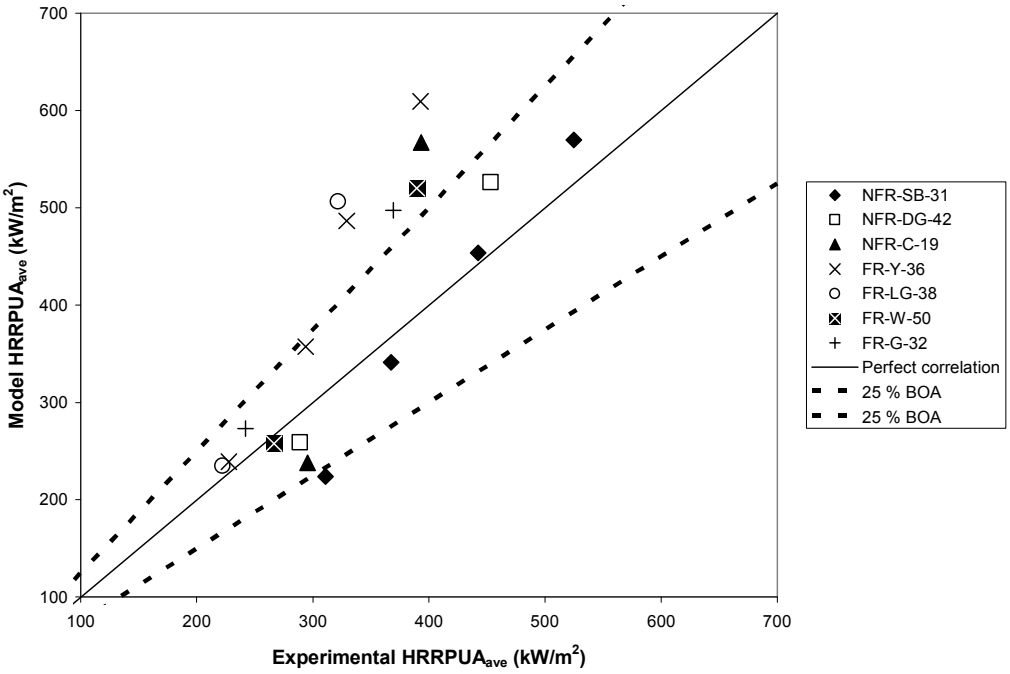
Model HRRPUA$_{ave}$ (kW/m^2)
Experimental HRRPUA$_{ave}$ (kW/m^2)
700
600
500
400
300
200
100
100
200
300
400
500
600
700
NFR-SB-31
NFR-DG-42
NFR-C-19
FR-Y-36
FR-LG-38
FR-W-50
FR-G-32
Perfect correlation
25 % BOA
25 % BOA

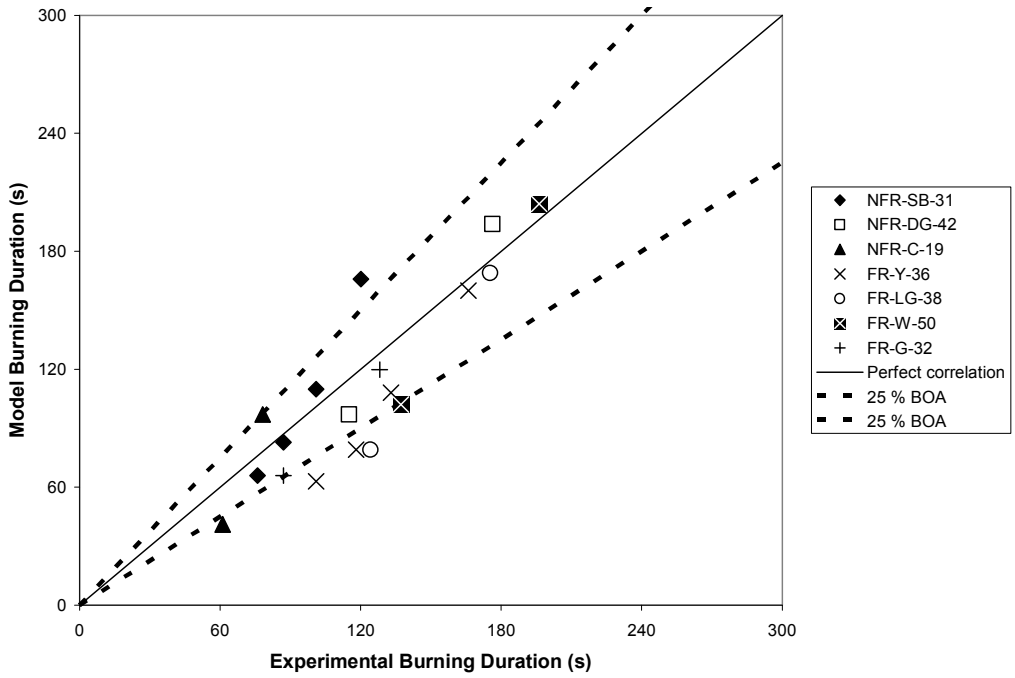

Figure 8-35: Linear regression analysis on maximum HRRPUA, average HRRPUA and burning duration between direct method and experiments for all polyurethane foams

The linear regression analysis on the maximum and average HRRPUA have showed that several data points with greater magnitude, corresponding to the higher exposure heat fluxes have fallen outside the upper limit of the acceptance boundary. This means the model is overpredicting the maximum and average HRRPUA as seen in the trends of FR-Y-36 in Figure 8-32. The analysis on the burning duration shows the data points have less scatter and are closer to the region of acceptance compared to the maximum and average HRRPUA. The accuracy achieved for the maximum HRRPUA, the average HRRPUA and the burning duration are 72, 61 and 67 % respectively. In conclusion, the accuracy assessment shows that the direct method mostly produces better prediction at low heat flux than at high heat flux. The heat flux specific accuracy of the default predictions at 30 kW/m^2 ranges from 41 to 87 % while at 50 kW/m^2, the accuracy ranges from 13 to 97 %. As the accuracies associated with NFR-SB-31 have an opposite trend to the rest of the foams, excluding NFR-SB-31 portrays a more representative range of accuracy, 62 to 87 % for 30 kW/m^2 and 13 to 56 % for 50 kW/m^2. Using the averaged 3 point shift improves the method specific accuracy but only slightly from 56 to 63 %.

8.8 Compatibility between FDS 5 and Gpyro in Pyrolysis Modelling

In order to improve the FDS 5 predictions of the experimental burning behaviour, the kinetic properties, E, A and Δh_r of the first and second reactions are refined using the genetic algorithm of Gypro[27,115] which is coupled with its pyrolysis model. The refinement process searches for a set of optimal kinetic properties which produces the closest comparison between the outputs of the pyrolysis model and the experimental results supplied. It is crucial to establish the similarities and differences between the pyrolysis model of FDS 5 and the pyrolysis model of Gpyro since the refined kinetic properties from Gpyro are intended as the inputs of FDS 5. The decomposition rate in Gpyro is calculated via Equation (3-2)[115] which has the same form as the decomposition rate in FDS 5 seen in Equation (3-1). When gaseous fuel is released from the solid phase cell and the solid density remains constant, the cell size in Gpyro would reduce to conserve mass[115]. This is essentially the same as the cell shrinking behaviour in FDS 5 described previously.

Despite the similarities, Gpyro does differ from FDS 5 in certain aspects. For the chosen decomposition scheme, Scheme 2, the thermophysical properties, λ and c_p of FDS 5 change linearly from foam to melt over a defined temperature range. Beyond this range, λ and c_p remain constant as either foam or melt. Similar feature is not available in Gpyro where the temperature dependency of the thermophysical properties is essentially a power function[115] which is unable to reproduce the same temperature dependent function specified in FDS 5. In order to compensate for this in the property estimation process, the effective thermophysical properties which are constant with temperature are used. These effective properties are calculated in a way which incorporates the effect of linear transition in the thermophysical properties of FDS 5. Details of the calculations are described later.

FDS 5 and Gpyro have similar back side boundary condition which consists of convective heat losses but the specification between the two models is slightly different. 'VOID' is invoked in FDS 5 where the component layer is backed against

an open void at ambient temperature. By default, the convective heat transfer coefficient is determined as the greater value between natural and forced convections[17]. When the fuel in a solid phase cell is completely consumed, the burning rate and convective heat flux to the cell are set to zero and its temperature returned to ambient value. In Gpyro, the convective heat transfer coefficient is user defined and a fixed value of 10 W/m^2K is used. When the solid fuel is fully consumed in Gpyro, the burning rate goes to zero but the surface remains at the final equilibrium temperature.

The representation of flame in FDS 5 and Gpyro is also different. FDS 5 uses mixture fraction model where the flame exists within a gas phase cell if both the gaseous fuel and oxygen are present. At each time step, the rate of mixing between the fuel and oxygen within the cell is governed by a few semi-empirical equations[17]. In Gpyro, the flame is represented as a constant radiative heat flux defined by the user which is invoked at the user specified ignition time of the material. As such, the burning behaviour simulated in FDS 5 and Gpyro is affected by the different physics of flame. The flame in FDS 5 has a finite growth and decay duration while the flame in Gpyro reaches maximum heat flux instantaneously upon ignition. As inputs of Gpyro, the ignition times of polyurethane foams at different heat fluxes are obtained from the cone experiments. The flame heat flux is not measured experimentally due to the difficulty in tracking the recessing surface of burning foam. Instead, the simulated flame heat fluxes from FDS 5 are specified in Gpyro and the calculation process to obtain this simulated flame heat flux is described in the next section.

8.8.1 Transforming Flame Heat Flux in FDS 5 to Gpyro

Rhodes et al.[57] and Hopkins et al.[58] reported that the flame heat flux received at the surface of a sample under the cone heater is a constant value because the geometry and shape of the flame is tall and narrow which means the majority of the flame heat flux received at the surface originates from the lower part of the flame, mostly below the top of the cone heater. The radiation from the upper part and the tip of the flame does not reach the surface. The flame heat flux required by Gpyro is estimated from the FDS 5 simulations performed for each foam which use the experimental material

properties listed in Table 8-13 as inputs. Although the HRRPUA comparison between the simulations and experiments are not ideal for certain foams, this is believed not to affect the value of flame heat flux significantly because of the common geometry and shape of the simulated flame whereby the radiation received by the surface originates mostly from the flame underneath the cone heater. In the model, the flame heat flux is recorded at the centre of the sample and Figure 8-36 compares the results of NFR-SB-31 from 10 and 5 mm gas phase meshes at different exposure heat fluxes.

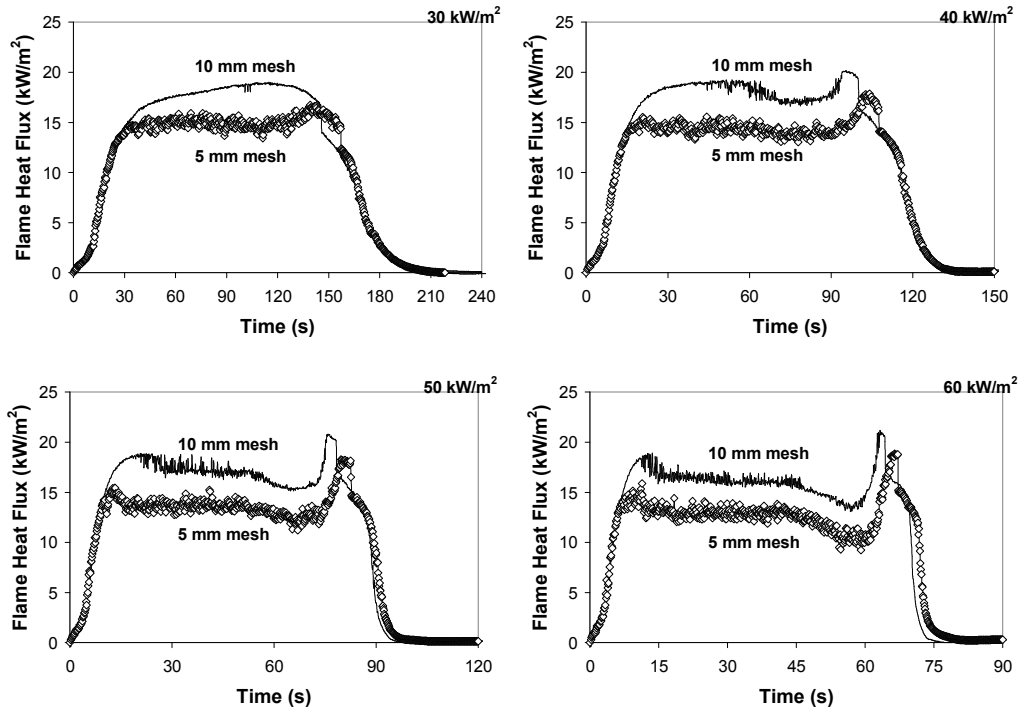

Figure 8-36: FDS 5 flame heat fluxes of NFR-SB-31 obtained at centre of sample from simulations at 10 and 5 mm gas phase meshes at 30, 40, 50 and 60 kW/m^2

Figure 8-36 shows a progressive reduction in the simulated flame heat flux when the exposure heat flux increases. In the model, the flame heat flux received at the surface mostly originates from the significant fuel and oxygen mixing region. With the increase in exposure heat flux, the distance between this significant mixing region and the sample surface is believed to increase which lowers the flame heat flux recorded. Over the burning period, the flame heat flux remains fairly constant except for the peak prior to the heat flux decay. The peak is noted to correspond with the decay of the flame height and it also appears more prominent towards higher exposure heat flux where the flame height decays more rapidly. Hence, before all the fuel is

consumed, the significant fuel and oxygen mixing region is shifted downwards following the flame height reduction and becomes closer to the sample surface thus producing this peak in the simulated flame heat flux.

The flame heat flux obtained from 10 mm gas phase mesh is consistently greater by approximately 4 kW/m^2 than the value from 5 mm mesh due to the different gas phase resolutions. Similar trends are also observed for the other polyurethane foams so their results are not repeated. The greater flame heat fluxes from the 10 mm gas phase mesh are used for all the Gpyro simulations. The ignition time, t_{ig} and the simulated flame heat flux, $\dot{q}''_{fl}$ at the different exposure heat fluxes are tabulated in Table 8-17 for all the foams tested.

Table 8-17: Ignition times and simulated flame heat fluxes of different polyurethane foams at 30, 40, 50 and 60 kW/m^2 for application in Gpyro

Sample code	t_{ig} (s) and $\dot{q}''_{fl}$ (kW/m^2) at different heat fluxes (kW/m^2)							
	30		40		50		60	
	t_{ig}	$\dot{q}''_{fl}$	t_{ig}	$\dot{q}''_{fl}$	t_{ig}	$\dot{q}''_{fl}$	t_{ig}	$\dot{q}''_{fl}$
NFR-SB-31	5.13	18	3.42	18	2.52	17	1.97	16
NFR-DG-42	5.14	19	N/A	N/A	3.22	17	N/A	N/A
NFR-C-19	7.38	18	N/A	N/A	2.14	16	N/A	N/A
FR-Y-36	7.77	18	4.16	17	3.03	15	2.20	14
FR-LG-38	14.00[a]	18	N/A	N/A	3.50	15	N/A	N/A
FR-W-50	11.00	18	N/A	N/A	2.40	15	N/A	N/A
FR-G-32	11.81	17	N/A	N/A	2.57	14	N/A	N/A

The ignition times reported in Table 8-17 is similar to those in Table 8-2, except for FR-LG-38 where the extensive ignition time of the second repetition at 30 kW/m^2, 234 s is excluded as an outlier. The flame heat flux reported is calculated as the average between the leading and trailing 90 % of the maximum flame heat flux over the constant region. The maximum flame heat flux used excludes the prominent peak near the decay. With increasing exposure heat flux, the calculated average flame heat flux shows a progressive reduction in magnitude, similar to the trend seen in Figure 8-36.

[a] The extensive ignition time of the second repetition of FR-LG-38 is not included in the calculation.

For the range of exposure heat fluxes and the different foams simulated, the flame heat flux at the centre of the sample is found to range between 14 and 19 kW/m^2 for an average HRRPUA ranging from 200 to 600 kW/m^2. The flame heat fluxes reported in this research have compared well with most published values in the literature. Hostikka et al.[120] performed multiple CFD simulations of flaming combustion under cone heater and reported a range of flame heat flux at the centre of the sample from 12 to 17 kW/m^2 for HRRPUA ranging between 100 and 400 kW/m^2. Summarising the values from several research on different types of material, Babrauskas[121] reported the flame heat flux ranges from 10 to 30 kW/m^2. However, Kramer et al.[54] reported flame heat flux between 36 and 58 kW/m^2 based on graphical analysis of surface recession rate of polyurethane foam under non-flaming and flaming conditions.

Comparing with the research of Kramer et al.[54], there are a number of notable differences which potentially contribute towards the disagreement in values for flame heat flux. First of all is the difference in experimental setup where Kramer et al. have used customised sample holder which exposed the foam on the top and also on all four sides. This means the convective heat transfer of the flame in their research differs from this research where the foam sample was contained in an aluminium cup. Their findings also concluded that the convective heat transfer of flame is depended on the sample configuration which affects the burning behaviour. Secondly, the range of flame heat flux reported by Kramer et al. was based on the analysis of surface recession rate which might not correlate with the decomposition and combustion of foam. Hence, there could be potential error with the analysis and parameters with a more direct relation such as mass loss rate should be considered instead.

Ideally, to estimate the properties for 5 mm gas phase simulations using the genetic algorithm of Gpyro, the flame heat fluxes should be determined from the 5 mm gas phase mesh. However, due to the extensive run time of Gpyro, this has not been performed and the flame heat fluxes from the 10 mm gas phase mesh are used. For the simulated scenarios investigated in this research, the run time of a single genetic algorithm simulation amounts to ~7 days on a computer system with 2.4 GHz of processing speed and 2 GB of processing memory. The constant 4 kW/m^2 difference between 10 and 5 mm meshes contributes to approximately 5 – 8 % reduction in the

total radiative heat flux for the 5 mm mesh. The total radiative heat flux is the sum of radiative heat fluxes from both the cone heater and the flame.

8.8.2 Transforming Thermophysical Properties in FDS 5 to Gpyro

As mentioned before, a set of effective thermal conductivity (λ_{eff}) and specific heat ($c_{p,eff}$) are used for the Gypro simulations to compensate for the linear change in magnitude of the same properties within FDS 5. The calculation to establish λ_{eff} and $c_{p,eff}$ utilise the same method as calculating ρ_{eff} in Scheme 2 where ρ in Equation (8-11) is replaced by either λ or c_p. The values of λ and c_p for foam and melt are obtained via the Hot Disk experiments while for mixture, the values are determined from Equation (8-13). The percentage of temperature range occupied by the different physical states, foam, mixture and melt are established from the TGA results as illustrated in Scheme 2. Table 8-18 shows the effective thermophysical properties calculated for use in Gypro simulations.

Table 8-18: Effective thermophysical properties of different polyurethane foams for Gpyro simulations

Effective thermophysical property	Polyurethane foams tested						
	NFR-SB-31	NFR-DG-42	NFR-C-19	FR-Y-36	FR-LG-38	FR-W-50	FR-G-32
λ_{eff} (W/mK)	0.107	0.111	0.101	0.111	0.112	0.117	0.105
$c_{p,eff}$ (J/kgK)	2600	2334	2312	2313	2325	2203	2464

8.8.3 Compatibility Assessment between FDS 5 and Gpyro

The compatibility of Gpyro with FDS 5 is assessed by comparing the sample mass loss rate from both models using the same material properties as model inputs. The FDS 5 simulations utilise Scheme 2 which is the multi reactions scheme, 10 mm gas phase mesh and the material properties listed in Table 8-13 as model inputs. The Gpyro simulations have the same decomposition scheme and inputs as FDS 5 except for λ and c_p where the calculated effective values in Table 8-18 are used. Also, to simulate ignition and the subsequent flaming combustion in Gpyro, the ignition times and flame heat fluxes from Table 8-17 are specified. Figure 8-37 shows the sample mass loss rate comparison between FDS 5 and Gpyro for NFR-SB-31. Both models are able to simulate the level burning behaviour exhibited by polyurethane foam at

low heat flux and the two stage burning behaviour at high heat flux. The overall magnitude predicted by FDS 5 and Gpyro is similar but both models do vary to some extent over the different phases of the fire.

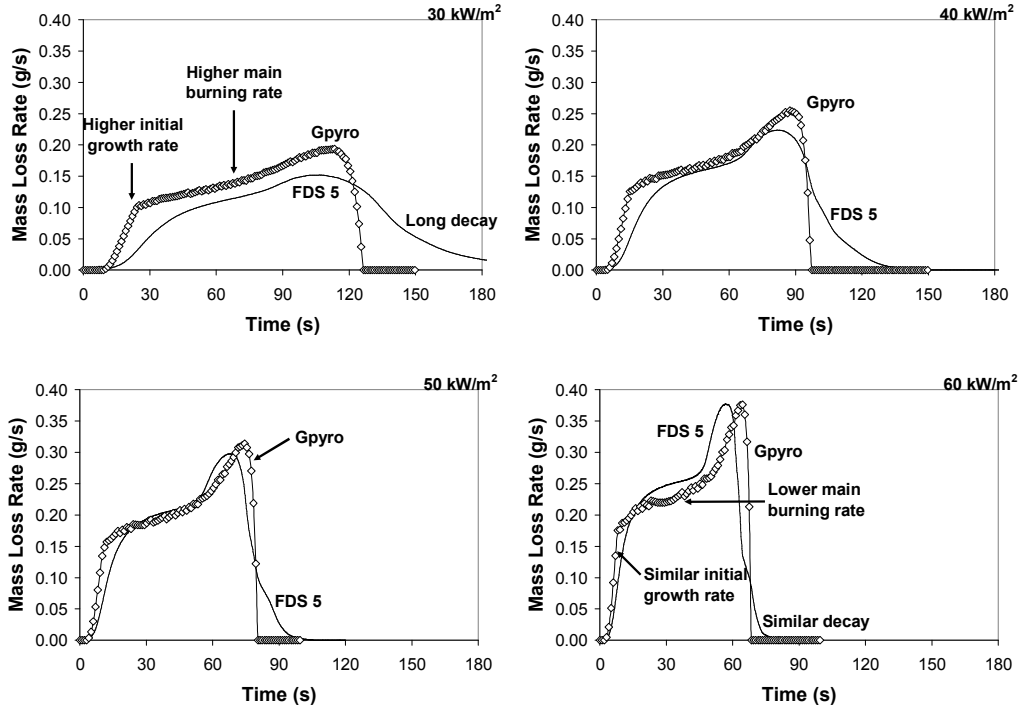

Figure 8-37: Sample mass loss rate of FDS 5 and Gpyro for NFR-SB-31 at 30, 40, 50 and 60 kW/m^2

During the initial growth phase, the Gpyro results at 30 kW/m^2 show a greater and earlier mass loss rate when compared to FDS 5 but this difference reduces with the increase in exposure heat flux. The difference is attributed to the variation in the representation of the flame and the thermophysical properties between the models. The flame heat flux in FDS 5 builds up gradually depending on the flame height and size but in Gpyro, a constant heat flux is added immediately upon ignition. In terms of thermophysical properties, λ_{eff} in Gpyro simulation, ranging from 0.101 – 0.117 W/mK is greater than λ_{foam}, ranging from 0.048 – 0.050 W/mK which is the initial value in FDS 5. Thus, the material modelled in Gpyro has better initial heat conduction capability. Likewise $c_{p,eff}$ in Gpyro simulation, ranging from 2203 – 2600 J/kgK is smaller than $c_{p,foam}$ in FDS 5, ranging from 2359 – 2996 J/kgK which means the energy required to heat up the material in Gpyro is also less. The instant growth of

flame heat flux couples with the lower thermal inertia of the material modelled give Gpyro a greater sample mass loss rate than FDS 5 over the initial growth phase.

The main burning phase consists of two stages, the first stage is a level plateau and the second stage is the subsequent peak. The peak appears less prominent at 30 kW/m^2 but it becomes more noticeable as the exposure heat flux increases. Comparing over the main burning phase, the sample mass loss rate from FDS 5 is initially less than Gpyro at 30 kW/m^2 but as the exposure heat flux increases, the magnitude of FDS 5 becomes greater and eventually surpasses Gpyro at 60 kW/m^2. Lastly, for the decay phase, the flame size in FDS 5 reduces gradually as the fuel content is exhausted. This produces a tail in the sample mass loss rate curve which is not seen in the Gpyro results. The comparison of the decay phase between the two models is the worst at 30 kW/m^2 but it improves towards higher exposure heat fluxes as the tail shortens due to more rapid decay of the flame size in FDS 5 following the increase in the decomposition rate. The models comparison for the other polyurethane foams is similar to Figure 8-37 so their results are not repeated.

The compatibility assessment performed reveals that at 30 kW/m^2, both models compare poorly due to the slow initial growth rate and the extensive tail towards the end of the mass loss rate curve in FDS 5. These trends are mainly attributed to the difference between the models in representing the temperature dependency of thermophysical properties and the radiative heat flux from flame. Despite the poor comparison at 30 kW/m^2, as the exposure heat flux increases, relatively good improvements are noted which validate the compatibility between FDS 5 and Gpyro.

8.9 Kinetic Properties Estimated with Genetic Algorithm of Gpyro

Since FDS 5 and Gpyro are compatible with each other, the genetic algorithm in Gpyro is used to estimate the E, A and Δh_r for the two reactions of Scheme 2. The estimated kinetic properties are later used in FDS 5 simulations of the different polyurethane foams. The following sections described the features of the genetic algorithm in Gpyro and the results of the property refinement process.

8.9.1 Genetic Algorithm in Gpyro

Genetic algorithm is an evolutionary search tool based on Darwinian theory and it is suitable for problems exhibiting nonlinearity with high dimensionality such as the decomposition of material governed by several changeable material properties[27,115]. Within Gpyro, its pyrolysis model and the genetic algorithm are coupled. The pyrolysis model simulates the experiment while the genetic algorithm finds a set of optimal solution which provides the closest agreement between the model outputs and the experimental results provided for comparison. The property estimation process initiates through the generation of an initial population consisting of a number of individuals, in this case, an individual is the set of E, A and Δh_r for the two reactions of Scheme 2. Each kinetic property is known as a gene which experiences evolution in the form of systematic and random changes to its value over the number of user defined iterations or generations. The run time of the simulation and also the optimal solution obtained eventually are governed by the range of the defined search boundary, the number of generations and individuals utilised and the experimental results supplied for comparison.

In each generation, the sets of kinetic properties are tried successively as inputs to the pyrolysis model and the simulated outputs are compared with the experimental results. The compared results in this research are the average sample mass loss rate and the average cumulative mass loss of the repeated cone experiments for each exposure heat flux. The sample mass loss rate measured by the load cell contains significant amount of noise thus the sample mass loss rate supplied is actually back-calculated by dividing HRRPUA by the effective heat of combustion. Gpyro then automatically computes the cumulative mass loss from the sample mass loss rate supplied. Based on the closeness between the model results and the experimental results, the fitness of each individual is computed where the individual with greater fitness has a higher probability of being selected to reproduce offspring for the next generation. To prevent premature convergence to a particular solution, a set of kinetic properties can only be selected a number of times which is defined by the user.

Further selection of the same individual will then prompt the algorithm to randomly choose a different individual from the population for reproduction.

An offspring for the next generation are generated from the linear combination of the genes from two parents. Again to prevent early convergence of the solution and also to adequately explore the search boundaries, the genes of an offspring are subjected to probabilistic mutation. The user defined probability of mutation is assigned to every gene and two types of mutation can occur. The first type of mutation involves a complete replacement of the current property with a new value while the second type of mutation is a partial replacement where the magnitude varied depends on the severity of mutation defined by the user. Finally, the new generation is created by replacing the parents with the offspring. Table 8-19 contains the parameters related to the genetic algorithm (GA) of Gpyro, their definition and the values used.

Table 8-19: Definitions and input values for parameters of Gpyro's genetic algorithm

GA parameter	Definition	Value[a]
NINDIV	Number of individuals	20
NGEN	Number of generations	200
MAXCOPIES	Maximum number of selection for one individual to reproduce	6
WHOLEGENEFRAC	Fraction of genes not produced by linear combination	0.5
PHI	Fitness metric weighting	1
FITEXPONENT	Constant to raise fitness	2.0
EPS	Constant to prevent infinite fitness	0.05
PMUT	Probability of mutation	0.15
VMUTMAX	Severity of mutation	0.4

For this research, the number of individuals, NINDIV in each generation is 20 and the number of generations, NGEN for the entire simulation is 200. The maximum number of time an individual can be selected for reproduction per generation, MAXCOPIES is set to 6. The fraction of genes that is not produced via the process of linear combination of two parents, WHOLEGENEFRAC is set to 0.5 in which case, the genes originating entirely from one parent are used. The parameters associated with the fitness calculation, PHI, FITEXPONENT and EPS are set to 1, 2 and 0.05 respectively. During the comparison between the model outputs and the experimental results supplied, PHI is the fitness metric weighting which can be adjusted to achieve more emphasis on a particular set of experimental measurements. In this research, the

[a] Most values are the program defaults except for the number of individuals and the number of generations.

same weighting is applied to the mass loss rate and the cumulative mass loss at different heat fluxes hence all the comparisons made contribute equally towards the fitness value. FITEXPONENT is the power which the fitness value is raised to while EPS is specified to prevent the fitness value from becoming infinite when the difference between the model and experimental results becomes small. Lastly, regarding mutation, the probability of mutation, PMUT is set to 0.15 and the severity of mutation, VMUTMAX for partial replacement is set to 0.4. Changes made on the parameters governing the reproduction, mutation and fitness calculation can potentially affect the outcome of the property estimation process so assessing the sensitivity of these parameters should be the focus of future research.

8.9.2 Search Boundary and Statistical Distribution of Kinetic Properties

Gpyro is able to produce one global set of estimated properties for a group of experimental results collected at multiple experimental conditions. Therefore, for this research, a single set of kinetic properties specific to each polyurethane foam are estimated from the experimental results at different exposure heat fluxes. Again, similar to the compatibility assessment between FDS 5 and Gpyro, the ignition times and flame heat fluxes from Table 8-17 and the effective thermophysical properties from Table 8-18 are specified for the property estimation process. The ignition times and flame heat fluxes represent flaming combustion in Gpyro while the effective thermophysical properties represent the temperature dependency of the same properties in FDS 5. The search boundaries allocated for E, A and Δh_r are tabulated in Table 8-20 and the unit presented for these properties are the same unit used in Gpyro. Due to the large magnitude of A and Δh_r, their range gap is significantly wider than E and this generates a wide search range for the genetic algorithm which can prolong the estimation process. Conveniently, Gpyro allows a material property to be presented in logarithmic form to resolve this issue. So both A and Δh_r are searched in this fashion to narrow their search range. The logarithmic value is included within brackets in Table 8-20. The subscripts '*1*' and '*2*' denote the first and second reactions while the subscripts '*min*' and '*max*' denote the minimum and maximum of the boundary.

Table 8-20: Search boundaries of kinetic properties in Gpyro for different polyurethane foams

Kinetic property	Polyurethane foams tested, types of boundary and boundary value						
	NFR-DG-42	**FR-Y-36**	**FR-W-50**	**FR-G-32**	**NFR-SB-31**	**NFR-C-19**	**FR-LG-38**
	Default	**Default**	**Default**	**Default**	**Extended**	**Extended**	**Extended**
$E_{1,min}$ (kJ/mol)	69				69	69	69
$E_{1,max}$ (kJ/mol)	121				121	121	121
$A_{1,min}$ (s^{-1})	6.47×10^{3} (3.8)				6.47×10^{3} (3.8)	6.47×10^{3} (3.8)	6.47×10^{3} (3.8)
$A_{1,max}$ (s^{-1})	8.45×10^{8} (8.9)				8.45×10^{8} (8.9)	8.45×10^{8} (8.9)	8.45×10^{8} (8.9)
$\Delta h_{r1,min} \cdot 10^{3}$ (J/kg)	575 (5.76)				575 (5.76)	575 (5.76)	575 (5.76)
$\Delta h_{r1,max} \cdot 10^{3}$ (J/kg)	1288 (6.11)				1467* (6.17)	1467* (6.17)	1288 (6.11)
$E_{2,min}$ (kJ/mol)	120				120	120	120
$E_{2,max}$ (kJ/mol)	274				274	313*	274
$A_{2,min}$ (s^{-1})	4.62×10^{6} (6.7)				4.62×10^{6} (6.7)	2.82×10^{3}* (3.4)	4.62×10^{6} (6.7)
$A_{2,max}$ (s^{-1})	3.36×10^{19} (19.5)				3.36×10^{19} (19.5)	3.36×10^{19} (19.5)	3.36×10^{19} (19.5)
$\Delta h_{r2,min} \cdot 10^{3}$ (J/kg)	178 (5.25)				178 (5.25)	178 (5.25)	149* (5.17)
$\Delta h_{r2,max} \cdot 10^{3}$ (J/kg)	295 (5.47)				295 (5.47)	295 (5.47)	295 (5.47)

The boundary values of the default range in Table 8-20 are the minimum and maximum kinetic properties from a number of individual SDT experiments. For *E* and *A*, the selected properties are determined from the SDT experiments with ~3 mg foam sample at 1, 5, 20 and 60 °C/min. For Δh_r, the selected properties are obtained from the SDT experiments within the consistent and recommended regions for DSC, involving both foam and melt samples. The default range is used as the first search boundary for all polyurethane foams and the optimal solution obtained for each foam is checked against the minimum and maximum of the boundary. If the refined kinetic properties are at the boundary, this means that there are potentially better solutions beyond the current search range. In this case, a new genetic algorithm simulation is performed with the breached boundary extended by 25 % of its default value. Using the default range, the optimal solution is obtained for NFR-DG-42, FR-Y-36, FR-W-50 and FR-G-32 but different extended ranges are required to obtain the optimal solution for NFR-SB-31, NFR-C-19 and FR-LG-38. The extended boundary values are marked with an asterisk in Table 8-20.

The genetic algorithm produces one best fit solution for each generation. Figure 8-38 shows the cumulative distribution function (CDF) and the probability density function (PDF) of the best fit solutions for NFR-SB-31 over 200 generations. The black

symbol represents CDF and the white symbol represents PDF. As indicated on the plot, the optimal solution over the entire simulation is denoted by 'Opt' and the maximum and minimum boundary values of each kinetic property are denoted by 'Min' and 'Max'. The subscripts '*1*' and '*2*' denote the first and second reactions.

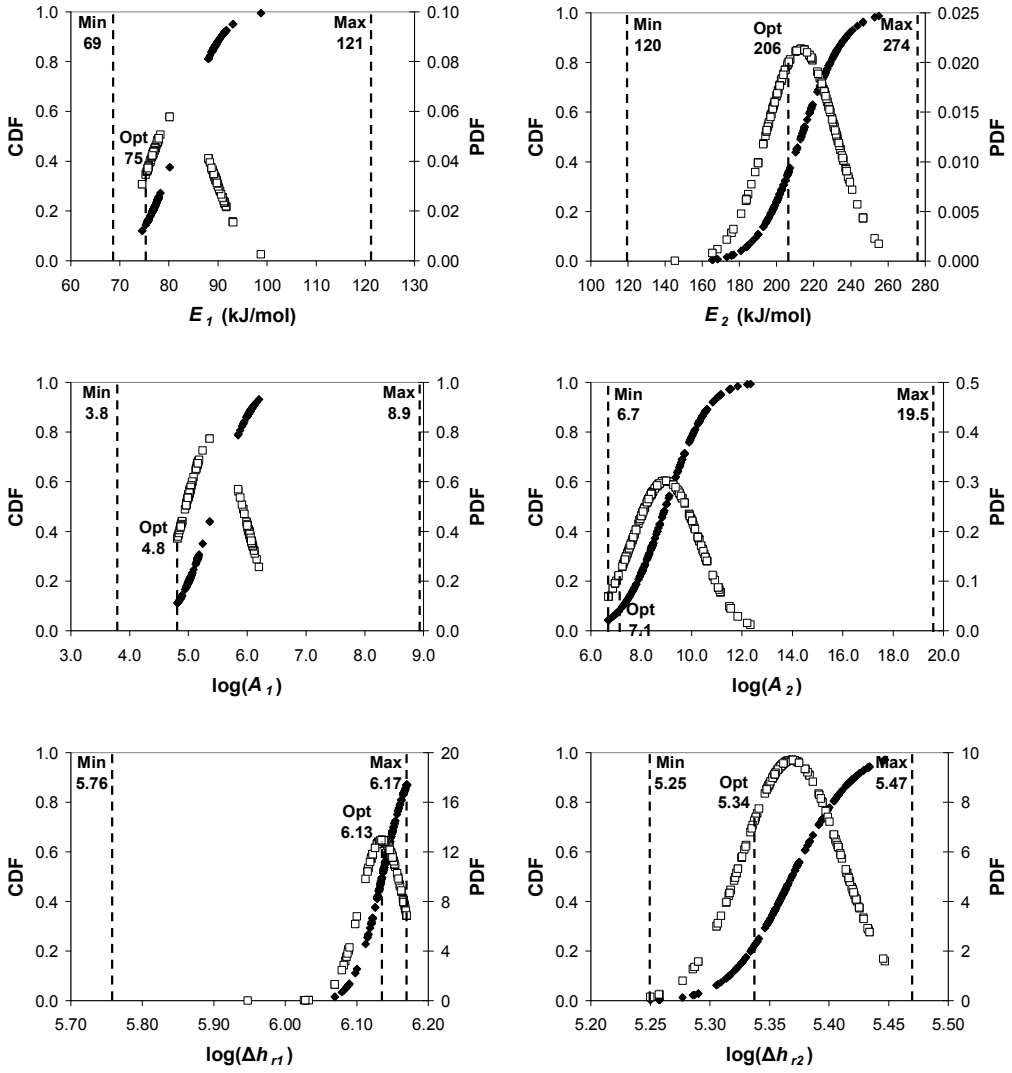

Figure 8-38: CDF and PDF of 200 best fit solutions for NFR-SB-31

Figure 8-38 shows the CDF sums up to unity at the end of the search range and the PDF has a bell shape curve. The optimal solution is contained within the search boundary and it does not breach the minimum and maximum of the range. The trend of CDF and PDF is similar for the other polyurethane foams so those results are not reproduced here. The optimal solution or the set of refined kinetic properties for all the polyurethane foams are tabulated in Table 8-21, denoted by 'Est'. The

experimentally derived properties denoted by ‘Exp’ and the difference compared to the estimated property, ‘Diff’ are also included. The difference is represented as the percentage of the experimentally derived values.

Table 8-21: Gpyro estimated and experimentally determined kinetic properties for different polyurethane foams tested

Kinetic properties		Polyurethane foams tested						
		NFR-SB-31	**NFR-DG-42**	**NFR-C-19**	**FR-Y-36**	**FR-LG-38**	**FR-W-50**	**FR-G-32**
E_1 (kJ/mol)	Est	75	99	90	82	99	92	100
	Exp	88	85	99	94	87	78	114
	Diff (%)	-15	16	-10	-13	14	17	-13
A_1 (s^{-1})	Est	6.82×10^{4}	2.40×10^{6}	4.47×10^{5}	2.95×10^{4}	3.59×10^{5}	2.36×10^{5}	4.98×10^{6}
	Exp	2.18×10^{5}	8.87×10^{4}	2.19×10^{6}	1.23×10^{6}	2.01×10^{5}	2.80×10^{4}	1.30×10^{8}
	Diff (%)	-9	29	-11	-27	5	21	-17
Δh_{r1} (J/g)	Est	1357	983	1285	845	621	762	1092
	Exp	891	768	1023	848	793	610	672
	Diff (%)	52	28	26	0	-22	25	62
E_2 (kJ/mol)	Est	206	226	256	220	196	227	242
	Exp	150	151	247	210	206	178	164
	Diff (%)	38	49	4	5	-5	27	47
A_2 (s^{-1})	Est	1.25×10^{7}	8.56×10^{7}	5.00×10^{5}	1.11×10^{9}	2.54×10^{8}	5.58×10^{10}	3.57×10^{7}
	Exp	3.06×10^{9}	4.60×10^{9}	3.07×10^{17}	2.42×10^{14}	9.52×10^{13}	3.81×10^{11}	4.58×10^{10}
	Diff (%)	-25	-18	-67	-37	-40	-7	-29
Δh_{r2} (J/g)	Est	218	200	206	211	214	193	216
	Exp	233	279	295	198	178	217	264
	Diff (%)	-6	-28	-30	6	20	-11	-18

The temperature dependent part of the decomposition rate is an Arrhenius expression, also known as the rate constant, k. As seen in Equation (3-17), the expression contains the constants, E and A which function as a pair. Due to the exponential nature of the relationship, the changes in E should be compared with the changes in $\ln(A)$ instead of A. Thus, the percentage difference reported for A in Table 8-21 is calculated on the basis of $\ln(A)$. From Table 8-21, the absolute percentage difference of E, A and Δh_r between the estimated values and the experimental values can vary as little as 0 % or as much as 70 % for the different polyurethane foams. The average taken by including the different foams produces a clearer depiction of the global trend. For the first and second reactions respectively, the average difference is 14 and 25 % for E, 17 and 32 % for A and 31 and 17 % for Δh_r.

The results show that the average difference between the estimated and experimental properties relates to the magnitude of the kinetic properties and also the allocated search range. A kinetic property with greater magnitude and allocated a greater search range produces a greater difference between its experimentally derived value and its Gpyro estimated value. As seen from Table 8-21, the magnitude of E and A from the second reaction is consistently greater than the first reaction and from Table 8-20, the allocated search range is also greater. As a result, the average difference in E and A is greater for the second reaction. For Δh_r, the opposite is noted where the first reaction possesses greater magnitude and search range. As such, the average difference of Δh_r for the first reaction is noted to be greater.

Table 8-22 shows the range of kinetic properties from Gpyro estimation, denoted by 'Est' and those determined experimentally, denoted by 'Exp'. Including all the polyurethane foams, the Gpyro estimated values of E, A and Δh_r have a narrower range when compared with the experimentally derived properties except for Δh_r of the first reaction.

Table 8-22: Range of kinetic properties from Gpyro estimation and experimental derivation

Reactions		Range of kinetic properties					
		E (kJ/mol)		A (s^{-1})		Δh_r (J/g)	
		min	max	min	max	min	max
1	Est	75	100	2.95×10^{4}	4.98×10^{6}	621	1357
	Exp	78	114	2.80×10^{4}	1.30×10^{8}	610	1023
2	Est	196	256	5.00×10^{5}	5.58×10^{10}	193	218

	Exp	150	247	3.06×10^{9}	3.07×10^{17}	178	295

The results from the direct method show that for most of the foams simulated, the model HRRPUA consistently overpredicts the experimental HRRPUA, especially at exposure heat flux greater than 30 kW/m^2. In attempt to match the experimental results supplied for comparison, the Gpyro genetic algorithm has selected E and A such that the reaction rate of the second reaction is lowered. The decomposition rate in Equation (8-14) shows that the reaction rate can be lowered when the value of E increases or the value of A decreases or both. For all polyurethane foams, a consistent trend is noted between the refined E and A of the second reaction and their experimentally derived values. E has increased while A has decreased to lower the reaction rate with the exception to E of FR-LG-38 which shows 5 % reduction. However, any effect this has on the reaction rate of FR-LG-38 can be considered negligible as its A reduces far more significantly by 40 % to lower the reaction rate. In contrast to the second reaction, the first reaction shows that any changes in either E or A are cancelled by a similar counter changes in the other parameter such that the reaction rate remains constant.

8.9.3 Gpyro Modelling using Optimal Solution as Inputs

During the property estimation process, the pyrolysis model of Gpyro produces the sample mass loss rate and the cumulative mass loss at different heat fluxes using each set of kinetic properties as inputs. These outputs are compared with the supplied experimental results at the respective heat flux to determine the fitness of the solutions. Figure 8-39 compares the sample mass loss rate of the optimal or fittest solution with the experimental results supplied. The results of the base case foams, NFR-SB-31 and FR-Y-36 are presented.

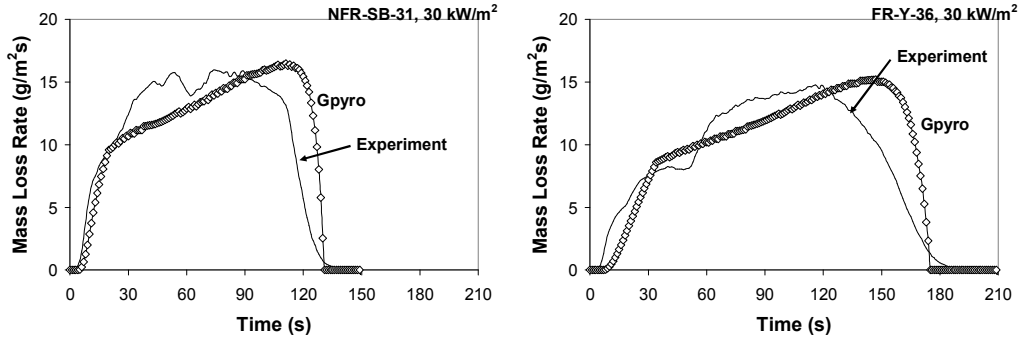

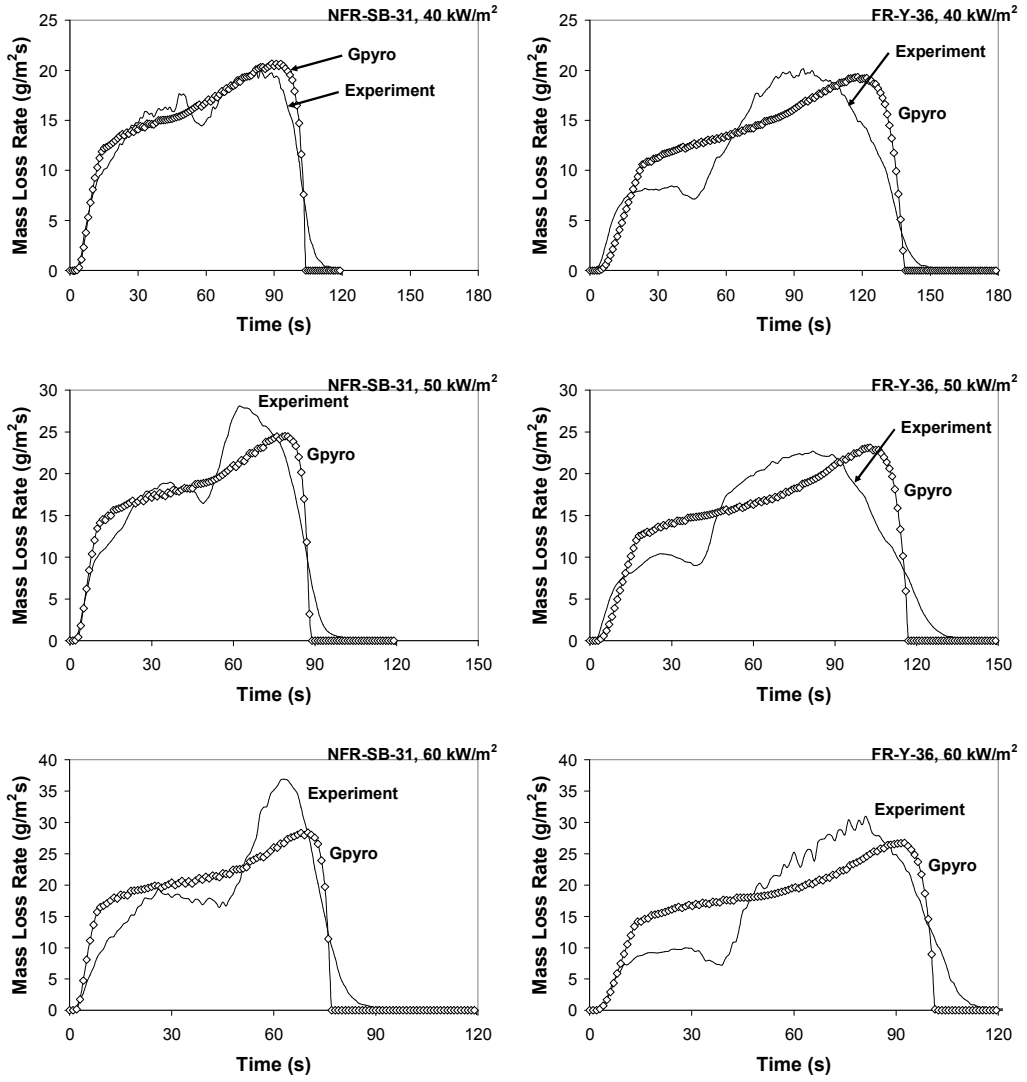

Figure 8-39: Comparison between Gpyro mass loss rate of optimal solution and experimental mass loss rate at 30, 40, 50 and 60 kW/m^2 for NFR-SB-31 and FR-Y-36

The primary difference between the two foams is the relatively better prediction over the first burning stage in the case of NFR-SB-31 compared to FR-Y-36. Also, the model manages to predict the second burning stage of NFR-SB-31 at 40 and 50 kW/m^2 but in the case of FR-Y-36, the plateau burning behaviour of the second stage has not been captured satisfactorily. The simulation results of other foams collectively show the multi reaction scheme, Scheme 2 struggles to capture the extensive level burning behaviour caused by the fire retardant mechanisms of the foams. These fire retardant mechanisms are not specifically addressed in the model used.

Table 8-23 shows the foam specific and heat flux specific fitness of the optimal solution for each polyurethane foam. The foam specific fitness is an output of Gpyro which is computed as the sum of fitness from all the heat fluxes simulated. The heat flux specific fitness is calculated by dividing the foam specific fitness equally by the number of heat fluxes simulated.

Table 8-23: Foam specific fitness and heat flux specific fitness of the optimal solution for different polyurethane foams

Type of Fitness	Polyurethane foams tested						
	NFR-SB-31	NFR-DG-42	NFR-C-19	FR-Y-36	FR-LG-38	FR-W-50	FR-G-32
Foam specific	686	312	345	470	400	287	327
Heat flux specific	172	156	173	118	200	144	164

A larger magnitude in Table 8-23 is indicative of a better fitness for the optimal solution. NFR-SB-31 and FR-Y-36 are simulated at 40 and 60 kW/m^2 in addition to the two common heat fluxes at 30 and 50 kW/m^2. As such, their foam specific fitness consisting of four heat flux specific fitness are relatively higher than the other foams. FR-LG-38 and FR-Y-36 have the best and worst heat flux specific fitness respectively. For the worst fitness, the comparison of FR-Y-36 as seen in Figure 8-39 shows the model struggles to capture the restricted burning behaviour of the first stage and also the extended plateau burning behaviour in the second stage. For the best fitness, Figure 8-40 compares the model and experimental mass loss rate of FR-LG-38 where the prediction at 30 kW/m^2 appears better when compared to 50 kW/m^2. Again, the model is noted to struggle in modelling the plateau burning behaviour of the first and second stages at 50 kW/m^2.

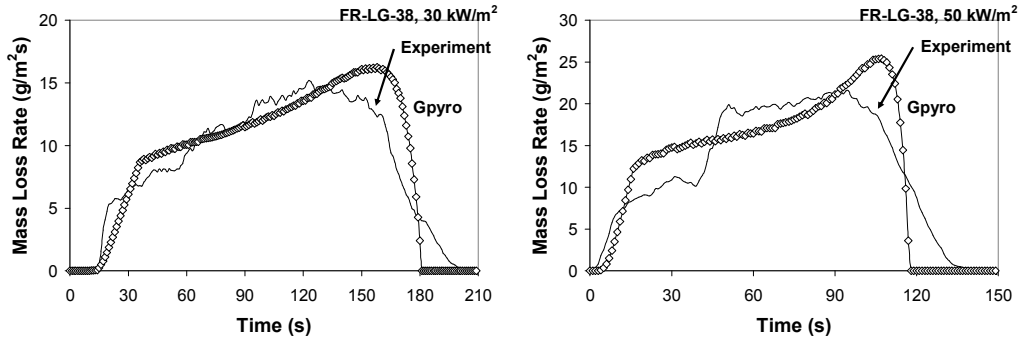

Figure 8-40: Comparison between Gpyro mass loss rate of optimal solution and experimental mass loss rate at 30 and 50 kW/m^2 for FR-LG-38

8.10 FDS 5 Modelling of 1-Dimensional Burning Behaviours of Polyurethane Foams using Gpyro Estimated Kinetic Properties as Inputs, Refined Method

The same simulations performed during the direct method are repeated with the kinetic properties, E, A and Δh_r of the first and second reactions being replaced by the Gpyro estimated values listed in Table 8-21. This method is also referred as the refined method in this research. Figure 8-41 shows the model and experimental HRRPUA comparison of the base case foams, NFR-SB-31 and FR-Y-36 at all the exposure heat fluxes. The different regions analysed during the linear regression analysis are depicted on the plot.

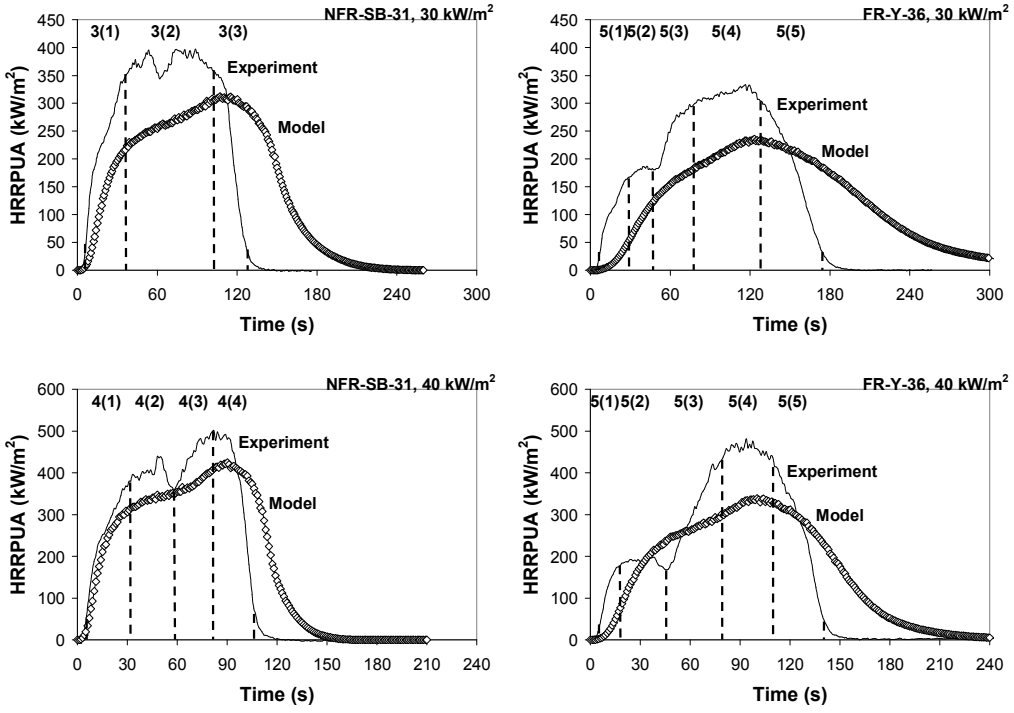

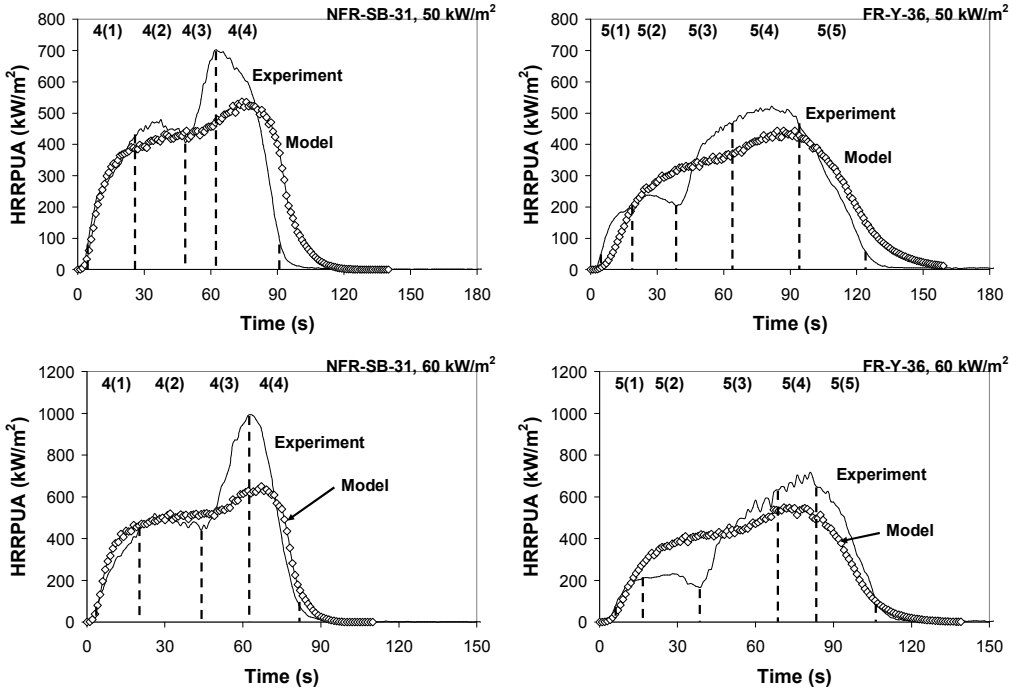

Figure 8-41: Comparison between FDS 5 HRRPUA by refined method and experimental HRRPUA at 30, 40, 50 and 60 kW/m^2 for NFR-SB-31 and FR-Y-36

For NFR-SB-31, the model shows that there is a delay in the initial growth at 30 kW/m^2 but when the exposure heat flux increases, the model prediction of the growth becomes progressively better. The model consistently underpredicts the HRRPUA and more notably over the second stage than the first stage. In fact, the model is able to capture the burning behaviour of the first stage at 50 and 60 kW/m^2. The greatest difference is noted between the model and experimental HRRPUA at 60 kW/m^2 over the second burning stage where the model underpredicts by approximately 400 kW/m^2. This mismatch is partly due to the constant effective heat of combustion, 25 MJ/kg that is applied. According to the experimental results in Table 8-2, the effective heat of combustion is seen to increase suddenly from the constant 25 MJ/kg to 27 MJ/kg at 60 kW/m^2 and this change has not been incorporated in the simulation.

For FR-Y-36, some trends are similar to NFR-SB-31 including the delay to the initial growth which improves with increasing heat flux and the consistent underprediction of HRRPUA. Despite having refined kinetic properties as inputs, the model still struggles to reproduce the extensive level burning behaviour seen over the two stages which is an inherent feature of the FR foams due to their fire retardant mechanisms.

The first plateau stage is not captured at any of the heat fluxes simulated where the model underpredicts at 30 kW/m^2 and overpredicts at higher heat fluxes. At 60 kW/m^2, the model shows the maximum overprediction of the first stage, approximately 200 kW/m^2. Different to NFR-SB-31 where the model struggles to predict the second burning stage at high heat fluxes, for FR-Y-36, the model actually shows improved prediction of the second stage as the heat flux increases.

The trends seen in the other foams are similar to those observed in NFR-SB-31 and FR-Y-36 so these results are not reproduced here. The common trends include the delay of the initial growth which improves with increasing heat flux and the consistent underprediction of HRRPUA. For all heat fluxes, the difference in the maximum HRRPUA between the model and experiment is mostly around 100 kW/m^2, except for NFR-SB-31 which shows greater difference of 200 and 400 kW/m^2 at heat flux of 50 and 60 kW/m^2 respectively. Therefore, in comparison with the direct method, the refined method has achieved a better overall comparison with the experimental results for most foams. From this qualitative comparison, the refined method predicts better at high heat flux than at low heat flux, a trend that is opposite to the direct method.

8.10.1 Linear Regression Analysis for Refined Method

In order to quantify the accuracy of FDS 5 modelling with the refined kinetic properties as inputs, the linear regression analysis is performed for the model and experimental HRRPUA, similar to the approach described previously for the direct method. The analysis is performed for the different analysis regions depicted in Figure 8-41 and the definition of each region is summarised in Table 8-14. The linear regression analysis for NFR-SB-31 and FR-Y-36 are showed in Figure 8-42 and the different symbols used on the plot represent the different analysis regions. Again, the line of perfect correlation and the two dashed lines forming the boundary of acceptance are used to gauge the accuracy of the refined method. The boundary is set to 25 % of the greatest experimental HRRPUA and the data points located within the boundary are considered to have acceptable accuracy.

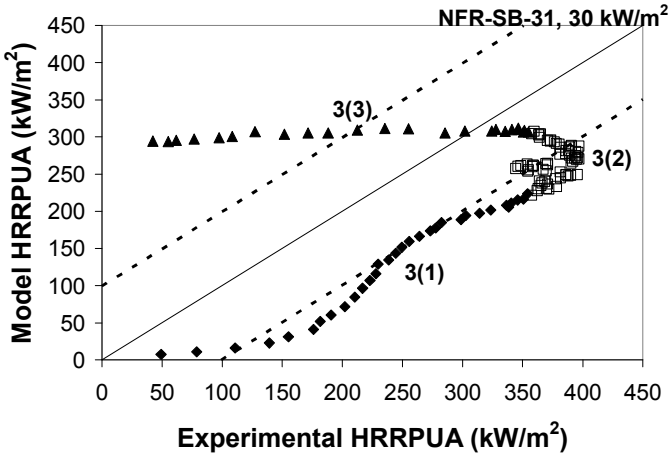
NFR-SB-31, 30 kW/m2
Model HRRPUA (kW/m2)
Experimental HRRPUA (kW/m2)
3(3)
3(2)
3(1)

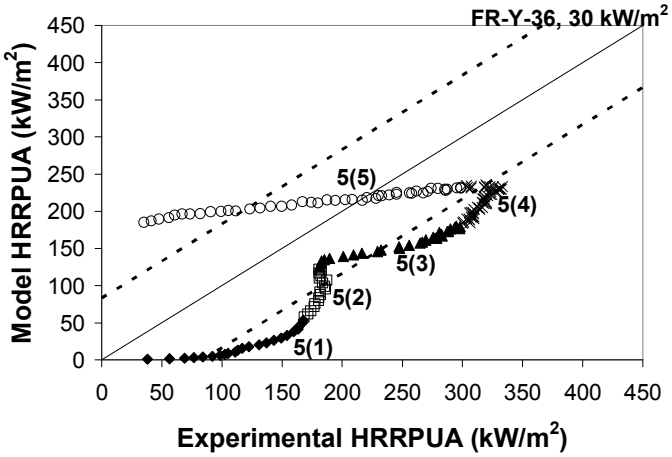
FR-Y-36, 30 kW/m2
Model HRRPUA (kW/m2)
Experimental HRRPUA (kW/m2)
5(5)
5(4)
5(3)
5(2)
5(1)

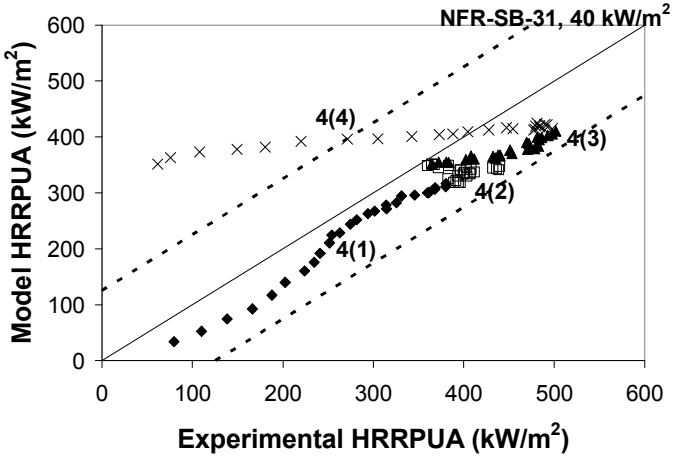
NFR-SB-31, 40 kW/m2
Model HRRPUA (kW/m2)
Experimental HRRPUA (kW/m2)
4(4)
4(3)
4(2)
4(1)

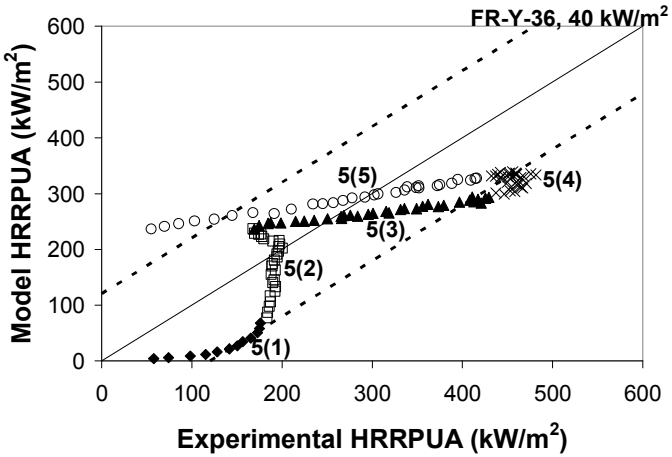
FR-Y-36, 40 kW/m2
Model HRRPUA (kW/m2)
Experimental HRRPUA (kW/m2)
5(5)
5(4)
5(3)
5(2)
5(1)

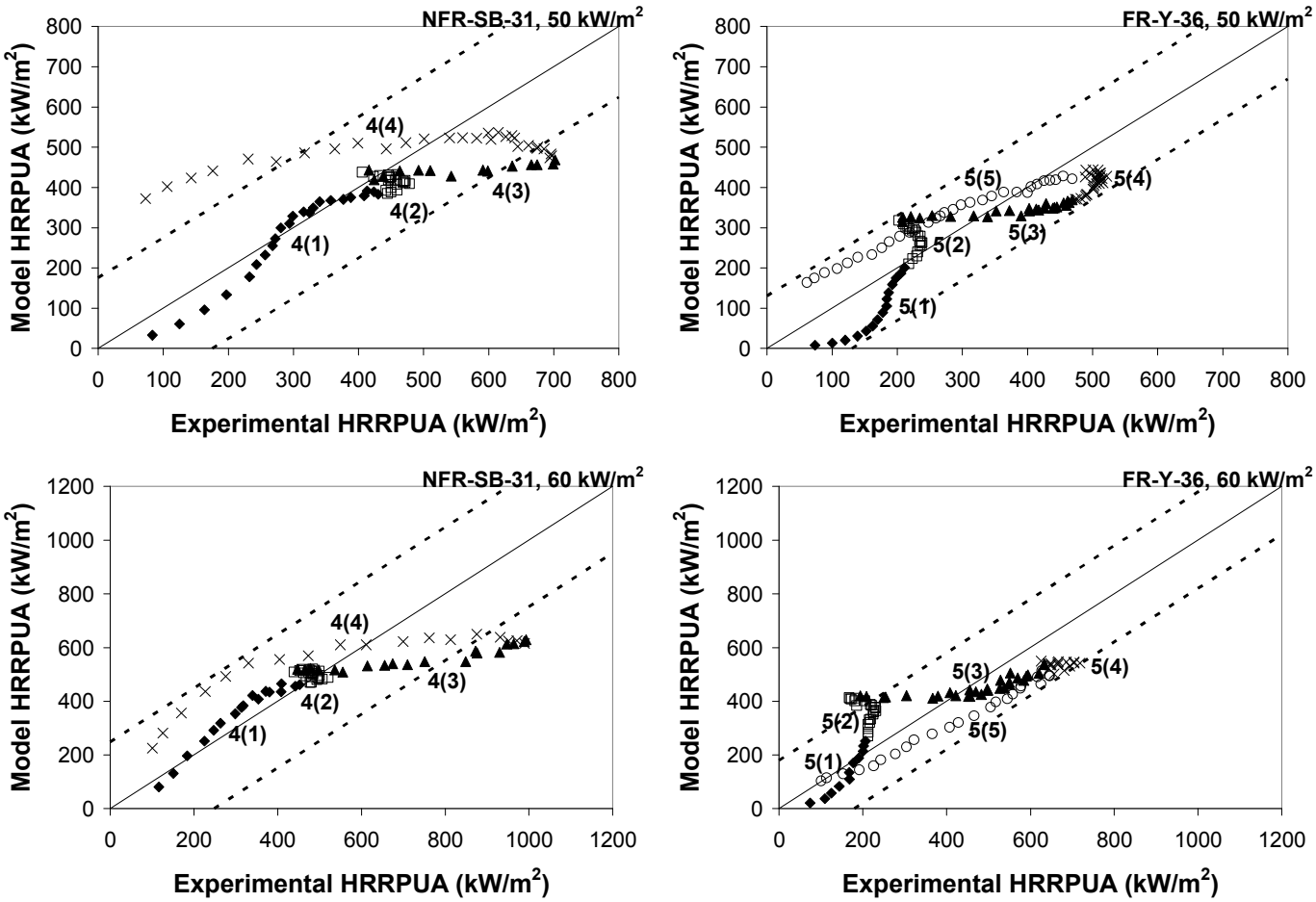

Figure 8-42: Linear regression analysis on HRRPUA between refined method and experiments for NFR-SB-31 and FR-Y-36 at 30, 40, 50 and 60 kW/m^2

Using the results at 30 and 50 kW/m^2 as example, the outcome of the linear regression analysis on both base case foams is explained. For NFR-SB-31 at 30 kW/m^2, the results are actually very similar to those from the direct method where the model underpredicts over the initial growth and single plateau regions while overpredicting in the decay region. In the case of FR-Y-36, the model mostly underpredicts for all of the regions except during the later part of the decay region. At 50 kW/m^2, the results from NFR-SB-31 and FR-Y-36 shows the model has produced better prediction when compared to 30 kW/m^2. For NFR-SB-31, most of the data points over the different regions are within the boundary of acceptance, except over the leading second peak region and towards the end of the trailing second peak region. The results of FR-Y-36 show that all of the data points analysed are within the boundary of acceptance. The pattern seen in the linear regression analysis consistently reflects the same trend seen between the model and experimental HRRPUA curves in Figure 8-41. Given the similarity between the other foams and the base case foams presented, the linear regression analysis for the other foams are not reproduced here.

8.10.2 Accuracy Assessment of Refined Method

The same four classes of accuracy used to describe the modelling accuracy achieved by the direct method are also applied to quantify the refined method. These are the region specific accuracy, the heat flux specific accuracy, the foam specific accuracy and the method specific accuracy. For the simulation results with heat flux specific accuracy of less than 80 %, the curve fitting shifts are applied to improve the comparison with the experimental results. Table 8-24 shows the region specific accuracies and the heat flux specific accuracies of the refined method for all the polyurethane foams tested at the different exposure heat fluxes. The values in brackets are the accuracies determined using the averaged 3 point shift and the single point shift.

Table 8-24: Region specific accuracies and heat flux specific accuracies of refined method for all polyurethane foams tested at 30, 40, 50 and 60 kW/m^2

Sample code	Heat flux (kW/m^2)	Number of regions	Region specific accuracies (%)					Heat flux specific accuracy (%)
			1	2	3	4	5	
NFR-SB-31	30	3	22 (94,78)	32 (74,45)	58 (71,58)	N/A	N/A	35 (79,56)
	40	4	100	100	100	76	N/A	94
	50	4	100	100	64	62	N/A	82
	60	4	100	100	58	78	N/A	84
NFR-DG-42	30	3	66	96	71	N/A	N/A	82
	50	4	100	100	100	85	N/A	97
NFR-C-19	30	3	13 (91,22)	32 (15,46)	60 (67,60)	N/A	N/A	32 (47,42)
	50	4	100	100	100	75	N/A	94
FR-Y-36	30	5	22 (100,100)	39 (100,100)	27 (60,43)	8 (14,8)	73 (82,80)	34 (62,56)
	40	5	67 (100,100)	100 (100,100)	85 (91,97)	32 (29,19)	83 (87,90)	74 (78,78)
	50	5	100	100	100	100	100	100
	60	5	100	70	93	100	100	91
FR-LG-38	30	3	46 (95,95)	42 (56,56)	56 (80,80)	N/A	N/A	47 (81,81)
	50	5	100	100	100	100	100	100
FR-W-50	30	5	100 (100,100)	100 (100,100)	31 (96,76)	23 (63,60)	85 (94,89)	63 (90,83)
	50	5	100	45	78	91	100	86
FR-G-32	30	5	43 (100,-)	92 (100,-)	100 (100,-)	63 (91,-)	39 (46,-)	69 (85,-)
	50	5	100	88	100	19	100	83

The region specific accuracies and the heat flux specific accuracies of NFR-SB-31 and FR-Y-36 share a very similar trend. Low accuracies are noted at 30 kW/m^2 due to the characteristic delay of the initial growth but above 30 kW/m^2, the accuracies improve with the majority being greater than 70 %. The trend in accuracies corresponds well with the comparison of HRRPUA curves in Figure 8-41 and the linear regression analysis in Figure 8-42. For the curve fitting shifts applied, the averaged 3 point shift in particular has produced significant improvement to the accuracy, especially at 30 kW/m^2. This is possible as the original mismatch between the model and experiment is mainly in the horizontal time. Using the estimated kinetic properties as inputs, the refined method has managed to establish a fairly consistent trend among all the different foams where the model predictions at high heat flux, 50 kW/m^2 are better than those at low heat flux, 30 kW/m^2. This is in contrast with the direct method which tends to predict better at low heat flux.

Table 8-25 summarises the heat flux specific accuracies, the foam specific accuracies and the method specific accuracy of the refined method. The values reported in brackets are the results when the averaged 3 point shift and the single point shift are applied.

Table 8-25: Heat flux specific accuracies, foam specific accuracies and method specific accuracy of refined method for all polyurethane foams

Sample code	Heat flux specific accuracy (%) at different heat fluxes (kW/m^2)				Foam specific accuracy (%)
	30	40	50	60	
NFR-SB-31	35 (79,56)	94	82	84	74 (85,79)
NFR-DG-42	82	N/A	97	N/A	89
NFR-C-19	32 (47,42)	N/A	94	N/A	63 (70,68)
FR-Y-36	34 (62,56)	74 (78,78)	100	91	75 (83,81)
FR-LG-38	47 (81,81)	N/A	100	N/A	74 (90,90)
FR-W-50	63 (90,83)	N/A	86	N/A	74 (88,84)
FR-G-32	69 (85,-)	N/A	83	N/A	76 (84,-)
				Method specific accuracy (%)	75 (84,81)

The heat flux specific accuracies in Table 8-25 collectively show that the refined method is able to produce better prediction of HRRPUA as the exposure heat flux increases. Without applying curve fitting shifts, most of the foams have a foam specific accuracy greater than 70 % except for NFR-C-19 which is the lowest at 63 %. NFR-DG-42 shows a foam specific accuracy of 89 % which is the highest. The application of curve fitting shifts improves the accuracy further. Through the averaged

3 point shift, the best and worst foam specific accuracies are 90 and 70 % for FR-LG-38 and NFR-C-19 respectively while through the single point shift, these accuracies are 90 and 68 % for the same set of foams. Comparing with the best and worst accuracies achieved by the direct method which are 79 and 37 % by default, 93 and 47 % by the averaged 3 point shift and 86 and 35 % by the single point shift, the refined method has greatly improved the worst accuracy. This validates the ability of Gpyro's genetic algorithm in refining the kinetic properties which produce better predictions when used as inputs in FDS 5. In terms of the method specific accuracy, the refined method achieves 75 % by default, 84 % by the averaged 3 point shift and 81 % by the single point shift. Comparing with 56, 63 and 56 % from the direct method, this once again illustrates the improvement in accuracy achieved by the refined method.

Figure 8-43 shows the linear regression analysis on the maximum HRRPUA, the average HRRPUA and the burning duration between the refined method results and the experimental results. The plots include all the foams at the different heat fluxes tested experimentally and also simulated numerically. The boundary of acceptance (BOA) for all three parameters is set to 25 % of the experimental values.

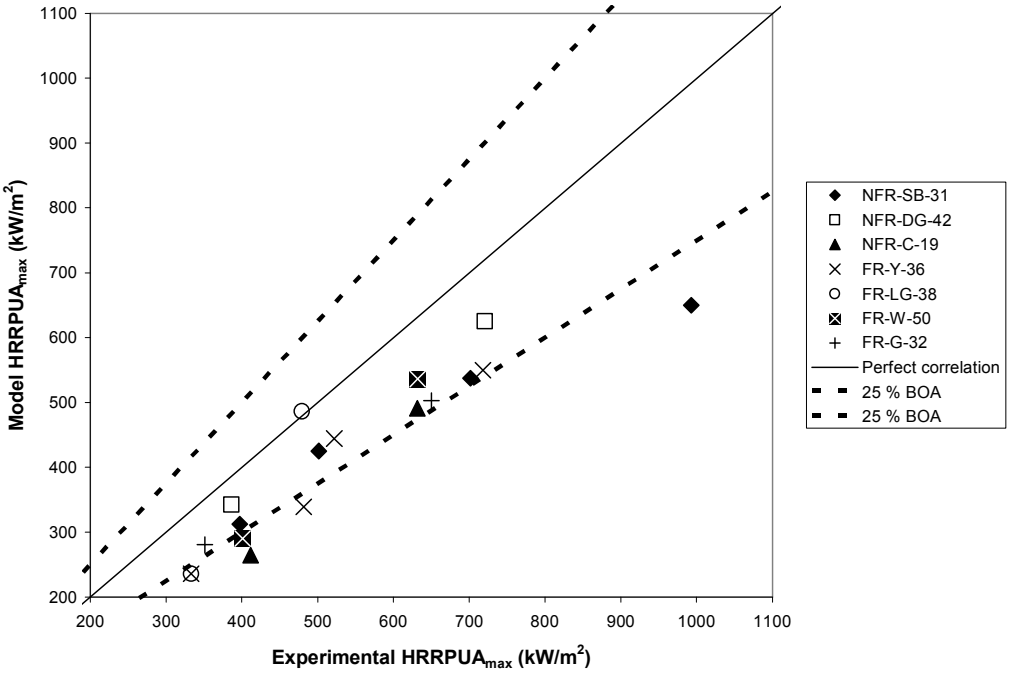
Model HRRPUA$_{max}$ (kW/m^2)
Experimental HRRPUA$_{max}$ (kW/m^2)
NFR-SB-31
NFR-DG-42
NFR-C-19
FR-Y-36
FR-LG-38
FR-W-50
FR-G-32
Perfect correlation
25 % BOA
25 % BOA

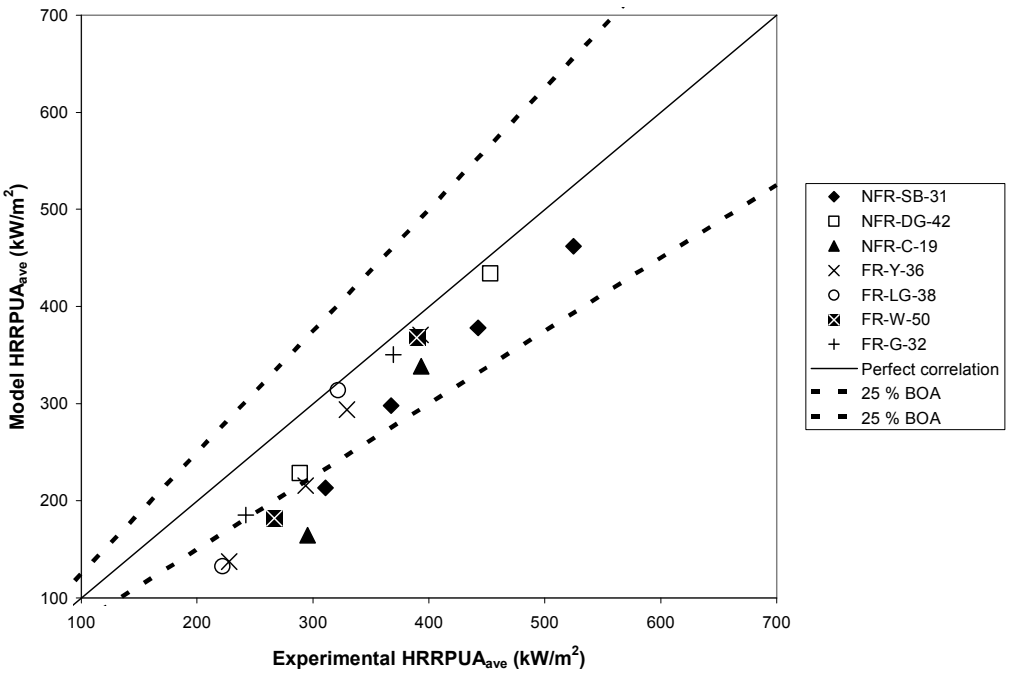
Model HRRPUA$_{ave}$ (kW/m^2)
Experimental HRRPUA$_{ave}$ (kW/m^2)
NFR-SB-31
NFR-DG-42
NFR-C-19
FR-Y-36
FR-LG-38
FR-W-50
FR-G-32
Perfect correlation
25 % BOA
25 % BOA

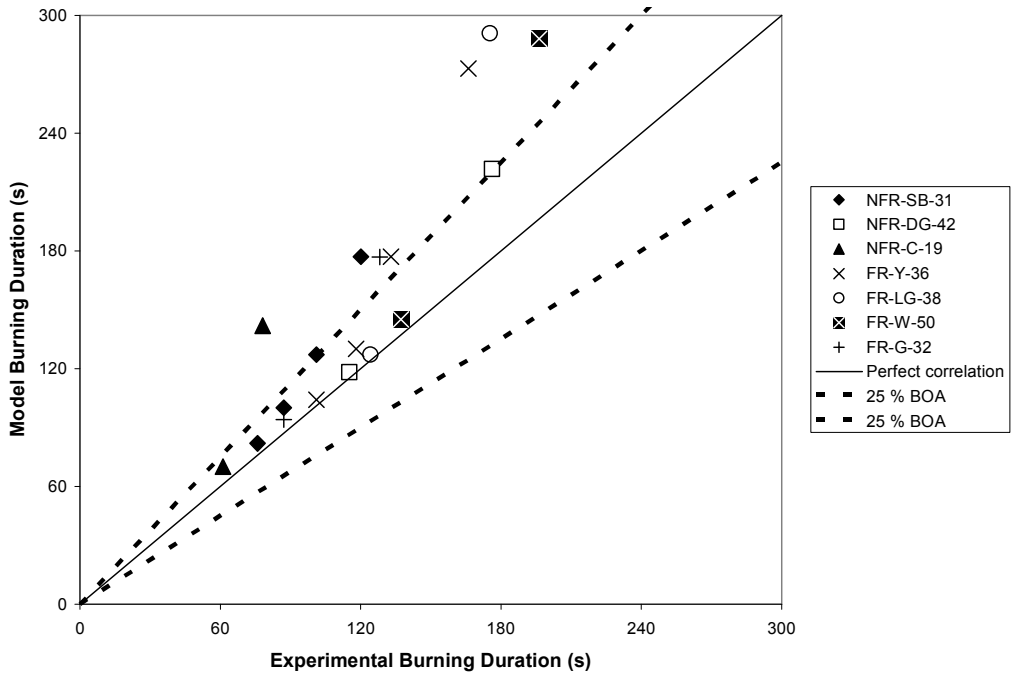

Figure 8-43: Linear regression analysis on maximum HRRPUA, average HRRPUA and burning duration between refined method and experiments for all polyurethane foams

For the maximum and average HRRPUA, almost all of the data points fall under the line of perfect correlation which indicates the model is underpredicting these parameters. Consequently, the model overpredicts the burning duration which is reflected in the burning duration analysis where most of the data points are located above the line of perfect correlation. In all three plots, a few data points are beyond the boundary of acceptance and these are mostly the low heat fluxes where the refined method struggles to predict. The trends in the maximum and average HRRPUA and the burning duration have corresponded well with the pattern of HRRPUA curves seen in Figure 8-41. In comparison with the direct method, the data points plotted are closer together showing less scatter. The reported accuracy for the maximum HRRPUA, the average HRRPUA and the burning duration are 67, 67 and 50 % respectively. In conclusion, the accuracy assessment of the refined method shows better prediction at high heat flux than at low heat flux, in contrast to the direct method. The heat flux specific accuracy of the default predictions at 30 kW/m^2 ranges from 32 to 82 % while at 50 kW/m^2, the accuracy ranges from 82 to 100 %. Overall, the refined method shows a much improved method specific accuracy of 75 %

compared to the direct method with 56 %. Using the averaged 3 point shift improves the accuracy of the refined method further to 84 %.

8.11 Shortcomings of Direct Method and Refined Method

The direct method and the refined method are both affected by the inherent differences between the model and the experiment. According to Equation (8-14), the decomposition rate in FDS 5 is implemented to be solely dependent on temperature but in reality, other factors such as the sample mass and the local oxygen concentration could also be influential. The chosen decomposition scheme for the pyrolysis model consists of two sets of kinetic properties representing the first and second reactions of foam decomposition in the TGA experiments but the scheme does not specifically address the fire retardant mechanisms of the FR foams. In the cone experiments, the notable change from foam into melts during which the sample experiences significant change in its density and thickness are also not modelled directly by FDS 5. Lastly, a majority of the model inputs used are the material properties developed under non-fire conditions.

As a result of all these differences, the direct method which utilises solely the material properties developed experimentally has not been able to produce consistent predictions for the burning behaviours of all the foams. The model struggles particularly at high heat flux such as 50 kW/m^2 and most of the heat flux specific accuracies are less than 40 %. The direct method achieves a method specific accuracy of 56 %. The refined method also experiences the aforementioned issues but these effects are mathematically compensated to a certain extent by the kinetic properties estimated with genetic algorithm. The method specific accuracy achieved is 75 % but even so the outcome of the linear regression analysis shows that the refined method tends to perform better at high heat flux, 50 kW/m^2 than at low heat flux, 30 kW/m^2. While the inherent differences between the model and the experiment still contribute towards the inferiority of the predictions at low heat flux, the main cause is the different flame representations between FDS 5 and Gpyro. The effects of different flame representations have on FDS 5 and Gpyro results are depicted in Figure 8-37.

At 30 kW/m^2, the FDS 5 results show delay during the initial growth phase and extensive tail in the decay phase when compared with the Gpyro results.

In Gypro, the flame is represented by the immediate onset of the full user specified flame heat flux at ignition. As such, during property estimation, the kinetic properties are refined under the scenario of immediate flame onset. Different to Gpyro, the flame heat flux in FDS 5 grows more gradually in accordance with the flame height. Thus, when the Gpyro refined kinetic properties are used as FDS 5 inputs, FDS 5 underpredicts the HRRPUA. This is because the simulated flame in FDS 5 which increases gradually in size does not possess the same intensity as the immediate flame onset in Gpyro. Using FR-Y-36 as an example, Figure 8-44 compares the flame heat fluxes of FDS 5 from the refined method with the flame heat fluxes specified in Gpyro for the estimation process. The FDS 5 simulations are performed with a gas phase mesh of 5 mm.

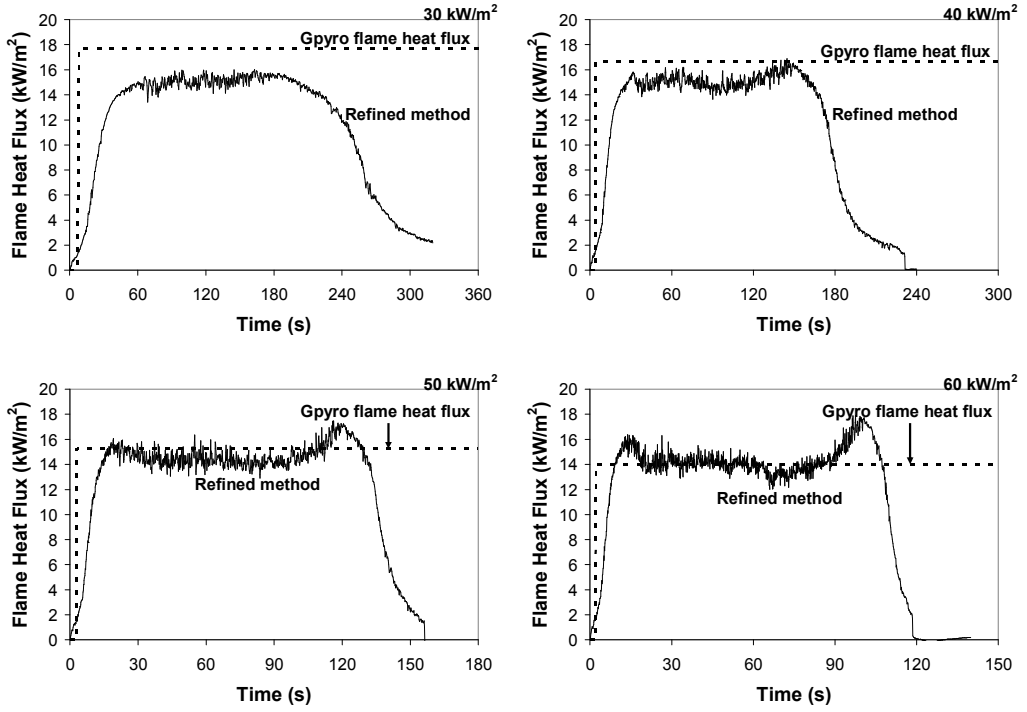

Figure 8-44: Comparison of flame heat fluxes specified in Gpyro and from refined method for FR-Y-36 at 30, 40, 50 and 60 kW/m^2

The comparison of FDS 5 and Gpyro flame heat fluxes in the other foams are similar and they are not reproduced here. Besides the different representation of the growth

and decay of the flame, the flame heat fluxes over the main burning process in FDS 5 are noted to be lower than the values specified in Gpyro which contributes further to the underprediction of HRRPUA by the refined method. The flame heat fluxes specified in Gpyro are obtained from FDS 5 simulations with 10 mm gas phase mesh and as presented previously in Figure 8-36 for NFR-SB-31, these are consistently greater than the flame heat fluxes from 5 mm gas phase mesh which is adopted in the refined method. The difference in flame heat flux from 10 and 5 mm meshes is a result of the different gas phase resolutions.

The greatest difference between FDS 5 and Gpyro flame heat fluxes is seen at the low exposure heat fluxes while at higher heat fluxes, the comparison improves. While this common trend is similar, not all the simulated foams possess the same magnitude of improvements as certain foams show better FDS 5 and Gpyro flame heat flux comparison than the others. The closer flame heat flux comparison at high heat fluxes and the varying magnitude of improvement between different foams are believed to be related to the difference in the kinetic properties estimated for the different foams and the validity of the semi-empirical equations governing fuel and oxygen mixing in FDS 5. The inferior flame heat flux comparison at low heat fluxes is a reason for the poorer prediction of the refined method. As the flame heat flux comparison improves at high heat fluxes, the prediction of the refined method also improves subsequently.

8.12 Conclusions

This chapter discusses the 1-dimensional burning behaviours of polyurethane foams under cone calorimeter for heat flux ranging between 30 and 60 kW/m^2. FDS 5 is used to simulate the burning behaviours of the foams tested and the accuracy of the model is reported. In this research, seven polyurethane foams are tested and four of which contain fire retardant additives such as melamine and halophosphate. From the HRRPUA curves, the NFR foams show two types of burning behaviour which changes according to the exposure heat flux. At low heat flux, a single level plateau is noted but at high heat flux, the burning behaviour gradually develops into two stages.

Due to the fire retardant mechanisms of FR foams, their burning behaviour consistently shows two stages at all heat fluxes.

Besides the HRRPUA curves, the cone calorimeter experiments also produce results such as the ignition time, the average mass loss rate, the total heat released, the effective heat of combustion and the peak and average HRRPUA. The FR foams demonstrate better fire resistive qualities such as longer time to ignition, lower effective heat of combustion and lower mass loss and heat release rates. The total heat released is found to correlate well with the foam density where the denser foams with higher fuel content produce greater total heat released. The NFR foams are found to have greater effective heat of combustion than the FR foams, the former range from 24 – 27 MJ/kg while the latter range from 21 – 24 MJ/kg. In terms of the maximum and average HRRPUA, the NFR foams also show greater magnitude when compared with the FR foams. For maximum HRRPUA, NFR foams at 30 kW/m^2 range from 400 – 430 kW/m^2 while FR foams range from 360 – 420 kW/m^2. At 50 kW/m^2, the former range from 650 – 750 kW/m^2 while the latter range from 500 – 690 kW/m^2. In terms of average HRRPUA, NFR foams at 30 kW/m^2 range from 290 – 320 kW/m^2 while FR foams range from 240 – 270 kW/m^2. At 50 kW/m^2, the former range from 400 – 450 kW/m^2 while the latter range from 330 – 390 kW/m^2.

From five different decomposition schemes, the most suitable scheme to model the cone experiments is found to be Scheme 2, the multi reaction scheme which consists of two reactions representing the first and second reactions in the decomposition of polyurethane foam in the SDT experiments. Two different approaches are undertaken to model the cone experiments in FDS 5, these are the direct method and the refined method. In the direct method, FDS 5 inputs consist of experimentally determined material properties and these include the thermophysical properties, the kinetic properties and the combustion property. The thermophysical properties are λ and c_p which are developed from the Hot Disk experiments and ρ_{eff} and d_{eff} which are effective values calculated according to the modelling assumptions made. The kinetic properties are E, A and Δh_r developed from the SDT experiments. The combustion property is $\Delta h_{c,eff}$ developed from the cone experiments. In the refined method, the FDS 5 inputs remain the same as those used in the direct method except for the kinetic

properties which are refined using the genetic algorithm of Gypro. The kinetic properties are estimated by the genetic algorithm based on the supplied cone results which are the sample mass loss rate and the cumulative mass loss.

The accuracy of the direct method and the refined method are assessed using linear regression analysis that compares the model and experimental HRRPUA. The direct method is found to predict better at low heat fluxes while the refined method is found to predict better at high heat fluxes. Using refined kinetic properties, the foam specific accuracy of the refined method has improved, 63 – 89 % compared to the direct method, 37 – 79 %. Overall, the refined method achieves a higher method specific accuracy than the direct method, 75 % compared to 56 %. The improvement in the accuracy of the refined method shows that the genetic algorithm in Gpyro is suitable for estimating kinetic properties for pyrolysis modelling in FDS 5. Although the modelling described in this research utilises a simpler decomposition scheme than some of those described in the literature, FDS 5 coupled with the property estimation ability from Gpyro is able to consistently capture the 1-dimensional burning behaviours of polyurethane foam to a reasonable accuracy.

Chapter 9. 2-Dimensional Flame Spread Behaviours of Polyurethane Foam and FDS 5 Modelling

9.1 Introduction

In the study on the 1-dimensional burning behaviour of polyurethane foams under the cone calorimeter experiments in Chapter 8, Fire Dynamics Simulator, Version 5[17] (FDS 5[a]) has been used to predict the heat release rate of the fire. The numerical modelling utilises the pyrolysis model in FDS 5 which requires a number of material properties as the model inputs. Table 9-1 shows the material properties investigated which are inputs of the pyrolysis model in FDS 5. These are categorised into thermophysical, kinetic and combustion properties. A few material properties that are not investigated in this research are excluded from the table. These include emissivity, absorption coefficient, mass fraction of material components and the yields of solid residue and gaseous fuel. Some of these properties are either not utilised by the decomposition scheme implemented in the pyroylsis model or simply remain as the model defaults which are assumed to be the best estimates.

Table 9-1: Material properties used as inputs of the pyrolysis model in FDS 5 to simulate burning behaviours of polyurethane foams

Category	Material property
Thermophysical	Thermal conductivity, λ (W/mK)
	Specific heat, c_p (J/kgK)
	Density, ρ (kg/m^3)
	Thickness, d (mm)
Kinetic	Activation energy, E (kJ/mol)
	Pre-exponential factor, A (s^{-1})
	Reaction order, n
	Heat of reaction, Δh_r (J/g)
Combustion	Effective heat of combustion, $\Delta h_{c,eff}$ (MJ/kg)

In this chapter, the burning behaviour of polyurethane foams at a domestic mattress-scale is first investigated experimentally. The experiments globally proceed in a 2-dimensional opposed-flow spread fashion. The pyrolysis model in FDS 5 is then used to simulate this flame spread process where the material properties that have been

[a] Version 5.5.3, SVN number 7031.

experimentally developed or iteratively refined at small-scale are used as the model inputs. As discussed in Section 8.7 and 8.10, two different modelling approaches known as the direct method and the refined method are applied. The direct method uses the experimentally developed material properties as inputs while for the refined method, part of the material properties as inputs are refined by the genetic algorithm of Gpyro[27]. Among the material properties, only the kinetic properties are subjected to refinement while the thermophysical and combustion properties remain as the experimental values. Previously, in the modelling of 1-dimensional cone experiments, the overall accuracy achieved by the direct method and the refined method is 56 and 75 % respectively.

In the literature, Prasad et al.[42] conducted flame spread experiments on polyurethane foam slabs and also used FDS 5 for the heat release rate modelling. The foam slab was 100 mm thick and measured 1200 mm along the sides and a line burner was used to ignite the foam slab along one edge. The flexibility of FDS 5 pyrolysis model allows the design of various schemes to represent the solid phase decomposition of the fuel so the authors assessed the suitability of a few decomposition schemes in simulating the burning behaviour of the foam under cone calorimeter. A two layers scheme was found to produce the closest comparison with the experiment and it was implemented to model the flame spread experiment. The authors defined the activation energy and pre-exponential factor in the model by specifying the reference rate, reference temperature and heating rate of the thermogravimetric analysis (TGA) experiment. The heats of reaction and the thermophyiscal properties used as input were obtained from the literature. Lastly, the combustion property was determined from the microcalorimeter experiment. Figure 8-6 compares the heat release rate between the experiment and FDS 5 performed by Prasad et al..

From Figure 8-6, the simulation results overpredict the start and growth of the foam slab fire but underpredict the peak heat release rate. In this study, the experimental setup of the foam slab is similar to Prasad et al. but the modelling approach taken is different. From the numerical modelling of the cone experiments, a suitable decomposition scheme to describe the 1-dimensional burning behaviour of polyurethane foams was developed. Different from the two layers scheme used by

Prasad et al., the scheme in this chapter is a multi reactions scheme which consists of a single material component in a single layer. Two solid phase reactions are implemented to represent the two decomposition reactions of polyurethane foam seen in the TGA results. The detailed discussions on the thermophysical, kinetic and combustion properties used as the model inputs are provided in later section. The polyurethane foam tested in the flame spread experiments is NFR-SB-31 listed in Table 2-1 and more details on the physical and chemical attributes of this foam is provided in Chapter 2.

9.2 Setup of Flame Spread Foam Slab Experiments

Three experiments in total were carried out under the furniture calorimeter for this study. The samples tested were a single 120 mm slab and two replicates of 100 mm slab. Except for the difference in thickness, the other physical dimensions of all three slabs are identical, measuring 1000 mm along the width and 2000 mm along the length. The 120 mm slab tested was the precursor of this study so its experimental setup in Figure 9-1 is slightly different compared to the 100 mm slabs in Figure 9-2.

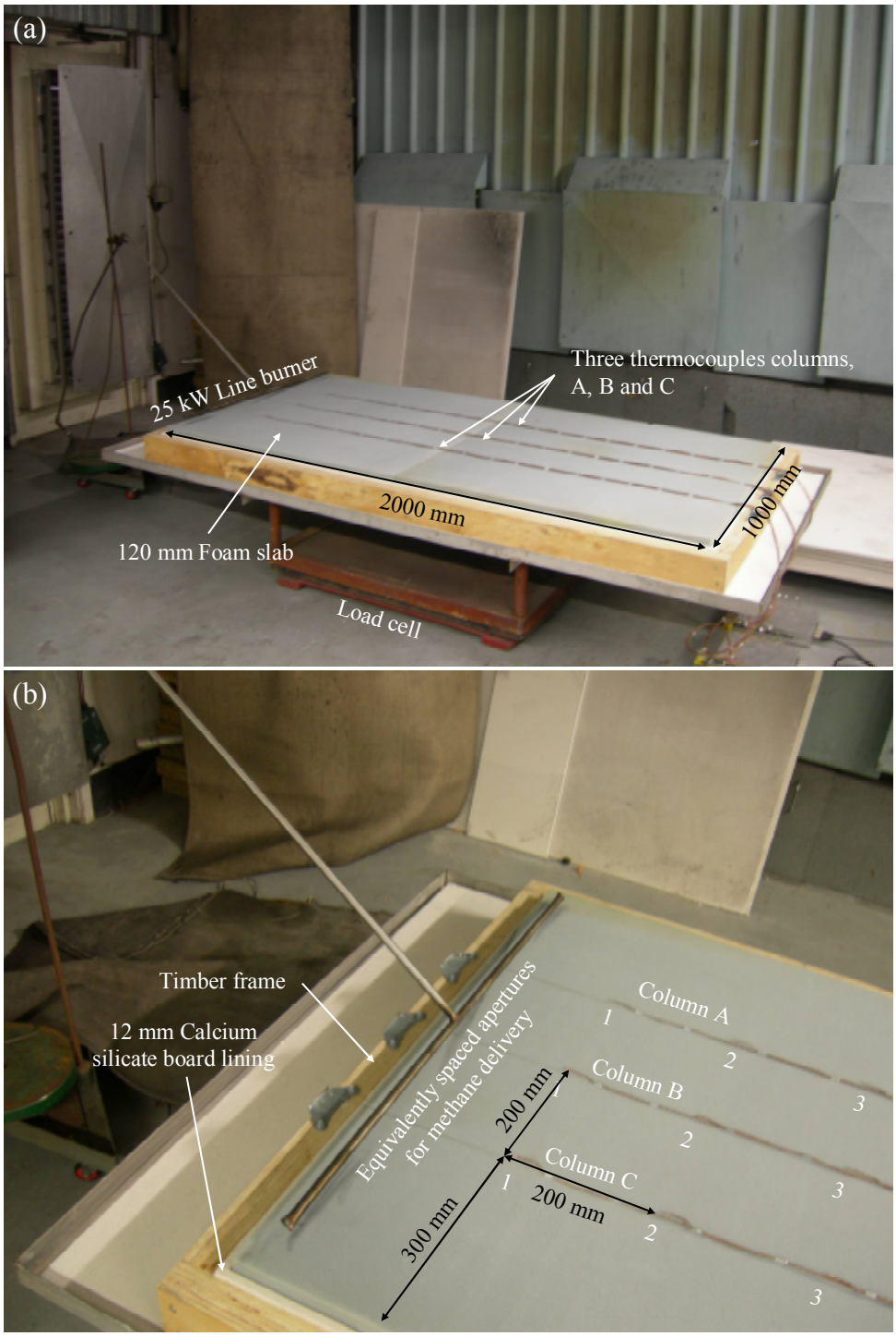

Figure 9-1: Experimental setup of 120 mm slab (a) and burner configuration (b)

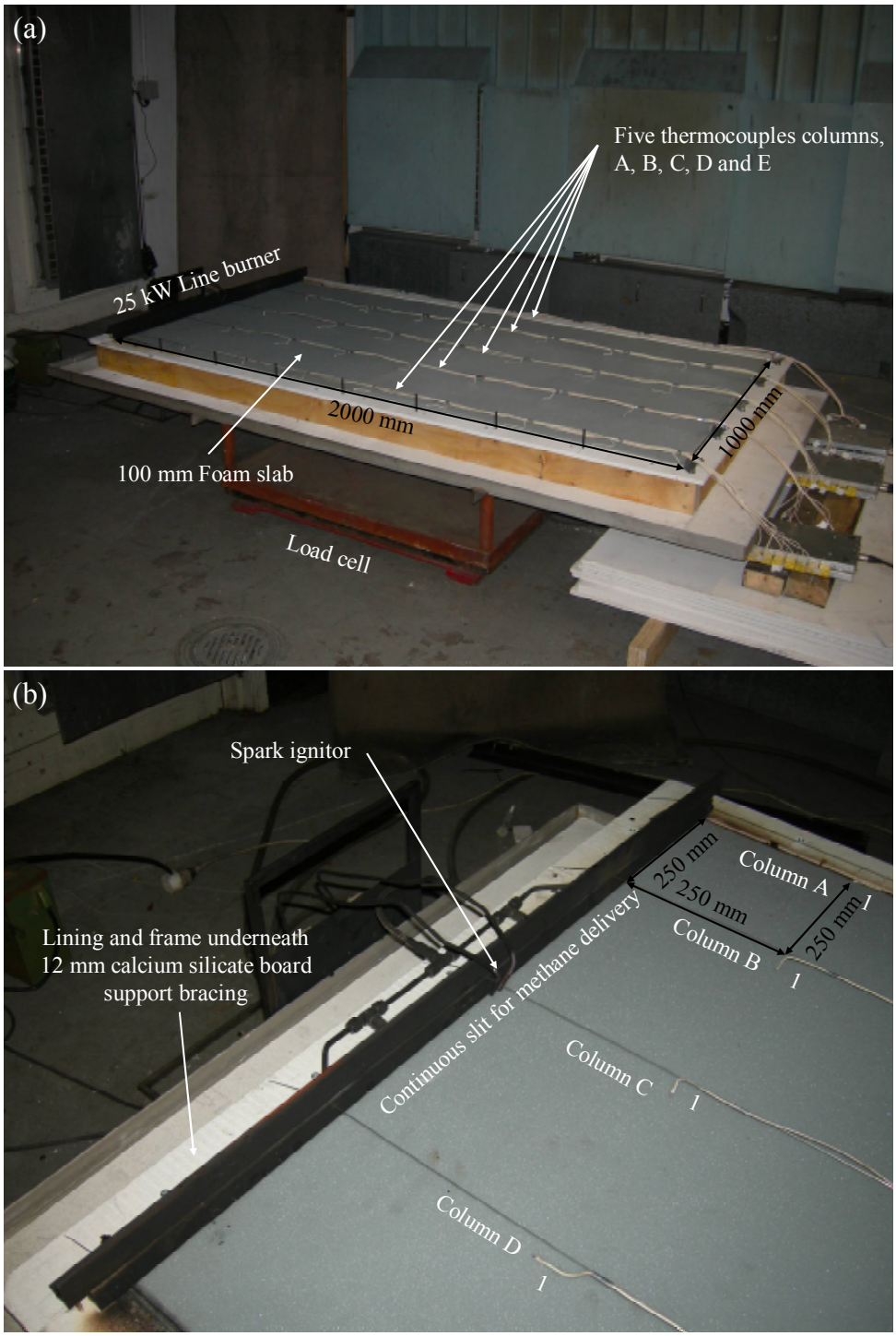

Figure 9-2: Experimental setup of 100 mm slab (a) and burner configuration (b)

In general, the sample was lined with 12 mm calcium silicate board and contained within a timber frame for structural support. The whole setup was located on top of a platform and the sample mass was measured using a load cell. A 25 kW LPG line

burner was used to ignite the sample at one end along the width and the turn on duration for the burner was 120 s. During the experiment, the combustion products produced from the fire was collected by the exhaust hood and then sampled and measured by the oxygen (O_2), carbon dioxide (CO_2) and carbon monoxide (CO) gas analysers.

The experiment with 120 and 100 mm slabs differed in the arrangement of thermocouples and the line burner's design. From Figure 9-1, the experiment involving 120 mm slab used three thermocouples columns at the surface of the sample to measure the temperature of the pyrolysis front. These columns were identified as A, B and C respectively and each contained nine individual thermocouples numbered 1 to 9. Column B was located through the middle of the sample and Column A and C were located on either side. Column A and C were 300 mm from the edge of the sample and 200 mm apart from Column B. The individual thermocouples along each column were located 200 mm apart from one another. In the experiments involving 100 mm slab, five thermocouples columns were used, labelled A to E with each containing eight individual thermocouples numbered 1 to 8. Figure 9-2 shows that the separation between the columns and between the individual thermocouples along each column was identical, 250 mm.

The line burner used to ignite the 120 mm slab was a stainless steel tube with a number of 3 mm openings spaced equivalently at 50 mm apart, except at both edges of the burner where the separation was 30 mm. The delivered LPG gas diffused through these openings and was manually ignited by the open flame from a hand held propane torch. Due to the separation between the openings, the flame front produced by this burner was found to be non-continuous thus the width of the sample was not ignited uniformly. Despite the non-uniform ignited front, this did not seem to have a significant effect on the flame spread as the fire rapidly involved the whole sample width soon after ignition. An improved burner design was implemented for the experiments involving 100 mm slab where the burner has a continuous ~0.25 mm slit from which the LPG gas was forced through and then ignited by a spark ignitor. This burner design produced a continuous flame front igniting the width of the sample uniformly.

9.3 2-Dimensional Burning Behaviours of Polyurethane Foam

From the gas concentrations measured by the gas analysers, the oxygen depletion calorimetry[11] is applied to calculate the heat release rate of the fires. The calculations involved are similar to those used for the cone calorimeter experiments described in ISO 5660-1:1993[12] except for the exhaust flow rate which is specific to the furniture calorimeter determined using Equation (9-1)[122].

$$\dot{m}_e = 26.54 \frac{A_{duct} k_c}{f(\mathrm{Re})} \sqrt{\frac{\Delta p}{T_e}} \tag{9-1}$$

The following sections describe the heat release rate and experimental observations of the 120 and 100 mm foam slab fires. The calculated experimental results and the flame spread analysis are also discussed.

9.3.1 Heat Release Rate and Experimental Observations of 120 mm Foam Slab Experiment

Figure 9-3 shows the experimental heat release rate curve of the 120 mm foam slab and also included on the plot are the actual progress of the fire at different intervals after ignition.

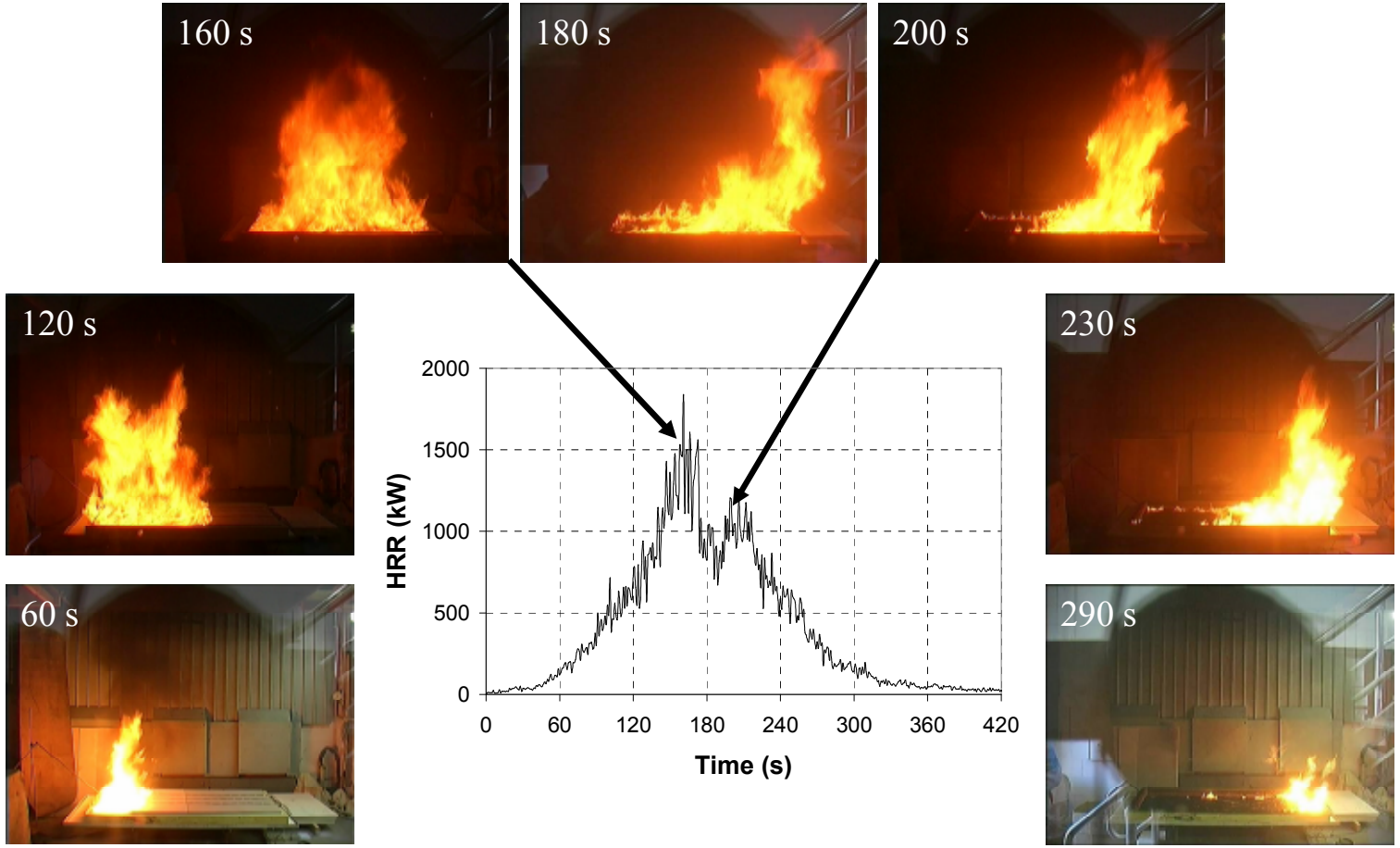

Figure 9-3: Heat release rate curve of 120 mm foam slab with actual fire progress at different intervals

Due to the design of the burner, the burning region developed initially was not even but this was soon rectified as the foam decomposed into melts and the flame spread rapidly to ignite the entire width of the sample. The flame heat flux from the developed burning region drove the pyrolysis front forward as the flame began to spread along the slab as seen at 60 s. The LPG supply to the line burner was turned off at 120 s and by this stage, the fire covering 1000 mm of the sample length had become self sufficient. The pyrolysis front was able to forage forward igniting the virgin foam closely followed by the burning region which imposed the radiative heat flux originating from the flame. The heat release rate was noted to increase continuously and turning off the burner did not have a notable impact on the results.

At 160 s, the heat release rate reached peak of 1500 kW just as the pyrolysis front arrived at the opposite end of the sample. Over the next 20 s, the burning area of the fire reached maximum, approximately 2.0 m^2 covering the entire sample. The first half of the sample rapidly burned out at 180 s causing the decay in the heat release rate to 800 kW. At 200 s, the heat release rate was able to increase to 1000 kW as a result of the slight increase in burning area due to the complete collapse of the last segments of foam structure into melts. From 230 s onwards, the fire entered the steady decay phase as the remaining fuel was consumed.

9.3.2 Heat Release Rate and Experimental Observations of 100 mm Foam Slab Experiment

Figure 9-4 shows the heat release rate curves of 100 mm foam slabs and also the progress of the fire at different intervals after ignition. The solid line is the heat release rate curve of the first replicate while the dashed line is that of the second replicate. Since the trend of heat release rate between both replicates is similar, only the fire progress of the first replicate is shown on the plot and discussed.

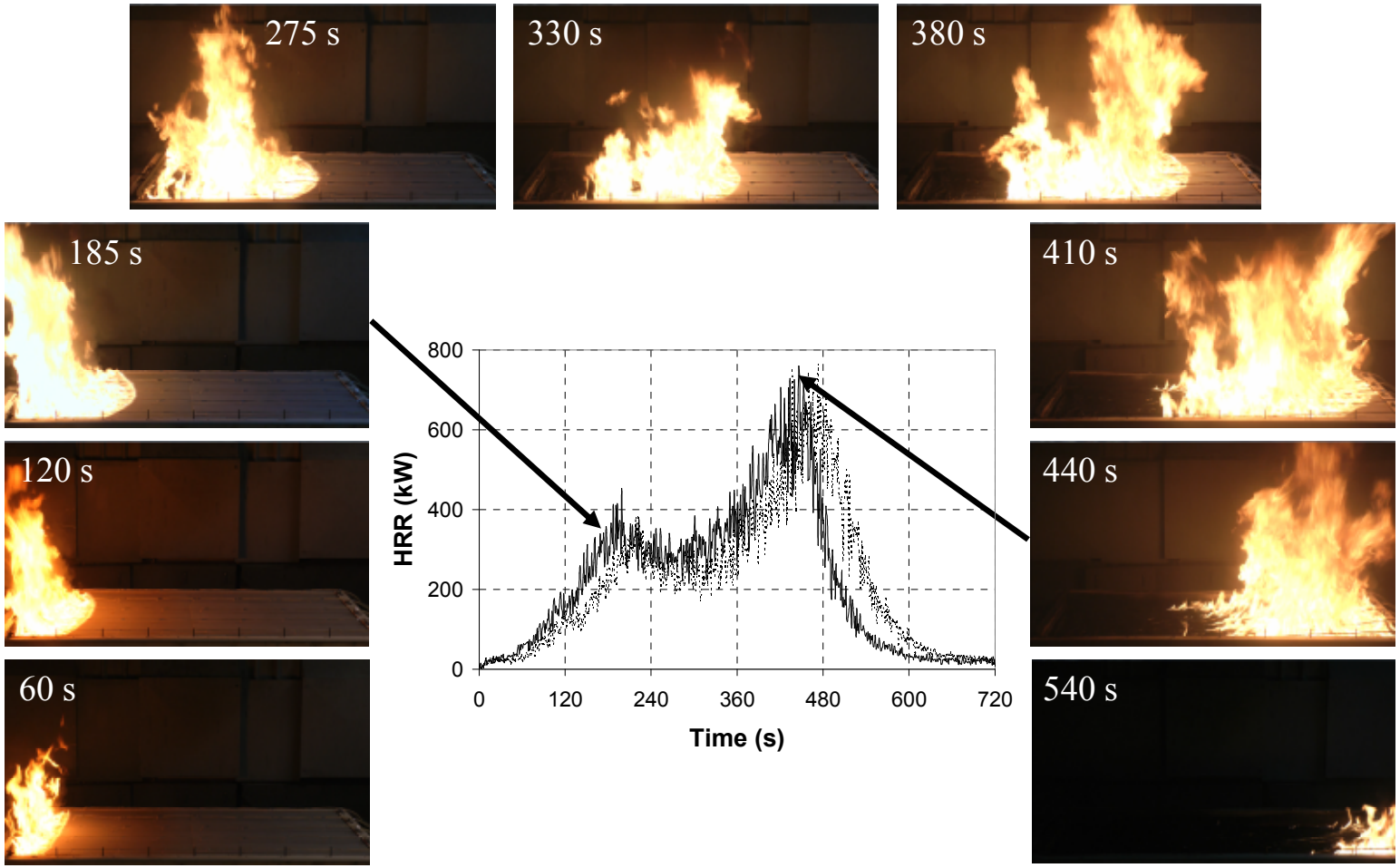

Figure 9-4: Heat release rate curve of 100 mm foam slabs with actual fire progress of the first replicate at different intervals

The continuous slit of the burner uniformly ignited the foam slab along its width. At 60 s after ignition, the burning region developed a uniform pyrolysis front. As the middle of the sample received more radiation, the pyrolysis front became bowed as seen at 120 s and the separation between the pyrolysis front and burning region appeared to increase. This bowing phenomenon was not observed previously in the 120 mm foam slab experiment because of the close proximity of the pyrolysis front to the burning region where its turbulent flame constantly disrupted the formation of the bowed pyrolysis front.

The heat release rate curves showed continuous increase in magnitude until 185 s where it reached approximately 360 kW and for the next 150 s, the heat release rate ranged between 260 and 360 kW. Over this plateau period, the burning behaviour was characterised by the constant burning area where the fire consistently covered approximately 600 mm of the sample length which is equivalent to an area of 0.6 m^2. These equivalent burning segments can be seen from the fire progress at 185, 275 and 330 s. While the heat release rate had remained constant, the dynamics of the fire were noted to vary over this period. From the close up in Figure 9-5, the separation between the pyrolysis front and the burning region at 185 s was seen reaching maximum, approximately 250 mm compared to 120 mm previously at 120 s.

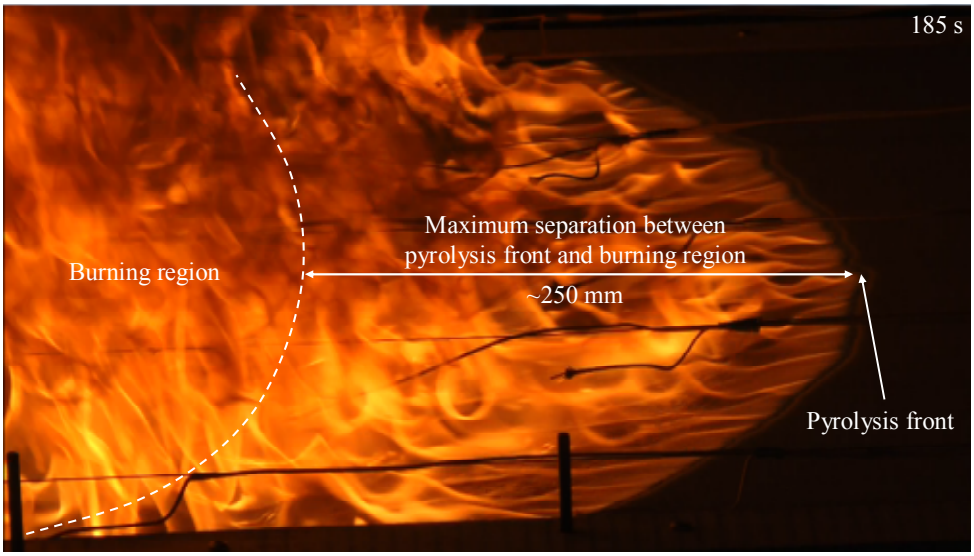

Figure 9-5: Maximum separation between pyrolysis front and burning region in first 100 mm foam slab experiment

At 275 s, the first 250 mm of the foam slab began to burn out, reducing the intensity of the burning region. The burning region of 100 mm slabs struggled to catch up to the pyrolysis front but in the previous case of 120 mm slab, the burning region was always trailing closely behind the pyrolysis front. The dynamics of the fire changed once more at 330 s indicating the end of the plateau region and the start towards the increase to peak heat release rate. At this stage, the first 250 mm of the foam slab had completely burned out and the separation between the pyrolysis front and the burning region has noted to reduce compared to the separation previously seen at 275 s. These variations in the dynamics of the fire at constant heat release rate such as the changes in separation between the pyrolysis front and the burning region and the burn out of the initial foam segments are due to the lower fuel content of the 100 mm slabs compared to the thicker 120 mm slab.

Trailing closely behind the pyrolysis front as seen at 330 s, the burning region was able to impose greater radiation on the pyrolysis front which enhanced the spread rate. At 380 s, the fire covered approximately 800 mm of the sample length which was 200 mm more than during the plateau period and the heat release rate continued to increase towards the peak magnitude. The pyrolysis front reached the opposite end of the foam slab at 410 s just as the heat release rate started to peak and the burning area reached a maximum of 1.0 m^2. The peak heat release rate was 700 kW at 440 s and the burning area was approximately 1.0 m^2, these give 700 kW/m^2 on a per unit area basis and this maximum fire intensity is comparable to that from the 120 mm slab which is approximately 750 kW/m^2. After 460 s, the fire entered the steady decay phase as the remaining fuel was consumed.

9.3.3 Experimental Results and Flame Spread Analysis

From the heat release rate and sample mass measured, the average mass loss rate ($\dot{m}_{ave}$), total heat released (q_{tot}), effective heat of combustion ($\Delta h_{c,eff}$), peak heat release rate ($\dot{q}_{pk}$) and average heat release rate ($\dot{q}_{ave}$) are determined and listed in Table 9-2. These parameters are the same as those determined in the cone calorimeter experiments and their definition are described in Section 8.4.2 to 8.4.5.

Table 9-2: Average mass loss rate, total heat released, effective heat of combustion, peak heat release rate and average heat release rate of 120 and 100 mm foam slabs

Foam slab experiment	Replicate	Experimental parameters				
		$\dot{m}_{ave}$ (g/s)	q_{tot} (MJ)	$\Delta h_{c,eff}$ (MJ/kg)	$\dot{q}_{pk}$ (kW)	$\dot{q}_{ave}$ (kW)
120 mm	1	39.2	172.6	25.3	1834	658
100 mm	1	17.0	155.3	24.9	760	311
	2[a]	N/A	156.2	N/A	762	290

The 20 % increase in sample thickness produces more than two times increase to the magnitude of $\dot{m}_{ave}$, $\dot{q}_{pk}$ and $\dot{q}_{ave}$. As explained before, these differences are mainly due to the different fire dynamics observed between the 120 and 100 mm foam slabs. The 120 mm foam slab shows more rapid spread and intense burning behaviours because the burning region followed the pyrolysis front closely. Differently, the 100 mm slabs show slower spread as the burning region trailed the pyrolysis front over the first half of the experiments. The intensity of the burning region is also reduced as the earlier ignited foam segments gradually burned out as the fire progressed.

As the burning area changes during fire spread, a direct comparison for $\dot{m}_{ave}$ and $\dot{q}_{ave}$ cannot be made between the foam slabs and the per unit area values of the cone samples. Due to the greater fuel content from the extra thickness, the 120 mm foam slab achieved q_{tot} of 173 MJ which is greater compared to 156 MJ of the 100 mm foam slabs. The values of q_{tot} for the foam slabs can be derived from the total heat released of the 50 mm cone samples, ranging from 38 – 41 MJ/m^2. The values of $\Delta h_{c,eff}$ for the foam slabs is a constant 25 MJ/kg, similar in magnitude to the values found from the cone experiments tested between 30 and 50 kW/m^2. The burning area at $\dot{q}_{pk}$ in the case of 120 and 100 mm slabs are 2.0 and 1.0 m^2 respectively so $\dot{q}_{pk}$ per unit area of the 120 mm slab is 920 kW/m^2 and for 100 mm slabs, the peak is 760 kW/m^2. This range of peak heat release rate falls between the exposure heat flux of 50 and 60 kW/m^2 under the cone calorimeter.

The thermocouples columns used in the experiments are installed at fixed position on the top surface of the sample. The purpose of the thermocouples is to capture the

[a] The sample mass measurements of the second replicate were corrupted during the data collection process so the average mass loss rate and the effective heat of combustion were undetermined.

temperature of the pyrolysis front from which the spread rate of the fires can be calculated. The solid temperatures measured by the thermocouples are valid until the collapse of the foam structure into melts which then exposes the thermocouples to flame. In this case, the temperature of the gas rather than the solid is being measured. Figure 9-6 shows the temperatures measured at the centre of the slab, Column C for the first 100 mm foam slab replicate. Each individual thermocouple along the column is numbered, '1' being 250 mm from the ignitor and '8' being 2000 mm from the ignitor. The temperature measurements by the other columns in the other experiments show similar trends so the results are not repeated.

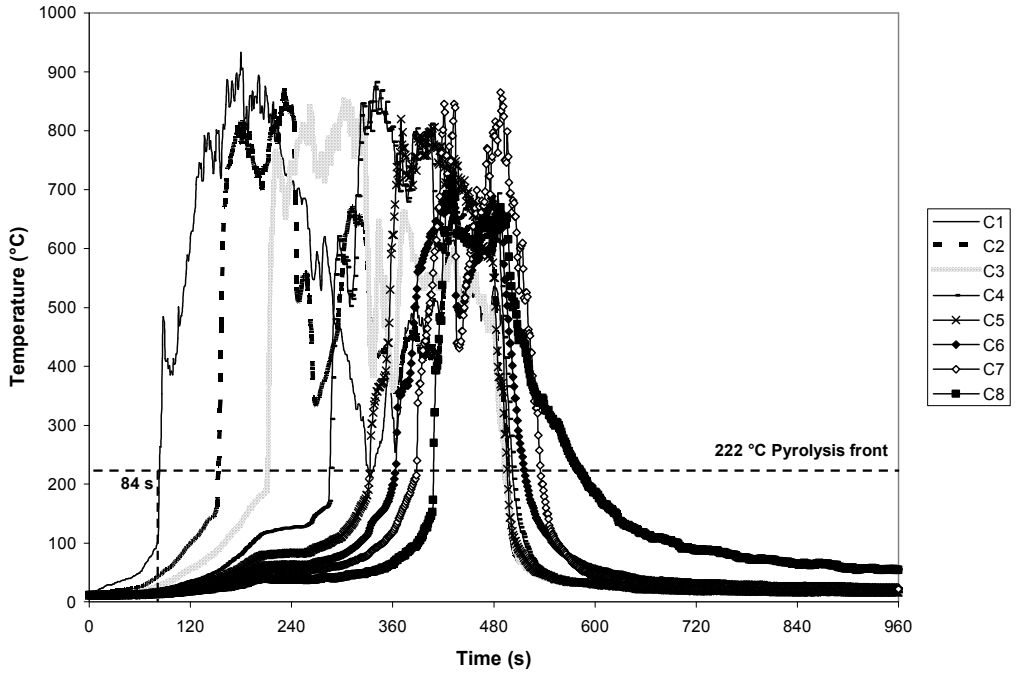

Figure 9-6: Surface temperatures at centre of first 100 mm foam slab replicate

The temperature measurements show that the pyrolysis front reached the individual thermocouples in the order of 1 to 8 which is the closest from the burner to the farthest from the burner. The temperature measured increases slowly at first as the pyrolysis front approaches the thermocouple but when the front touches the thermocouple, the temperature is seen to increase almost vertically towards a gas temperature ranging between 700 and 900 °C. As the fuel burned out, the temperature measured reduces to the ambient temperature again.

The temperature range of polyurethane foam decomposition is available from the TGA results in Chapter 4. Over a range of tested heating rate from 1 to 60 °C/min, the starting decomposition temperature for NFR-SB-31 ranges from 206 to 239 °C according to Table 4-1 which gives an average of 222 °C. The starting temperature is defined as the temperature where the mass loss rate is 10 % of the difference between the maximum and minimum of the first reaction of foam decomposition. As indicated on Figure 9-6, 222 °C is applied as the nominal temperature of the pyrolysis front from which the distance travelled by this front and also the amount of time taken can be determined. Comparing with the experimental observations made, 222 °C gives a reasonable indicator for the location of the pyrolysis front. From Figure 9-6, C1 measures 222 °C at 84 s after ignition and according to the observation in Figure 9-7, the pyrolysis front is seen just reaching C1 at the same instant. In the research by Robson et al.[123] which also investigated flame spread on polyurethane foam slabs, a temperature of 300 °C has been used in their thermal imaging analysis to determine the appropriate flame area. While 222 °C is less than 300 °C, it is still within 200 to 300 °C which is the range of starting temperature for foam decomposition proposed by Robson et al..

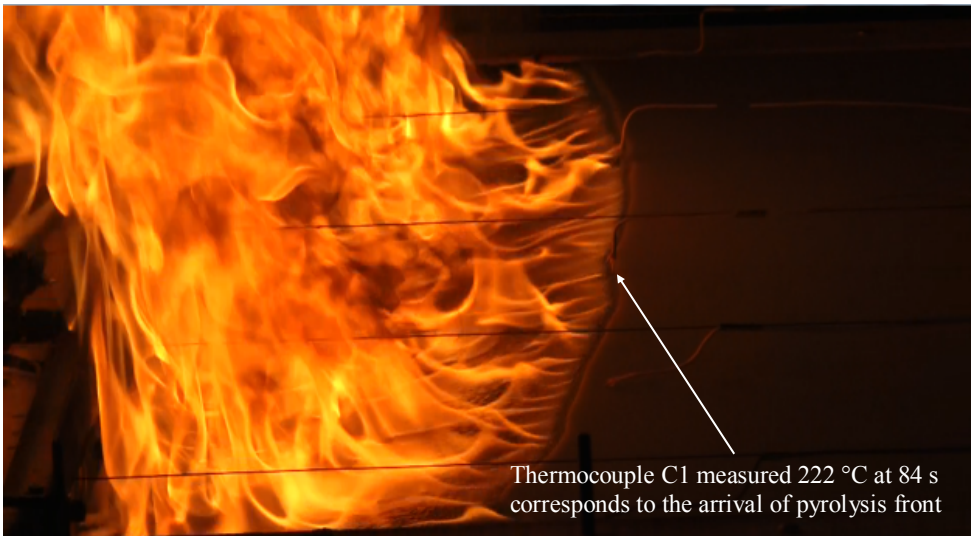

Figure 9-7: Arrival of pyrolysis front at thermocouple C1 at 84 s corresponds well with 222 °C measured by the thermocouple in first 100 mm foam slab experiment

For 120 and 100 mm foam slabs, Figure 9-8 shows the position of the pyrolysis front along the sample and the time taken to reach that position. From this information, a

spread rate of the pyrolysis front is calculated as the average velocity over each segment defined by the spacing between the individual thermocouples along a column, 200 mm for 120 mm slab and 250 mm for 100 mm slabs. The measurements from all the thermocouples columns are included in the figure.

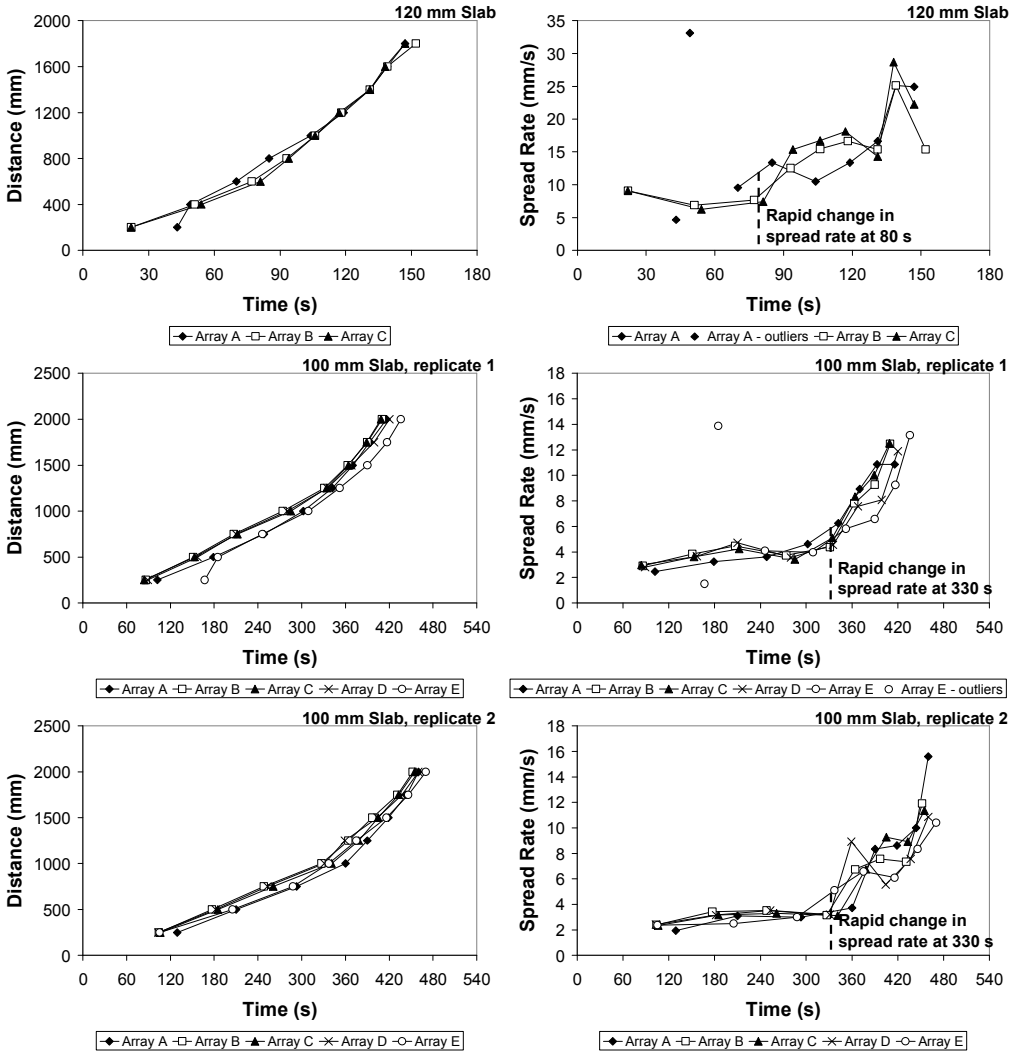

Figure 9-8: Distance travelled and spread rate of pyrolysis front versus time of all thermocouples columns for 120 and 100 mm foam slabs

The different columns show comparable results which validate the 2-dimensional nature of the fires. The results of 120 mm foam slab show that the fire requires less time to cover the same distance as the 100 mm slabs and thus the greater spread rate associated with the former. The spread rate shows an exponential trend and this is similar for the two different thicknesses tested but in terms of maximum magnitude, the 120 mm slab is approximately two times faster than the 100 mm slab, 26 mm/s

compared to 12 mm/s. Indicative of a more rapid spread, the fire of 120 mm slab also shows its low spread rate region is short, lasting 80 s where the magnitude ranges from 7 to 9 mm/s. However, for the 100 mm slabs, the constant initial spread rate ranges between 3 and 4 mm/s which is lower than 120 mm slab and it lasts 330 s before the rapid upturn. The average spread rate for 120 mm slab is 12 mm/s while for the 100 mm slab, the average spread rate ranges between 4 to 5 mm/s. A few outliers seen at the start of the fire are a result of some experimental errors. In the case of 120 mm slab, the outliers are caused by the non-uniform initial flame front and in the case of the first 100 mm slab replicate, the edge thermocouples measured the lining temperature rather than that of the foam.

The trends seen in the plot of distance covered and spread rate agree with the experimental observations made. The greater spread rate associated with the 120 mm foam slab is a result of the close proximity of the burning region to the pyrolysis front thus allowing the front to receive more radiation from the burning region and forages forward. The wider separation noted between the pyrolysis front and the burning region in the case of 100 mm foam slabs means that the front is not able to receive enough radiation from the burning region. Furthermore, the burn out of foam segments ignited earlier also contributed to the reduced intensity of the fire and thus the spread rate. The upturn in the spread rate of the 100 mm slabs at approximately 330 s corresponds to the reduced separation between the pyrolysis front and the burning region and in this case, the front receives more radiation to progress forward more rapidly. This eventually leads to the peak heat release rate of the fires. Similar flame spread results on foam slabs were also reported by Robson et al.[123] where greater slab thickness produces greater flame spread rate. The authors investigated foams with density ranging between 15.9 and 19.3 kg/m^3 and slabs having thickness from 25 to 100 mm with sides measuring from 500 to 1400 mm.

9.4 FDS 5 Modelling of 2-Dimensional Burning Behaviours of Polyurethane Foams

As mentioned earlier, different to the two layers scheme developed by Prasad et al.[42], the approach adopted in this research is a multi reactions scheme. In Chapter 8, reasonable comparison with the heat release rate from cone experiments over a range of heat fluxes has been achieved using this decomposition scheme. The multi reactions scheme contains two reactions representing the two stages of decomposition observed in the TGA results of foam. Besides using different decomposition scheme, the approach in this research also differs from Prasad et al. in terms of the specification of the thermophysical and kinetic properties. These are listed and discussed in Table 9-3.

Table 9-3: Different specification of thermophysical and kinetic properties in FDS 5 of this research and Prasad et al.

Material properties		Differences compared to Prasad et al.
Thermophysical	λ	Prasad et al. specified the thermal conductivity and specific heat for the layer of foam and melt and these properties remain constant with changes in temperature. This research specified temperature dependent thermal conductivity and specific heat where these properties changes from those of foam into melt with increasing temperature.
	c_p	
	ρ	Prasad et al. specified the density and thickness for the layer of foam and melt. This research specified an effective value for the density and thickness of the single layer.
	d	
Kinetic	E	Prasad et al. specified the reference rate, reference temperature and heating rate from which FDS 5 calculates the appropriate activation energy and pre-exponential factor. This research directly specified the activation energy and pre-exponential factor.
	A	

The temperature dependency of λ and c_p and also the effective density and thickness are determined from the TGA results. As discussed in Section 8.5.2, this is done based on the assumption made regarding the changes to the sample's physical state over the range of decomposition temperature. Table 9-4 shows the material properties experimentally developed and those refined by Gpyro, both at small-scale for modelling the 2-dimensional flame spread in FDS 5. The subscripts '*1*' and '*2*' denote

the first and second reactions of the foam decomposition. The kinetic properties first reported are those determined experimentally and the kinetic properties in brackets are those refined by the genetic algorithm of Gpyro[27].

Table 9-4: Material properties developed experimentally at small-scale and those refined by Gpyro at small-scale as FDS 5 inputs to simulate 2-dimensional flame spread on foam slabs

Material property	Values		
λ (W/mK)	$T \leq 222$ °C 0.049	222 °C $\leq T \leq$ 310 °C 0.049 – 0.186	$T \geq 310$ °C 0.186
c_p (J/kgK)	$T \leq 222$ °C 2996	222 °C $\leq T \leq$ 310 °C 2996 – 2053	$T \geq 310$ °C 2053
ρ (kg/m^3)	297		
d (mm)	12.50 mm for 120 mm slab, 10.40 mm for 100 mm slab		
E_1 (kJ/mol)	88 (75)		
A_1 (s^{-1})	2.18×10^5 (6.82×10^4)		
n_1	0.00		
Δh_{r1} (J/g)	891 (1357)		
E_2 (kJ/mol)	150 (206)		
A_2 (s^{-1})	3.06×10^9 (1.25×10^7)		
n_2	0.00		
Δh_{r2} (J/g)	233 (218)		
$\Delta h_{c,eff}$ (MJ/kg)	25		

Besides those properties in Table 9-4, FDS 5 also requires the specification of the stretch factor, the cell size factor (S), the back side boundary condition and the chemical formula of the gaseous fuel. The stretch factor is set to 1 and S is set to 0.43 in order to produce uniform 0.1 mm solid phase cell size. 'VOID' is specified as the back side boundary condition and the chemical composition for NFR-SB-31 listed in Table 2-1 is specified as the chemical formula of the gaseous fuel in FDS 5. In Section 8.5.6 and 8.5.7, the sensitivity of heat release rate to different solid phase cell sizes and back side boundary conditions have been assessed for 1-dimenisonal burning. These inputs used were validated to produce the best agreement with the experimental results.

Based on the actual dimensions, the foam slab is modelled in FDS 5 as an obstruction measuring 2000 mm in length, 1000 mm in width and 100 mm in height. The obstruction conforms to the two gas phase mesh sizes investigated, 50 and 25 mm. Only the top surface of the obstruction is assigned as the foam while the other surfaces remain inert, not undergoing any solid phase reaction. The difference in fuel content between the 120 and 100 mm foam slab is accounted through the specification

of their respective effective thicknesses listed in Table 9-4. The line burner is specified as a 50 mm vertical plane obstruction located at one end of the foam slab and extending the entire width of the slab. The burner surface not facing the foam slab is assigned inert while the other surface facing the foam slab is assigned a user defined heat release rate per unit area. For 50 mm gas phase mesh, the constant fire size assigned is 500 kW/m^2 and since the surface area is 0.050 m^2, the actual burner output of 25 kW is achieved. For the finer 25 mm gas phase mesh, the lower 25 mm surface is assigned as the burning surface while the upper 25 mm is assigned inert. The fire size specified is 1000 kW/m^2 and since the burning area is 0.025 m^2, the burner output of 25 kW is achieved.

Despite reasonable success at modelling the 1-dimensional burning behaviour of cone experiments, both the experimentally determined properties and the Gpyro refined properties do not appear to support the 2-dimensional flame spread of the foam slabs. As such, several modelling options are investigated in attempt to reproduce the flame spread process observed experimentally. These include reducing the gas phase mesh to 1 mm and also varying the burner's physical design, its heat release rate output and its turn on duration. However, these methods are deemed futile and inevitably, the remaining options involved altering the material properties specified as the model inputs.

The specific material properties altered are the kinetic properties and this investigation focuses on the kinetic properties that have been refined by Gpyro. The first attempt involved setting the heat of reaction to zero which essentially assumes the amount of energy absorbed for decomposition is negligible. To certain extent, this assumption is reasonable as the energy released following combustion based on the effective heat of combustion specified is at least 18 times greater in magnitude when compared to the heat of reaction. However, this approach still fails to produce the flame spread phenomenon seen in the experiments. In FDS 5, the decomposition rate is represented by Equation (3-1) and since $n = 0$ for the selected scheme, the decomposition rate is governed by E and A. The decrease of E or the increase of A or both result in greater decomposition rate. Thus, the second attempt involved reducing E of both reactions by a fixed percentage. Numerous simulations were performed in

search of the best fit values of *E* that produce the closest agreement between the model and experimental heat release rates. It was found that a general reduction of 20 to 30 % was necessary in order to produce flame spread with this multi reactions scheme. The following sections compare and discuss the heat release rate and flame spread analysis between the model and the experiments.

9.4.1 Comparison of Model and Experimental Results for 120 mm Foam Slab

Figure 9-9 compares the best fit model results of 120 mm slab at gas phase mesh size of 50 mm with the experimental heat release rate. The Smokeview images and experimental observations depicting the progress of the fire at different time intervals are also included on the plot. Simulations were also performed for the 120 mm slab at 25 mm gas phase mesh and the best fit model results are presented later.

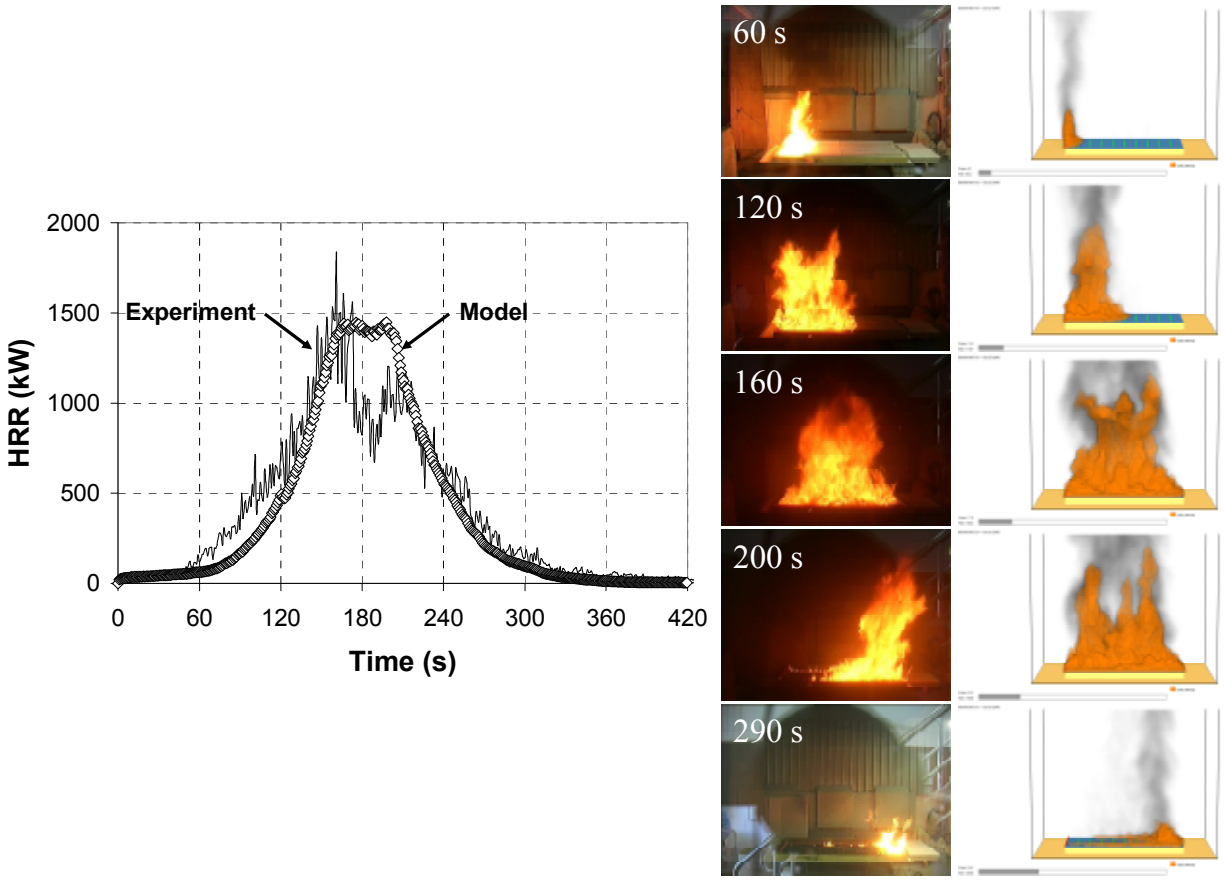

Figure 9-9: Comparison between model and experimental heat release rates of 120 mm foam slab at 50 mm gas phase mesh size

A 26.4 % reduction of the original Gpyro refined *E* is required to produce the best fit heat release rate comparison with the experiment. Due to the exponential relationship of the decomposition rate, the specification of a precise set of values for *E* is necessary hence the percentage of reduction is presented in three significant figures. The comparison shows that the model is able to simulate the growth rate and the maximum heat release rate of the fire. This is reflected by the comparable fire progress between the experimental and simulated pyrolysis front at 60, 120 and 160 s. The model predicts the peak heat release rate of 1500 kW but it struggles to reproduce the two peaks seen in the experimental results. The second peak is a slight resurgence of the heat release rate following the decomposition of the last foam segments into melts which leads to a slight increase in the burning area. The model overpredicts this second peak and the Smokeview image at 200 s reflects this where the simulated foam slab is seen burning at maximum area but in the experiment, half of the sample has already burned out. For the decay phase, the model manages to capture the experiment again.

9.4.2 Comparison of Model and Experimental Results for 100 mm Foam Slab

Figure 9-10 compares the best fit model results of 100 mm slab at gas phase mesh size of 50 mm against the experimental heat release rate. The Smokeview images and experimental observations are included to compare the progress of the fire at different time intervals.

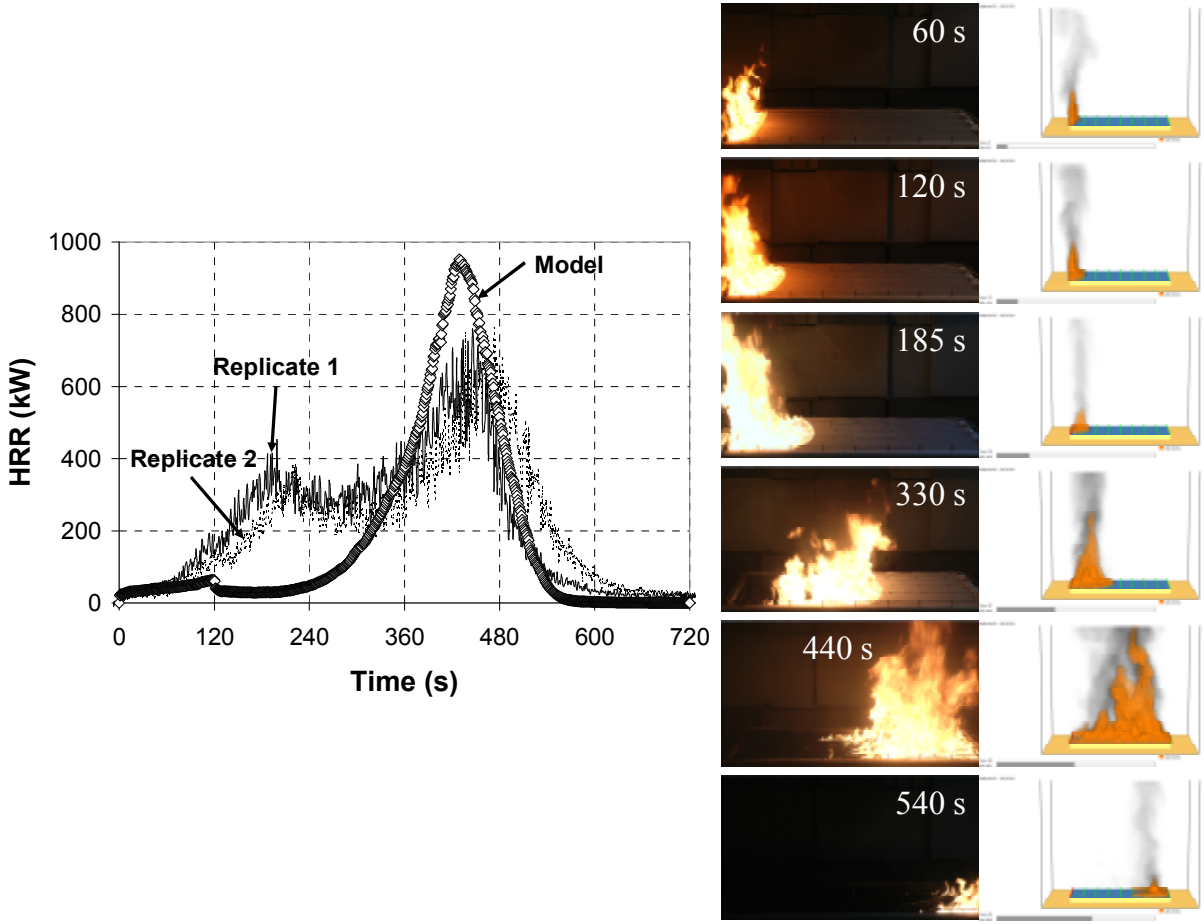

Figure 9-10: Comparison between model and experimental heat release rates of 100 mm foam slabs at 50 mm gas phase mesh size

Different to the reduction factor of *E* used for modelling 120 mm slab, 22.4 % is required to achieve the best fit heat release rate comparison with the 100 mm slab experiments. The comparison shows that the model struggles to simulate the initial growth and subsequent plateau burning behaviour exhibited by the experiment. The plateau burning behaviour is characterised by the formation of constant burning area over an extended period, from 185 to 330 s after ignition. When the burner is turned off in the model at 120 s, the simulated fire becomes dormant for approximately 120 s. The Smokeview image at 185 s shows that without the radiative heat flux from the burner, the burning region actually reduces. The model heat release rate starts to increase at 240 s and eventually overpredicts the maximum heat release rate, reaching 900 kW compared to the experimental value of 700 kW. Despite capturing the growth to peak heat release rate, the Smokeview images at 330 and 440 s show that the simulated fire is actually behind in terms of the distance covered and the model is unable to simulate the burn out of initial segments which is a key feature in the 100 mm slab experiments. For the decay phase, the model produces reasonable comparison with the experiments.

9.4.3 Sensitive Nature of Flame Spread Modelling

Table 9-5 shows the changes in kinetic properties required to produce the best fit heat release rate for the 120 and 100 mm foam slabs simulated at different sizes of gas phase mesh. For identification, the simulation set for 120 mm slab is denoted 'a' while 'b' represents the simulation set for 100 mm slab, this is followed by the percentage of *E* reduced and the suitable gas phase mesh size. For the mesh sizes investigated, 50 mm mesh amounts to ~200 k cells and 25 mm mesh amounts to ~1.9 million cells. Using a computer system with 3.4 GHz of processing speed and 16 GB of processing memory, the run time for 50 and 25 mm mesh is ~14 and ~150 hours respectively. The two *E* specified represent the first and second reactions of the foam decomposition, denoted by the subscript '*1*' and '*2*' respectively.

Table 9-5: Values of *E* specified as FDS 5 inputs to model 2-dimensional flame spread foam slab experiments

Kinetic Property	Sets		
	a-26.4-50	**a-28.0-25**	**b-22.4-50**
E_1 (kJ/mol)	55.2	54.0	58.2
E_2 (kJ/mol)	151.6	148.0	159.9

With 50 mm gas phase mesh, the fire of 120 mm foam slab is modelled by the reduced *E* of a-26.4-50 as seen in Figure 9-9. However, when the same set of properties are used to model 100 mm foam slab, they result in much higher heat release rate so the greater *E* values from b-22.4-50 have to be used to lower the decomposition rate and produce the best fit comparison as depicted in Figure 9-10. Therefore, even under the same gas phase mesh size, different reduction factor for *E* is required to model the 120 and 100 mm foam slabs due to the distinct difference in the dynamics of the fires observed experimentally. The fire of the 120 mm slab is noted to be rapid and intense where it grows towards peak heat release rate and then decay from thereafter. Differently, the fires of the 100 mm slab are less intense where they start off slowly and enter an extended plateau burning phase characterised by the constant burning area due to the lower fuel content of the samples. Furthermore, certain fire dynamics are specific to the 100 mm slabs. These include the increased distance between the pyrolysis front and the burning region which reduces the spread rate of the fires and the burn out of the initial foam segments which reduces the

intensity of the burning region. Eventually, after the plateau burning phase, the fires of 100 mm slab also reach maximum heat release rate and decay thereafter.

The sensitivity of the model results towards the change in gas phase mesh is investigated for the 120 mm slab and it is found that a different reduction factor for *E* is required to produce the best fit comparison at a finer gas phase mesh. From Figure 9-11, the use of *E* from a-26.4-50 in the simulation with a mesh size of 25 mm results in a delay of approximately 50 s in the heat release rate curve. To eliminate this delay, the decomposition rate needs to increase via further reduction in *E* and the values from a-28.0-25 are found to produce a reasonable comparison with the experimental results. Overall, the model input, *E* is found to be a sensitive parameter due to its exponential relationship with the decomposition rate where small changes made to *E* as seen in Table 9-5 can lead to significant variations on the heat release rate curve.

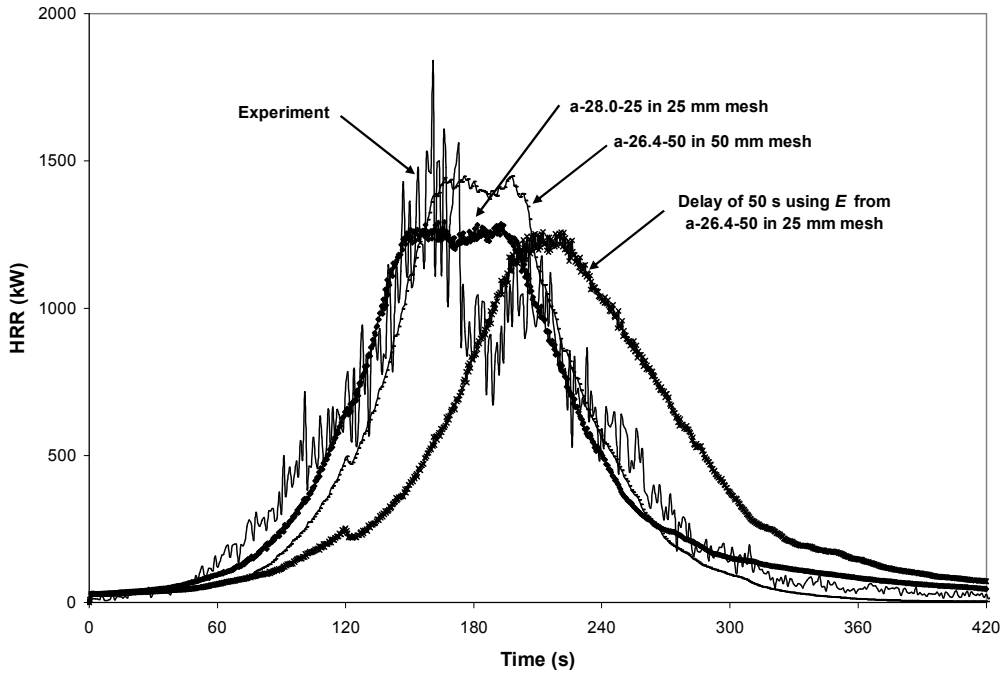

Figure 9-11: Comparison between model and experimental heat release rate of 120 mm foam slab at 50 and 25 mm gas phase mesh sizes

9.4.4 Comparison of Model and Experimental Results for Flame Spread Analysis

During the simulations, the surface temperature of the foam slab is measured at the precise same locations where the actual thermocouples are placed in the experiments. Again, using 222 °C as the indicator of the pyrolysis front, Figure 9-12 compares the distance travelled and the spread rate of the pyrolysis front in the experiments with those in the simulations for 120 and 100 mm foam slabs. The 2-dimensional nature of the fire means that the variation in the results among the columns is minimal in both the experiment and the model. Hence, the average of all the columns is presented and compared instead of the individual columns.

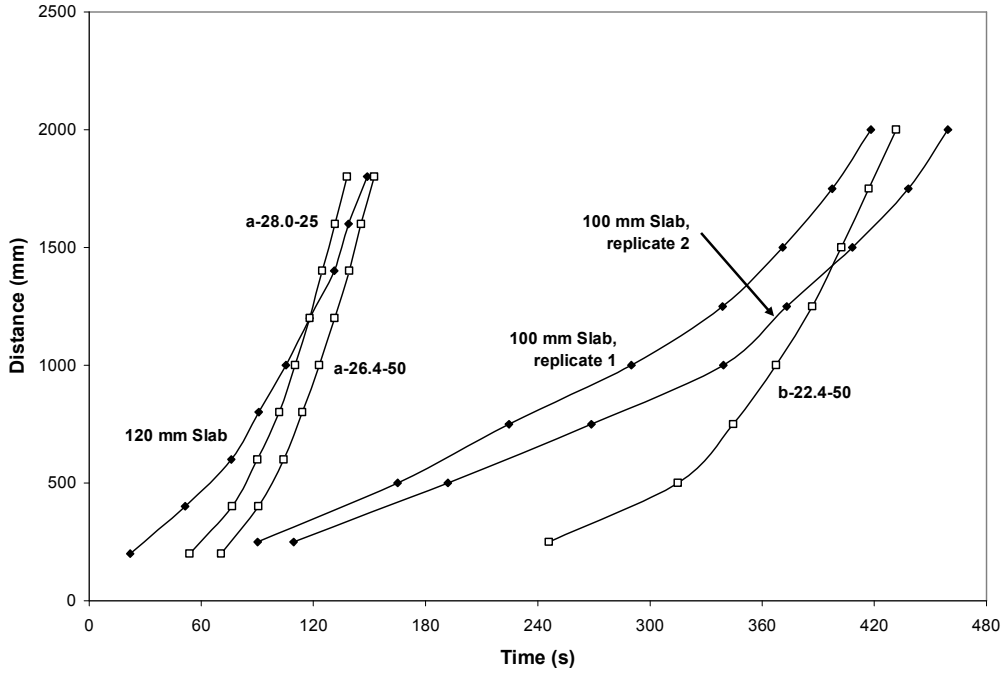

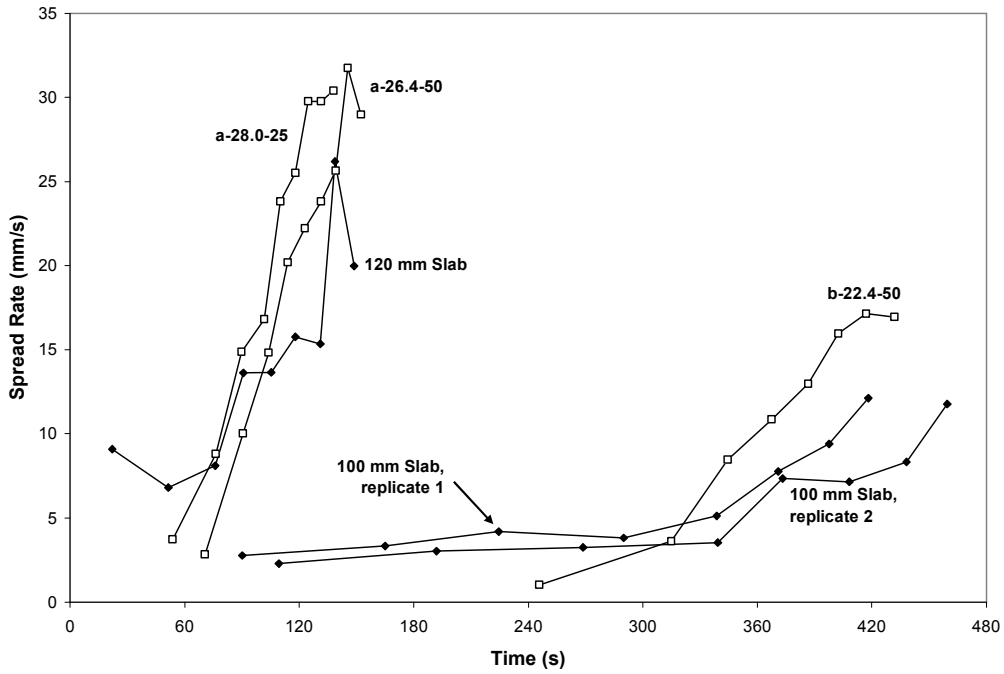

Figure 9-12: Average distance travelled and average spread rate of the pyrolysis front versus time for experiment and FDS 5 of 120 and 100 mm foam slabs

The comparison shows that the model underpredicts the distance covered by the pyrolysis front initially and this is more obvious in the case of 100 mm slab because the model is unable to address the experimental fire dynamics caused by the lower fuel content of the sample. However, as the fire progresses further, the comparison between model and experiment improves. Comparing the trend of the spread rate between the model and the experiment, the model is noted to achieve consistently greater peak magnitude. The maximum spread rate achieved for the simulations of 120 mm slab is 32 mm/s and it is 17 mm/s for the 100 mm slab. For the experiments, these are 26 and 12 mm/s for 120 and 100 mm slabs respectively. In terms of average, the spread rate between the model and the experiment are similar. For 120 mm slab, the average model spread rate is 12 to 13 mm/s and for 100 mm slabs, it is 5 mm/s. In the experiments, these are 12 mm/s and 4 to 5 mm/s for 120 and 100 mm slabs respectively.

The trends of heat release rate comparison in Figure 9-10 and 9-11 are also reflected in the trends of distance covered and spread rate of the pyrolysis front in Figure 9-12. From Figure 9-11, the simulated heat release rates of the 120 mm slab, a-26.4-50 and

a-28.0-25 underpredict the experiment initially but after 120 s, the comparison improves. Similarly, above 120 s, Figure 9-12 shows the model is seen producing closer comparison for distance covered and also starting to overpredict the spread rate. From Figure 9-10, the simulated heat release rate of the 100 mm slab, b-22.4-50 severely underpredicts the initial growth and plateau burning period of the experiments but after 360 s, the comparison improves. The simulated distance covered in Figure 9-12 shows a similar trend where the comparison becomes closer above 360 s. The upturn in the experimental spread rate occurs at approximately 330 s leading to the increase towards peak heat release rate and Figure 9-12 shows the simulated spread rate also manages to capture this phenomenon at almost the same instant.

9.5 Shortcomings of Flame Spread Foam Slabs Modelling

In Valencia's research[25], the findings showed that the material properties determined or developed from material-scale TGA experiment when used as FDS 5 inputs have failed to produce the burning behaviour of polyurethane foam at small-scale cone experiment. Similarly, the findings from this research show that neither the experimentally developed nor the Gpyro refined material properties are able to produce the opposed-flow spread of 120 and 100 mm foam slabs in FDS 5. The simulated decomposition rate needed to be increased through further reduction of E in order to recreate the experimental flame spread scenarios. This reduction factor of E compensates for the crucial physical phenomena which are not addressed adequately by the model. Examples of these are the melting behaviour of foam leading to the transport of fuel, the porous nature of the foam structure, the changes in material's density and thickness when the foam decomposes into melts, the 3-dimensional heat transfer processes and the representation of flame which is a zone consisting of reactive radicals undergoing rapid chemical reactions. In general, the reduction factor ranges between 20 and 30 % for E refined by Gpyro but given the sensitive nature of the parameter, the precise factor required could change for E determined via different methods.

The current representation of the fuel at material level in FDS 5 still has not addressed the aforementioned physical phenomena which are crucial to the fire development, especially the foam melting behaviours and the subsequent melt flow dynamics. Therefore, despite being able to create flame spread in FDS 5 using the reduced *E* as inputs, the model still lacks the resolution to capture certain dynamics of the fires. In the 120 mm slab simulations, the model single peak in Figure 9-9 does not capture the second peak of the experiment which is caused by the slight increase in burning area following the decomposition of the remaining foam into melts. In the 100 mm slab simulation, the model results in Figure 9-10 underpredict the extensive plateau region of the fire which is characterised by the prolonged interval with constant burning area due to the lower fuel content of the sample. The significant differences found between the burning behaviours of 120 and 100 mm foam slabs are also related to the foam melting behaviours which are essential to the overall decomposition of foam. Within the literature[89,124,125] and also addressed previously in Chapter 7, some on-going investigations are being carried out to implement a melting model which can address this issue.

The difficulty in simulating flame spread on foam slabs with FDS 5 prompts an assessment to determine the amount of radiative heat flux from the line burner received on the surface of the foam slab. The setup of the experiment is seen in Figure 9-13 for the position 12.5 mm away from the line burner.

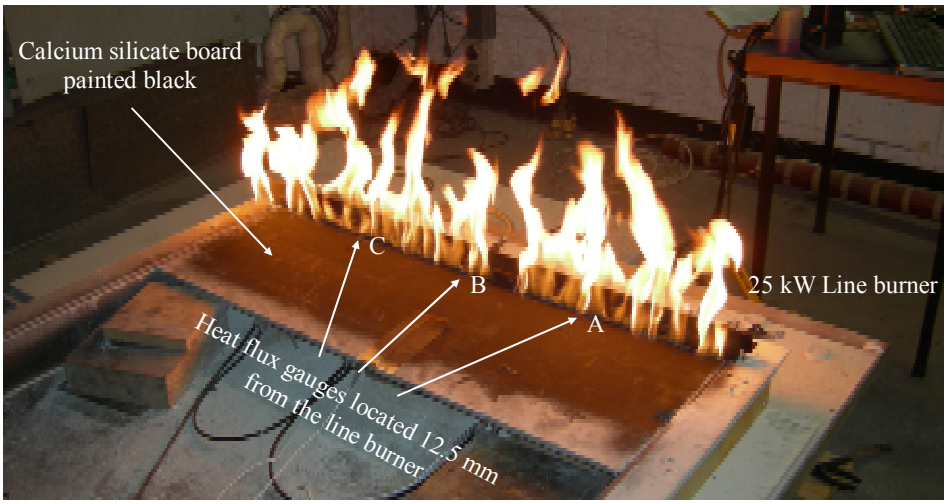

Figure 9-13: Experimental setup to measure radiative heat flux from 25 kW line burner at different locations on sample surface

Three side mounted water cooled Schmidt-Boelter heat flux gauges were used to measure the radiative heat flux. These gauges protruded through three openings on a calcium silicate board and remained level with the surface of the board which represented the slab surface. The board was painted black to minimise reradiation. Measurements were taken along three columns, at the centre and at 250 mm apart on both sides. These are labelled A, B and C as seen in Figure 9-13. Each column contained the identical measurement points located at 12.5, 25.0, 50.0, 75.0, 100.0, 150.0 and 200.0 mm away from the burner. The line burner was set to produce 25 kW of heat release rate and once the measured heat flux achieved steady state, a 60 s continuous recording was made. The same setup is also simulated in FDS 5 with different gas phase meshes of 50 and 25 mm and Figure 9-14 compares the experimental and model results.

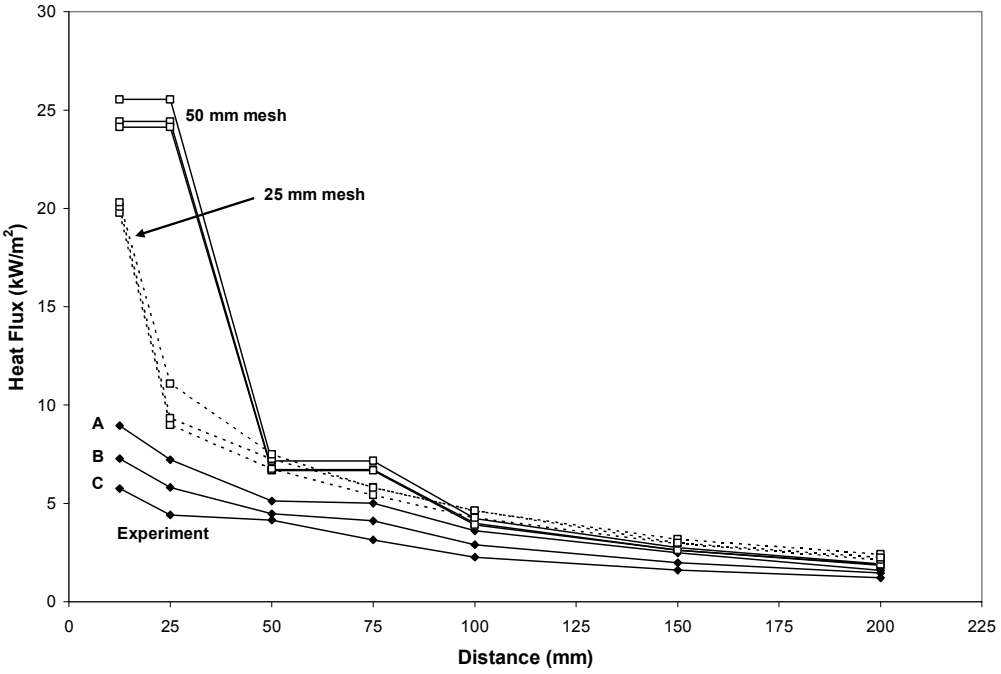

Figure 9-14: Comparison between model and experimental radiative heat flux from 25 kW line burner at different locations on sample surface

The average heat flux over 60 s is presented for all the experimental measurement points. The variation in the experimental measurements is noted to increase for position closer to the burner due to the turbulent nature of the flame but this is within

2 kW/m^2. Thus, the heat flux comparison between the different columns is considered to be similar. From the results, the flame from the burner does not appear to impose great heat flux onto its vicinity. In fact, the heat flux measured at 12.5 mm from the burner is less than 10 kW/m^2. This heat flux level is found to be comparable to the critical and minimum ignition heat fluxes for upholstered furniture composite[107]. Therefore, it can be concluded that the flame from the burner does not contribute significantly in terms of radiative heat flux to the flame spread process and it only serves to ignite the foam slabs. The flame spread process is driven by the flame heat flux from the burning region and also the high reactivity of the flame which contains large quantity of reactive radicals. From Figure 9-14, the model results after 60 s of steady state for 50 and 25 mm meshes overpredict the radiative heat flux received especially nearing the burner. This is to be expected due to the constant radiative fraction from flame in FDS 5[17] which is adopted in this research and also the thin nature of the experimental flame. The model and experiment comparison improves for positions at 50 mm and further away from the burner.

Besides the lack of detailed representation of fuel at material level, the difficulty in simulating opposed-flow spread on foam slabs in FDS 5 is also due to a number of other reasons. In the modelling of cone experiments which show 1-dimensional burning, reasonable model predictions were obtained between 30 and 60 kW/m^2 of exposure heat flux. This range is much greater than the heat flux initially imposed by the burner on the slab surface as seen in Figure 9-14. So FDS 5 predictive capability has not been investigated for heat fluxes less than 30 kW/m^2 which are crucial to the early phase of the flame spread process. From Figure 9-14, the heat flux received by the pyrolysis front after ignition will be small thus the initial flame spread would rely on the high reactivity of the flame. However, the effect of flame reactivity on solid phase decomposition is not addressed yet in FDS 5 as the solid and gas phases are completely decoupled. Despite having a relatively simple experimental setup, the opposed-flow spread is not an easy phenomenon to model numerically due to the small preheated region of the fuel compared to the concurrent flame spread[117]. Often, the preheated area of the fuel in opposed-flow spread can be smaller than the numerical grid size used thus the temperature of the front cannot be resolved accurately. This research has showed the material properties that are either

experimentally developed or refined by Gpyro at small-scale are not able to support flame spread in FDS 5. However, to be fair, the suitability of these properties for medium and large-scale simulations should first be assessed in the form of 1-dimensional burning which becomes a practical challenge from an experimental perspective.

9.6 Conclusions

The opposed-flow spread behaviour of 2000 mm long and 1000 mm wide foam slabs is investigated experimentally at two different thicknesses, 120 and 100 mm. The burning behaviours observed experimentally are significantly different between the two thicknesses. For 120 mm slab, the heat release rate increased to a peak value of 1500 kW in 160 s after ignition. As the initial foam segments burned out, the heat release rate reduced but it resurged later, forming a second peak of 1000 kW as the remaining foam decomposed into melts resulting in the slight increase of burning area. Thereafter, the fire entered into a steady decay phase. For 100 mm slabs, the heat release rate increased to 360 kW at 185 s and entered a plateau burning region with a slight decrease in the heat release rate of 100 kW over the period of 150 s. In this region, the burning behaviour was characterised by a constant burning area due to the burn out of initial foam segments. Throughout the plateau burning region, a distinct separation was noted between the pyrolysis front and the burning region. At 330 s, this separation was noted to reduce so the burning region was able to impose more radiative heat flux on the pyrolysis front. The heat release rate then started to increase and reached a peak of 700 kW at 440 s. After that, the fire entered into a steady decay phase.

When the material properties developed experimentally and those refined by Gpyro, both at small-scale are used as FDS 5 inputs, the model is unable to numerically simulate the opposed-flow spread seen experimentally. Numerous modelling options are investigated and eventually, the option of reducing E is chosen to increase the decomposition rate to enable flame spread on the foam slabs modelled. A reduction of 20 to 30 % of the original E is required to match the simulated heat release rate with

the experimental results. Even with this approach, the model still struggles to predict certain dynamics of the fires seen in the experiments. For the 120 mm slab simulations, the model manages to predict the initial growth, the 1500 kW peak and the decay of the fire but it fails to capture the second peak. For the 100 mm slab simulation, the model fails to reproduce the plateau burning behaviour and also overpredicts the peak heat release rate, 900 kW instead of 700 kW. It is more difficult for the model to predict the 100 mm foam slab fires because their flame spread behaviour is less intense due to the lower fuel content of the samples. The dynamics of the fire include the changes in separation between the pyrolysis front and the burning region and also the burn out of initial foam segments. To capture these phenomena, the detailed representation of the fuel at material level is necessary, especially to address the foam melting behaviours and melt flow dynamics which has not been implemented yet in FDS 5.

The progress of the pyrolysis front is inferred from the surface temperatures measured by the thermocouples located on the surface of the foam slab. A nominal temperature of 222 °C is used to identify the location of the pyrolysis front. The surface temperatures at the same locations are also measured in the model which initially underpredicts the distance covered by the pyrolysis front but as the fire progresses further, the comparison with the experiments improves. The model produces a greater maximum spread rate when compared to the experiment but for the average spread rate, the model and experimental values are similar. For 120 mm slab, the maximum and average spread rates in the experiment are 26 mm/s and 12 mm/s and in the model, these are 32 mm/s and 12 to 13 mm/s respectively. For 100 mm slab, the maximum and average spread rates in the experiment are 12 mm/s and 4 to 5 mm/s and in the model, these are 17 mm/s and 5 mm/s respectively. Both experimentally and numerically, the trend in the distance covered and the spread rate of the pyrolysis front also reflects the trend observed in the heat release rate curves. In the 100 mm slab experiments, the increase towards the peak heat release rate coincides with the rapid increase in the spread rate which is captured reasonably well by the model. Besides the absence of more detailed fuel representation, the difficulty of using FDS 5 to simulate the opposed-flow spread on foam slabs is also caused by other issues. These include the uncertain predictive capability of FDS 5 at low exposure heat flux,

the inadequate representation of flame reactivity in FDS 5 and the inherently short preheated region associated with opposed-flow spread whereby the temperature of the pyrolysis front cannot be resolved accurately by the numerical grid.

Chapter 10. Conclusions and Recommendations for Future Research

10.1 Conclusions

In this research, the decomposition and burning behaviours of polyurethane foams were studied experimentally at different scales and orientations. The experimental burning behaviours, mainly the heat release rate were simulated numerically using a pyrolysis model and the accuracy of the model was quantified. Seven polyurethane foams were tested and these consisted of three non-fire retardant (NFR) and four fire retardant (FR) foams. The experimental investigations were carried out using numerous experimental techniques which include simultaneous differential scanning calorimetry and thermogravimetric analysis (SDT), Hot Disk Thermal Constants Analyser, Sample Feeding Vertical Cone, cone calorimeter and flame spread on domestic mattress-scale foam slab. The numerical investigations focused primarily on Fire Dynamics Simulator, Version 5 (FDS 5[a]) where its inbuilt pyrolysis model was applied to simulate the cone and foam slab experiments. The numerical investigations also utilised the genetic algorithm of Gpyro to refine part of the FDS 5 inputs to improve the comparison between model and experiment. The inputs refined were the kinetic properties which govern the decomposition rate in FDS 5.

The SDT experiments showed the decomposition under nitrogen consists of two pyrolysis reactions. The first reaction was the foam decomposition into melts and gases while the second reaction was the further decomposition of the remaining melts into gases. The melting behaviour of foam was also evident from the Sample Feeding Vertical Cone experiments carried out. The decomposition in SDT experiments under inert environment such as nitrogen is representative of the decomposition during a fully developed fire where oxygen is assumed to be consumed within the flame and not able to reach the fuel surface to cause oxidation. Numerically, to represent fuel decomposition, the flexibility of FDS 5 pyrolysis model allows the user to device

[a] Version 5.5.3, SVN number 7031.

different decomposition schemes for the solid fuel in the model. From five different schemes available in FDS 5, a multi reactions scheme was found to best represent the heat release rate of polyurethane foam under cone calorimeter and it was implemented for the subsequent numerical investigations. Representative of the foam decomposition behaviours noted in the SDT experiments, this multi reactions scheme consisted of two reactions converting solid fuel into gaseous fuel.

Besides providing information on the decomposition behaviours of polyurethane foams, the results from differential scanning calorimetry (DSC) and thermogravimetric analysis (TGA) of SDT experiments also produced the necessary kinetic properties for FDS 5 modelling. These kinetic properties were the activation energy (E), pre-exponential factor (A) and reaction order (n) determined from the TGA results while the heat of reaction (Δh_r) was determined from the DSC results. The determination of E, A and n were investigated using a number of graphical techniques and in order to be compatible with the multi reactions scheme implemented in FDS 5 pyrolysis model, these kinetic properties were calculated using the normalised Inflection Point Methods where $n = 0$. The kinetic properties used as FDS 5 inputs were determined as the average from four different heating rates, 1, 5, 20 and 60 °C/min tested on ~3 mg foam sample. For the seven polyurethane foams investigated in this research, E and A of the first reaction ranged from 78 – 114 kJ/mol and 2.80×10^{4} – 1.30×10^{8} s^{-1} respectively while for the second reaction, these ranged from 150 – 247 kJ/mol and 3.06×10^{9} – 3.07×10^{17} s^{-1} respectively.

Δh_r for the first and second reactions were determined from the changes in heat flow and sample mass over these reactions. A region of consistent heat of reaction was found for the second reaction by testing of the melt samples between 5 and 20 °C/min with mass between ~20 and ~50 mg. For the second reaction, Δh_r ranges from endothermic 178 – 295 J/g. A consistent region was not found for the first reaction because the maximum sample mass that could be tested was ~10 mg due to the porous nature of the foam sample. The recommended Δh_r for the first reaction was determined at 5 °C/min for ~3 and ~10 mg samples which was found to be endothermic 610 – 1023 J/g.

The thermal conductivity (λ) and specific heat (c_p) of the polyurethane foams and their melts were determined at ambient temperature using the Hot Disk method. The values of λ and c_p for the polyurethane foams ranged from 0.048 – 0.050 W/mK and 2359 – 2996 J/kgK respectively while for melts, these ranged from 0.186 – 0.198 W/mK and 1958 – 2061 J/kgK respectively. Within FDS 5, these properties were specified as temperature dependent parameters where their magnitude changes from those of foam into melt with increasing temperature. The temperature dependent functions were developed based on assumptions made regarding the different physical states of the sample during SDT experiments which are foam, melt and a mixture of both. In the multi reaction scheme, the solid fuel was considered as a single material component but since the sample has three different physical states, effective density (ρ_{eff}) and thickness (d_{eff}) were used for modelling. Once again, these were calculated based on the assumptions made regarding the different physical states of the sample. For the different foams, ρ_{eff} ranged from 243 – 364 kg/m^3 while d_{eff} ranged from 4.00 – 6.80 mm.

The 1-dimensional burning behaviour of polyurethane foams was investigated using the cone calorimeter. The NFR foams showed changes in the burning behaviour, from a level plateau at low heat flux into two stages at high heat flux. For FR foams, consistent two stage burning behaviour was noted at all the heat fluxes tested due to the foams' fire retardant mechanisms. The effective heat of combustion ($\Delta h_{c,eff}$) for FDS 5 modelling was determined from the cone results and it ranged from 21 – 25 MJ/kg. In FDS 5 modelling of the 1-dimensional cone experiments, two different approaches were considered, the direct method and the refined method. The direct method used the aforementioned material properties which were determined experimentally as the FDS 5 inputs. The refined method utilised the genetic algorithm of Gpyro to refine specifically the kinetic properties in order to improve the comparison between FDS 5 and experiment. The pyrolysis model in Gpyro was similar to FDS 5 hence the same multi reactions scheme was also implemented in Gpyro. Through a number of iterations, the genetic algorithm searched for the optimal set of kinetic properties within the defined boundaries which produced the closest agreement between the Gpyro outputs and the experimental results supplied for comparison. For the polyurethane foams tested, the range of refined E, A and Δh_r for

the first reaction were 75 – 100 kJ/mol, 2.95×10^{4} – 4.98×10^{6} s^{-1} and 621 – 1357 J/g respectively. For the second reaction, E, A and Δh_r ranged from 196 – 256 kJ/mol, 5.00×10^{5} – 5.58×10^{10} s^{-1} and 193 – 218 J/g respectively. Using linear regression analysis to compare the model and experimental heat release rates, the accuracy of the direct method was found to be 56 % while the accuracy of the refined method was higher at 75 %.

The 2-dimensional flame spread behaviours of the base case NFR foam were investigated in the foam slab experiments at two different thicknesses, 120 and 100 mm. The burning behaviours between the 120 and 100 mm foam slabs were found to be different, the former showed rapid and intense opposed-flow spread while the latter showed slower and less intense flame spread. When the material properties determined experimentally or refined by Gpyro, both at small-scale were used as FDS 5 inputs, the model was not able to produce flame spread on the foam slab. Other modelling options were investigated to capture the experimental results and reducing E was found to allow flame spread. The approach of reducing E is a temporary solution to the problem as FDS 5 does not yet have the features to properly address certain phenomena noted in the experiments such as the foam melting behaviours, the melt flow dynamics and the reactive nature of the flame.

10.2 Recommendations for Future Research

There are still areas in the experimental and numerical aspects of this research that are uncertain and require further study. This section lists a number of recommendations for future work related to this research.

10.2.1 Content of Fire Retardant Additives in Polyurethane Foams and Melts

The decomposition behaviour of FR-G-32 melt in TGA experiment seen in Figure 4-11 was noted to occur at lower temperature compared to the other melts. This is believed to be due to FR-G-32 melt containing higher phosphorus content than the melts of other foams because in the form of phosphoric acid, it is known to act as

catalyst for the decomposition of melt[36]. Therefore, it is desirable to perform elemental analysis to ascertain the phosphorus content within the melts of different polyurethane foams.

The concentration of melamine used within FR-Y-36, FR-LG-38 and FR-W-50 is believed to be the cause for the different char formation behaviours observed in Figure 7-10 during the Sample Feeding Vertical Cone experiments. From the elemental analysis, the higher nitrogen content of FR-Y-36 and FR-LG-38 indicated a higher melamine concentration within their formulations than FR-W-50. However, this assessment is qualitative and the actual concentration of melamine used remained unknown. Currently, within the literature, a few experimental techniques[126,127,128] have been developed to detect melamine in food and also to measure the concentration. Thus, it is desirable to investigate the application of these techniques to measure the melamine concentration in polyurethane foam.

10.2.2 Characteristics of Kinetic Properties

From Chapter 3 and 4, there are distinct trends in the E, A and n between the first and second reactions of the foam decomposition. The values of E and A for the first reaction are noted to be consistently smaller than the second reaction while the values of n for the first reaction are consistently greater than the second reaction. These trends are consistent among the kinetic properties developed by each graphical technique. It is desirable to investigate and determine which TGA results influence the trend of these kinetic properties. These results include the range of reaction temperature, the amount of sample mass decomposed and the mass loss rate of the reaction. Understanding the influencing factors behind these trends will explain the variations among the kinetic properties developed from the different graphical techniques and also for the different polyurethane foams.

10.2.3 Sensitivity Analysis for DSC Experiments on Polyurethane Foams and Melts

In Chapter 5, a region of consistent heat of reaction was determined for the decomposition of melts which ranges from 5 to 20 °C/min in terms of heating rate and ~20 to ~50 mg in terms of sample mass. Outside this consistent region, the heat of reaction was noted to change significantly. In this research, the SDT experiments were carried out for the melt samples at 1, 5, 20 and 60 °C/min with ~3, ~10, ~20 and ~50 mg of sample mass. Thus, this consistent region is only bounded by two sets of experimental results and it is of interest to perform more SDT experiments to ascertain the boundary of this consistent region. For instance, at 3, 10, 15, 25, 30, 35, 40 and 50 °C/min of heating rate and at 15, 25, 30, 35, 40 and 45 mg of nominal sample mass.

Due to the porous nature of the foam sample, the alumina cup used in the SDT experiments can only contain up to ~10 mg of sample mass. Thus far, no consistent region was identified for the heating rates and sample mass tested. The tested heating rates were 1, 5, 20 and 60 °C/min and the sample mass were ~3 and ~10 mg. It is desirable to determine a consistent region for foam sample by carrying out SDT experiments at the discrete heating rates proposed above for the melt sample and also at 5 and 7 mg of nominal sample mass.

10.2.4 Addressing Offset, Curvature and Chemical Issues of DSC Experiments

The treatment of offset[67] and curvature[74] has an impact on the heat of reaction determined. In Chapter 5, the offset and curvature has been crudely removed via a user defined heat flow baseline. Therefore, it is of interest to estimate both offset and curvature more accurately. For the offset, the temperature dependent function representing the heat capacity of foams and melts should be developed while to address the curvature, the additional radiation heat flow should be quantify. Similar to the approach proposed by Rath et al.[64], this additional radiation heat flow specific to each experiment can be obtained by rerunning the experiment with sample cup containing the char residue and measuring the heat flow. From the literature, chemical

issues such as the changes in yield and composition of the decomposition products with heating rate can affect the heat of reaction determined. Thus, it is desirable to incorporate Fourier transform infrared (FTIR) spectroscopy[25] to determine the concentration of various gaseous products released from the decomposition of polyurethane foam.

10.2.5 Thermophysical Properties at Elevated Temperature

When heated, the thermophysical properties of foam are known to change with increasing temperature[25] so it is desirable to develop the temperature dependent relationships for fire modelling. Besides being implemented as the inputs of FDS 5[17,18], the temperature varying thermophysical properties measured from Hot Disk experiments, especially the specific heat can be used to develop the temperature dependent heat capacity function needed for estimating the offset in DSC experiments. Some of the necessary upgrades for this elevated temperature application include the use of high temperature Hot Disk sensor and the construction of a temperature controlled furnace to house the samples and sensor setup. The current sensor is kapton insulated with operating temperature between -240 and 170 °C and for higher temperature application, mica insulated sensor should be used which operates between 130 and 720 °C[97].

10.2.6 Melting Model for Polyurethane Foams

The results from the Sample Feeding Vertical Cone experiments in Chapter 7 were obtained from a single heat flux, 50 kW/m^2. It is of interest to investigate the decomposition and melting behaviours of the vertically oriented polyurethane foams at different heat fluxes and oxygen concentrations. From these results, a set of empirical formula describing the decomposition and melting behaviours can be developed and incorporated into FDS 5 as a simple melting model.

10.2.7 Compatibility between Cone Sample Setup and FDS 5 Boundary Conditions

In Figure 8-28, the four sides of the prepared cone sample experienced convective heat losses and since the sample was not restrained against the sample holder, there were also some convective heat losses from the bottom due to the poor contact. Although the burning behaviour of this setup remains 1-dimensional and the setup is relatively simple to construct experimentally, it has introduced some uncertainties numerically because in FDS 5 modelling, the backing of this sample setup can neither be considered as 'VOID' nor 'INSULATED'. Specifying the former allows convective heat losses from the backside boundary while the latter means no heat losses.

Therefore, it is desirable to recreate these boundary conditions experimentally so as to minimise the discrepancy between the model and experiment. 'VOID' can be recreated by removing the sample holder covering the bottom of the current setup and this would require an alternative load cell setup to structurally support the sample during the cone experiment. 'INSULATED' can be recreated by using an alternative sample holder made from calcium silicate board where only the sample's top surface is exposed while the other sides are all insulated.

10.2.8 Effective Heat of Combustion for Combustion of Melt and Foam

According to the literature[42,54,112,118], the combustion of the melts which is the second stage in foam burning behaviour is capable of releasing higher amount of heat when compared to the first stage, the combustion of foam. It is of interest to test the collected melts from foam melting experiments using the cone calorimeter to determine the melts' effective heat of combustion. In FDS 5 modelling, the effective heat of combustion for foam and melt can be specified as inputs to better represent the greater amount of heat released over the second stage. The effective heat of combustion for foam can be determined over the first stage using Equation (8-9).

10.2.9 Parallel Processing for Genetic Algorithm Simulation

In Section 8.9, the Gpyro simulations were performed using a standalone computer system with 2.4 GHz of processing speed and 2 GB of processing memory which requires 7 days for relatively simple simulation involving 20 individuals and 200 generations. It is desirable to perform the simulations with parallel processing which would be able to accommodate more individuals and generations for similar amount of run time. With parallel processing ability, the sensitivity of the estimated properties to the changes in genetic algorithm parameters such as the number of individuals and generations can be studied in more details.

10.2.10 Future Numerical Modelling

In Chapter 8 and 9, the FDS 5 modelling of cone and foam slab experiments utilised a simple decomposition scheme, the multi reactions scheme which decomposes the solid fuel into gaseous fuel via two solid phase reactions. The flexibility of the pyrolysis model of FDS 5 actually allows for more advanced scheme to be designed. It is desirable to investigate if a more sophisticated decomposition scheme can improve the heat release rate predictions. For example, the foam can be modelled as multiple layers of foam and melt components where the foam decomposition is represented by residue formation scheme and the melt decomposition is represented by single reaction scheme.

Following the shortcomings identified in Section 9.5 of Chapter 9, future research should focus on developing new sub-models within FDS 5 to address the melting behaviours exhibited by polyurethane foam and also the porous nature of the material. The melting of foam introduces heat and mass transfers which are not accounted for in the current pyrolysis model. The porous nature of foam will affect the heat transfer through the solid. Through statistical study, Lefebvre et al.[106] have demonstrated that foam porosity is dependent on the catalyst used in the manufacturing process and the content of ethylene oxide in the polyol used as raw ingredient. In their research, an experimental apparatus was developed to assess the porosity of foam as a measure of pressure drop. Lastly, the existing radiation sub-model should also be investigated to

assess the model sensitivity on pyrolysis and combustion, particularly the absorption coefficient of the solid.

FDS 6 was released towards the conclusions of this research and this version is still relatively new, undergoing early developments. As such, the functionality of FDS 6 pyrolysis model has not been evaluated by this research. Furthermore, the material properties developed are based on the pyrolysis model in FDS 5 hence these inputs might not be applicable for FDS 6. It is of interest for future research to validate the pyrolysis model of FDS 6.

10.2.11 Opposed-Flow Spread of Polyurethane Foam with Different Thicknesses and Different Density

In Chapter 9, significant difference was noted between the opposed-flow spread behaviours of 120 and 100 mm foam slabs. The flame spread of 100 mm slab was slower and less intense while the 120 mm slab showed more rapid spread. In the literature, research by Pitts[118] and Robson et al.[123] have demonstrated that the flame spread behaviours of polyurethane foam slabs with different density and thickness could potentially vary. Therefore, it is of interest to investigate the changes in flame spread behaviour by testing foam slab of different thicknesses, ranging between 50 and 200 mm and also of the different densities included in this research.

Chapter 11. References

[1] Wikipedia, List of polyurethane applications, 2013, http://en.wikipedia.org/wiki/List_of_polyurethane_applications, 16th April 2013.

[2] European Association of Flexible Polyurethane Foam Blocks Manufacturers, Flexible polyurethane foam in everyday life, http://www.europur.com/index.php?page=73, 16th April 2013.

[3] Extract from the New Zealand Building Code, Department of Building and Housing, Wellington, New Zealand, 2012.

[4] C. R. Wong, "Contribution of upholstered furniture to residential fire fatalities in New Zealand", Fire engineering research report, University of Canterbury, Christchurch, 2001.

[5] C. M. Fleischmann and G. R. Hill, "Burning Behaviour of Upholstered Furniture", *Proceedings* of the 10th International INTERFLAM Conference, INTERFLAM '04, Edinburgh, Scotland, 5-7 July, 2004, Interscience Communications Limited, London, England, 2004, pp. 907-916.

[6] H. Denize, "The combustion behaviour of upholstered furniture materials in New Zealand", Fire engineering research report, University of Canterbury, Christchurch, 2000.

[7] N. Girgis, "Full-scale compartment fire experiments on upholstered furniture", Fire engineering research report, University of Canterbury, Christchurch, 2000.

[8] E. A. Young, "Standardising design fires for residential and apartment buildings: upholstered furniture fires", Fire engineering research report, University of Canterbury, Christchurch, 2007.

[9] G. R. Hill, "Burning behaviour of upholstered furniture", Master's thesis, University of Canterbury, Christchurch, 2003.

[10] V. Babrauskas and R. D. Peacock, "Heat release rate: The single most important variable in fire hazard", *Fire Safety Journal*, Vol. 18, No. 3, 1992, pp. 255-272.

[11] M. L. Janssens, "Measuring rate of heat release by oxygen consumption", *Fire Technology*, Vol. 27, No. 3, 1991, pp. 234-249.

[12] ISO 5660-1:1993, Fire tests -- Reaction to fire -- Part 1: Rate of heat release from building products -- (Cone calorimeter method), International Organization for Standardization, Geneva, Switzerland, 1993.

[13] ISO 9705:1993, Fire tests – Full-scale room test for surface products, International Organization for Standardization, Geneva, Switzerland, 1993.

[14] C/ VM2, Verification Method: Framework for Fire Safety Design, Department of Building and Housing, Wellington, New Zealand, 2012.

[15] Commentary for Verification Method C/ VM2, Department of Building and Housing, Wellington, New Zealand, 2012.

[16] C. Wade, G. Baker, K. Frank, A. Robbins, R. Harrison, M. Spearpoint and C. Fleischmann, "B-RISK User Guide and Technical Manual", BRANZ Study Report 282, BRANZ Ltd, Porirua City, New Zealand, 2013.

[17] K. McGrattan, R. McDermott, S. Hostikka and J. Floyd, "Fire Dynamics Simulator (Version 5) User's Guide, FDS Version 5.5, *SVN Repository Revision*: 6997", NIST Special Publication 1019-5, National Institute of Standards and Technology, Gaithersburg, MD, 2010.

[18] K. McGrattan, H. Baum, R. Rehm, W. Mell, R. McDermott, S. Hostikka and J. Floyd, "Fire Dynamics Simulator (Version 5) Technical Reference Guide, Volume 1: Mathematical Model, FDS Version 5.5, *SVN Repository Revision*: 6909", NIST Special Publication 1018-5, National Institute of Standards and Technology, Gaithersburg, MD, 2010.

[19] G. Rein, C. Lautenberger, A. C. Fernandez-Pello, J. L. Torero and D. L. Urban, "Application of genetic algorithms and thermogravimetry to determine the kinetics of polyurethane foam in smoldering combustion", *Combustion and Flame*, Vol. 146, No. 1-2, 2006, pp. 95-108.

[20] E. Kim, C. Lautenberger and N. Dembsey, "Property Estimation For Pyrolysis Modeling Applied To Polyester FRP Composites With Different Glass Content", *Proceedings* of the 11th International Conference on Fire and Materials, San Francisco, CA, 26-28 January, 2009, Interscience Communications Limited, London, England, 2009, pp. 61-76.

[21] A. Matala, S. Hostikka and J. Mangs, "Estimation of pyrolysis model parameters for solid materials using thermogravimetric data", *Proceedings* of the 9th International Symposium on Fire Safety Science, Karlsruhe, Germany, 21-26 September, 2008,

International Association for Fire Safety Science, London, England, 2009, pp. 1213-1223.

[22] R. Bilbao, J. F. Mastral, J. Ceamanos and M. E. Aldea, "Kinetics of the thermal decomposition of polyurethane foams in nitrogen and air atmospheres", *Journal of Analytical and Applied Pyrolysis*, Vol. 37, No. 1, 1996, pp. 69-82.

[23] C. Y. H. Chao and J. H. Wang, "Comparison of the Thermal Decomposition Behaviour of a Non-Fire Retarded and a Fire Retarded Flexible Polyurethane Foam with Phosphorus and Brominated Additives", *Journal of Fire Sciences*, Vol. 19, No. 2, 2001, pp. 137-156.

[24] F. E. Rogers and T. J. Ohlemiller, "Pyrolysis Kinetics of a Polyurethane Foam by Thermogravimetry; A General Kinetic Method", *Journal of Macromolecular Science: Part A – Chemistry*, Vol. 15, No. 1, 1981, pp. 169-185.

[25] L. B. Valencia, "Experimental and numerical investigation of the thermal decomposition of materials at three scales: application to polyether polyurethane foam used in upholstered furniture", PhD's thesis, University of Edinburgh, Edinburgh, 2009.

[26] T. J. Ohlemiller and J. R. Shields, "Aspects of the Fire Behaviour of Thermoplastic Materials", NIST Technical Note 1493, National Institute of Standards and Technology, Gaithersburg, MD, 2008.

[27] C. Lautenberger, "Gpyro – A Generalized Pyrolysis Model for Combustible Solids, Users' Guide, Version 0.700", Department of Mechanical Engineering, University of California, Berkeley, CA, 2009.

[28] D. Price, Y. Liu, G. J. Milnes, R. Hull, B. K. Kandola and A. R. Horrocks, "An Investigation into the Mechanism of Flame Retardancy and Smoke Suppression by Melamine in Flexible Polyurethane Foam", *Fire and Materials*, Vol. 26, No. 4-5, 2002, pp. 201-206.

[29] BS 5852:2006, Methods of test for assessment of the ignitability of upholstered seating by smouldering and flaming ignition sources, British Standards Institution, London, England, 2006.

[30] BS 4735:1974, Laboratory method of test for assessment of the horizontal burning characteristics of specimens no larger than 150 mm × 50 mm × 13 mm (nominal) of cellular plastics and cellular rubber materials when subjected to a small flame, British Standards Institution, London, England, 1974.

[31] AS/NZS 1530.3:1999, Methods for fire tests on building materials, components and structures – Simultaneous determination of ignitability, flame propagation, heat release and smoke release, Standards Australia, Sydney, Australia, 1999.

[32] Technical Bulletin 117, Requirements, Test Procedure and Apparatus for Testing the Flame Retardance of Resilient Filling Materials Used in Upholstered Furniture, Bureau of Home Furnishings and Thermal Insulation, Sacramento, CA, 2000.

[33] Part 25 – Airworthiness Standards: Transport Category Airplanes, Appendix F to Part 25, Part I – Test Criteria and Procedures for Showing Compliance with § 25.853, or § 25.855, Federal Aviation Administration, Washington, DC, 1972.

[34] C. Denecker, J. J. Liggat and C. E. Snape, "Relationship Between the Thermal Degradation Chemistry and Flammability of Commercial Flexible Polyurethane Foams", *Journal of Applied Polymer Science*, Vol. 100, No. 4, 2006, pp. 3024-3033.

[35] H. C. Ashton, "Fire Retardants", *Functional Fillers for Plastics*, Second Edition, M. Xanthos (Eds.), Wiley-VCH, Weinheim, Germany, 2010, pp. 309-350.

[36] N. Grassie and G. A. Perdomo Mendoza, "Thermal Degradation of Polyether-Urethanes: Part 2 – Influence of the Fire Retardant, Ammonium Polyphosphate, on the Thermal Degradation of Poly(Ethylene Glycol)", *Polymer Degradation and Stability*, Vol. 10, No. 1, 1985, pp. 43-54.

[37] N. Grassie and G. A. Perdomo Mendoza, "Thermal Degradation of Polyether-Urethanes: Part 4 – Effect of Ammonium Polyphosphate on the Thermal Degradation of Polyether-Urethanes Prepared from Methylene Bis(4-Phenylisocyanate) and Low Molecular Weight Poly(Ethylene Glycols)", *Polymer Degradation and Stability*, Vol. 11, No. 2, 1985, pp. 145-166.

[38] S. V. Levchik, "Introduction to Flame Retardancy and Polymer Flammability", *Flame Retardant Polymer Nanocomposites*, A. B. Morgan, C. A. Wilkie (Eds.), John Wiley & Sons. Inc., Hoboken, NJ, 2007, pp. 1-30.

[39] L. B. Valencia, T. Rogaume, E. Guillaume, G. Rein and J. L. Torero, "Analysis of principal gas products during combustion of polyether polyurethane foam at different irradiance levels", *Fire Safety Journal*, Vol. 44, No. 7, 2009, pp. 933-940.

[40] A. Tewarson, "Generation of Heat and Chemical Compounds in Fires", *The SFPE Handbook of Fire Protection Engineering*, Third Edition, P. J. DiNenno et al. (Eds.), National Fire Protection Association, Quincy, MA, 2002, pp. 3-82 to 3-161.

[41] H. H. Saber, A. Kashef, A. C. Bwalya and G. D. Lougheed, "Numerical and experimental investigations of fire behaviour due to polyurethane foam and wood cribs in a medium-sized residential room", Research Report # RR-291, NRC Institute for Research in Construction, Ottawa, ON, 2010.

[42] K. Prasad, R. Kramer, N. Marsh, M. Nyden, T. Ohlemiller and M. Zammarano, "Numerical Simulation Of Fire Spread On Polyurethane Foam Slabs", *Proceedings* of the 11th International Conference on Fire and Materials, San Francisco, CA, 26-28 January, 2009, Interscience Communications Limited, London, England, 2009, pp. 697-708.

[43] G. Rein, A. Bar-Ilan, A. C. Fernandez-Pello, J. L. Ellzey, J. L. Torero and D. L. Urban, "Modelling of One-Dimensional Smoldering of Polyurethane in Microgravity Conditions", *Proceedings* of the 30th International Symposium on Combustion, Chicago, IL, 25-30 July, 2004, Combustion Institute, Pittsburgh, PA, Vol. 30, No. 2, 2005, pp. 2327-2334.

[44] C. R. Houck, J. A. Joines and M. G. Kay, "A Genetic Algorithm for Function Optimization: A Matlab Implementation", Technical Report NCSU-IE TR 95-09, North Carolina State University, Raleigh, NC, 1995.

[45] V. M. Gorbachev, "A solution of the exponential integral in the non-isothermal kinetics for linear heating", *Journal of Thermal Analysis and Calorimetry*, Vol. 8, No. 2, 1975, pp. 349-350.

[46] H. S. Kalsi, "Indicators and Display Devices", *Electronic Instrumentation*, Third Edition, H. S. Kalsi (Eds.), Tata McGraw-Hill, New Delhi, India, 2010, pp. 25-63.

[47] H. L. Friedman, "Kinetics of thermal degradation of char-forming plastics from thermogravimetry. Application to a phenolic plastic", *Journal of Polymer Science Part C: Polymer Symposia*, Vol. 6, No. 1, 1964, pp. 183-195.

[48] C. Lautenberger, E. Kim, N. Dembsey and C. Fernandez-Pello, "The Role of Decomposition Kinetics in Pyrolysis Modelling – Application to a Fire Retardant Polyester Composite", *Proceedings* of the 9th International Symposium on Fire Safety Science, Karlsruhe, Germany, 21-26 September, 2008, International Association for Fire Safety Science, London, England, 2009, pp. 1201-1212.

[49] S. G. Viswanath and M. C. Gupta, "Estimation of nonisothermal kinetic parameters from a TG curve by the methods of overdetermined system and inflection point", *Thermochimica Acta*, Vol. 285, No. 2, 1996, pp. 259-267.

[50] A. Matala, C. Lautenberger and S. Hostikka, "Generalized direct method for pyrolysis kinetic parameter estimation and comparison to existing methods", *Journal of Fire Sciences*, Vol. 30, No. 4, 2012, pp. 339-356.

[51] D. S. W. Pau, C. M. Fleischmann, M. J. Spearpoint and K. Y. Li, "Determination of kinetic properties of polyurethane foam decomposition for pyrolysis modelling", *Journal of Fire Sciences*, 2013, DOI: 10.1177/0734904113475858.

[52] R. Font, A. Fullana, J. A. Caballero, J. Candela and A. Garcia, "Pyrolysis study of polyurethane", *Journal of Analytical and Applied Pyrolysis*, Vol. 58-59, 2001, pp. 63-77.

[53] Y. Zhang, Z. Xia, H. Huang and H. Chen, "Thermal degradation of polyurethane based on IPDI", *Journal of Analytical and Applied Pyrolysis*, Vol. 84, No. 1, 2009, pp. 89-94.

[54] R. H. Kramer, M. Zammarano, G. T. Linteris, U. W. Gedde and J. W. Gilman, "Heat release and structural collapse of flexible polyurethane foam", *Polymer Degradation and Stability*, Vol. 95, No. 6, 2010, pp. 1115-1122.

[55] L. B. Valencia, T. Rogaume and E. Guillaume, "New Method For Simulating The Kinetic Of Toxic Gases Production Of Upholstered Furniture Fire", *Proceedings* of the 11th International Conference on Fire and Materials, San Francisco, CA, 26-28 January, 2009, Interscience Communications Limited, London, England, 2009, pp. 685-695.

[56] R. Chang, "Thermochemistry", *Chemistry*, Seventh Edition, R. Chang (Eds.), McGraw-Hill, New York, NY, 2002, pp. 205-244.

[57] B. T. Rhodes and J. G. Quintiere, "Burning rate and flame heat flux for PMMA in a cone calorimeter", *Fire Safety Journal*, Vol. 26, No. 3, 1996, pp. 221-240.

[58] D. Hopkins Jr. and J. G. Quintiere, "Material fire properties and predictions for thermoplastics", *Fire Safety Journal*, Vol. 26, No. 3, 1996, pp. 241-268.

[59] C. A. Wade, "BRANZFIRE Technical Reference Guide 2004", BRANZ Study Report 92 (revised), Building Research Association of New Zealand, Judgeford, Porirua City, New Zealand, 2004.

[60] J. E. J. Staggs, "The heat of gasification of polymers", *Fire Safety Journal*, Vol. 39, No. 8, 2004, pp. 711-720.

[61] P. Gabbott, "A Practical Introduction to Differential Scanning Calorimetry", *Principles and Applications of Thermal Analysis*, P. Gabbott (Eds.), Blackwell Publishing, Oxford, England, 2008, pp. 1-50.

[62] Department of Chemistry, Colorado State University, TA training presentations on DSC at CSU, 2006, http://www1.chm.colostate.edu/Files/CIFDSC/dsc2000.pdf, 3rd November 2012.

[63] S. R. Sauerbrunn, D. C. Armbruster and P. D. Shickel "Differential Photocalorimetry: Advancements for the Analysis and Characterization of Free Radical, Cationic and Hybrid Photopolymers", TA Instruments, New Castle, DE, 1997.

[64] J. Rath, M. G. Wolfinger, G. Steiner, G. Krammer, F. Barontini and V. Cozzani "Heat of wood pyrolysis", *Fuel*, Vol. 82, No. 1, 2003, pp. 81-91.

[65] Presentation slides, Good Laboratory Practice (GLP) in Thermal Analysis, Research Instruments, Singapore, 2011.

[66] R. B. Cassel "How Tzero™ Technology Improves DSC Performance, Part I: Flat Baselines and Glass Transition Measurements", TA Instruments, New Castle, DE, 2001.

[67] R. B. Cassel "How Tzero™ Technology Improves DSC Performance, Part III: The Measurement of Specific Heat Capacity", TA Instruments, New Castle, DE, 2001.

[68] R. B. Cassel "How Tzero™ Technology Improves DSC Performance, Part II. Peak Shape and Resolution", TA Instruments, New Castle, DE, 2001.

[69] R. B. Cassel "How Tzero™ Technology Improves DSC Performance, Part V: Reducing Thermal Lag", TA Instruments, New Castle, DE, 2001.

[70] R. B. Cassel "How Tzero™ Technology Improves DSC Performance, Part VI: Simplifying Temperature Calibration for Cooling Experiments", TA Instruments, New Castle, DE, 2002.

[71] S. I. Stoliarov and R. N. Walters "Determination of the heats of gasification of polymers using differential scanning calorimetry", *Polymer Degradation and Stability*, Vol. 93, No. 2, 2008, pp. 422-427.

[72] L. Waguespack and R. Blaine "Design of a New DSC Cell with Tzero™ Technology", TA Instruments, New Castle, DE, 2001.

[73] L. C. Thomas "Interpreting Unexpected Events and Transitions in DSC Results", TA Instruments, New Castle, DE, 1997.

[74] M. G. Wolfinger, J. Rath, G. Krammer, F. Barontini and V. Cozzani "Influence of the emissivity of the sample on differential scanning calorimetry measurements", *Thermochimica Acta*, Vol. 372, No. 1-2, 2001, pp. 11-18.

[75] A. Matala, "Estimation of solid phase reaction parameters for fire simulation", Master's thesis, Helsinki University of Technology, Espoo, 2008.

[76] A. Chipperfield, P. Fleming, H. Pohlheim and C. Fonseca, "Genetic Algorithm Toolbox For Use with MATLAB®, User's Guide, Version 1.2 ", ACSE Research Report No. 512, Department of Automatic Control and Systems Engineering, University of Sheffield, Sheffield, England, 1994.

[77] J. D. Peterson, S. Vyazovkin and C. A. Wight "Stabilizing effect of oxygen on thermal degradation of poly(methylmethacrylate)", *Macromolecular Rapid Communications*, Vol. 20, No. 9, 1999, pp. 480-483.

[78] M. Schubnell, "Temperature and Heat Flow Calibration of A DSC-instrument in the Temperature Range Between -100 and 160 °C", *Journal of Thermal Analysis and Calorimetry*, Vol. 61, No. 1, 2000, pp. 91-98.

[79] F. P. Incropera and D. P. Dewitt, "Appendix A, Thermophysical Properties of Matter", *Fundamentals of Heat and Mass Transfer*, Fifth Edition, F. P. Incropera and D. P. Dewitt (Eds.), John Wiley & Sons Inc., Hoboken, NJ, 2002, pp. 903-932.

[80] D. Drysdale, "Fire Science and Combustion", *An Introduction to Fire Dynamics*, Third Edition, D. Drysdale (Eds.), John Wiley & Sons, West Sussex, England, 2011, pp. 1-34.

[81] R. B. Cassel "How Tzero™ Technology Improves DSC Performance, Part IV: MDSC® Enhancement", TA Instruments, New Castle, DE, 2001.

[82] N. Grassie and G. A. Perdomo Mendoza, "Thermal Degradation of Polyether-Urethanes: 5. Polyether-Urethanes Prepared from Methylene Bis(4-Phenylisocyanate) and High Molecular Weight Poly(ethylene Glycols) and the Effect of Ammonium Polyphosphate", *Polymer Degradation and Stability*, Vol. 11, No. 4, 1985, pp. 359-379.

[83] N. Grassie and G. A. Perdomo Mendoza, "Thermal Degradation of Polyether-Urethanes: Part 1 –Thermal Degradation of Poly(Ethylene Glycols) Used in the Preparation of Polyurethanes", *Polymer Degradation and Stability*, Vol. 9, No. 3, 1984, pp. 155-165.

[84] N. Grassie and G. A. Perdomo Mendoza, "Thermal Degradation of Polyether-Urethanes: Part 3 – Polyether-Urethanes Prepared from Methylene Bis(4-Phenylisocyanate) and Low Molecular Weight Poly(Ethylene Glycols)", *Polymer Degradation and Stability*, Vol. 10, No. 3, 1985, pp. 267-286.

[85] C. W. Lautenberger, "A Generalized Pyrolysis Model for Combustible Solids", PhD's thesis, University of California, Berkeley, 2007.

[86] S. E. Gustafsson, "Transient plane source techniques for thermal conductivity and thermal diffusivity measurements of solid materials", *Review of Scientific Instruments*, Vol. 62, No. 3, 1991, pp. 797-804.

[87] ISO 22007-2:2008, Plastics -- Determination of thermal conductivity and thermal diffusivity -- Part 2: Transient plane heat source (hot disc) method, International Organization for Standardization, Geneva, Switzerland, 2008.

[88] T. G. Cleary and J. G. Quintiere, "Flammability Characterization of Foam Plastics", NISTIR 4664, National Institute of Standards and Technology, Gaithersburg, MD, 1991.

[89] K. M. Butler, T. J. Ohlemiller and G. T. Linteris, "A Progress Report on Numerical Modeling of Experimental Polymer Melt Flow Behavior", *Proceedings* of the 10th International INTERFLAM Conference, INTERFLAM '04, Edinburgh, Scotland, 5-7 July, 2004, Interscience Communications Limited, London, England, 2004, pp. 937-948.

[90] M. A. Abdelrahman, S. M. Said, A. Ahmad, M. Inam and H. Abul-Hamayel, "Thermal Conductivity of Some Major Building Materials in Saudi Arabia", *Journal of Building Physics*, Vol. 13, No. 4, 1990, pp. 294-300.

[91] A. Bouguerra, A. Aït-Mokhtar, O. Amiri and M. B. Diop, "Measurement of thermal conductivity, thermal diffusivity and heat capacity of highly porous building materials using transient plane source technique", *International Communications in Heat and Mass Transfer*, Vol. 28, No. 8, 2001, pp. 1065-1078.

[92] S. A. Al-Ajlan, "Measurements of thermal properties of insulation materials by using transient plane source technique", *Applied Thermal Engineering*, Vol. 26, No. 17-18, 2006, pp. 2184-2191.

[93] Application note nr. 9, Thermal Transport properties in nano fluids, Hot Disk AB, Uppsala, Sweden, 2009.

[94] M. Gustavsson and S. E. Gustafsson, "Thermal conductivity as an indicator of fat content in milk", *Thermochimica Acta*, Vol. 442, No. 1-2, 2006, pp. 1-5.

[95] Y. He, "Rapid thermal conductivity measurement with a hot disk sensor: Part 2. Characterization of thermal greases", *Thermochimica Acta*, Vol. 436, No. 1-2, 2005, pp. 130-134.

[96] MatWeb, Material Property Data, 1996-2012, http://www.matweb.com/search/QuickText.aspx?SearchText=polyol, 17th February 2012.

[97] Instruction Manual, Hot Disk Thermal Constants Analyser Windows 95/98 Version 5.0, Hot Disk AB, Uppsala, Sweden, 1999.

[98] Y. He, "Rapid thermal conductivity measurement with a hot disk sensor: Part 1. Theoretical considerations", *Thermochimica Acta*, Vol. 436, No. 1-2, 2005, pp. 122-129.

[99] Y. Wang, F. Zhang, X. Chen, Y. Jin and J. Zhang, "Burning and dripping behaviors of polymers under the UL94 vertical burning test conditions", *Fire and Materials*, Vol. 34, No. 4, 2010, pp. 203-215.

[100] UL 94, the Standard for Safety of Flammability of Plastic Materials for Parts in Devices and Appliances testing, Underwriters Laboratories, Northbrook, IL, 1996.

[101] J. Zhang, T. J. Shields and G. W. H. Silcock, "Effect of Melting Behaviour on Upward Flame Spread of Thermoplastics", *Fire and Materials*, Vol. 21, No. 1, 1997, pp. 1-6.

[102] J. Sherratt, "The Effect of Thermoplastic Melt Flow Behaviour on The Dynamics of Fire Growth", PhD's thesis, University of Edinburgh, Edinburgh, 2001.

[103] D. S. W. Pau and C. M. Fleischmann, "Melting Rate of Polyurethane Foam in a Vertical Orientation", *Proceedings* of the 12th International INTERFLAM Conference, INTERFLAM '10, Nottingham, England, 5-7 July, 2010, Interscience Communications Limited, London, England, 2010, pp. 581-592.

[104] J. L. Throne, "Methods of Heating Sheet", *Understanding Thermoforming*, J. L. Throne (Eds.), Carl Hanser Verlag, Munich, Germany, 2008, pp. 101-128.

[105] ISO 5657:1997, Reaction to fire tests -- Ignitability of building products using a radiant heat source, International Organization for Standardization, Geneva, Switzerland, 1997.

[106] J. Lefebvre, B. Bastin, M. Le Bras, S. Duquesne, C. Ritter, R. Paleja and F. Poutch, "Flame spread of flexible polyurethane foam: comprehensive study", *Polymer Testing*, Vol. 23, No. 3, 2004, pp. 281-290.

[107] F. Chen, "Radiant ignition of New Zealand upholstered furniture composites", Fire engineering research report, University of Canterbury, Christchurch, 2001.

[108] J. L. Neviaser and R. G. Gann, "Evaluation of Toxic Potency Values for Smoke from Products and Materials", *Fire Technology*, Vol. 40, No. 2, 2004, pp. 177-199.

[109] R. A. Orzel, S. E. Womble, F. Ahmed and H. S. Brasted, "Flexible Polyurethane Foam: A Literature Review of Thermal Decomposition Products and Toxicity", *International Journal of Toxicology*, Vol. 8, No. 6, 1989, pp. 1139-1175.

[110] B. C. Levin, E. Braun, M. Paabo, R. H. Harris and M. Navarro, "Reduction of Hydrogen Cyanide Concentrations and Acute Inhalation Toxicity From Flexible Polyurethane Foam Combustion Products by the Addition of Copper Compounds. Part 4. Effects of Combustion Conditions and Scaling on the Generation of Hydrogen cyanide and Toxicity From Flexible Polyurethane Foam With and Without Copper Compounds", NIST Interagency Report 4989, National Institute of Standards and Technology, Gaithersburg, MD, 1992.

[111] J. U. Ezinwa, L. D. Robson, M. R. Obach, D. A. Torvi and E. J. Weckman, "Evaluating Models for Predicting Full-Scale Fire Behaviour of Polyurethane Foam Using Cone Calorimeter Data", *Fire Technology*, 2011.

[112] J. Lefebvre, B. Bastin, M. Le Bras, S. Duquesne, R. Paleja and R. Delobel, "Thermal stability and fire properties of conventional flexible polyurethane foam formulations", *Polymer Degradation and Stability*, Vol. 88, No. 1, 2005, pp. 28-34.

[113] Q Series™ Getting Started Guide, SDT Simultaneous DSC-TGA, TA Instruments, New Castle, DE, 2007.

[114] V. Babrauskas, "A6 Cone Calorimeter testings", *Fire Safety of Upholstered Furniture – the final report on the CBUF research programme*, B. Sundstrom (Eds.), Interscience Communication Limited, London, UK, 1995, pp. 339-355.

[115] C. Lautenberger, "Gpyro – A Generalized Pyrolysis Model for Combustible Solids, Technical Reference, Version 0.700", Department of Mechanical Engineering, University of California, Berkeley, CA, 2009.

[116] C. Lautenberger, G. Rein and C. Fernandez-Pello, "The application of a genetic algorithm to estimate material properties for fire modeling from bench-scale fire test data", *Fire Safety Journal*, Vol. 41, No. 3, 2006, pp. 204-214.

[117] C. Lautenberger, W. Wong, A. Coles, N. Dembsey and C. Fernandez-Pello, "Large-Scale Turbulent Flame Spread Modeling With FDS5 On Charring And Noncharring Materials", *Proceedings* of the 11th International Conference on Fire and Materials, San Francisco, CA, 26-28 January, 2009, Interscience Communications Limited, London, England, 2009, pp. 367-378.

[118] W. M. Pitts, "Role of two stage pyrolysis in fire growth on flexible polyurethane foam slabs", *Fire and Materials*, Vol. 38, No. 3, 2014, pp. 323-338.

[119] V. Babrauskas, "The Cone Calorimeter", *The SFPE Handbook of Fire Protection Engineering*, Third Edition, P. J. DiNenno et al. (Eds.), National Fire Protection Association, Quincy, MA, 2002, pp. 3-63 to 3-81.

[120] S. Hostikka and J. Axelsson, "Modelling of the radiative feedback from the flames in cone calorimeter", Nordtest Technical Report 540, Nordtest, Espoo, Finland, 2003.

[121] V. Babrauskas, "Heat Release Rates", *The SFPE Handbook of Fire Protection Engineering*, Third Edition, P. J. DiNenno et al. (Eds.), National Fire Protection Association, Quincy, MA, 2002, pp. 3-1 to 3-37.

[122] P. A. Enright, "Heat release and the combustion behaviour of upholstered furniture", PhD's thesis, University of Canterbury, Christchurch, 1999.

[123] L. Robson, D. Torvi, M. Obach and E. Weckman, "Effects of Thickness and Ignition Location on Flame Spread Rates in Furniture Calorimeter Tests of Polyurethane Foam", *Proceedings* of the 11th International Symposium on Fire Safety Science, Christchurch, New Zealand, 9-14 February, 2014.

[124] K. M. Butler, E. Onate, S. R. Idelsohn and R. Rossi, "Modeling Polymer Melt Flow Using the Particle Finite Element Method", *Proceedings* of the 11th International INTERFLAM Conference, INTERFLAM '07, London, England, 3-5 September, 2007, Interscience Communications Limited, London, England, 2007, pp. 929-940.

[125] K. M. Butler, "Model of Melting and Dripping Thermoplastic Objects in Fire", *Proceedings* of the 11th International Conference on Fire and Materials, San Francisco, CA, 26-28 January, 2009, Interscience Communications Limited, London, England, 2009, pp. 341-352.

[126] L. He, Y. Liu, M. Lin, J. Awika, D. R. Ledoux, H. Li and A. Mustapha, "A new approach to measure melamine, cyanuric acid, and melamine cyanurate using surface enhanced Raman spectroscopy coupled with gold nanosubstrates", *Sensing and Instrumentation for Food Quality and Safety*, Vol. 2, No. 1, 2008, pp. 66-71.

[127] M. Lin, L. He, J. Awika, D. R. Ledoux, H. Li and A. Mustapha, "Detection of melamine in gluten, chicken feed, and processed foods using surface enhanced Raman spectroscopy and HPLC", *Journal of Food Science*, Vol. 73, No. 8, 2008, pp. 129-134.

[128] L. Zhu, G. Gamez, H. Chen, K. Chingin and R. Zenobi, "Rapid detection of melamine in untreated milk and wheat gluten by ultrasound-assisted extractive electrospray ionization mass spectrometry (EESI-MS)", *Chemical Communications*, No. 5, 2009, pp. 559-561.